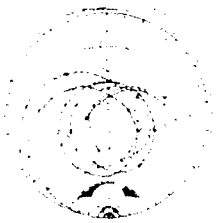

6th Annual Review of Progress in

APPLIED COMPUTATIONAL ELECTROMAGNETICS

at the

Naval Postgraduate School

Monterey, CA

March 19-22, 1990

CONFERENCE PROCEEDINGS

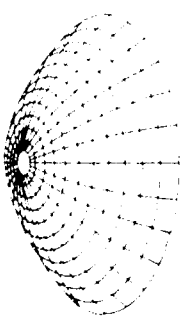

CONFERENCE PROCEEDINGS

6th Annual Review of Progress in

APPLIED

COMPUTATIONAL

ELECTROMAGNETICS

at the

Naval Postgraduate School

Monterey, CA

March 19-22, 1990

SYMPOSIUM PROGRAM COMMITTEE CHAIRMAN

Scott Ray

Sponsored by

The Applied Computational Electromagnetics Society

and DOD/USA ECOM, USAISEC, NOSC, NPS, DOE/LLNL

THE NAVAL POSTGRADUATE SCHOOL

TABLE OF CONTENTS

SESSION 6: NEW TECHNIQUES

SESSION 7: NEC APPLICATIONS

SESSION 8: PARTIAL DIFFERENTIAL EQUATION BASED METHODS

SESSION 9: HIGH FREQUENCY METHODS AND CODES

SESSION 10a: VALIDATION

SESSION 10b: MODELING EM INTERACTION WITH BIOLOGICAL MEDIA

SESSION 11: SURFACE INTEGRAL EQUATION CODES AND APPLICATIONS

PAPER SUBMITTED BUT NOT PRESENTED

SESSION 1A - "SPECIAL REPORTS - INVITED TALKS"

Using Advanced Artificial Intelligence Techniques to Create Analysis Plans for Cosite Electromagnetic Interference Problems

Costas Tsatsoulis

Center for Computer-Aided Systems Engineering
Department of Electrical and Computer Engineering
The University of Kansas
Lawrence, KS 66045
(913) 864-7749
tsatsoul%tisl@kuhub.cc.ukans.edu

ABSTRACT

In this paper we describe the use of a prototypical, advanced Artificial Intelligence system to generate analysis plans in problems of cosite electromagnetic interference. The design of communication systems generally follows well developed methodologies that have been successfully extended to distributed networks with many nodes. When nodes for different networks are collocated in a somewhat confined area interference occurs because of mutual coupling between antennas. Over the past ten years several computer programs have been developed to perform Electromagnetic Interference (EMI) and Electromagnetic Compatibility (EMC) analyses for situations of collocated networks. We have used the concepts and techniques of *Case-Based Reasoning* to develop a system (called ASP) that automatically and intelligently generates analysis plans for EMI/EMC problems. ASP expertly sets-up analysis runs for complex communications systems, can select between various available tools and algorithms, can sequence various analysis runs, and can automatically learn how to avoid failures and incorrect analysis techniques. ASP is incorporated within COEDS, an engineering workstation-based shell for interoperability analysis engines, and it is the first step toward an intelligent engineering workstation for interoperability analysis of collocated communications equipment.

1. Introduction

The military communications environment can be characterized in part by a distributed network whose nodes have a high density of operating frequencies, that is, as a complex and dense electromagnetic environment. When nodes for different networks are collocated in a somewhat confined area, such as is found aboard ships and other mobile communications platforms, interference occurs because of mutual coupling between antennas. Difficulties arise when collocated equipment interfere to such an extent that interoperability is defeated. Reports have shown that EMI can be a major source of degradation and failure in communications systems [1]. In light of these, interoperability analysis plays a significant role in the system design process.

Over the past ten years several computer programs have been developed to perform Electromagnetic Interference (EMI) and Electromagnetic Compatibility (EMC) analyses for situations of collocated networks. The methodologies employed for analysis have been sufficient but laborious [2]. The programs developed require extensive data preparation and careful control of data management, and produce large volumes of tabular data which are difficult to interpret and even more difficult to use in a design process. To provide a user-friendly interface to these analysis programs

the University of Kansas developed COEDS, the Communications Engineering Design System. COEDS is a shell around the EMI/EMC analysis codes, and it provides a graphical user interface, data flow and program control, a test plan generator, and a postprocessor that presents the analysis data into a graphical, thought enhancing format [3,4].

Unfortunately, even when using the user-friendly engineering workstation environment offered by COEDS, the generation of reliable analysis data is a complex process. The engineer using COEDS and the available analysis programs must be an expert in communications system design and in the use of analysis codes. Sometimes analysis data can be useless if an inappropriate tool is used. Other times the data can be obtained only by using multiple analysis tools in concert; for example, to generate interference limited link reliability, one must use one code to generate interference noise, and then another one to analyze the link given the interference data.

In our work we developed a system called ASP that automatically generates runs for the analysis of collocated communications systems. ASP uses advanced Artificial Intelligence (AI) techniques to model the expertise and intelligent behavior of the human engineer. It succeeds in expertly and correctly developing analysis plans for EMI/EMC analysis. The reasoning process employed by ASP is based on *Case-Based Reasoning*, a new methodological approach to the problems of automated reasoning. Case-Based Reasoning is a general paradigm for reasoning from experience, and allowed us to model the expertise of a human engineer easily and quickly.

The rest of this paper is organized as follows: in Section 2 we will briefly present Case-Based Reasoning; in Section 3 we will describe the domain of application and COEDS; in Section 4 we will discuss the application of CBR in analysis run generation and will show examples of how ASP operates; Section 5 will present our conclusions and future directions.

2. Case-Based Reasoning

2.1. Brief Overview of Case-Based Reasoning

There are two broad research targets in AI. The first tries to understand the nature of intelligence and human thought. It examines cognitive behavior and looks for principles that play general descriptive and explanatory roles. The second seeks to create intelligent artifacts and to develop a technology of intelligence.

Case-Based Reasoning is an AI paradigm that addresses both research agendas. Case-Based Reasoning is based on psychological theories of human cognition. It is also a new methodological approach in AI that provides the foundations for a new technology of intelligent systems.

Avoiding the details of the theory Case-Based Reasoning, we can describe it as based on the intuitive notion that human expertise is not based on rules or other formalized structures, but on experiences. Human experts *differ* from novices in their ability to relate problems to previous *ones*, to reason based on analogies between current and old problems, and to use solutions from old experiences.

The process of reasoning using experiences or cases can be described by the following steps:

1. **Retrieve:** Given a new problem, retrieve a similar past case from memory. The past case contains the prior solution.

2. **Modify:** The old solution is modified to conform to the new situation, resulting in a proposed solution.

3. **Test:** The proposed solution is tested for successful solution of the current problem.

4. Learn: If the solution fails, explain the failure and learn it to avoid repeating it. If possible, repair the failure, generate a new proposed solution and return to step **3.** If the solution succeeds, incorporate it into the case memory as a successful solution, and stop.

Case-Based Reasoning has been used in many prototypical systems applied in a variety of domains, including manufacturing, design, law, medicine, battle planning, and so forth. Case-Based Reasoning is a methodology that is still under research, and new developments are bound to change its directions [5,6].

2.2. Intelligent Systems: Expert systems vs. Cases

Before we present ASP we should address the question of why Case-Based Reasoning. In other words, why should an engineer prefer Case-Based Reasoning for the development of intelligent systems over the other techniques and methodologies of AI. More specifically, expert systems have been used in the last ten years to develop many intelligent systems for real-life applications. Expert systems are heuristic, rule-based programs that have been used extensively to simulate intelligent behavior [7]. They were studied extensively in the 1970's, they are an established, well-understood technology, and there currently exist dozens of tools that can help an engineer develop expert systems. Why then should the engineer use a new, advanced technique as Case-Based Reasoning, instead of using a tested, and often applied AI methodology like expert systems?

The basic unit of an expert system has been an *IF-THEN* rule. A rule comprised a conditional test-action pair, e.g. *IF condition, THEN action.* Several hundred rules might be required to handle a typical diagnostic or repair task; design tasks tend to require thousands of rules, as, for example, in R1, an expert system for the design of VAX computers that uses over 10,000 rules [8]. Building and using rule-based expert systems became very popular; they are easy to develop as a prototype, and very powerful in their results. As experience with rule-based expert systems increased, so did the understanding and awareness of some basic short-comings of the rule-based paradigm.

The first problem is *knowledge-acquisition.* To build an expert system a knowledge engineer had to interview human experts (informants) and to try to elicit appropriate knowledge in the form of rules. This knowledge was difficult to uncover. The human expert could not make a list of hundreds of rules he or she used, because the expert most often did not use rules in problem solving. The process of knowledge acquisition became very tedious and tiring for both the knowledge engineer and the expert. Often it resulted in incorrect rules, since the expert was forced to express his or her expertise in a format (rules) that did not truly reflect the way he or she thought. Knowledge acquisition became known as a bottleneck in the construction of expert systems [7].

The second problem is that expert systems lack memory. For example, when a medical diagnosis expert system was presented with a patient, it might use hundreds or even thousands of rules to reach a diagnosis. When presented with exactly the same case again, it would have to re-use the same set of rules to reach the exact same conclusion. This lack of memory led to computational inefficiencies. Furthermore, a program without memory is destined to repeat the same mistakes and failures, and will never learn from them.

The third problem is related to robustness. If an expert system was given a problem that did not match its rules fully, it would be incapable of producing an answer. The knowledge of an expert system is limited to its rules, and if no rules are applicable the system has no alternatives.

The behavior of human experts in no way matches that of a rule-based expert system. The central feature of expertise is *experience.* An expert is someone who has vast knowledge in a specialized domain, who has witnessed numerous cases in a domain,

and has generalized this experience to apply it to new situations. When confronted with a problem an expert is reminded of previous, similar problems and their respective resolutions. Even rules that the expert may be using are rooted in actual experiences, which have been distilled into a general formula of action. Thus, the basic unit of knowledge for an expert is not a *rule* but a *case*. Human experts acquire knowledge by assimilating new cases. Consequently, it is easy to acquire expert knowledge if the knowledge engineer asks for cases and experiences, rather than for rules. Experts can easily articulate their experiences and the knowledge acquisition bottleneck is solved in Case-Based Reasoning.

Second, human experts remember their experiences. Similarly, Case-Based Reasoning systems are memory systems that remember all problem solving instances. Case-Based Reasoning systems keep adding to their experiences and knowledge and can grow as a more advanced reasoning system. Case-Based Reasoning systems learn from experience and add to their knowledge both successful cases and failures, so that they can avoid repeating the same mistakes.

Third, human experts can reason by analogy. If a designer is faced with a completely new problem he or she will not give up. Instead the engineer will attempt to solve the problem by relating it to other ones and will try to arrive to a composite solution based on a number of previous cases. Even if the expert is faced with a problem for which there is no exact similar experience, the expert is still capable of coming up with approximate or probable solutions that need to be tried out for correctness. Case-Based Reasoning systems can construct solutions to novel problems, too. By reasoning from analogy with past cases Case-Based Reasoning systems can address new and unknown problems, and are not constrained to solving only a limited set of known problems.

In conclusion, the technology of Case-Based Reasoning promises to offer new, improved methodological approaches to the creation of intelligent systems. Case-Based Reasoning provides the developer of intelligent systems with ease in knowledge acquisition, learning capabilities that will allow the system to evolve and improve from experience, and robustness in its reasoning and problem solving process.

3. The Domain of Application: Interoperability Analysis

We were interested in developing an intelligent system that would assist a communications system design engineer in analyzing his or her design for EMI/EMC. The vehicle for the analysis would be the COEDS environment on an engineering workstation.

As discussed in the Introduction, COEDS is a shell that has been developed to provide a user-friendly, graphical interface, and data postprocessor to interoperability analysis codes. At this time COEDS contains COSAM II [9] for interference and degradation analysis, and LINCAL [10] for link analysis. COSAM II operates under two different modes, a System Performance Score (SPS) and a Necessary Desired Power (NDP) mode. The calculated products are the desired Signal to Noise Ration (SNR), Bit Error Rate (BER), Articulation Index (AI). Intermediate products are Excell Interference Level (EIL) and Tune Power (PINO).

The purpose of COEDS is to analyze RF communication systems. The analysis is to be used in the design of Navy shipboard exterior communication systems. COEDS performs the data and resource management leaving the engineer with more time to produce an acceptable design. COEDS also displays the results of the analysis in a thought enhancing format, using graphics, color, and visualization.

4. ASP - The Analysis and Simulation Planner

To further assist the engineer during the analysis of collocated communications systems we developed ASP, the Analysis and Simulation Planner. ASP is an intelligent,

case-based system that generates analysis plans. The use of ASP simplifies the use of COEDS and the EMI analysis codes, and also functions as a prototypical demonstration of the applicability of advanced AI techniques in computational electromagnetics.

The inputs to ASP are the description of a communications system, environmental information (noise environment, global position, etc.), and the analysis goals, that is what kind of information should be the final result of the analysis run. ASP will then use Case-Based Reasoning techniques to generate an *analysis plan*. An analysis plan represents the set of actions that must be taken to realize the analysis goals specified. The actions are analyses that must be sequenced, combined and run. After the analysis plan is generated it is evaluated and stored in a Case Memory. If the analysis plan fails it is identified as an error and stored as a failure. If it succeeds, it is executed and the results are presented to the engineer in the COEDS format.

Here we will not give any details of the internals of the intelligent system other than mention that it uses Case-Based Reasoning methodologies to reason. Instead we will present three simple examples of ASP's execution and provide some explanation of the reasoning process.

4.1 Example 1

Example 1 consists of a simple two transmitter, one receiver system. The user has described the system and asked for ASP to generate an analysis plan to compute the System Performance Score (SPS) value:

Case ID: 10
Input: Transmitters TX1, TX2
Receiver RX1
Output: SPS

Next, ASP identified cases similar to the given problem and produced the following solution:

Actions:
(input TX1 RX1) (output PINO-1)
(input PINO-1) (output EIL-1)
(input EIL-1) (output UPS-1)
(input TX2 RX1) (output PINO-2)
(input PINO-2) (output EIL-2)
(input EIL-2) (output UPS-2)
(input UPS-1 UPS-2) (output SPS)

The above actions imply the following: First compute the PINO value for transmitter TX1 and receiver RX1; next use this PINO value to compute the value of EIL; use this value to find the UPS between TX1 and RX1; do the same for computing the UPS value between TX2 and RX1; finally, use the two UPS values to compute the required value of the System Performance Score (SPS).

In finding the solution ASP had to find similar old cases that were executed successfully, avoid known failures, and put together a solution from the past cases. In this specific example ASP did not need to perform any *adaptation*, that is it did not need to modify the candidate solution to reflect the realities of the current problem.

4.2. Example 2 - Adapting Solutions

In this example we demonstrate ASP's ability to adapt past solutions given the peculiarities of the current problem. We have used the same system as above, only this time have included wideband architectures:

Case ID: 18
Input: Transmitters TX1, TX2
Receiver RX1
Output: SPS

The solution generated by ASP was the following:

Actions:
(input TX1 RX1) (output PINO-1)
(Input PINO-1) (output WB-EIL-1)
(input WB-EIL-1) (output UPS-1)
(input TX2 RX1) (output PINO-2)
(Input PINO-2) (output WB-EIL-2)
(input WB-EIL-2) (output UPS-2)
(input UPS-1 UPS-2) (output SPS)

The solution was modified to express the need to calculate EIL using the wideband EIL code rather than the standard EIL analysis routines. ASP knows a large number of adapta-

tion rules that allow it to modify solutions to fit the present configuration of the communications system. Adaptation rules are used for different environments, system architectures (wideband, microwave, frequency hopping, etc.), and so forth.

4.3. Example 3 - Partial Retrieval

In this example we show how ASP can retrieve parts of old cases and use them to solve current problems. The user did not give specific devices to the system, but only requested that an analysis be performed to calculate UPS if the EIL were known. The system was able to retrieve the analysis actions independent of the communications system associated with them:

Case ID: 20
Input: PINO
Output: UPS

The solution generated by ASP was the following:

Actions:
(input PINO) (output EIL)
(input EIL) (output UPS)

5. Summary and Conclusions

We have described ASP, a Case-Based intelligent system that can generate analysis plans for analyzing collocated communications equipment. ASP is a simple example of how advanced AI techniques can have a tremendous impact on the domain of computational electromagnetics. ASP is capable of modeling the cognitive processes of human analysis experts, can learn from its mistakes, remembers its problem solving experiences, and can reason analogically by combining and modifying past experiences.

ASP can simplify the process of analyzing shipboard communication systems and provide a powerful enhancement to COEDS. ASP has been completely developed and tested on a number of communications systems. In the future we will embed ASP into the COEDS shell, creating an integrated, intelligent analysis environment on an engineering workstation. ASP will receive its inputs automatically from COEDS and will send its analysis plans directly to COEDS for testing and execution.

ASP provides the communications system design engineer with yet another improvement of her environment. Intelligent tools like ASP do not intend to replace the human expert, but to free her from the tedious parts of the design and analysis process, allowing her to concentrate on the creative part of the design. Use of intelligent systems in the design, analysis, and simulation of systems in general, and in computational electromagnetics in particular, will have immediate and strong impact on the quality of designs.

6. Acknowledgements

The author would like to acknowledge the help of Dr. J. Holtzman who helped him understand COEDS and the domain of EMI/EMC. Perry Alexander developed the code for ASP.

7. References

[1] Jaquish, J.J.e., "We Have Met the Jammer - and He is Us", *Journal of Electronic Defense*, vol. 11, no. 8, 1988, 34-36.

[2] Rockway, J.W., S.T. Li, D.E. Baran and W. Kowalyshyn, "Design Communication Algorithm (DECAL)", *IEEE International Symposium on Electromagnetic Compatibility*, 1978.

[3] Alexander, P., P. Magis, J. Holtzman and S. Roy, "A Methodology for Interoperability Analysis", *MILCOM-89*, 1989.

[4] Holtzman, J., Alexander, P., P. Magis, and S. Roy, *Communications Engineering Design System - Final Report*, Technical Report TR-7150-39, 1989.

[5] Hammond, K.J., *Case-Based Planning*, Boston: Academic Press, 1989.

[6] Riesbeck, C.K. and R.C. Schank, *Inside Case-Based Reasoning*, Hillsdale, NJ: Lawrence Erlbaum Associates, 1989.

[7] Hayes-Roth, F., D.A. Waterman and D.B. Lenat (Eds)., *Building Expert Systems*, Reading, Mass.: Addison-Wesley, 1983.

[8] van de Brug, A., J. Bachant and J. McDermott, "The Taming of R1", *IEEE Expert*, vol. 1, no. 3, 1986.

[9] Clubb, K. et al., *The COSAM II (DECAL/PECAL) Wideband and Narrowband RF Architecture Analysis Program User's Manual*, Consulting Report ECAC-CR-86-112, ECAC, Annapolis, Maryland, 1987.

[10] Roder, C. et al., *A Method for Evaluating the Received Signal Statistics of a Communications Link Termination on a Naval Ship*, Consulting Report ECAC-CR-79-126, ECAC, Annapolis, Maryland, 1979.

SESSION 1B - "USER INTERFACES FOR EM MODELING CODES"

Development of GEMCOP, an Expert System for GEMACS and GAUGE.

R. Fisher - Science & Engineering Associates
6100 Uptown Blvd. Suite 700
Albuquerque, NM 87110

E. L. Coffey - Advanced Electromagnetics
5617 Palomino Dr. NW
ALbuquerque, NM 87120

Lt. T. Timmerman - WL/AWE
Weapons Laboratory
Kirtland AFB, New Mexico 87117-6008

ABSTRACT

GEMACS (General Electromagnetic Modeling for Analysis of Complex Systems) is perhaps the most comprehensive electromagnetic analysis tool available today. As for most large and complex codes, GEMACS tends to frustrate the potential user with modeling complexities which can obscure and hinder the application and use of the program. The next logical step is the development of an expert system which acts as an interface to the GEMACS and GAUGE (Graphical Analysis for the Users of GEMACS) programs to provide the user with a menu driven access to all features of the codes. A Phase I SBIR program was successfully completed last year demonstrating the feasibility for developing just such a program. A Phase II SBIR contract is presently underway to complete the development and implementation of this program, which is called GEMCOP (GEMACS COntrol Program). This program will act as a step-by-step guide for the users of GEMACS in the development, execution and interpretation of electromagnetics analysis with GEMACS/GAUGE. This paper will discuss the objectives and status for GEMCOP. The functions and features for the program will be discussed along with its structure and operation.

Overview of GEMCOP

The purpose of the development of GEMCOP is to complete an expert control shell program for the GEMACS/GAUGE codes which will allow the user to solve complex EM problems without having a detailed knowledge of how to operate either GEMACS or GAUGE. This will be accomplished through the inclusion of specific menu options for the controlled development of complete GEMACS models which can be executed and analyzed under the control of this program. Interactive script files will be included which enhances the decision making abilities of the program and which minimize the user level of expertise in either running GEMACS or GAUGE.

In order to minimize the demands on the user for detailed knowledge of the GEMACS code and the various data statement types and forms, GEMCOP will provide as much decision support information as possible during the development and execution of a GEMACS problem. This means that after the user has described the type of problem that is desired to solve, the menus will request information from the user which is required to complete the setup

This work supported by the Weapons Laboratory and Rome Air Development Center under contract F29601-89-C-0074.

and execution as well as guide the user to logical conclusions about appropriate techniques and modeling procedures.

The specific objectives of the GEMCOP development effort are:

- Develop a user friendly, menu driven control program for GEMACS/GAUGE
- Minimize requirement for user's knowledge of GEMACS/GAUGE
- Include program "hooks" for inclusion of additional features/programs
- Integrate capabilities of GEMACS/GAUGE for pre/post processing support
- Create script file for the execution of user applications
- Provide for multi-layer Build capabilities

Table 1. summarizes the philosophy for the development of GEMCOP. This philosophy forms the basis for the development of the architecture and interfaces for the program. This allows for the development of the specific menu options to support the user in applications for GEMACS and GAUGE.

Table 1. Points of Philosophy for the GEMACS Control Program

Fundamental purpose of GEMCOP is to remove user's intimidation of using GEMACS and GAUGE for EM analysis.

Make the code "self-teaching" and easy to use.

The user is asked to specify the goals of the problem early in the session.

A record of past operations and current state will be maintained to guide the user with dynamic menus through an entire problem.

GEMCOP will focus on the thorough development of techniques/applications which meet the needs of the majority of users as opposed to trying to make the program everything to all users.

Often used/required functions will be supported through "hot keys".

Menus will be dynamic in providing only those options which make sense from the users application standpoint and the history of previous selections.

Provide a user's "safety net" through prompting, advice windows, error checking, file and data coordination.

Support specific applications areas such as:

- Antenna analysis
- EMC/EMI
- Scattering
- Antennas on structures
- Multiple region
- Dry lab of test setups

VAX version will operate with GEMCOP and GAUGE on the PC and exercise GEMACS on the VAX.

Primary code documentation will be through PDL comments in the code.

Code integration will occur as each program module becomes available.

Place as few requirements on the user's knowledge of GEMACS as possible.

Functions/Features of GEMCOP

Table 2. summarizes the basic features of the GEMCOP program necessary to implement the philosophy. These features determine the structure for the program and the specific support which will be provided to the users.

Table 2. Features of GEMCOP

- Structured menus for assisting the GEMACS/GAUGE user.
- Ability to create/review/modify/analyze/output GEMACS:
  - Geometry files (GEOMETRY)
  - Command Set files (COMMANDS)
  - Topology/connectivity files (BUILD)
  - Task files (TASKS)
- Ability to execute GEMCOP generated files to exercise GEMACS and GAUGE.
- Ability to execute other tasks/programs specified by the user during setup.
- Ability to perform error checking for GEMACS:
  - Geometry files (GEOMETRY)
  - Command Set files (COMMANDS)
  - Topology/connectivity files (BUILD)
  - Task files (TASKS)
  - Application Physics
- "Self teaching" window descriptions of menu choices and their implications.
- Ability to support archival/retrieval of GEMACS files and to act as a code/data interface and manager.
- Facilitate input/output through data management and translation of GEMACS terminology to the users.
- Ability to run on a PC or VAX.
- Code documentation will be included in each program module in detailed PDL comments.
- Ability to estimate execution time and status of estimated time remaining for completion.

The primary function of the GEMCOP program is to make the GEMACS/GAUGE code combination less intimidating and much easier to use. This will be accomplished through a menu driven program which supports a number of specific operations, some of which are directly related to GEMACS and/or GAUGE requirements, and others that are more DOS or utility oriented. The key top level functions for GEMCOP are: File operations (FILES), task/configuration state monitoring (TASKS), multi-layer geometry modeling (BUILD), GEMACS command file generation (COMMANDS), geometry file creation and editing (GEOMETRY), problem/program execution (EXECUTE), analysis of input and output data (ANALYZE), various utility operations (UTILITY) and output to printers, plotters, etc. (HARDCOPY).

In addition, other features such as hot-key support of all major options in the program will function to provide knowledgeable users with a quick interface to any portion of the menu desired without having to step through the menus one at a time. Another function is the support of script files for performing specific operations with GEMACS. The program will also provide a "safety net" for users which will catch the most common errors in GEMACS use and help the user to correct or work around them. Figure 1 illustrates the main menu screen for GEMCOP. This screen consists of an information bar along the top, the main menu bar just under it, the pull-down menu and response screen area and a hot-key assignment bar along the bottom.

GEMCOP Code/Data Interface Management

One of the principal functions of the GEMCOP program is as a code/data interface and manager. This function is accomplished through structured menus which interface the user with GEMACS/GAUGE code requirements without placing a demand on the user for a high degree of knowledge of GEMACS or GAUGE. GEMCOP supports the user by being able to read, create, review, modify and save key GEMACS files. These files include geometry, commands, build (multiple region connectivity). It also works with scripts and task configuration information, to simplify the overall use of the code.

GEMCOP Input/Output Facilitator

GEMCOP will have the ability to archive and retrieve files. This is a capability which is distinct from the standard read/write performed by DOS. The archive process will save header information with each file which describes the allows the user to describe the file and its pertinent parameters so that is essentially cataloged for later retrieval and use. The retrieve option works specifically on archived files to read the header information and present the user with a summary of exactly what the file being retrieved is. The archive feature will allow the user to store file/problem descriptive information in a library database which can be scanned and sorted on key words. All pertinent file linkages and problem or task states will be stored in the header so that everything required to fully "revive" the archived file or problem will be present.

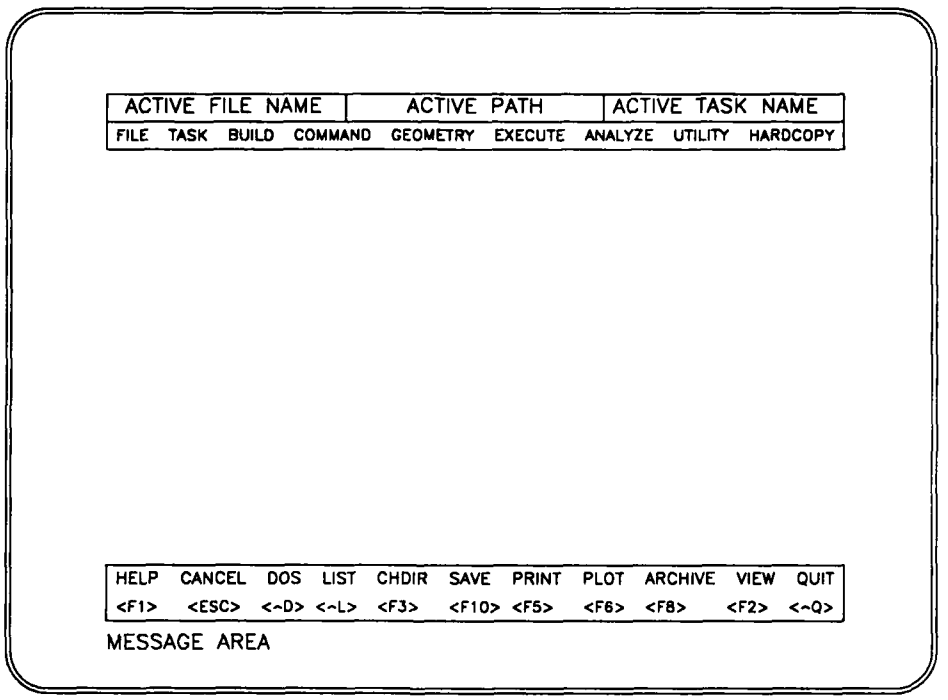

Figure 1. Main Menu Screen for GEMCOP

GEMCOP Task/Problem Configuration Management

The GEMCOP program will maintain memory of the task configuration for the user. This will be used to provide the user with dynamic menus which can help move the user through the creation, execution and analysis of a GEMACS problem. Information on what has already been done along with problem requirements will allow the program to guide the user to the next logical steps.

GEMCOP Analysis Capabilities

Another major function of the program is in the area of data analysis. GEMCOP will aid in the analysis of data by providing specific support for reviewing, printing, plotting, modifying, comparing and sorting GEMACS data in various ways.

GEMCOP Multiple Region Modeling

The construction and evaluation of coupled multiple region problems in difficult at best. The GEMCOP program will provide an approach for handling these regions through the BUILD function. BUILD allows the user to create a complex topological problem geometry from a conceptual viewpoint to make sure all aspects of the problem are completely defined. It will also ensure that various connected regions are connected where they are supposed to be.

Specifically, the BUILD option will offer the following capabilities:

- graphical view of problem topology
- unlimited nesting of regions
- handling of both serial and parallel regions
- unlimited aperture connections for coupling
- acts as coordinator/interface for apertures between regions
- allows use of user assigned names, definitions and quantities
- prompting for required region specific data

Figure 2 depicts a sample screen showing how a multiple region geometry might appear. The names assigned to the various apertures would be user names such as those shown. The BUILD option will allow the automatic generation of this geometry as the user enters information on the various regions and their connections. By using BUILD, the user will be assured of creating the correct geometry file for representing a given problem.

GEMCOP Expert Script Files

A script language processor (SLP) will be used to interpret function and application scripts designed to provide the user with interactive guidance in the operation of GEMACS/GAUGE and the evaluation of their output data.

GEMCOP Error Checking/User Instruction Capabilities

The file/data coordination and error checking capabilities of GEMCOP will provide a "safety net" for the user. It will provide prompting for information when such information is required to continue processing. It will provide advice on recommended selections at various stages in the program.

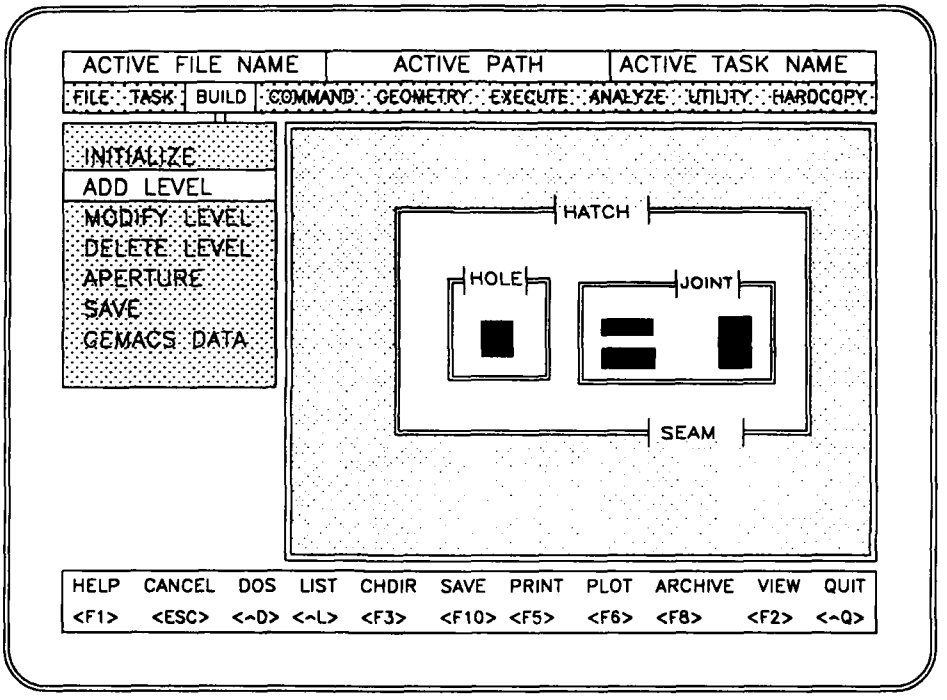

Figure 2. Multiple Region Geometry Screen (BUILD)

The error checking will be under the user's control so that it can be performed on a command by command basis or all at once at the end of some problem construction.

Summary of GEMCOP Functions

In summary, GEMCOP provides a comprehensive user interface which will be both easy to use and powerful. GEMCOP will be able to translate to/from GEMACS and the user's language. It will provide smart hardcopy and preview options, paving the way for report quality output. Different levels of assistance will be available according to the level of knowledge of the user. The use of script files will provide for expansion of capabilities. GEMCOP's dynamic menus will give the user confidence that the selections that he is making are reasonable and will produce sensible results. The GEMCOP interface will make it difficult to make a mistake when running GEMACS or GAUGE.

Menu Descriptions for GEMCOP

The top level menus which will be supported in GEMCOP are illustrated in Figure 3. The selection and organization of the menus/options was the result of extensive evaluations of the interface requirements for GEMACS/GAUGE as well as the anticipated support requirements for applying these codes and analyzing output data from them. Figure 4 shows the nature of typical menu types which will be used with the GEMCOP program. The basic menu screen consists of the top information line, the top menu bar and the bottom menu bar.

The information line is used to provide the user with information concerning the path and files be used by the program at any given time. The nature and organization of the information on this line may change according to where the user is in the GEMCOP program.

The top menu bar provides the user with the basic, top level menu selections for GEMCOP. These consist of FILE, TASK, BUILD, COMMAND, GEOMETRY, EXECUTE, ANALYZE, UTILITY and HARDCOPY. When the user selects one of these menu items, either by moving the curser to highlight the choice and pressing "enter", or by pressing the first character of the menu item, a pull-down menu, such as shown for command, appears.

The bottom menu bar provides the user with active hot-key choices for performing specific functions or obtaining help. This menu bar will contain different options according to the operations currently being performed by the user in GEMCOP. Some options, such as HELP, CANCEL and SAVE, will always be in this menu line.

Another type of menu which will be used in GEMCOP is the pop-up menu. This type of menu is illustrated in Figure 4 where the HIGHLIGHT SCRIPT pop-up menu has been activated by the choice of COMMAND SCRIPTS from the COMMAND pull-down menu. Pop-up menus will typically be used at levels below the first pull-down options.

Script windows will appear whenever user interaction/intervention may be required and more specifically for scripted problems or applications. The script window for MAKEPTS is shown in Figure 4. Scrollable windows or items

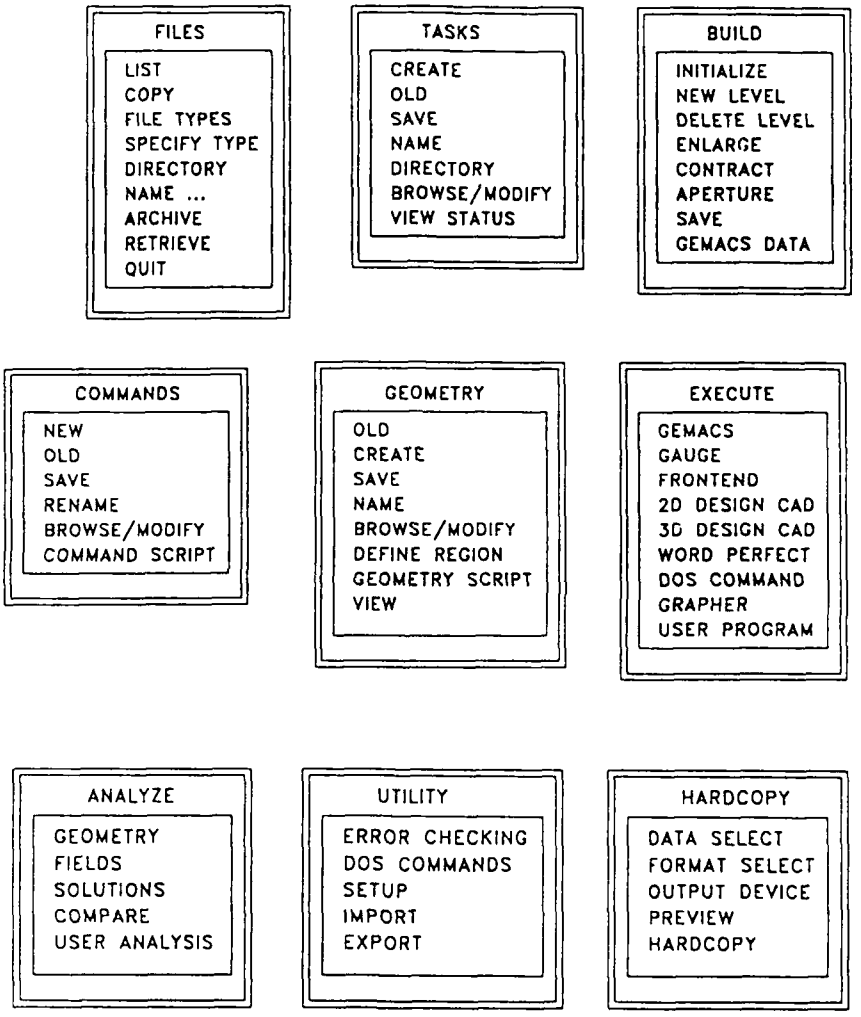

Figure 3. GEMCOP Top Level Pull-Down Menus

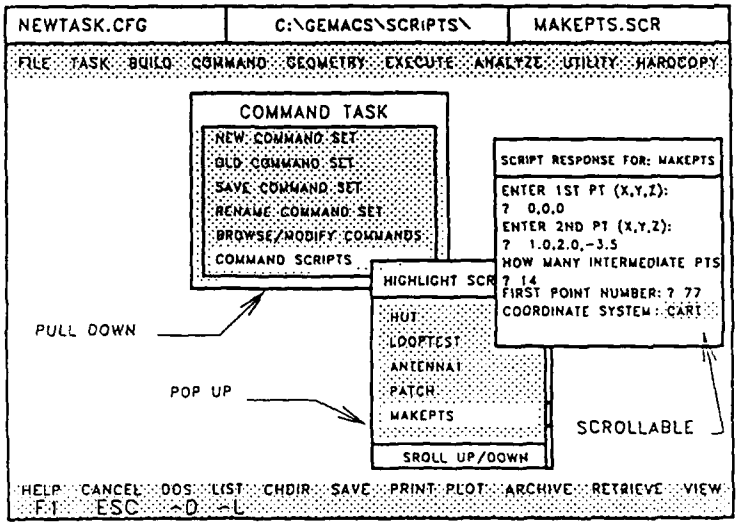

Figure 4. Sample GEMCOP Menu Types

will also be used in GEMCOP. For example, the HIGHLIGHT SCRIPT window is scrollable (note scroll bar along right edge of window in Figure 4) and the coordinate system selection bar in the script window can be scrolled to select the desired coordinate system. Finally, dialogue boxes will be used to provide the user with a convenient method for inputing specific data into GEMCOP (i.e. file names, etc.).

The first level of menus are all of a pull down nature. That is, when a top level menu option is selected, one of these menus is pulled down from the menu selection bar to provide specific choices available with the selected option.

The GEMCOP menus will be dynamic. This means that as the user moves through the program building up a problem for execution by GEMACS, menu options which are currently available or recommended will be highlighted or otherwise emphasized. Items which are not available or are not currently recommended will appear at low intensity and will not be selectable. This dynamic feature of the GEMCOP menu structure will further aid the user in moving through the program to establish inputs for the GEMACS code and in subsequently analyzing the output data from it.

GEMCOP Applications/Script Files

The purpose of the script file approach in GEMCOP is to provide support for specific applications without hard wired code that must be changed for each use. The script files will make use of replaceable parameters in an ASCII text file with FORTRAN-like syntax to allow for the development of general purpose application files suitable for working a particular class of problems.

The script files can be applied to geometry file creation, command file generation, analysis, program execution and other areas covering requirements of GEMACS or GAUGE.

The script file language will have support for such features as operators, functions, repetitive execution (looping), conditional execution, nested scripts, output display to the user, prompting for user input and jumps (relative to the present position in the script). Initially, an interpreter will be used to read and execute the script files. This interpreter will be designated as the Script Language Processor (SLP).

The GEMCOP SLP will also allow screen outputs to display information to the user. This will allow interactive processing of macros through screen display of messages and variables. For example, based on the nature of the model which may have been developed for an application, the user can be appraised of model/technique limitations such as the maximum frequency at which the model provides accurate results.

The combination of all these features available under the Script Language Processor (interpreter) will allow the development of very powerful script files for performing complex problem solving with GEMACS.

GEMCOP Development Status

The Phase II SBIR program under which GEMCOP is being developed began in September, 1989. The architecture for the program has been established and the design of the code has been started. The first operational prototype for the full GEMCOP code is scheduled for December, 1990. Delivery of the completed code and its documentation to the sponsors is scheduled for April, 1991.

GEMACS/GAUGE MOM MODEL EDITOR (MODELED)

Jeffrey A. Evans
Decision-Science Applications, Inc.
1300 Floyd Ave Suite 5
Rome, NY 13440
(315) 339-6184
FAX (315) 339-6923

ABSTRACT

GAUGE (Graphical Aids for the Users of GEMACS) is a PC based graphics package to help an engineer interactively build geometric models of real world structures (aircraft, antennas, ships, etc.). These models are then submitted to GEMACS (General Electromagnetic Model for the Analysis of Complex Systems) or another numerical analysis code for electromagnetic (EM) analysis. The capability to interactively and graphically develop geometry models reduces the overall time required to perform an EM analysis, and it has increased the accuracy and detail of the model.

This paper describes the program MODELED, its graphical interface and its utility in EM modeling and analysis. MODELED is a supplement to the GAUGE package that allows an engineer to semiautomatically alter a model for analysis under different EM conditions.

INTRODUCTION

Systems modeled under a given set of EM conditions constitute a baseline model. The MOM solution technique is used to model electrically small-to-moderate structures. For MOM the analyst uses short wire segments and surface patches to represent the physical structure. This type of model is commonly referred to as a wireframe model. In GEMACS a typical wire segment modeling guideline is that the segments should be no longer than a tenth of a wavelength and the length of a segment should be at least five to ten times its radius.

When analysis of a system under different EM conditions is required, changes to the baseline model are required to satisfy the different EM conditions. Previously, manual model editing was necessary to add or cut wires (possibly hundreds) to stay within the modeling guidelines. MODELED automates this editing thus saving substantial time over the previous manual method. The time saved by automating this process is orders of magnitude over the manual method.

MODELED is functionally equivalent to the GAUGE Graphic Processor and Preprocessor. The Postprocessor of GAUGE was omitted from MODELED to allow for the wire subdivision algorithms. One portion of the Postprocessor that was kept is the Color by option. The engineer can thus still color the model in several ways to highlight different parameters. Because MODELED is a preprocessing option, the main MODELED input menu is selected from the preprocessor menu as show in figure 1.

The remainder of the menus accessed from the Main Menu are the same menus as in GAUGE. The other additional submenu under the Preprocessor is the Integrity option. This capability was not incorporated into the original version of GAUGE. It will be discussed later in this paper

<<< MODELED >>>	Pre-processor	MODELED Options
(F-1 Help)	(F-1 Help)	(F1 Help)
		This model is valid
D) Draw model	A) Add	up to 6000.0 Mhz
V) View options	E) Edit	==========
P) Parameters	R) Renumber	
S) Show/noshow	I) Integrity	>Regrid Options<
T) Text/axes/leg.	D) Delete	Wires Only : OFF
E) prE-process	T) Trans/rotate	Wires & Areas: OFF
U) Utilities	F) reFlect	by Frequency : OFF
H) Hardcopy	S) Save model	Freq. (MHz) : 6000.0
R) Read model	C) Conversion	by Wire Ratio: OFF
C) Color	L) Lines/curves	Ratio(>=1) : 1
Q) Quit	M) Model editor	Set Radii : ON
	X) eXit	
		>Radii Options<
		Assign Radii : OFF
		Check Radii : OFF
		Update Radii : OFF
		Accept(F9) Exit(F10)

Figure 1. MODELED Menus

To illustrate the usefulness of MODELED, 3 examples are presented in this paper; 1) Bistatic Scattering from a cube; 2) A communications hut with an antenna on top; and 3) An aquila rpv.

BISTATIC SCATTERING FROM A CUBE

The case of scattering from a MOM cube was presented at the 1988 ACES Review in the paper GAUGE[2]. The initial cube, figure 2, was constructed from plates (.1 meter on a side) being rotated and translated to form the 6 sides of the cube. The plates were then converted to wires via the conversion algorithm in the GAUGE preprocessor. The resultant wireframe cube is valid for about 300MHz.

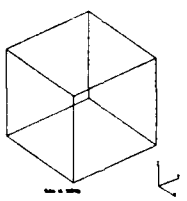

Fig 2 Wireframe Cube

Now consider performing the analysis on the cube at a frequency of 1200MHz. The wires defining the edges of the cube now are long compared to a wavelength. In order to correct the model each edge of the cube should be subdivided into 4 subsections. Also the sides of the cube should also be subdivided. There are several manual methods of subdividing this model, but they all involve considerable time to add the new wires (total new wires) and then deleting the old wires. MODELED can perform the above operation by asking for

wire and area ratio subdivision and then specifying a 4:1 ratio. The resultant cube is shown in figure 3. The shrink option is used to show the individual wires.

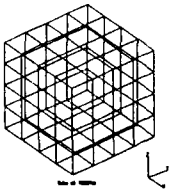

Figure 3 Cube at 1200MHz (ratio)

The frequency subdivision option will give an equivalent model to that shown if figure 3. The algorithm for frequency based subdivision is similar to that used by Heighway and Biddecombe [3]. The subdivided cube is show in fig 4.

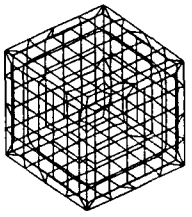

Figure 4 Cube at 1200MHz (freq.)

HUT WITH T-BAR ANTENNA

A slightly more complex structure for GEMACS analysis is the communications hut with a T-bar antenna on top shown in figure 5a. This model has MOM wires that form both closed surfaces (e.g. the hut) and free hanging wires (e.g. the T-bar). The user may wish to concern himself only with the antenna on the top of the hut. The hut can be put in noshow mode and any editing performed by MODELED will be limited to the antenna as shown in figure 5b.

Figure 5a & b Comm. Hut and T-Bar antenna

The antenna is currently valid for about 600MHz. Using the wires only, frequency subdivision with a target frequency of 2400MHz, we obtain the antenna as shown in figure 6. The hut can then be retrieved from noshow and the entire geometry can be saved into a new geometry file.

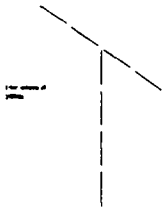

Figure 6 T-Bar antenna at 2400MHZ

If we had started with the antenna in figure 6 we could easily generate the original antenna by specifying a target lower frequency in the menu. This is a trivial case, but if we had a dipole array we get a significant editing time savings. Also, by reducing the number of elements in the model for lower we can realize a disk space and computer run time savings during an analysis.

AQUILA RPV

The Aquila RPV example shows how a MODELED can work on various portions of a complex geometry. The original geometry is shown in figure 7.

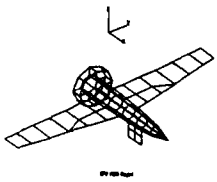

Figure 7 Aquila RPV

By placing different parts of the geometry in show only mode the modeler can apply different editing schemes to the geometry. An example of the utility of this approach is shown when the placement of an antenna on an airframe is needed. Where the antenna is to be placed can be modeled with a finer grid spacing to give a better approximation for the analysis. Figure 8 shows the RPV after three regions of it were regridded at different ratios.

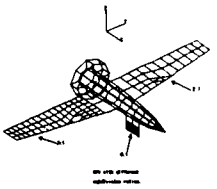

Figure 8 RPV after editing with MODELED

INTEGRITY CHECKING OF GEMACS GEOMETRY

GEMACS uses straight wire segments in its method of moments methodology to represent a physical structure. There are several general guidelines that should be followed when generating these structures. The guidelines used by MODELED include the following:

- Segments must be short compared to a wavelength. Lengths of 0.1 lambda are adequate for most purposes.
- Actual wires should be modeled with the actual radius. Other wires in the model should use a wire radius about one-fifth of the segment length.
- Segments with lengths differing by more than a factor of two should not be joined.
- Small angles (less than about 20 degrees) between joined segments should be avoided.

These Modeling Guidelines are used by MODELED in the regridding of a geometry and as a basis for the integrity checking. A full discussion of these guidelines is contained in the GEMACS Users Manual[4].

```
INTEGRITY
 (F1-Help)
A) wire Angle
L) wire Length
R) Radius check
S) Surface area
M) liMiting wire
D) reDisplay
X) eXit
```

Figure 9 Integrity check menu

SUMMARY/FUTURE ENHANCEMENTS

The MODELED program was written in response to a need to be able to interactively alter/validate a MOM EM model. The program provides these capabilities and it also provides a platform for adding new editing and validation functions for the GAUGE package. The following list are recommended improvements and enhancements that could be incorporated into the MODELED program. This list is by no means complete and not all of these may be deemed necessary in the future. They are provided as a reference/starting point for the programmer.

- Regridding for highly reentrant regions in Subdivision.
- Upgrade ratio subdivision.
- Banded Renumbering.
- Distance Renumbering.

- Subdividing an n-sided polygon, user selects the sides.
- Integrity check for plates attached to a cylinder.
- Integrity check for wires connected to plates and patches.
- Refining the superpolygon superdivision

REFERENCES

[1] Upshaw, G., Grage, M., Siarkiewicz, K. R., "Graphics Programming for electromagnetic Modeling," Northrup Corp., presented at the Fourth Annual Review of Progress in Applied Computational Electromagnetics at the Naval Postgraduate School, Monterey, CA, March 1988

[2] Lockyer, A., Tulyathan, P., M., Siarkiewicz, K. R., "GRAPHICAL AIDS FOR USERS OF GEMACS (GAUGE)," Northrup Corp., presented at the Fourth Annual Review of Progress in Applied Computational Electromagnetics at the Naval Postgraduate School, Monterey, CA, March 1988

[3] "Two dimensional automatic mesh generation for the finite element electromagnetics package PE2D", Heighway E. A., and Biddlecombe, C. S., IEEE Transactions on Magnetics, Vol MAG-18, No. 2 Mar 1982, pp. 594-598.]

[4] Kadlec, D. L., Coffey, E. L., General Electromagnetic Model for the Analysis of Complex Systems (GEMACS) Version 4 User Manual, The BDM Corporation, RADC-TR-87-68, Vol I, May 1987.

[5] Lockyer, A., Tulyathan, P., Coffey, E., Grage, M., Upshaw, G., GRAPHICAL AIDS FOR THE USERS OF GEMACS (GAUGE), Northrup Corporation, RADC-TR-88-316, Feb. 1989.

[6] Evans, J. GEMACS/GAUGE METHOD OF MOMENTS MODEL EDITOR, Decision-Science Applications, RADC Technical report in publication.

MMP-3D: A Package for Computation of 3D Electromagnetic Fields on PCs and Workstations

Lars Bomholt, Peter Regli, Christian Hafner and Pascal Leuchtmann

Electromagnetics Group
ETH Zurich
Zurich, Switzerland

Abstract

The MMP-3D (Multiple MultiPole) package is an implementation of the GMT (Generalized Multipole Technique) for 2D and 3D electromagnetic scattering problems in linear, homogeneous and isotropic materials. It includes a portable numerical kernel and graphic interfaces for workstations and personal computers. The characteristics of the programs are presented along with an example.

1 Overview of the Method

The MMP-3D (Multiple MultiPole) package is an implementation of the GMT (Generalized Multipole Technique) [1] for 2D and 3D electromagnetic scattering problems. It is a tool for computing time harmonic fields in linear, homogeneous and isotropic media. Via Fourier transform also scattering of non-sinusoidal excitations can be computed.

The field is expanded in solutions of the time harmonic Maxwell equations, mostly cylindrical and spherical multipole expansions of finite order with multiple origins (*multiple multipoles*). The expansions are matched on the boundary using point matching with overdetermined systems of equations. The strength of the MMP-3D code lies in nearfield calculations and in computations involving dielectric or lossy media.

The main part of preparing input is to discretize the boundary and to choose locations and orders for the multipoles (pole setting). Results of the computation are mostly the residues in the matching points and plots of the field components on rectangular grids. For input and output it is essential to provide graphic tools.

2 Overview of the Package

Numerical programs can be kept portable contrarily to graphics programs which depend very much on the hardware, the operating system and on the graphic libraries used. The MMP-3D package therefore consists of several separate programs running on different computers.

The numerical kernel of the MMP-3D program is portable among different computers. Graphic input and output programs are the *mmptool* for Sun Workstations under SunView and a separate editor and plot program for MS-DOS machines with the GEM graphic desktop. For communication between the programs files in ASCII format are used because of their machine independence. The *mmptool* can also interactively exchange information with one or several kernels running on the same or on remote machines.

3 The Numerical Kernel

The MMP-3D numerical kernel is written in FORTRAN 77 using as few as possible nonstandard extensions. It compiles and runs on UNIX workstations and mainframes, on PCs , and on transputer networks. Models are full 3D with possible symmetries about $X = 0$, $Y = 0$, or $Z = 0$. The expansions currently implemented are

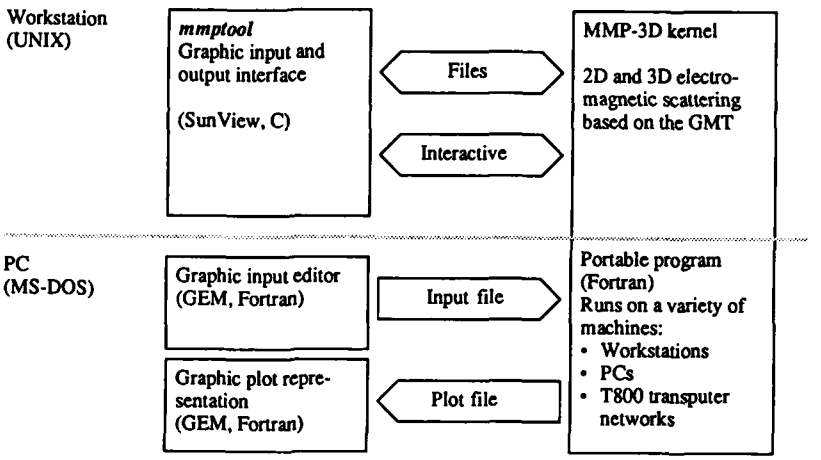

Figure 1: *Overview of the programs in the MMP-3D package*

- Cylindrical TE, TM and TEM expansions
- Spherical TE and TM expansions
- Plane waves, waveguide modes
- Thin wire expansions (see [2])
- Connections

Connections are combinations of one or several of the above expansions together with parameters. They enable the user to construct more special expansions or to include the results of previous calculations for iterative computations. In addition to field continuity conditions and impedance boundary conditions also additional equations and constraints in form of integrals are implemented. Results can be computed as plots on rectangular grids or arbitrary set of points as well as in form of integrals over lines, planes and volumes.

The size of the source code is around 200kB, the size of the executable depends on the compiler and is between 200kB and 300kB. Memory requirements are about 10MB of memory for a problem with 1000 unknowns, which is already fairly large. The performance compared to other codes running on the same machines is very good [3].

The minimum requirements for reasonable work is a 386-based PC with 4MB of memory.

Parallelization of parts of the code makes it possible to run the program on INMOS T800 transputer networks [4]. Currently we are using AT-compatible boards that hold 9 transputers with a total of 28MB of memory. The speed is comparable to a CONVEX C1 machine with a single user. The networks can easily be fitted to the size of the problem.

4 Graphic Interface on UNIX Workstations

The *mmptool* for Sun workstations (see fig. 2) is a graphical front end which allows model definition and visualization of the results in 3-dimensional space. It is programmed in C using the SunView graphic desktop and implements the following features:

- Window based interface with buttons, pop-up menus etc.
- Multiple views in different windows on the same screen

- Parallel and perspective projections, shading and hidden surface removal
- Mouse controlled file manipulations
- Job management and interactive computations with one or more kernels running on local or remote machines

2D and 3D models can be constructed by mouse with the following geometric objects

- Parametric curves like straight lines, circles, elliptical and parabolic arcs, B-splines
- Parametric surfaces like spheres, product surfaces of two curves, bodies by rotation of any of theabove curves
- Readjustable uniform and variably spaced discretization
- Transformations like translation, rotation and scaling, duplications
- Assisted pole setting

Results of a computation with the MMP program are the errors on the surface and plots of the field components. The principles of the representation and examples have already been shown in [5]. Since then additional possibilities have been added and include now

- Vectorial display of $\vec{E}$,$\vec{H}$,$\vec{S}$, surface currents and charges on several arbitrary surfaces at a time. Dynamic range of the vectors is enhanced by using variable length, width and color.
- Contour maps, color or grayscale maps, and hedgehog charts for scalar quantities on any surface.

All representations can be animated. This greatly improves intellegibility. Hardcopies can be made with PostScript. Development on this interfaced still continues. It will soon be converted to X-Windows, which makes it portable to most UNIX based workstations and PCs.

5 Graphic Interface on PCs

A simpler, but still powerful mouse based graphic interface is available for PCs running MS-DOS and the GEM desktop. The input program allows discretization of the boundary and computer assisted pole setting along with representation of the error distribution on the surface. The output program is the same as for the 2D MMP codes. It allows animated representations of of scalar and vector fields on quadratic surfaces. For hardcopies device independent GEM metafiles are used.

For running these programs a XT-compatible PC is sufficient. Animation requires either a fast harddisk or a sufficiently large virtual disk.

6 Example

A short example is given for illustration. The configuration is a hole of diameter $d = 0.6m$ in a thick metallic sheet. A plane wave of wavelength $\lambda = 2m$ is incident perpendicularly. Behind the hole there is a dielectric lens ($\epsilon_r = 3$) and an absorbing sphere ($\sigma = 0.1Sm^{-1}$). The problem has been calculated in full 3D using 2 planes of symmetry. It has 452 matching points and 25 expansions. Time for discretization is about 2 hours starting from the idea. Figure 3 shows the model during construction.

The rectangular matrix has 428 columns and 2112 rows. CPU time on a CONVEX C1 for one run is 1070 seconds for determining the parameters, 77 for computation of the errors, and 39 for a plot on 600 field points. Results are shown in figure 4.

7 Availability

The kernel [6] and the graphic interface for PCs will be made available soon as public domain source code. For further information please contact the authors.

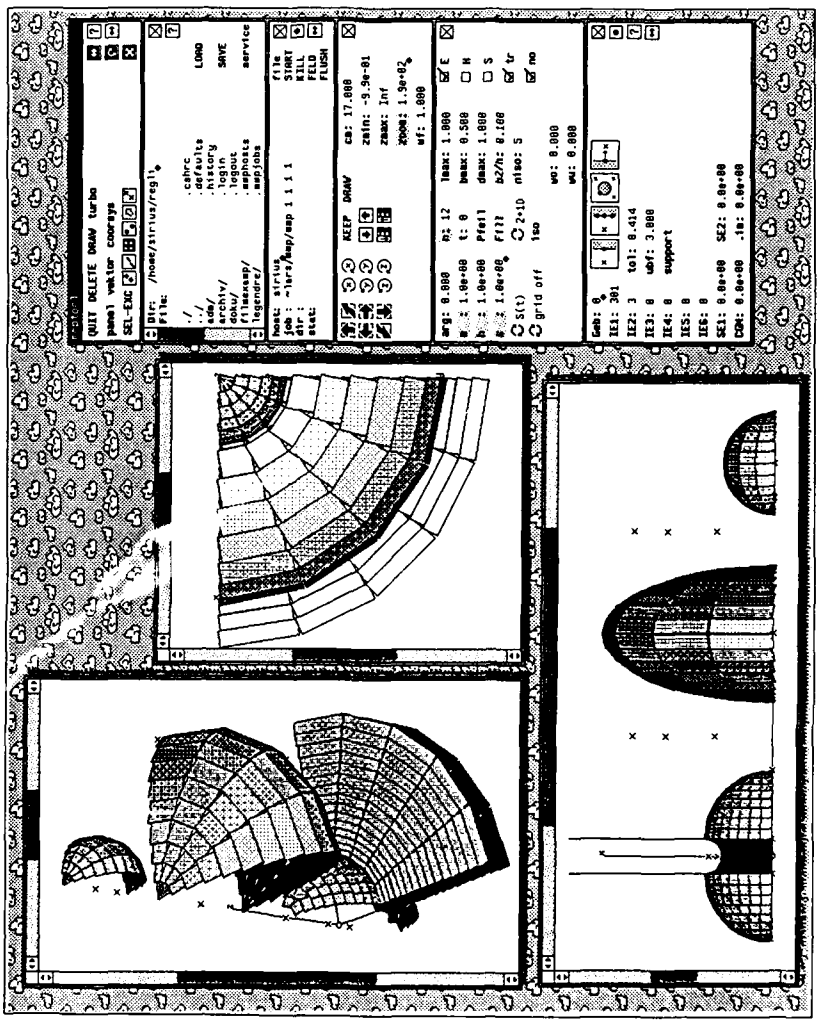

Figure 2: *View of the screen of a workstation running the* mmptool

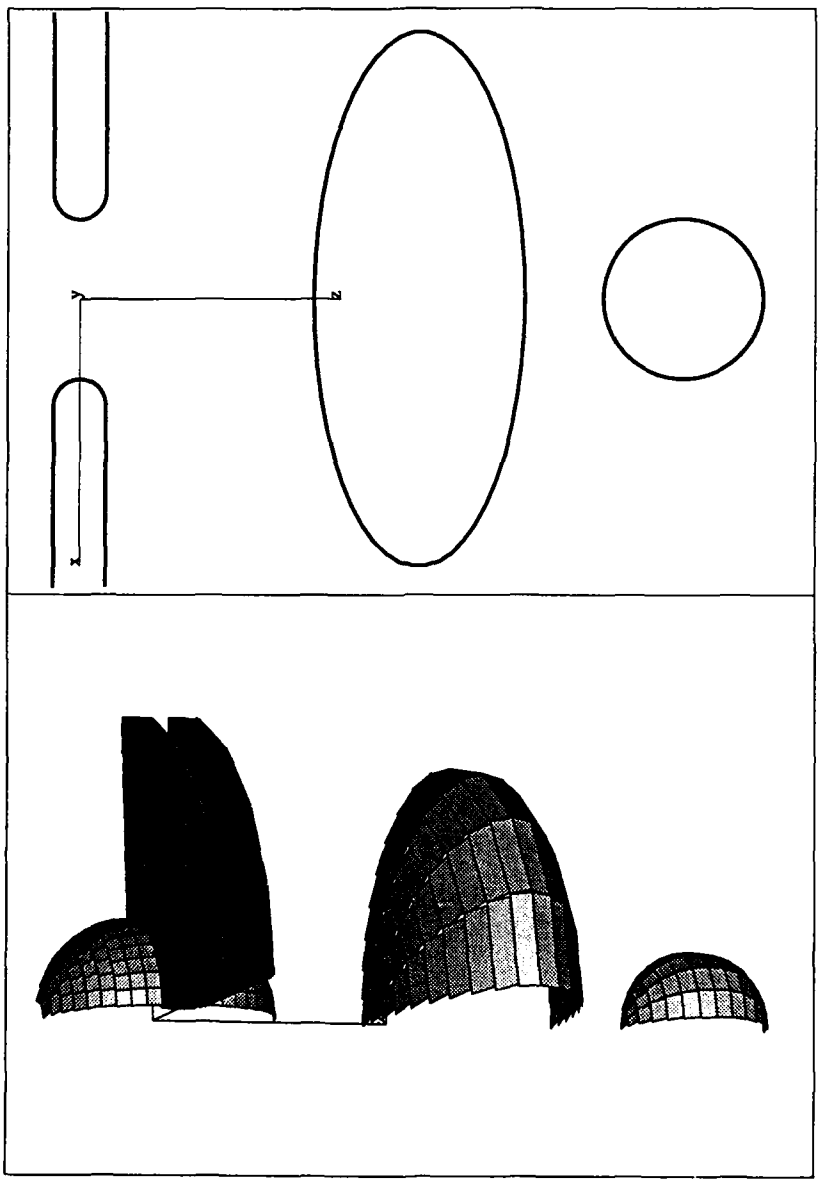

Figure 3: Top: ***Physical model of the example (see text).*** Bottom: ***MMP-model. The rectangles are matching points.***

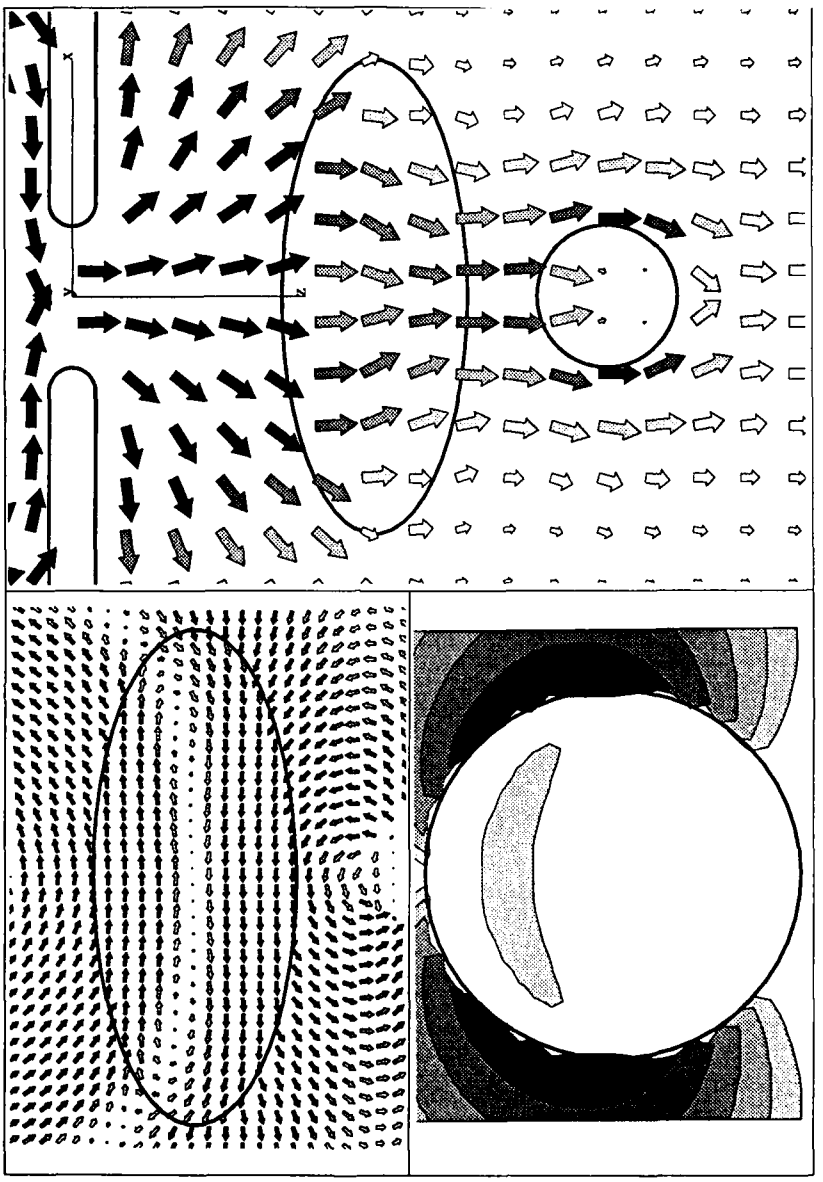

Figure 4: Top: *Poynting field mean time value (power flux)* Bottom left: *Detail: Electric field $\vec{E}(t)$ near the lens.* Bottom right: *Detail: Poynting field $\vec{S}(t)$ around the absorbing sphere (iso-lines).*

References

[1] A. Ludwig, "A new technique for numerical electromagnetics," *IEEE AP-S Newsletter*, vol. 31, pp. 40–41, Feb. 1989.

[2] P. Leuchtmann and L. Bomholt, "Thin wire feature for the MMP-code." In this conference.

[3] N. Kuster, "6 types of canonical problems based on one geometrical model," in *ACES Special Issue on Canonical Problems*, Applied Computational Electromagnetics Society, 1990. To appear in spring 1990.

[4] Ch. Hafner and L. Bomholt, "Implementation and performance of MMP-programs on transputers," in *5th Annual Review of Progress in Applied Computational Electromagnetics (ACES), Conference Proceedings*, (Monterey), Mar. 1989.

[5] P. Regli, Ch. Hafner, and N. Kuster, "Graphic output routines of the MMP-program package on PCs and SUN workstations," in *5th Annual Review of Progress in Applied Computational Electromagnetics (ACES), Conference Proceedings*, (Monterey), Mar. 1989.

[6] L. Bomholt, *MMP-3D — A Computer Code for Electromagnetic Scattering based on the GMT*. PhD thesis, ETH Zurich, 1990. To be published.

AUTOMATION OF THE GEOMETRY DATA FOR THE NEC AND THE ESP USING THE SUPER-3D

J. Peng, J. Choi, and C. A. Balanis
Telecommunications Research Center
College of Engineering and Applied Sciences
Arizona State University
Tempe, AZ 85287-7206

Abstract

In this paper, antenna patterns and monostatic scattering patterns for various objects are obtained using the numerical electromagnetics computer codes (NEC [1] and ESP [2]) based on an interactive graphics program GEOM developed recently at the Telecommunications Research Center at Arizona State University. The GEOM is constructed based upon the three-dimensional Macintosh graphics software Super-3D[3] which can create geometries consisting of elements such as polygons and lines. The geometry can be created by entering the geometry data either by the key board or by the mouse. The interactive graphics program GEOM can transform the geometry data created by the Super-3D to the NEC and the ESP input geometry data format so that the electromagnetics quantities of interest can be computed. Some antenna patterns and monostatic scattering patterns are calculated and compared with experimental data. Also, the previous data obtained through a direct geometry input procedure to the numerical electromagnetics computer codes are used for comparison.

Introduction

Computational electromagnetics have been widely used due to the recent innovations in modern digital computers with large memory and fast speed. Recently, the development of interactive graphics computer programs, which can aid the usage of the existing electromagnetics computer programs, such as the ESP and the NEC, have attracted many electromagnetics researchers and scientists. The use and the development of such programs aid the users of the EM codes to understand more clearly the nature of the EM problems by displaying graphically the geometry of the object under study and the resulting electromagnetics quantities of interest.

The GEOM is a system designed to reduce the time required for antenna and scattering model calculations by providing the user with partial automation of the geometry data entry and the data display process. Previously other interactive graphics packages, such as IGUANA[4] and GAUGE[5], had been developed and they can be used interactively with the NEC[1] and the GEMACS[6], respectively. However, there are no such interactive graphics program available for the ESP geometry data entry. This gives the authors a motivation to develop an interactive graphics package

which can be used not only with the ESP but also with the NEC. However, the development of the GEOM is just at the initial stage, and much work needs to be done in the near future.

The GEOM is developed based on the Macintosh 3-D graphics software Super-3D (copyrighted by Silicon Beach Software, Inc.). The detailed features of the Super-3D are not presented in this paper, but it has similar features as any ordinary CAD. Once the geometry of interest (of the antenna or scatterer) is created by the Super-3D, the geometry data created by this software can be accessed by a word processing software such as Microsoft Word. Then the data is transmitted to the main frame computer (such as IBM-3081 or VAX-8600) through the ETHERNET. After transmission, the data is transformed to the input geometry data format of the ESP or the NEC for the electromagnetics calculations. The use of the GEOM not only saves time for entering the data, but it also allows the user of the electromagnetics codes to have a better visual display of the problem under consideration.

The systematic flow chart for the GEOM is as follows:

Table.1. Systematic Flow Chart

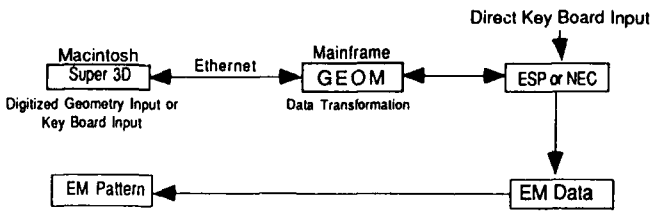

* The direction of arrow represents the transportability from one stage to another.

Numerical Examples

The main purpose of this section is to illustrate the application of the interactive graphics program GEOM. In order to achieve this goal, we compute the backscattering patterns of a dihedral corner reflector. Then these results are compared to the measured and the previous data obtained through the direct input procedure for the geometry data. Also, antenna patterns of a scaled model helicopter are calculated using the NEC and the ESP.

1. Backscattering RCS of a dihedral

In Figure 1, the backscattering RCS of a 90° dihedral corner reflector at a frequency of 10 GHz is calculated by the NEC and the ESP. Each plate of the dihedral reflector has dimensions of 2" by 2" and a thickness of 0.8 mm. For

both computer codes, the direct input procedure and the GEOM input procedure for the geometry data are used to obtain the backscattering RCS pattern. It is evident that both produce exactly the same results. These results are also compared to the measured data obtained at the ASU compact range.

At scattering angles near -180°, -90°, 0°, 90°, and 180°, where the thickness of the plate might play an important role in the scattering patterns, agreement between the measurement and the NEC is better than between the measurement and the ESP. The reason is that the model used for the ESP code does not account for the thickness of the plate. On the other hand, the radii of wires used to model the dihedral corner reflector in the NEC code serve as a thickness of the plate. The previous study [7] showed that the inclusion of edge plates along the side of the dihedral reflector improves the agreement between the measured data and the values obtained by the ESP.

2. Radiation patterns of an antenna mounted on the scaled helicopter model

The radiation patterns of an antenna on scaled model of a helicopter are calculated using the NEC and the ESP, and they are displayed in Figures 2. The scaled model of a helicopter is created using the Super-3D, and then these data are transformed through the GEOM for the EM calculations. A center fed dipole antenna of length 1.23 m is used on the helicopter, and the operating frequency is 64 MHz. The antenna is not grounded to main body.

In Figure 2, antenna patterns for a scaled model helicopter should be symmetric in the roll and the yaw planes, since the helicopter model is symmetric about the y-z plane. However, the ESP results do not exhibit the symmetry property in these planes. If the Subroutine Plate 3 in the ESP code neither chooses the same common edge as the generating side nor divides the same generating side into the identical segmentation for the same structure, the ESP code will place different overlapping modes for the physically same structures. As a result, the pattern might not be symmetric. One way of avoiding this possibility is either to use smaller segment size at the expense of computing time or to specify the generating side for each plate in the model.

Conclusion

Even though the GEOM is just at the initial stage of automation of the geometry data for the numerical electromagnetics codes, such as the NEC and the ESP, it provides the user with the partial automation of the geometry data entry and the data display process. To illustrate the application of the GEOM, antenna patterns for the scaled model of a helicopter are calculated. Also, scattering patterns of a 90° dihedral corner reflector are presented. Our next goals are to make this interactive graphics package more user friendly and to include the 3-D graphics capability for the EM quantities into the GEOM.

Acknowledgement

This work was supported by the Advanced Helicopter Electromagnetics Industrial Associates Program and NASA Grant NAG-1-1082.

References

[1] G. J. Burke and A. J. Poggio, " Numerical Electromagnetics code(NEC)-Method of moments Parts 1, 2, and 3," Naval Ocean Systems Center, San Diego, CA, NOSC TD 116(revised), 1980.

[2] E. H. Newman, " A user's manual for electromagnetic surface patch code : ESP Version 4," Ohio State University, ElectroScience Lab., Rep. 716199-11, Dept. of Electrical Engineering prepared under contract NSG 1498 for NASA, Langley Research Center, Hampton, VA. Aug. 1988.

[3] Copy righted by Silicon Beach Software, 9770 Carroll Center Road Suite J, San Diego, CA, 92126.

[4] Unisys corporation, " Interactive Graphics Utility for Automated NEC Analysis (IGUANA) for Version 4.1," prepared under contract No. N66001-83-D-0094 for Naval Ocean Systems Center, San Diego, CA. 92110.

[5] A. J. Lockyer, P. Tulyathan, G. Upshaw, and M. Grage, " GAUGE User's Manual," Northrop Corporation prepared under contract No. F30602-87-C-0110 for Rome Air Development Center, May, 17, 1988.

[6] K. R. Siarkiewicz, " An Introduction to the General Electromagnetic Model for the Analysis of Complex Systems (GEMACS)," RADC-TR-78-181, Rome Air Development Center (RBTC), Griffiss AFB, NY 13441.

[7] K. Liu and C. A. Balanis, "Comparison of Antenna and Scattering Patterns by the NEC and ESP codes," Conference Proceedings for the 5th annual Review of Progress in Applied Computational Electromagnetics, pp. 1-8, March 20-24, 1989.

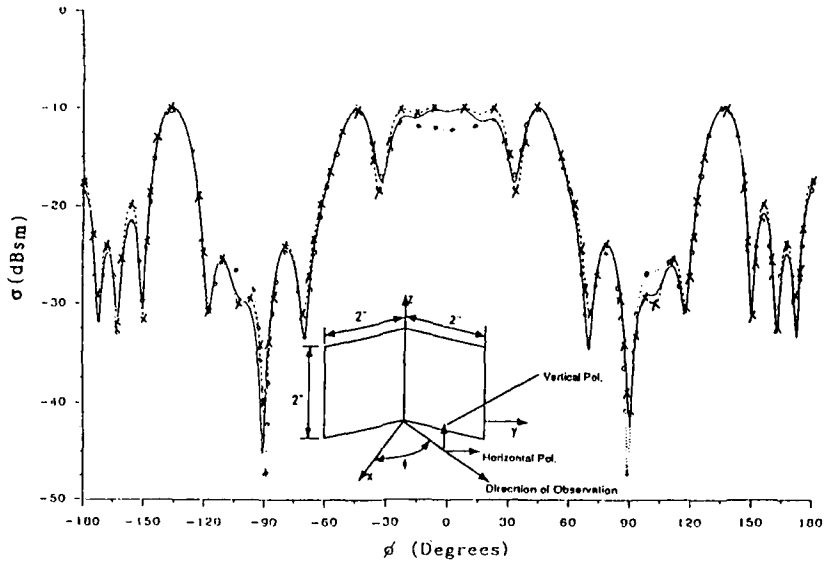

Horizontal-Horizontal; Frequency=10 GHz.

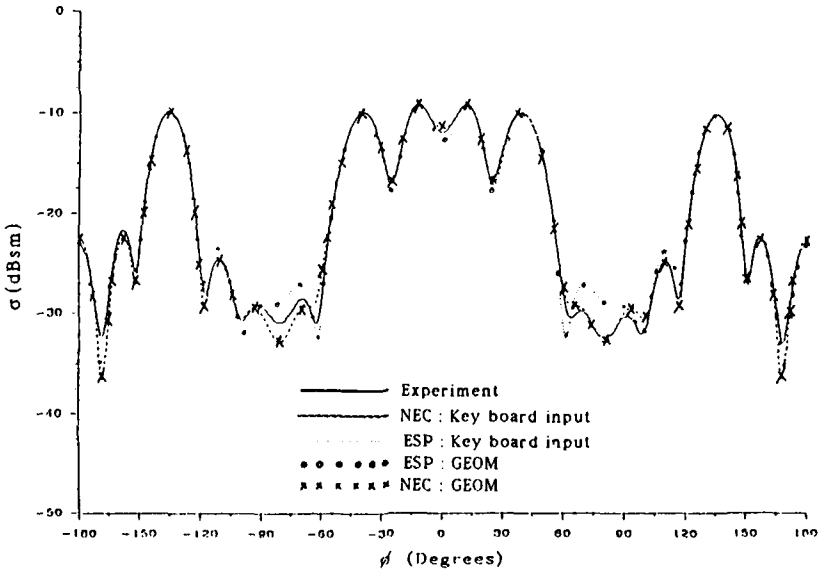

Vertical-Vertical: Frequency=10 GHz.

Figure 1. Backscattering RCS patterns of 90°dihedral corner reflector.

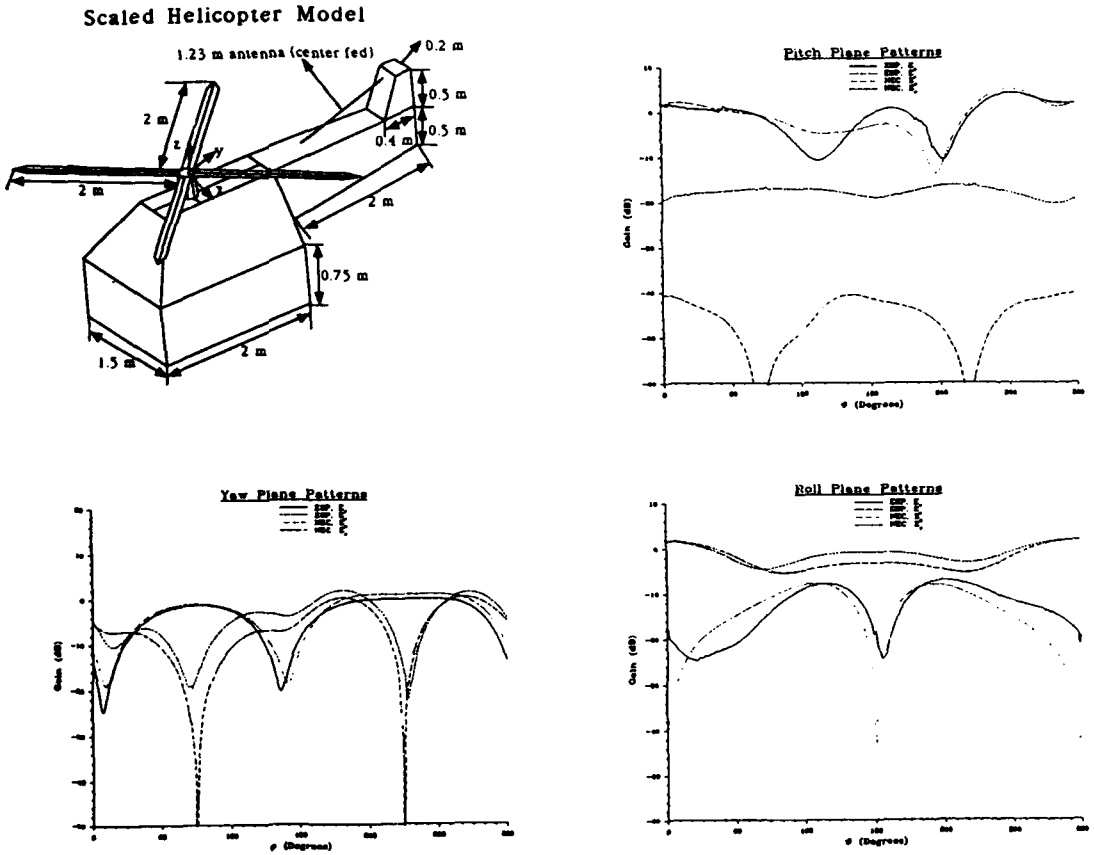

FIGURE 2: Radiation patterns of a center fed antenna of length 1.23 m mounted on a scaled helicopter model (frequency = 64 MHz).

SESSION 2 - "MOMENT METHOD THEORY"

ITERATIVE MOMENT METHOD IN SCATTERING PROBLEMS

H. Dominik
Institut für Hochfrequenztechnik
Technische Universität Braunschweig
P.O.Box 3329 , D-3300 Braunschweig
Federal Republic of Germany

1 Introduction

The solution of scattering problems with the moment method involves the inversion of large linear equation systems, which have to be solved with iterative methods to avoid numerical inaccuracy. Using the Moment Iteration Method in [1] leads to the inversion of only small parts of the complete impedance matrix at each iteration step. The disadvantage of this method is a slow convergence depending on a random choise of the locations for the basis and weighting functions, which requires a convergence test at each iteration step. Choosing shifted locations for the basis functions leads to an excellent convergence for a special class of scattering problems due to the coefficients of the impedance matrix. Combining this method with the Integrated Square Error Criterion (ISEC) presented in [2] enforces the convergence at each iteration step even for ill-conditioned matrices.

2 Theory

Starting with the linear operator equation

$$Lf = g \tag{1}$$

the method of moment leads with the choice of basis functions ϕ_i and weighting functions w_j to an approximation for the solution

$$f = \sum_{i=1}^{M} \alpha_i \phi_i \,, \tag{2}$$

which involves the inversion of the $M \times M$-matrix system

$$[L_{ij}][\alpha_i] = [g_j] \,. \tag{3}$$

The coefficients of the matrix are defined by $L_{ij} =< L\phi_i, w_j >$ and $g_j =< g, w_j >$, where $<>$ denotes the inner product.

The choice of

$$f^{(n)} = f^{(n-1)} + F^{(n)} \tag{4}$$

leads to an iterative process for the n-th approximation, with

$$F^{(n)} = \sum_{i=1}^{N} \alpha_i \phi_i \, . \tag{5}$$

The ϕ_i are basis functions defined only on a subdomain of the operator, but $F^{(n)}$ is valid on the total domain with zero values on the rest of the operator domain. N is arbitrary in the intervall $1 \leq N \leq M$. The deviation from the solution follows then to

$$R^{(n)} = g - Lf^{(n)} \tag{6}$$

$$R^{(n)} = g - Lf^{(n-1)} - LF^{(n)} \tag{7}$$

$$R^{(n)} = R^{(n-1)} - LF^{(n)} \, . \tag{8}$$

Taking the inner product of the last equation with weighting functions w_j on the subdomain and requesting $< R^{(n)}, w_j >= 0$ leads to a matrix system

$$[l_{ij}][\alpha_i] = [R_j] \, , \tag{9}$$

with $l_{ij} =< L\phi_i, w_j >$ and $R_j =< R^{(n-1)}, w_j >$. The unknown α_i follow from the inversion of the last equation, which is now a $N \times N$-matrix system.

3 Choice of Basis Functions

To prevent a necessary convergence test you can use shifted basis functions for each iteration step. As shown in Fig. 1 the domain of the solution is splitted up into segments with pulse functions as basis functions on each segment. At each step the iterative method described above is applied to three segments involving the inversion of a 3×3-matrix. The considered segments of successive iteration steps are shifted as shown one segment. After the completion of one cycle the iteration process starts again with the first three segments until the error exceeds a desired accuracy. Alternatively the segment-shifting of successive iteration steps can be choosen in a different manner, which can be advantageous for some problems.

4 The Integrated Square Error Criterion

When the iteration process is not convergent, the method has to be combined with the Integrated Square Error

$$\mathrm{err}^{(n)} = \int |\mathrm{R}^{(n)}|^2 \mathrm{dx} \, , \tag{10}$$

which modifies (4) with a variational parameter $\eta^{(n)}$ to

$$f^{(n)} = f^{(n-1)} + \eta^{(n)} F^{(n)} , \tag{11}$$

with the parameter defined by $\eta^{(n)} = A^{(n)^*}/B^{(n)}$. Introducing this parameter enforces a minimisation of the error at each iteration step to

$$\mathrm{err}^{(n)} = \mathrm{err}^{(n-1)} - \frac{|\mathrm{A}^{(n)}|^2}{\mathrm{B}^{(n)}} , \tag{12}$$

with

$$A^{(n)} = \int R^{(n-1)^*} F^{(n)} \tag{13}$$

$$B^{(n)} = \int |F^{(n)}|^2 dx . \tag{14}$$

5 Scattering of Parallel Strips

An incident electromagnetic field E_{inc} with wavelength λ induces a current density J_S on the strips shown in Fig. 2. J_S follows from the integral equation

$$\int H_0^{(2)}(k|x - x'|) J_S(x') dx' = \frac{4}{k\eta} E_{\mathrm{inc}}(x) \tag{15}$$

with integration over all strips. $H_0^{(2)}$ is a Bessel function of the third kind, $k \approx 2\pi/\lambda$ and η the impedance of free space. Using pulse basis functions and delta functions as weighting functions (point matching) one get an excellent approximation for J_S after the 1st cycle as seen in Fig. 3, which shows the induced current on a single strip for the 1st and the 50th cycle. The Integrated Square Error versus the number of the cycles is seen in Fig. 4. In this case you get a better *convergence without the* Integrated Square Error Criterion.

Fig. 5 shows the induced currents on 5 parallel strips, Fig. 6 the Integrated Square Error versus the number of the cycles for two different segment-shiftings of successive iteration steps. As in Fig. 3 you get a very good approximation for the solution after the 1st cycle. Comparing the computation times for the inversion of the matrices shows, that the time spending for one cycle is about 5 times quicker for curve a) and 12 times quicker for curve b) in Fig. 7 than the inversion of the complete $M \times M$-matrix.

6 Scattering of a Dipole

The induced current $I(z)$ on a thin dipole with length $2L$ and radius a is described with [3] by

$$\frac{\eta}{4\pi jk} \int_{-L}^{L} I(z') \left[2r^2(1 + jkr) - (\rho^2 + a^2)(3 + 3jkr - k^2r^2)\right] \frac{e^{-jkr}}{r^5} dt = -E_{inc}(z) , \tag{16}$$

with $r = \sqrt{\rho^2 + a^2 + (z - t)^2}$ and ρ, z the cylindrical coordinates on the dipole. Using pulse basis functions and point matching yields the Integrated Square Error in Fig. 7 for two dipoles of different lenghts. For the short dipole one get a good convergence. The Integrated Square

Error Criterion deteriorates the convergence, but is necessary for the $\lambda/2$-dipole.

The implementation of this method into MININEC [3] and Richmond [4] yields similar results. Only for short dipoles one get an efficient convergence. To improve the convergence, I have programmed the reaction integral equation in [4] with overlapping sinusoidal current distributions shown in Fig. 8 as basis and weighting functions. Choosing an offset Δ_{off} for the basis functions extending over two segments modifies the elements of the impedance matrix and results in the Integrated Square Errors in Fig. 9, which shows a good convergence for increasing Δ_{off} without the Integrated Square Error Criterion.

References

[1] Lindell, I.V.; Nikoskinen, K.I.: "Application of Moment Iteration Method (MIM) to Electromagnetic Field Computation", AEÜ, Vol.42, No. 4, 1988, pp. 248-253

[2] Van den Berg, P. M.: "Iterative Computational Techniques in Scattering Based Upon the Integrated Square Error Criterion", IEEE Trans. Antennas and Propagation, Vol. AP-32, No. 10, Oct. 1984, pp. 1063-1071

[3] Richmond, J.H.: "A Wire-Grid Model for Scattering by Conducting Bodies", IEEE Trans. Antennas and Propagation, Vol. AP-14, No. 6, Nov. 1966, pp. 782-786

[4] S.T.Li, J.W. Rockway, J.C.Logan, D.W.S.Tam: "Microcomputer tools for communications engineering", Artech House Inc., Washington ST., Dedham, MA, 1983

[5] J.H. Richmond: "Computer program for thin wire structures in a homogeneous conducting medium", Ohio State Univ., Jun. 1974, NASA-CR-2399

Figures

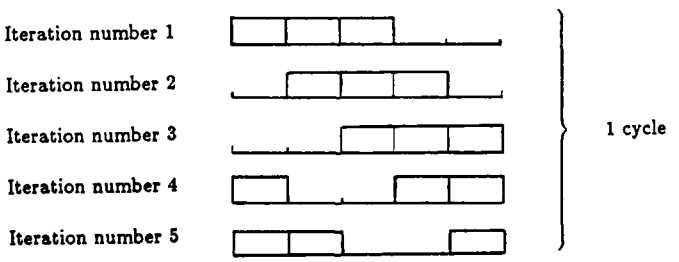

Figure 1: Shifted pulse basis functions for 1 cycle

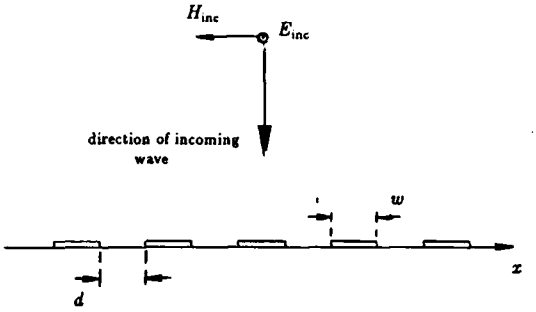

Figure 2: 5 parallel strips with perpendicular incidence of an incoming electromagnetic wave

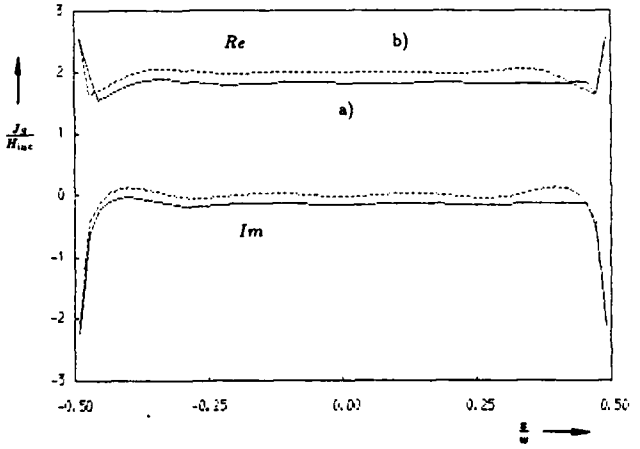

Figure 3: Real and imaginary part of the induced current density J_S on a single strip ($kw = 24, M = 55, N = 5$, 1 segment-shifting of successive iteration steps)
a) After 1st cycle
b) After 50th cycle

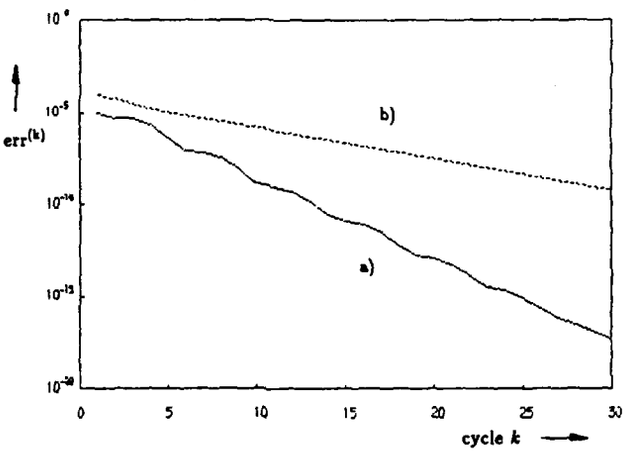

Figure 4: Integrated Square Error $err^{(k)}$ versus the number of cycles for a single strip ($kw = 24, M = 55, N = 5$, 1 segment-shifting of successive iteration steps)
a) Without ISEC
b) With ISEC

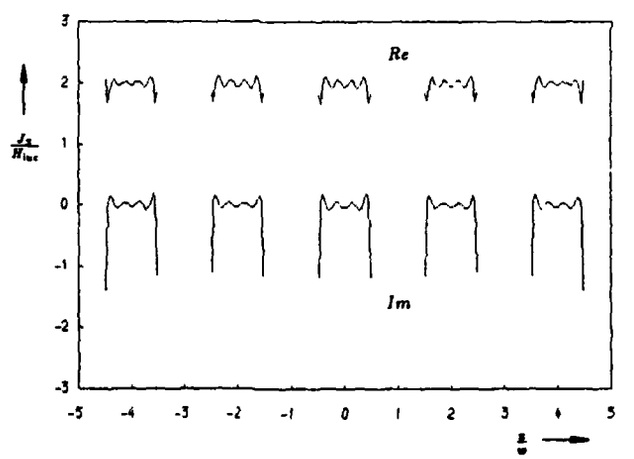

Figure 5: Real and imaginary part of the induced current density J_S on 5 parallel strips after the 1st cycle ($kw = 24, d = w$, M=150, $N = 30$, 30 segment-shiftings of successive iteration steps)

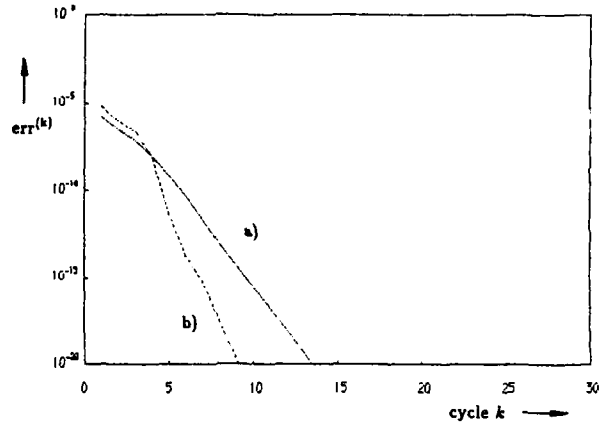

Figure 6: Integrated Square Error $err^{(k)}$ versus the number of cycles for 5 parallel strips ($kw = 24, d = w$)
a) $M = 150, N = 15$, 10 segment-shiftings of successive iteration steps
b) $M = 150, N = 30$, 30 segment-shiftings of successive iteration steps

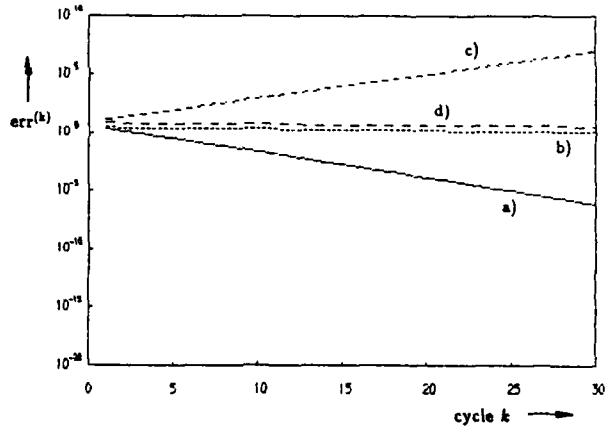

Figure 7: Integrated Square Error $err^{(k)}$ versus the number of cycles for a single dipole (λ=1 m , a=0.001 m , $M = 29, N = 3$, 1 segment-shifting of successive iteration steps)
a) L = 0.1 m (without ISEC) b) L = 0.1 m (with ISEC)
c) L = 0.5 m (without ISEC) d) L = 0.5 m (with ISEC)

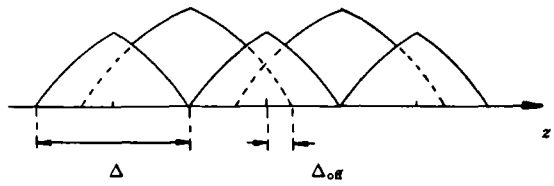

Figure 8: Overlapping sinusoidal basis functions on each segment of length Δ with offset Δ_{off} for the basis functions extending over two segments

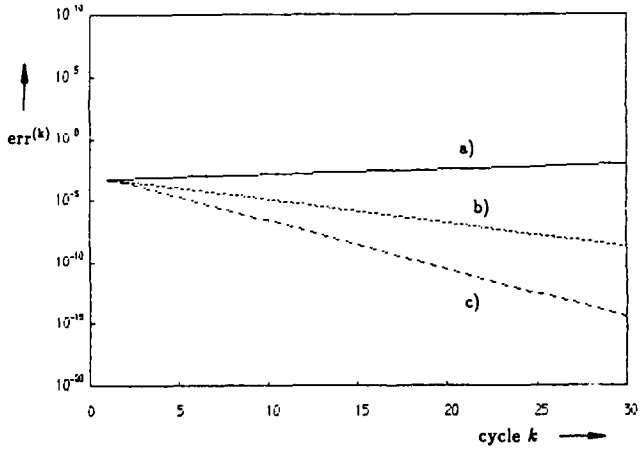

Figure 9: Integrated Square Error $err^{(k)}$ versus the number of cycles for a single dipole without ISEC (λ=1 m , L = 0.5 m , a=0.001 m , $M = 29, N = 3$, 1 segment-shifting of successive iteration steps)
a) Δ_{off}=0 b) Δ_{off}=0.1 Δ c) Δ_{off}=0.2 Δ

THE SPECTRAL ITERATION TECHNIQUE (SIT) APPLIED TO 3D HOMOGENEOUS DIELECTRIC SCATTERERS

A. McCowen and T. V. Tran University of Wales, Swansea

(This work has been carried out with the support of Procurement Executive Ministry of Defence)

INTRODUCTION

For some time now doubts have been expressed about the validity of using the spectral iteration technique (SIT) for solving the electromagnetic problems associated with electrically large scatterers. This potentially powerful numerical technique for the rapid convergence of electromagnetic problems has been prone to difficulties over convergence. In particular there has until recently, been a noticeable absence of any results in the literature for TE incident waves. Mackay and McCowen [1988] have shown that the matrix interpretation of the SIT (MSIT) can be applied as an iterative technique to solve the standard (volume formulation) Methods of Moments for 2D homogeneous dielectric and conducting scatterers. The results yield currents on the body, and hence far-fields, exactly as predicted by the Method of Moments. As with the Method of Moments the MSIT, in its present form, yields erroneous results for conductors since it is based on volume formulation. However, the results for homogeneous dielectric and lossy dielectric cylinders have shown excellent agreement with analytic solutions (circular cylinders only) and, as shown by Mackay and McCowen [1989], the convergence rate is very rapid for both TE and TM cases. This paper will show how the MSIT has been extended into 3D in the code MSIT3D for homogeneous dielectric and lossy dielectric scatterers. This code has recently been developed at Swansea and shows, for the first time, that the SIT can be made to work in 3D.

THE MSIT

The electric field integral equation (EFIE) is written as

$$\int_{\text{volume}} \underline{\underline{G}}(\underline{r}, \underline{r}') \cdot \underline{J}(\underline{r}')\, dr' = -\underline{E}(\underline{r}) \qquad (1)$$

where $\underline{J}$ is the current distribution on the scatterer, $\underline{E}$ is the scattered electric field distribution and $\underline{\underline{G}}$ is the free-space Green's dyad. This integral is of convolution form in the spatial domain and can be transformed, usually by the fast Fourier Transform (FFT), into the spectral ($\underline{k}$-space) domain where the problem can be computed more efficiently. In addition defining the problem in the spectral domain considerably reduces the computer

storage associated with the Green's matrix.

The basic outline of the original SIT as proposed by Bojarski [1971] is shown in Table I in which $\underline{J}^{(n)}(\underline{r})$ is the nth estimate of the unknown current distribution on the scatterer of volume V. The scheme is started with an initial guess of the current distribution. The associated electric field $\underline{E}^{(n)}(\underline{r})$, for the nth estimate $\underline{J}^{(n)}(\underline{r})$, is determined by transforming equation (1) into the spectral domain to determine $\tilde{\underline{E}}^{(n)}(\underline{k})$ which can subsequently be transformed back into the spatial domain to yield $\underline{E}^{(n)}(\underline{r})$. Boundary condition can then be enforced to yield the next estimate of $\underline{E}^{(n+1)}(\underline{r})$. Similarly the next estimate of $\underline{J}$ is determined via computations in the spectral domain and subsequent enforcement of boundary conditions to yield $\underline{J}^{(n+1)}(\underline{r})$. The boundary conditions on $\underline{J}$ are usually that of the physical requirement of confining the current distribution to the volume V. As can be seen from Table I, only the Green's matrix $\tilde{\underline{G}}(\underline{k})$ in the spectral domain is required to be stored which represents a considerable saving in computer memory over the storage of $\underline{G}$ in the spatial domain.

TABLE I

spatial domain		*spectral domain*
$\underline{J}^{(n)}(\underline{r})$	$\underline{r}\epsilon V$	$\longrightarrow \tilde{\underline{J}}^{(n)}(\underline{k})$
0	$\underline{r}\notin V$	
$\underline{E}^{(n)}(\underline{r})$		$\longleftarrow \tilde{\underline{E}}^{(n)} = \tilde{\underline{G}} \cdot \tilde{\underline{J}}^{(n)}$
$\underline{E}^{(n+1)}(\underline{r})$		$\longrightarrow \tilde{\underline{E}}^{(n+1)}(\underline{k})$
$\underline{J}^{(n+1)}(\underline{r})$		$\longleftarrow \tilde{\underline{J}}^{(n+1)} = \tilde{\underline{G}}^{-1} \cdot \tilde{\underline{E}}^{(n+1)}$

In its original form the SIT suffers from significant convergence difficulties. This is due to the pointwise sampling of the analytic Green's matrix in $\tilde{\underline{G}}(\underline{k})$ which contains a singularity in the spectral domain at $|k| = k_o$. The MSIT, however, samples the Green's term in the spatial domain. This is tantamount to setting up the Method of Moments problem which turns the EFIE of equation (1) into the matrix equation

$$\begin{bmatrix} G_v^{11} & G_v^{12} & G_v^{13} \\ G_v^{21} & G_v^{22} & G_v^{23} \\ G_v^{31} & G_v^{32} & G_v^{33} \end{bmatrix} \begin{bmatrix} \underline{J}_x \\ \underline{J}_y \\ \underline{J}_z \end{bmatrix} = \begin{bmatrix} \underline{E}_x \\ \underline{E}_y \\ \underline{E}_z \end{bmatrix} \qquad (2)$$

where the vectors $\underline{E}_{inc} = [\underline{E}_x, \underline{E}_y, \underline{E}_z]^T$ and $\underline{J} = [\underline{J}_x, \underline{J}_y, \underline{J}_z]^T$ represent the known incident electric field and unknown current distribution on the scatterer. The MSIT uses Van den Berg's [1984] conjugate contrast–source truncation (CCST) algorithm to iteratively solve the 3D version of equation (2). In this scheme the solution for the current $\underline{J}$ is constructed from a sequence of global basis functions each of which is successively generated by spectral iteration. A variation principle is applied to minimise an error norm.

The 3D current vector $\underline{J}$ is approximated by $\underline{J}^{(n)}$ in the nth iteration of the scheme, see Table II, where

$$\underline{J}^{(n)} = \underline{J}^{(o)} + \sum_{i=1,n} \eta^{(i)} \underline{j}^{(i)} \qquad (3)$$

$\underline{J}^{(o)}$ represents the initial guess, which is taken to be the zero vector, $\eta^{(n)}$ (scalar) is a variational parameter and $\underline{j}^{(n)}$ is a variational function. At each iteration a 3D field residual $\underline{F}^{(n)}$ is determined by

$$\underline{F}^{(n)} = \underline{E}_{inc} - G\,\underline{J}^{(o)} - \sum_{i=1,n} \eta^{(i)} \underline{j}^{(i)}$$

$$= \underline{F}^{(n-1)} - \eta^{(n)} \underline{f}^{(n)} \qquad (4)$$

and $$\underline{f}^{(n)} = G\,\underline{j}^{(n)} \qquad (5)$$

$\eta^{(n)}$ is generated in such a way as to reduce the field residual squared magnitude, $err^{(n)}$ at each iteration where

$$err^{(n)} = < \underline{F}^{(n)}, \underline{F}^{(n)} >$$

$$= \sum_{i,j,k} [F_1^{(n)*} F_1^{(n)} + F_2^{(n)*} F_2^{(n)} + F_3^{(n)*} F_3^{(n)}] \qquad (6)$$

and i, j and k span the range of grid points over the domain of the object. The "second minimisation step" included in Table II further reduces $err^{(n)}$ and hence improves convergence but at the expense of storing in computer memory the previous $\underline{f}^{(n-1)}$ and $\underline{j}^{(n-1)}$ vectors.

It should be noted that each of the six different G_{ν}^{ij} matrices in equation (2) needs to be extended (by at least a factor of two) to produce a circulant matrix suitable for the application of an FFT. As shown by McCowen and Tran [submitted] a further expansion of the spatial matrices is required (typically to a factor of three), while maintaining their circulancy, to achieve convergence of the MSIT.

TABLE II

spatial domain	spectral domain
$n = 0$	$\underline{E}^{(0)}(\underline{r}) = \underline{\mathcal{E}}^{(0)}(\underline{r})$ $\mathrm{err}^{(0)} = \langle \underline{E}^{(0)}, \underline{E}^{(0)} \rangle$
$n = n + 1$	
$\underline{E}^{(n-1)}(\underline{r})$ $\underline{r}\in V$; 0 $\underline{r}\notin V$	$\longrightarrow \tilde{\underline{E}}^{(n-1)}$
$\underline{j}^{(n)}(\underline{r})$	$\longleftarrow \tilde{\underline{j}}^{(n)} = (\tilde{\underline{G}}')^{-1}\, \tilde{\underline{E}}^{(n-1)}$
$\underline{j}^{(n)}(\underline{r})$ $\underline{r}\in V$; 0 $\underline{r}\notin V$	$\longrightarrow \tilde{\underline{j}}^{(n)}$
$\underline{f}^{(n)}(\underline{r})$	$\longleftarrow \tilde{f}^{(n)} = \tilde{\underline{G}}' \cdot \tilde{\underline{j}}^{(n)}$
$A^{(n)} = \langle \underline{E}^{(n-1)}, \underline{f}^{(n)} \rangle$	
$B^{(n)} = \langle \underline{f}^{(n)}, \underline{f}^{(n)} \rangle$	
if $n > 1$	$\underline{j}^{(n)}(\underline{r})$, $\underline{f}^{(n)}(\underline{r})$ and $B^{(n)}$ are modified as follows (second minimization step)
	$C^{(n)} = \langle \underline{f}^{(n)}, \underline{f}^{(n-1)} \rangle$
	$\xi^{(n)} = C^{(n)*} / B^{(n-1)}$
	$B^{(n)} := B^{(n)} - \xi^{(n)} C^{(n)}$
	$\underline{j}^{(n)} := \underline{j}^{(n)} - \xi^{(n)} C^{(n)}$
	$\underline{f}^{(n)} := \underline{f}^{(n)} - \xi^{(n)} \underline{f}^{(n)}$
	$\eta^{(n)} = A^{(n)*} / B^{(n)}$
	$\underline{J}^{(n)}(\underline{r}) = \underline{J}^{(n-1)}(\underline{r}) + \eta^{(n)} \underline{j}^{(n)}(\underline{r})$
	$\underline{E}^{(n)}(\underline{r}) = \underline{E}^{(n-1)}(\underline{r}) - \eta^{(n)} \underline{f}^{(n)}(\underline{r})$
	$\mathrm{err}^{(n)} = \langle \underline{E}^{(n)}, \underline{E}^{(n)} \rangle$

RESULTS

In this section we wish to show detailed results from a few of the particular examples to be presented in the paper, all of which were generated on a VAX 8700. Firstly, Figure 1 shows the normalised bistatic RCS due to plane wave incidence on a $0.191\lambda_0$ dielectric sphere. The figure compares the analytic E and H-plane solutions to those obtained using the MSIT which are equivalent, as with all the examples, to the Method of Moments solutions with pulse basis functions. The sphere was discretised into $(0.04775\lambda_0)$ cubes which generated 96 unknowns. 4 iterations were required to achieve convergence with a total CPU of 35 sec.

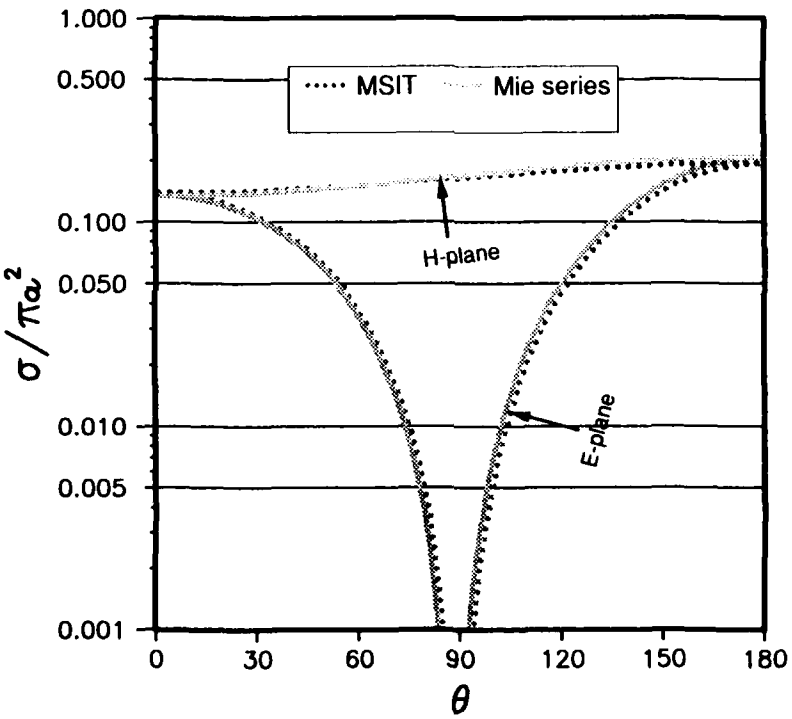

Figure 1: Normalised bistatic RCS from a pure dielectric $0.191\lambda_0$ with relative permittivity 4.43. $\theta = 0^\circ$ is the angle of backscatter.

Figure 2 shows similar results for a larger sphere of lossy dielectric material. ($0.075\lambda_0$) cubes were used to discretise this sphere which generated 4416 unknowns. Only 10 iterations were needed to achieve convergence with a total CPU of 53 mins. Table III shows the print out from the MSIT3D code after each iteration for this particular example. The right-hand column lists the ratio, $\| \underline{E}^{(n)} \| / \| \underline{E}^{i} \|$, the normalised integrated square error, which we specify to be less than 0.5 E-3 for convergence in all our examples.

TABLE III

$\| E^i \| = 0.788$

N	$\|\underline{J}^{(n)}\| / \Delta V$	$\|\underline{E}^{(n)}\|$	$\|\underline{E}^{(n)}\| / \|\underline{E}^{i}\|$
1	22.732	0.354	0.449
2	22.735	0.8527E-1	0.108
3	22.461	0.4154E-1	0.527E-1
4	22.857	0.1803E-1	0.229E-1
5	22.752	0.1028E-1	0.130E-1
6	22.691	0.4860E-2	0.617E-2
7	22.671	0.1766E-2	0.224E-2
8	22.684	0.9897E-3	0.126E-2
9	22.677	0.5454E-3	0.692E-3
10	22.679	0.2739E-3	0.348E-3

REFERENCES

N. N. Bojarski
"K-space formulation of the electromagnetic scattering problems", Tech. Rep., AFAL-TR 71-75, March 1971.

P. M. Van den Berg
Iterative computational techniques in scattering based upon the integrated square error criterion", IEEE Trans. Antennas Propagat., Vol AP-32, pp 1063-1071, October 1984.

. J. Mackay and A. McCowen
Matrix interpretation of the Spectral Iteration Technique", IEEE Trans. Antennas Propagat., ol 36, pp 950 - 955, July 1988.

J. Mackay and A. McCowen
Convergence criteria for the extended Matrix version of the Spectral Iteration Technique", EE Antennas Propagat., Vol AP-37, pp 1150 - 1155, September 1989.

McCowen and T. V. Tran
Matrix interpretation of the Spectral Iteration Technique for 3D dielectric scatterers in the onance region", Submitted for publication.

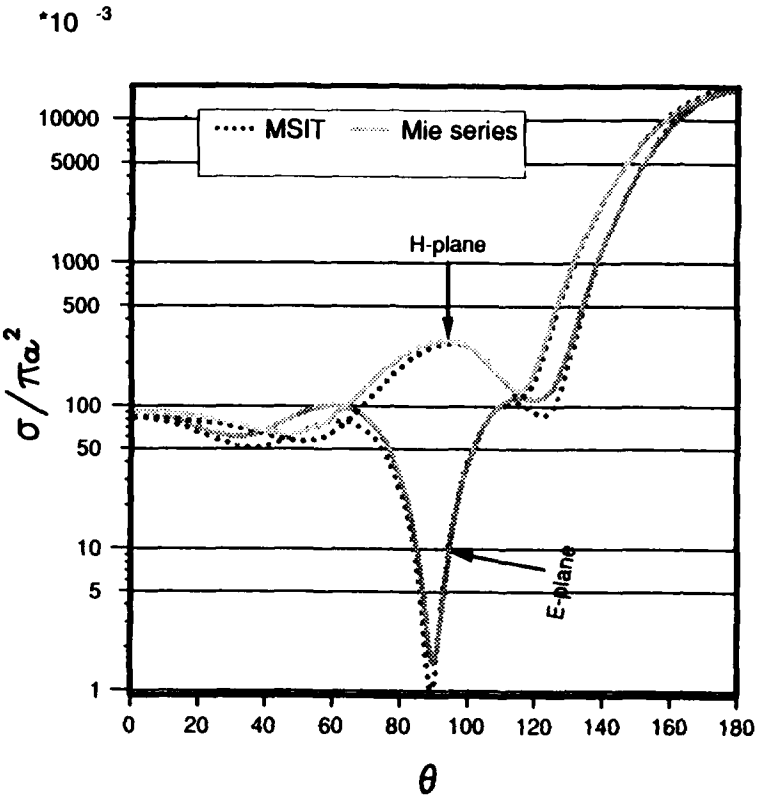

Figure 2: Normalised bistatic RCS from a lossy-dielectric $1.05\lambda_0$ sphere with complex relative permittivity 1.5 - j 1.5. $\Theta = 0^{\circ}$ is the angle of backscatter.

Some Modifications to the Numerical Electromagnetics Code and their Effects

T. H. Hubing
University of Missouri-Rolla
Rolla, MO 65401

J. F. Kauffman
North Carolina State University
Raleigh, NC 27695

Abstract

The Numerical Electromagnetics Code (NEC2) does not always yield consistent or accurate results when analyzing configurations that contain thin conductive surfaces or configurations with sources located near a wire-surface attachment. This paper evaluates modifications to the code designed to "test the limits" of the NEC2 algorithm. These modifications can significantly increase the amount of time required for the algorithm to run and do not necessarily belong in a "general purpose" EM modeling code. Nevertheless, the modified code is able to analyze configurations that the unmodified algorithm is unable to analyze and the results obtained using the modified code can help the user to understand where certain types of error originate.

Introduction

The Numerical Electromagnetics Code [1] is a general-purpose moment-method computer program capable of analyzing the electromagnetic scattering properties of a variety of wire-surface geometries. Several other general-purpose moment-method codes are available, however NEC is unique in that it is the only widely-distributed, well-documented code that analyzes surfaces by solving a form of the magnetic field integral equation (MFIE). MFIE-based algorithms have certain computational advantages over algorithms that analyze surfaces by solving the electric field integral equation (EFIE). However, MFIE-based codes do not model electrically thin conductive surfaces efficiently. The inability of the Numerical Electromagnetics Code to analyze geometries with thin metal plates significantly limits its potential applications.

Another limitation of the NEC algorithm is its inability to accurately calculate the input impedance of sources located near a wire-surface attachment point. The method used by NEC2 to model wire-surface attachments analyzes simple configurations accurately and efficiently, however a more detailed wire-attachment model is required for many applications.

The purpose of this paper is to investigate the thin-surface and wire-attachment limitations of NEC2. In the course of this investigation, modifications to the algorithm will be introduced. These modifications expand the scope of the algorithm at the expense of requiring additional computation.

Thin Surfaces

The form of the MFIE used by NEC2 to analyze conductive surfaces is,

$$\boldsymbol{J_s}(x) = 2\hat{n}\times\boldsymbol{H^i} + 2\hat{n}\times\int_s \boldsymbol{J_s}(x')\times\nabla' G(x,x')\,ds \quad . \tag{1}$$

The $2\hat{n}\times\boldsymbol{H^i}$ term is the component of $\boldsymbol{J_s}(x)$ that is due directly to the incident magnetic field. The $2\hat{n}\times\int_s \boldsymbol{J_s}(x')\times\nabla' G(x,x')\,ds$ term is the component of $\boldsymbol{J_s}(x)$ induced by the fields from the induced surface currents at all points on the surface except the neighborhood of the point $x' = x$. A detailed derivation of Equation (1) can be found in [2].

Conductive surfaces are represented as a collection of surface "patches" in NEC2. The surface current on each patch that is not connected to a wire is described by two impulse functions. The two impulses represent components of current flowing in each of two orthogonal directions on the surface. This modeling technique is referred to as point matching since the boundary conditions are enforced at individual points on the surface. The surface integral on the right hand side of

Equation (1) is reduced to a simple multiplication, which significantly reduces the time required to compute the values of the impedance matrix.

The surface current integral in Equation (1) is only used to calculate off-diagonal terms of the impedance matrix. Large smooth surfaces result in well-conditioned diagonally dominant impedance matrices [3]. Small errors in the calculation of off-diagonal terms do not tend to significantly affect the accuracy of the result when analyzing large surfaces. Relatively small surfaces or thin plates, on the other hand, are more sensitive to errors in the calculation of the off-diagonal terms. The analysis of small or thin surfaces requires a more careful evaluation of the integral in Equation (1). In other words, a weighting function other than an impulse is needed. For our purposes, a pulse function was considered to be the best trade-off between an impulse function and more complex weighting functions that would require considerably more computation time. Flexibility and ease of data entry was a primary consideration.

When point matching is used, it is not necessary to know the exact shape of a patch or the location of its edges. Pulse weighting functions require the shape and location of the patch to be known but they do not require a knowledge of how a patch is oriented relative to the other patches. Switching from impulse to pulse weighting functions required two basic modifications to the algorithm:

1. Describing the patch geometry to the necessary subroutines
2. Using this data to evaluate the surface integral in Equation (1).

The original code accepted a variety of patch shapes and even allowed a patch to be defined with an arbitrary, unspecified shape. The only data used by the algorithm was the patch area and center point location. In order to facilitate both of the tasks listed above, only rectangular patches are permitted in the modified code.

The subroutine DATAGN was modified to read or calculate the corner points of each surface patch and store them in the common block, PCORNR. The single multiplication that used to perform the integration in Equation (1) was replaced by a double sum of the form,

$$\int_s J_s(x')\, G(x,x')\; ds \approx \frac{A}{N^2} \sum_{i=1}^{N} \sum_{j=1}^{N} J(x_{ij})\, G(x,x_{ij}) \qquad (2)$$

where: J = constant pulse amplitude

A = area of surface patch

N^2 = # of subpatches

x_{ij} = center point of $(ij)^{th}$ subpatch

This simple method for estimating the value of the surface integral is referred to as the mid-point rule [4]. It is similar to trapezoidal rule integration in terms of efficiency and error but it avoids problems that can occur when the integrand has singularities at the end-points. Larger values of N result in more accurate evaluations of the integral at the expense of additional computation time. When N equals 1, this method is equivalent to the original point-matching technique.

Note that if G(x,x') is fairly constant over the surface of the patch, relatively small values of N are required. However, when G(x,x') is a strong function of position (as it is for example when evaluating the interaction between two patches on opposite sides of a thin plate), larger values of N are necessary to achieve a given level of accuracy. The NEC2 subroutine HINTG was modified to do the midpoint rule integration. The value of N is stored in the variable NPATCH at the beginning of the modified subroutine. The subroutine UNERE, which evaluates a form of the EFIE for

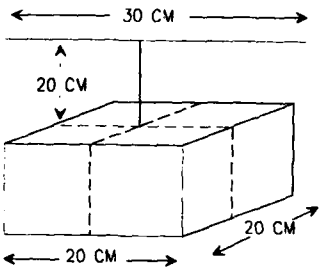

Figure 1: Wire-T Configuration

analyzing wire-to-surface interactions was also modified to perform a midpoint rule integration. The value of N used for this integration is stored in the variable NSTEP. NSTEP and NPATCH are independent of one another, since the accuracy of the surface integration required for the EFIE may not be the same as the accuracy required for evaluation of the MFIE.

In order to evaluate the effect of this modification to the NEC2 code, one of the example problems from the NEC2 User's Guide [1] was analyzed using different values for NPATCH and NSTEP. The configuration is illustrated in Figure 1. It consists of a 1 volt, 300 MHz source driving a wire-T relative to a 20x20x10 cm metal box resting on a ground plane.

As the User's Guide points out, a lossless structure over a ground plane should have an average power gain of 2.0. The calculated average power gain for this example however, is about 1.8 indicating that the calculated input impedance (about $181 + j218$ ohms) may be inaccurate.

The User's Guide cites the relatively crude way that the patches are modeled as the probable source of the error, however a closer examination of this and other examples reveals another problem. During the course of this work, it was observed that inconsistent results were obtained whenever a voltage source was located on a wire segment with one end attached to a surface patch. The reason for this relates to the way that voltage sources are modeled by the program [3]. The error can usually be reduced by using shorter segment lengths in the vicinity of a patch attachment and placing at least one segment between the surface and the segment containing the source. This was done for the example in Figure 1 by subdividing the surface-attached wire segment into 3 smaller segments of equal length. The source was located on the center segment making it the same height above the surface.

The program was run again and the new value calculated for the input impedance was 176 - j413 ohms and the average power gain was 1.82. This was significantly different from the 181 + j218 ohm impedance that was originally calculated but even this value is not correct. Another modification to the NEC2 code intended to improve the accuracy of wire-to-surface attachment calculations was applied and the new calculated value of the input impedance became 195 + j260 ohms. (This modification is described in the next section.) Using this impedance as a starting point, Table 1 shows the effect of increasing the values of the variables NPATCH and NSTEP. Note that in this example, the results stabilize for values of NPATCH and NSTEP greater than 5.

Table 1: Effect of NPATCH and NSTEP on Wire-T

NSTEP	NPATCH	NINT	INPUT Z	AVE. PG
1	1	48	195+j260	1.81
5	1	48	188+j258	1.87
15	1	48	188+j258	1.87
15	5	48	174+j272	1.89
15	15	48	174+j272	1.89
5	15	48	174+j272	1.89
1	15	48	180+j274	1.84

Wire-to-Surface Attachments

Errors related to the use of point matching can generally be overcome without modifying the algorithm by simply using a larger number of patches to represent the surface when sufficient computing resources are available. However, there is another source of error that arises when using NEC2 to analyze small or thin surfaces with a wire-to-surface attachment point that cannot be compensated for without modifying the algorithm.

NEC2 allows wires to be attached to a surface at patch centers. The procedure for analyzing wire-surface attachments used by NEC2 is based on a technique used by Albertsen et al [5]. When a wire surface attachment is made, NEC2 divides the region near the attachment point into four subpatches as illustrated in Figure 2. The expansion of the surface current density in this region must satisfy the following condition,

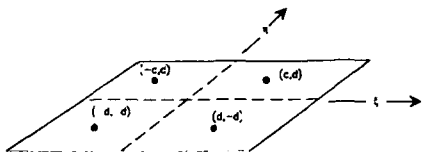

Figure 2: Wire Attachment Point

$$\nabla_s \cdot \boldsymbol{J}_s(\xi,\eta) = \boldsymbol{J}_o(\xi,\eta) + I_o\,\delta(\xi,\eta) \qquad (3)$$

where ∇_s denotes surface divergence, $\boldsymbol{J}_o(\xi,\eta)$ is a continuous function in the region of the attachment, and I_o is the wire current flowing onto the surface. The expansion function used by NEC2 is,

$$\boldsymbol{J}_s(\xi,\eta) = I_o f(\xi,\eta) + \sum_{j=1}^{4} g_j(\xi,\eta)\,[\boldsymbol{J}_j - I_o f_j] \qquad (4)$$

$$\text{where } f(\xi,\eta) = \frac{\xi\hat{\xi} + \eta\hat{\eta}}{2\pi(\xi^2+\eta^2)}$$

$$\boldsymbol{J}_j = \boldsymbol{J}_s(\xi_j,\eta_j)$$

$$f_j = f(\xi_j,\eta_j)$$

and ξ_j,η_j are the coordinates at the centers of patch j. The interpolation functions $g_j(\xi,\eta)$ used by NEC2 are:

$$g_1(\xi,\eta) = \frac{1}{4d^2}(d+\xi)(d+\eta) \qquad (5a.)$$

$$g_2(\xi,\eta) = \frac{1}{4d^2}(d-\xi)(d+\eta) \qquad (5b.)$$

$$g_3(\xi,\eta) = \frac{1}{4d^2}(d-\xi)(d-\eta) \qquad (5c.)$$

$$g_4(\xi,\eta) = \frac{1}{4d^2}(d+\xi)(d-\eta) \qquad (5d.)$$

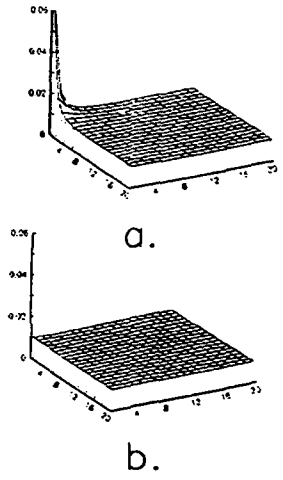

Figure 3: Current Expansion Functions for a Patch with a Wire Attachment

A plot of the magnitude of this current expansion function for the case $\boldsymbol{J}_1 = \boldsymbol{J}_2 = \boldsymbol{J}_3 = \boldsymbol{J}_4$ is shown in Figure 3a. The surface current expansion in Equation (4) is used *only when computing the electric field at the center of the attached wire segment due to the surface current on the four surrounding patches.* An impulse expansion of this patch current is used to calculate the fields at all of the other wire segment centers.

This technique for analyzing wire-surface attachments is relatively simple. It doesn't require excessive computation and it doesn't place severe restrictions on the size or placement of wire attachment regions. However the errors introduced by this simple technique may be unacceptable, particularly in situations where an accurate calculation of the input impedance of a source on a wire near a surface attachment point is desired.

One source of error arises from the fact that the surface current expansion, Equation (4), is defined over a square region centered at the wire attachment point even when the patch to which

the wire is connected is not square. Since the unmodified NEC2 does not consider the shape of a patch when performing a surface integration, there would be little to gain by defining the wire attachment region to be a specific shape. However, with the modifications described in the previous section, surface integrations are performed using specific patch dimensions. If the wire attachment current expansion function is not modified, the surface integration would be performed twice in some areas and not at all in others.

Two modifications are required to make the program integrate the surface current expansion function over the correct patch surface. First, the limits of the integration in Equation (4) must be changed to correspond to the corners of the patch. This is done by modifying the subroutine PCINT. Second, the interpolation functions, Equations (5), must be modified so that the points ξ_j,η_j are at the centers of the four subpatches. The new interpolation functions can be written:

$$g_1(\xi,\eta) = \frac{1}{4d_1d_2}(d_1+\xi)(d_2+\eta) \tag{6a.}$$

$$g_2(\xi,\eta) = \frac{1}{4d_1d_2}(d_1-\xi)(d_2+\eta) \tag{6b.}$$

$$g_3(\xi,\eta) = \frac{1}{4d_1d_2}(d_1-\xi)(d_2-\eta) \tag{6c.}$$

$$g_4(\xi,\eta) = \frac{1}{4d_1d_2}(d_1+\xi)(d_2-\eta) \tag{6d.}$$

where d_1 and d_2 are the ξ and η components of the distance to the center of each subpatch. This modification to the interpolation functions was also made in the subroutine PCINT.

There is a second source of error with this wire-attachment method that is not quite as apparent. This error arises from the fact that two different current expansion functions are used to represent the current in the region of a wire attachment. The current expansion function in Equation (4) is used to calculate the electric field at the center of the *attached* wire segment due to the current on the four subpatches,

$$E_{attached} = \int_s J_s(\xi,\eta)\, G(w,\xi,\eta)\, ds \ . \tag{7}$$

while the electric field at the center of *non-attached* wire segments is calculated using an impulse expansion of the current on the four subpatches,

$$E_{non\text{-}attached} = \sum_{j=1}^{4} J_j\, A\, G(w,\xi,\eta) \ . \tag{8}$$

The variable w represents the coordinates at the center of the wire segment at which the field is evaluated in Equations (7) and (8) and A is the area of one subpatch.

Two types of error result from this approximation. One source of error is due to the fact that in many configurations, particularly those involving wire segments located close to a surface, $G(w,\xi,\eta)$ can vary significantly over the integration surface. However, even when $G(w,\xi,\eta)$ is relatively constant in the region of a wire attachment, error is introduced.

To illustrate this, assume for the moment that all of the wire segments except for the attached segment are relatively far from the attachment subpatches and the $G(w,\xi,\eta)$ can be approximated as a constant, G, over the surface of integration, Equation (7) can be written,

$$E = G \int_s J_s(\xi,\eta)\, ds \tag{9}$$

substituting for $J_s(\xi,\eta)$ using Equation (4) and filling in the integration limits for the first of the four subpatches,

$$E_{attached} = G \int_0^{2d_1} \int_0^{2d_2} \left[I_o f(\xi,\eta) + \sum_{j=1}^{4} g_j(\xi,\eta) (J_j - I_o f_j) \right] ds \tag{10}$$

The electric field due to the current in the first subpatch calculated using Equation (8) making the same assumption is,

$$E_{non-attached} = G J_1 A \quad . \tag{11}$$

In order to determine how good this approximation is, we can evaluate the integral of Equation (10) assuming for the moment that $J_1 = J_2 = J_3 = J_4$ and that $d_1=d_2=d$. The field due to the ξ component of the current is given below. By symmetry, a similar result can be obtained for the η component.

$$E_{attached} = G \int_0^{2d_1} \int_0^{2d_2} \left[I_o f(\xi,\eta) + \sum_{j=1}^{4} g_j(\xi,\eta) (J_j - I_o f_j) \right] ds = G \left[I_o \frac{d}{\pi} (3 - 2\sqrt{2} - 1) + J_1 A \right] \tag{12}$$

The term at the far right, $J_1 A$, is equivalent to the approximation of Equation (11). However, there is an additional term, which is a function of I_o, that the approximation neglects. Therefore even when G can be considered relatively constant over the integration, the two current expansion functions used to represent patches attached to wire segments are not equivalent.

Another way to view this is illustrated in Figure 3. The current expansion functions in Figure 3a. and Figure 3b. are both used to represent the current on the same patch for different calculations. However, the volume under each of these curves is not equal. The moment method program calculates a single value for J based on two inconsistent expansion functions. This introduces error into the calculated value of J.

The actual error term is highly dependent on the integration technique used in the vicinity of the wire attachment. When using midpoint rule integration, the calculated volume under the curve in Figure 3a. is very dependent on N because of the singularity at the origin. The value of N used for this integration is stored in the variable NINT in the subroutine PCINT. Larger values of N increase the accuracy of the calculation in Equation (10), but do not necessarily reduce the error term.

One way to eliminate this error would be to define the expansion function, Equation (4) and the integration technique so that the volume under each of the surface curves in Figure 3 is equal. This is difficult to do without restricting the shape of the wire-attachment region. Another approach that also eliminates the error due to the non-constant $G(w,\xi,\eta)$, is to use the same expansion function

Table 2: Effect of Modified CMSW on Wire-T

VERSION OF CMSW	NINT	INPUT Z	AVE. PG
ORIGINAL	10	161-j384	1.83
ORIGINAL	12	163-j295	1.82
ORIGINAL	24	173+j77	1.80
ORIGINAL	48	174+j136	1.80
MODIFIED	10	160-j298	1.91
MODIFIED	12	163-j199	1.91
MODIFIED	24	173+j206	1.89
MODIFIED	48	174+j272	1.89
MODIFIED	66	174+j272	1.89

for all of the calculations. The impulse expansion is too simplistic to provide an accurate representation of the patch currents in the area of a wire attachment, so the program was modified to use the expansion of Equations (4,6) to calculate all of the electric fields due to currents on patches connected to wire segments. This was done by modifying the subroutine CMSW. As expected, this significantly increased the amount of time required to calculate the values of the impedance matrix for configurations with many wire segments. The original impulse expansion function for the subpatches was still used to calculate patch-to-patch interactions, because it was felt that the increase in accuracy resulting from this change would not justify the increased amount of computation.

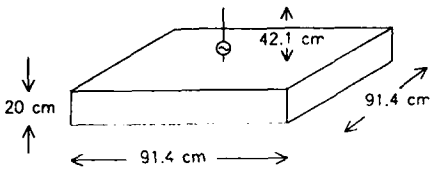

Figure 5: Wire Attachment Example

Table 2 gives the calculated values of input impedance and average power gain for the wire-T configuration in Figure 1 using both the modified and unmodified versions of the subroutine CMSW. The variable NINT represents the number of subpatches used to perform the integration in Equation (4). Note that both versions of the code stabilize for values of NINT somewhere between 25 and 48, but they result in two different solutions. The input impedance calculated with the unmodified algorithm corresponds to a reflection coefficient magnitude of 0.7 when attached to a 50-ohm cable. The input impedance calculated using the modified version of CMSW corresponds to a reflection coefficient magnitude of 0.85, which agrees with the measured value of reflection coefficient obtained using a network analyzer and a copper model of this configuration [3].

Figure 5 shows a configuration consisting of a 42.1 cm wire above a 91.4 x 91.4 x 20 cm conductive surface. The wire is driven by a voltage source located on the wire 8 cm above the surface. This configuration was analyzed using both the modified and unmodified versions of the NEC2 code in the frequency range 125 - 215 MHz. Both the top and bottom of the surface were divided into 25 square patches and the sides were each divided into 5 patches lengthwise. Since the conductive surface is neither small or thin at these frequencies, one might expect point matching to be sufficiently accurate. This is indeed the case as indicated by the plot in Figure 6, which shows that setting the variables NPATCH and NSTEP equal to 1 (as opposed to 15) had little effect on the calculated input conductance. However, the modified wire-attachment technique had a significant effect on the calculations as illustrated in Figure 7. This result shows how the error introduced by using two different expansion functions to represent the surface patches at a wire attachment can significantly affect the calculated input impedance near the attachment point.

Since one of the modifications made to the code was designed to correct a problem that can occur when using non-square patches, this configuration was analyzed again with the top and bottom

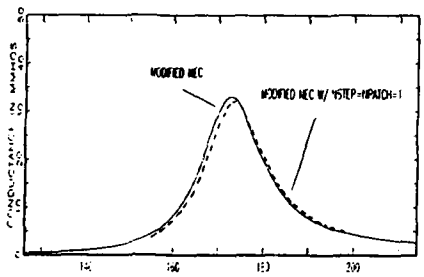

Figure 6: Effect of Point Matching

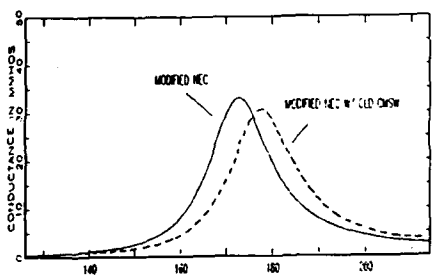

Figure 7: Effect of Modified Wire Attachment

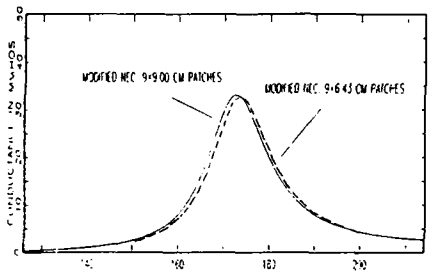

Figure 8: Effect of Patch Shape with Modified Code

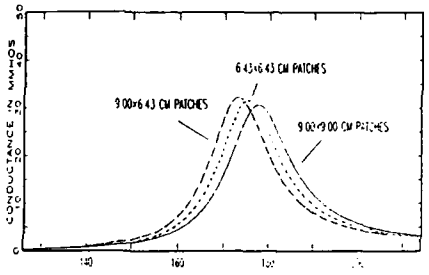

Figure 9: Effect of Patch Shape with Original Code

surfaces divided into 35 (9.00 x 6.43 cm) rectangular subpatches. The configuration being modeled was unchanged, so ideally there should be little change in the calculated results. This is indeed the case using the modified code as shown in Figure 8, however the results from the unmodified code are significantly different as shown in Figure 9.

Conclusions

The Numerical Electromagnetics Code (NEC2) is limited in its ability to analyze even moderately thin conductive surfaces and configurations with a source located near a wire-to-surface attachment. Modifications have been described that can improve the ability of the algorithm to model some types of configurations at the expense of requiring additional computation. In general, the improvement in accuracy applies only to specific types of configurations and the decreased efficiency due to these modifications can be significant.These modifications and their effects should be of interest to anyone trying to test the limits of NEC2 or model configurations that NEC2 isn't able to model accurately.

References

[1] G. J. Burke and A. J. Poggio, *Numerical Electromagnetics Code (NEC)-Method of Moments*, Naval Ocean Syst. Center, San Diego, CA, NOSC Tech. Document 116, Jan. 1981.

[2] A. J. Poggio and E. K. Miller, "Integral Equation Solutions of Three-Dimensional Scattering Problems", *Computer Techniques for Electromagnetics*, R. Mittra editor, Pergamon Press, 1973, Chapter 4.

[3] T. H. Hubing, "Modeling the Electromagnetic Radiation from Electrically Small Sources with Attached Wires", Ph. D. dissertation, North Carolina State University, May, 1988.

[4] A. Ralston and P. Rabinowitz, *A First Course in Numerical Analysis*, McGraw-Hill, 1978, p.432.

[5] N. C. Albertsen et al., "Computation of Radiation from Wire Antennas on Conducting Bodies", *IEEE Transactions on Antennas and Propagation*, vol. AP-22, Mar 1974, pp. 200-206.

The Effects of Mantissa Length on MiniNEC Accuracy

Don Metzger and John Norgard
ECE Dept., University of Colorado
Colorado Springs, CO 80933

Abstract: A method for analyzing the effects which numerical representation have on the accuracy of mathematical algorithms is developed. A comparison with both analytical and experimental results from FFT computations demonstrates the accuracy of the method. Results are given when the method is applied to the MiniNEC code. MiniNEC computations are effected by less than 3% when single precision numbers are used for problems requiring about 500,000 operations (a single wire with 56 segments).

Introduction

With increases in computational power, problems with large numbers of computations (additions, multiplications etc.) are becoming commonplace. One area of concern in obtaining accurate results, is the precision with which floating point values are represented. The use of single precision or double precision quantities effects the memory requirements, speed and accuracy of the results. While the effects of numerical representation on memory and speed are readily evaluated, the effects on the accuracy of the result are not. Assuming that the exponent part of a floating point number is of sufficient size to avoid overflow or underflow, the primary effects on accuracy will be determined by the number of bits used to represent the mantissa.

In this work, a method is presented which allows modification of the mantissa of the result of any floating point mathematical operation. The method is verified by comparison with results for FFT's, where analytical results are available. This method is then applied to the MiniNEC code to determine how mantissa length effects accuracy of the result. Results from altering the mantissa length in different sections of the code (matrix fill, matrix solve etc.) are also discussed.

Experimental Procedure

Floating Point Math on the Macintosh

The Apple Macintosh offers a particularly good platform for calculating the errors introduced into numerical calculations due to limited precision. The heart of

floating-point mathematics on the Macintosh is the Standard Apple Numeric Environment (SANE). SANE is a library of routines that handles all floating point calculations in the absence of a hardware floating point unit. SANE implements the full ANSI-IEEE Std 754 for Binary Floating Point Arithmetic. SANE has only one entry point, different mathematical operations are performed by examining the passed opcode and branching appropriately. It is this structure with a single entry point and passed opcodes which can be exploited to study the reduction of precision in the mantissa.

As an example of how SANE works, consider adding two floating-point numbers. When a program needs to add two numbers, it pushes the addresses of the operands onto the stack, then pushes an address for the result, then pushes an opcode telling SANE to add the numbers, and calls SANE by implementing a system trap. The system trap goes to a look-up table in memory to find the address of SANE and jumps to that location. In order to control all floating point math on the Macintosh, it is merely required to change the address in the look-up table to that of another routine (newSANE).

It is possible to avoid writing a newSANE routine which must handle all necessary mathematical functions. If the address of the original SANE routine is stored before it is modified, newSANE can simply call SANE to perform all math functions. Thus, when SANE returns from its calculations, it returns to newSANE which has all the information necessary (result address and the opcode) to perform the appropriate truncation or rounding of the mantissa.

It is possible to turn-on or turn-off the reduction of precision being performed by newSANE at any point in a numerical algorithm. It is also possible to change the number of bits of precision as the computations proceed. In addition, it is possible to differentiate between types of mathematical operations, reducing precision in some case, while not effecting others. In summary, this method of controlling the precision of calculations offers great flexibility, while being applicable to any algorithm.

There are three precisions of real numbers allowed by SANE: 1) "single" 32 bits with a 23 bit mantissa, 2) "double" 64 bits with a 52 bit mantissa, and 3) "extended" 80 bits with a 64 bit mantissa. The mantissa for each precision is in sign-magnitude representation. These representations are consistent with IEEE Std 754. For this work, the "extended" format was used for all floating point numbers.

Rounding

As mentioned above, the extended format has a mantissa with 64 significant bits. In general, it is desired to limit the mantissa to fewer bits, denoted as b. When a floating point operation occurs, the result may have more than b significant bits and, thus, must be reduced to b bits. The three general methods for reducing to b bits are truncation, rounding and random rounding. Because rounding is the most

commonly used method of reducing precision, discussion and results are limited to it.

Rounding may be accomplished by adding a binary 1 in the b+1 bit location and then truncating by setting all bits from b+1 to 64 to binary 0. An interesting case for rounding is that for which the b+1 bit is 1 and all bits from b+2 to 64 are 0 before the rounding begins. For this case, the value to be rounded lies halfway between the numerical representations to which it is possible to round. For this method of rounding, rounding up will always occur.

Results for a Decimation-in-Frequency FFT

In order to check the accuracy of the methodology, results from the method used here are compared with those published concerning a well studied mathematical algorithm, the FFT. The errors introduced in a standard radix-2, decimation in frequency, FFT algorithm[1] are shown in figure 1. The data from this work is compared to that from Oppenheim and Weinstein[2], who present both analytical and experimental results. In general, there is good agreement. Results for truncation and random rounding also show good agreement, but are not included here for the sake of brevity.

Results for MiniNEC

Figure 2 shows the geometry to be analyzed. A straight dipole is driven in the center. The errors due to reduced precision will be tracked by considering the input impedance of the antenna.

Figures 3 and 4 show the input resistance and input reactance, respectively, when the antenna is divided into 40 segments. The horizontal scale is the number of significant bits in the mantissa. The results denoted "Fill" are when only the matrix fill portion of the algorithm has the number of bits indicated, all other parts of the computation have 64 bit mantissas. Those denoted "Solve" are when only the matrix factor and solve portions use limited precision. Finally, those denoted "Fill & Solve" are for limited precision in the fill, factor and solve parts of the algorithm. The input resistance has more error due to the fill than due to the solve, whereas, the input reactance has more error due to the solve. Both parameters are well converged to the limiting value when 24 bits are used for the mantissa. This is a typical mantissa size for single precision math.

Figure 5 shows the error in the real and imaginary parts of the input impedance when the number of unknowns is varied. These results are for limited precision in the fill, factor and solve portions of the algorithm. Of course, as the number of unknowns is varied, MiniNEC calculates different values of the input

impedance due to the changing number of unknowns. To determine the effects of limited precision, the input impedance is calculated with a 64 bit mantissa and with a 24 bit mantissa. The absolute value of the difference of these two results, divided by the values from the 64 bit case, multiplied by 100% are the percent error. It can be seen that the error for 36 unknowns or more, approaches and exceeds 1% in the imaginary part of the input impedance. The error in the real part is between 2 and 4 orders of magnitude less.

Figure 6 shows the same data as figure 5 except that the horizontal scale is the number of mathematical operations whose results were changed. The number of mathematical operations can be counted by incrementing a counter in newSANE each time it is called. The case of 56 unknowns requires a little over 500,000 floating point operations to perform the calculation. While this represents an execution time in the range of minutes on a personal computer without a math coprocessor, there are numerous systems that can do this number of calculations in fractions of a second (if the speed claims are credible). The implications are significant. These results show that errors on the order of 1% can be produced in very short order, when single precision numbers are used.

It is interesting to note the disparity in the amount of error introduced into the real and imaginary parts of the input impedance. Figure 7 shows one possible explanation for this disparity. This figure shows input impedance as a function of dipole length when the number of segments remains constant at 40 and a 64 bit mantissa is used. Indicated are the values for the length of 48.75 m, the length used in figures 3-6 above. The slope of the imaginary part is much greater than that of the real part. Thus, a slight deviation due to limited precision will produce greater error for the imaginary part than for the real part. It could be argued that, since the imaginary part is close to zero in magnitude at the chosen length, while the real part is near 70, an error of the same magnitude will be larger in percent error in the imaginary part due to its small value. However, the exponent part of the floating point number contains most of the information concerning the magnitude of the number and it is not modified in this work. It is expected that the error due to limited mantissa size should be the same regardless of the size of the exponent. The data show not only a larger percentage of error, but also a larger magnitude of error for the imaginary part.

Conclusions

A flexible method for determining the effects of finite register length in the mantissa of a floating point number, on the accuracy of calculations has been developed. This method has been verified by comparison with published results for FFT's. Dependences between the error introduced by limited precision and the number of operations, the number of significant bits and the rate of change of the solution, have been shown. The generality of the method allows it to be applied to

any mathematical algorithm. The authors solicit suggestions for appropriate applications of the method.

References

[1] C. S. Burrus and T.W. Parks, *DFT/FFT and Convolution Algorithms*. New York: Wiley-Interscience, 1985, pp. 109-111

[2] A. V. Oppenheim and C. J. Weinstein, "Effects of Finite Register Length in Digital Filtering and the Fourier Transform," *Proceedings of the IEEE*, vol. 60, pp. 957-976, Aug. 1972

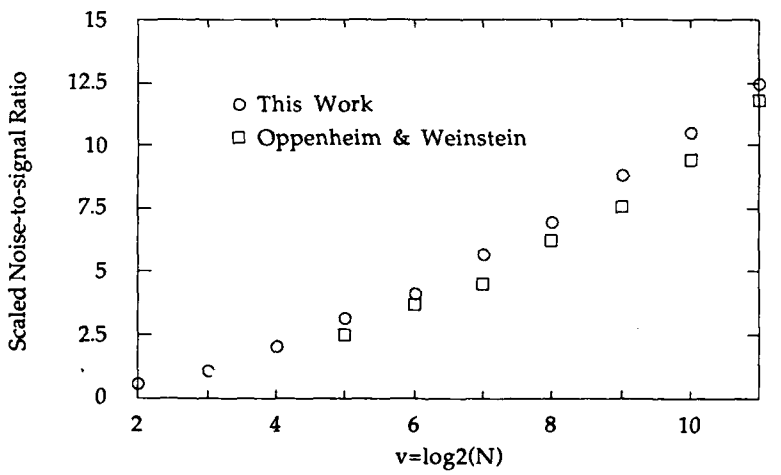

Fig 1: Decimation-in-frequency FFT output noise variance divided by output signal variance expressed in units of 2^{-2b} for rounding.

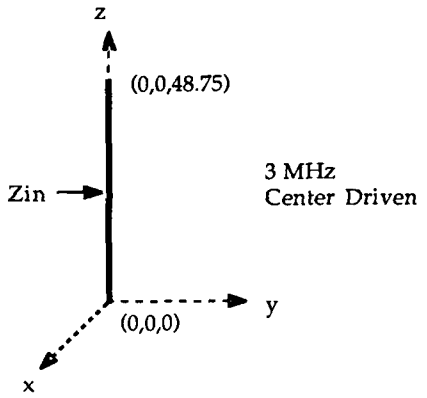

Fig. 2: Geometry used for the results given in figures 3-6.

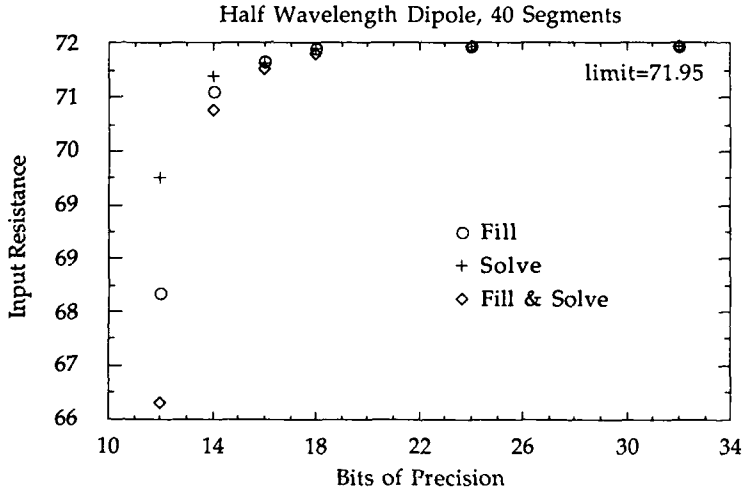

Fig. 3: Variation of the input resistance with bits of precision when the precision is limited in only the matrix fill, only the matrix solve and in both.

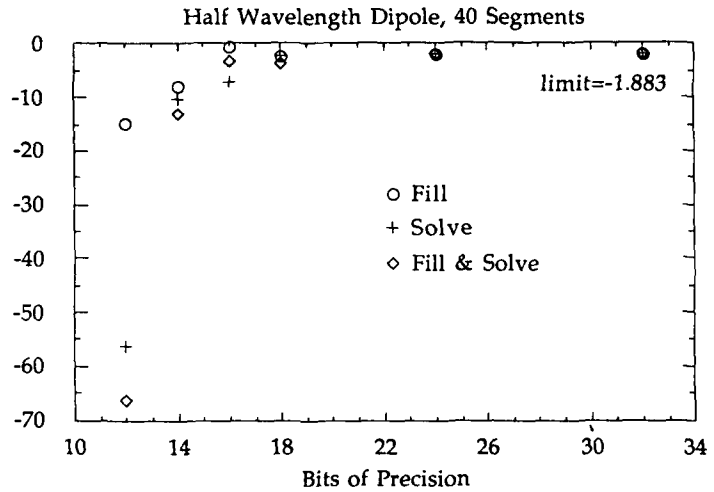

Variation of the input reactance with bits of precision when the precision s limited in only the matrix fill, only the matrix solve and in both.

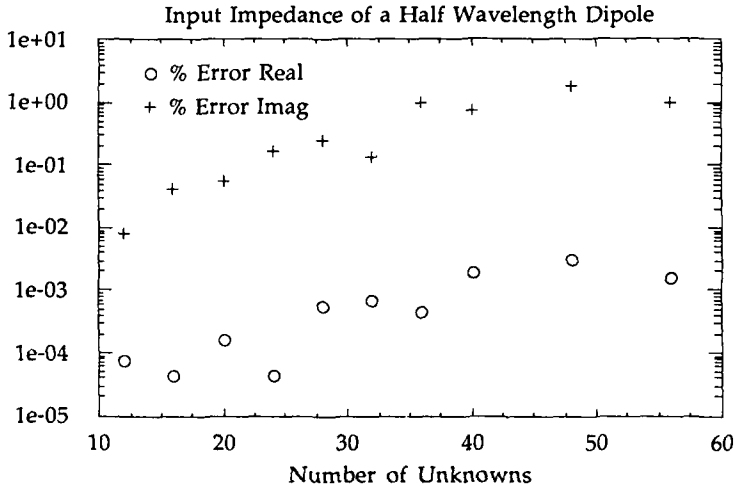

Fig. 5: Percent Error in the input impedance (24 bit mantissa).

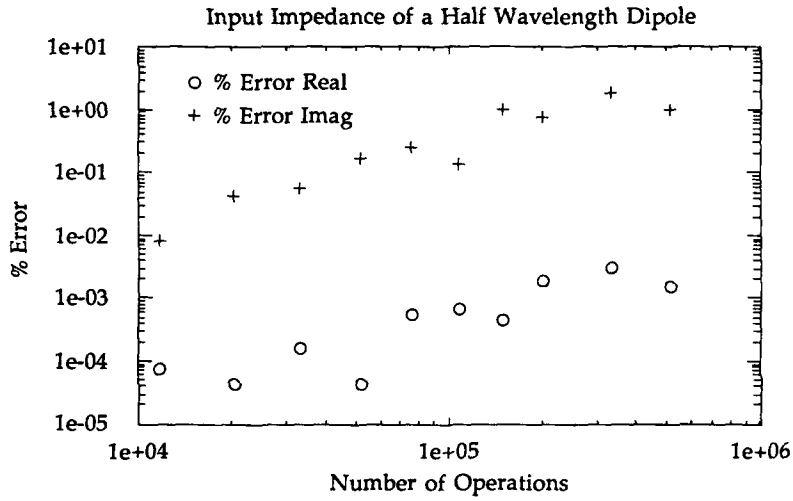

Fig. 6: Percent Error in the input impedance (24 bit mantissa).

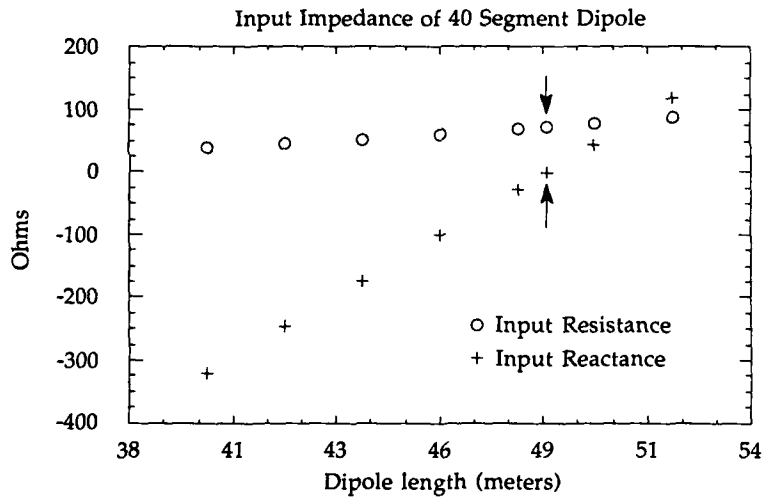

Fig. 7: Variation of the input impedance of a center driven dipole with dipole length (64 bit mantissa). The values indicated by the arrows are for the length shown in figure 2.

SESSION 3 - "POSTER PAPERS"

THE SPECTRAL ITERATION TECHNIQUE (SIT) APPLIED TO 2D STRATIFIED DIELECTRIC SCATTERERS

A. McCowen and V. C. W. Chu University of Wales, Swansea

INTRODUCTION

The successful development of the extended matrix version of the spectral iteration technique (MSIT), and in particular its rapid convergence when applied to 3D homogeneous dielectric scatterers, as shown by McCowen and Tran [1990], has lead the authors to consider its application to inhomogeneous problems. Such problems arise in a variety of applications ranging from biological effects of RF radiation to frequency selective surfaces (FSS) and dielectric or RAM-coated conducting scatterers. The future application of the MSIT to a highly inhomogeneous problem, such as the human body, is improbable; however, if the inhomogeneity is limited to 2 types of material, as in the case of the other applications mentioned above, then the MSIT may have a future role. This paper reports the first results of applying spectral iteration to inhomogeneous scatterers. The simplest case of 2D stratified structures is considered and the authors also comment on the development of the reported scheme into 3D.

THE MSIT

The MSIT iteratively solves the Method of Moments volume formulation which can be written, in matrix form, as

$$G \underline{J} = \underline{E}_{inc} \qquad (1)$$

where $\underline{E}_{inc}$ is the known incident electric field, $\underline{J}$ is the unknown current distribution on the scatterer and G is determined from the free space Green's function. For a homogeneous 2D scatterer G can be written as a 2 x 2 partitioned block Toeplitz Toeplitz block (BTTB) matrix for TE incidence and can be reduced to a BTTB matrix for TM incidence which are conditions on G necessary to apply the MSIT as reported by Mackay and McCowen [1988]. For ease of notation we take the later case and write the BTTB matrix, for the 2D scatterer shown in Figure 1, as follows

$$G = \begin{bmatrix} C_1 & D_1 & D_2 \\ D_1 & C_1 & D_1 \\ D_2 & D_1 & C_1 \end{bmatrix} \qquad (2)$$

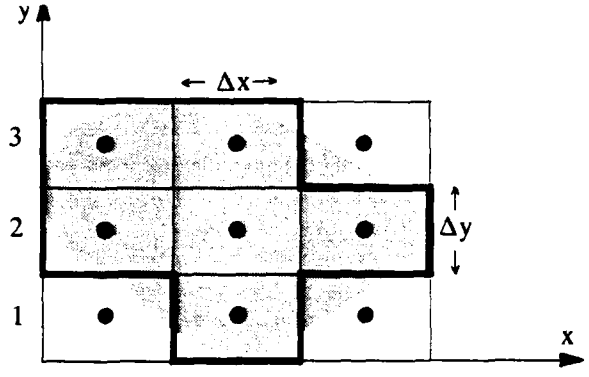

Figure 1: A 2D scatterer of arbitrary shape. The solid lines refer to its approximation by the rectangular cells of the mesh.

where C_1 is a Toeplitz matrix with diagonal terms dependent on the relative permittivity, ϵ_1, which may be complex. If the scatterer now comprises of material ϵ_1 in layers 1 and 2 and ϵ_2 in layer 3 then equation (1) may be written as

$$\begin{bmatrix} C_1 & D_1 & D_2 \\ D_1 & C_1 & D_1 \\ D_2 & D_1 & C_2 \end{bmatrix} \begin{bmatrix} \underline{J}_1 \\ \underline{J}_2 \\ \underline{J}_3 \end{bmatrix} = \begin{bmatrix} \underline{E}_1 \\ \underline{E}_2 \\ \underline{E}_3 \end{bmatrix} \qquad (3)$$

where C_2 is dependent on ϵ_2 and the resulting Green's matrix is no longer BTTB. The system of equations in equation (3) can be rearranged to turn the matrix into BTTB form as follows

$$\begin{bmatrix} C_1 & D_1 & C_2 & D_1 & D_2 \\ D_1 & C_1 & D_1 & C_2 & D_1 \\ D_2 & D_1 & C_1 & D_1 & C_2 \\ * & D_2 & D_1 & C_1 & D_1 \\ * & * & D_2 & D_1 & C_1 \end{bmatrix} \begin{bmatrix} \underline{J}_1 \\ \underline{J}_2 \\ 0 \\ 0 \\ \underline{J}_3 \end{bmatrix} = \begin{bmatrix} \underline{E}_1 \\ \underline{E}_2 \\ \underline{E}_3 \\ ? \\ ? \end{bmatrix} \qquad (4)$$

where the * values in the matrix may be arbitrary Toeplitz matrices provided the block Toeplitz form is maintained and the ? values in the $\underline{E}$ vector are unknown values. Equation (4) is now in the form which may be solved iteratively by the MSIT. The matrix in equation (4) becomes the "core" matrix which needs to be extended (by at least a factor of two) to produce a circulant matrix suitable for the application of an FFT and further extended (typically to a factor of three) for the MSIT to achieve convergence.

RESULTS

The 2D MSIT code developed by Mackay and McCowen [1988] has been adapted to provide confirmation of the scheme's validity. Two examples of the results to be presented are now given.

The first example is that of TM incidence on an infinite cylinder with a $0.7\lambda_0$ square cross-section as shown in Figure 2. A thin layer, $0.07\lambda_0$ thick, of a different lossy dielectric is at one edge of the cylinder. The square was uniformly discretised with a

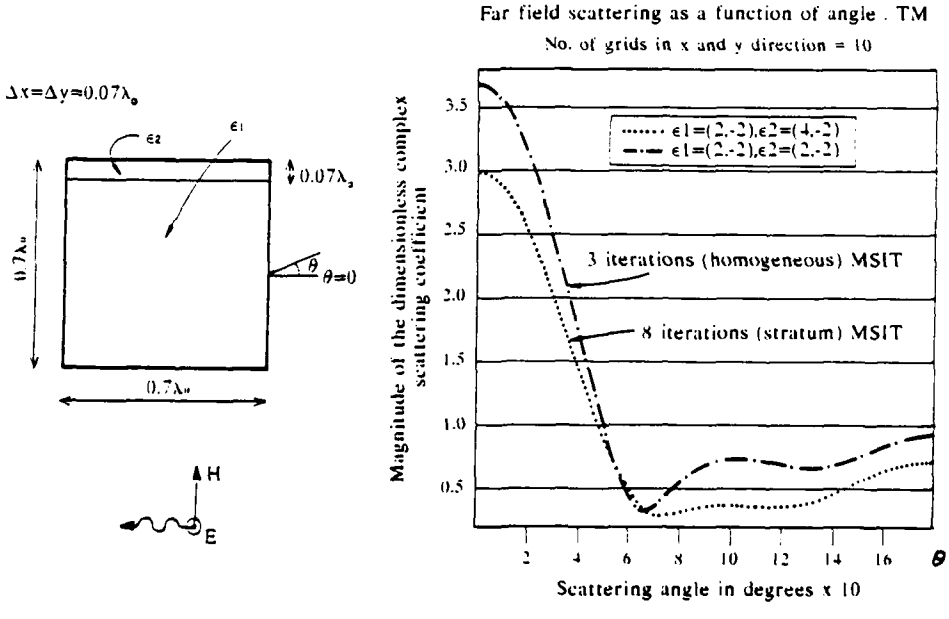

Figure 2: The normalised complex scattering amplitude from the inhomogeneous scatterer shown, compared with the equivalent homogeneous scatterer.

$0.07\lambda_o$ mesh yielding a problem with 200 unknowns. The MSIT took 8 iterations to converge compared with 3 iterations for the equivalent homogeneous problem. The complex scattering amplitude of the inhomogeneous cylinder is also shown in Figure 2 and is compared to that from the same homogeneous cylinder.

The second example, shown in Figure 3a, is that of a thin dielectric slab, with a $0.01\lambda_o$ thick conductor of length $0.4\ \lambda_o$ on its surface. The object was meshed with a 10 x 10 grid, with $\Delta x = 0.1\lambda_o$ and $\Delta y = 0.01\lambda_o$ yielding 188 unknowns. The MSIT took 3 iterations to converge and used 16 secs of CPU on a VAX8700. The complex scattering amplitude is also shown in Figure 3a, while the volume current distribution is shown in Figure 3b.

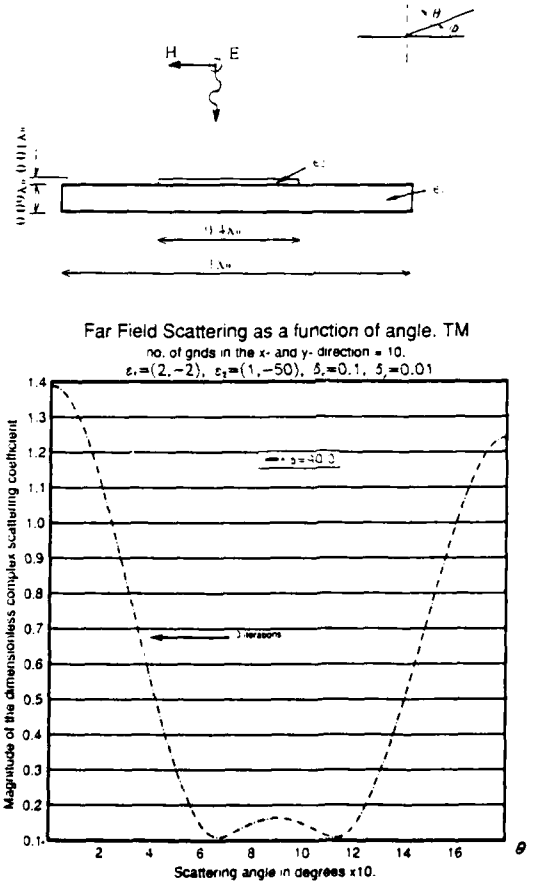

Figure 3: (a) The normalised complex scattering amplitude from the thin dielectric cylinder shown which is partially coated with a perfect conductor.

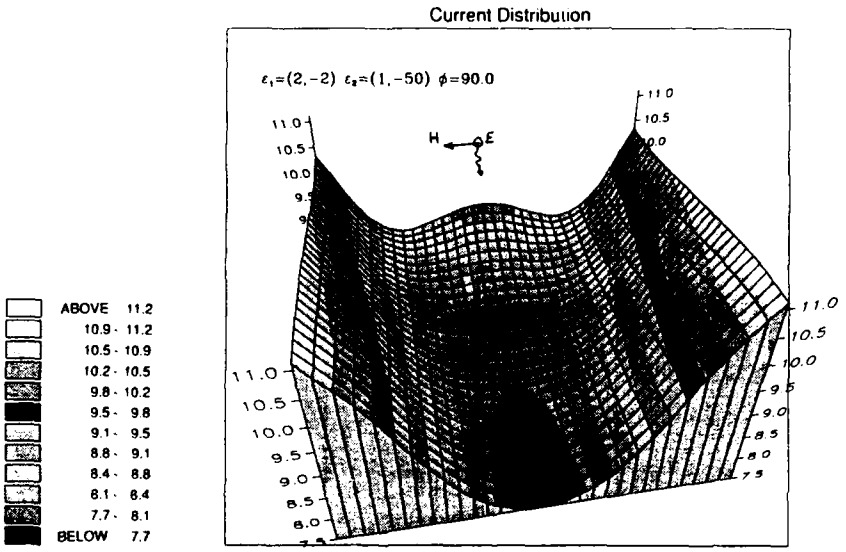

Figure 3: (b) The current distribution within the volume of cylinder in Figure 3(a).

COMMENTS

Spectral Iteration has been successfully used on 2D scatterers of limited inhomogeneity. It is important to note that the modifications to the MSIT, in their present form, are difficult to code for both TE incidence or 3D. A generalisation of this work is being developed for arbitrary geometry e.g. coated curved surfaces, and results for both TE incidence and 3D are envisaged by the end of the year. As inferred by the expansion of the matrix given in equation (4), the computer storage requirements for the scheme exceed those for the homogeneous problem by approximately a factor of 2. It is worth noting, however, that the total storage requirement for the homogeneous scheme, which is discussed *in detail by McCowen and Tran [submitted], is comparable to that required by the* Conjugate Gradient FFT scheme.

REFERENCES

A. McCowen and T. V. Tran
"The Spectral Iteration Technique (SIT) applied to 3D homogeneous dielectric scatterers", This Proceedings.

A. J. Mackay and A. McCowen
"The Matrix interpretation of the Spectral Iteration Technique", IEEE Trans. Antennas Propagat., Vol 36, pp 950 - 955, July 1988.

A. McCowen and T. V. Tran
"Matrix interpretation of the Spectral Iteration Technique for 3D Dielectric Scatterers in the Resonance Region", submitted for publication.

A METHODOLOGY FOR THE GENERATION OF MOM MODELS FOR LARGE, COMPLEX SURFACES"

By
Mark T. Gross, Andrew L. Drozd, and Alfred D. Paoni
Kaman Sciences Corporation
258 Genesee Street
Utica, New York 13502

Abstract

This paper presents a detailed methodology for automating the generation of Method of Moment (MOM) models for complex systems. The methodology consists of: (1) developing a parameterization to initially represent the complex surface and then employing techniques to refine the parameterized results; and (2) employing an automated technique to create MOM wire gridded surfaces consistent with the requirements of the General Electromagnetic Model for the Analysis of Complex Systems (GEMACS). The methodology provides a mechanism for generating the majority of a MOM model quickly and facilitates rescaling for different frequencies. It also establishes a mechanism for generating a MOM mesh representation for a surface using any specified wire segment length. The methodology is general enough to be applicable to nearly any geometry shape. The Graphical Aids for the Users of GEMACS (GAUGE), was used in conjunction with this modeling approach to provide a mechanism for visualizing a model.

Introduction

This paper first discusses the development of a parameterization technique which is used to represent a complex surface. What follows is a description of how this parameterization is used in conjunction with an automated approach for generating a MOM wire grid for that surface. The majority of the modeling effort, hence, the discussions, is directed towards the development of a suitable surface parameterization.

The approach in developing the parameterization involves the definition of the basic geometry cross-sections at known points. These cross-sections characterize the shape and proportion of the surface to be modeled. This description is then refined using smoothing functions and/or curve-fitting techniques. Finally, the refined parameterization is forced to comply with high-fidelity measurement data by employing scaling procedures. The scaling procedures are intended to constrain approximations introduced during the initial parameterization and to establish a realistic 3-D representation of the actual surface. The parameterization results are then used to generate a MOM mesh to any desired degree of granularity. Granularity refers to the specification of appropriate point distances, and corresponding wire segment lengths and length-to-radius ratios in order to conform to suitable MOM modeling guidelines.

The flexibility introduced into the methodology facilitates the generation of MOM geometry descriptions using any predefined maximum segment length, and permits MOM modeling and analyses for the same geometry over a broad range of frequencies. This approach is in contrast to the "manual", point-by-point technique discussed in much of the literature. The methodology focuses on establishing reasonable characterizations of the exterior surface topology of a complex system. One important fallout of the methodology development is that it is general enough to be used in conjunction with other MOM or "finite element" modeling tools.

The impetus for developing the methodology was to facilitate the creation of a library of GEMACS [1] models for a variety of complex systems. These models would then be used to perform various assessments to evaluate electromagnetic radiation and scattering, radar cross-section (RCS), EMI/EMC, EMP, HPM, ECM and ECCM, jamming susceptibility, and antenna performance. The GAUGE [2] graphical interface was used to visualize the models developed for the library. Interactive graphics

and CAD features in GAUGE are tailored directly towards electromagnetic modeling and model verification.

The discussions which follow describe the details of the methodology and how it was implemented to support the development of a library of GEMACS/MOM models. The problems encountered in its implementation, as well as related issues which must be addressed for future refinements in the approach are indicated. Finally, an example is presented to illustrate the effectiveness of the methodology.

Surface Parameterization

Parameterization is defined as the procedure for generating a function of two independent variables (parameters) characterizing a complex surface including its various contours. The parameterization relies on the availability of physical measurement data obtained from an actual system and/or a scale model, in conjunction perhaps, with the use of scaled system drawings. The process involves shaping, contouring, or model "editing" to achieve a reasonably accurate representation of the surface. This latter aspect can be achieved by means of smoothing functions and "curve-fitting" techniques. This section discusses one method for the parameterization of a generic complex surface using limited information and data. The data referred to in the following discussions is obtained from a small-scale model of the subject, and a cut-away blueprint or diagram. This data is used iteratively to characterize a complex surface where each iteration enhances the fidelity of the parameterization. The majority of the surface parameterization can be established without measurements of the actual full-scale surface.

The initial parameterization step is automated by using scanned images of a cut-away diagram. This represents a consistent, automated first step in the methodology. The scanned image technique is used in conjunction with a MacPaint or a PC-Paint + software program [3, 4], for example, which is modified to retain the pixel coordinates of the cursor location whenever a "mouse-down event" occurs (i.e., when a mouse button is depressed). The surface contours or cross-sectional curves are approximated using spline functions *through* known (Cartesian) points. These points are first generated by using the automated procedure described above. The surface function is initially defined by linear combinations of spline curves approximating the cross-sectional shapes. The resultant parameterizations of the surface are represented by the following expressions:

$$x(z, t) = x_i(t)\left|1 - \frac{z - z_i}{z_{i+1} - z_i}\right| + x_{i+1}(t)\left|\frac{z - z_i}{z_{i+1} - z_i}\right|,$$

$$y(z, t) = y_i(t)\left|1 - \frac{z - z_i}{z_{i+1} - z_i}\right| + y_{i+1}(t)\left|\frac{z - z_i}{z_{i+1} - z_i}\right|$$

where $z_i \leq z < z_{i+1}$.

The functions $x_i(t)$ and $y_i(t)$ are splines approximating the surface's cross section at z_i, where z is the primary axial coordinate of the shape being modeled.

Refinement of the initial, unscaled surface parameterization is achieved through the use of constraint data taken from a small-scale model, for example. Typically, the constraint data consists of height or thickness functions along the primary axial coordinate of the shape being modeled. This is used to

rescale the surface function such that its height and thickness match the constraint data. Next, this refined parameterization is used to systematically generate a MOM mesh to the desired degree of granularity.

Some limitations and issues with the parameterization should be considered. First, the parameterization relies on the existence of a natural axial coordinate as a reference from which to generate the surface function and to incorporate the constraint data. In the case of aircraft models, this implies that such features as wings, nacelles, and stabilizers must each be modeled separately and then be connected in order to create the final model. This introduces "bookkeeping" functions into the methodology which are associated with the attachment and identification of areas (points, segments) where any two sections must join together. The bookkeeping issues of primary concern in the case of aircraft systems are: (1) the identification of wire segments characterizing windows, radomes, and other surface apertures, and (2) providing a method of attaching major components together (e.g., the wing to the fuselage). In order to address such issues, further parameterizations of these areas are needed. These parameterizations are then used in the grid generation procedure to establish points corresponding to these junctions which are then stored into auxiliary files.

Aside from the required bookkeeping, another issue that was addressed in the parameterization development and which affects grid-generation, is the "normalization" of the variable, t, for each cross-section. Normalization refers to fixing the range of t to maintain uniformity in the way that one cross-section "connects" to the next. This is further discussed in the following section of this paper.

In review, the parameterization consists of multiple stages of refinement of an initial, approximate characterization of a complex surface. This initial parameterization is a crude, not-to-scale representation of the actual shape, generated using a cut-away diagram, for example. Next, the initial parameterization is manually refined and smoothed to more accurately reflect the correct shape. After this smoothing is performed, data is taken from a small-scale model and used to constrain the surface representation, in order to match the shape of the model. Finally, measurements of the full-scale system may be incorporated to finalize and further refine the surface parameterization.

The discussion which follows describes the grid generation procedure developed as part of this methodology. The algorithm discussed is basic, and the details of its practical implementation are omitted.

Grid-Generator Algorithm

The grid-generating algorithm assumes that an appropriate parameterization is specified and that the coordinates of points representing attachment areas for separate components of a model, including windows and apertures, are also defined. The algorithm provides for the generation of MOM GEMACS geometry input file(s) and a set of auxiliary files which contain the coordinate locations and surface characterizations of apertures.

This algorithm works satisfactorily, provided that the surface features of the actual model do not vary too quickly. This is important because the algorithm "steps" along the axial coordinate (e.g., fuselage station) to generate points used to define the wire grid. Step size increments are currently fixed, therefore, if quickly-varying contours are encountered during the stepping procedure, then certain details or variations of the surface might be "stepped over". It is also important to assure that the initial cross-sectional "slices" are connected domains. Otherwise, the grid generation portion of this methodology may not be successfully used due to the complexity involved in extending the wire mesh from a single, connected cross-section to a multiply-connected cross-section. Connected domains are those for which any two points can be joined by a suitably chosen curve residing entirely within its interior [5].

For each step in the axial coordinate, z, the grid-generation method proceeds as follows. First, a set of parameter values (t) for points on a cross-section are generated using the parameterization described above. Secondly, this set of values is used in conjunction with the axial coordinate, z, of the cross-section to generate point coordinates, while verifying that the point resides either on an aperture or at a junction between two components. Finally, "connect points" commands are generated which join the points of contiguous cross-sections to form the wire-gridded surface. This procedure is further illustrated in the flow chart shown in Figure 1.

As mentioned above, an issue which affects the grid-generation algorithm is the "normalization" of the variable, t, for each cross-section. The definition of the surface parameterization requires two cross-sectional splines to be used in characterizing any single section. Each of these splines may have a different number of nodes or points which define them. A reasonable normalization for t was chosen to be 2π. This works well when the spline nodes defining the cross-sections are evenly spaced with respect to arc length.

Note that Cartesian coordinates are used to define the nodes. The reason for not using polar coordinates was to avoid difficulties associated with multiple MOM points having azimuthally equal angles. This condition creates difficulties in choosing the correct parameter values for such points in the grid-generation procedure.

The algorithm (Figure 1) discussed in this section illustrates the majority of the practical issues that are involved in generating a usable MOM geometry data deck. There are many improvements and modifications that are possible. For example, techniques for adjusting step size increments to within a desired tolerance, or the generation of triangular gridding as opposed to rectangular, may be incorporated into the basic algorithm. The next section further illustrates some aspects involved in obtaining the surface parameterization and in generating the wire-grids for sample cross-sections.

Example

The following example illustrates how the methodology was used to generate a wire-grid model of the cockpit portion of the B-1. The initial parameterization of the B-1 cockpit is based on first scanning the cross-section images shown in Figure 2. Although the images have been distorted through numerous stages of photocopying and reduction, they still provide a suitable starting point for the parameterization procedure, since the basic shape is reasonably preserved. The parameterization based on the scanned images must be rescaled to compensate for any distortion errors. This is done by utilizing scale-model measurement data (i.e., constraint data) obtained from a 1/72 scale plastic model.

Some difficulties were encountered when performing the scale-model measurements. These were primarily related to limitations in the measurement instruments themselves and in demonstrating measurement precision. Before confidence can be achieved in developing a model for a complex system, a method must be implemented to obtain reliable data. In this respect, known reference points on the object being modeled must be firmly established. In the case of the B-1, measurements were also taken on the actual system to further refine and verify the model. It was found that the parameterization results and the actual system measurements were in agreement to within 10 cm. The reference frame from which the constraint data is obtained should correspond to the coordinate system of the parameterized shape, which in turn is related to the aircraft coordinate system. When the constraint data is incorporated into the parameterization, a GAUGE-viewable prototype is generated to verify shape and proportion. The final model, along with the necessary auxiliary files, contain point and segment information corresponding to the desired frequency or wavelength of concern. The auxiliary files consist of interface points for the connection of individual components of the model.

Views of the B-1 cockpit section that were generated using GAUGE are shown in Figures 3 and 4. These correspond to two levels of refinement for the parameterization. The segment lengths for this prototype model were generated without regard to any specific frequency. The methodology is flexible enough to permit rescaling for any frequency(ies) of interest.

Summary

This paper has presented a methodology for generating MOM (GEMACS) wire grid models using limited data. This methodology is built around the idea of iteratively refining a surface parameterization. The grid generation scheme presented is primitive and improvements are possible. It does, however, demonstrate the importance of keeping track of point and segment numbers, and assuring connectivity with particular attention given to window and radome location coordinates. This procedure can be extended to modeling structural details for finite element, boundary element, or computational fluid dynamics (CFD) analyses. The methodology can be used to support any or all of these modeling thrusts in parallel.

The methodology has been implemented using a set of three software programs written in C language [6, 7]. The next step is to implement the methodology as a flexible, unified program that can support detailed modeling of complex surfaces for any MoM-based application.

It is acknowledged that the utilities within GAUGE to generate input data for GEMACS are powerful, yet limited in certain respects. For example, GAUGE cannot be easily used to model irregular, complex contours to a high-degree of resolution. The methodology described in this paper exploits the current power and capabilities of GAUGE, and complements it by adding a more flexible capability to model complex contours and shapes.

Acknowledgements

The unclassified work described in this paper was performed under USAF Contract No. F30602-88-D-0025. The objective of this contract was to develop a library of GEMACS models of USAF test assets. The authors wish to thank Mr. Kenneth R. Siarkiewicz and Mr. Tim Blocher of RADC for their support and assistance in the on-going development and implementation of this methodology.

References

[1] Lockyer, A. J., Tulyathan, P., Coffey, E. L. III, Grage, M. J., and Upshaw, G., "Graphical Aids for the Users of GEMACS (GAUGE)," RADC-TR-88-316, February 1989

[2] Coffey, E. L. and Kadlec, D., "General Electromagnetic Model for the Analysis of Complex Systems (GEMACS)", RADC-TR-87-68, Vol. I-IV, May 1987.

[3] Claris Corporation, "MacPaint", 1989.

[4] Mouse Systems, "PC-Paint + ", 1989.

[5] Kaplan, W., Advanced Calculus, Third Edition, Addison-Wesley, 1984.

[6] Symantec Corporation, "THINK C 4.0," 1989

[7] Dow, G. H., "Art Class," Oop Demonstration Program Using THINK C, Symantec Corporation, 1989.

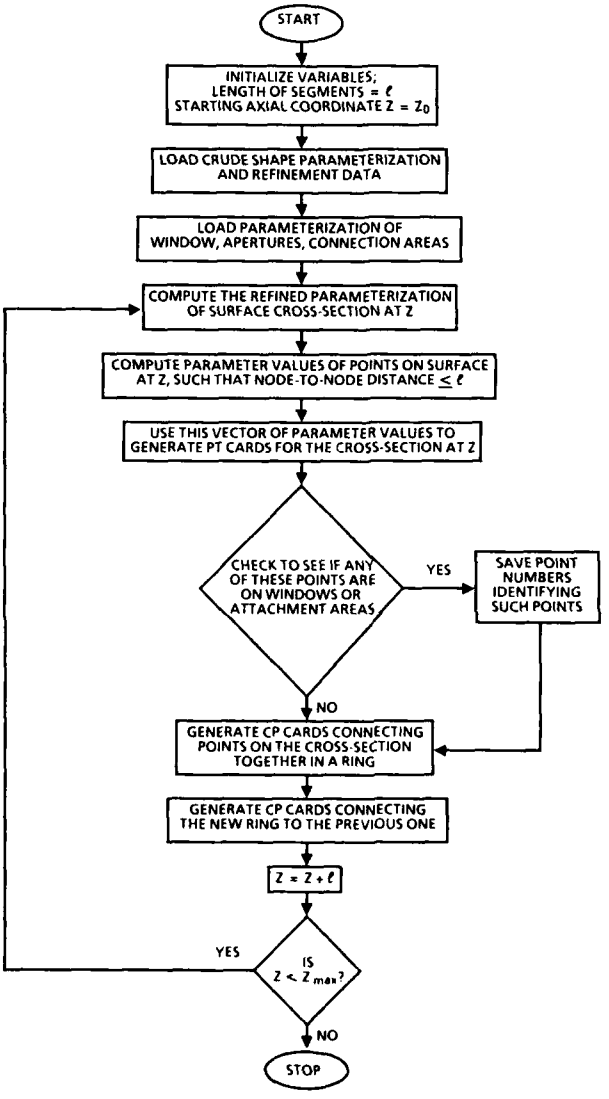

Figure 1. Grid-generator Flowchart

Figure 2. Cut-away Diagram of Surface Contours at Known Stations

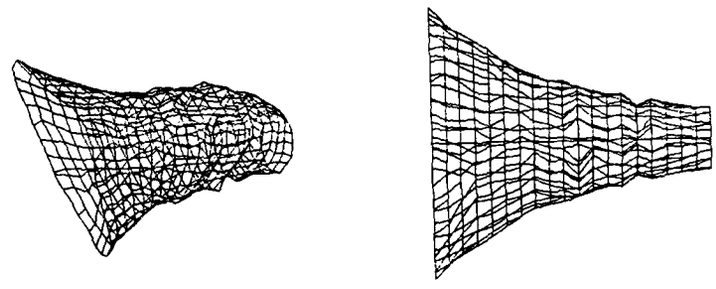

Tilted View Top View

Figure 3. MOM Surface Characterization Using Initial Parameterization

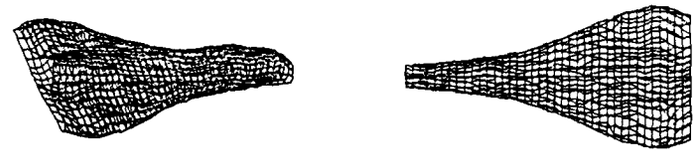

Tilted View Top View

Figure 4. MOM Surface Characterization Using Refined Parameterization

VALIDATION OF A VOLUME-INTEGRAL CODE FOR EDDY-CURRENT NONDESTRUCTIVE EVALUATION

Harold A. Sabbagh, L. David Sabbagh
Sabbagh Associates, Inc., 4639 Morningside Drive, Bloomington, IN 47401,

and

John R. Bowler, Steven A. Jenkins
University of Surrey, Guildford, Surrey GU2 5XH, England

Abstract

Eddy-current methods are often used in the nondestructive evaluation of conducting structures. In the simplest procedure, a single current-carrying coil is scanned over the conducting workpiece, inducing eddy-currents into the structure. If there is a defect (which could be a crack, or some other conducting anomaly), then the driving-point impedance of the coil changes slightly. The variation of the change in impedance with position of the probe coil is, in some sense, a signature of the defect. Such single-coil sensors, however, are sensitive to lift-off, which is the height of the coil above the workpiece.

Differential eddy-current probes are attractive because of their insensitivity to lift-off effects. By using two similar coils wound in opposition, or connected to a bridge circuit, we have a sensor that detects variations in the magnetic field along a line joining their centers. The impedance plane response of a differential probe to a flaw is somewhat more complicated than the signal from a single-winding probe, but this is a price one must be prepared to pay for nullifying the lift-off signal.

We have developed a computational model and code that will efficiently solve several problems in eddy-current nondestructive evaluation (NDE), including the single and differential probe problems described above. The model is fully three-dimensional and is based on a volume integral equation that is discretized using the method of moments, and is then solved iteratively using conjugate gradients and FFT techniques [1,2]. Three-dimensional pulse functions are used for expansion and testing. Problems with 12,000 unknowns are being routinely solved on the Alliant FX/4 minisupercomputer in reasonable times, as well as on a Sun 4/360 workstation that is coupled to a Sky Warrior array processor.

In this paper we describe two validation tests. Both tests are concerned with the change of impedance of a coil system as it is scanned over a known crack in a metallic workpiece. In both cases computations based on the model are compared with accurate experimental results.

The first test compares the computed impedance of a single air-core coil with highly accurate experimental data [6]; the results are in excellent agreement. This test will appear in the collection of Canonical Problems, that will be published by ACES in the Spring of 1990.

The second test involves a three-coil differential system that has recently been suggested as a benchmark problem for the evaluation of electromagnetic numerical modeling codes [3]. Experimental results for this test are reported in [4,5].

Although the second benchmark problem examines the probe response due to a surface slot in a finite conducting slab, we have, instead, computed the signals due to a similar flaw in a half-space conductor. It is possible to adapt our model to a finite slab, but this introduces edge effects that we wish to avoid. Instead, we demonstrate an effective method for calculating the differential signal due to the slot; this aspect of the problem is of particular interest because it has proved to be very difficult to determine this signal by using finite-element methods [3].

Test One

The problem we are modeling is based on a benchmark experiment described in [6], and

shown in Figure 1. A single coil is scanned along the positive X-axis over a slot (produced by electro-discharge machining, or EDM). The coordinate axes are symmetrically placed with respect to the slot. All parameters are listed in Table 1 [6].

Table 1: Parameters of Test Experiment (see Figure 1)

The coil	
Inner radius (a_2)	6.15 ± 0.05mm
Outer radius (a_1)	12.4 ± 0.05mm
Length (b)	6.15 ± 0.1mm
Number of turns (N)	3790
Lift-off (l)	0.88 mm
The test specimen	
Conductivity (σ)	$3.06 \pm 0.02 \times 10^7$ S/m
Thickness	12.22 ± 0.02mm
The defect	
Length ($2c$)	12.60 ± 0.02mm
Depth (h)	5.00 ± 0.05mm
Width (w)	0.28 ± 0.01mm
Other parameters	
Frequency	900 Hz
Skin depth at 900 Hz	3.04mm
Isolated coil inductance	221.8 ± 0.04mH
Isolated coil DC resistance	660Ω
Isolated coil resonant frequency	26 kHz (100 pF leads)
	47.1 kHz (2 pF leads)

Using the model described above we have computed the change in impedance versus position, and have plotted the magnitude and phase in Figures 2 and 3, which includes the experimental data for comparison. The agreement is excellent, and probably comes near to the experimental error. In arriving at the computed results, we used 32 cells along the length of the slot, 8 across the width, and 8 in depth, for a total of 6,144 unknowns for the anomalous current density. We believe that the problem size can be reduced considerably by using first-order (piecewise linear) expansion functions for the three anomalous current components, but continuing to use pulse functions for testing.

Test Two

The coil arrangement for the second test consists of an air-core exciting coil that encloses two matched air-core sensing coils connected in a differential mode, as in Figure 4. A 3mm thick dielectric slab separates the base of the coil support from the workpiece. This slab has no significant effect on the field; therefore, the excitation coil has a fixed effective lift-off of 8mm.

The flaw region, Figure 5, was discretized by dividing the slot into 64 elements along the length of the slot, 4 across the slot, and 8 layers in depth, giving a total of 2048 cells. Because the anomalous current density due to the presence of the flaw has three components, there are a total of 6,144 unknowns, as in the first test.

The test piece shown in Figure 5 is made of austenitic steel, type 18-10M0, with a conductivity of 1.7×10^6 S/m, and a relative magnetic permeability of unity. The inspection frequency was 500 Hz. Using this information, and the above mesh, we needed 4674 CPU seconds to calculate and store the matrix elements on a Sun 4/260 workstation. (All CPU times quoted

used a Sky Warrior array processor for implementing the FFT's.)

The probe parameters in Figure 4 are now used to calculate two incident fields, one for the driving coil and one for the two sensing coils (the reciprocity theorem allows us to reverse the roles of the sensing coils). These incident fields need only be computed once per scan if the probe stays inside the computed area of the fields. We performed two scans, one perpendicular to the slot, the other parallel to it. The fields for the perpendicular scan took 160 CPU seconds to compute, whereas the fields for the parallel scan took twice as long, because we scanned a larger area.

A perpendicular scan can be performed by starting with the probe centered on the flaw and calculating the differential voltage at 1mm increments through 40 mm total displacement. the results of such a numerical scan are presented in Figure 6. The axes are scaled by a constant term, α, which is the product of the number of turns in the driving and sensing coils. It took approximately 120 CPU seconds to compute each point shown.

Figure 7 shows the numerical results for a scan parallel to the slot. Again, this scan started with the probe centered on the flaw and then moved in 1mm increments through 60mm total displacement. It took approximately 250 CPU seconds to compute each point for this configuration.

Figure 8 compares the results of the two previous scans with experimental data [5]. The experimental data available to the authors does not contain absolute phase information or absolute magnitude information, so the experimental data has been normalized to $(1,0)$ for the parallel results, and $(0,1)$ for the perpendicular. The normalization point was chosen to be the point of maximum magnitude of signal for the probe close to the slot. The experimental data shown was collected on a 30mm thick plate, 330mm long in the dimension of the slot length, and 285mm in the dimension of the slot width. The numerical results show good agreement to the experimental results, even though we are looking at only a half-space, therefore ignoring completely the effects of the finite thickness of the slab. We are also ignoring the effects of the sides of the slab, so our solution will diverge for large offsets of the probe. We plan to recompute this solution, taking into account the presence of the edges of the slab. The volume integral model and code should easily accomodate this added complication.

References

[1] J. R. Bowler, L. D. Sabbagh, and H. A. Sabbagh, "A Theoretical and Computational Model of Eddy-Current Probes Incorporating Volume Integral and Conjugate Gradient Methods", IEEE Trans. Magnetics, Vol. 25, No. 3, May 1989, pp. 2650-2664.

[2] H. A. Sabbagh, J. R. Bowler, and L. D. Sabbagh, "A Volume Integral Code for Eddy-Current Nondestructive Evaluation", Journal of the Applied Computational Electromagnetics Society, Vol. 4, No. 1, Spring 1989, pp. 3-22.

[3] L. R. Turner, ed., *Proceedings of the Vancouver TEAM Workshop*, NTIS Report ANL/FPP/TM-230, 1988.

[4] J. C. Verite, COMPEL, Vol. 3, No. 3, pp. 167-178, 1984.

[5] J. C. Verite, A. Bossavit, J. Cahouet, and Y. Crutzen, eds., *TEAM Workshop and Meeting on the Applications of Eddy-Current Computations*, (Commission of European Communities, Brussels 1989).

[6] S. K. Burke, "A Benchmark Problem for Computation of ΔZ in Eddy-Current Nondestructive Evaluation (NDE)." Journal of Nondestructive Evaluation, Vol. 7, Nos. 1/2, 1988, pp. 35-41.

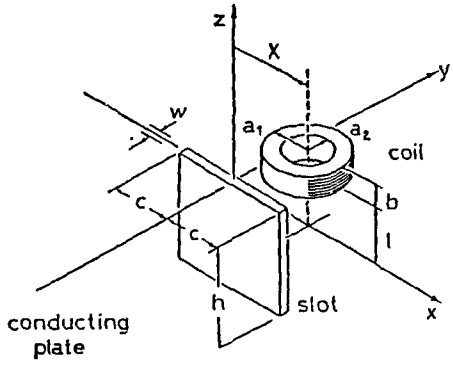

Figure 1. Schematic configuration for the benchmark experiment. The coil and slot parameters are given in Table 1.

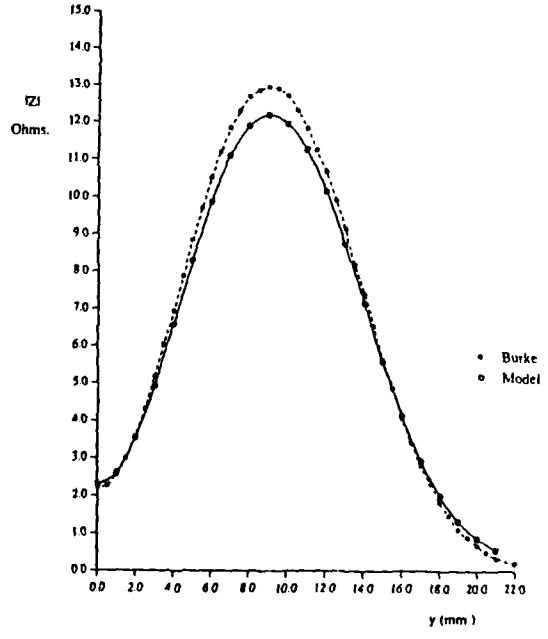

Figure 2. Comparison of the magnitude of impedance vs. position. The solid dots are the experimental data of [6], and the open circles are computed results.

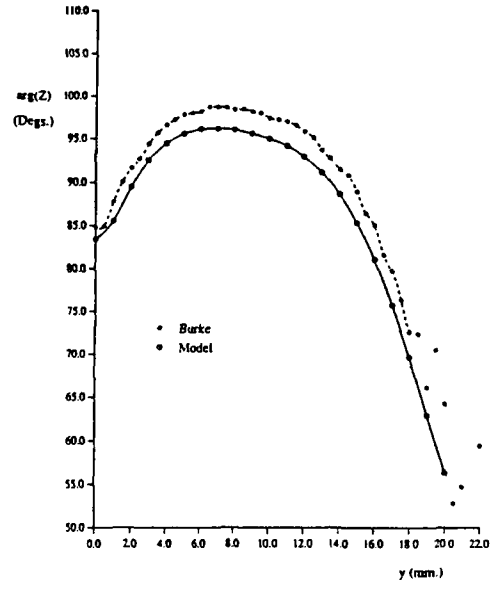

Figure 3. Comparison of the phase of impedance vs. position. The solid dots are the experimental data of [6], and the open circles are computed results.

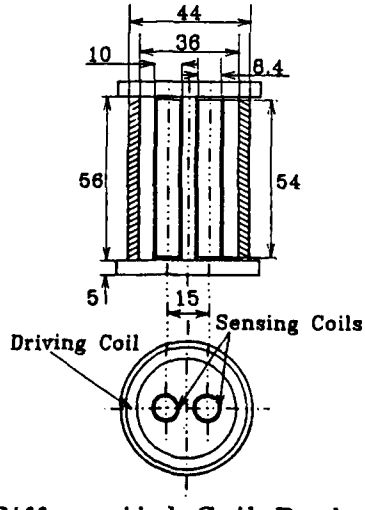

Differential Coil Probe

Figure 4. Differential eddy-current probe. Dimensions are in mm.

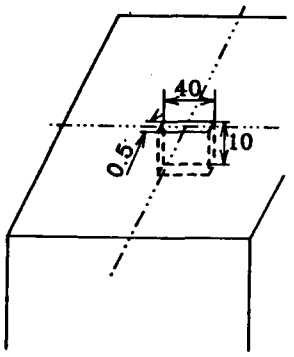

Figure 5. Slot in slab of austenitic steel.

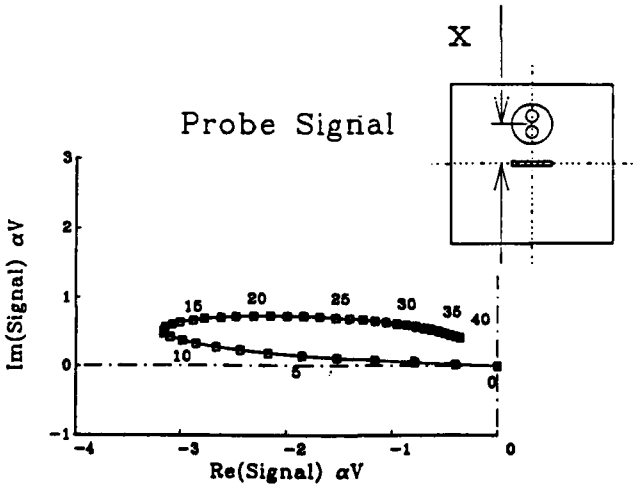

Figure 6. Differential probe response for scan perpendicular to slot.

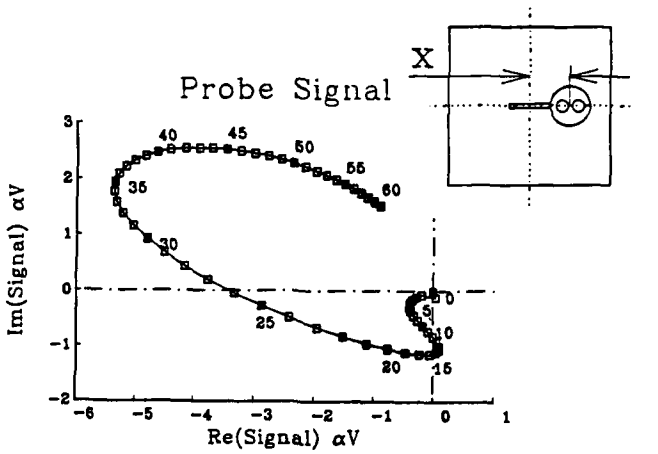

Figure 7. Differential probe response for scan parallel to slot.

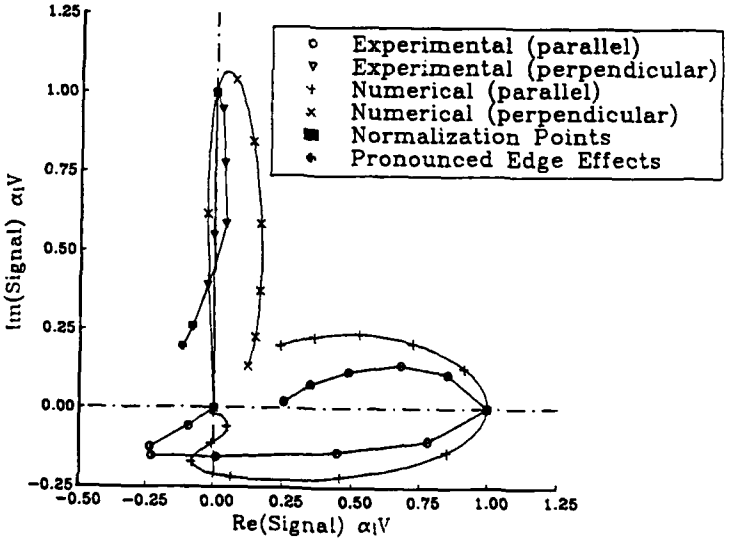

Figure 8. Comparison between experimental and computed signals for differential probe.

THE CASE AGAINST STAIRCASING

Richard Holland
Consultant to Lockheed Aeronautical Systems Company
1625 Roma NE
Albuquerque, NM 87106

The staircase representation of oblique surfaces has a long history of use in solving Maxwell's equations by time-domain finite differencing (TDFD). Its obvious advantage is one of extreme ease of application, especially in comparison with actual oblique surface implementation. Moreover, the general belief has been that any accuracy deficiencies resulting from its use could be eliminated by resorting to finer meshing. (In other words, there has been an attitude of shifting the resource burden from the analyst to the computer.)

From 1966 until the last two years, TDFD was primarily used as an EMP coupling evaluation tool. In this application, one usually looks for orientations which maximize coupling. For this scenario, staircasing works quite well.

Recently, however, there has been a major application of TDFD to RCS evaluation. This is quite a different situation, as vehicles may be designed to minimize radar backscatter in the direction of illumination. For instance, it is common to expect the poynting vector to strike major surfaces of the target at very shallow or grazing angles. It does not seem to be commonly understood that staircased TDFD, applied to this situation, may yield totally specious answers, often two orders of magnitude high. Moreover, these answers do not, in general, quickly converge to the correct RCS as cell size becomes small.

The main purpose of this presentation is to give examples showing how bad staircase-based RCS results can be. A secondary purpose is to review a technique for eliminating the staircasing approximation and its associated error.

FLAT PLATE ILLUMINATED OBLIQUELY AT 5 DEG

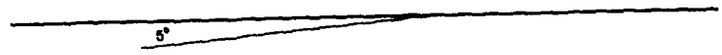

STAIRCASE TILTED PLATE ILLUMINATED HORIZONTALLY

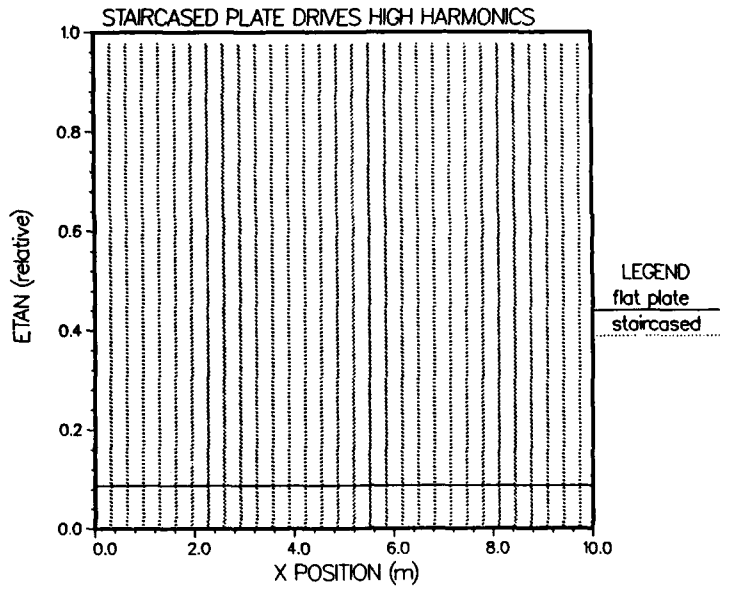
STAIRCASED PLATE DRIVES HIGH HARMONICS
ETAN (relative)
1.0
0.8
0.6
0.4
0.2
0.0
0.0
2.0
4.0
6.0
8.0
10.0
X POSITION (m)
LEGEND
flat plate
staircased

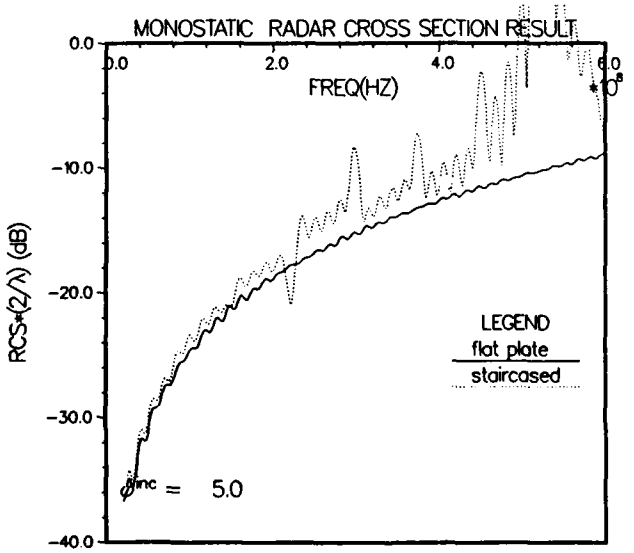
MONOSTATIC RADAR CROSS SECTION RESULT
0.0
2.0
4.0
6.0
FREQ(HZ)
*10^8
RCS*(2/λ) (dB)
-10.0
-20.0
-30.0
-40.0
LEGEND
flat plate
staircased
φinc = 5.0

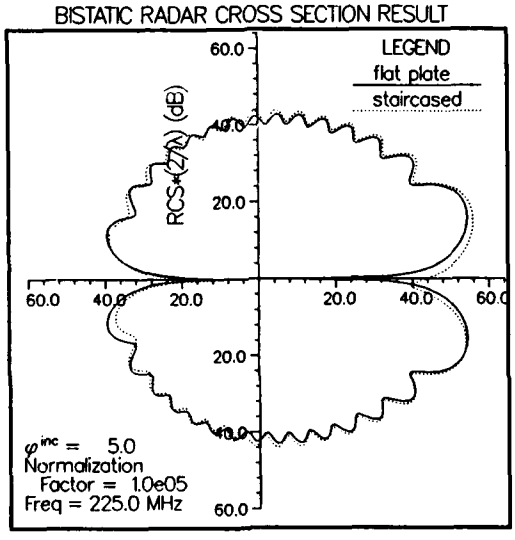
BISTATIC RADAR CROSS SECTION RESULT
LEGEND
flat plate
staircased
RCS (dB)
60.0
40.0
20.0
20.0
40.0
60.0
20.0
40.0
60.0
φ inc = 5.0
Normalization
Factor = 1.0e05
Freq = 225.0 MHz

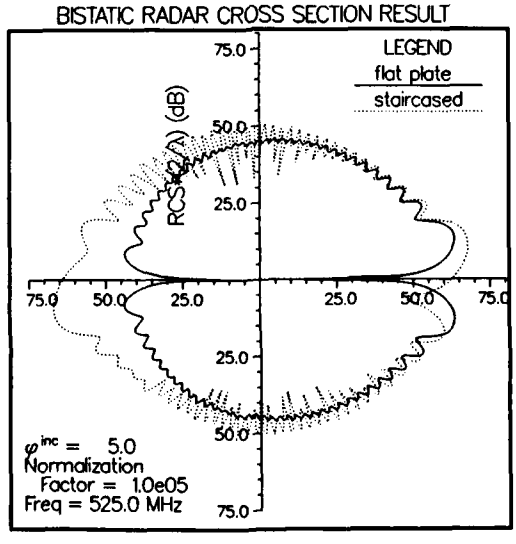
BISTATIC RADAR CROSS SECTION RESULT
LEGEND
flat plate
staircased
RCS (dB)
75.0
50.0
25.0
75.0
50.0
25.0
25.0
50.0
75.0
25.0
50.0
75.0
φ inc = 5.0
Normalization
Factor = 1.0e05
Freq = 525.0 MHz

FACETED CYLINDER 25 CELLS ACROSS DIAMETER

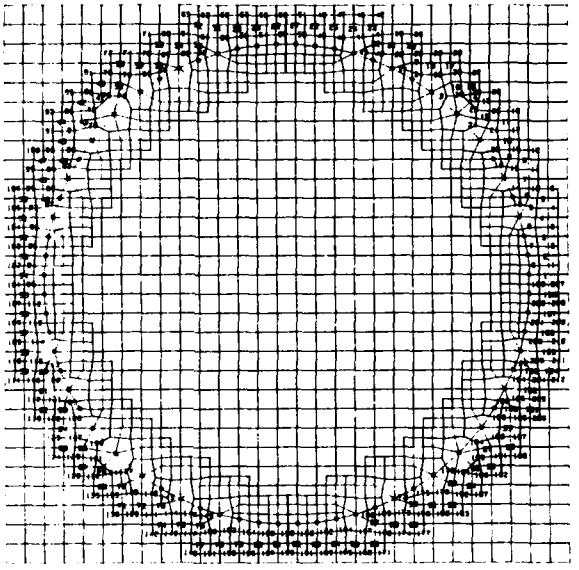

STAIRCASED CYLINDER 50 CELLS ACROSS DIAMETER

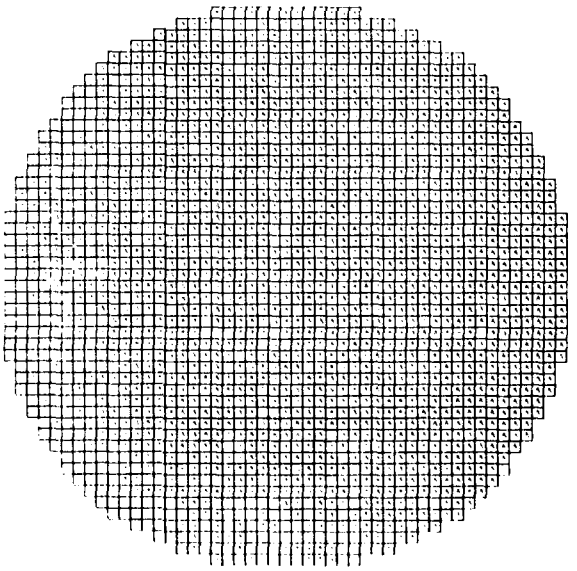

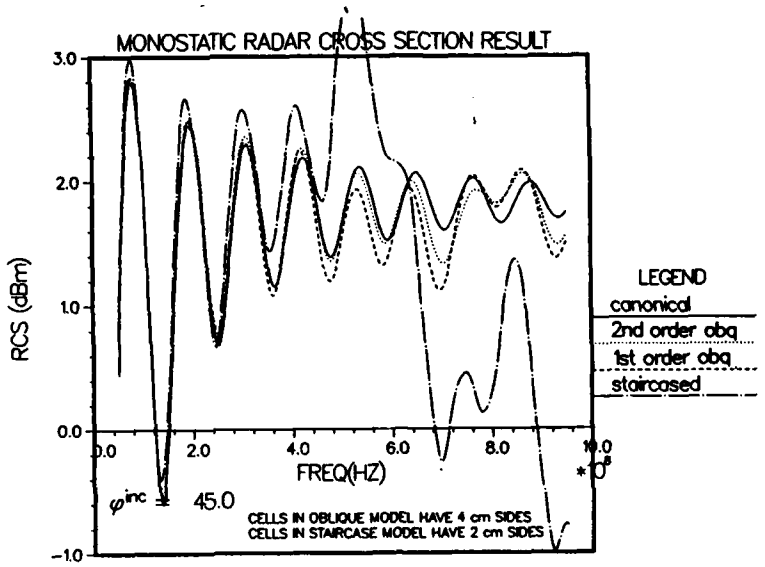
MONOSTATIC RADAR CROSS SECTION RESULT
RCS (dBm)
3.0
2.0
1.0
0.0
-1.0
2.0
4.0
6.0
8.0
FREQ(HZ)
φ^{inc} = 45.0
CELLS IN OBLIQUE MODEL HAVE 4 cm SIDES
CELLS IN STAIRCASE MODEL HAVE 2 cm SIDES
LEGEND
canonical
2nd order obq
1st order obq
staircased

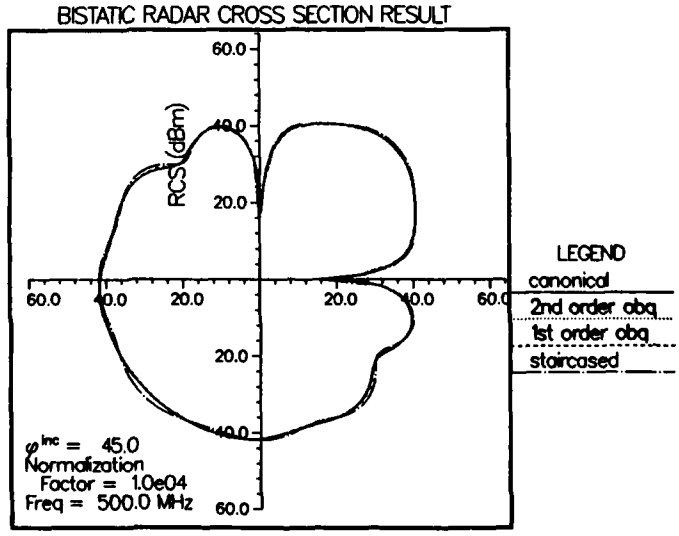
BISTATIC RADAR CROSS SECTION RESULT
RCS (dBm)
60.0
40.0
20.0
20.0
40.0
60.0
φ^{inc} = 45.0
Normalization
Factor = 1.0e04
Freq = 500.0 MHz
LEGEND
canonical
2nd order obq
1st order obq
staircased

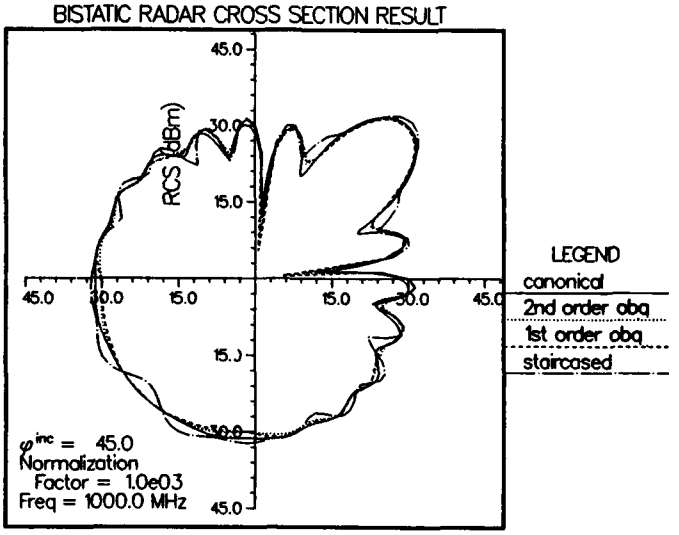

CONCLUSIONS

1. STAIRCASED MODELS DETERMINE COMPLEX RESONANT FREQUENCIES QUITE WELL.

2. STAIRCASED MODELS WILL DRIVE THESE RESONANCES VERY INACCURATELY.

3. EVEN MESHING 4 TIMES AS DENSELY DOES NOT MAKE STAIRCASING AS ACCURATE AS FACETING.

4. FOR GRAZING INCIDENCE, STAIRCASING MAY NOT WORK AT ALL, FOR ANY FINENESS OF GRID.

AN EFFICIENT ALGORITHM FOR THE ANALYSIS OF PASSIVE MICROSTRIP DISCONTINUITIES FOR MICROWAVE AND MILLIMETER WAVE INTEGRATED CIRCUITS IN A SHIELDING BOX

by

Achim Hill *
Compact Software
483 McLean Blvd
Paterson NJ 07504

ABSTRACT

A rigorous, fullwave analysis for arbitrary rectangular, passive microstrip components on a two layered substrate is presented. The method employs an algorithm which allows the efficient solution of the governing integral equation. The system matrix of the moment method is derived from a linear combination of elements in a precomputed index table. The table is obtained from a two dimensional, discrete fast Fourier transform. In the moment method procedure, the two dimensional surface current is represented by locally defined roof top functions.

Numerical results include the simulation of microstrip discontinuities such as right angle bends with and without compensated corner, open end and coupled step discontinuities.

Introduction

Numerous techniques have been developed in the past for the analysis of microstrip discontinuities [1]. The majority of these techniques are subject to certain geometry and frequency limitations which results in simplifications in the numerical treatment and leads to low computation times. With the increase in operating frequencies and the tendency to reach a higher density in circuit packages, rigorous fullwave solutions become progressively important. Accurate solutions require the incorporation of all dominating physical effects such as surface waves, interaction with the metallic enclosure and coupling effects between various circuit elements in close proximity. Various fullwave solution have been published [2-14] but the efficient numerical treatment still remains a challenge.

* This work was performed in part at Oregon State University

Numerical Formulation

The numerical formulation is set up for the configuration shown in figure 1. The source free media consists of three homogeneous, isotropic dielectric layers and is bounded by a box of perfectly conducting metal. Each layer r(r=1,2,3) of thickness H_r is characterized by its relative dielectric constant e_r. The box extends from x = 0 to x = a, y=0 to y = b with bottom and cover plates at z = 0 and z = c. The microstrip metallization of zero thickness and infinite conductivity is located at a dielectric interface. The standard moment method procedure is employed to determine the network function of a microstrip structure with ports located at the metallic walls. Using Galerkin's technique we solve the electric field integral equation in terms of the current distribution on the microstrip structure. The current on the metal interface is modeled by roof top functions as shown in figure 2.

After applying the testing procedure, the linear system of equations can be summarized as follows

$$\begin{bmatrix} V_x \\ V_y \end{bmatrix} = \begin{bmatrix} P_{xx} & P_{xy} \\ P_{yx} & P_{yy} \end{bmatrix} \begin{bmatrix} A_x \\ A_y \end{bmatrix} \qquad (1)$$

The left hand side represents the scalar product of the electric field on the metallized surface and a testing current. These vanish on the metal except for subsections where sources are defined. The system matrix P contains the testing products and the Green's dyadic of the associated boundary value problem. Vector A is formed by the expansion coefficients for the current. Details of the well known moment method formulation can be found elsewhere [6]. Here, only the equations relevant for the demonstration of the

efficient numerical treatment are repeated. The elements of the system matrix P can be written symbolically as

$$
\begin{aligned}
P_{xx}^{ij} &= \sum_m \sum_n G_{mn}^{xx} \cos k_{xm}x_{jx} \sin k_{yn}y_{jx} \cos k_{xm}x_{ix} \sin k_{yn}y_{ix} \\
P_{xy}^{ij} &= \sum_m \sum_n G_{mn}^{xy} \sin k_{xm}x_{jy} \cos k_{yn}y_{jy} \cos k_{xm}x_{ix} \sin k_{yn}y_{ix} \\
P_{yx}^{ij} &= \sum_m \sum_n G_{mn}^{yx} \cos k_{xm}x_{jx} \sin k_{yn}y_{jx} \sin k_{xm}x_{iy} \cos k_{yn}y_{iy} \\
P_{yy}^{ij} &= \sum_m \sum_n G_{mn}^{yy} \sin k_{xm}x_{jy} \cos k_{yn}y_{jy} \sin k_{xm}x_{iy} \cos k_{yn}y_{iy}
\end{aligned}
\qquad (2)
$$

where k_m, k_n and x,y represents the spectral and spacial coordinates respectively. G_{mn} symbolizes the contribution of the Green's dyadic and the basis functions for the current distribution.

Notice, in (2) for each combination (i,j) of basis functions, a two dimensional summation needs to be performed to establish the moment matrix. This process is rather time consuming and in general exceeds the time requirements for the solution of the linear system (1).

In order to reduce the computing time necessary for the formation of the moment matrix two techniques are suggested. Instead of performing the two dimensional summation for each pair (i,j) in P only one evaluation of a suitable two dimensional summation is performed for each dyadic. All elements of the moment matrix (i,j) per dyadic are then obtained from the precomputed two dimensional summation. The second acceleration technique constitutes the use of two dimensional fast fourier transform algorithms. These are used to perform the summations described in the previous sentence.

In order to employ FFT routines, the representation of the moment matrix has to be transformed into a suitable form. In addition the interface is uniformly discretized in x and y direction such that

$$
\begin{aligned}
x_{ix} &= p_{ix}\,\Delta x && , \quad p_{ix} = 0,1,\ldots,M \\
y_{iy} &= s_{iy}\,\Delta y && , \quad s_{iy} = 0,1,\ldots,N \\
x_{iy} &= \left(p_{iy} + \frac{1}{2}\right)\Delta x && , \quad p_{iy} = 0,1,\ldots,M-1 \\
y_{ix} &= \left(s_{ix} + \frac{1}{2}\right)\Delta y && , \quad s_{ix} = 0,1,\ldots,N-1
\end{aligned}
\tag{3}
$$

where M and N are the total number of subdivisions in x and y direction respectively.

After using trigonometric identities and substituting (3) into (2) the system matrix P can be rewritten as

$$
\begin{aligned}
P_{xx}^{ij} &= f_{xx}(p_{jx}-p_{ix}\,,\,s_{jx}-s_{ix}) - f_{xx}(p_{jx}-p_{ix}\,,\,s_{jx}+s_{ix}) \\
&\quad + f_{xx}(p_{jx}+p_{ix}\,,\,s_{jx}-s_{ix}) - f_{xx}(p_{jx}+p_{ix}\,,\,s_{jx}+s_{ix}) \\
P_{xy}^{ij} &= f_{xy}(p_{jy}+p_{ix}\,,\,s_{jy}+s_{ix}) - f_{xy}(p_{jy}+p_{ix}\,,\,s_{jy}-s_{ix}) \\
&\quad + f_{xy}(p_{jy}-p_{ix}\,,\,s_{jy}+s_{ix}) - f_{xy}(p_{jy}-p_{ix}\,,\,s_{jy}-s_{ix}) \\
P_{yy}^{ij} &= f_{yy}(p_{jy}-p_{iy}\,,\,s_{jy}-s_{iy}) + f_{yy}(p_{jy}-p_{iy}\,,\,s_{jy}+s_{iy}) \\
&\quad - f_{yy}(p_{jy}+p_{iy}\,,\,s_{jy}-s_{iy}) - f_{yy}(p_{jy}+p_{iy}\,,\,s_{jy}+s_{iy})
\end{aligned}
\tag{4}
$$

with

$$f_{xx}(u,v) = \sum_m \sum_n G_{mn}^{xx} \cos \frac{m\pi u}{M} \cos \frac{n\pi v}{N}$$

$$f_{xy}(u,v) = \sum_m \sum_n G_{mn}^{xy} \sin \frac{m\pi (u + 1/2)}{M} \sin \frac{n\pi (v + 1/2)}{N} \qquad (5)$$

$$f_{yy}(u,v) = \sum_m \sum_n G_{mn}^{yy} \cos \frac{m\pi u}{M} \cos \frac{n\pi v}{N}$$

The number of spectral samples required for a converged solution can exceed the upper limit M and N in the FFT routines. In this case the quantities G in (5) need to be presampled before they can be submitted to the FFT routines. This procedure is exemplified for the xx dyadic. F_{xx} in (4) is rewritten as

$$\sum_m \sum_n G_{mn}^{xx} \cos \frac{m\pi p}{M} \cos \frac{n\pi s}{N} = \sum_m \sum_n G_{mn}^{xxee} \cos \frac{m\pi p}{M} \cos \frac{n\pi s}{N}$$

$$+ (-1)^s \sum_m \sum_n G_{mn}^{xxeo} \cos \frac{m\pi p}{M} \cos \frac{n\pi s}{N} + (-1)^p \sum_m \sum_n G_{mn}^{xxoe} \cos \frac{m\pi p}{M} \cos \frac{n\pi s}{N} \qquad (5)$$

$$+ (-1)^{(s+p)} \sum_m \sum_n G_{mn}^{xxoo} \cos \frac{m\pi p}{M} \cos \frac{n\pi s}{N}$$

with the presampled quantity G_{mn}^{xxpq}

$$G_{mn}^{xxpq} = \sum_{i_p} \sum_{j_q} (m+i_pM \ , \ n+j_qN) \qquad (6)$$

where p = even or odd or q = even or odd.

Terminal impedances Z are derived from an energy formulation [6]

$$Z = - \frac{\int EJdxdy}{I^2}$$

and are post processed to determine the network matrix of the metal interface.

Results

To demonstrate the capabilities of the algorithm, network characteristics of various discontinuities are presented. The reflection coefficient of an open microstrip stub is compared to simulated results obtained from Super-Compact [16]. The stub was 5mm long and 0.5mm wide and was situated on a dielectric substrate with a permittivity of 9.8. Figure 3 shows the phase of the reflection coefficient, and the agreement is obvious.

The effect of compensating microstrip right angle bends has been discussed in [15]. Figure 4 compares the S parameter of a microstrip right angle bend with and without compensation. A square with the side length s=0.25*w was cut out of the corner region as indicated in figure 4 and leads to a reduction of the reflection S11. The line connecting to the corner was 0.635mm wide, 3.175mm long and was deposited on a 0.635mm alumina substrate.

The effect of interacting step discontinuities is shown in figure 5. Two cases are simulated and the result of each case is compared to results obtained from Super-Compact. In the first case the two steps are separated by a transmission line section of width w=3*w1 and length l=8*w1. The S parameter for this case are almost identical to those obtained from Super-Compact (figure 5 a and b) and suggest that a decoupled treatment of the two steps is a valid assumption. For the second case, the separation of the two steps was reduced to l=w1. As can be seen from figure 5 c, there is a significant difference of about 3db for the magnitude of S11 between the fullwave solution and the case where decoupled steps are assumed. For this example the linewidth w1 was 0.5mm, the w1/h ratio was 1 and the relative dielectric constant was chosen to be 9.8.

Summary

An algorithm has been presented which enhances the previously developed moment method for the full wave analysis of passive microstrip structures in a shielding box. The enhancement is accomplished by the use of index tables that are computed from 2D FFT routines. Elements of the associated moment matrix are then derived from a simple linear combination of the elements in the index table. S parameter were computed for various MMIC structures to demonstrate the capability of the presented technique.

REFERENCES

[1] Itoh Ed T., "Numerical Techniques for Microwave and Millimeter Wave Passive Structures," John Wiley & Sons, 1989.

[2] Koster N.H.L., Jansen R. R., "The Microstrip Step Discontinuity: A Revised Description," IEEE Trans. on Microwave Theory and Tech., vol. MTT-34, pp. 213-222, February 1986.

[3] Katehi P. B., Alexopoulos N.G., "Frequency-Dependent Characteristics of Microstrip Discontinuities in Millimeter-Wave Interated Circuits," IEEE Trans. on Microwave Theory and Tech., vol. MTT-33, pp. 1029-1035, October 1985.

[4] Jackson R.W., Pozar D.M., "Full-Wave Analysis of Microstrip Open-End and Gap Discontinuity," IEEE Trans. on Microwave Theory and Tech., vol MTT-33, pp. 1036-1042, October 1985.

[5] Jansen R.H., "Hybrid Mode Analysis of End Effects of Planar Microwave and Millimetrewave Transmission Lines," IEEE Proceedings, vol. 128, Pt.H, no. 2, pp. 77-86, April 1981.

[6] Rautio J.C., Harrington R.F., "An Electromagnetic time-harmonic analysis of shielded microstrip circuits," IEEE trans. on Microwave Theory and Tech., vol. MTT-35, pp. 726-730, August 1987.

[7] Jansen R.H., "The Spectral-Domain Approach for Microwave Integrated Circuits," IEEE Trans. on Microwave Theory and Tech., vol. MTT-33, pp. 1043-1056, October 1985.

[8] Jackson R.W., "Full-Wave, Finite Element Analysis of Irregular Microstrip Discontinuities," IEEE Trans. on Microwave Theory and Tech., vol. MTT-37, pp 81-89, January 1989.

[9] Skrivervik A., Mosig J. R., "Equivalent Circuits of Microstrip Discontinuities Including Radiation Effects." IEEE MTT-S Intl. Microwave Symp. Digest, pp. 1147-1150, 1989.

[10] Harokopus W. P., Katehi P.B., "An Accurate Characterization of Open Microstrip Discontinuity Including Radiation Losses," IEEE MTT-S Intl. Microwave Symp. Digest, pp. 231-234, 1989.

[11] Wertgen W., Jansen R.H., "Spectral Iterative Techniques for the Full-Wave 3D Analysis of (M)MIC Structures," IEEE MTT-S Intl. Microwave Symp. Digest, pp. 709-712, 1988.

[12] Jansen R.H., Wiemer L., "Full-Wave Theory Based Development of mm-wave Circuit Models for Microstrip Open End, Gap, Step, Bend and Tee," IEEE MTT-S Intl. Microwave Symp. Digest, pp. 779-782, 1989.

[13] Dunleavy L.P., Katehi P.B., "A Generalized Method for Analyzing Shielded Thin Microstrip Discontinuities," IEEE Trans. on Microwave Theory and Tech., vol. MTT-36, pp. 1753-1766, December 1988.

[14] Nakatani A., Maas S., Castaneda J., "Modeling of High Frequency MMIC Passive Components," IEEE MTT-S Intl. Microwave Symp. Digest, pp. 1139-1142, 1989.

[15] Hoffmann, R.K., "Integrierte Mikrowellenschaltungen."

[16] Super-Compact, PC Version 4.0, Compact Software, Paterson, NJ, 1990.

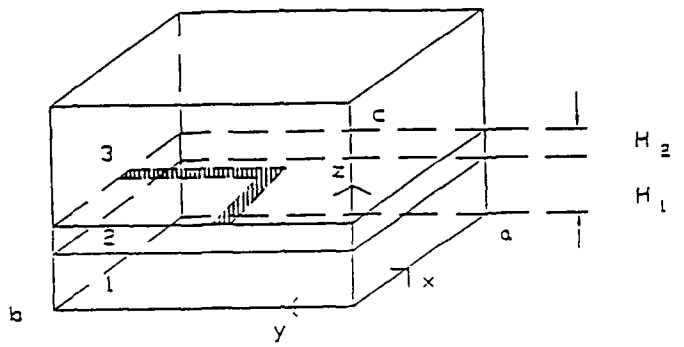

Figure 1. Microstrip discontinuity in shielded box.

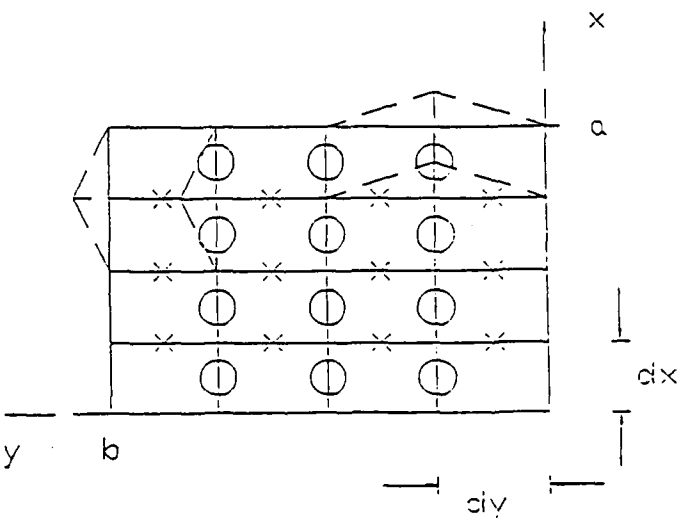

Figure 2. Discretization of conductor surface. Crosses represent center of x-directed current; circles represent centers of y-directed currents.

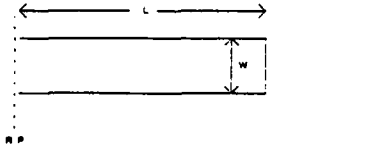

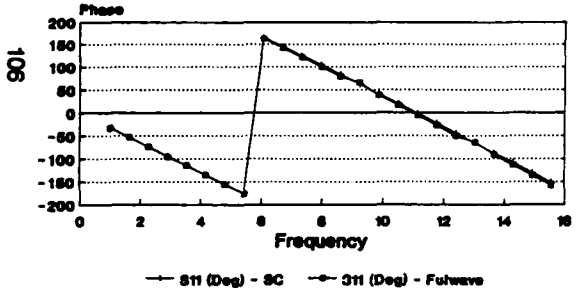

Length = 6mm, Width = 0.6mm
er = 9.8, Height = 0.6mm,
Box 9mm by 7mm by 60mm

Figure 3. Open Stub Reflection

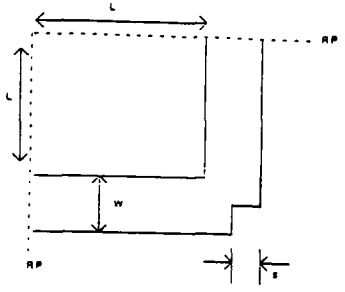

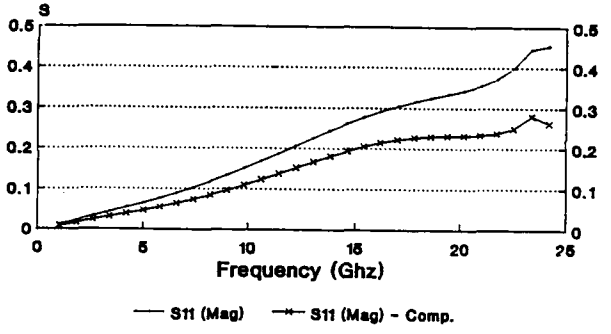

w/h = 1, er = 9.8, w = 0.635mm
Box dimension 6.35mm by 6.35mm by 635mm
l/w = 6

Figure 4(a). Right Angle Bend
Effect of Compensation

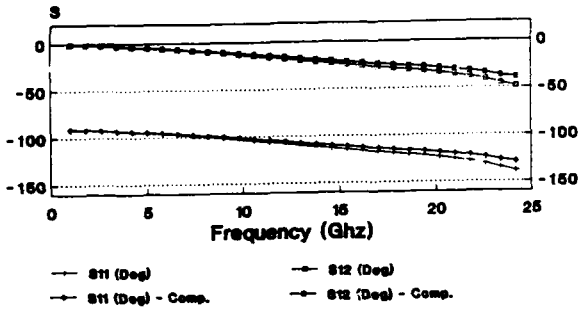

w/h = 1, er = 9.8, w = 0.635mm
Box dimension 6.35mm by 6.35mm by 635mm
l/w = 5

Figure 4(b) Right Angle Bend
Effect of compensation

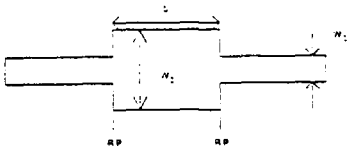

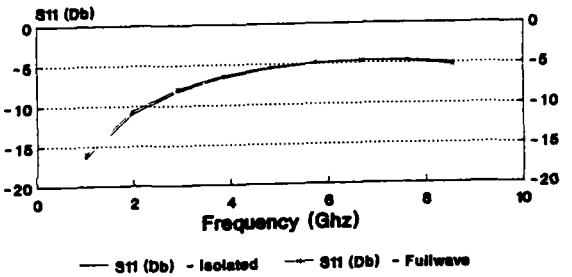

w1/h = 1, w2/h = 3, h = 0.6mm
er = 9.8
Box = 13 * w1 by 18 * w1 by 100 * w1

Figure 5(a). Step Discontinuity
Isolated vs. Coupled Analysis
I = 8 * w1

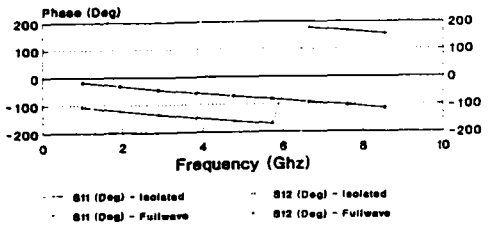

w1/h = 1, w2/h = 3, h = 0.6mm
er = 9.8
Box = 13 * w1 by 18 * w1 by 100 * w1

Figure 5(b) Step Discontinuity
Isolated vs. coupled analysis
I = 8 * w1

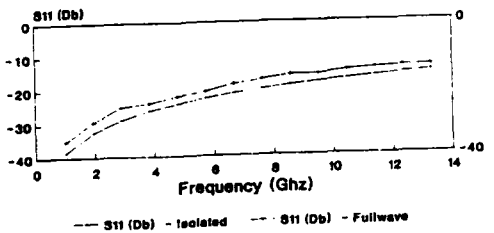

w1/h = 1, w2/h = 3, h= 0.6mm
er = 9.8
Box: 13*w1 by 11*w1 by 100*w1

Figure 5(c) Step Discontinuity
Isolated vs. coupled analysis
I = w1

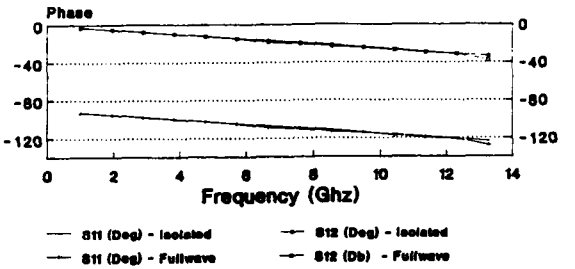

w1/h = 1, w2/h = 3, h= 0.6mm
er = 9.8
Box: 13*w1 by 11*w1 by 100*w1

Figure 5(d) Step Discontinuity
Isolated vs. coupled analysis
I = w1

Full Wave Computation of Electromagnetic Wave Excitation, Propagation, and Absorption at the Ion Cyclotron Frequency in Fusion Experiments*

D. B. Batchelor and E. F. Jaeger
Oak Ridge National Laboratory

High-power electromagnetic waves at frequencies ranging from a few megahertz to a few hundred gigahertz serve many important functions in modern fusion experiments. Probably the most important application is plasma heating. Ignition of a fusion reactor will require a plasma to be heated until the average particle energy is ~10 keV (temperature > 10^8 K). This is routinely accomplished in existing large devices. Waves at the ion cyclotron frequency (typically f = 30 to 100 MHz) are very important for fusion devices because of low cost/unit power compared to other frequency regimes and because of their ability to directly heat fusile ions. These waves are also useful for modifying the velocity distribution for improved stability and to drive currents which affect plasma equilibrium. Study of this frequency range is, however, greatly complicated by long wavelengths compared to device size, nonsymmetric device geometry, and the tendency of the waves to linearly transform to shorter wavelength modes. Geometrical optics is generally inapplicable. Thus, codes have been developed to solve the vector wave equation in toroidal geometry for hot plasmas having anisotropic, spatially nonuniform, dispersive constitutive relations.

In this paper we describe the code ORION [1–4] developed at Oak Ridge National Laboratroy and present illustrative applications to a range of fusion experiments. Specific applications of the code include detailed modeling of the antennas used to launch the waves, calculation of wave propagation throughout the plasma, and modeling of the absorption of the waves by the plasma.

1. Mathematical Formulation

For purposes of this paper we restrict consideration to toroidally axisymmetric devices such as tokamaks (Fig. 1) [5,6]. These devices consist of a toroidal shell vacuum vessel, assumed to be perfectly conducting, filled with a hot magnetized plasma. The plasma is contained by a magnetic field $\mathbf{B}^0(\mathbf{x})$, which on the time scale of the wave motion, 1/f, is steady state. The field lines of this equilibrium magnetic field wrap helically around the device and form approximately elliptical, nested surfaces called flux surfaces. The plasma density and temperature are approximately constant on flux surfaces; therefore, it is sometimes convenient to introduce a radial like coordinate, ψ, which labels the flux

*Research sponsored by the Office of Fusion Energy, U.S. Department of Energy, under contract DE-AC05-84OR21400 with Martin Marietta Energy Systems, Inc.

surfaces. The magnetic field strength does not follow the flux surfaces but varies roughly as 1/R, where R is the distance from the axis of symmetry. Another convenient coordinate is the poloidal angle, θ, which is measured the short way around the torus (see Fig 1).

Conceptually the wave formulation is straightforward. The waves of interest have periods much shorter than any other time scale (e.g., heating time or plasma flow time) and the absorption processes are linear, so we may safely assume the solutions to be time harmonic. Thus, the wave equation is simply the $\nabla\times\nabla\times\mathbf{E}$ Maxwell's equation,

$$\nabla \times \nabla \times \mathbf{E} - \frac{\omega^2}{c^2}\,\sigma\cdot\mathbf{E} = i\omega\mathbf{J_{ext}} \tag{1}$$

where σ is the plasma conductivity tensor operator and $\mathbf{J_{ext}}$ is the external current due to the antenna. Boundary conditions are that the tangential components of $\mathbf{E}$ vanish on the conducting wall. A second version of the code, which is needed for certain applications as explained below, introduces the potentials $\mathbf{A}$ and Φ along with the Coulomb gauge $\nabla\cdot\mathbf{A} = 0$. Then the waves are described by

$$\nabla^2\mathbf{A} + \frac{\omega^2}{c^2}\,\sigma\cdot\mathbf{A} + \frac{i\omega}{c^2}\,\sigma\cdot\nabla\Phi = -\mathbf{J_{ext}} \tag{2}$$

$$\nabla\cdot(\sigma\cdot\nabla\Phi) - i\omega\,\nabla\cdot(\sigma\cdot\mathbf{A}) = -\rho_{ext} \tag{3}$$

where ρ_{ext} is the external charge on the antenna. The boundary conditions are $\mathbf{A}_t = 0$ and $\Phi = 0$ on the conducting wall.

The field quantities and source terms can be expanded as a Fourier series in ϕ:

$$\mathbf{E}(r,\theta,\phi) = \sum_N \mathbf{E}_N(r,\theta)\, e^{iN\phi} \qquad \mathbf{J}_{ext}(r,\theta,\phi) = \sum_N \mathbf{J}_N(r,\theta)\, e^{iN\phi} \tag{4}$$

Since the plasma and boundary are uniform in the ϕ coordinate, the Fourier modes are uncoupled. The matrix to be inverted is two-dimensional (2-D), although the structure of the summed fields is three-dimensional (3-D). The 2-D equations obtained by substituting Eq. (4) into Eqs. (1)-(3) are solved by finite difference techniques.

2. Plasma Constitutive Relation:

The primary challenge in this work is to correctly model the current distribution induced in the plasma by the wave fields. To place the complexity of plasma wave phenomena in perspective, recall that in a uniform volume of air there are two basic waves: acoustic waves, which are longitudinal, and light waves, which are transverse. These waves are non-dispersive ($v_{phase} = \omega/k = const$) and except in the most extreme cases are uncoupled. However, in a hot magnetized plasma an infinite number of distinct waves exist [7]. Polarizations range from purely longitudinal (electrostatic waves) to purely transverse (electromagnetic waves). Phase speed and wavenumber can vary appreciably over short distances within the plasma volume. Waves can be very strongly absorbed, with damping length $< \lambda$. And local matching of wavenumber and polarization can occur, resulting in conversion from one wave type to another.

The simplest model is the cold plasma approximation. In the older literature, particularly in the ionospheric propagation field, this is referred to as magneto-ionic theory [8]. If the average particle velocity, $v_{thermal}$, is much smaller than the wave phase velocity, $v_{phase} = \omega/k$, the particles experience an oscillatory acceleration which is proportional to the local electric field. The wave-particle interaction is then approximately local in space and harmonic in time. The plasma current is of the form

$$\mathbf{J}_{plasma}(\mathbf{x},t) = \sigma(\mathbf{x},\omega)\cdot\mathbf{E}(\mathbf{x},t) \tag{5}$$

where $\sigma(\mathbf{x},\omega)$ is a nondiagonal tensor that depends locally on the equilibrium magnetic field vector $\mathbf{B}^0(\mathbf{x})$ and the densities of the various plasma particle species $n_j^0(\mathbf{x})$. This tensor is singular, permitting resonant absorption, at surfaces where the local cyclotron frequency ($\Omega_j = e_jB^0/m_jc$) equals the wave frequency for some species j. There also exist other resonances (wavenumber $k \rightarrow \infty$) called hybrid resonances and cutoffs, or surfaces of reflection ($k \rightarrow 0$), within the plasma volume.

This simple model describes the plasma response reasonably well over most of the plasma. However, near resonances the wave phase velocity, ω/k, decreases and may approach the particle thermal speed. Also near cyclotron resonance, the Doppler-shifted wave frequency in the particle frame of reference, $\omega - kv$, may equal the local cyclotron frequency. Here v is the particle velocity parallel to the wave. In either case the particle experiences a slowly varying accelerating field and may have coherent interactions with the wave over extended regions of space and time. In such cases the conductivity is a nonlocal, integral tensor operator on the wave field:

$$\mathbf{J}_{plasma}(\mathbf{x},t) = \int d^3\mathbf{x}'dt'\ \sigma(\mathbf{x},\mathbf{x}',t,t')\cdot\mathbf{E}(\mathbf{x}',t') \qquad (6)$$

This introduces dissipation throughout the plasma volume (not just at singular surfaces) and introduces a number of new, short-wavelength, electrostatic modes called Bernstein waves. The mathematical problem in this form is equivalent to an infinite-order differential system. In the ORION code the integral operator is expanded to second order in the gyromotion of the plasma particles about the equilibrium magnetic field [9]. In this expansion the conductivity tensor remains local, but now depends on a local wavenumber $\mathbf{k}$, which is determined from a local dispersion relation. In this formulation, conversion of the electromagnetic ion cyclotron modes to Bernstein modes is neglected but the energy lost from the incident ion cyclotron waves is adequately modeled.

3. Numerical Considerations

Two different situations occur in practice. Case (1): In most cases of interest the plasma densities in tokamaks are sufficiently high that the electron conductivity parallel to $\mathbf{B}^0$ is much greater than that perpendicular to $\mathbf{B}^0$. In that case the wave electric field parallel to $\mathbf{B}^0$, $\mathbf{E}_{||}$, is very much smaller than $\mathbf{E}_{\perp}$ and can be calculated perturbatively. The numerical approach in this case is to solve Eq. (1) for $\mathbf{E}_{\perp}$. Case (2): When low plasma densities are of interest, for example for modeling the outside edge near the antenna, the parallel conductivity may be much smaller so that $\mathbf{E}_{||}$ must be solved for directly. In this case the numerical approach is to solve Eqs. (2) and (3) for the potentials. This approach resolves mathematical difficulties associated with direct inversion of the $\nabla\times\nabla\times$ operator and properly includes electrostatic effects. Special care must be taken to ensure that the finite differencing scheme is consistent with the gauge condition $\nabla\cdot\mathbf{A} = 0$. The finite difference representation preserves the natural grouping of partial derivatives as they occur in the differential equation and in this sense is "conservative." In both cases the finite difference problem is solved by direct matrix inversion using the MA32 package [10] for sparse, unsymmetric systems. This method is based on Gaussian elimination using a modification of the frontal scheme of Hood [11]. It has the advantage that only a small part of the total matrix need be stored in memory at one time.

4. Results from the ORION Code

Figure 2 shows calculations for the poloidal cross section of the Alcator C-Mod tokamak, which is under construction at MIT. The height of the vacuum vessel is about 75 cm. The axis of symmetry is to the left of the cross sections shown, approximately 66 cm from the center. For these calculations, the plasma consisted of electrons with peak density $n_e = 4 \times 10^{14}$ cm^{-3}, deuterium ions with density $n_D = 0.96n_e$, and a minority hydrogen ion species with density $n_H = 0.04n_e$. The temperature of all species was $T = 2$ keV. The magnetic field strength at the center was $B_0 = 5.0$ T. The wave frequency was 80 MHz. The

antenna consists of a strap of width $L_s = 12.5$ cm located outside the plasma in the recessed area to right [see Fig. 2(a)]. The vertical dashed line is at the location of the hydrogen fundamental cyclotron resonance ($\Omega_H = \omega$). Another plasma resonance called the ion-ion hybrid resonance lies just to the left of the hydrogen fundamental. Figure 2(a) is a grey scale intensity plot of one component of the wave electric field, $Re\{E_x\}$. The free space wavelength at 80 MHz is 375 cm. However, it is seen that the high effective refractive index N of the plasma to these waves reduces the actual wavelength in the high density, central region to $\lambda = c/\omega N \sim 6$ cm. In the outer regions where the density is low, the refractive index is also small. Since the finite extent of the antenna in the toroidal direction induces a minimum toroidal wavenumber, $k_T = 1/\lambda_T \sim 1/L_s >> \omega/c$, and the radial wavenumber k_R satisfies $k_R^2 = N^2\omega^2/c^2 - k_T^2 < 0$. the radial wavenumber is imaginary at the outside of the plasma. The waves are therefore evanescent and must "tunnel" through to the inner region. One can see the focusing toward the center of the propagating waves due to the radially decreasing refractive index and the decrease in wave amplitude due to absorption at the cyclotron and hybrid resonances.

The primary quantity of interest in these calculations is the spatial distribution of power absorption. This, as shown in Fig. 2(b), occurs at the hydrogen cyclotron resonance and the ion-ion hybrid resonance. A check on the accuracy of the computation can be made by comparing the total absorbed power obtained by integrating $\mathbf{E}^* \cdot \sigma \cdot \mathbf{E}$ over the plasma volume with the total radiated power obtained by integrating $\mathbf{E}^* \cdot \mathbf{J}_{ext}$ over the antenna. For the present calculations, these agree to within 8%. This calculation also gives a useful quantity, the antenna load resistance. To obtain these results the grid consisted of 101 radial mesh points and 50 poloidal points. A total of 50 toroidal Fourier harmonics were included in the summed field, requiring 80 min of CPU time on a Cray 2. It was possible to perform these calculations with full memory storage; 9 million words were required.

An important application of codes such as ORION is to the detailed modeling of fields near the antenna structures. This is both for the purpose of understanding the radiation characteristics of the antennas and for minimizing high-voltage breakdown and sputtering due to near fields. A common technique for improving antenna performance is to eliminate stray toroidal electric fields by placing a Faraday shield consisting of conducting bars in the toroidal direction in front of the antenna.

Figure 3 shows a sequence of calculations for the DIII-D tokamak at General Atomics that focuses on the details of the fields near the antenna. This is a somewhat larger device than Alcator C-Mod, with a 260-cm-high vacuum vessel and a radius from the symmetry axis to the center of the cross section of 167 cm. For these calculations the peak electron density was $n_e = 8 \times 10^{13}$ cm^{-3} and the plasma temperature was $T = 3$ keV. The magnetic field at the center was $B_0 = 1.7$ T. In Fig. 3(a) the solution for $Im\{E_y\}$ was computed across the entire cross section using the version of ORION which solves Eqs. (2) and (3). In Fig. 3(b) the computational domain was reduced to that indicated by the rectangular box. Thus,

the density of grid points in this region was increased by a factor of about 3. Again, perfectly conducting boundary conditions were imposed at the edge of the domain, but reflections were eliminated in the portion of the boundary lying in the plasma by introducing an artificially large collisional absorption near the edge. Except near the artificial absorber the agreement between the solutions in Figs. 3(a) and 3(b) is good. Figure 3(c) shows the same case but with conducting metal rods inserted as a Faraday shield. One can see the field compressed between the shield blades and some perturbation of the radiated fields in the plasma region. These calculations have proved very useful in understanding the mechanism for increased plasma sputtering due to RF fields near antennas [4]. For this calculation the grid was an 85×85 rectangular mesh. Owing to the increased number of mesh points and increased number of equations per point ($A_{||}$ and Φ are now included) it was no longer possible to invert the matrix in full storage. A 100 million word disk file was required. Solution for each toroidal mode takes 16 min of Cray 2 time. The solutions shown in Fig. 3 represent a single mode.

5. Conclusion

We see that it has now become feasible to study wave phenomena in very complicated 2-D geometries and in nonuniform, dispersive, dissipative media. These calculations are of great practical importance for understanding the results of fusion experiments and for designing future devices. The assumption of a 2-D boundary is adequate for studying the penetration of the waves into the center of the plasma and for calculating the absorption profiles. *It would be desirable to include the three-dimensionality of the antenna structures* at the plasma edge. However, it does not appear computationaly feasible to include such a complicated medium as a hot plasma in a 3-D code at this time.

References

[1] E. F. Jaeger, D. B. Batchelor,H. Weitzner, and J. H. Whealton, *Comuput. Phys. Commun.* **40**, 33 (1986).

[2] D. B. Batchelor, E. F. Jaeger, and P.L. Colestock, *Phys. Fluids* B **1**, 1174 (1989).

[3] E. F. Jaeger, D. B. Batchelor, and M. D. Carter, *Nucl.Fusion*, **30**, 505 (1990).

[4] I. S. Lehrman, P. L. Colestock, and E. F. Jaeger, "Edge Modeling of ICRF Heated Plasmas on PLT," submitted to *Nucl.Fusion* (1990).

[5] L. A. Artsimovich, *Nucl.Fusion*, **12**, 215-252 (1973).

[6] John Wesson, *Tokamaks* (Oxford Science Publications, Oxford, England, 1987).

[7] K. Miyamoto, *Plasma Physics for Nuclear Fusion*, (MIT Press, Cambridge, Mass., (1989).

[8] K. G. Budden, *Radio Waves in the Ionosphere*, (Cambridge Univ. Press, Cambridge, England 1961).

[9] E. F. Jaeger, D. B. Batchelor, and H. Weitzner, *Nucl Fusion*, **28**, 53 (1988).

[10] I. S. Duff, MA32 – A Package for Solving Sparse Unsymmetric Systems Using the Frontal Method, Atomic Energy Researach Establishment Report AERE R.10079, H.M. Stationer's Office, London, 1981.

[11] P. Hood, *Int. J. Numer. Methods Engrg.* **10**, 379 (1976).

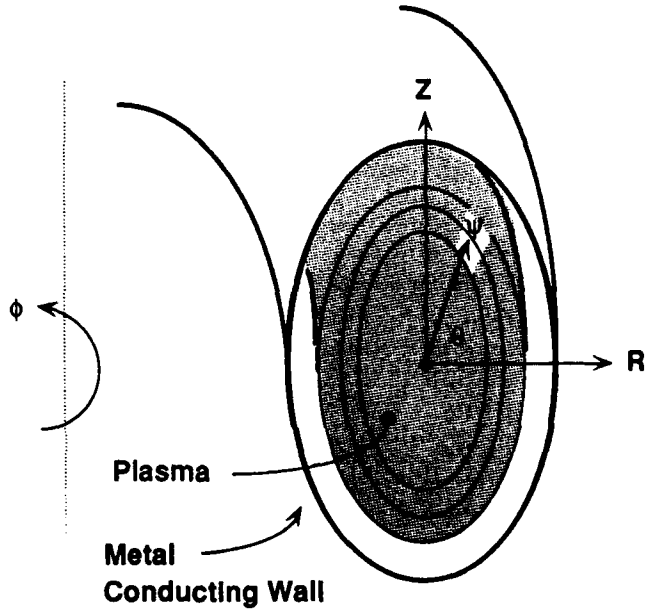

Fig. 1. Tokamak - toroidally symmetric geometry.

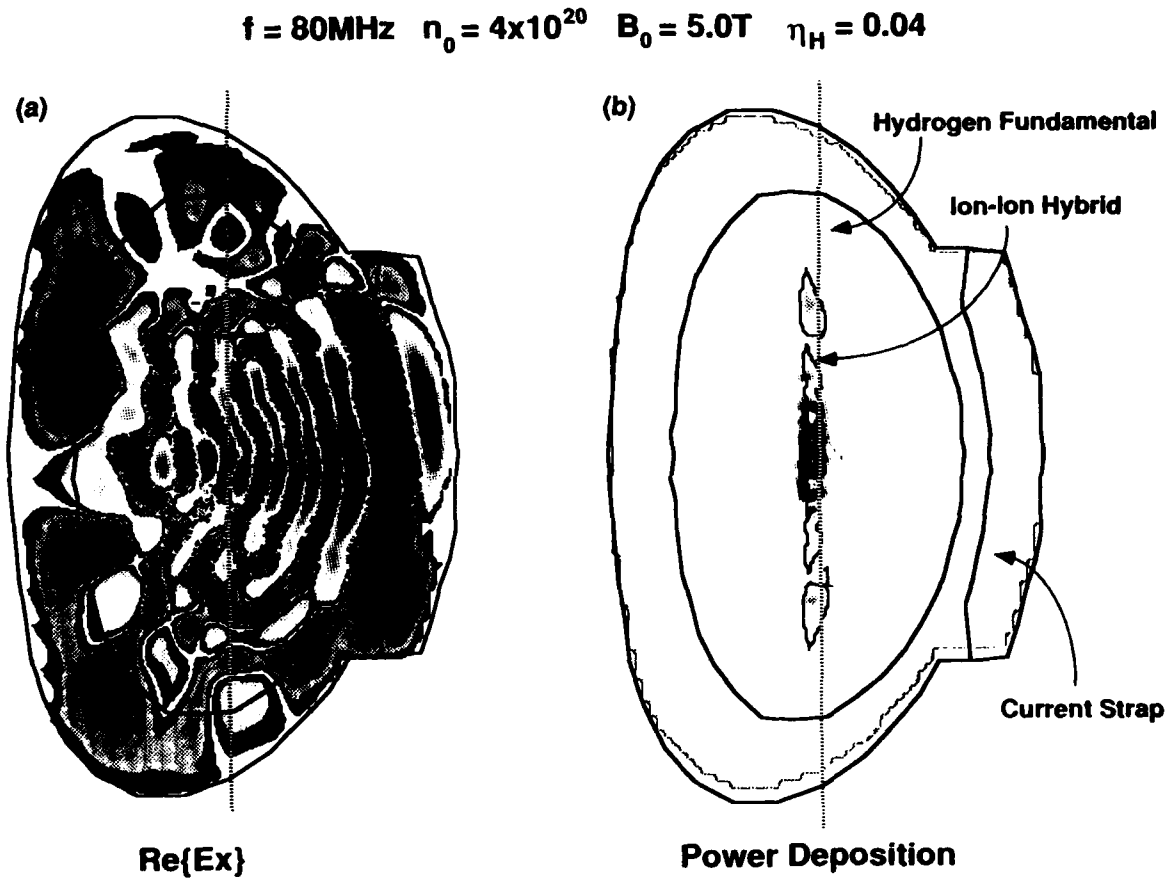

Fig. 2. Alcator C-mod D-H.

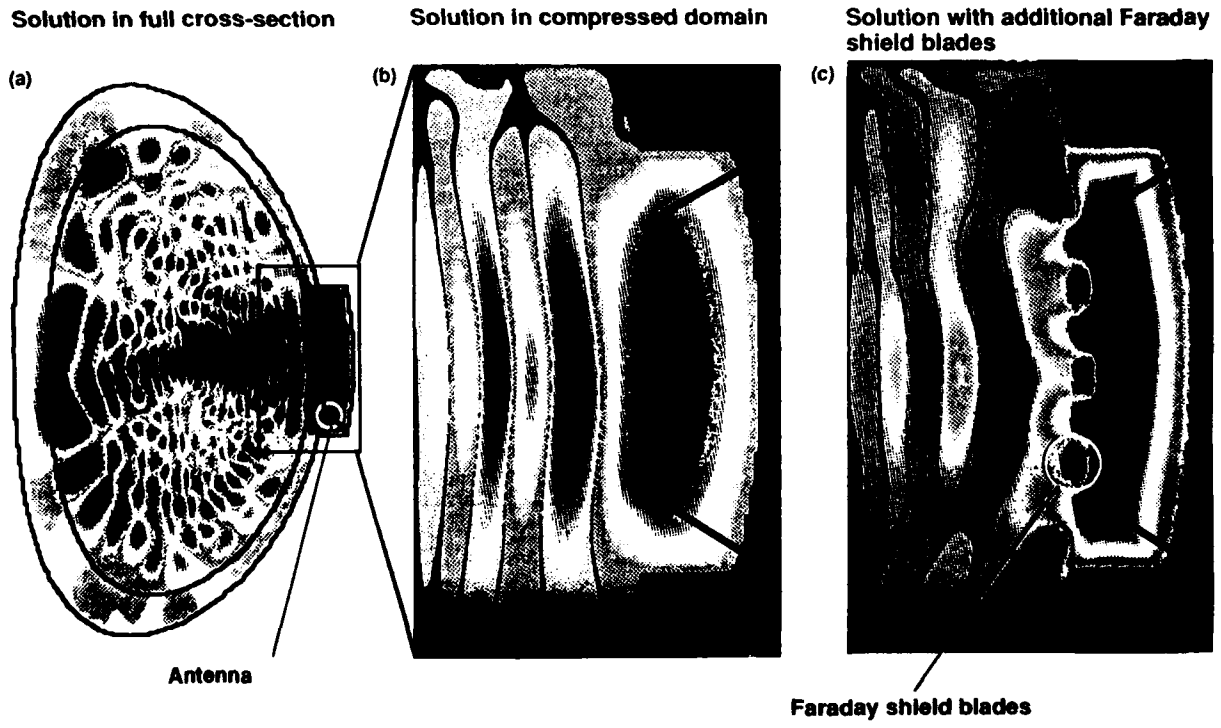

Fig. 3. Detailed modeling of antenna near fields in Tokamak geometry.

[10] I. S. Duff, MA32 – A Package for Solving Sparse Unsymmetric Systems Using the Frontal Method, Atomic Energy Researach Establishment Report AERE R.10079, H.M. Stationer's Office, London, 1981.

[11] P. Hood, *Int. J. Numer. Methods Engrg.* **10,** 379 (1976).

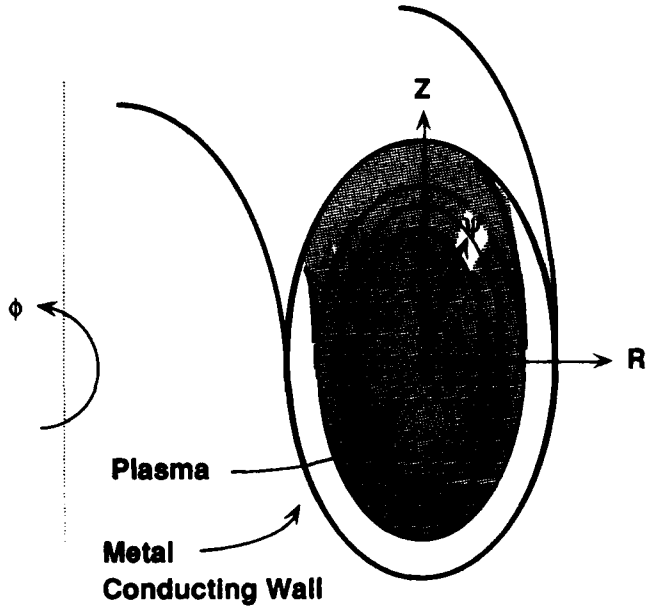

Fig. 1. Tokamak - toroidally symmetric geometry.

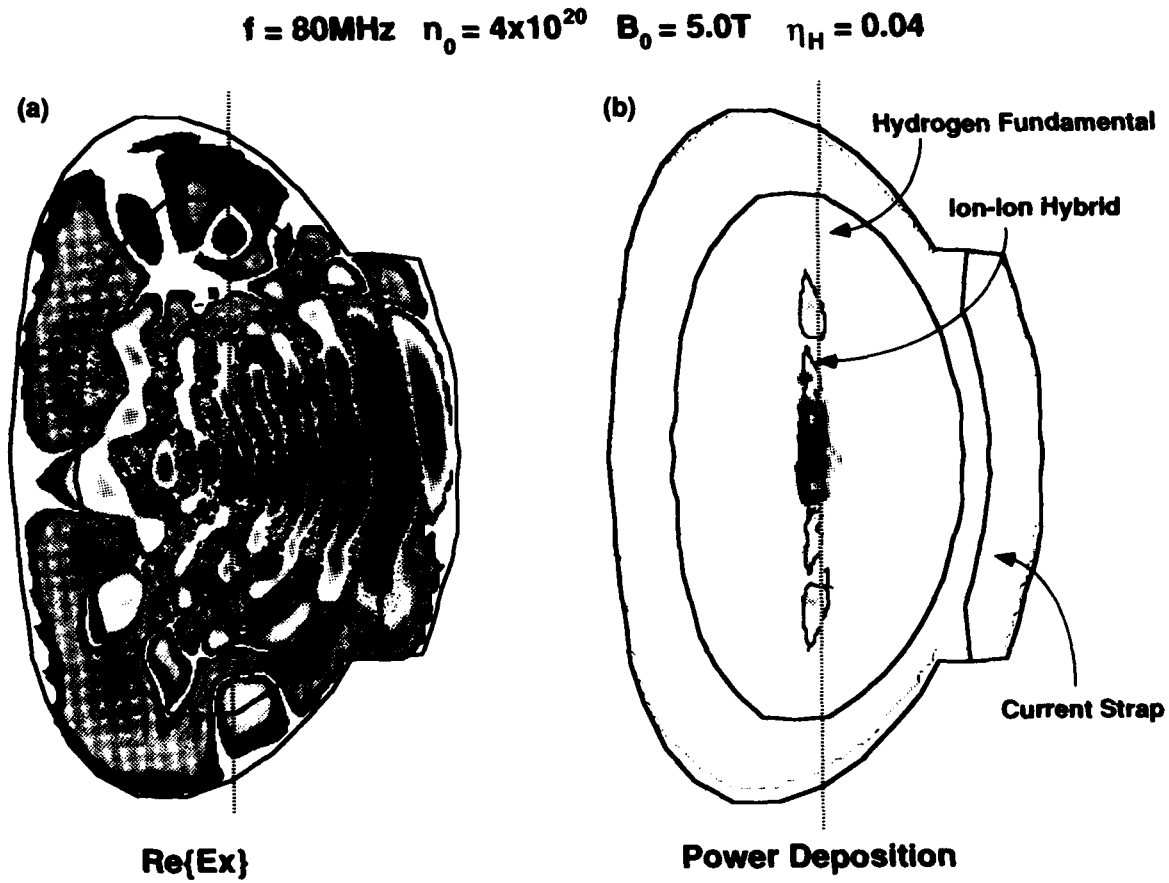

Fig. 2. Alcator C-mod D-H.

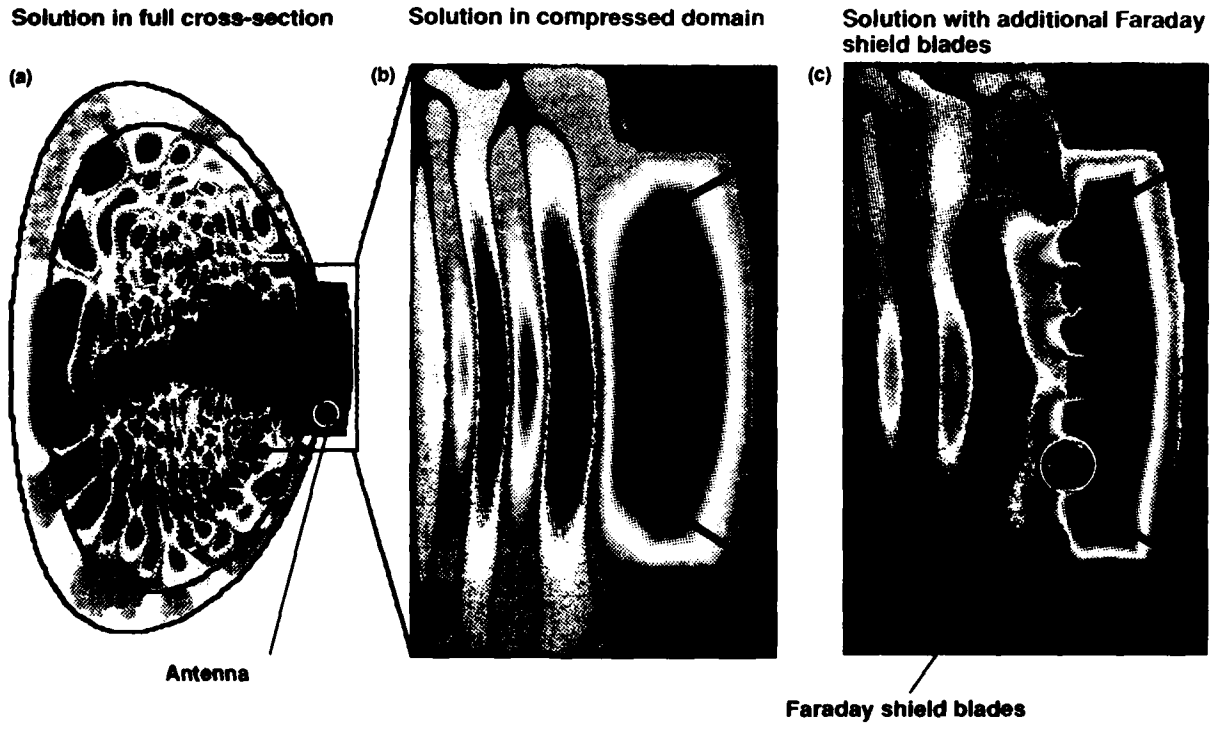

Fig. 3. Detailed modeling of antenna near fields in Tokamak geometry.

EXTRAPOLATION OF RADAR CROSS SECTION DATA INTO THE RAYLEIGH REGION USING A CROSSED DIPOLE METHOD

D. P. Allen and L. J. Teig
The MITRE Corporation
Burlington Road
Bedford, MA 01730

ABSTRACT

We have recently used a crossed dipole method to calculate the radar cross section RCS) of several aircraft for various frequencies and viewing angles in the Rayleigh region ecause noise in measured data prevented the direct use of those data at these small RCS alues.

This method involves representing the aircraft as two crossed dipoles, one representing ıe fuselage and the other representing the wings. An expression for the cross section ontribution of an individual dipole was taken from Section 17.8 of J. D. Jackson's Classical lectromagnetics [1] and modified to give:

$$\sigma = \frac{\sigma_o f^4 \cos^2\theta_1 \cos^2\theta_2}{\left(f_o^2 - f^2\right)^2 + f^2\left[\Gamma' + \Gamma f^2/f_o^2\right]^2}$$

'here f is the frequency and σ_o , f_o , Γ , and Γ' are constants to be determined for each ipole. The cosine terms are the dot products of a unit vector in the dipole axial direction and nit polarization vectors for the incident and scattered waves, respectively.

The four constants for each dipole were determined by using a nonlinear chi-squared fit to the measured data near resonance. The wing dipole used measurements at 0° azimuth while the body dipole used measurements at 90° azimuth. A ninth parameter used to determine the mixing of the two dipoles was fit to measured data at 45° azimuth. The cross section results generated by this method were compared with values generated by a modified version of D. R. Wilton's low-frequency method-of-moments code EFIE2. Results from this comparison will be presented in this paper.

INTRODUCTION

Much of the work that we do involves the use of the radar cross section (RCS) of complicated targets. Ideally, we would like to use RCS measurements of the actual target. Such measurements are not generally available, however, so we use the next best source of RCS data, scale model measurements, whenever they are available. Due to physical limitations of measurement ranges, such measurements sometimes include noise that reduces their accuracy. Figure 1 shows horizontal polarization RCS measurements of a scale model Beechcraft Duke aircraft at 6° elevation and 0° azimuth (nose-on; solid line); 45° azimuth (dashed line); and 90° azimuth (broadside; dotted line) taken as functions of frequency by SRI International for the United States Air Force. This figure shows that noise contributed significantly to the RCS values in the Rayleigh region for this target, introducing oscillations into an area that would normally exhibit a smooth, rapidly rising dependence on frequency.

An alternative to using measured data would be to use a method-of-moment code (e.g., EFIE2 [2], NEC [3], or RADCRCS) to calculate the target RCS. This approach can be slow and tedious, however, because the appropriate target computer models that have to be generated before running the code are usually very complex.

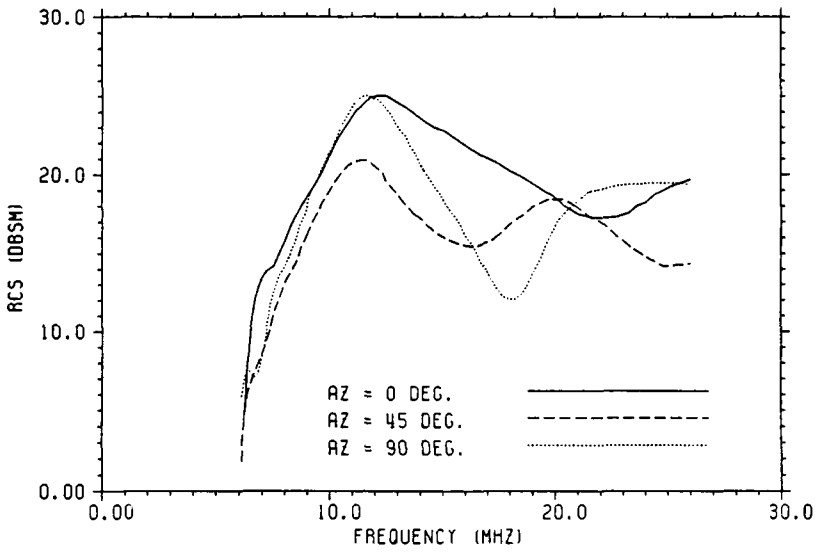

Figure 1. Scale Model RCS Measurements of the Beechcraft Duke

In order to avoid these problems, we developed the crossed dipole method. This method is used to accurately extrapolate measured RCS from the resonance peak area (which is presumably much freer of noise than the Rayleigh region), down into the Rayleigh region. The method also yields accurate RCS values at these frequencies for aspect angles for which there are no measurements.

This paper describes the crossed dipole method and its implementation. For validation, the crossed dipole extrapolations and the original measurements are compared with RCS values generated with our code EFIE.

THE CROSSED DIPOLE METHOD

The crossed dipole method involves representing the target as a pair of mutually perpendicular horizontal dipoles, one representing the wings and the other representing the fuselage. The dipole lengths approximate the length or span of these target body features. A third vertical dipole is not needed since, in the Rayleigh region, the RCS of an object is proportional to its length taken to the sixth power. The targets we deal with have much larger horizontal than vertical dimensions; thus, the contribution of such a vertical dipole would probably be negligible.

The expression for the cross section of an individual dipole is taken from the expression in Jackson [1] for the differential scattering cross section of an electric charge bound by a spherically symmetric, linear, restoring force and by other dissipative forces. We modify that expression to fix the dipole direction so that the charge oscillations will lie along the wing and fuselage directions as appropriate, while the original expression will allow the induced charge to oscillate along the incident electromagnetic wave polarization vector. This modification results in the double dot products mentioned below. The final expression is:

$$\sigma = \frac{\sigma_o f^4 \cos^2\theta_1 \cos^2\theta_2}{\left(f_o^2 - f^2\right)^2 + f^2\left[\Gamma' + \Gamma f^2 / f_o^2\right]^2} \qquad (1)$$

where f is the frequency and σ_o , f_o , Γ , and Γ' are parameters to be determined from the measured data. The cosine terms are the dot products of a unit vector in the dipole direction with unit polarization vectors for the incident and scattered waves, respectively. The parameter f_o is effectively the resonance frequency, or equivalently, the dipole length, while the parameters Γ and Γ' are related to the resonance width.

The dipoles have nulls in their radiation pattern along their axes, due to the dot products mentioned above. Thus, 0° elevation, broadside, horizontally-polarized radiation can only be due to fuselage dipole excitation, while 0° elevation, nose-on, horizontally-polarized radiation can only be due to the wing dipole excitation. The appropriate data set can thus be used to fit the dipole parameters for each dipole individually. We fit the parameters using the data around the resonance peak only, using an augmented version of the nonlinear least-squares fitting routine CURFIT from Bevington [4].

At aspect angles other than nose-on or broadside, or at elevation angles other than 0°, both dipoles will contribute to the target cross section. We have chosen to parametrize the combined cross section at those aspects with:

$$\sigma_{xx} = C*\left[\sqrt{\sigma^1_{xx}} + \sqrt{\sigma^2_{xx}}\right]^2 + (1-C)*\left[\left(\sqrt{\sigma^1_{xx}}\right)^2 + \left(\sqrt{\sigma^2_{xx}}\right)^2\right] \quad (2)$$

where σ_{xx} represents the combined RCS and σ^1_{xx} and σ^2_{xx} are the individual dipole cross sections. The subscript xx represents the polarization matrix component, e.g., HH or VH. The parameter C, which we call the coherence factor, multiplies the coherent sum of the individual dipole cross sections, while the factor (1-C) multiplies the incoherent sum of the individual dipole cross sections. An eyeball fit to the resonance region of 45° azimuth data is used to determine the value for this parameter.

At this stage, all the parameters of this method have been determined, and the crossed dipole model can be used by itself to represent the RCS of the target at Rayleigh region frequencies. These results can also be used to replace measured data at frequencies below the resonance peak where the results and the measurements diverge, yielding accurate RCS values through both the Rayleigh and resonance regions.

TESTING THE METHOD

To initially test this method on a complex target, we used calculated RCS values for a Learjet, for which we had an already existing triangular patch model. The calculations were done using our EFIE code, which is a modified version of the code EFIE2 written by Wilton, Rao, and Glisson [2]. The major modifications include:

1.) The ability to handle target models with up to 9,000 unknowns (current elements).
2.) The use of the SCAMP and TRIGPE modeling packages to create target models (these two programs were developed by the Syracuse Research Corporation and modified by us).
3.) Changes to the algorithm implementation to decrease the run time, and transferring the code to an array processor.

The Learjet model is shown in Figure 2a. This model has approximately 1000 current elements and a maximum edge length of one meter ($\lambda/10$ at 30 MHz). The method parameters were found as described above using the horizontal polarization 0° (nose-on), 45°, and 90° (broadside) azimuth curves, except that the elevation angle of the calculations was 6° rather than 0°. This was done to mimic the measurements shown in Figure 1. The fact that at this low elevation angle the appropriate dipole dominates the nose-on and broadside curves for this target allows the method to yield accurate results. Frequencies between 6 MHz and 26 MHz were used to fit both dipoles. The curves in Figure 2b, 2d and 2f show that the method reproduces the EFIE calculations well at frequencies below the lower fit frequency. The remaining curves show that the method yields correct RCS values at azimuths which were not

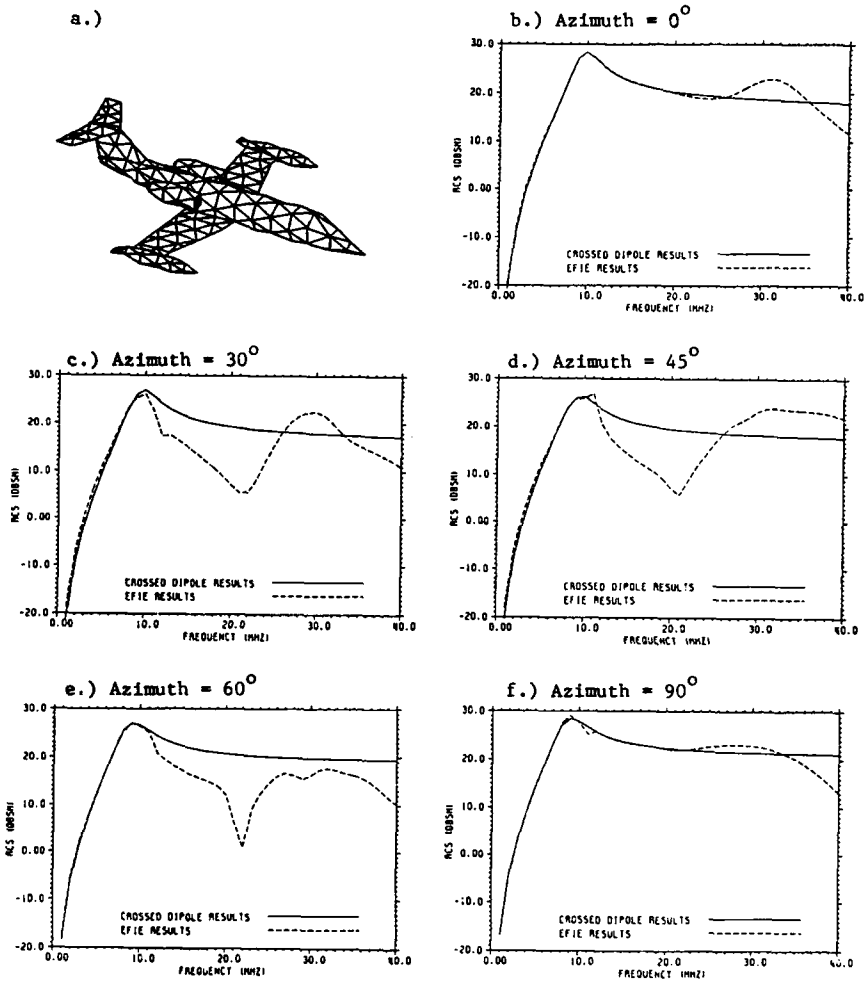

Figure 2. a.) EFIE Model of the Learjet
b.) through f.) Learjet Horizontal Polarization Crossed Dipole and EFIE RCS Calculations at 6° Elevation

used for the parameter fits. The curves also show that the agreement is poor above the resonance peak at aspects other than 0° and 90°.

VALIDATION

The measured scale model Beechcraft Duke data shown in Figure 1 were fit in the manner described above. For this case, the data between 8 and 18 MHz were used to fit both dipoles.

To validate the method, EFIE was run on the Duke target model shown in Figure 3a for the aspect angles for which we have measurements, as well as for other aspect angles. This model has approximately 2000 current elements, again with a one meter maximum edge length. The results of these computations are shown as the dashed curves in Figures 3b through 3f. The crossed dipole results (the solid curves) generated from the measured data and, where available, the original measurements (the dot-dashed curves in Figures 3b, 3d, and 3f) are also shown. The EFIE results agree with the measured data where the latter is valid. Below the resonant peak, the results of the dipole method agree with the EFIE calculations.

CONCLUSIONS

We have developed a fast, accurate method to extrapolate measured RCS data from the resonance region down in frequency into the Rayleigh region. The figures above show good agreement between the method and full method-of-moment calculations in that region at aspect angles at which the original measurements were taken, as well as at other aspect angles for which there are no measurements. The lack of good agreement above the first resonance between the method results and the measurements and calculations may be ameliorated by using a better method of combining the contributions of the two dipoles, i.e., appropriately phasing them. A follow-on study will examine this aspect.

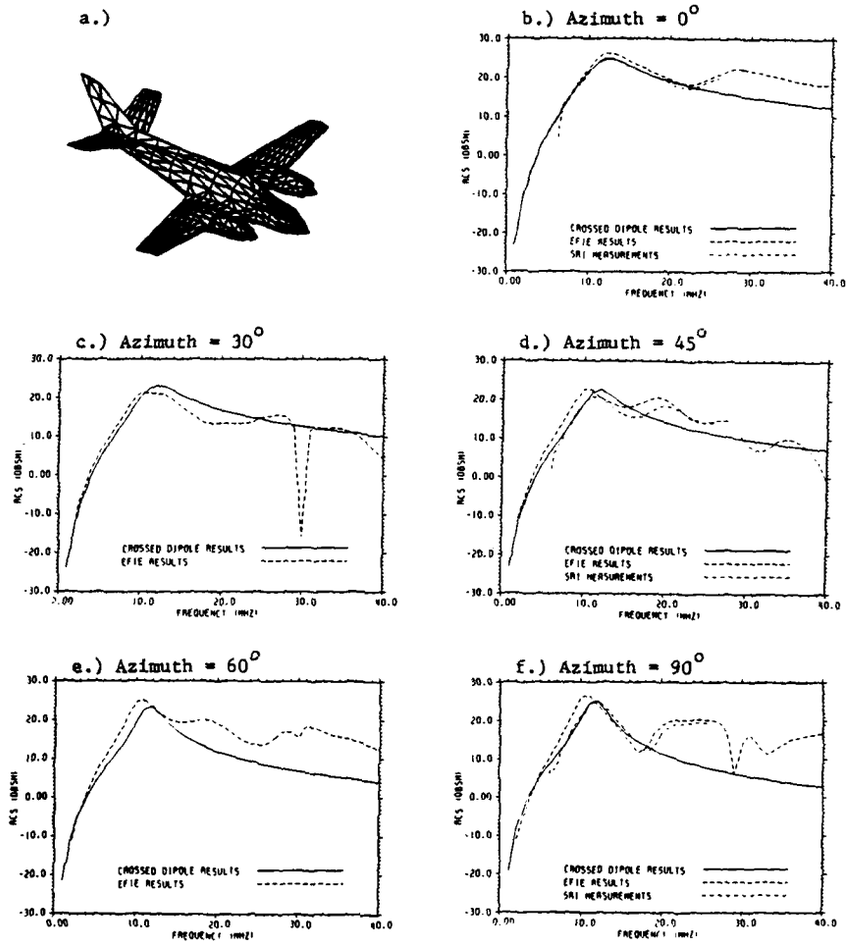

Figure 3. a.) EFIE Model of the Beechcraft Duke
b.) through f.) Duke Horizontal Polarization
Crossed Dipole and EFIE Calculations and
SRI International Measurements at 6° Elevation

Work on this paper was supported by the United States Air Force under contract number F19628-89-C-0001. The SRI International RCS measurements were made for the Naval Research Laboratories on contract number N00014-86-C-0404.

REFERENCES

1. Jackson, J. D., Classical Electromagnetics, Second Edition, John Wiley & Sons, Inc., New York, 1975.

2. Wilton, D. R. , Rao, S. S. M., and Glisson, A. W., "Electromagnetic Scattering by Surfaces of Arbitrary Shape," University of Mississippi, Rome Air Development Center Report RADC-TR-79-325, March 1980.

3. Burke, G. J., and Poggio, A. J., "Numerical Electromagnetics Code (NEC) - Method-of-Moments," Lawrence Livermore Laboratory Report UCID 18834, January 1981.

4. Bevington, P. R., Data Reduction and Error Analysis for the Physical Sciences, McGraw Hill Book Company, New York, 1969.

A MESH MODEL OF A COAXIAL TRANSMISSION LINE USING NEC

G. J. Burke
Lawrence Livermore National Laboratory

E. K. Miller
Los Alamos National Laboratory

A wire mesh is often used to represent a solid surface in Moment-Method modeling

- The mesh model is convenient
  - Thin wire modeling codes are readily available
  - Convenient to specify shape in terms of end points
  - Very easy to connect wire antennas
- A mesh can model either open or closed surfaces, while the MFIE surface model is limited to closed surfaces
- While EFIE surface codes are now available, they do not yet include ground effects, transmission lines, etc.

Wire grids can successfully model solid surfaces in many applications. But there are limitations –

- Grid models generally are accurate for impedance and far field but near field accuracy is limited by discrete current

- Physical modeling errors can result from
  - Mesh size $/\lambda$ too large
  - Incorrect wire radius
  - Preferred direction for current on the grid
- Sources of numerical modeling errors include
  - Segment length $/\lambda$ too large
  - Problems in modeling junctions
  - Erroneous loop currents

Theoretical and experimental studies of wire meshes provide some useful information –

- Tove Larsen, "A survey of the Theory of Wire Grids," *IRE Trans. MTT*, 1962 includes 83 references.

- Sir Horace Lamb, in 1898, derived a transmission coefficient for a mesh of parallel wires. With $\vec{E}$ along the wires –

$$T_p = 1 - \frac{1}{1 + \left(\frac{2d}{\lambda} \ln \frac{d}{2\pi a}\right)^2}$$

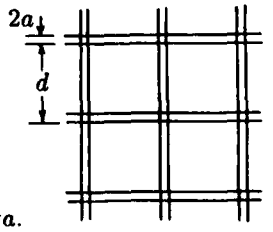

Thus $T_p = 0$ for equal surface area: $d = 2\pi a$.

The "equal surface area rule" is supported by other work...

Lee, Marin and Castillo, *IEEE Trans AP*, 1976 show that

- A mesh has excess inductance over that of a solid surface

$$\Delta L \approx \frac{\mu d}{2\pi} \ln\left(\frac{d}{2\pi a}\right)$$

- Interpretation of the capacitance of the mesh relative to surface depends on the form of the integral equation.

- Hence use $d = 2\pi a$ so that $\Delta L = 0$,
  or use loading $-\Delta L$ on segments???

The "equal surface area rule" is supported by other work...

- Moore and Pizer *Moment Methods in Electromagnetics*, 1984 —
  - $2\pi a = d$ is minimum radius. Up to 2.5 × area of *both* sides of open surface for accuracy in minor lobes ($2\pi a \approx 5d$)
  - Mesh size of 0.02 to 0.03 λ^2 recommended
  - Triangular mesh preferred

- A. C. Ludwig, *IEEE Trans. AP*, 1987 —
  - Considered exact solution for infinite cylinders
  - Showed minimum error in far field occurs when $2\pi a = d$.
  - $2\pi a > d$ increases error.

A wire mesh model of a coaxial transmission line is considered here to investigate the accuracy of mesh modeling

- The theory of a coaxial line is well established (R. W. P. King)
- Symmetry greatly reduces solution time (NEC3–GS code used)
- Problem: junctions at the ends may violate thin-wire limit.
- Three mesh types were used:

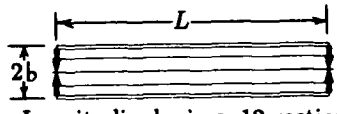

Longitudinal wires, 12 sections

Longitudinal cells, 12 sections

Diagonal cells, 8 sections

$b = L/10$

Segment length $= L/20$

Cell width $= d = L/20$

$2\pi a/d = 0.01, 0.1, 0.5, 1.0, 2.0, 3.0$

The coaxial transmission line exhibited very high Q Resonances

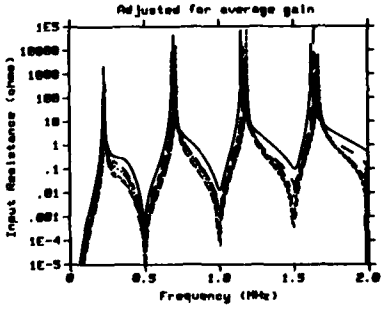

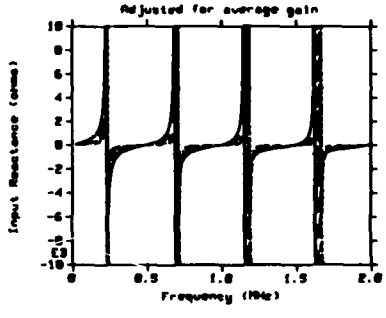

Bad things happen for large wire radius, indicating failure of the thin-wire approximation at the junction

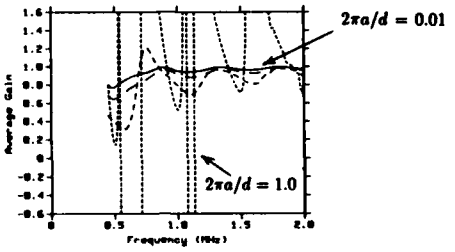

- Input resistance was corrected using the *Average Gain* $\bar{G}$

$$\hat{Z}_{in} = \bar{G}\Re(Z_{in}) + j\Im(Z_{in})$$

Computed values of $\hat{Z}_{in}$ were fit with a rational function for interpolation and to get poles and zeros

- Problem: $\hat{Z}_{in} = \bar{G}\Re(Z_{in}) + j\Im(Z_{in})$

Is not an analytic function of frequency, let alone rational.

But it worked ok if $\Re(Z) \ll \Im(Z)$ or $\bar{G} \approx 1$

For longitudinal-wire grid — $2\pi a \approx d$ is best

$-\Delta L$ loading helps ?

Zeros of Z approach $L/\lambda = n/2 + j0$

$2\pi a/d$	No loading	$-\Delta L$ loading
0.01	△	▲
0.1	□	■
0.5	◇	◆
1.0	⧗	⧗
2.0	▽	▼
3.0	○	●

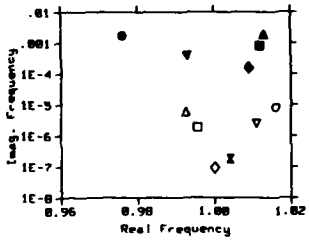

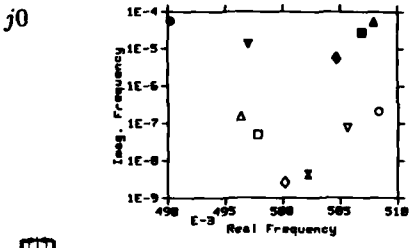

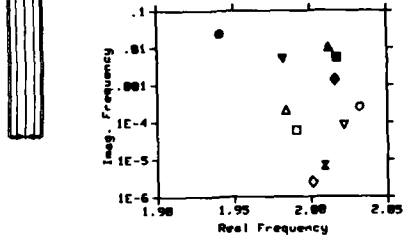

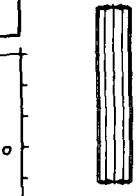

Longitudinal square cells yield more accurate zeros than longitudinal wires only

$2\pi a/d$	No loading	$-\Delta L$ loading
0.01	△	▲
0.1	□	■
0.5	◇	◆
1.0	⧗	⧗
2.0	▽	▼
3.0	○	●

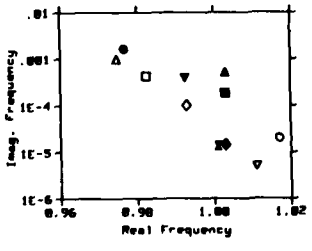

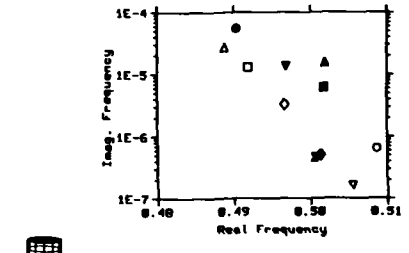

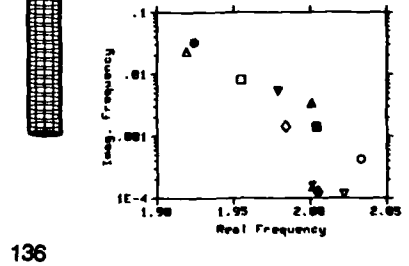

Diagonal square cells are close to longitudinal cells

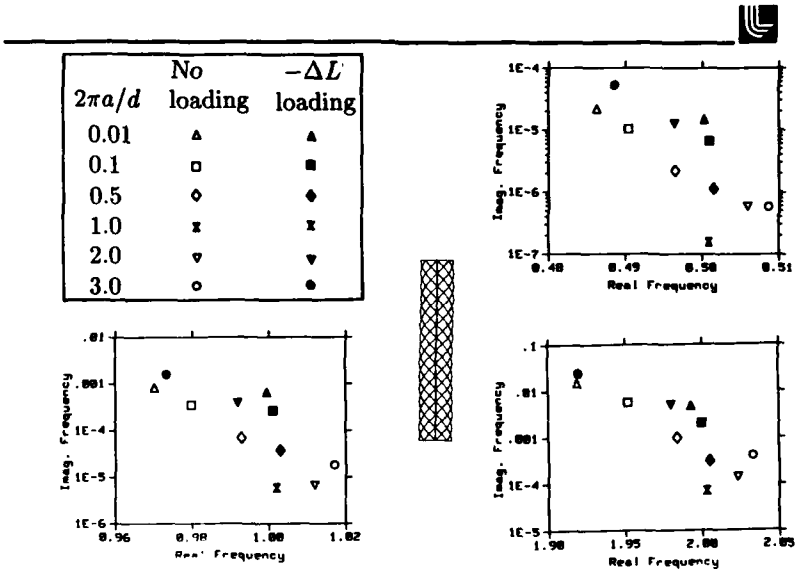

Poles of Z_{in} show a different behavior than zeros and are more distant from $L/\lambda = n/2 + 1/4$

Longitudinal wire grid —

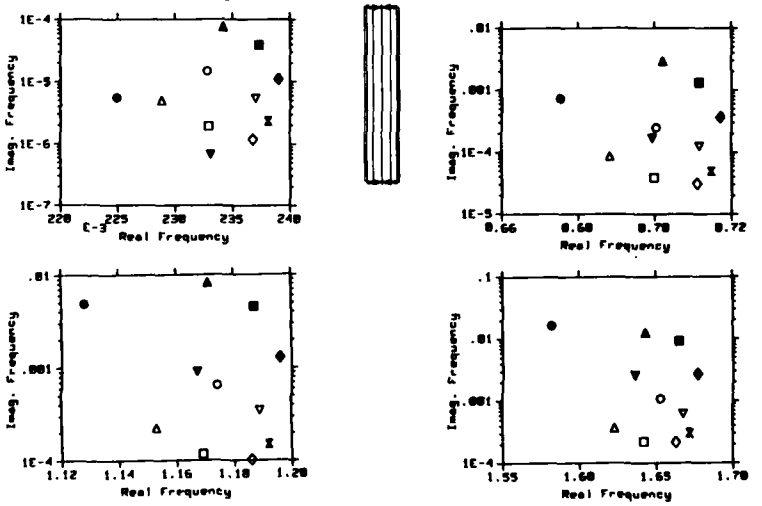

The cylinders were also excited as monopoles with a voltage source on a perfectly conducting ground plane

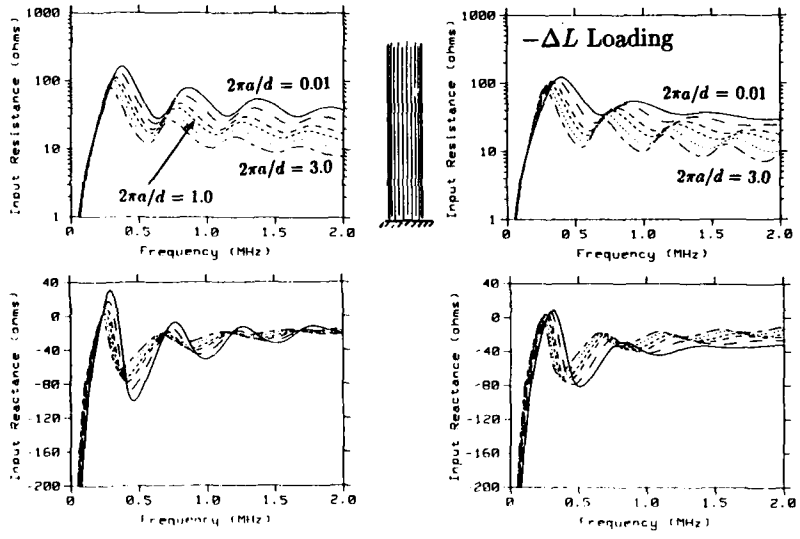

The cylinders were also excited as monopoles with a voltage source on a perfectly conducting ground plane

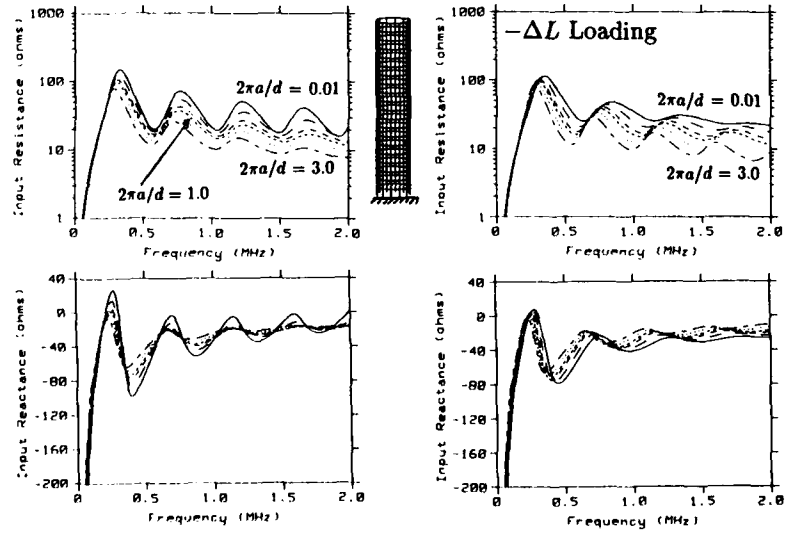

The cylinders were also excited as monopoles with a voltage source on a perfectly conducting ground plane

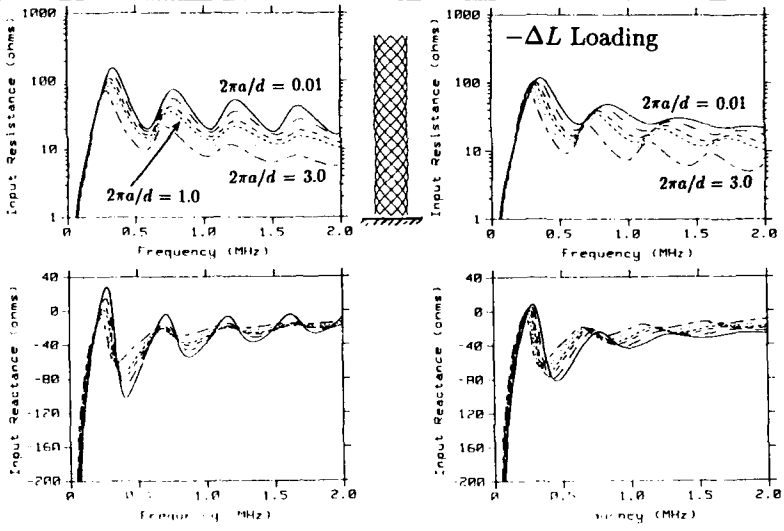

The first pole and zero of Z_{in} shift in the real part of L/λ with more shift in the pole

$2\pi a/d$	No loading	$-\Delta L$ loading
0.01	▲	▲
0.1	□	■
0.5	◇	◆
1.0	⧗	⧗
2.0	▼	▼
3.0	○	●

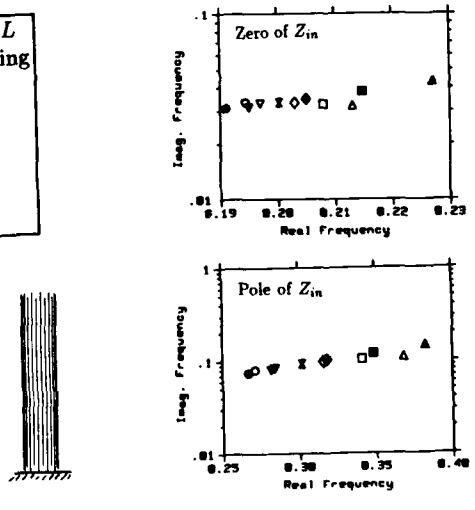

The first pole and zero of Z_{in} shift in the real part of L/λ with more shift in the pole

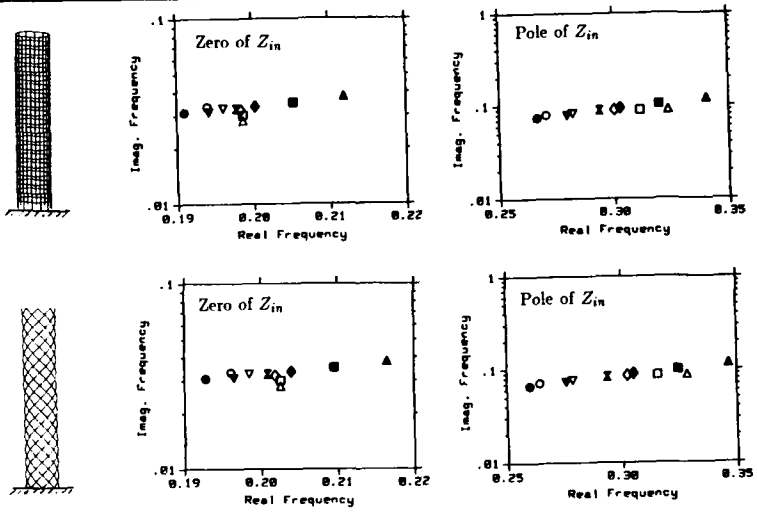

Conclusions —

- Coaxial transmission lines are hard to model
- The "equal area rule", $2\pi a \approx d$, gives the best results
- Negative inductive loading ($-\Delta L$) may help if $2\pi a < d$ but sometimes it makes thing worse.

OVERCOMING THE SMALL LOOP LIMITATION OF NEC FOR HFDF SSL RECEIVING ARRAYS

LT. CHRIS JENSEN, USN
RICHARD W. ADLER

NAVAL POSTGRADUATE SCHOOL
MONTEREY, CA

ABSTRACT

The small loop limitation for the NEC-MOM codes suggests that the circumference of a loop (in free space) be no smaller than .0001 wavelengths. This free space value does NOT apply in the case of a loop in the presence of conducting half-space, where a loop as large as a wavelength in circumference and a wavelength above the interface fails.

In a recent study of a High Frequency Direction Finding Single Site Location system with crossed loop arrays mounted very close to lossy ground, we avoided low frequency ranges where these NEC limits existed. NEC closely predicted the received currents induced in the loops when compared to measurements on a test array receiving known signals. A serendipitous user error in selecting a frequency produced unexpected but delightful results and reminded us that reciprocity does not include transmit and receive currents.

GOAL: EXERCISE A NEC MODEL OF AN HF SSL DF ARRAY FOR INCIDENT SKYWAVES OVER LOSSY GROUND.

BACKGROUND: A NEW NAVY HFDF SYSTEM HAS BEEN DEVELOPED FOR SHIPBOARD USE. A LAND-BASED VERSION OF THE CROSSED-LOOP ARRAY WAS INSTALLED OVER LOSSY GROUND AND TESTED BY THE MANUFACTURER. SIGNALS WERE RECEIVED FROM KNOWN TRANSMITTER SITES AND THE FREE-SPACE DF SYSTEM ALGORITHM WAS EXERCISED TO PREDICT THE LINE-OF-BEARING AND ELEVATION ANGLE OF THE RECEIVED WAVEFRONT.

EXTENSIVE TESTING OF THE ARRAY IS VERY EXPENSIVE. NEC WAS SELECTED TO DETERMINE TO WHAT EXTENT IT WAS POSSIBLE TO NUMERICALLY MODEL THE ANTENNA SYSTEM IN ITS LOSSY ENVIRONMENT AND TO PREDICT THE LOCATION OF THE INCIDENT SIGNALS.

PREVIOUS WORK IN HF CROSSED LOOP ARRAYS OVER GROUND DEMONSTRATED THAT THE INPUT IMPEDANCE AND GAINS PRODUCED BY NEC WERE SUBJECT TO HUGE ERRORS FOR LOW HF FREQUENCIES WHERE THE ELEMENTS WERE ELECTRICALLY VERY CLOSE TO THE GROUND.

ARRAY DESCRIPTION

A 32 ELEMENT Y-ARRAY WITH 70 M. LONG LEGS IS COMPOSED OF 1M. SQUARE CROSSED-LOOP ELEMENTS, MOUNTED 0.6M OFF THE GROUND.

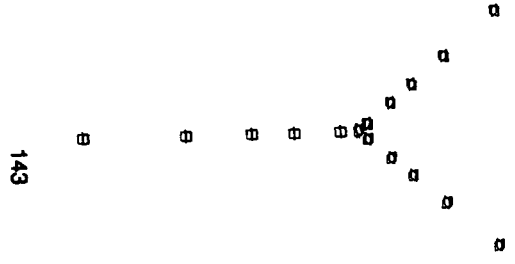

NEC Array Geometry - Oblique Angle (Not to Scale)

NEC Generated Array Geometry - Top View (To Scale)

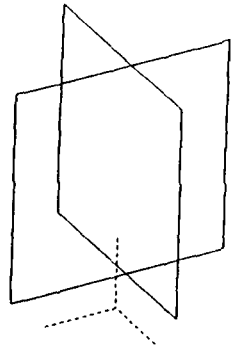

Crossed Loop Antenna Geometry (Oblique Angle)

THE LOOP CIRCUMFERENCE VARIES FROM 0.003 TO 0.4 WAVELENGTHS, WHICH IS WELL WITHIN THE ACCEPTABLE LIMITS FOR ACCURATE NEC MODELS IN FREE SPACE AND OVER PERFECT GROUND.

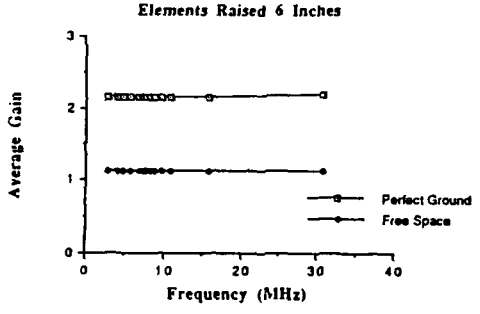

Average Gain (Normal Level)

WHEN FINITE GROUND IS INTRODUCED, THINGS "FALL APART" BELOW 10 MHZ, AS IS SEEN BY THE AVERAGE GAINS PERDICTED FOR 6 IN. HEIGHT ABOVE GROUND.

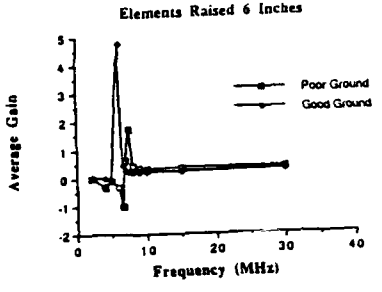

Average Gain (Normal Level)

AS THE HEIGHT IS INCREASED TO 5, 7.5 AND 10 FEET, THE WILD GYRATIONS IN AVERAGE GAIN GRADUALLY SUBSIDE, BUT THE ARRAY IS NOW IN A NON-REALISTIC MOUNTING GEOMETRY CONDITION.

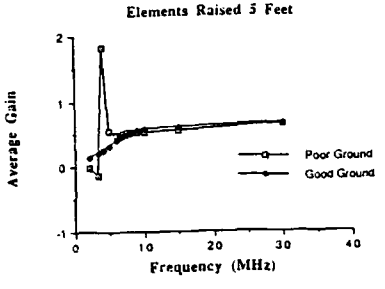

Average Gain (Elements Raised 5.0 feet)

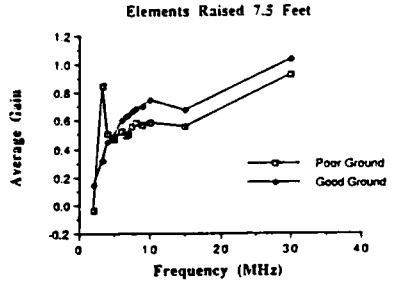

Average Gain (Elements Raised 7.5 feet)

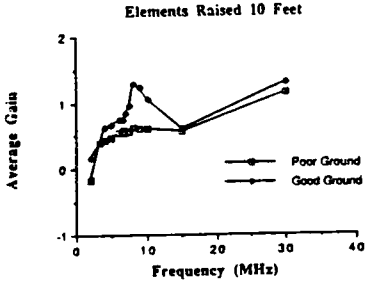

Average Gain (Elements Raised 10.0 feet)

AFTER SEEING THE POOR TRANSMIT PERFORMANCE OF THE LOOP ELEMENTS FOR LOWER HF FREQUENCIES, WE KNEW THAT WE COULD NOT USE NEC FOR THE RECEIVE ARRAY CALCULATIONS AT 3.333 AND 4.271 MHZ, THE TWO LOWEST FREQUENCIES FOR WHICH WE HAD MEASURED DATA. FOR THE HIGHER FREQUENCIES THE NEC RESULTS WERE WITHIN A FEW PERCENT OF THE MEASURED NUMBERS.

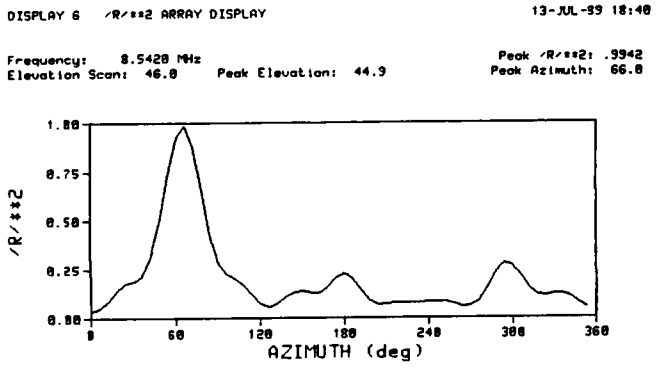

NEC Data Validation using ASDF (Sky Wave)

WHEN WE CONSIDERED RUNNING AT THE 3 AND 4 MHZ FREQUENCIES, WE DECIDED TO ELEVATE THE ARRAY TO 10 FT. AND SEE IF THE RESULTS WERE REASONABLE.

IN SETTING UP THE INPUT DATASET, WE INADVERTENTLY LEFT THE ARRAY CLOSE TO THE GROUND WHERE THE INPUT IMPEDANCE WAS BUGGY BUT TO OUR SURPRISE THE NEC DF RESULTS WERE JUST AS ACCURATE AS FOR THE HIGHEST FREQUENCIES!

THE INPUT RESISTANCE AT 3.333 MHZ WAS VERY LOW AND THE REACTANCE WAS ENORMOUS AS EXPECTED. X/R VARIED FROM 30,000:1 TO 200:1 FOR THE UNDER 7 MHZ RANGE.

THIS SHOWS WHY NEC RESULTS ARE SUBJECT TO LARGE ERRORS FOR THE TRANSMIT CURRENT CASE BUT IN THE RECEIVE CASE, THE LARGE REACTANCE, WHICH IS ACCURATELY PREDICTED, CONTROLS THE CURRENT INDUCED BY THE INCIDENT E-FIELDS!!!

SO, WE ARE REMINDED THAT RECIPROCITY OF TRANSMIT AND RECEIVE CURRENT DISTRIBUTIONS DOES NOT APPLY AND WE NOW MAY USE NEC, WITH CARE, TO ANALYZE CROSSED-LOOP HFDF RECEIVING ARRAYS NEAR GROUND.

SESSION 4 - "TIME DOMAIN METHODS AND APPLICATIONS"

A SPECIAL PURPOSE COMPUTER FOR THE TIME DOMAIN ADVANCE OF MAXWELL'S EQUATION

Ronal W. Larson, PhD
Poh H. Ng, PhD

Electro Magnetic Applications, Inc.
12567 West Cedar
Denver, CO 80228

ABSTRACT

Progress is reported on the construction of a special purpose computer designed for the efficient time advance of Maxwell's Equations. The design involves both paralleling and pipelining techniques with specialized hardware that takes advantage of the six-fold symmetry of Maxwell's equations.

A time speedup of a factor of about 500 over operation on a VAX is projected, with initial costs less than that of a VAX. Much of the time savings is achieved by enabling up to eight simultaneous pipelined operations on six (almost identical) boards. The remaining time savings is achieved by having twenty four simultaneous operations in and out of as many memory modules. Each field is drawn out once for its time advance and one other advance and then later (or earlier) for use in one other time advance; there are a minimum number of memory operations. The algorithms developed have a direct applicability for reducing computation time in general purpose computation as well.

Although there are few opportunities for modifying the hardware to handle such special cases as nonlinear problems, the hardware otherwise seems capable of handling all of the presently employed special cases in the time advance of Maxwell's Equations. A discussion will be given of the relative ease of using the same Maxwell Equation hardware also for:

1. *Boundary conditions*
2. Huygens' sources
3. Specified sources
4. Time-varying materials
5. Thin wires

Detailed design is presently underway using the conceptual design reported on below, with availability scheduled in 8 months. The work to be reported is the result of advances made during the first half of a Phase II SBIR contract from the U.S. Army's Harry Diamond Laboratories, under Prime Contract # DAAL02-89-C-0004.

1. INTRODUCTION

This is the first public report under the Phase II Small Business Innovative Research (SBIR) contract, and follows an earlier report dealing with the Phase I results [1]. In this first portion of the Phase II effort, we have made several major changes to the overall design, and have found several ways to reduce storage requirements for constants and to handle the equations auxiliary to the main Maxwell Equation advance equations.

In the first Phase I report, we showed how Maxwell's Equations could be simplified for use in a normalized form, which we then believed would be faster and cheaper to implement in hardware. In this phase, we decided that a different normalization would make for greater symmetry between the electric and magnetic field equations, and we also decided to include magnetic conductivity terms.

It now appears that it is just as fast and cheap to perform floating point operations. Thus the equations below are slightly different in appearance and no longer emphasize the simplest possible form (smallest number of constant multipliers), since it is appreciably less expensive to have multiple boards that are identical rather than slightly fewer operations on boards that are not identical.

The principal goal in the work is to achieve a very fast and cheap machine for very large problems. The present design goal is to obtain one time advance for all 6 staggered fields for 8 million cells every second. At the present time, the design described below is being implemented in hardware, using a fundamental clock speed of about 10 Megahertz.

2. BASIC EQUATIONS

We begin with the six Maxwell curl equations, which in vector form are:

$$\mu \frac{\partial \mathbf{H}}{\partial t} + \sigma_m \mathbf{H} + \nabla \times \mathbf{E} = \mathbf{M} \tag{2.1a}$$

$$\varepsilon \frac{\partial \mathbf{E}}{\partial t} + \sigma \mathbf{E} - \nabla \times \mathbf{H} = -\mathbf{J} \tag{2.1b}$$

Here, ε is the permittivity, μ the permeability, and σ and σ_m are respectively the electric and magnetic conductivities of the medium. M and J represent magnetic and electric current sources respectively.

The finite difference solution of these equations in the time domain may be accomplished by making use of a centered difference approximation of the time and space derivatives in the curl equations [2,3,4] or their integral forms. We also employ an apparently new normalization that puts both the E and H fields into the units of volts, using (for two of the six substitutions, with the others obvious by permutation):

$$D_x \; E_x \;>>>\; F(M=4) \tag{2.2a}$$

$$^{*}(\mu/\varepsilon)^{1/2} \; (D_y D_z / D_x) \; H_x \;>>>\; F(M=1) \tag{2.2b}$$

where the left hand side of the replacement (>>>) operation refers to equations (2.1), but the right hand nomenclature will be used hereafter.

After this substitution, we obtain six identical difference equations of the form:

```
F(L,M)=C1(M,NM)*F(L,M)
   -C4(M,NM)*(C2(M)*(F(L,MP2(M))-F(L3,MP2(M)))
                -C3(M)*(F(L,MP3(M))-F(L2,MP3(M))))
```
(2.3)

The field-specifying quantity, M, is a linear combination of M_0 and M_1, via the equation:

$$M = 3 \cdot M_0 + M_1 \tag{2.4}$$

where M_0 is a variable distinguishing between H (M_0=0) and E (M_0=1), while M_1 distinguishes between x (M_1=1), y (M_1=2) and z (M_1=3) so that M=1, 2, 3, 4, 5, and 6 means respectively H_x, H_y, H_z, E_x, E_y, and E_z. Thus, we see that the new form of Equation (1) allows a positive permutation of the variables x, y, z.

Equation (1) also has an implied M_0 reversal of meaning in the terms L, L2, and L3. If M refers to a magnetic variable (M_0=0) then MP2 and MP3 refer to electric (M_0=1) and vice versa. Also, if M1 is an x-variable, then MP2 and MP3 are respectively y and z variables. Similarly, if M1 is y-directed (or z), then MP2 and MP3 are respectively z and x (or x and y) variables. The use of subtractions in the general form (1) is the only way to obtain positive permutations (which are thereby easy to remember).

Another item to discuss is the meaning of the terms: F(L3,MP2(M)) and F(L3,MP3(M))), where L2 and L3 are defined as:

```
L2=L+LD2(M,N)
L3=L+LD3(M,N)
```
(2.5)

LD2 and LD3 are predetermined offsets in i, j, or k by the appropriate number of cells. They depend on M and N, where N specifies the type of operation (advance, boundary, Huygens, etc) that is being conducted. The offsets are of three types:

1. by unity ($\Delta i=1$),
2. by the cells in a pencil ($\Delta j=1 \Rightarrow$ IH-1 cells, where IH is the number of cells in a pencil, and the numbering starts at 0), or
3. by the cells in a layer ($\Delta k=1 \Rightarrow$ IH • JH cells, where JH is the number of pencils in a layer).

These also are permuted so that if F(L,M)) respectively denotes x, y, and z, then F(L2,M) denotes offsets of J, K, and I; F(L3,M) denotes offsets of K, I, and J.

Lastly, we note that the offsets for F(L2,M) and F(L3,M) are positive when F(L,M) is a magnetic field (M_Q=0) and are negative when F(L,M) is an electric field (M_Q=1). In the six simultaneous equation approach, this is an important difference, since all of the offset E-fields required have not been time-advanced, while all the required offset H-fields have been time-advanced. Thus, in a six-equation hardware (or software) approach, the H-fields must be computed first, given the numbering system that has been employed. The constants are further described in the next section.

The five values needed to compute one of the fields are itself (previous iteration) and four of the opposite type fields resident on the edges of "its" face (the face used in the integral form of the equation. Figure 2.1 shows that only 12 (rather than 3x5=15) values of E and H are required to compute the three H-fields. However, because we compute along an x-pencil, two of the values are repeated in the x-direction, so that there are only 10 unique values: 1-6 are internal to the i,j,k call, while 7-10 come from outside as E-values.

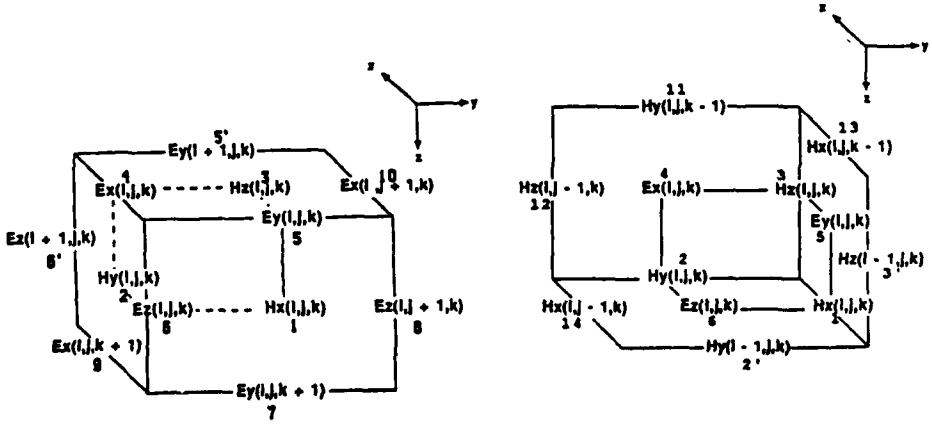

Figure 2.1 Three Faces Used with H and E Computations

For computational purposes it is convenient to think of E values as not only residing on edges of cubes, but also at the center of another set of faces which are offset from the H cubes by a negative 1/2 of a cube dimension in each of the three axis directions as shown in Figure 2.1b Again, one can think of 10 values as being required for the complete determination of the E-fields, but since six of these can be carried over from the H-field computations, only four new H-fields are being added: fields 11-14.

3. IMPLEMENTATION IN PIPELINING HARDWARE

In the previous paper, we described several ways that computation can proceed. We have settled on the coarsest approach, which is the processing of cells in "pencils", which are cells varying in i, but having the same j and k coordinates. Following the computation of a single pencil, a change is made in j, which continues until a layer is complete, whereafter k is changed. For any single cell, we see that it will always involve x, y, and z components, but that only two of the three possible offsets will occur. Thus, in pipelining the advance computations, it is possible to develop a "circular" system in which E-boards feed H-boards and vice-versa.

The present implementation of the pipelining and cross-connections is seen in Figure 3.1. Four separate memory banks at the right edge can be simultaneously accessed through the switch Sw1. The curl (or line integral) subtract operations are performed in the boxes labeled D2 and D3, where the numbers refer to the same L2 and L3 operations described above. The symbol "D" is used to denote a "doublet" processor. This is a commercially available chip with two 32 pin inputs and a 32 pin output, capable of simultaneously (in pipelined fashion) performing either an add (or subtract) and subsequent multiply, or the converse. Since our constants are rarely changing, these two operations can be performed every 100 nanoseconds, with only a single clock step required to change the multiplying constant when required. These would be changed simultaneously whenever required by the problem space geometry.

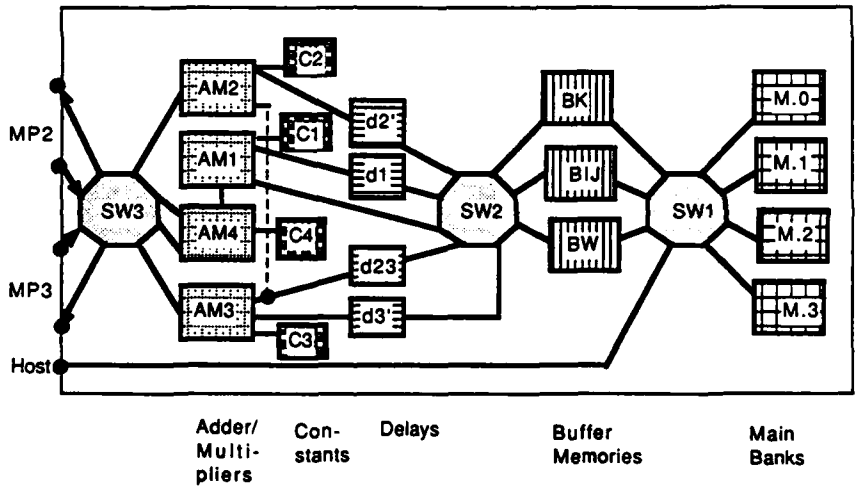

Figure 3.1 Schematic of One of Six Pipelined Boards

The outputs of D2 and D3 are fed (through Switch 2) to D4, which has the same doublet arrangement; the inputs are first subtracted and the resultant multiplied by C4. The output of D4 is fed to D1; this unit has a different ordering, with the subtraction being the final operation. The first operation is a multiplication of F(L,M) by C1(M,N), remembering that this is the field being advanced (say Hx), whereas the field coming from D4 is of the opposite type (differences in Ey and Ez, in this example).

After leaving D1, the newly advanced field is handled differently for H and E fields. The former is immediately rerouted back through the D2 and D3 doublets in order to be used to update the associated E-fields. The E-fields are ready for "immediate" return to memory. In order to simplify the memory operations, return is made of all fields simultaneously, as further described in the next section.

4. MEMORY MANAGEMENT

With the assumed size (200^3 = 8 million cells), a total memory for 6 fields and associated constants will be in excess of 200 Megabytes, when using 4 byte (32 bit) logic. Dynamic Random Access Memory (DRAM) cells will be used for this large computer memory, since they are appreciably cheaper than the faster Static RAMs (SRAMs). However, a typical random access time for DRAM is 180 nanoseconds. Since the same DRAM chip can retrieve or store numbers sequentially in 50 nanoseconds, the design now includes provision for a small SRAM between the main memory and the processing chips to be able to pick up this factor of three in speed, by using "page mode" addressing: a full row (or "page" of memory at one time.

The current design is oriented towards the new (and cheapest) 4 Megabit DRAM chips, with 1024 rows and 1024 columns per chip. In this design, a full row of memory (1024 columns) will be retrieved at one time, stored in SRAM, and then used as required. This row from memory could cover a part of a very long pencil or could cover several shorter pencils, depending on the geometry being analyzed. The next part of space will, however, always come from a different bank of memory, with four interleaved banks for each field, giving 24 total banks.

It was originally proposed that each pencil would be in one of four separate banks. It would then be possible to read three cells (for H-fields, the present and to the left and above; for E-fields, present, right, and below) and write one all in the same time step. The present scheme simplifies this even one step further, since fields will be retained after first use (main for H, right for E) for a subsequent operation (left for H, main for right) In this way, a fourth bank is always available for communication of results back to the host computer and/or other housekeeping functions, while the second and third are being respectively used for the fields above (H) or below (E), and for rewriting back into memory. The same board can be used for three-board or single-board operation, albeit at a slower rate.

Refreshing of memory must be built in to the memory management scheme also. With the present approach, approximately 12 clock ticks will be used at the end of every 1024 cells (a chip row) for this function, thus adding about 1% overhead for the memory refresh function. This is appreciably less time than with other schemes which would require changing memory banks every pencil. This is also much simpler in terms of addressing changes, since a change in mid memory-row would require additional refresh operations and/or loss of memory locations when pencil lengths did not fit neatly into the 1024 memory columns within a memory row.

In this first 8 million cell design with 4 Megabit DRAM chips, each of the four banks of the six fields will have two million cell locations. The table below shows the total allocation of 392 chips across fields and banks. To allow for future growth, we allocate 16 wires for addressing both the rows and columns.

	cell locations (millions)	bytes (millions)	bits (millions)	4 MBit Chips
per bank	2	8	64	16
per field	8	32	256	64
6 field total	8	192	1576	392

5. BOUNDARY CONDITIONS

The standard first order Mur [5] boundary condition requires backstorage of the (edge) fields. We have developed a new approach which calculates the boundary condition in two steps, thereby eliminating the need for the back storage. That portion of the computation which requires the older fields is done before time advancing, while the advance field portion is done afterwards. Although this doubles the time required for boundary condition implementation, the removal of a need for backstorage simplifies the storage considerably. The new normalized form becomes:

implementation, the removal of a need for backstorage simplifies the storage considerably. The new normalized form becomes:

$$F(L,M)=C1(M,NM)*F(L,M) -C4(M,NM)*F(L3,M) \quad (5.1)$$

Now, the term NM is used to specify whether the constants are appropriate for before or after field advance. Because the boundary conditions take only a few percent of the advance computation time, the doubling of the time is not a significant factor. Note that only M appears in this equation, indicating that a switch needs to be thrown to keep all computations on the same board (unlike the advance operations). A switch to accomplish this is shown in Figure 3.1.

In the first paper, we noted that the Mur first order form could be simplified, after which the form above could be used directly. A second form was found to be a little more accurate. We also have explored the use of conditions on both the E- and H-fields as proposed by Fang and Mei [6] and find that they can be included in the above formulation as well. Attenuative terms (not included in the Mei formulation) can be handled through the constants.

6. HUYGENS' SOURCES

The Huygens' sources are added as an interpolation between a small number of sources also stored in the same field memories at memory locations L2.

$$F(L,M)=F(L,M)+F(L2,M)+ P*(F(L2+1,M)-F(L2,M)) \quad (6.1)$$

The interpolation distance is P, and is obtained from a separate accumulator designed only for that purpose, through the equation:

$$T (I, J, K) = L2'+ P$$

This special accumulator is virtually the only hardware that is not used throughout all computations. The alternative is an additional several percent more storage of both L2' and P.

7. THIN WIRES AND OTHER FUNCTIONS

The previous paper described modifications to the equations to be used when thin wires are in the problem space. No change has been made in these forms of the equations. Specifically, the format does not allow for inclusion of transmission line equations for voltage and current on these thin wires.

It was originally proposed that a separate doublet would be used for adding sources M and J. The present approach utilizes Doublet D2 in a subsequent addition, since it takes so little extra time to go back and add the few sources apt to appear in most problems.

If material parameters change during a run, then time must be allocated to read these constants into their separate memories between time advance steps.

8. SUMMARY

The first portion of the SBIR phase II study continues to be encouraging, with the project speed and cost goals apparently still attainable. Numerous additional problems have been encountered and solved as the initial design, concentrating on the time advance equations, has matured and the auxiliary equations have been analyzed more closely. It still appears that the total problem can be handled within 120% of the time required for the time advance alone, which itself appears to be achievable in only about 1% more time than the minimum of one cell per clock tick.

REFERENCES

[1] Larson, R. W. et al, "Special Purpose Computers for the Time Advance of Maxwell's Equations", IEEE Transactions on Magnetics, (Special Issue reporting on the Third Biennial Conference on Electromagnetic Field Computation, Held in Washington, DC Dec, 1988), July 1989, pp 2913-2915.

[2] Larson, Ronal W. et al, "Numerical Approaches to the Solution of Electromagnetic/Coupling Problems", EMA-88-R-25, March 1988, SBIR Final Report to HDL.

[3] Yee, Kane S., "Numerical Solution of Initial Boundary Value Problems Involving Maxwell's Equations in Isotropic Media," IEEE Trans. Antennas & Propag.,Vol. AP-14, No. 3, May 1966, pp. 302-307.

[4] Rudolph, T.H. and P.H. Ng, "Time Domain Solution of Maxwell's Equations by Finite Difference Methods (with preface introduction to the computer codes)," EMA-88-R-65, September 1988.

[5] Mur, G., "Absorbing Boundary Conditions for the Finite Difference Approximations of the Time-Domain Electromagnetic-Field Equations," IEEE Trans. EMC, Vol. EMC-23, No. 4, November, 1981.

6] Fang, Jiuyuan, and Mei, K.K, "A Super-Absorbing Boundary Algorithm for Solving Electromagnetic Problems by Time-Domain Finite-Difference Method", 1988 IEEE AP-S International Symposium, Syracuse Univ., June, 1988.

Electromagnetic Propagation on an Unstructured Finite Element Grid

John Ambrosiano and Scott Brandon
University of California, Lawrence Livermore
National Laboratory, Livermore, California

Rainald Löhner
CMEE School of Engineering and Applied Science,
The George Washington University,
Washington, D. C.

Introduction.

Standard techniques for computing electromagnetic solutions in the time domain rely on finite differences. These so called FDTD (Finite Difference Time-Domain) methods[1,2] are applicable to a broad range of problems and are both reliable and accurate. However, the regular lattices of points on which the finite difference operators are defined can be too restricting for geometrically demanding problems. In particular, problems in which there is scattering from an object of complicated shape, or problems requiring extreme local refinement of zones, are not well suited to a regular finite difference grid.

Geometric flexibility can be achieved by abandoning the regular latticework of sample points and adopting an unstructured grid. An unstructured grid connects a given point to an arbitrary number of other grid points. Typically the points are connected to form triangles in 2-D or tetrahedra in 3-D. An unstructured grid allows one to place the grid points anywhere one chooses so that boundaries can be fit with ease. One can also refine local areas of interest, either ab initio or dynamically, without affecting the resolution in other parts of the problem domain.

In this paper we present a technique for solving Maxwell's equations on an unstructured grid. Our approach is based on the Taylor-Galerkin finite element method. We will give some numerical examples of wave propagation and scattering and discuss the fundamental accuracy of the method. Although our examples are in two dimensions the results are easily generalized to 3-D.

The Taylor-Galerkin method applied to electromagnetics.

In the time domain, electromagnetics is a hyperbolic problem. Until recently, it was believed that finite elements were not a good match to hyperbolic systems of partial differential equations (PDE's). However, Taylor-Galerkin methods[3,4] have proven very successful in such applications — specifically in computational fluid dynamics (CFD). The idea behind the Taylor-Galerkin formulation is very simple. One first specifies a temporal truncation error by expanding the unknown in a Taylor series. The PDE is then used to replace partial derivatives in time with partial derivatives in space. Finally a Galerkin approximation is applied to the spatial derivative operators. To illustrate, consider the simple linear hyperbolic system in 1-D

$$\frac{\partial u}{\partial t} = -\frac{\partial f(u)}{\partial x} = -c\frac{\partial u}{\partial x} \tag{1}$$

where $c \equiv \partial f(u)/\partial u$ is the characteristic speed which is independent of u for linear problems. Expand the unknown at time level $n+1$ about the value at time level n

$$u^{n+1} = u^n + \Delta t\left(\frac{\partial u}{\partial t}\right)^n + \frac{1}{2}\Delta t^2\left(\frac{\partial^2 u}{\partial t^2}\right)^n + O(\Delta t^3) \tag{2}$$

Substituting expressions for the time derivatives from (1) into (2) we obtain

$$u^{n+1} = u^n - c\Delta t\left(\frac{\partial u}{\partial x}\right)^n + \frac{1}{2}c^2\Delta t^2\left(\frac{\partial^2 u}{\partial x^2}\right)^n \tag{3}$$

This procedure is similar to one for deriving the Lax-Wendroff scheme[5], and in fact, if one replaces the derivatives with centered finite differences, Lax-Wendroff is obtained. Instead we apply the Galerkin approximation. We expand u^n as

$$u^n(x) = \sum_i u_i^n N_i(x) \tag{4}$$

where $N_i(x)$ is the node-based linear basis or shape function and u_i is the value of u at node i. On substituting (4) into (3) and taking the inner product with another shape function $N_j(x)$ we obtain

$$\sum_i \langle N_j \mid N_i\rangle \delta u_i = -c\Delta t \sum_i \left\langle N_j \mid \frac{\partial N_i}{\partial x}\right\rangle u_i^n - \frac{1}{2}c^2\Delta t^2 \sum_i \left\langle \frac{\partial N_j}{\partial x} \mid \frac{\partial N_i}{\partial x}\right\rangle u_i^n \tag{5}$$

Here $\langle F \mid G\rangle \equiv \int F(x)G(x)dx$ is the inner product and $\delta u \equiv u^{n+1} - u^n$. The left-hand side contains the (consistent) mass matrix. The matrix appearing in the second-order term on the right-hand side will be recognized as the stiffness matrix. It is the presence of this extra term which accounts for the enhanced phase accuracy and stability of the Taylor-Galerkin scheme over previous finite element formulations for hyperbolic problems. Eq. 5 can be written in a more compact form

$$M_C \delta \mathbf{u} = \mathbf{f} \tag{6}$$

where $\delta\mathbf{u}$ and $\mathbf{f}$ are nodal vectors. The consistent mass matrix can be inverted by a simple iterative technique. Denoting as M_L the lumped mass matrix we write

$$\delta \mathbf{u}^{k+1} = M_L^{-1}\left\{\mathbf{f} - M_C \delta \mathbf{u}^k\right\} \tag{7}$$

It has been found in practice that three iterations suffice. Wathen[6] has recently analyzed the convergence rate and found it sufficiently fast to be consistent with this experience.

To apply this method to electromagnetic propagation we merely rewrite Maxwell's equations in a standard hyperbolic form. For example, for vacuum fields in 2-D:

$$\frac{\partial}{\partial t}\begin{pmatrix} E_x \\ E_y \\ E_z \\ B_x \\ B_y \\ B_z \end{pmatrix} = -\frac{\partial}{\partial x}\begin{pmatrix} 0 \\ cB_z \\ -cB_y \\ 0 \\ -cE_z \\ cE_y \end{pmatrix} - \frac{\partial}{\partial y}\begin{pmatrix} -cB_z \\ 0 \\ cB_x \\ cE_z \\ 0 \\ -cE_x \end{pmatrix} \tag{8}$$

where now c is the speed of light. The components are linearly interpolated from the nodes of triangles on an unstructured grid.

The method just described is basically the finite element equivalent of the Lax-Wendroff scheme. A second-order Leapfrog Taylor-Galerkin scheme can also be derived. Expand $\mathbf{E}^{n+1}$ and $\mathbf{E}^n$ about $\mathbf{E}^{n+\frac{1}{2}}$

$$\mathbf{E}^{n+1} = \mathbf{E}^{n+\frac{1}{2}} + \frac{1}{2}\Delta t\frac{\partial \mathbf{E}^{n+\frac{1}{2}}}{\partial t} + \frac{1}{8}\Delta t^2\frac{\partial^2 \mathbf{E}^{n+\frac{1}{2}}}{\partial t^2} + O(\Delta t^3) \tag{9}$$

$$\mathbf{E}^{n} = \mathbf{E}^{n+\frac{1}{2}} - \frac{1}{2}\Delta t\frac{\partial \mathbf{E}^{n+\frac{1}{2}}}{\partial t} + \frac{1}{8}\Delta t^2\frac{\partial^2 \mathbf{E}^{n+\frac{1}{2}}}{\partial t^2} + O(\Delta t^3) \tag{10}$$

Then perform similar expansions for $\mathbf{B}^{n+\frac{3}{2}}$ *and* $\mathbf{B}^{n+\frac{1}{2}}$ *about* $\mathbf{B}^n$. On subtracting the expansions and substituting expressions for the time derivatives we obtain

$$\mathbf{E}^{n+1} = \mathbf{E}^n + c\Delta t\nabla \times \mathbf{B}^{n+\frac{1}{2}} \tag{11}$$

$$\mathbf{B}^{n+\frac{3}{2}} = \mathbf{B}^{n+\frac{1}{2}} - c\Delta t\nabla \times \mathbf{E}^{n+1} \tag{12}$$

One then applies the Galerkin approximation to (11) and (12). The advantage of the Leapfrog scheme is that, although phase errors are somewhat greater, it is dissipation-free.

Donea[3] has analyzed Taylor-Galerkin schemes for linear advection and has found that they have good stability and low phase error. We expect these qualities to carry over to electromagnetic applications. The somewhat dissipative nature of the Lax-Wendroff Taylor-Galerkin (LWTG) scheme may be inappropriate for some applications. In such cases the Leapfrog Taylor-Galerkin (LFTG) is a better option. Figure 1 shows the time histories of field energy for a test problem comparing the LWTG and LFTG formulations. In this problem a perturbation in the B_z component at the center of a square domain produces an outgoing circular wave. The domain was first discretized into square cells and then into triangles by dividing the cells along their diagonals. This gave us approximately 1800 triangles of equal size h. A wavelength was resolved by about 8 nodes. In each case the Courant number $\nu = c\Delta t/h = 1/2$. Our choice of parameters was designed to exaggerate the differences in energy conservation which are plainly seen in the figure. As claimed, the leapfrog version is energy-conserving.

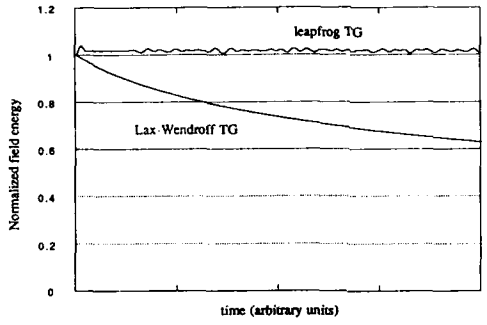

Figure 1. Comparison of energy time histories for the LWTG and LFTG schemes.

Another special consideration to be given electromagnetic applications concerns the additional constraints on the solutions. In vacuum the fields must satisfy $\nabla \cdot \mathbf{E} = 0$ and $\nabla \cdot \mathbf{B} = 0$. If one takes the divergence of the Faraday and Ampere Laws, one finds that if the divergence constraints are satisfied initially, they are satisfied for all time. This follow directly from the fact that $\nabla \cdot \nabla \times \mathbf{B} = \nabla \cdot \nabla \times \mathbf{E} = 0$. However this may not be true in the discrete approximation. In the conventional central finite difference approximation on a staggered mesh the divergence of the curl vanishes identically and therefore the divergence constraints on the fields are preserved by the time marching algorithm. In our Taylor-Galerkin schemes *divergence constraints are not satisfied exactly.* However, we believe this is not a problem for typical applications. Our experience has shown that the divergence errors are small, local, non-accumulating, and consistent with the order of the method. As evidence we present figure 2. Here we define the relative error in the divergence of $\mathbf{E}$ as

$$\epsilon \equiv \frac{| \nabla \cdot \mathbf{E} |}{| \partial E_x/\partial x | + | \partial E_y/\partial y |} \tag{13}$$

For the expansion of a circular wave on a regular square lattice of nodes using LWTG, we present three solutions: one with 20×20 nodes, one with 40×40, and one with 80×80. One can see that the maximum relative error does not accumulate with time. Furthermore, each level of refinement reduces the error by almost an order of magnitude. Thus we expect good answers for any problem that is reasonably zoned. These cases further suggest that Taylor-Galerkin and adaptive refinement would be a powerful combination.

Some numerical examples.

Our first example shows the advantage of an unstructured grid for local refinement. The grid is long and has a very small wire located within it. The upper and lower boundaries are periodic so that the grid actually represents an array of wires. The wire is located within the densely-zoned region of Figure 3(a) and its radius is only $1/300th$ of the width of the region. The unstructured grid allows us to use these very fine zones near the wire

and smoothly match to coarser zones in the remainder of the region. The total number of zones in this grid is 3614. If we were forced to use a uniform grid with one zone representing the wire, we would need 540,000 zones. A closeup of the zones near the wire is shown in figure 3(b). This grid was generated automatically using a method known as the advancing front[7].

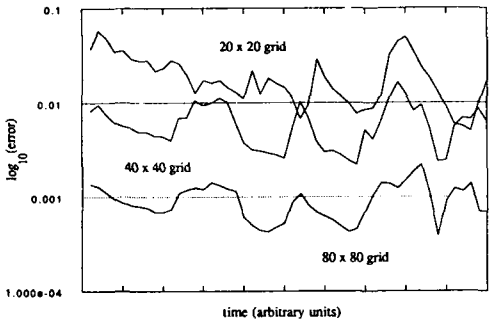

Figure 2. Maximum relative error in divergence of E as a function of time for grids with different resolution.

We use a TM polarization, i.e., E_z parallel to the wire, and introduce a half-cycle plane wave from the left. Figure 4 depicts the solution sometime after the wave has encountered the wire. Figure 4(a) shows contours of E_z while 4(b) shows us a closeup of the magnetic field vectors near the wire. This example illustrates the advantage of an unstructured grid in situations were small obstacles or features must be included in a large-scale simulation.

Our next example demonstrates the ability of finite elements combined with an unstructured grid to handle complex geometries. Although suggestive of certain applications, it is not intended to be realistic. Figure 5(a) depicts the results of a scattering simulation. A two-cycle TE-polarized plane wave incident from the left strikes the surface of an armoured tank. We can see the reflections from various parts of the tank along with evidence of a cavity resonance on the underside. This is because our computational tank is two-dimensional. Figure 5(b) shows the grid for this calculation. The grid was again generated automatically using the advancing front technique.

A more quantitative example is the scattering a plane wave by a circular cylinder for which there is an analytic solution[8]. Figure 6 shows the computed and analytic values of the scattered amplitude as a function of angle for $ka = 5$, where k is the wavenumber of the incoming wave and a is the cylinder radius. The agreement is evidently very good with only some slight loss of amplitude for the lobes at approximately 70°.

Conclusions.

The Taylor-Galerkin method is found to be useful for electromagnetic applications. Two different formulations have been considered — each with advantages and disadvantages. The Lax-Wendroff style scheme has excellent phase accuracy, but is slightly dissipative, the amount of dissipation depending inversely on the Courant number. The leapfrog

variant is non-dissipative, but not as accurate. Both methods are at least second-order accurate. Neither guarantees that divergence constraints are locally satisfied, however the errors introduced are small if the problem is properly zoned. For problems involving propagation or scattering, the divergence errors should not be a concern.

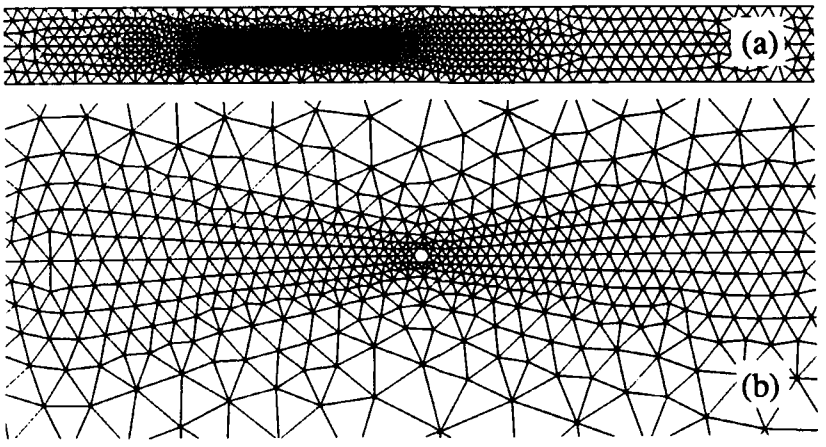

Figure 3. An unstructured grid surrounding a fine wire. (a) The entire simulation region; (b) a closeup of the region surrounding the wire.

Taylor-Galerkin schemes on unstructured grids offer a great advantage for electromagnetic problems. They allow small features to be zoned within a large-scale problem with a minimum number of zones. They also allow complicated geometric objects to be realistically represented. This approach could make time-domain electromagnetic calculations the technique of choice for an even broader class of applications.

Acknowledgement.

We thank the many colleagues who gave us useful advice and suggestions. We specifically thank Scott Ray, Dale Nielsen, and Peter Rambo of LLNL. We are indebted to Rick Devore of the Naval Research Laboratory who performed the scattering calculation on the circular cylinder. This work was performed under the auspices of the U. S. Department of Energy by Lawrence Livermore National Laboratory under contract no. W-7405-Eng.-48.

References.

1. Yee, K. S., *IEEE Trans. Antennas. Propagat.*, **AP-14**, 302 (1966).
2. A. Tavlove and K. R. Umashankar, in *Progress in Electromagnetics Research*, M. A. Morgan, Ed., Elsevier, New York,1990, pp. 287-373.
3. J. Donea, L. Quartapelle, and V. Selmin, *J. Comput. Phys.*, **70**, 463 (1987).

4. R. Löhner, K. Morgan and O. C. Zienkiewicz, *Int. J. for Num. Meth. in Fluids*, 4, 1043 (1984).
5. R. D. Richtmyer and K. W. Morton, *Difference Methods for Initial-Value Problems*, John Wiley, New York, 1967, pp. 300-306
6. A. Wathen, *IMA J. Num. Analysis*, 7, 449 (1987).
7. R. Löhner, *Comm. Appl. Num. Meth.*,4, 123 (1988).
8. R. F. Harrington, *Time-Harmonic Electromagnetic Fields*, McGraw-Hill, New York, 1961, pp. 232-245.

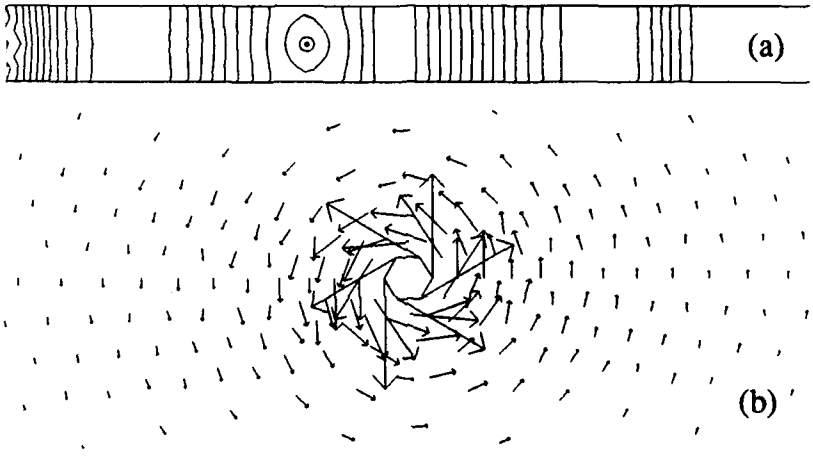

Figure 4. Solution for a half-cycle plane wave impinging on a fine wire. (a) Contours of the z-component electric field (along the wire); (b) the magnetic field vectors near the wire.

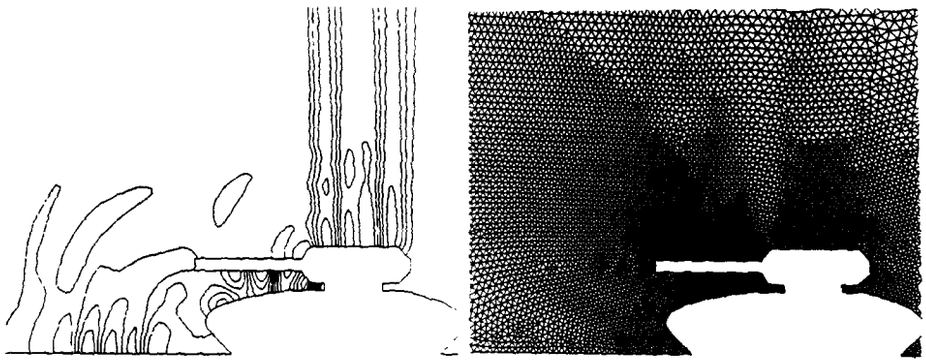

Figure 5. A two-cycle plane wave scatters off an armoured tank. (a) Contours of the z-component magnetic field; (b) the unstructured grid for the problem.

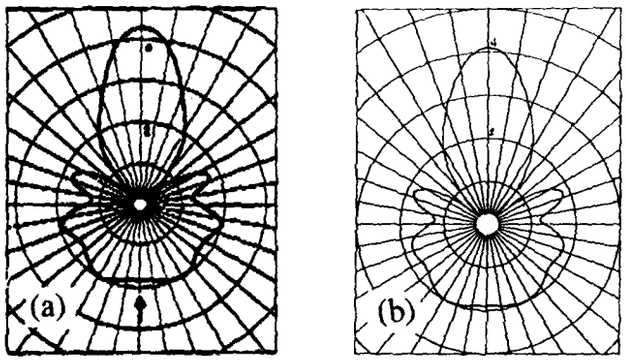

Figure 6. Relative amplitude as a function of angle for a plane wave scattering off a circular cylinder for ka=5: (a) analytic solution, (b) computed solution. Courtesy of Rick Devore, Naval Research Laboratory, Washington, D. C.

ANALYSIS OF RADAR ABSORBENT MATERIAL (RAM) COATED HF WIRE ROPE ANTENNAS USING THE TLM METHOD

G.K. Gothard, F.J. German, and L.S. Riggs
Department of Electrical Engineering
200 Broun Hall
Auburn University, AL 36849

Typical examples of ships systems performance degradation resulting from electromagnetic interference (EMI) include false targets, false bearings, and radiation pattern blockage. The cumulative effects of these types of equipment problems have been known to result in mission delays and aborted exercises. In many cases the best solution in relieving the above mentioned ships systems performance degradation is to employ radar absorbent materials (RAM) which have the ability to radically attenuate RF radiation. The transmission line modeling or matrix (TLM) method has been used as a numerical modeling approach for the assessment of radar reflectivity/absorbability of RAM coated shipboard HF wire rope antennas.

The basic principle of the TLM method is the modeling of space using a mesh of interconnected transmission lines. This mesh is excited at time zero, and the voltage and currents at each node in the mesh are recorded as time is stepped. The equivalence between electromagnetic field quantities and voltages and currents on transmission lines is use to calculated electric and magnetic fields as a function of time. The TLM method provides a time domain analysis of electromagnetic interaction and provides all six field quantities at each node in the mesh.

In this analysis of the RAM coated wire rope antenna the TLM method is employed to determine near field quantities. Using the equivalence principle, a near-to-far field transformation algorithm is used to determine the far field quantities from near field quantities. Subsequently, the radar cross section (RCS) of the RAM coated and uncoated wire antenna are determined in order to ascertain the effective attenuation of the RAM coating.

INTRODUCTION

All large motor-driven ships have certain electromagnetic interference (EMI) problems associated with them. This is because the closed environment of the ship contains many devices, such as the communications system and the motor, which radiate electromagnetic fields of various frequencies. These fields can couple with metallic surfaces or components on the ship generating currents which may interfere with other electronic devices. EMI is especially evident on naval ships because of the large number of shipboard electromagnetic radiators.

Law has listed many of these manmade EMI producing devices in Shipboard Electromagnetics [1]. For example the shipboard communications system has RF radiators operating at HF (3-30 MHz), VHF (30-300 MHz), UHF (300-3000 MHz), SHF (3-30 GHz), and EHF (30-300 GHz) frequencies. Different shipboard electromagnetic systems might be radiating at the same time while involved in weapons detection, tracking, navigation, communications and a wide variety of other tasks. Another system is the shipboard receiver system which can generate EMI within itself. Other systems contributing to EMI are the shipboard motors and generators, circuit breakers, switches and relays, engine ignition systems, fluorescent lighting, heaters, power supplies, PA systems, computers and all other electrical devices.

Typical shipboard problems [1] due to EMI producing devices include false radar targets, false alarms, false bearings, false tuning, communication and display screen distortions and radiation pattern blockage. While shipboard EMI can never be completely eradicated, it can be significantly reduced with protective measures. According to Law [1], some of these protective measures include decoupling, shielding, power reduction and the use of RAM.

One very prominent part of a naval ship is the wire rope antenna system. These wires are typically made of phosphor-bronze material and are five-sixteenth inch in diameter, and operate in the 3 to 30 MHz range [2]. These antennas are often constructed by erecting long (10 m) vertical wire ropes to transmit and receive over a full three hundred and sixty degrees (omnidirectional). These long vertical wire ropes can interfere with radar tracking and other information retrieval systems. As the shipboard radar systems sweep through the wire rope antennas, out-of-band energy reflections off of the wire rope antennas can cause some of the afore-mentioned EMI problems such as false targets on radar displays.

One proposed method of decreasing the RF energy reflections is to coat the wire rope antennas with a radar absorbent material (RAM). RAM has the ability to radically attenuate RF reflections. As a result, a RAM coating can significantly reduce back-scattered fields such as those reflected back into the radar systems from the wire rope antennas. The personnel of SEMCIP, the Shipboard Electromagnetic Compatibility Improvement Program, are currently testing RAM-coated wire in order to determine the attenuation

provided by the coating. They are interested in the theoretical trends to compare with the experimental data. The thrust of this project is to investigate these trends and to determine the maximum theoretical attenuation.

ABSORBERS

There are various types of absorbing materials that can be used to attenuate radiation. One type is the broadband absorber which yields high attenuation over a large frequency range. Another type is the resonant absorber which is set to provide maximum attenuation at a discrete frequency. A third type operates by having the complex permittivity equal to the complex permeability, and therefore the characteristic impedance of the material is equal to that of free space.

The ideal absorber would have a characteristic impedance equal to free space at all frequencies (broadband) and would have a high value of magnetic and dielectric loss. This would allow an incident wave to penetrate the absorber with no reflection, and the magnetic and dielectric losses would attenuate the wave to the desired level. At low frequencies these material parameters can be realized. However, the complex permittivity and permeability of a medium are highly frequency dependent in a nonlinear fashion, and at microwave frequencies the magnetic loss of most materials is much less than the dielectric loss.

At microwave frequencies, the characteristic impedance of any broad band absorber can not be equal to the characteristic impedance of free space. This impedance mismatch precludes the use of a flat sheet of absorbing material because of large reflections off the air/absorber interface. When using this type of absorbing material, the geometry of the material must be altered to provide a gradual impedance transformation from that of free space. A conical or pyramidal profile is usually used.

A resonant absorber provides maximum attenuation, or is tuned, to a single frequency. The best type of resonant absorber is a quarter wave resonator, which has a layer of material one quarter of a wavelength thick (at the desired frequency) with a metallic backing [3]. Figure 1 shows a wave incident upon a quarter wave resonator. Part of the incident wave is reflected from the air/material boundary and the rest is transmitted into the material. The wave propagating in the material is reflected back and forth from the metallic backing to the material/air interface yielding a series of emergent waves. Since the electrical thickness of the material is a quarter wavelength all the emergent waves are in phase with each other but out of phase with the reflected wave. Therefore if the sum of the initial reflected wave and emergent waves are equal to zero the total reflection will be zero. To realize this the sum of the emergent waves must be equal in amplitude to the initial reflected wave.

Using transmission line theory, the quarter wave resonant absorber can be considered as a quarter wave transformer backed by a short circuit [3]. This yields the input impedance condition

$$Z_{input} = Z_0 \tanh(kd) \qquad (1a)$$

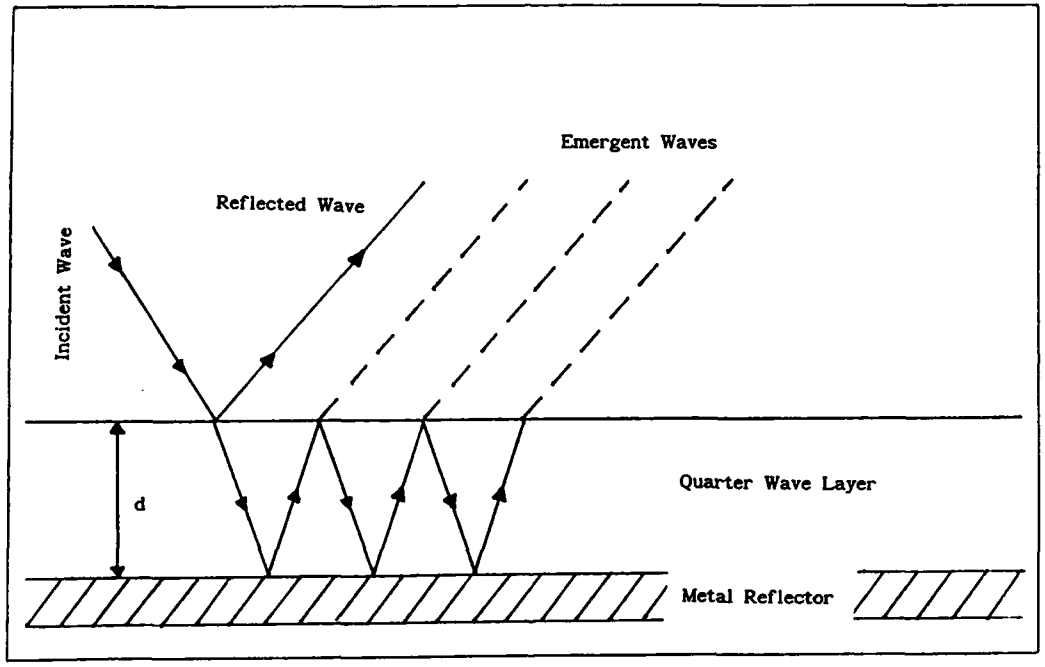

Figure 1 Quarter Wave Resonant Absorber with Metallic Backing Showing the Incident Wave, Initial Reflected Wave and the Emergent Waves

where the propagation coefficient k is

$$k = j\frac{2\pi}{\lambda}\sqrt{\mu_r \varepsilon_r} \qquad (1b)$$

and d is the thickness of the layer. For zero reflection the tanh(kd) of 1a should be solved for unity.

The frequency of interest for this project was restricted to a narrow band in the microwave range, and the geometry of the object considered (wire rope antenna) was not conducive to employing broadband materials with their conical or pyramidal profiles. Therefore a resonant absorber was the optimal choice for the RAM coating used on the wire rope antennas. This project deals only with the analysis of resonant absorbers applied to wire rope antennas.

APPROACH USED FOR THE INVESTIGATION

The transmission line modeling (TLM) method was used in this analysis of the RAM-coated wire rope antennas. Several modifications to the TLM method were needed to determine electromagnetic scattering. These modifications included absorbing boundary conditions and plane wave excitation [4]. The modified TLM algorithm, GTEC2, was used to determine the near fields scattered by an infinite circular cylinder. Then a near-to-far field transformation algorithm was used to transform the near-field data to the far field. The far-field data is necessary for the calculation of the RCS.

Referring to Figure 2, the radius (a) of the wire analyzed in all cases was 3/16 inch. The parameters varied in the study were the RAM permittivity (ε), permeability (μ), conductivity (σ), thickness (r-a) and the frequency of excitation. A plane wave was simulated on the TLM mesh and was used as the wave incident upon the scatterer. This wave is shown in Figure 2 to have a transverse magnetic (TM) polarization, however the transverse electric (TE) polarized incident wave was also considered. Once the total near fields were obtained via TLM, the incident field was subtracted to yield the scattered near fields which were to be transformed to the far field.

EXAMPLE CALCULATIONS

The method used to determine the RCS yielded a bistatic result. This can be seen in Figure 3 where the RCS is shown for a receiver moved from the source location through 180 degrees. The backscattered region corresponds to the 180 degree point and the forward scattered region corresponds to the 0 degree point. The various curves on the plot of Figure 3 are for different radii of the RAM material with all other parameters held constant (see listing of RAM parameters on Figure 3). It is interesting to note that maximum reduction in RCS due to the RAM coating is different for different thicknesses of RAM depending on the receiver location. For example, a thicker layer of RAM gave the minimum RCS at about 115 degrees whereas a thinner coating gives the minimum RCS in the backscattered region (180 degrees). This result is important for the case when the source and victim are not the same system.

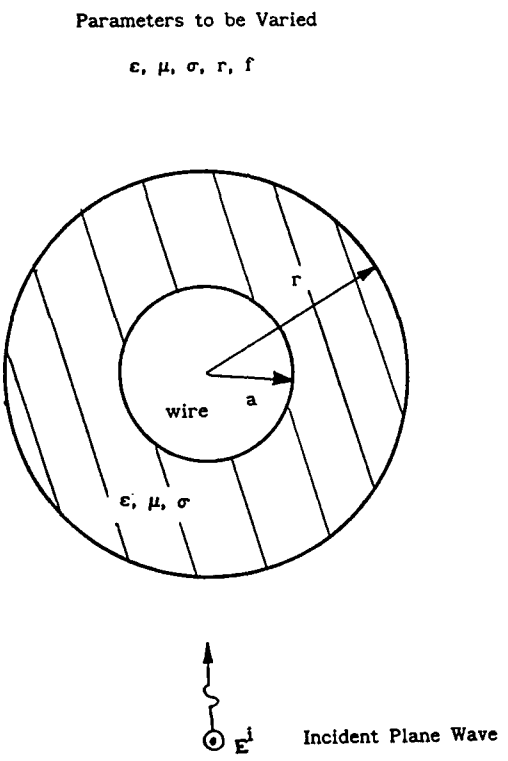

Figure 2 Geometry of the Wire with RAM Coating Used for Analysis, and a List of the RAM Parameters to be Varied

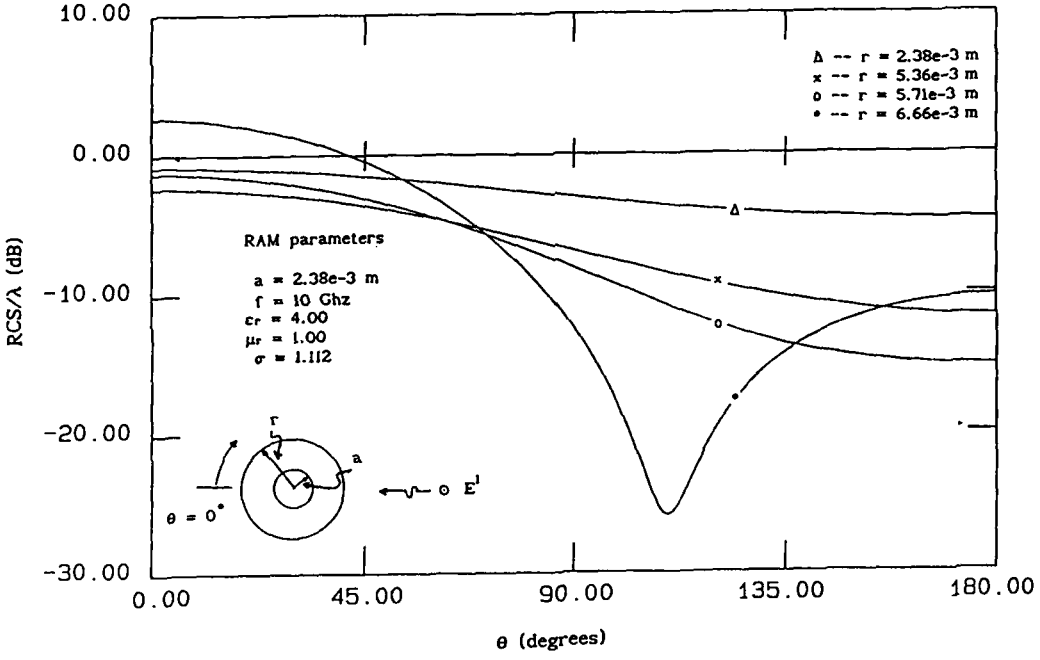

Figure 3 Bistatic RCS of RAM-Coated Circular Cylinder for TM Polarization. Each Line on Plot Corresponds to a Different RAM Thickness

Cases for both the transverse electric (TE) and transverse magnetic (TM) polarized incident waves were examined. Figure 4 is the monostatic RCS for TE illumination and Figure 5 is the monostatic RCS for TM illumination. In both these figures the thickness of the RAM is varied and all other parameters are held constant. The monostatic RCS for the uncoated wire is the left most point on the figures and corresponds to a diameter of 3/16 inch. Comparing the RCS of Figures 4 and 5 at the point where the RCS of Figure 5 (TM) is at a minimum shows that the magnitude of the RCS of Figure 4 (TE) at the same point is significantly lower. This implies that in terms of backscattered power TM illumination is the worst case. Based on this comparison RCS and attenuation calculations were carried out for TM illuminations only.

Figure 6 is a plot of the attenuation (in dB) with the radius of the RAM coating varied and all other parameters held constant (see RAM parameters on Figure 6). The attenuation has been defined as the ratio of the scattered power with the RAM coating on the wire to the scattered power without the RAM coating on the wire. The maximum attenuation is shown to be approximately 12 dB, and this maximum occurs at the point where the wavelength of the incident wave is a quarter wavelength in the RAM.

Figure 7 is a plot of the attenuation with the frequency varied from 8 to 12 Ghz and all other parameters held constant (see RAM parameters on Figure 7). The radius of the RAM is fixed such that at 10 GHz the maximum possible attenuation is obtained. This plot shows that the attenuation generally decreases as the frequency is moved away from 10 GHz. This decrease is because the RAM was "tuned" to provide maximum attenuation at 10 GHz. As the frequency is shifted away from this point the electrical thickness of the RAM changes.

Figure 8 is a plot of the attenuation with the permittivity varied and all other parameters held constant (see RAM parameters on Figure 8). This plot shows that as the permittivity is varied the attenuation generally decreases. The permittivity (and the permeability) defines the electrical thickness of a material, and any change in these parameters changes this thickness. Since the thickness of the RAM (with a permittivity of ε_r = 10.27) was adjusted to provide maximum attenuation , changing the permittivity of the RAM changed the electrical thickness of the RAM and therefore the attenuation decreased.

Figure 9 is a plot of the attenuation with the conductivity varied and all other parameters held constant (see RAM parameters on Figure 9). It is evident from this plot that as the conductivity of the material decreases the attenuation approaches zero and as the conductivity increases the attenuation increases, but only up to a point. The point when the attenuation begins to decrease is reached when the increased conductivity makes the RAM "look" like a metallic material. At this point, reflections off this material at the air-RAM interface cause the attenuation to decrease.

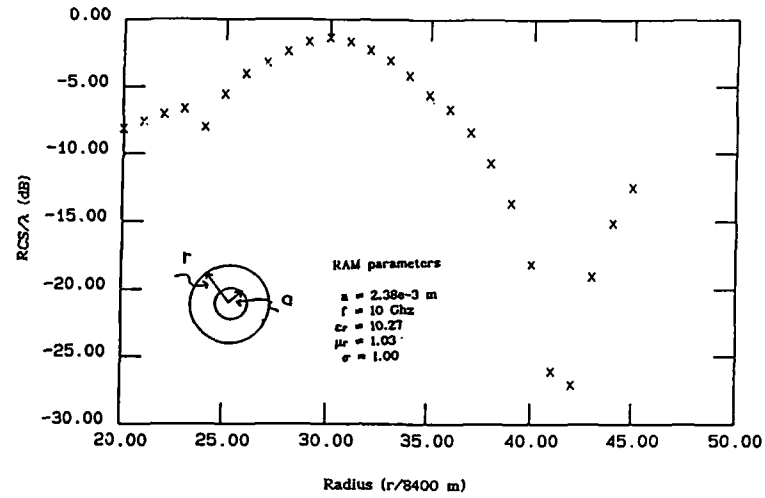

Figure 4 Monostatic RCS of RAM-Coated Circular Cylinder for TE Polarization with Radius of RAM Varied

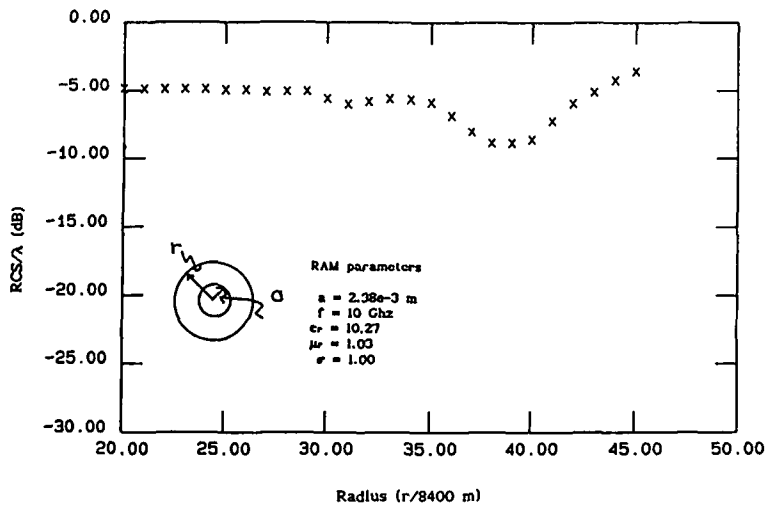

Figure 5 Monostatic RCS of RAM-Coated Circular Cylinder for TM Polarization with Radius of RAM Varied

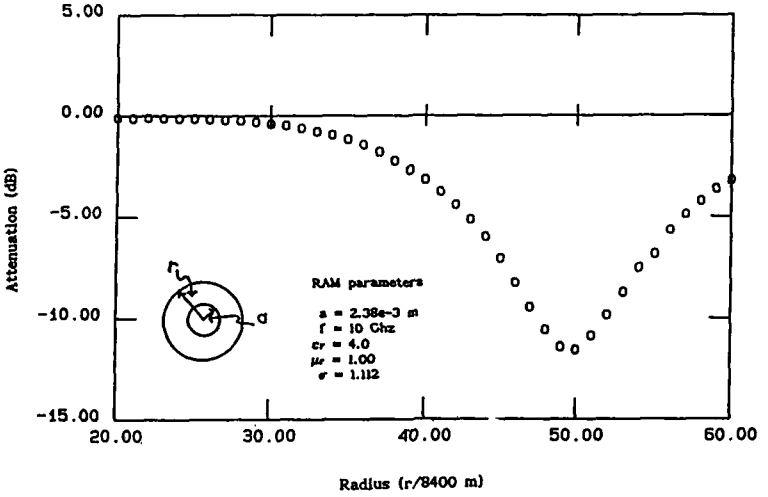

Figure 6 Monostatic Attenuation of RAM-Coated Circular Cylinder for TM Polarization with Radius of RAM Varied

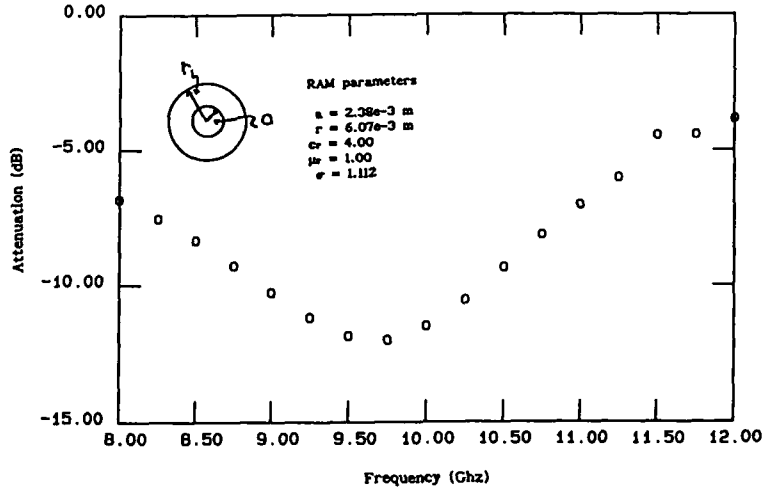

Figure 7 Monostatic Attenuation of RAM-Coated Circular Cylinder for TM Polarization with Frequency of Incident Wave Varied

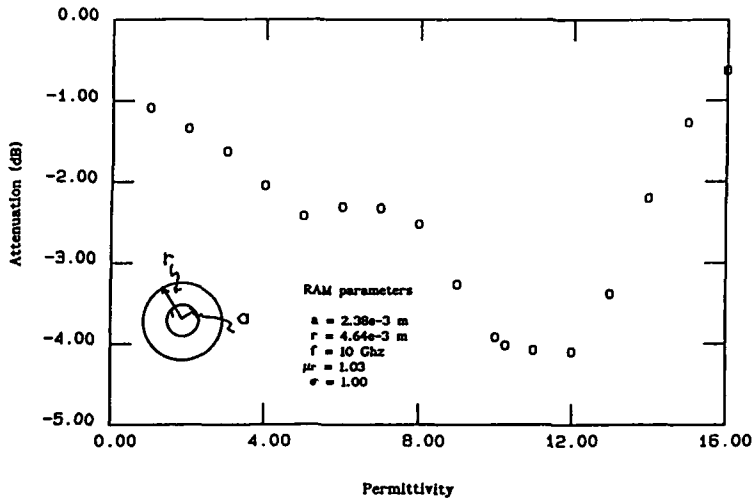

Figure 8 Monostatic Attenuation of RAM-Coated Circular Cylinder for TM Polarization with the Permittivity of the RAM Varied

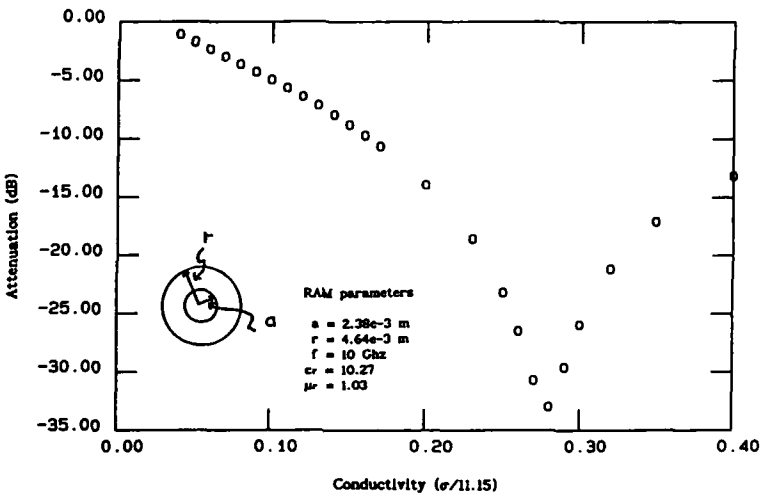

Figure 9 Monostatic Attenuation of RAM-Coated Circular Cylinder for TM Polarization with the Conductivity of the RAM Varied

CONCLUSIONS

RCS calculations for TE- and TM-polarized waves incident upon a RAM-coated wire were carried out. Based on a comparison of these results, it was concluded that, generally, the backscattered field for the TM illumination was greater than that for TE illumination. Therefore, for a worst case analysis, one need only consider TM illumination.

For a given RAM/wire geometry and material parameters, RAM having a large value of dielectric loss factor (sigma) caused the attenuation to be larger than RAM having a smaller value of sigma...up to a point. This is due to the reflectivity of the material increasing with an increase in sigma. At some point, the reflectivity of the material cancels out the benefits of the sigma-induced attenuation in the RAM.

When the RAM is a quarter wavelength thick at a design frequency fo, the attenuation is maximized for that design frequency. When the frequency is shifted away from fo, the attenuation generally decreases.

Based on the experimental data, it appears that the planar approximation of the wire rope antenna for the backscattered area is fairly accurate. For a given set of RAM parameters, the maximum attenuation does occur when the RAM is one quarter of a wavelength thick in the material. However, it does not necessarily follow that this is always the case. Further research is necessary in this analysis of narrow band "tuned" RAM. The analysis should be extended to include wire antennas of various diameters. Attenuation should be calculated at different frequencies, such as the S-band or K-band, in order to see how resonant absorbers tuned for operation in these bands perform.

Recently the TLM algorithm was modified to include complex permeability, and it is now possible to include magnetic losses as well as electric losses in absorbing or lossy materials. We are currently in the process of obtaining measured attenuation data and accurate material parameters for the RAM from the personnel of SEMCIP. Experimental data will be obtained and compared to the measured data, and this will be the subject of a future paper.

References

[1] P. E. Law, Jr., *Shipboard Electromagnetics,* Dedham, MA: Artech House, 1987.

[2] P. E. Law, Jr., *Shipboard Antennas*, Dedham, MA: Artech House, 1986.

[3] Communique from Plessey Materials, "An Introduction to Microwave Absorbent Materials," Towcester, Northants, U.K.

[4] F. J. German, G. K. Gothard, L. S. Riggs, P. M. Goggans, "The Calculation of Radar Cross Section (RCS) Using the TLM Method," *Int. J. Numerical Modeling: Elec. Networks, Devices and Fields*, accepted for publication for Nov., 1990 issue.

RADAR CROSS SECTION (RCS) CALCULATION OF TWO AND THREE DIMENSIONAL SCATTERERS USING THE TLM METHOD

F.J. German, G.K. Gothard and L.S. Riggs
Department of Electrical Engineering
200 Broun Hall
Auburn University, AL 36849

ABSTRACT

The transmission line matrix (TLM) method of electromagnetic analysis is a well known numerical technique for the simulation of complicated three dimensional electromagnetic systems. The technique has been applied to a wide variety of electromagnetic interaction problems with success.

Recently, we have applied the TLM method to the analysis of scattering from structures in unbounded spaces. In this paper we will present results for the RCS of several two and three dimensional scatterers calculated using the symmetrical condensed node TLM technique. We will also discuss the development of an efficient truncation boundary condition for use with the symmetrical condensed node TLM method as well as a field continuation condition for efficiently launching plane waves onto a TLM mesh. The results obtained with the TLM technique are shown to be in very good agreement with those obtained from analyses based on the method of moments.

INTRODUCTION

The transmission line matrix (TLM) method is a numerical scheme for determining the time domain solution to the Maxwell equations in three dimensional space. The TLM method has been used extensively to solve a wide range of electromagnetic interaction problems [1]. The application of the technique to problems involving unbounded space has been limited to the estimation of the response of structures, such as surface currents induced on aircraft, to nuclear electromagnetic pulses (NEMP) where extremely accurate results are often not required [2]. To date, no work has been reported involving the use of TLM for calculating the electric and magnetic fields at observation points which lie in the far field of a scatterer which are required for calculating the radar cross section (RCS) of the scatterer.

Traditional techniques used for RCS calculations involve the use of the method of moments (MoM), the physical theory of diffraction (PTD), and the geometric theory of diffraction (GTD); the latter two methods being used when the objects of interest have dimensions on the order of many wavelengths at the frequency of interest. The MoM is limited to scattering objects involving maximum dimensions of a few wavelengths.

This paper presents the use of the TLM method for the computation of the RCS of complex scatterers. This is an attractive technique for RCS calculation since the addition of apertures, cavities, and arbitrary, time-varying, non-linear material parameters does not change the formulation of the TLM algorithm - only the input data specifying the geometry must be changed. In addition, the upper frequency limit at which accurate results can be obtained is limited only by the available computer resources and not by assumptions inherent to the numerical scheme.

Problems involving scattering in unbounded spaces using TLM have been limited in the past due to several complications. Namely, the excitation of infinite plane waves on a finite mesh, the truncation of the mesh boundaries to simulate unbounded space when irregularly graded/anisotropic meshes are used, and the transformation of the TLM generated near fields to the far field to allow RCS prediction. In this paper, we present our approach to each of these problems and give results for the RCS of several two and three dimensional scatterers. Our results are shown to be in very good agreement with both measurements and data from other analytical techniques.

TLM BASICS

The basis of the TLM method is the well understood concept of a three dimensional circuital model of space wherein voltages and currents in the circuit are equivalent to the electric and magnetic field quantities and lumped inductors, capacitors, and resistors represent the permeability, permittivity, and conductivity of the space being modeled. In the TLM method, the equivalent circuit is replaced by a three dimensional mesh of interconnected transmission lines. The time domain impulse response to this transmission line mesh is then determined by tracking pulses as they scatter throughout the mesh until the desire

simulation time is reached. Once this impulse response is found, steady state frequency domain data can be extracted via a Fourier transform. The upper frequency limit for which the impulse response will yield accurate data is determined by the coarseness of the mesh used. The general rule of thumb that has been used in the past is to use at least ten TLM cells per wavelength. As we will show in this paper, however, this requirement can be relaxed somewhat when using the symmetrical condensed TLM method provided that the mesh is fine enough to model the field variation.

For all of the work presented here we have used the symmetrical condensed TLM node which is shown in Figure 1. This particular version of the TLM procedure has been shown to be more accurate and computationally more efficient than previous formulations of the TLM technique [3]. For two dimensional problems a "slice" from a three dimensional mesh is used; i.e., only a subset of the full three dimensional scattering matrix is used. While a complete analytic assessment of the symmetrical condensed node propagation characteristics has yet to be performed, preliminary analysis and numerical experimentation show that this variant of the TLM method displays improved propagation characteristics over other previous TLM models.

ABSORBING BOUNDARY CONDITIONS FOR TLM

Obviously, only a finite TLM mesh can be modeled by a computer. Thus, in order to model electromagnetic interaction problems involving unbounded space, some means of terminating the finite TLM mesh to simulate an unbounded space must be used. From a computational standpoint, it is desired to employ the truncation conditions as close to the scatterer as possible. On the other hand, the truncation planes must be far enough away from the scatterer so that non-physical reflections from the truncation boundaries don't pollute the desired field data.

Truncation of a TLM mesh is accomplished by specifying an appropriate reflection coefficient for voltage pulses at the outer edges of the mesh. For a mesh using cubic cells and modeling an isotopic medium determination of the appropriate reflection coefficient is straightforward. Recently, we have formulated a set of truncation conditions which are applicable to irregularly graded/anisotropic TLM meshes [4].

Consider the case of a cubic TLM cell modeling a block of space with material parameters ε_r and μ_r. The reflection coefficient for mesh termination should simulate the voltage pulse travelling from the link transmission line with unity normalized characteristic impedance to an infinite space with normalized impedance $\sqrt{\mu_r/\varepsilon_r}$ and is given by

$$\rho = \frac{\sqrt{\mu_r/\varepsilon_r} - 1}{\sqrt{\mu_r/\varepsilon_r} + 1}$$

For the case of a rectangular block of space with dimensions u,v, and w in the x,x, and z coordinate directions, the following immitances are defined [5]:

$$Y_x = 2\left[\frac{v\ w}{u}\frac{\varepsilon_r}{c\Delta t} - 2\right]$$

$$Y_y = 2\left[\frac{u\ w}{v}\frac{\varepsilon_r}{c\Delta t} - 2\right]$$

$$Y_z = 2\left[\frac{v\ u}{w}\frac{\varepsilon_r}{c\Delta t} - 2\right]$$

$$Z_x = 2\left[\frac{v\ w}{u}\frac{\mu_r}{c\Delta t} - 2\right]$$

$$Z_y = 2\left[\frac{u\ w}{v}\frac{\mu_r}{c\Delta t} - 2\right]$$

$$Y_z = 2\left[\frac{v\ u}{w}\frac{\mu_r}{c\Delta t} - 2\right]$$

where c is the speed of light and Δt is the TLM time step.

If we define effective material constants as

$$\varepsilon_{rx} = (Y_x + 4)\frac{c\Delta t}{2}$$

$$\varepsilon_{ry} = (Y_y + 4)\frac{c\Delta t}{2}$$

$$\varepsilon_{rz} = (Y_z + 4)\frac{c\Delta t}{2}$$

$$\mu_{rx} = (Z_x + 4)\frac{c\Delta t}{2}$$

$$\mu_{ry} = (Z_y + 4)\frac{c\Delta t}{2}$$

$$\mu_{rz} = (Z_z + 4)\frac{c\Delta t}{2}$$

The above equations show that the use of rectangular (as opposed to cubic) cells in a TLM mesh introduces anisotropies into the model that must be accounted for when terminating the mesh. To account for this,

the two orthogonal voltage pulses encountering a truncation plane must be weighted by *different* reflection coefficients. The reflection coefficient is given by

$$\rho = \frac{F - 1}{F + 1}$$

where the factor F is determined by the voltage pulse being truncated. For the port numbering shown in Figure 1, Table 1 gives the F factor associated with each voltage pulse.

TABLE I

Voltage Pulses	F
V_1 and V_{12}	$\frac{\sqrt{Zz + 4}}{\sqrt{Yx + 4}}$
V_2 and V_9	$\frac{\sqrt{Zy + 4}}{\sqrt{Yx + 4}}$
V_3 and V_{11}	$\frac{\sqrt{Zz + 4}}{\sqrt{Yy + 4}}$
V_4 and V_8	$\frac{\sqrt{Zx + 4}}{\sqrt{Yy + 4}}$
V_5 and V_7	$\frac{\sqrt{Zx + 4}}{\sqrt{Yz + 4}}$
V_6 and V_{10}	$\frac{\sqrt{Zy + 4}}{\sqrt{Yz + 4}}$

PLANE WAVE SOURCE CONDITIONS

The truncation conditions of the previous section are applied to voltage pulses which are associated with the total field which is the sum of the incident (usually plane wave) excitation and the fields scattered from the object under study. This leads to difficulties when the incident excitation is an infinite plane wave propagating on a two or three dimensional TLM mesh. The result is that the incident excitation tends to "fall" off of the mesh along with the outgoing scattered field. Our approach has been to apply the truncation conditions to the voltage pulses at the mesh boundary - these voltage pulses are associated with the *total* field. Then we re-inject pulses back into those ports with the correct magnitude of the incident field, which is usually an analytic function. This is equivalent to applying truncation conditions to the outward propagating scattered fields and applying one dimensional symmetry conditions to the incident infinite plane wave. A quantitative

description of this technique for the two dimensional case can be found in [4].

NEAR-TO-FAR FIELD TRANSFORMATION

In order to keep the computer expenditure from becoming prohibitive, only the fields in the near field of the scatterer can be calculated with TLM. These near fields are then transformed to the far field using a near-to-far field transformation based on the equivalence principle [6]. To accomplish this a rectangular virtual surface is defined which completely encloses the scatterer and the tangential fields at all cells on this surface are stored. From these field values, equivalent electric and magnetic currents are obtained and then integrated (summed) over the free-space Green's function to yield the vector magnetic and electric potentials from which the fields in the far zone of the scatterer are readily obtained, and hence, the RCS.

TLM SIMULATION RESULTS

In order to test the quality of the absorbing boundary conditions and plane wave source conditions, the RCS of several two and three dimensional scatterers are presented.

Two Dimensional Cylinders: The first example is a perfectly conducting square cylinder with several different coatings. The geometry and results for the bistatic RCS are shown in Figure 2 for three different coatings including a magnetic one. The excitation is TE polarized. The TLM results are compared with those obtained using a MoM code and the agreement is excellent. For the TLM calculations, the mesh used was 20 x 40 cells (symmetry was employed). with the conducting cylinder having a width of 20 cells, and the virtual surface taken five cells from the dielectric surface.

Since TLM models usually employ a cartesian mesh, the effects of approximating curved surfaces (i.e., "staircasing") must be investigated. Figure 3 shows the geometry and bistatic RCS for a perfectly conducting coated circular cylinder subjected to a TM polarized incident plane wave. The total cylinder diameter (including dielectric) was 40 cells and the total mesh size was 100 x 50 cells. Conducting boundaries were used both between nodes and at nodes in order to more effectively model the curvature of the cylinder. As in the square cylinder case, excellent agreement is obtained with the MoM results.

The same conducting cylinder was then illuminated with a TE polarized incident plane wave and the RCS results are shown in Figure 4. Notice that while the general trends of the RCS were predicted by the TLM analysis, agreement is not as good as in the previous cases. This discrepancy is thought to be a consequence of staircasing the cylinder surface when circumferentially flowing surface currents are present. We are currently investigating the feasibility of developing a TLM mesh that can conform to the surface of arbitrary scatterers to improve accuracy without requiring an extremely large mesh.

Three Dimensional Examples: To verify the procedure for three dimensional scatterers we have calculated the bistatic RCS of a perfectly conducting cube. Each face of the cube was modeled using 20 x

20 cells. Symmetry was again employed yielding a total mesh size of 48 x 24 cells. The TLM calculated RCS is compared to measurements from [7]. Figure 7 shows the RCS for a cube that is 0.75λ per side and agreement with the measurements is very good. The cell size in this case is 0.0375λ.

Next, we calculated the RCS for a conducting cube 1.5λ per side. To do this we used the time domain impulse response from the 0.75λ case and performed the Fourier transform at a higher frequency. For this case the cell size is 0.075λ and as can be seen form Figure 6 agreement with the measured RCS is quite good.

Still using the same impulse response, we Fourier transformed at a frequency which made the cell size 0.15λ. The RCS is compared to measurements in Figure 6 and agreement is still fairly good even though the 0.1λ cell size criteria has been violated.

Finally, we have analyzed a dielectric cube (ε = 4.0) that was 0.2566λ per side. The mesh was the same size as that used for the conducting cube. The results in Figure 8 show excellent agreement with those obtained from a volume integral MoM solution from [8].

CONCLUSIONS

This paper has validated the use of the TLM method for RCS calculations. Absorbing boundary conditions, plane wave source conditions, and a near-to-far field transformation have been presented. Comparisons with other methods and measurements show good agreement for cell sizes as large as 0.15λ. Problems were encountered for TE excitation of two dimensional circular cylinders and this is thought to be due to the cartesian approximation to the cylindrical surface. The TLM is a powerful technique for RCS calculations since arbitrary geometries and material parameters may be modeled without complicating or changing the algorithm in any way. While we have transformed Fourier transformed field values to the far field to calculate RCS, the actual time domain fields can be transformed. This would prove useful for investigating the response of scatters to a wide band pulsed illumination.

REFERENCES

[1] W.J.R. Hoefer, "The transmission line matrix method - theory and applications," IEEE Trans. Microwave Theory Tech., MTT-33, no. 10, 1985, 882-893.

[2] P.B. Johns and A. Mallik, "EMP response of aircraft structures using TLM," 6th Symposium and technical Exhibition on Electromagnetic Compatibility, Zurich, 1985.

[3] P.B. Johns, "A symmetrical condensed node for the TLM method," IEEE Trans. Microwave Theory Tech., MTT-35, no. 4, 1987, 370-377.

[4] F.J. German, G.K. Gothard, L.S. Riggs and P.Goggans, "The calculation of radar cross section (RCS) using the TLM method," to be published in International Journal of Numerical Modelling: Electronic Networks, Devices and Fields, vol.2, no. 4, 1990.

[5] D.A. Al-Mukhtar and J.E. Sitch, "Transmission-line matrix with irregularly graded space," Proc. IEE, vol. 128, no. 6, 1981, 299-305.

[6] A. Taflove and K. Umashankar, "Radar cross section of general three-dimensional scatterers," IEEE Trans. Electromagnetic Compatibility, EMC-25, 1983, 433-440.

[7] R. Penno, P.K. Murthy and G.A. Thiele, "Results of the application of the hybrid iterative method to scattering from a cube," IEEE AP-S International Symposium Digest, 1987, 526-529.

[8] S. Ching-Chuan, "Electromagnetic scattering by a dielectric body with arbitrary inhomogeneity and anisotropy," IEEE Trans. Ant. and Prop., AP-37, 1989, 384-389.

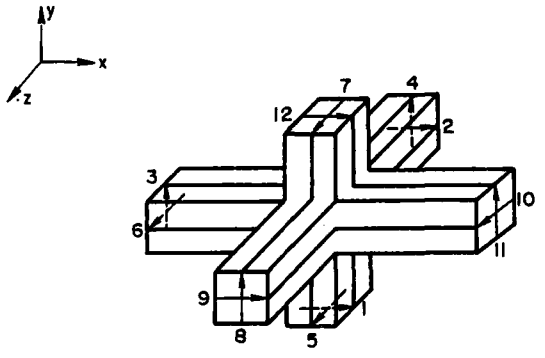

Figure 1 The symmetrical condensed TLM node with all port voltages shown

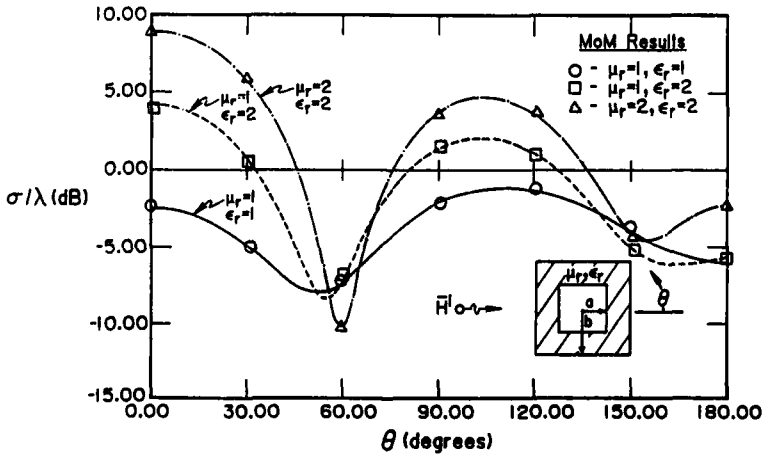

Figure 2 Bistatic RCS of coated square cylinder for TE polarization.
(ka = 1.0, kb = 1.5)

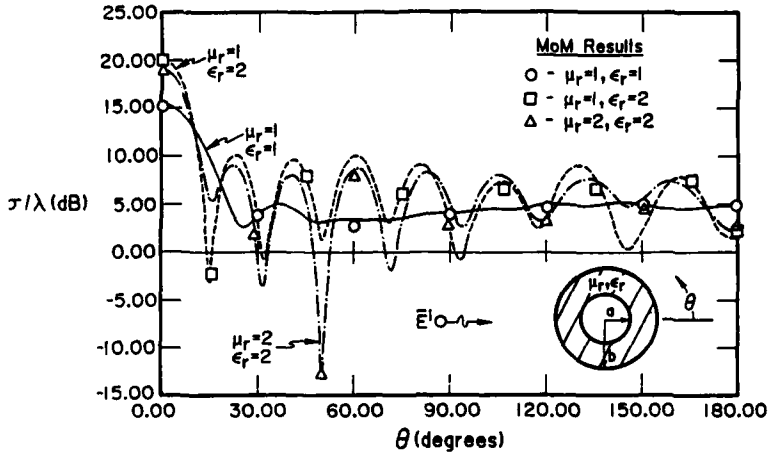

Figure 3 Bistatic RCS of coated circular cylinder for TM polarization. (ka = 2π, kb = 3π)

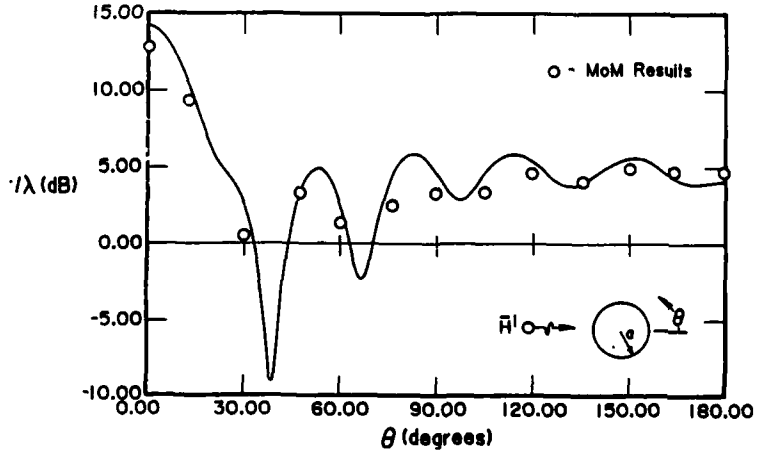

Figure 4 Bistatic RCS of conducting circular cylinder for TE polarization. (ka = 2π)

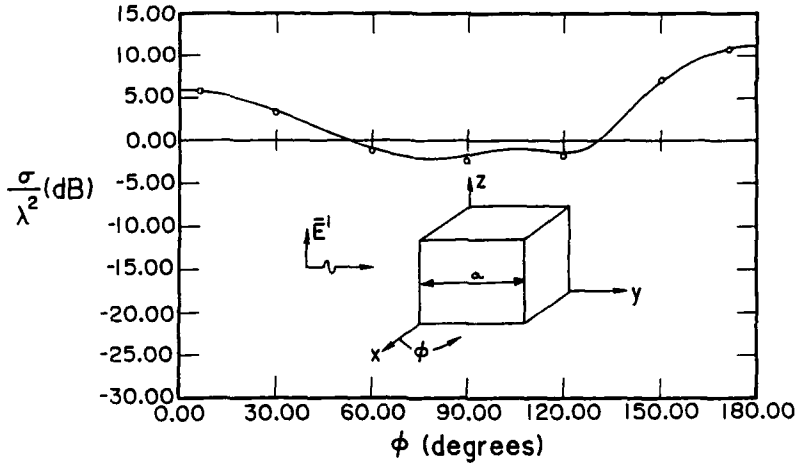

Figure 5. Geometry of conducting cube scatterer and bistatic RCS. Cube is 0.75λ per side. (——— - TLM, o - measurements from [7])

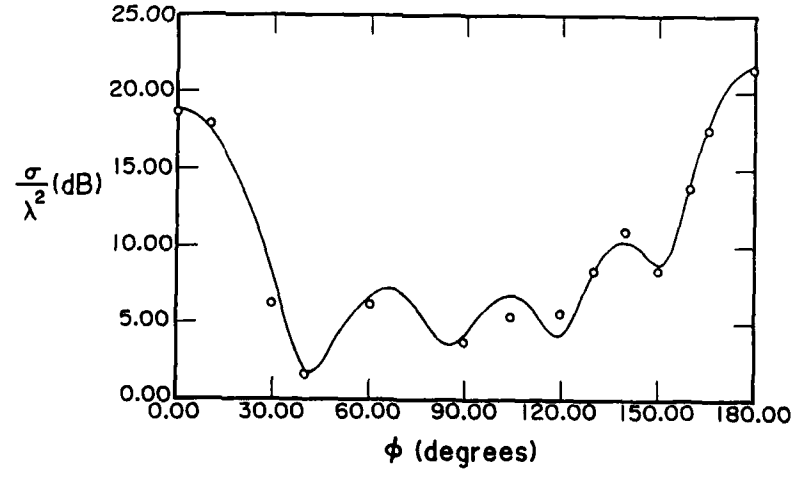

Figure 6. Bistatic RCS of conducting cube with 1.5λ per side. (——— - TLM, o - measurements

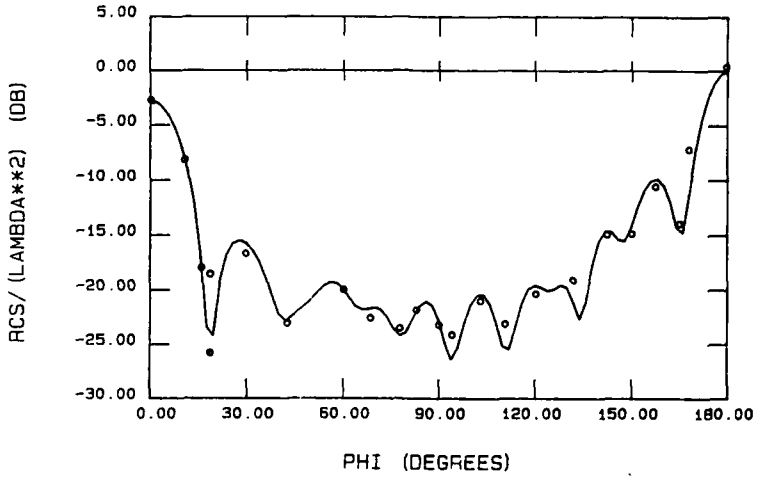

Figure 7. Bistatic RCS of conducting cube with 3.0λ per side.
(——— - TLM, o - measurements

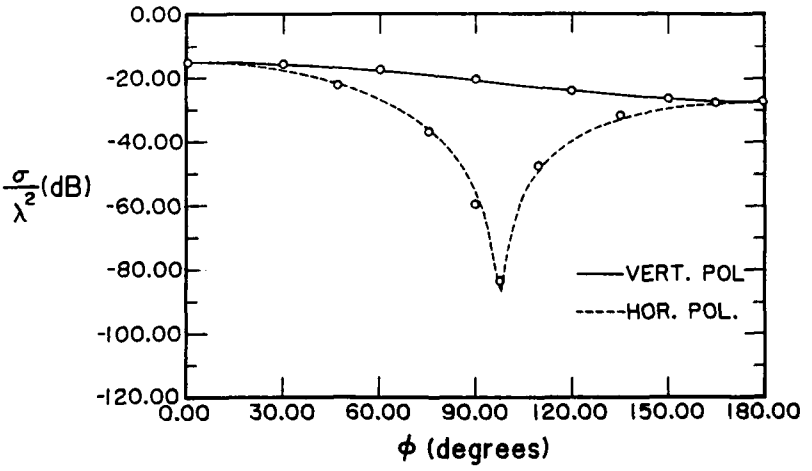

Figure 8. Bistatic RCS of dielectric cube 0.2566λ per side, $\epsilon_r = 4$.
(—— & - - - - TLM, o - from [6])

ANALYSIS OF THE INPUT IMPEDANCE OF A CAVITY-BACKED APERTURE ANTENNA USING THE TLM METHOD

S.L. Ponder, F.J. German, and L.S. Riggs
Department of Electrical Engineering
200 Broun Hall
Auburn University, Alabama 36849

The cavity-backed aperture antenna is a useful device for applications requiring a small, flush-mounted radiator. The input admittance of the slot-excited cavity-backed aperture antenna is well-documented; however, there is very little information available regarding the input impedance of the cavity-backed aperture antenna excited by a coaxial probe in the cavity.

In this paper, the TLM method is used to determine the input impedance of the probe-excited cavity-backed aperture antenna, loaded with a dielectric. The antenna and a length of transmission line are modeled as a set of boundaries in a three-dimensional cartesian mesh. The TLM method makes all six cartesian field components available at each point (or node) in the mesh, allowing the computation of antenna's input impedance over a wide range of frequencies.

It is shown that the TLM method can be used to model TEM propagation along a coaxial transmission line and to compute the characteristic impedance of the coaxial line. Antenna aperture distribution data generated by the TLM method is presented as well as preliminary results of a TLM analysis of the antenna's aperture admittance.

Introduction

The cavity-backed aperture antenna is a useful device for applications requiring a small, flush-mounted radiator. The use of dielectric loading materials allows the antenna to be miniaturized for use when space is at a premium. These antennas have found use on the fuselages of aircraft and missiles, in orbiting satellites, and in hyperthermia applicators . While the input impedance of these antennas is well-documented for the slot-excited configuration ([1]-[3]), there is little information available regarding the input impedance of the cavity-excited configuration. This paper describes the results of using TLM analysis to determine the input impedance of the cavity-excited cavity-backed aperture antenna.

Antenna Geometry

Two examples of cavity-backed aperture geometries are shown in Figure 1. Figure 1(a) depicts an antenna excited by a coaxial line that is attached directly to the the slot (aperture). Figure 1(b) shows the same type of antenna excited by a coaxial probe in the cavity. The dimensions of the cavity are usually chosen so that it acts as an iris-terminated waveguide operating in its fundamental mode. The aperture itself may be a narrow slot as shown, or it may have the same dimensions as the cavity wall in which it is located. The antenna's surfaces are metallic and are made of whatever alloy is best suited to the operating environment (e.g. lightweight metals for aircraft antennas.)

Figure 1 shows the two most common methods of exciting a cavity-backed aperture antenna. The configuration in Figure 1(a) works well for low microwave frequencies. In Figure 1(b), the slot is excited indirectly by the cavity field; this configuration works well at higher microwave frequencies. The cavity is excited by either a probe (shown) or a small loop. It is the configuration of Figure 1(b) that will be analyzed using the TLM method.

Using TLM to Solve for the Input Impedance of a Coaxially-Fed Cavity-Backed Aperture Antenna

The TLM method can be used to easily determine the input impedance of a variety of antennas, including cavity-backed aperture antennas. In a TLM analysis, the device being analyzed is modeled as a set of boundaries in a three dimensional cartesian mesh. The TLM method makes all six cartesian field components available at each point (or node) in the mesh. If the device being modeled is a coaxially-fed cavity-backed aperture antenna of the type in Figure 1(b), the input impedance can be determined by using TLM-generated field values within the coaxial line at the point where the coaxial line connects to the cavity. Evaluating these fields over the proper line integrals yields values for voltage and current, the ratio of which is the antenna's input impedance.

Coaxial Line Model

A valid model of a coaxial transmission line had to be developed in order to accurately compute the input impedance of a cavity-backed aperture antenna excited by a probe in its cavity. The coaxial line model had to be capable of properly supporting TEM propagation and had to display a consistent characteristic impedance along its length. Before a TLM analysis of a cavity-backed antenna was attempted, a thorough TLM analysis was made of the coaxial line model to be used with the antenna.

A coaxial line was modeled in the TLM cartesian mesh. The coax was terminated into continuation boundaries [4] at both ends of the line, simulating an infinitely long coaxial line. A TEM mode was excited at the first node of the model and the magnitude of the radial component of **E** was observed along the line. It was evident from the results of this simulation that the TEM mode of propagation becomes dominant within five nodes away from the excitation point, and it continues uninterrupted along the length of the line. Thus, it was demonstrated that the coaxial line model would support the TEM mode of propagation.

The characteristic impedance of the coaxial line model was calculated at several points along the length of the line. Because all field components were available at each point inside of the coaxial line model, the relationships

$$I = \int \mathbf{H} \cdot d\mathbf{l} \tag{1}$$

$$V = -\int \mathbf{E} \cdot d\mathbf{l} \tag{2}$$

$$Z = \frac{V}{I} \tag{3}$$

were used to find the characteristic impedance of the coaxial line. The characteristic impedance, Z, was found to be consistent along the length of the line and was in good agreement with values predicted using exact equations.

Cavity-Backed Aperture Antenna Model

A TLM model of the cavity-backed aperture and coaxial line was needed to compute the input impedance to the the antenna. The simplest configuration was chosen: a cavity of the type in Figure 1(b), with no ground plane and with aperture dimensions equal to the dimensions of the cavity wall. This is a simple open ended waveguide configuration. This model and its dimensions are shown in Figure 2, with radiation in the x-direction. The coaxial probe is centered inside the cavity.

Dielectric Loading of the Cavity

It was desired that the aperture be one half-wavelength long at some frequency within the range of interest. The aperture in Figure 2 is one half-wavelength long at 9.375 GHz; but, this frequency is also

the cutoff frequency of the cavity's fundamental mode (corresponding to the TE_{10} mode in a waveguide.) This problem was overcome by loading the cavity with a dielectric in order to reduce the wavelength inside of the cavity. Teflon ($\varepsilon_r = 2.1$) was chosen as the dielectric because it can easily be machined to fit inside of a cavity-backed aperture antenna of the type shown in Figure 2. The cutoff frequency of the fundamental (TE_{10}) mode is reduced to 6.5 GHz by loading the cavity with teflon. The cutoff frequency for the next higher (TE_{20}) mode is 12.9 GHz; thus, at 9.375 GHz, the aperture is one half-wavelength long and single-mode propagation exists in the cavity.

A coaxial line model was chosen with an inner conductor diameter of 1 mm and an outer conductor diameter of 6 mm; the dielectric material in the coax is air. One end of the coaxial line was terminated at the antenna and the other end was terminated in a continuation boundary to simulate infinite length or a matched source. The same tests used to verify the validity of the coaxial line model above were repeated for this model. The coaxial line model supported TEM propagation and exhibited a characteristic impedance of 84 ohms.

Analysis of Input Impedance

The input impedance of the antenna model in Figure 2 is found in much the same way as the characteristic impedance of the coaxial line model. Since the TLM method makes all six field quantities available at every node in the modeled mesh, the fields within the coax at the input of the cavity can be used to calculate the input impedance of the cavity-backed aperture antenna.

Using the field quantities at the junction of the coaxial line and the cavity could introduce errors due to fringing effects around the junction. This problem was avoided by calculating the impedance in the coaxial line at a point five nodes below the coax-to-cavity junction. Using the necessary components of **E** and **H** in the coaxial line air gap five nodes below the junction, equations (1) through (3) are applied to yield the impedance of the coaxial line at that point. Since the coaxial line model is ideal, this impedance can be transformed to the load impedance using the following equation:

$$Z_l = Z_o \cdot \frac{(Z_o - Z_x - e^{-2\gamma d}(Z_x + Z_o))}{(Z_x - Z_o - e^{-2\gamma d}(Z_x + Z_o))} \qquad (4)$$

where Z_o is the characteristic impedance of the coaxial line, Z_x is the impedance calculated at a point on the coaxial line, d is the distance from the load (coax-to-cavity junction) to the point where Z_x is calculated, and Z_l is the impedance of the load (the input impedance of the antenna.) The propagation constant $\gamma = j\beta$ (where β is the phase constant) for the lossless coaxial line model.

Analysis of the Antenna Model

The preceding method was used to find the input impedance of the cavity-backed aperture antenna model with a probe diameter of 1 mm.

The probe length was varied from 0.0 mm (no probe in the cavity) to 8.0 mm (probe contacting the upper wall of the cavity) in 0.5 mm increments. For each probe length, an analysis of the input impedance of the antenna was made over a range of frequencies. Some of the data from this analysis is presented in Figure 3 (a-e). Note that for a probe length of 4 mm (Figure 3(c)), the real part of the input impedance at the first resonance (7.9 GHz) is 80 ohms, which is very close to the coaxial line's impedance of 84 ohms. The peak in the magnitude of E_y occurring at 7.9 GHz in Figure 4 (the probe length used in the analysis for Figure 4 was also 4 mm) is attributed to the excellent match between the coaxial line and the input of the antenna at that frequency. A comparison of the data in Figures 4 and 3(c) concludes that the optimum probe length for this antenna when used with 84 ohm coax is approximately 4 mm and the optimum operating frequency is 7.9 GHz.

Figure 5 presents the input impedance as a function of probe length for the cavity-backed aperture antenna at two fixed input frequencies. The frequencies 7.9 GHz (Figure 5(a)) and 13.1 GHz (Figure 5(b)) were chosen because they correspond to the peaks in the magnitude of E_y as shown in Figure 4.

Aperture Distributions

A TLM analysis of the antenna in Figure 2 was made in order to determine the E-field and H-field distributions across the aperture. The probe was extended 4 mm into the cavity (probe length = 4 mm) and its diameter was 1 mm, the same diameter as the coaxial line's inner conductor. The antenna was excited by forcing a TEM mode on the coaxial line at its continuation boundary termination. The magnitude of E_y was observed at a point located 0.5 mm outside of the aperture center. Figure 4 shows a plot of the magnitude of E_y versus input frequency obtained from this analysis. Plots of the aperture distribution of the antenna model excited at 7.9 GHz are shown in Figure 6. The probe length was maintained at 4 mm and propagation is in the x- direction. The distributions shown are only for one half of the aperture; in order to conserve computer resources, a magnetic symmetry boundary (ρ = 1.0) was placed through the center of the antenna and a TLM analysis was performed on one half of the antenna. The symmetry boundary occurs at node number 1 in Figure 6; thus, the plots begin at the center of the aperture and extend to one side (z = 0 in Figure 2). Figure 6(b) is in very good agreement with data published by Adams [2].

Aperture Admittance

An important parameter of the cavity-backed aperture antenna is the slot admittance. Because the TLM method provides all six field components for each point in its mesh, the method can be used to calculate slot admittances. The power flowing through the slot and the voltage across the slot are easily calculated using the TLM method. The power flow definition of admittance is then applied to the TLM-generated results to compute the slot admittance. This procedure can be applied to apertures of other geometries, e.g. irises in waveguides, capacitive and inductive waveguide junctions, and diaphragms in waveguides.

A simple aperture geometry that is readily analyzed using the TLM method is that of a waveguide cross-section. The power flow through the cross-section of a 3.5 x 2.5 cm waveguide was calculated with TLM. Figure 7 presents a comparison of TLM- generated power flow data with data calculated using exact equations; good agreement between exact and calculated data is exhibited over a broad range of frequencies. The power flow data obtained in this analysis can be used to calculate the admittance (impedance) of the waveguide. This example provides a foundation for computing the aperture admittance of more complicated radiating structures such as the cavity-backed aperture antenna considered above.

Conclusion

The TLM method has been used to investigate the behavior of a cavity-backed aperture antenna. It was shown that the TLM method can accurately model a coaxial transmission line and calculate its characteristic impedance. The same method used for calculating the characteristic impedance of a coaxial line is used to calculate the input impedance of a cavity-backed aperture antenna with several input probe lengths. Aperture distributions are also calculated for the antenna using TLM.

REFERENCES

[1] J. Galejs, "Admittance of a Rectangular Slot Which Is Backed by a Rectangular Cavity," IEEE Trans. Antennas Propagat., vol. AP-11, pp. 119-126, March 1963.

[2] A.T. Adams, "Flush Mounted Rectangular Cavity Slot Antennas-Theory and Design," IEEE Trans. Antennas Propagat., vol. AP-15, pp. 342-351, May 1967.

[3] S.A. Long, "Experimental Study of the Impedance of Cavity- Backed Slot Antennas," IEEE Trans. Antennas Propagat., vol. AP-23, pp. 1-7, Jan. 1975.

[4] F.J. German, G.K. Gothard, L.S. Riggs, and P. Goggans, "The Calculation of Radar Cross Section (RCS) Using the TLM Method," to be published in International Journal of Numerical Modelling: Electronic Networks, Devices, and Fields, vol. 2, no. 4, 1990.

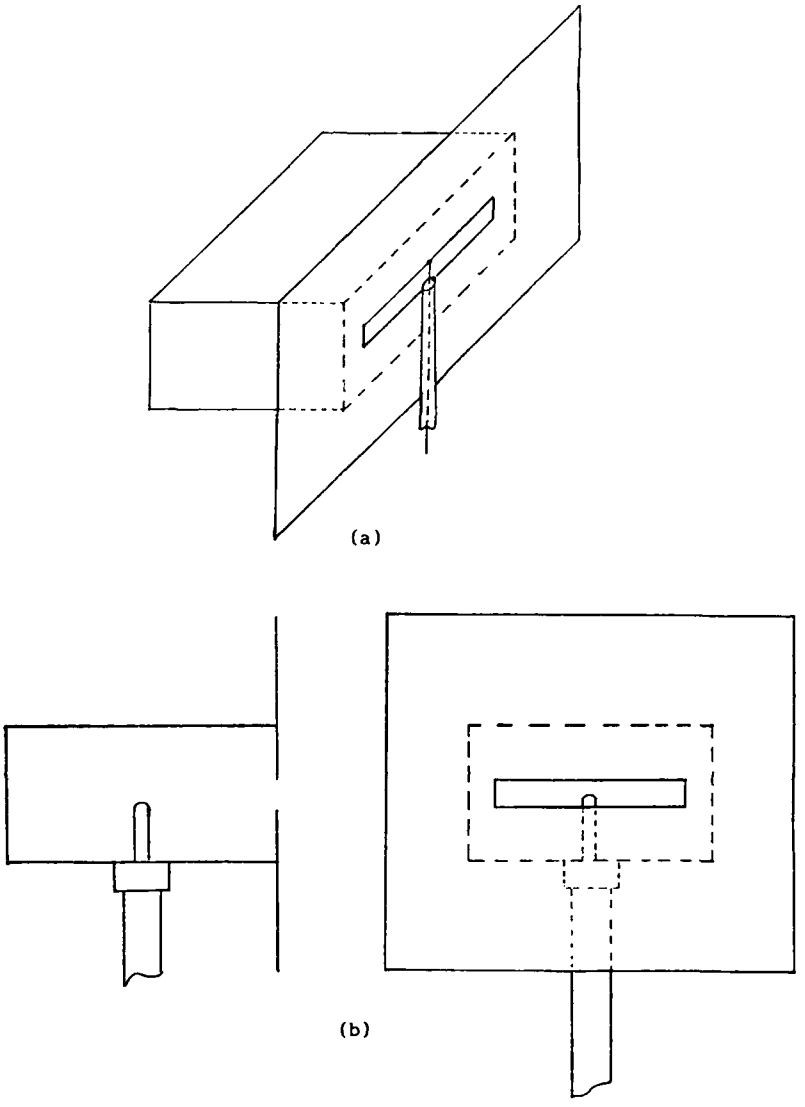

Figure 1: Typical cavity backed aperture antenna geometries. (a): Cavity-backed aperture antenna excited at the slot with a coaxial line. (b): Cavity-backed aperture antenna excited by a coaxial probe in the cavity.

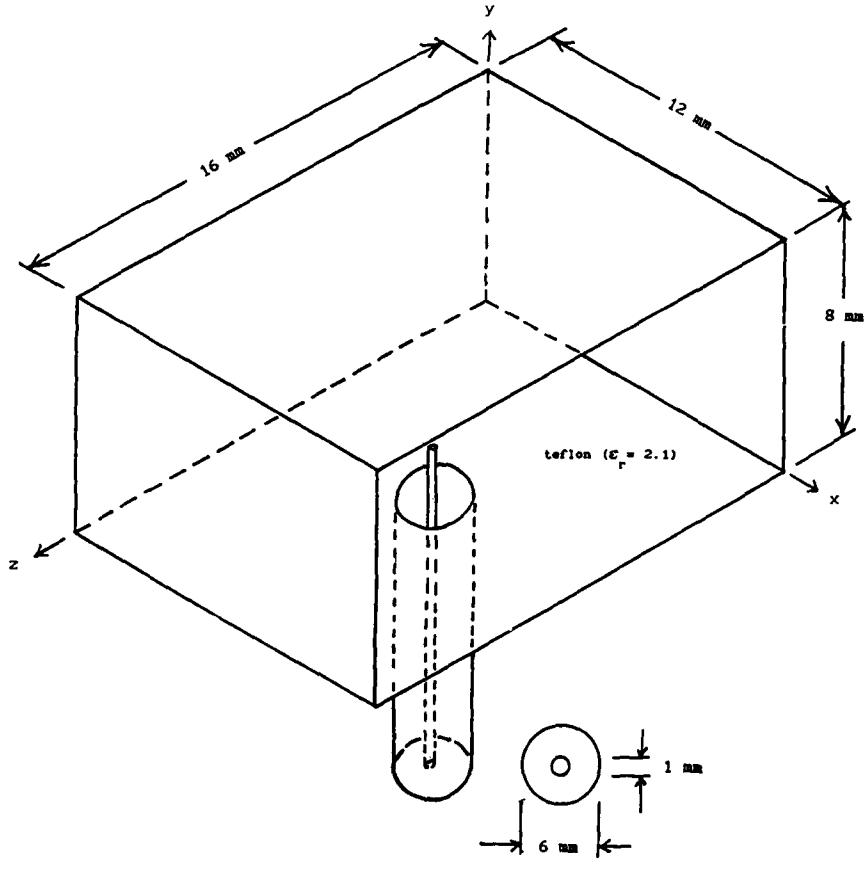

Figure 2: Geometry of the teflon-filled rectangular cavity-backed aperture antenna. The antenna is fed by a coaxial transmission line with a characteristic impedance of 84 ohms. Radiation is in the x- direction.

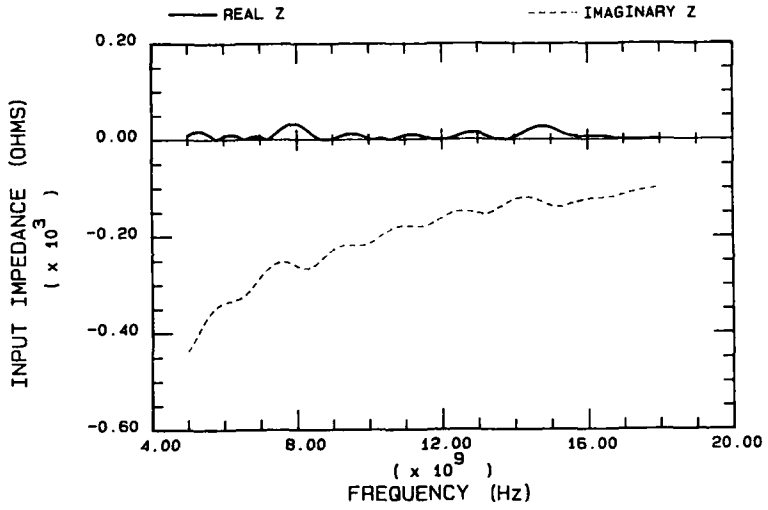

(a): Probe length = 0.0 mm (no probe in the cavity.)

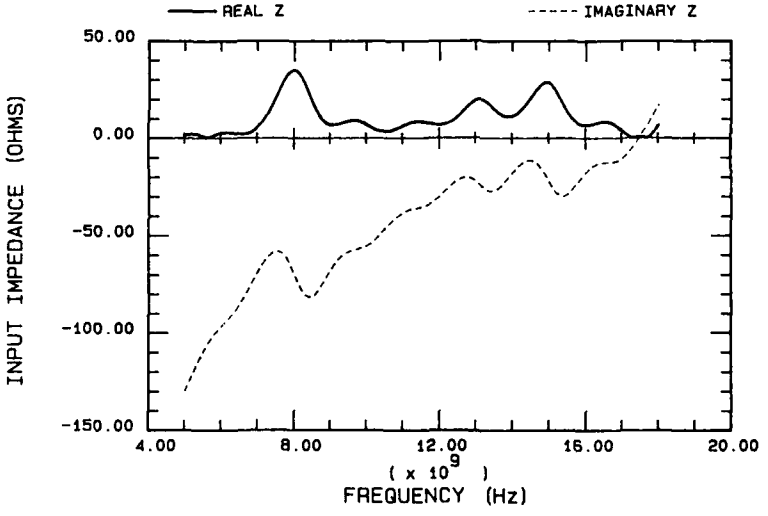

(b): Probe length = 2.0 mm.

Figure 3: Input impedance of the teflon-filled cavity-backed aperture antenna (see Figure 2) at various probe lengths.

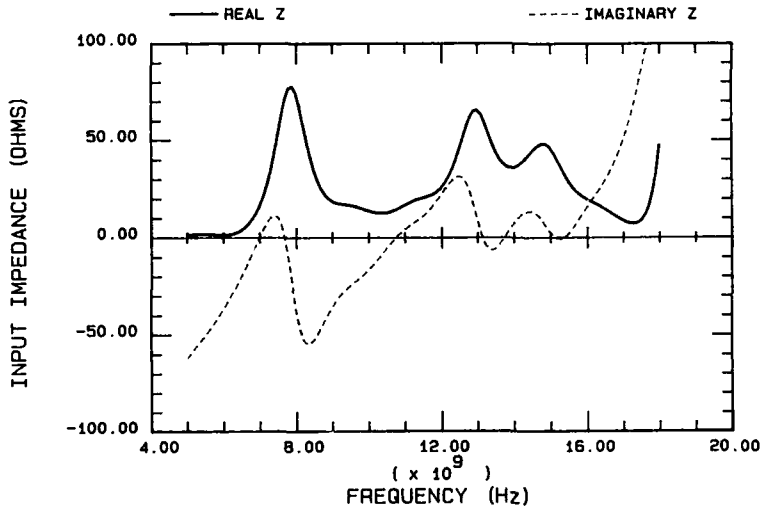

(c): Probe length = 4.0 mm.

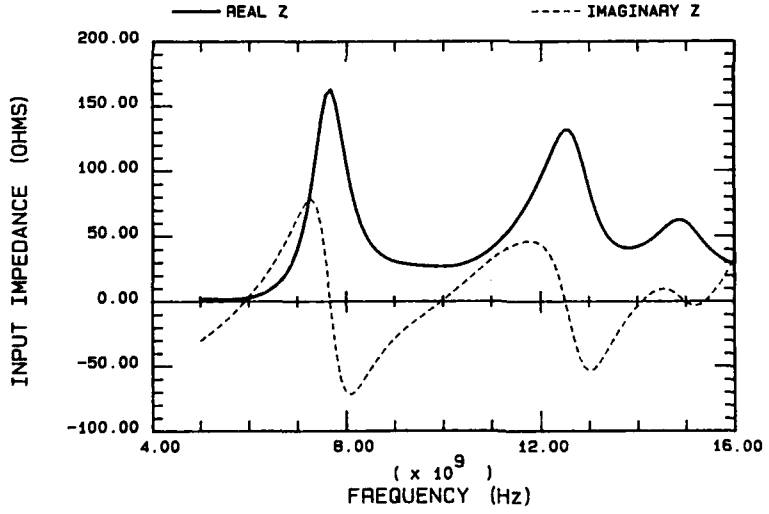

(d): Probe length = 6.0 mm.

Figure 3: Input impedance of the teflon-filled cavity-backed aperture antenna (see Figure 2) at various probe lengths.

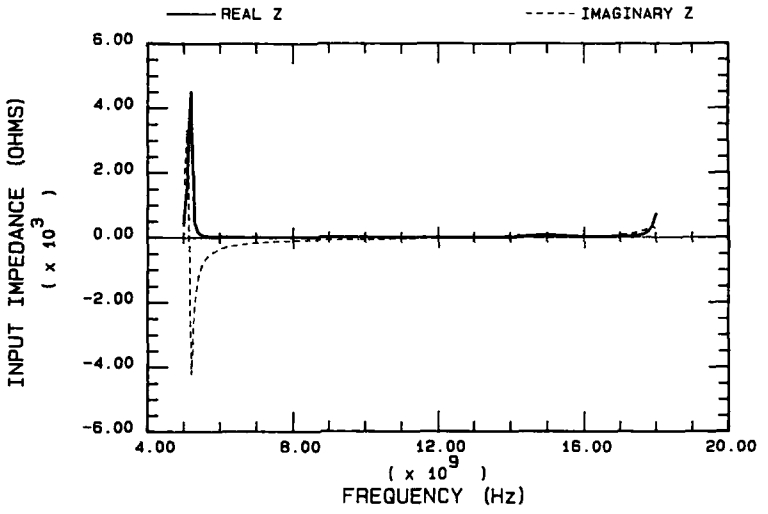

(e): Probe length = 8.0 mm. (Probe touching upper wall of cavity)

Figure 3: Input impedance of the teflon-filled cavity-backed aperture antenna (see Figure 2) at various probe lengths.

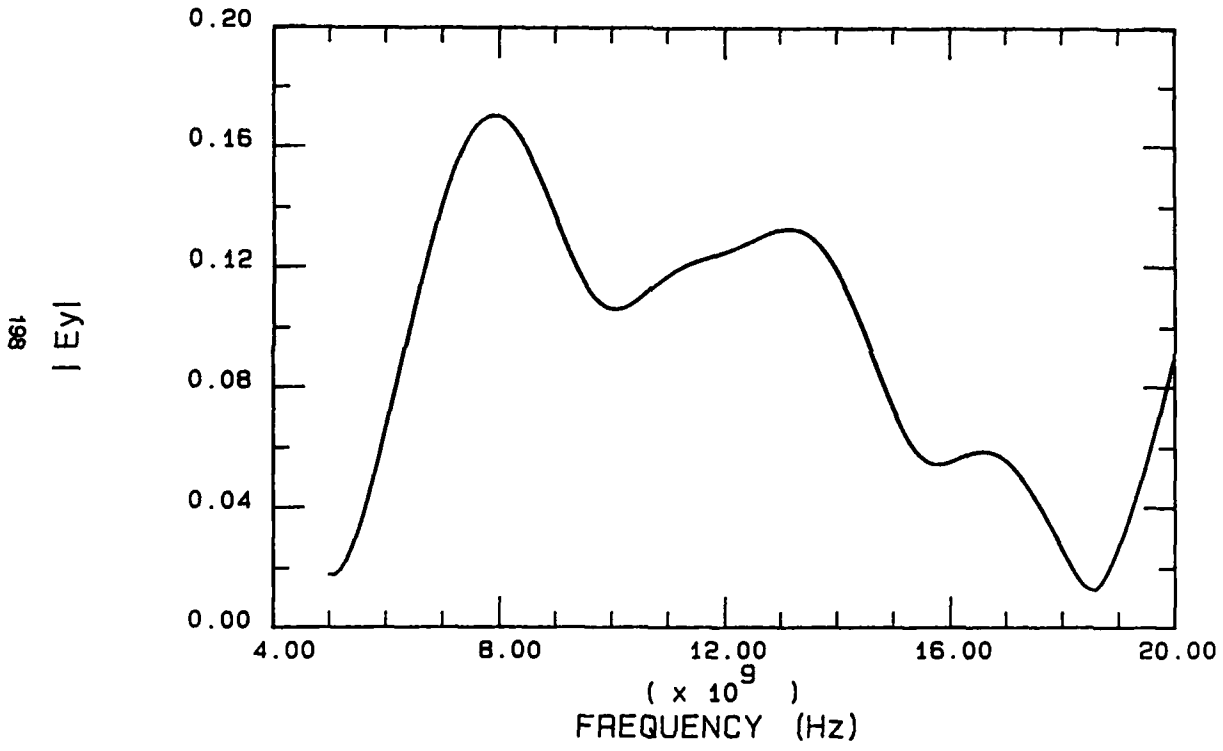

Figure 4: *Magnitude of Ey at a point* 0.5 mm outside of the aperture center. A probe length of 4 mm was used for this case.

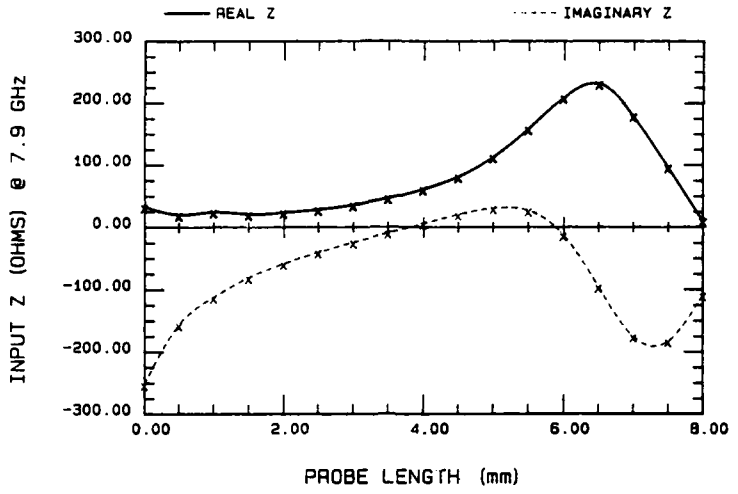

(a)

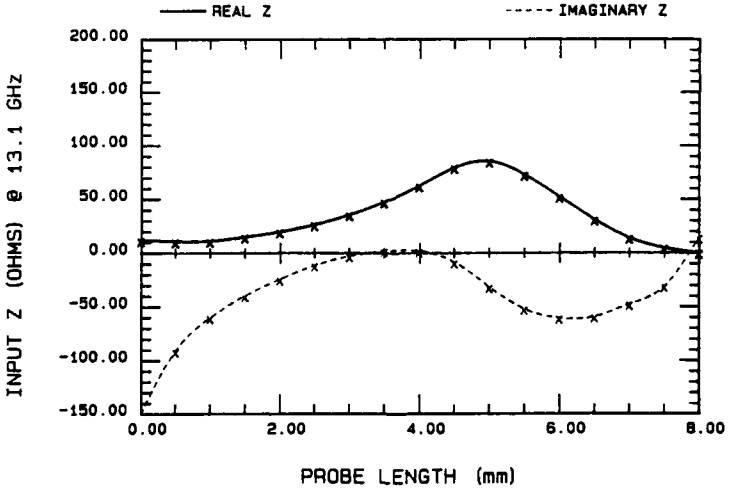

(b)

Figure 5: Input impedance versus probe length for the teflon-filled cavity-backed aperture antenna of Figure 23. (a): Antenna excited at 7.9 GHz. (b): Antenna excited at 13.1 GHz.

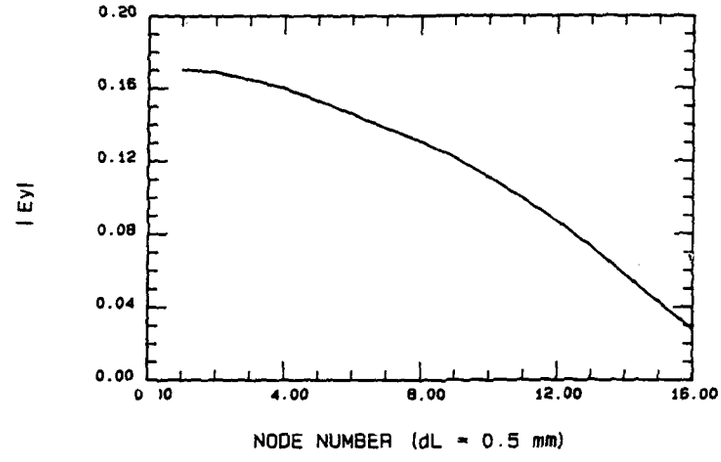

(a)

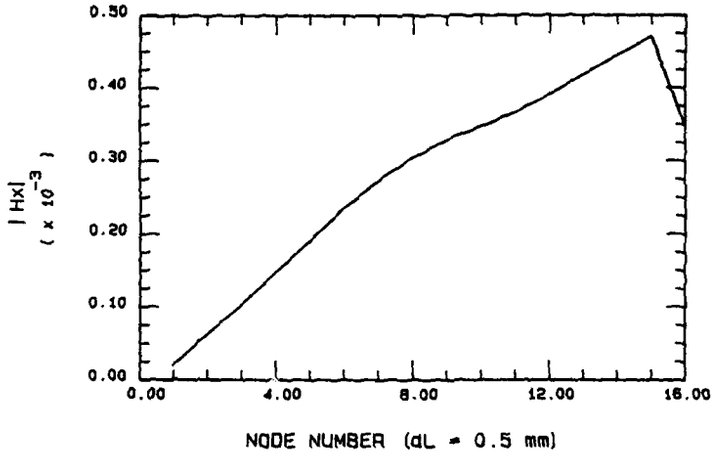

(b)

Figure 6: Aperture distribution for the antenna of Figure 2 excited at 7.9 GHz. (a): Magnitude of Ey extending from the center of the aperture to the right aperture boundary. (b): Magnitude of H in the direction of radiation, also extending from the center of the aperture to the right aperture boundary. There is a magnetic (ρ = 1.0) symmetry boundary at node number 1.

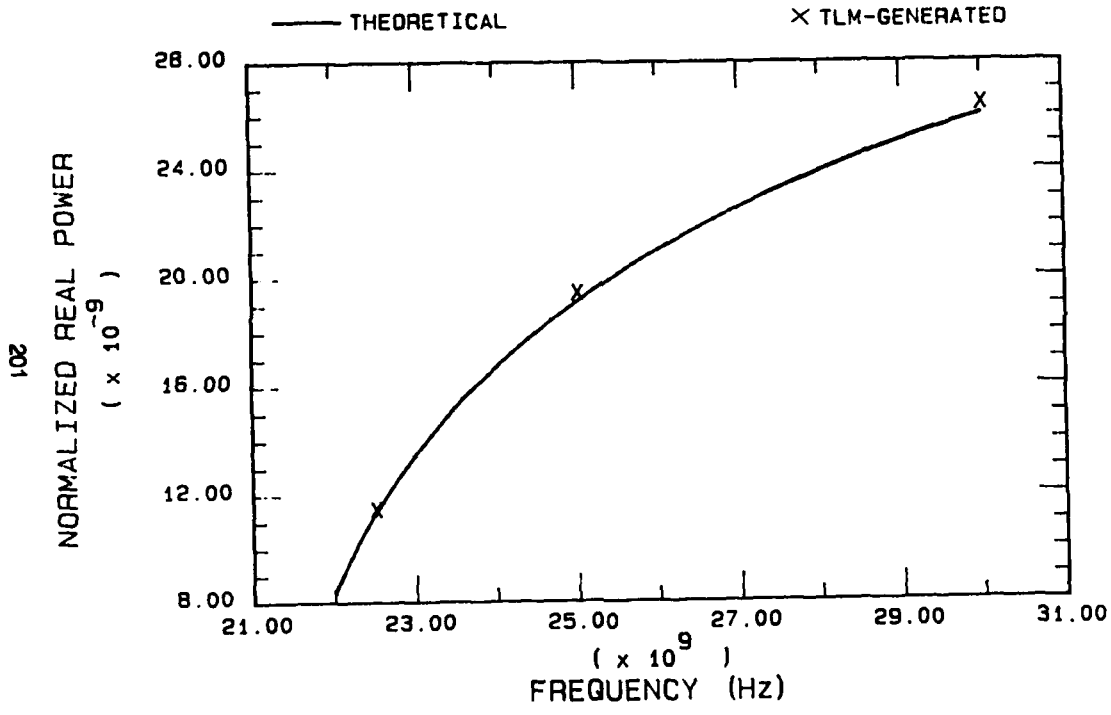

Figure 7: Comparison of TLM- generated power flow through a waveguide cross-section and data from exact equations. Data is generated for a 3.5 x 2.5 cm waveguide.

A Comparison of C and FORTRAN Languages Applied to a Time Domain Finite Difference Application

Robert J. Balestri
Booz·Allen & Hamilton Inc.
4330 East West Highway
Bethesda, MD 20814

INTRODUCTION

With the maturing of the C programming language and the emphasis placed on C in academia, the question of its merits relative to FORTRAN for scientific applications naturally arises. Other languages, such as PL1, APL, Algol and Pascal, have received similar attention over the years only to vanish into specialized applications if they survive at all. The best known scientific applications of C are for graphics processes and the Mathematica™ code. There is a natural curiosity to determine if C offers any clear advantages over FORTRAN that justify the effort required to learn the language. Learning a new programming language is often as difficult as learning a new spoken language and significant benefits are required to justify the expenditure of the required effort.

It seems to this author that "language bashing" and "language zealotry" have become a major activity in scientific and engineering circles. Indeed, it is this author's personal experience that a lot of people seem to spend more time extolling the merits of a particular programming language or word processor than the merits of the programs or words being processed.

Among the latest arrivals in the area of programming languages is C, developed during the early 70's by Dennis Ritchie of Bell Laboratories as the system language for UNIX. Benefits ascribed to C include transportability, modularity and host machine interfaces allowing access to operating system functions for the program. Generally, topics such as speed, maintenance of arithmetic precision, code size and the overhead associated with function calls are not addressed. These issues are extremely important to electromagnetics modeling.

The objective of this paper is to address these issues in a manner pertinent to computational electromagnetics. A two dimensional time domain finite difference (TDFD) application was chosen for three reasons. First, TDFD codes are computationally intensive with operations that can be severally affected by round off error. Second, TDFD algorithms can be highly modular using matrix operations supporting the use of separate functions to perform many operations. Third, since the time evolution of the field is usually desired, TDFD naturally leads to intensive output of intermediate results.

This paper will compare the performance of the Microsoft 5.0 and WATCOM 7.0 C compilers with that of the Microsoft 4.2 and Ryan-McFarland 2.42 FORTRAN compilers for AT class PCs. Comparisons include code size, I/O time requirements, execution speed and round off errors. Some general observations on the requirements to implement/learn C will be discussed as well as transportability issues.

The Electromagnetic TDFD Problem

The problem chosen to benchmark the languages, code architecture and machines is that presented in Figure 1 which is modeled after Figure 2 of Yee[1] for a TM wave impinging on a perfectly conducting square. For TM waves, the equations for the electric and magnetic field corresponding to Yee's equations (14a-14c) are:

$$E_z^{n+1}(i,j) = E_z^n(i,j) + Z\frac{\delta\tau}{\delta x}\left[H_y^{n+\frac{1}{2}}(i+\tfrac{1}{2},j) - H_y^{n+\frac{1}{2}}(i-\tfrac{1}{2},j)\right] - Z\frac{\delta\tau}{\delta x}\left[H_y^{n+\frac{1}{2}}(i,j+\tfrac{1}{2}) - H_y^{n+\frac{1}{2}}(i,j-\tfrac{1}{2})\right] \quad (1)$$

$$H_x^{n+\frac{1}{2}}(i,j+\tfrac{1}{2}) = H_x^{n-\frac{1}{2}}(i,j+\tfrac{1}{2}) - \frac{1}{Z}\frac{\delta\tau}{\delta y}\left[E_z^n(i,j+1) - E_z^n(i,j)\right] \quad (2)$$

$$H_y^{n+\frac{1}{2}}(i+\tfrac{1}{2},j) = H_y^{n-\frac{1}{2}}(i+\tfrac{1}{2},j) - \frac{1}{Z}\frac{\delta\tau}{\delta x}\left[E_z^n(i+1,j) - E_z^n(i,j)\right] \quad (3)$$

where (i,j) represent the spatial grid indices of $i\delta x, j\delta y$. The temporal index n represents the time step $n\delta\tau$. The magnetic field space/time grid is offset by ½ grid increment from the electric field grid. Z is the impedance of the media, taken here as free space.

Computational Approaches

There are several approaches to solving equation 1-3. The code developed is not intended to be optimal, but rather to exercise certain features of codes. The E-field and H-field arrays

---

[1] Kane S. Yee, "Numerical Solution of Initial Boundary Value Problems Involving Maxwell's Equations in Isotropic Media," IEEE Trans. Antennas and Propagation, vol AP-14, pp. 302-307, May 1966.

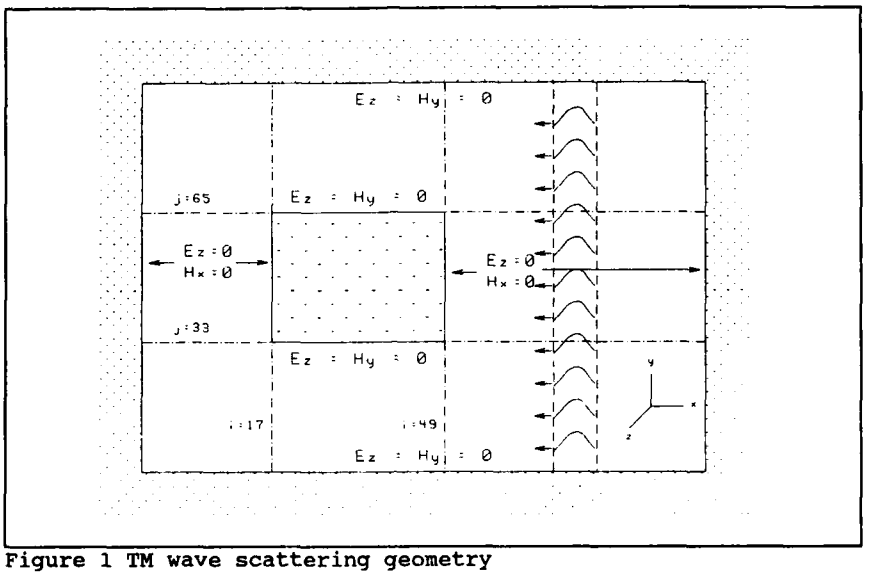

Figure 1 TM wave scattering geometry

are initialized at τ=0 for all space. Then, equations 2 and 3 are use to update the H-field for all space using the lagged values of the E-field. This is followed by using equation 1 to update the E-field for the current time. This procedure is repeated for all times of interest. The E- and H-field components are then each stored in a single array. This necessitates looping over the spatial grid twice for each time step. Alternatively, two arrays may be used for the field values, one corresponding to the previous time step and the other to the current times step. This method employs only a single loop over the spatial grid for each time step. The operations count is the same for each approach but the time required will be compiler dependent due to optimization procedures. For this study, the dual array method was chosen to exercise conditional branching within the innermost loop.

Boundary conditions can be included by checking array indices to determine the proper condition for each cell at each time step. An alternative is to perform the field updates only in the region where propagation takes place and setting the boundary values to the value initially and using these values for each time step. Finally, a third approach is to define a boundary condition array corresponding to each element of the field arrays and multiply equations 1-3 by the boundary condition value during field updates. This is the procedure chosen here in order to make the computations vector process oriented. The boundary condition array operating

on equations 1-3 can be viewed as an inner product of a column of the boundary condition array with the column of the fields arrays.

For both C and FORTRAN, two code structures were used to implement the functions required. Version 1 corresponds to a single in-line module for the entire process. That is, no subroutines or functions were used. Version 2 of each code segmented the process into functional procedures with the subsequent calls from the main procedure. For each structure, field output was omitted to determine the impact of I/O on run times for the FORTRAN and C versions of the code. Listings of the In-Line and Modular FORTRAN and C codes are contained in Appendices A and B respectively.

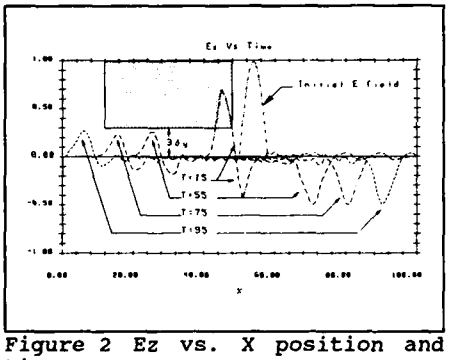

Figure 2 Ez vs. X position and time

RESULTS

Typical output is presented in Figure 2 for the z component of the electric field at 3 increments below the obstacle for several time steps. These results agree with [1].

Comparison are presented in Table 1 for each code and I/O configuration on two different computers. The consistent result is that modularization increases the execution time by 25-30% independent of the language or compiler. This is not particularly surprising when one considers the overhead associated with setting up and executing subroutine or function calls.

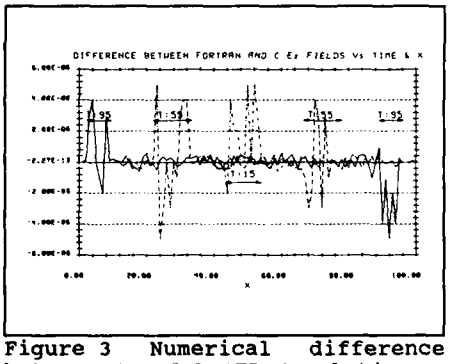

Figure 3 Numerical difference between C and FORTRAN solution

Based on this example, it is can be stated that FORTRAN executed at least as fast or faster than C. While this may appeal to FORTRAN defenders, it is somewhat misleading. There is only a 7-8% difference between the minimum FORTRAN and maximum C execution time for any case. Extrapolating such differences to other problems and computers is probably unwarranted.

All four of these compilers utilize the math co-processor for

floating point operations. There were no significant differences in the numerical precision of the results. The difference between the C and FORTRAN solutions are shown in Figure 3.

The most meaningful differences are in the size of the code generated for each case. These differences are summarized in Table 2 where the code size, less the array storage requirements, for the configurations is presented. It is clear that FORTRAN produces consistently larger code the does C. This is most likely due to the libraries used by the compilers. FORTRAN libraries, especially for I/O, are much more generalized than C libraries. Watcom's C compiler produced significantly smaller code than did the Microsoft C compiler.

	Compaq Portable II @ 8 Mhz				Compaq Portable III @ 12 Mhz (Ram Disk I/O)			
	MSF	RMF	MSC	WCC	MSF	RMF	MSC	WCC
In-Line_WIO	465	446	463	472	333 (326)	321 (316)	329 (319)	341 (329)
In-Line_NIO	427	412	427	433	310 (311)	301 (300)	310 (310)	315 (315)
In-Line I/O Cost	38 9%	34 8%	36 8%	39 9%	23 (16)	20 (16)	19 (19)	16 (14)
Modular_WIO	621	633	673	642	447 (438)	453 (444)	480 (470)	458 (448)
Modular_NIO	587	587	637	597	429 (429)	428 (428)	461 (461)	433 (434)
Modular I/O Cost	34 6%	46 8%	36 6%	45 7%	18 (9)	25 (16)	19 (9)	25 (14)
In-Line/ Modular_WIO	.75	.70	.68	.74	.74	.71	.69	.74
In-Line/ Modular_NIO	.73	.70	.67	.73	.72	.70	.67	.73

MSF - Microsoft FORTRAN Ver 4.2 MSC - Microsoft C Ver 5.0
RMF - RyanMcFarland FORTRAN Ver 2.42 WCC - Watcom C Ver 7.0
_WIO - With I/O _NIO - Without I/O
Note: All times in seconds

able 1 Execution time comparisons

Language	FORTRAN				C			
Vendor	Microsoft		Ryan McFarland		Microsoft		Watcom	
Case	WIO	NIO	WIO	NIO	WIO	NIO	WIO	NIO
In-Line	32191	27215	35721	31989	25683	22469	17821	15113
Modular	36037	35119	40397	39359	26921	26575	18881	18639

WIO - With I/O
NIO - Without I/O

Table 2 Executable code size in bytes for different cases

CONCLUSIONS

While C is designed to construct modular code, results presented in Table 1 indicate that the relative price for implementing this modularity is somewhat higher in C than FORTRAN. However, if code size is important, C clearly produces tighter executable code. The relative value of this is up to the user.

It is clear to this author that it is easier to accomplish many things in C than the comparable function using FORTRAN. However, the system interfaces and graphic capabilities of C reside in the libraries and these libraries and their interfaces are compiler, vendor and version dependent as well as machine dependent. In the case of Microsoft, these C libraries are accessible to the FORTRAN user.

C requires a much higher level of discipline on the part of the programmer. There are simply too many ways of achieving identical results in C. The determined coder can make much more difficult code in C than in FORTRAN. In summary, C and FORTRAN are very comparable. For the FORTRAN programmer, the extensive variable and function declarations required by C will be a strong impediment to using the language. On the other hand, access to the system functions, dynamic storage allocation, and a relatively standard graphic library are good reasons to consider learning the language. The C compilers used here clearly generate efficient executing code and they both processed the same source code. This was also the case for the FORTRAN compilers.

ANALYSIS OF WAVEGUIDE-FED THICK-WALLED SLOT RADIATOR WITH PARASITIC WIRES

Sembiam Rengarajan, Andrew Potter *, Wing Li **
Department of Electrical and Computer Engineering
California State University
Northridge, Ca. 91330

* Hughes Aircraft Company
Space and Communications Group
El Segundo, Ca. 90009

**Hughes Aircraft Company
Radar Systems Group
El Segundo, Ca. 90009

INTRODUCTION

Clavin developed an antenna consisting of a waveguide fed slot with two parasitic monopole elements which resulted in equal E and H plane patterns [1]. This element was analyzed previously using approximate distributions for the E field in the slot and the monopole currents [2]. A major weakness of this approach was that it could not predict the resonant characteristics accurately. A study of an array of Clavin elements showed that they exhibited less mutual coupling than a similar array of slots [3]. A recent investigation of such an array showed scan-independent performance [4]. There is a need to determine the scattering characteristics of this element based on an accurate theoretical model for antenna applications. This paper fills such a need.

METHOD OF ANALYSIS

Figure 1 shows the geometry of the problem under discussion. A square ended slot of a width a and length 2b is cut in a broad wall of a rectangular waveguide with wall thickness t. The slot is offset from the center of the guide by a distance x_o. Two monopoles of height h are placed symmetrically about the center of the slot. The monopoles are separated by a distance 2d. It is assumed that the broad wall containing the slot and monopoles extends to an infinite perfectly conducting ground plane.

By using Schelkunoff's equivalence principle, the domain of this problem is divided into three regions; the waveguide interior, the external half space containing the two monopoles, and a cavity region to account for wall thickness. For the purpose of solving

SESSION 5A - "WAVEGUIDES AND MICROWAVE CIRCUITS"

the problem in each of these regions infinitely thin perfectly conducting sheets are placed in each slot aperture and equivalent magnetic currents which are surrogates to aperture electric fields are placed on the conducting sheets.

For narrow slots, longitudinal components of the aperture E fields can be ignored. In the exterior half space, in addition, the wires are replaced by equivalent electric currents induced on them. The transverse distribution of the slot E field has been assumed constant. This excites the monopoles with an odd symmetry. The waveguide interior is excited by a TE_{10} mode source. By enforcing the continuity of longitudinal component of the magnetic fields across the slot apertures and by equating the total tangential E along the monopoles to zero, we obtain three coupled integro-differential equations given below.

$$-H_z^{int} + H_{z1}^{cav} = H_z^{inc} \qquad (1)$$

$$H_{z2}^{cav} - H_z^{ext} - H_z^{m1} - H_z^{m2} = 0 \qquad (2)$$

$$E_{ys} + E_y^{m1} + E_y^{m2} = 0 \qquad (3)$$

Since the monopole currents exhibit odd symmetry, it is sufficient to satisfy the boundary conditions on one of them. Expressions for H_z^{int}, H_{z1}^{cav}, H_z^{inc}, H_{z2}^{cav}, and H_z^{ext} appear in the literature [5,6]. The remaining fields can be obtained from the vector potentials for the corresponding electric or magnetic equivalent currents.

The integral equations have been solved by the method of moments. The slot aperture E field has been expanded in terms of entire domain sinusoidal functions longitudinally with uniform transverse variations. Monopole currents have been expressed in terms of a set of pulse functions. In equations (1) and (2), testing functions exhibiting sinusoidal longitudinal variations with a Dirac type delta function at the transverse center have been chosen.This has been possible because of a Hallen type formulation employed in equation (3). A Pocklington type formulation would have resulted in a numerical triple integration in place of a double integration. A point matching scheme at centers of all sub-domains and the edge point of the monopole has been employed in equation (3). The mathematical formulation and the numerical technique employed in this work assure that no more than numerical double integrals are required to be performed. The resulting matrix equations can be expressed in the form:

$$\begin{bmatrix} [Z'_{11}] & [Z'_{12}] & [0] \\ [Z'_{21}] & [Z'_{22}] & [Z_{12}] \\ [0] & [Z_{21}] & [Z_{22}] \end{bmatrix} \begin{bmatrix} \underline{\beta}_j \\ \underline{\beta}'_j \\ \underline{\alpha}_k \\ B \end{bmatrix} = \begin{bmatrix} \underline{\gamma}_i \\ \underline{0} \\ \underline{0} \end{bmatrix}$$

Here $\underline{\beta}_j$ and $\underline{\beta}'_j$ are the column sub-matrices containing the coefficients of expansion for the slot E field, $\underline{\alpha}_k$ are the coefficients of expansion for the monopole currents and B is the even constant arising from Hallen's formulation. The $\underline{\gamma}_i$ are the excitation terms. The "self" terms for the slot and monopoles are shown by dashed lines. These parts of the moment method matrix have been validated by comparing the results obtained from our "self" matrices for an isolated slot or a pair of dipoles to similar results previously published in the literature.

The slot self terms are obtained for a special case of the compound slot terms, i.e. when the tilt angle is 0^o [5]. Typical matrix elements for the remaining sub-matrices are:

$$[Z_{12}]_{mn} =$$

$$+\frac{d}{2\pi}\int_{-b}^{b}\int_{-yn-\delta y/2}^{-yn+\delta y/2}\left(\frac{e^{jk_0(d^2+y'^2+z'^2)^{1/2}}}{(d^2+y'^2+z'^2)}\left(jk_0+\frac{1}{(d^2+y'^2+z'^2)^{1/2}}\right)\sin\left[\frac{m\pi(z'+b)}{2b}\right]\right)dy'dz'$$

$$[Z_{21}]_{mn}=$$

$$\frac{j}{c}\int_0^{y_m}\int_{-b}^{b}\int_{-a/2}^{a/2}\sin\left[\frac{n\pi(z'+b)}{2b}\right](x'+d)\left(jk+\frac{1}{[(x'+d)^2+y^2+z^2]^{1/2}}\right)\times$$

$$\frac{e^{jk_0[(x'+d)^2+y^2+z^2]^{1/2}}}{[(x'+d)^2+y^2+z^2]}\sin[k_0(y_m-y')]\,dx'dz'dy'$$

$$[Z_{22}]_{mn}=$$

$$\int_{y_m-\delta y/2}^{y_m+\delta y/2}\left\{\frac{e^{-jk_0[r_m^2+(y_m-y')^2]^{1/2}}}{[r_m^2+(y_m-y')^2]^{1/2}}-\frac{e^{-jk_0[(2d)^2+(y_m-y')^2]^{1/2}}}{[(2d)^2+(y_m-y')^2]^{1/2}}\right\}dy'$$

$$+\int_{-y_m-\delta y/2}^{-y_m+\delta y/2}\left\{\frac{e^{-jk_0[r_m^2+(y_m-y')^2]^{1/2}}}{[r_m^2+(y_m-y')^2]^{1/2}}-\frac{e^{-jk_0[(2d)^2+(y_m-y')^2]^{1/2}}}{[(2d)^2+(y_m-y')^2]^{1/2}}\right\}dy'$$

NUMERICAL RESULTS AND DISCUSSION

Figure 2 shows a typical plot of the monopole current distribution with a comparison to the sinusoidal distribution which has been the approximation employed in previous works [1,2,3]. The slot electric field distribution is nearly a half sinusoid characterized by a dominant contribution by the first expansion mode. In reduced height guide for large offsets the slot field can deviate substantially from such a behavior even at resonance as observed in [6]. Figure 3 shows far field E and H plane patterns. These two patterns are nearly equal over a substantial angular region. The dimensions are optimum as given in [1,2] and the patterns are in good agreement with those in [2]. Figure 4 shows the behavior

of normalized slot resonant length as a function of offset. The resonant length increases with offset. The effect of monopoles is to increase the resonant length. Figure 5 shows the resonant conductance of the slot which is found to increase with offset. Conductance increases when monopoles are introduced and it is greater in reduced height waveguides.

CONCLUSION

This paper has presented results on scattering characteristics of a Clavin element, containing a longitudinal broad wall slot and two parasitic monopole elements. Coupled integral equations have been formulated and solved by the method of moments. The results presented in this paper should find applications in the design of arrays of Clavin elements.

REFERENCES

[1] A. Clavin, D.A. Huebner, F.J. Kilburg, " An improved Element for Use in Array Antennas," IEEETrans. Antennas Propagat., Vol. AP-22,no. 4, pp. 521-526, July, 1974.

[2] A. B. Papierez, S. M. Sanzgire and S. R. Laxpati,"Analysis of antenna structure with equal E and H plane patterns," IEE, Vol. 124, no. 1, pp 25-30, Jan., 1977

[3] R. Elliott,"On the mutual admittance between Clavin elements," IEEE Trans. Antennas Propagat.,Vol. AP-28,no. 6, pp 864-870, Nov., 1980

[4] K. T. Ng and B.A. Munk,"Scan Independent Slot Arrays With Parasitic Wire Arrays in Stratified Medium.", IEEE Trans. antennas Propagat., Vol. AP-36, no.4, pp. 483-495, Apr. 1988.

[5] S. Rengarajan, " Compound radiating slots in a broad wall of a rectangular waveguide", IEEE Transactions on Antennas and Propagation, Vol. AP-37, no.9, pp. 1116-1123, Sept. 1989.

[6] G. Stern and R.Elliott,"Resonant length of longitudinal slots and validity of circuit representation: theory and experiment," IEEE Trans. on Antennas and Propagat., Vol. AP-33,no. 11,pp. 1264-1271, Nov., 1985

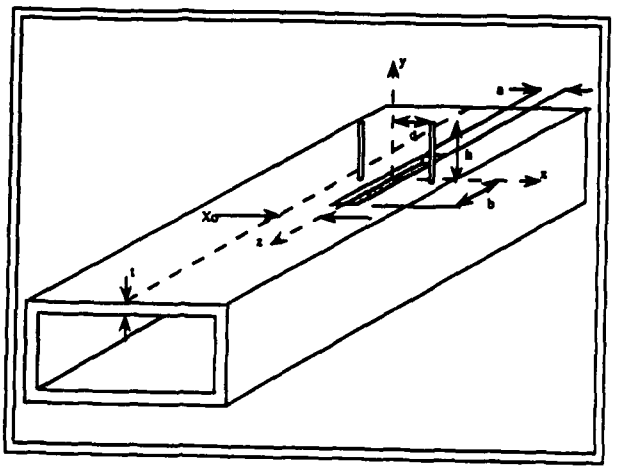

Figure 1
Waveguide With Slot and Monopoles

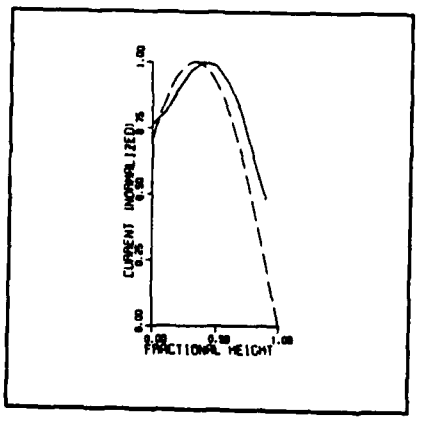

Figure 2
Typical Monopole Current (————)
Sinusoidal Current (_ _ _)

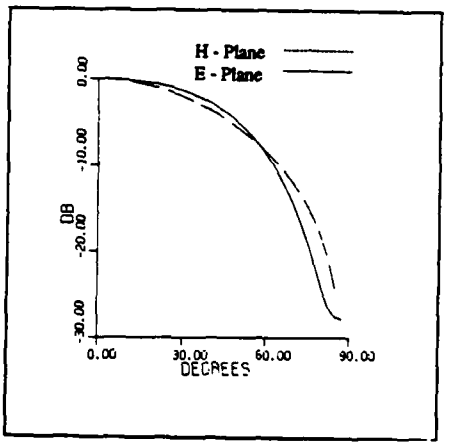

Figure 3
Far Field Pattern

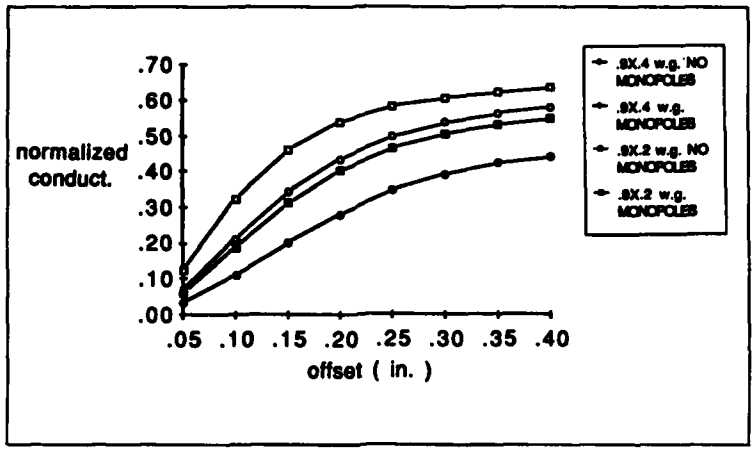

Figure 5
Normalized Resonant Slot Conductance

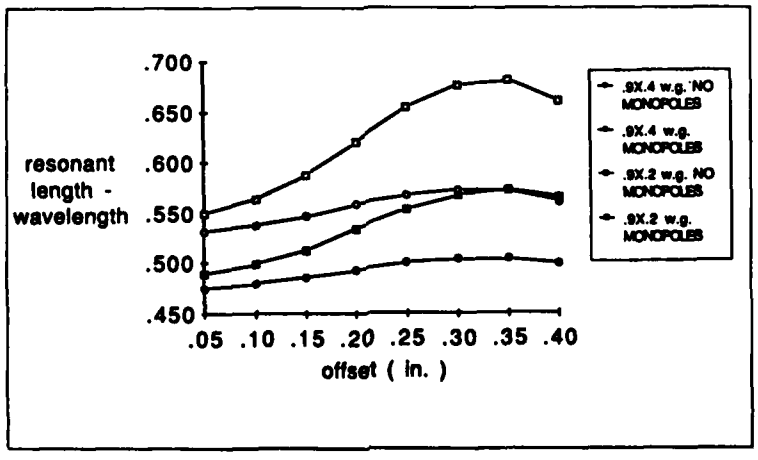

Figure 4
Normalized Resonant Length vs. Offset

SESSION 5B - "EMI/EMC"

ANALYSIS OF ELECTROMAGNETIC INTERFERENCE EFFECTS IN SPACECRAFT GENERATED BY ELECTROSTATIC DISCHARGES USING THE METHOD OF MOMENT

Reinaldo Perez
Jet Propulsion Laboratory
California Institute of Technology

ABSTRACT

Electromagnetic computer codes based on the Method of Moment can be used as tools for analyzing spacecraft electromagnetic interference effects resulting from environmentally generated Electrostatic Discharges (ESD) between solar arrays and spacecraft structure. First an equivalent circuit model is used to calculate the induced transient voltages at several likely locations on the spacecraft. The Method of Moment technique is subsequently employed to model the induced current distribution on the spacecraft structure and calculate the resulting near electric fields. Finally, a method is shown to use the IEMCAP and SEMCAP electromagnetic compatibility analysis programs to perform field-to-wire coupling analyses between the previously calculated fields and spacecraft electronics.

INTRODUCTION

Spacecraft charging immunity has been an important consideration since the early 1970's when it was found that operational anomalies in orbit could be correlated with activity in the energetic plasma environment which spacecraft must survive. Prior to the knowledge of Electrostatic Discharges (ESD) hazards, thermal considerations were the major design factor for the exterior surface configuration of spacecraft. Exterior surfaces like thermal blankets, optical surface reflection, and solar cells comprise most of the exterior material of spacecraft and are made of very good electrical insulators. The differential voltage which builds up between the metal structure of the spacecraft and these dielectric surfaces can cause ESD with subsequent anomalies showing up in the spacecraft's electronics.

Recent data obtained from geosynchronous orbiting satellites has indicated that the surface of these satellites can charge to hundreds (in sunlight) and even thousands of volts (in eclipse). Dense plasma clouds of energetic particles [1] are injected into the region of the geosynchronous altitude during geomagnetic storm

activity. In a staedy state, every insolated part of the spacecraft immersed in this plasma will come into electrical equilibrium by developing surface charges of the proper sign and magnitude such that the net current (deposition and release of charge particles from the surface of the spacecraft) is zero. This equilibrium potential of the surface is the potential difference between the surface and ambient plasma sheath.

It has been known that electron and ion irradiation of insulators can produce accumulation of charges sufficient to cause dielectric breakdown [2]. The problem of spacecraft charging has been associated to space-plasma electrons and ions incident on the dielectric materials used on the exterior of satellites. In Figure 1 an illustration is shown of the electron and ion interactions related to charge build up in insulators. The surface in the plasma becomes negatively charged due to electrons which have a much smaller mass than ions, but have a much greater velocity than ions and impact the surface at a much higher rate.

Energetic electrons and ions incident on the insulator penetrate the surface of the material. Some of the electrons and ions undergo ellastic (coulombic) collisions with the atoms of the material and are "backscattered". The remaining electrons interact inelastically with the orbital electrons of the atoms generating electron-hole pairs by ionization. Some of the electrons produced by ionization escape from the surface of the material as secondary electrons. Both secondary and backscattered electrons reduce the net excess charge that enters the material from from the initial electron flux. The remaining electron-hole pairs act as carriers; producing a region of radiation-induced conductivity in the insulator. The charge accumulated by the insulator can drift under the influence of its own field. If the charge can not drift and removed by an electrode attached to the material, charge build up can occur producing an electric field which, if strong enough, can cause dielectric breakdown.

It has been postulated [3] that the anomalous behavior of geosynchronous spacecraft is due to electrostatic charging of the various spacecraft surfaces to large negative potentials and the subsequent discharging. The electromagnetic pulses produced by the discharges and the induced currents on the spacecraft are large enough that can interact with the electronic logic circuits, and cause voltage and current spikes large enough to change logic states. Several out of a series of Electromagnetic Compatibility (EMC) problems that can arise from ESD are illustrated in Figure 2. The differential charging of the dielectric materials found in thermal blankets and solar arrays, and the subsequent discharging, is one of the major causes of EMC problems in spacecrafts.

In the past lumped-element electric circuit modeling of spacecraft have been used to analyze the ESD effects on several sensitive electronic circuits. The circuit elements consist of resistors, capacitors, inductors, and sources in several

different configurations depending on the type of spacecraft. The analyses have provided results in terms of voltages and currents at certain spacecraft locations but give very little information concerning some basic aspects of EMC such as cable-to-cable, field-to-cable and field-to-antenna coupling.

In this paper a method is proposed to bridge the gap between lumped-element electrical circuit analysis of electrostatic discharges in spacecraft and electromagnetic compatibility. The objective is accomplished by using the Method of Moment technique to calculate the fields produced by ESD-induced transient voltages which may occur ar several locations on the spacecraft. The calculated fields can then be used by EMC programs such as IEMCAP [4] and SEMCAP [5] to perform field-to-wire or field-to-antenna compatibility analyses.

COMMON APPROACHES TO ESD ANALYSIS IN SPACECRAFT

Charging Phase:

In spacecraft the "charging" process of an ESD event can be described by the net flow of all environmental source currents as described in equation 1.

$$\sum J = I_{SPACECRAFT} + \left(J_{PLASMA\ IONS} + J_{PLASMA\ ELECTRONS} + J_{SECONDARY} + J_{BACKSCATTER} + J_{PHOTO-EMISSIONS} \right) AREA \quad (1)$$

The interaction processes of the currents to account for charge build up and static electric fields can be accomplished accurately using the well known NASA Charging Analyzer Program (NASCAP) model [6] which was developed as an engineering tool to determine the environmental effects on spacecraft surfaces and systems.

The work herein described is focused on the charge build up which occurs in the glass-covered surface of solar arrays. Solar arrays often contain the largest area of dielectric material exposed to space plasma. This large build up of electrostatic potential in the solar arrays increases the likelihood of ESD events of several thousands of volts on the spacecraft structure which induces the subsequent anomalies associated with ESD. Though NASCAP can be used to calculate accurately the electrostatic potential accumulated on the surface of solar arrays (and any other dielectric surface), the simple geometry of solar arrays allows the use of approximations to calculate such potential.

Consider the dimensions of the solar arrays for a presently proposed NASA spacecraft where the length and width of each solar array panel is 5.6 x 2.8 meters respectively. If the capacitance of the glass-covered sections of the solar array (excluding the frame) is approximated (worst case) by using a parallel plate capacitor model then:

$$C = \frac{\epsilon_O \cdot \epsilon_R \cdot A}{D} = \frac{(8.85 \times 10^{-12})(3.8)(15.68)}{1.27 \times 10^{-4}} = 4.15 \times 10^{6}\ pF \qquad (2)$$

where

A = (5.6m x 2.8m)
D = 5 mils of fused quarz glass cover (typical number)
ϵ_O = permitivity in free space
ϵ_R = relative permitivity of quarz

In addition, it has been calculated that for the proposed orbit, the accumulated charge during the maximum charging period is of the order of 5.39×10^{-3} coulombs for the solar array. Using the simple relationship

$$V = \frac{Q}{C} \qquad (3)$$

The expected charged voltage is of the order of 1300 volts

Discharging Phase:

During this phase, shown in Figure 3, an ESD event with peak magnitude of 1300 volts is assumed to occur on the solar array surface. The arch discharge strikes a shielded cable which connects a temperature sensor on the solar array with a control box (Box 2) inside the spacecraft structure.

Modeling the discharging process of Figure 2 requires the lumped-element representation of Figure 4. In the Figure capacitance coupling is modeled between the cable and spacecraft (C_3), cable and solar array (C_4), solid conductor and cable shield (C_5), and between the space plasma and spacecraft/solar array (C_1 and C_2). Capacitance C_6 was previously calculated in equation 2. The modeling of Figure 4 has been "idealized" by avoiding mismatching effects between the shielded cable and its load, hence, the characteristic impedance of the cable is matched to its load

which is assumed for simplicity to be 50 ohms. In addition the model of Figure 4 is further simplified by considering the discharge on **only one cable** out of the over 100 signal/control and power cables that normally connect the solar array with spacecraft electronics. A more accurate model will require the representation of multiple types of capacitance effects between the many cables and the spacecraft, plasma, and solar array. The capacitance values of Figure 4 can be accurately obtained experimentally but some approximation (worst case) can be made using certain analytical close form expressions which can estimate the capacitance between conductors of varied geometrical configurations.

The circuit diagram representation of Figure 4 is shown in Figure 5. The purpose, as illustrated in the Figure, is to calculate the voltage and current transients at Z_L when an electrostatic discharge with a peak magnitude of 1300 volts occurs from the glass-covered solar array. To model the arch discharge the transient voltage is modeled to represent a typical ESD transient, with a rise-time of 3 nsec, pulse-length of 40 nse and decay-time of 10 nsec. In addition to the previously defined capacitance terms, resistance and inductance terms are added to properly represent the impedance of the cable shield, main conductor, and spacecraft structure as shown in Figure 5. To provide a "generalized" approach to the circuit model the resistance, capacitance, and inductance values of Figure 5 were calculated using several analytical expressions [7] and the results corresponding to the circuit parameters of Figure 5 were obtained to be:

C_1 = 158 pF R_s = 35 ohms
C_2 = 139 pF L_s = 2.91 uH
C_3 = 15.97 pF R_g = 8.88 u-ohms/square
C_4 = 13.38 pF $C_6 = 4.15 \times 10^6$ pF
C_5 = 165 pF

The values for the circuit elements in Figure 5, (stated above), allow the calculation of several parameters useful to assess the vulnerability of the victim circuit (Z_L) to the ESD event produced by solar array. The SPICE circuit analysis program is first used to calculate the voltage gain vs frequency of the victim (Z_L) with respect to the source voltage normalized to 1 volt. The objective is to assess the frequency sensitivity of the victim circuit to the resulting transient voltage and current which appears across Z_L during an electrostatic discharge. The result of this analysis is shown in Figure 6. The SPICE circuit analysis program is then used to perform the transient analysis described in Figure 5. The voltage and current at Z_L are evaluated and the results are shown in Figure 7. The results of Figure 7 show that approximately 240 volts will appear across Z_L. The 240 volts correspond to to the maximum peak of the induced transient voltage in Figure 7.

METHOD OF MOMENT AND MODELING THE INDUCED FIELDS

Discharge voltages induce current distributions on the conductor and shield of the cables connecting the sensors and power circuits of the solar array with the spacecraft electronics. In the problem of Figure 4 a method is needed to model the induced current distribution on the shielded cable by the voltage transient of Figure 7. The resulting current can then be used to calculate the fields generated by the cable inside the spacecraft structure.

In Figure 7 the physical layout of the shielded cable inside the spacecraft is modeled slighly different from that shown in Figure 4. The shield is grounded to the spacecraft through a "pigtail" connection, the load Z_L represents, as before, the input impedance of Box 2 in Figure 3. Figure 7 shows the corresponding "thin-wire" structure of the inner conductor, shield, and pigtail connection needed to model the current distribution by the Method of Moments. The length of the thin-wire segments used (a total of 22) is not physically larger than $\lambda/10$ for the frequency range of interest and assumed to be perfect conductors. The diameter of the segments is made to be equal to the diameter of the center conductor. The source voltage shown in Figure 8 correspond to the amplitude terms of the Fourier Transform of the transient voltage waveform in Figure 7.

In Figure 6, it was shown that the greatest sensitivity of the load Z_L to an applied voltage source corresponded to the frequency of about 17 MHz. This is further corroborated in Figure 7 where the highest peak of the induced transient voltage waveform across Z_L is found to occur at approximately 58 nsec, which is the intanteneous period corresponding to 17 MHz. Because the highest sensitivity of the circuit in Figure 5 is about 17 MHz, only the Fourier Transform of the major "lobe" of the transient waveform in Figure 7 is calculated. The amplitude terms of the Fourier Transform can be used as the source voltages in Figure 8 at the corresponding frequencies.

For the thin-wire model of Figure 9, the near electric field was calculated at several locations (P_1 through P_6) on both sides of the shielded cable as indicated in the Figure. These locations were chosen first, to study the dependance of field magnitude with proximity to the cable, and secondly, to study the effect of pigtails in near field calculations. Though electric field calculations can be made at several frequencies, the results shown in Table 1 are those for the frequency of 17 MHz which is the worst case for this particular problem. Notice the effect of increased field strength (P_4 through P_6) when a pigtail is used for grounding purposes. In the modeling, several geometrical aspects which need to be considered for field calculations were neglected. Electromagnetic phenomenae such as reflection, scattering and diffraction of waves within the geometrical boundaries of the spacecraft were not considered, as shown in Figure 9, by removing from Figure 8

the boundaries of the grounded spacecraft structure. Such electromagnetic effects can be modeled using Finite Element Methods (FEM) and Geometric Theory of Diffraction (GTD) techniques found in GEMACS [8].

USING EMC CODES FOR COMPATIBILITY STUDIES

The main objective in calculating the radiating fields from the shielded cable in Figure 8 due to an ESD event is to perform field-to-wire coupling analyses inside the spacecraft as illustrated in Figure 10. The analyses may reveal the presence of unacceptable levels of noise (in terms of coupled voltages) in nearby cables, wires and sensitive electronic equipment. Extensive field-to-wire coupling analyses can be performed using known EMC codes such as SEMCAP and IEMCAP. These programs require the accurate geometrical layout of all field sources and victim cables and the magnitude of the field sources must be known a priori.

The concept used in IEMCAP for field-to-wire coupling is the "illuminated transmission line" where the exposed cables are assumed to be adjacent to an aperture and the amount of RF energy coupled depends on the aperture size and location. A transmission line model (differential mode) is then used to compute the currents induced in the wire loads. Worst case electromagnetic field orientation is determined and used for the calculations. IEMCAP models the x, y, and z components of its field sources from the far-field approximation of the ambient sources present. The Method of Moment however, can provide accurate estimates of field strength at specific locations based on the modeling of the sources, and these capabilities are not presently available in IEMCAP which models its field sources as worst-case. For cables close to several apertures the superposition principle is used, and for circuits with ground plane return, the transmission line is formed by using the ground plane as primary cable.

In SEMCAP the induced voltage on the receptor (antenna or cable) is obtained by first calculating the fields at 1 meter from the antenna and/or cable using closed form analytical expressions to represent the fields from wires or antennas which serve as sources of emissions; then by using the $1/r$ (worst case) far field approximation, the field decay is calculated at the antenna and/or cable which serves as victim circuits. The Method of Moments however, can provide accurate estimates of field strength at the location of victim circuits. The final step in SEMCAP and IEMCAP is to calculate the induced voltage on the antenna and/or wire from the field strength at their input terminals. In all these calculations provisions are made to consider shielding effects of radiators and receptors.

SUMMARY

A method has been shown for a three-step procedure to compute electromagnetic interference levels on cables and wires in a spacecraft due to electrostatic discharges from solar arrays. First the discharge event is modeled by an equivalent circuit represenation of all the elements involved. The induced voltage is then calculated on cables and wires located where the discharges would most likely occur. Secondly, the method of moment is used to calculate the generated fields from these cables by appropriate modeling of the current distribution. The final step demostrated how the calculated fields can be used to perform field-to-wire EMC analyses by using either IEMCAP or SEMCAP.

REFERENCES

[1] Inoye, G.T., et al "Final Report, Spacecraft charging analysis studies and analysis of the modified DSCS-II Flights 5 and 6 configuration, TRW Report," 1975.

[2] Gross,B., Dow, J. and Nablo, S. "Charge buildup in electron -irradiated dielectric," J. Applied Physics, 44:2459, 1973.

[3] Ling,D. "Common approach to solving SGEMP, DEMP and ESD survivability," Proc. of the Spacecraft Charging Technology Conference, Oct 27-29, 1976.

[4] RADC-TR-74-342, "Intrasystem Electromagnetic Compatibility Analysis Program (IEMCAP)," Rome Air Development Center, Air Force System Command, December 1974.

[5] TRW System Group, "Specification and Electromagnetic Compatibility Compatibility Analysis Program (SEMCAP)," One Space Park, Redondo Beach, California, October 1975.

[6] Katz, I. et al., 1977,1979; Schnuelle et al., 1979; Roche and Purvis, 1979 ; Rubin et al., 1980, "The NASA Charging Analyzer Program computer code, (NASCAP)"

[7] Massaro,M.J.,Green, T., Ling, D.,"A Charging Model for Three-Axis Stabilized Spacecraft," Proc. The Spacecraft Charging Technology Conference, Oct 27-29, 1976.

[8] Kadlec, D.L., Coffey, E.L., "General Electromagnetic Model

for the Analysis of Complex Systems (GEMACS)," Rome Air Development Center, Air Force System Command, 1983.

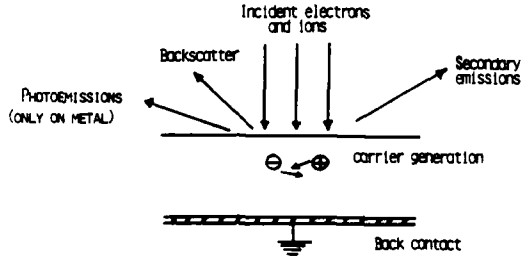

Figure 1. Electron and Ions Interactions Related to Charge Buildup in Insulators

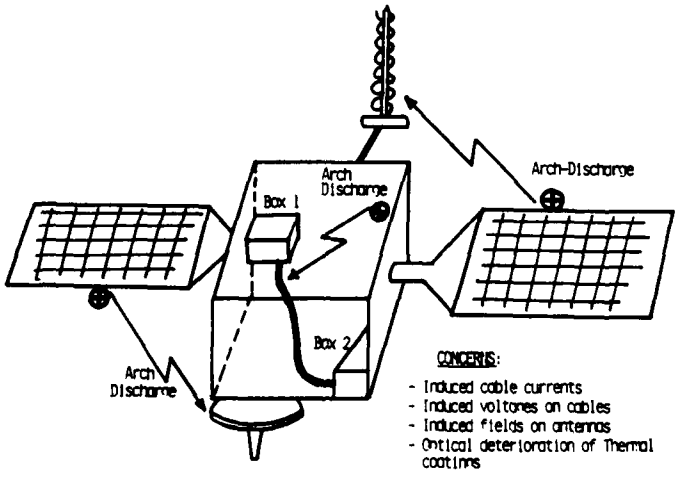

Figure 2. Electrostatic Discharges and their Effects on Spacecrafts

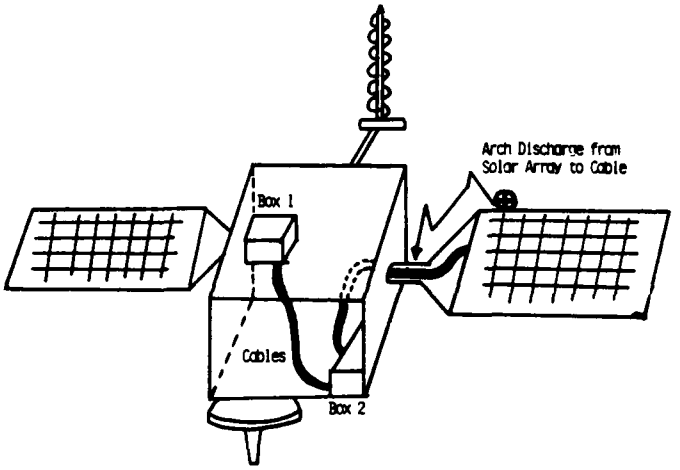

Figure 3. Typical ESD Event Between Solar Array and a Cable in a Spacecraft.

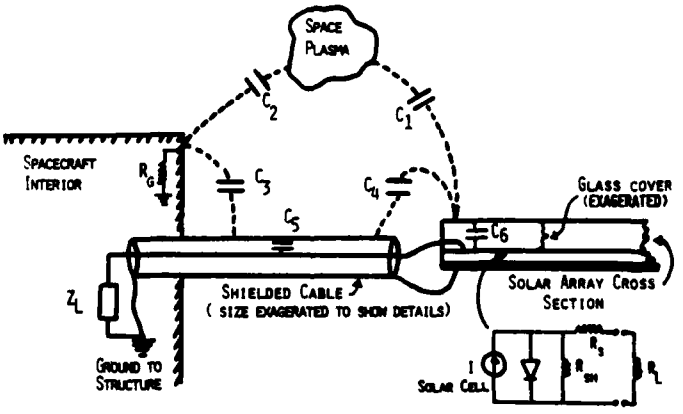

FIGURE 4. LUMPED ELEMENTS CIRCUIT PARAMETERS FOR SOLAR ARRAY-TO-SPACECRAF ESD EVENT.

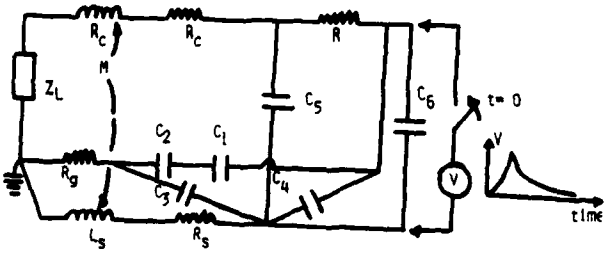

where:

L_s = Shield Inductance
R_s = Shield Resistance
M = Mutual Inductance (L_s = M) for tight coupling
R_c = Conductor Resistance
C_1 , C_2 , C_3 , C_4 , C_5 , C_6 = See Figure 4
Z_L = Load Impedance
R = High Impedance to "couple" ESD transient voltage "V" to C_1 /C_2 and C_4
R_g = Structure or "Ground" Impedance
V = Transient voltage

Figure 5. Circuit representation of Solar Array-to-Spacecraft ESD event

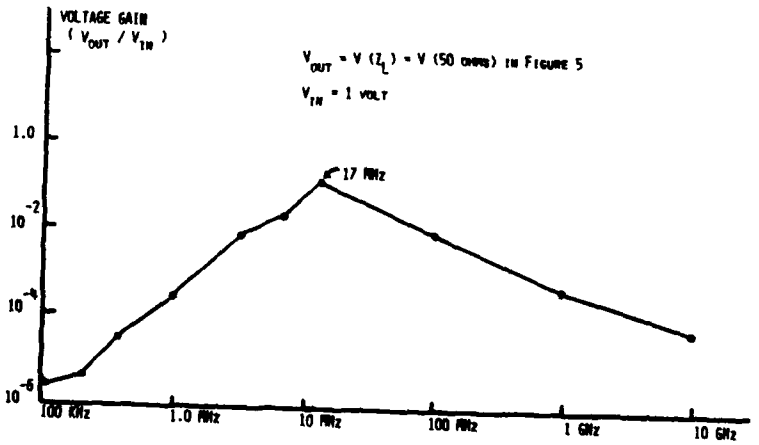

Figure 6. Voltage gain across Z_L due to a unitary voltage across C_6

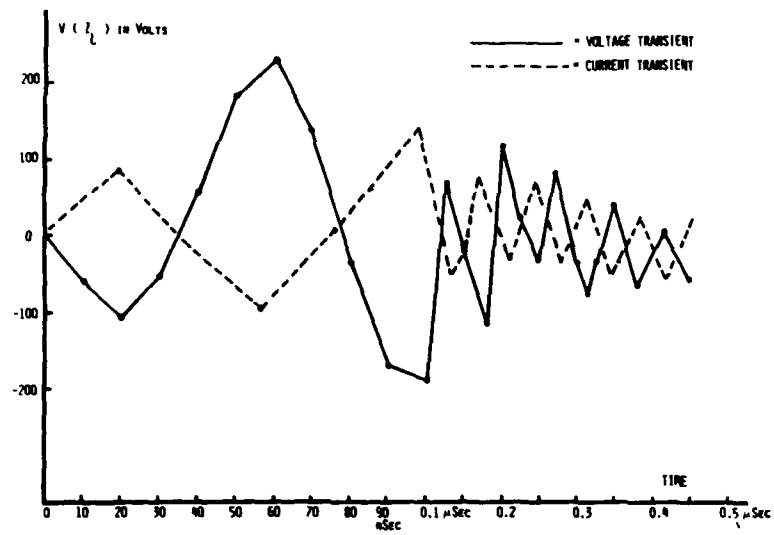

Figure 7. Induced Transient Voltage and Current on Z_L

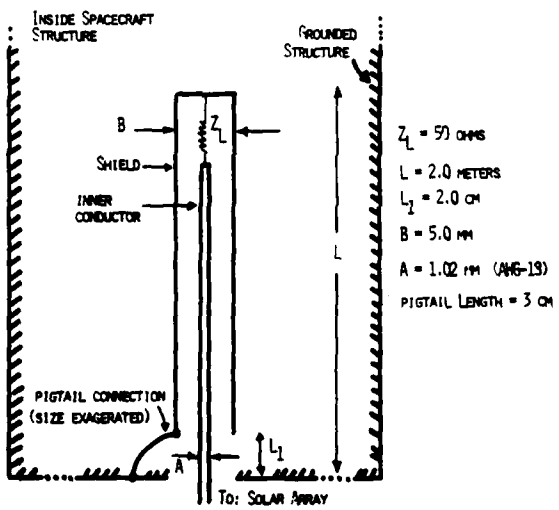

Figure 8. Physical Representation of Shielded Cable Inside Spacecraft Structure.

LOCATION	E_x (dBuV/m)	E_y (dBuV/m)	E_z (dBuV/m)
P_1	111.51	39.11	95.95
P_2	106.21	79.13	96.71
P_3	92.86	58.25	93.93
P_4	115.14	96.63	95.62
P_5	108.19	82.99	96.40
P6	94.54	61.07	93.99

Table 1. CALCULATED VALUES OF NEAR ELECTRIC FIELDS RADIATED FROM SHIELDED CABLE IN FIGURE 9.

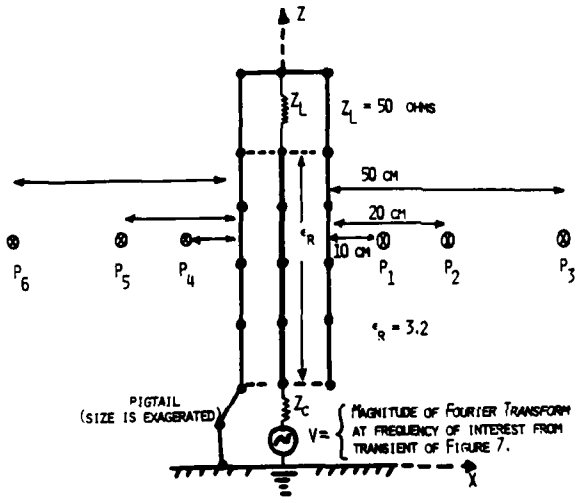

FIGURE 9. METHOD OF MOMENT MODELING OF SHIELDED INSIDE SPACECRAFT FOR ELECTRIC FIELD CALCULATIONS.

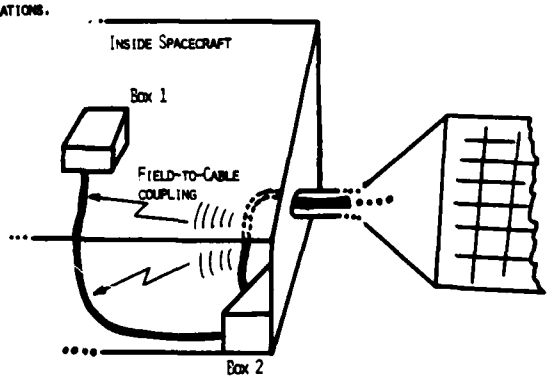

FIGURE 10. EXAMPLE OF FIELD-TO-WIRE COUPLING TO BE USED BY SEMCAP.

ELECTROMAGNETIC MODELING FOR COMMERCIAL EMI DESIGN AND ANALYSIS

Colin E. Brench
Digital Equipment Corporation
146, Main Street, Maynard, MA 01754

Abstract

The need for realistic electromagnetic modeling is becoming more acute in the world of commercial electromagnetic compatibility. Many rules of thumb and guidelines exist that help to minimize emissions from printed circuit boards and to design a shielded enclosure. However, with the ever increasing operating frequencies used in information technology equipment, the usefulness of these tools are dropping. This paper presents both the system design goals that the EMC engineer has to meet and the information that is available at the start of a new product. It is the goal of this paper to help strengthen the link between those developing electromagnetic models and the design engineers in the EMC community who need such tools.

Introduction

With the latest revision of the FCC Rules in Part 15, it is necessary to measure the radiated emissions from a product from 30MHz to an upper limit determined by the fastest clock in the system.

Fastest Clock	Upper Frequency Limit
< 108MHz	1 GHz
< 500MHz	2 GHz
< 1000MHz	5 GHz
> 1000MHz	5xFclock but <40GHz

Previously, testing, and hence design, were only required to 1GHz. As the highest frequency of concern increases there are fewer reasons to trust many of the traditional design approaches that are based on much lower frequency models. There is a need to upgrade the existing guidelines to meet these new boundary conditions, or ideally, to develop more precise methods.

There are a number of reasons for having good modeling tools other than the need to design an acceptable product. One of the difficulties faced by an EMC engineer is the lack of solid design information to back up his recommendations. Since many EMC designs are largely experience based they are hard to verify in any tangible way. Another challenge in developing a new product, is in setting the priorities between the needs of all the engineering disciplines: thermal, acoustic, shock and vibration, and industrial design. In order for this to take place each

discipline must be able to present a clear case for their requirements, and also know what alternatives are viable. It is important that, where possible, advantage is taken of similar design requirements, and that conflicts in design are worked out. For these cases electromagnetic modeling can play a key role in the variety of "what if" evaluations such that the optimum design can be achieved.

Statement of the Problem

There are two parts to the problem of EMI modeling: evaluating the sources of radiated energy and evaluating the enclosure shielding. While these two problems are often viewed independently, there can be a strong interaction between them.

The ultimate goal is not only to predict the level of radiated energy from circuitry which is located inside a "shielded" enclosure, but also to understand how those levels are modified by changes to any of the component parts of the system.

Radiated Energy Sources

There are three components to each radiated emission:

- o an rf energy source, (di/dt)
- o a means of coupling, (mutual impedance)
- o a radiating element, (antenna)

The primary sources are the rf currents in the PC board traces and IC bondwires. Secondary sources include the induced "common mode voltages" that can be measured between a heatsink and PC board groundplane, or across a PC board. The coupling from the sources to the radiating elements is known as the mutual impedance; at lower frequencies this is often capacitive or inductive coupling. The radiating elements are physical parts such as PC traces, connectors, heatsinks, etc. The mutual impedances between the noise sources and the radiating elements are critical to successfully combining the available information.

Enclosure Shielding

In order to understand the shielding of the system, it must be realized that there are two main requirements for a good shield. It must prevent energy from penetrating it (shielding effectiveness), and it must provide a return path for any currents induced into it by I/O filters or cable shields.

The shielding effectiveness equations in popular use provide the ratio of the incident plane wave, normal to the surface under investigation, to the normal, transmitted plane wave. In reality the fields are not plane waves and do not necessarily have normal incidence.

The return path problem is quite different. A given opening, designed for a specific shielding effectiveness, may not be adequate to suppress radiation caused by currents coupled directly to the enclosure by an I/O filter. In this case energy radiated by the apertures in the shield will be dependent upon a number of things such as: the dimensions of the opening, the frequency of concern, and the direction of current flow.

Starting Information

The first step in solving any problem is to determine what is actually known. At the beginning of a project there are mostly goals, ideas and some modeling information (based on someone's best guess) that can provide the basis for the design. There are a number of levels to this information, starting with the details of the integrated circuits and printed circuit boards, all the way through to the outside enclosure and system configurations.

Once the details of the variables within a system are known, the effects of them upon each other require evaluation. The influence of all these factors needs to be considered, and one of the keys to solving the problem is to know how much influence these factors actually have.

- Circuit/Device Simulation. Knowledge of the integrated circuit can be as minimal as its package size and clock rate or it could include extensive simulation data. Circuit analysis tools such as SPICE can be used to predict current waveforms together with the fourier analysis necessary to give the amplitudes at the various component frequencies. This information provides the basis for the source model and so is a key factor in the overall accuracy.

- Device Packaging. To use the noise source information effectively the radiating element(s) within the system must be modeled. To derive the model of an IC as an antenna, some details of the package need to be known: size, shape, internal bond wire routing, etc.

- Device Heatsink. Heatsinks can be significantly large in terms of the frequencies of interest. As such they can be good radiating elements. To determine how much they affect the radiated emissions it is necessary to analyze their antenna properties and to determine how much energy is coupled to them. A given device may have different geometry heatsinks in different situations.

- PCB Layout. For a simple printed circuit board the layout is usually crucial to minimizing radiation, but if large components such as connectors with daughter cards are present then the radiation characteristics will be dependent upon those larger parts.

- System Configuration. The mutual impedance effects between the source(s) and conductive parts of the system are very important to the EMC analysis. Details of the system assembly can provide

information on the internal wiring and the presence of adjacent PC boards with or without full internal groundplanes. In some cases the noise source may be adjacent to the shielded enclosure.

- o Open Area Needed for Cooling. To ensure adequate cooling a certain open area will be required. The industrial design can influence the location and orientation of these vents. If a high percentage of open space is required, the shielding becomes less predictable, due to the larger openings.

- o Types and Characteristics of I/O. The characteristics of the I/O from a computer are very important in defining what needs to be done to provide a "clean" port. A wide bandwidth signal will require a shielded cable, whilst an I/O for slower data may be filtered. In both of these cases rf energy will be conducted onto the shield and so be a possible source of radiation.

- o Materials Used. The material of the enclosure may be of concern particularly if it is not a simple metal box. A very thin conductive film may prove deficient for shielding low frequency sources.

- o Required Regulatory Limits. Once the noise sources have been evaluated, it is possible to compare the radiated power with that permitted by the various regulatory agencies and ensure that the enclosure provides the shielding needed to meet those requirements.

- o Upgrade Plans. Further consideration is needed for future upgrades to a product line. Almost all products will grow with time, a faster processor, more features, etc. If a given design is fully understood, it will be possible to make extrapolations for the new elements of the system.

Discussion

For today's EMC design it is possible to use SPICE models for circuit analysis, to provide the noise current waveforms in a conductor, or the expected voltage waveform on a heatsink. MiniNEC can then be used to create wire frame antenna models of heatsinks, PC boards, internal cables, etc., that will provide the radiation resistance and antenna reactance. By considering the antenna impedance in conjunction with the noise source impedance and amplitude, an estimate of the radiated energy can be made.

Unfortunately, the source, radiating element, and shielding of a system are not independent and the interactions between them need to be understood. When this is possible circuit models can be modified to correct for the radiation losses, and antenna models can be corrected to include the mutual impedance effects caused by a shielded enclosure and/or conductive planes.

It is also important to know where to concentrate during the EMC design effort. Commercial EMC design encompasses a wide range of products and the most cost effective, or time to market, solution will depend upon many factors. Should resources be used in minimizing the source, or in containing the energy at the system level? Until an overall picture of the system EMC, in conjunction with the product and its market, emerges, this is hard to answer.

Note that this paper only addresses directly radiated emissions. There are equally important issues concerning the rf voltages on I/O lines and ac power cords. Part of the shield design is to provide a good rf zero voltage reference (THE ground) for all I/O filters and/or cable shields.

Accuracy

Before generating extensive models it is important to consider the accuracy of the data available to the model. A SPICE model could have been based upon the best guess of the group responsible for the development of the IC. Printed circuit layout could be based on expected pin outs, expected functionality, and the assumption that everything will be ready when needed.

While the source of the data is by no means 100% accurate, the same is largely true for the measurements of the results. Even the best EMI test sites can have overall measurement errors of ±6dB, i.e. +100%/-50%.

This indicates that precision is not vital; rather, it is the ability to juggle the variables in an intelligent manner that makes an EMC analysis tool most valuable.

Conclusions

To obtain a quality EMC design, a great deal of information is required at the start of the project, not only concerning the sources and shielding, but also concerning the interactions of passive parts. In order to evaluate these effects, sophisticated tools are needed; the synergistic use of SPICE and MiniNEC being one example.

Any modeling tool will have limitations, therefore it is essential that the boundaries are understood, to ensure that the results obtained are valid. One boundary is the accuracy of the initial data. While accuracy is always a goal, it is not paramount to the EMC design, as speed and the ability to evaluate numerous configurations are most needed. For now, the task is to fill the gap between the back of an envelope and hours of mainframe CPU time.

SESSION 6 - "NEW TECHNIQUES"

Thin Wire Feature for the MMP-Code

P. Leuchtmann and L. Bomholt
Electromagnetics group, ETH Zurich
CH-8092 Zurich, Switzerland

Abstract

After a brief explanation of the original MMP-Code and its basic ideas, a new feature of this code is described: the modelling of thin wires in a way, which is very similar to that used in NEC. One of the basic principles of the MMP-Code, the use of overdetermined systems of equations, becomes a difficulty concerning the thin wires. The arising problems are described in the paper and rules for their solving are given. Some remarks on the validation of the results are given, and some successful applications of the new feature are presented.

1 The Original MMP-Code

The MMP-code (Multiple MultiPole) is a powerful tool for calculating electromagnetic fields. [1,6] The basic idea is, to expand the electromagnetic field $(\vec{E}, \vec{H})$ in a series of easily calculable fields:

$$\vec{E}(\vec{r}) \approx \vec{E}_0(\vec{r}) + \sum_{k=1}^{K} a_k \vec{E}_k(\vec{r}); \qquad \vec{H}(\vec{r}) \approx \vec{H}_0(\vec{r}) + \sum_{k=1}^{K} a_k \vec{H}_k(\vec{r}). \tag{1}$$

The K unknowns a_k are the same for the $\vec{E}$- and the $\vec{H}$-series and each pair $(\vec{E}_k, \vec{H}_k)$, $k = 1 \ldots K$, fulfills Maxwell's equations of a linear, isotropic and homogeneous medium:

$$\text{rot}\, \vec{E}_k = i\omega\mu \vec{H}_k; \qquad \text{rot}\, \vec{H}_k = -i\omega\epsilon' \vec{E}_k. \tag{2}$$

The medium is described with the permeability μ and the complex permittivity $\epsilon' = \epsilon - \frac{\sigma}{i\omega}$, where ϵ is the real permittivity, σ is the conductivity and ω is the angular frequency. ($e^{-i\omega t}$-time dependence!)

The zero indexed quantities in (1) are special solutions of the (possibly *inhomogeneous*) Maxwell equations and are present, if there are impressed sources or a given excitation.

The unknowns a_k in (1) are determined using the boundary and/or continuity conditions for the field. The MMP-code uses an overdetermined system of equations, which is found by "point-matching" (imposing the boundary conditions for the field in many boundary points).

To find *easily calculable fields* $(\vec{E}_k, \vec{H}_k)$, two main procedures are useful, a "mathematical" procedure and a "physical" one. Developing the original MMP-code, the mathematical procedure was used first.

1.1 Mathematical Procedure to Find Expansion Functions

Maxwell's equations (2) may be solved by the "separation of the variables". [1,5] The procedure may be applied successfully, when either a cartesian, a cylindrical or a spherical coordinate system is used. The results are plane waves, cylindrical waves or spherical waves respectively. The waves mainly used in the MMP-code have a decreasing behaviour for large distances from the origin of the coordinate system and are singular at the origin itself. They are called *multipoles*. Theoretically, there is an infinite number of different waves for each origin, starting with the dipole, quadrupole, etc. For numerical purposes, only a finite number of these waves can be used. The "local behaviour" of the multipole-fields makes it possible, to use them for modelling the total field in a somewhat constructive way: 1) the field domain is surrounded by a number of origins of different coordinate systems, 2) each of these origins is "carrier" of several waves

$(\vec{E}_k, \vec{H}_k)$ and 3) the waves of one origin are mainly used for modelling the field in the closer vicinity of that origin. [1,2]

All expansion fields $(\vec{E}_k, \vec{H}_k)$ found by the mathematical procedure have the important advantage, that the field components at any position $\vec{r}$ may be calculated by the evaluation of simple *analytical* formulae.

The singularity of a multipole field can be interpreted as a (non isotropic) point-source of the field. The notion of sources of the fields leads to a second, more physical way to find expansion fields $(\vec{E}_k, \vec{H}_k)$.

1.2 Physical Procedure to Find Expansion Functions

Any physical Maxwell field (fulfilling (2) in the field domain D) is produced by sources (current density $\vec{j}$ and charge density ϱ) located outside (or on the boundary of) D. The sources $\vec{j}$ and ϱ are restricted by the charge conservation principle, in our case: $\operatorname{div} \vec{j} = i\omega\varrho$. Therefore, $\vec{j}$ alone describes all the sources[1].

On the other hand, any current distribution $\vec{j}_k$ which is located completely outside D produces a specific field $(\vec{E}_k, \vec{H}_k)$ in D, which is possibly useful for the expansion (1) of the total field. The relationship between $\vec{j}(\vec{r}')$ and $\vec{E}(\vec{r})$ is given by the following integral representation of the electric field (EFIE) [1,3]:

$$\vec{E}(\vec{r}) = \frac{1}{4\pi i\omega\varepsilon'} \int \left(\vec{j} \frac{G}{R^2} (1 - ikR - k^2R^2) - (\vec{j} \cdot \vec{R}) \vec{R} \frac{G}{R^4} (3 - 3ikR - k^2R^2) \right) dV'. \tag{3}$$

Here and in the following, k is the wave number of the medium in D and

$$\vec{R} = \vec{r} - \vec{r}'; \qquad R = |\vec{R}|; \qquad G = G(\vec{r}, \vec{r}') = \frac{e^{ikR}}{R}. \tag{4}$$

The integration range is the area, where $\vec{j}(\vec{r}')$ is nonzero. The magnetic field $\vec{H}$ may then be calculated using the first equation in (2).

The advantage of formula (3) is, that one can now think in terms of sources rather than in terms of fields to produce expansion terms $(\vec{E}_k, \vec{H}_k)$. For many practical cases, this is very helpful, because one knows approximately, where the currents can flow. E.g., for scattering problems, the real physical currents can only flow on the conductor-surfaces, which are — at the same time — boundaries of the field domain.

On the other hand, the main disadvantage of (3) is its complexity: The evaluation of an integral for each field point $\vec{r}$ must be performed numerically — a very laborious task.

It is a lucky chance, that there exist current distributions $\vec{j}(\vec{r}')$ for which the integral (3) may be evaluated analytically for any given field point $\vec{r}$. This is the case for certain straight line currents, as we shall show in the next section.

2 Thin Wires

Suppose a thin line current $I(z')$ on the z-axis of a cylindrical coordinate system (ρ, ϕ, z). $I(z')$ is nonzero only for $z_1 \le z' \le z_2$. The corresponding current distribution is $\vec{j}(\vec{r}') = I(z')\delta(\rho')\vec{u}_z$, with the Dirac-$\delta$ and the unit vector $\vec{u}_z$. In this case, (3) reduces to the line integral

$$\vec{E}(\vec{r}) = \frac{-1}{4\pi i\omega\varepsilon'} \int_{z_1}^{z_2} I(z') \left[\left(k^2 G + \frac{\partial^2 G}{\partial z^2} \right) \vec{u}_z + \frac{\partial^2 G}{\partial\rho\partial z} \vec{u}_\rho \right] dz'. \tag{5}$$

[1] Also non-physical sources (e.g. with magnetic charges), produce a Maxwell-field *in* D, as long as the sources are located outside D. For this paper, we are not interested in such cases.

2.1 Harmonic Current Distribution on a Straight Wire Segment

The integral (5) can be evaluated analytically, if the current $I(z')$ fulfills the harmonic differential equation

$$\frac{d^2I}{dz'^2} + k^2 I = 0; \qquad k^2 = \omega^2 \mu \epsilon', \tag{6}$$

i.e., if the current has the form $I(z') = a\cos kz' + b\sin kz'$. Note, that k is the wavenumber of the surrounding medium. The parameters a and b may have any complex value. Without loss of generality, we choose the coordinate system, so that $z_1 = 0$ and $z_2 = l$. Then, we obtain the following expressions for the field components:

For $I(z') = a\cos kz'$:

$$E_\rho = \frac{a}{4\pi i\omega\epsilon'\rho}\left[G_l\left(k(z-l)\sin kl - \frac{\rho^2+(z-l)^2 ikR_l}{R_l^2}\cos kl\right) + G_0\frac{\rho^2+z^2 ikR_0}{R_0^2}\right], \tag{7-1}$$

$$E_z = \frac{-a}{4\pi i\omega\epsilon'}\left[G_l\left(k\sin kl + (z-l)\frac{1-ikR_l}{R_l^2}\cos kl\right) - G_0 z\frac{1-ikR_0}{R_0^2}\right], \tag{7-2}$$

$$H_\phi = \frac{-a}{4\pi\rho}\left[G_l\left(iR_l\sin kl + (z-l)\cos kl\right) - G_0 z\right]. \tag{7-3}$$

For $I(z') = b\sin kz'$:

$$E_\rho = \frac{-b}{4\pi i\omega\epsilon'\rho}\left[G_l\left(k(z-l)\cos kl + \frac{\rho^2+(z-l)^2 ikR_l}{R_l^2}\sin kl\right) - G_0 kz\right], \tag{8-1}$$

$$E_z = \frac{b}{4\pi i\omega\epsilon'}\left[G_l\left(k\cos kl - (z-l)\frac{1-ikR_l}{R_l^2}\sin kl\right) - G_0 k\right], \tag{8-2}$$

$$H_\phi = \frac{b}{4\pi\rho}\left[G_l\left(iR_l\cos kl - (z-l)\sin kl\right) - G_0 iR_0\right]. \tag{8-3}$$

The abbreviations $R_0 = R|_{z'=0}$, $R_l = R|_{z'=l}$ $G_0 = G|_{z'=0}$, $G_l = G|_{z'=l}$ were used (see (4)!). The other components of the field, E_ϕ, H_ρ and H_z, are zero. We shall write $(\vec{E}_c, \vec{H}_c)$ for the field (7) and $(\vec{E}_s, \vec{H}_s)$ for (8).

2.2 Constant Current on a Straight Wire Segment

For the special case $I(z') = c$ in the intervall $[0, l]$, the integral (5) delivers the expressions

$$E_\rho = \frac{-c\rho}{4\pi i\omega\epsilon'}\left[G_l\frac{1-ikR_l}{R_l^2} - G_0\frac{1-ikR_0}{R_0^2}\right], \tag{9-1}$$

$$E_z = \frac{-c}{4\pi i\omega\epsilon'}\left[G_l(z-l)\frac{1-ikR_l}{R_l^2} - G_0 z\frac{1-ikR_0}{R_0^2} + k^2\int_0^l G\,dz'\right], \tag{9-2}$$

$$H_\phi = \frac{c\rho}{4\pi}\int_0^l G\frac{1-ikR}{R^2}dz'. \tag{9-3}$$

We shall write $(\vec{E}_o, \vec{H}_o)$ for this field. It must not be confused with $(\vec{E}_0, \vec{H}_0)$ in (1).

2.3 Long Curved Wire with Arbitrary Current Distribution

The fields $(\vec{E}_s, \vec{H}_s)$, $(\vec{E}_c, \vec{H}_c)$ and $(\vec{E}_o, \vec{H}_o)$ may be *superimposed* and are then associated with the current

$$I(z') = a\cos kz' + b\sin kz' + c. \tag{10}$$

This gives three degrees of freedom (the parameters a, b and c) for modelling a (thin wire-)current, which is definitely not sufficient in a generic case. To model an arbitrary current on a long and possibly curved wire, the whole wire can be cut into short segments. Then, on each segment one has three free parameters. They can be determined by imposing a) boundary conditions of the *field* on the surface of the wire and b) continuity conditions of the *current* along the wire.

Condition a) is based on the field and means mainly, that the tangential $\vec{E}$-field on the surface of the wire must be zero. This is a continuous condition along the whole surface, i.e. an equation of functions rather than an equation of numbers.

Condition b) is based on the current and means, that not only the current $I(z')$, but also — due to the *charge conservation principle* — its first derivative must be continuous. The current (10) fulfills both of these continuities along the segment, but not at the junction between segments. Thus, two equations for each junction must be fulfilled — if one really wants to satisfy both, the continuity of the current and the continuity of the derivative of the current. Note that this is *not* always necessary: As an alternative, it may be better to satisfy the field boundary conditions.

We tested different possibilities: the continuous current version (only continuous current), the smooth current version (current and its derivative continuous, like NEC) and pure field versions (only field conditions are imposed). In the continuous current version, only two parameters per segment, a and b were used, in order to avoid the numerical integration in the evaluation of the field (9). In the smooth current version, three parameters, a, b and c were used on each segment.

The continuity conditions for the current of an N-segment wire deliver $N-1$ equations at the segment *junctions* and another $N-1$ equations for the continuity of the current's derivative. The resulting system of equations contains all the unknowns. $N-1$ (resp. $2N-2$) of them may be eliminated, leaving significantly less unknowns for the fulfilling of the field boundary conditions. It is shown in the appendix, how the elimination of $N-1$ (resp. $2N-2$) unknowns may be done *by hand*.

3 Numerical Investigations

In this section, we discuss the various alternatives of imposing (field-)boundary and/or (current-)continuity conditions. The following statement must be kept in mind: If the field boundary conditions are fulfilled on the whole surface of the wire, the current becomes *automatically* continuous and smooth. The opposite is *not* true: Even a smooth current does not automatically imply a satisfied field boundary condition.

In the original MMP-code, only the field boundary conditions are implemented. A $\lambda/2$-antenna with a length/radius ratio of 200 has been successfully modelled using 100 multipoles along the axis with totally 500 unknowns [4]. Following the same procedure, a thinner antenna would request even more unknowns. This is due to the mentioned local behaviour of the multipole fields. Using the new feature, a wire is modelled by the fields $(\vec{E}_c, \vec{H}_c)$, $(\vec{E}_s, \vec{H}_s)$ and $(\vec{E}_o, \vec{H}_o)$, which are better adapted to the wanted *field* than the multipoles are. Especially, the number of unknowns does not increase, when the wire becomes thinner.

On a conductor, the tangential electric field and the normal magnetic field must be zero[2]. In the case of a thin wire, using the fields $(\vec{E}_c, \vec{H}_c)$, $(\vec{E}_s, \vec{H}_s)$ and $(\vec{E}_o, \vec{H}_o)$, only the longitudinal $\vec{E}$-field, E_z, must be matched to zero. The other tangential component, E_ϕ, and the normel component, H_ρ, vanish in any case.

Following the extended point matching technique of the MMP-code, [1] matching points (MP's) on the surface of the wire are chosen. Due to the rotational symmetry of the wire fields, it is sufficient to introduce MP's only on a line parallel to the axis of the wire. Depending on how many parameters are free on each segment (1, 2 or 3), at least the same number of MP's must be used. The use of more MP's leads to an overdetermined system of equations and — at the same time — to a smoother error distribution on the

[2] In the case of impedance boundary condition, the tangential electric and magnetic field are related to each other

surface [5]. The latter is less evident in the case of thin wire fields, because these fields are already smooth in the direction of the wire.

3.1 Field Boundary Condition Versus Current Continuity Condition

A $\lambda/2$-dipole antenna was excited with a plane wave, polarized parallel to the antenna. The wire has been modelled with different numbers of segments (10...50) and different numbers of MP's. The locations of the MP's were chosen in various ways. a) Segment-wise modelling: The number of MP's per segment is constant along the wire, and the MP's are shifted only within the segment. (1...10 MP's per segment) b) Whole-wire-modelling: The MP's are located along the wire independently from the segments with continuously varying density along the wire, either more MP's in the center of the antenna or more MP's at its ends. In all cases, the biggest errors (=longitudinal electric field) occurred at the end of the antenna. This result has been expected, since the (electric) field has its greatest magnitude at the end. More important is the fact, that the wire fields $(\vec{E}_c, \vec{H}_c)$, $(\vec{E}_s, \vec{H}_s)$ and $(\vec{E}_o, \vec{H}_o)$ *cannot model the field at the end of a wire in an exact way*. This is, because one always has other than longitudinal currents at the end of a wire, and those currents produce a field (locally) essentially different from that of a line source. For a first view, this seems hopeless, but it is not! If one is interested in the exact field at the end of the antenna, one can model it by multipoles, which act only locally. If one is not interested in this field — and this is the normal case — one should just not place MP's too close to the end. Experience shows, that the last MP should never be closer than a quarter of a segment length by the end. If this rule is respected, all arrangements of MP's give quite similar and good results. As an example, six particular results of the same arrangement are shown in fig. 1 on the next page.

Note, that a free end of a wire is a particularly hard task for the least squares technique in the solution procedure of an overdetermined system of equations, because the wanted field is almost singular at that point. A small percentage error becomes actually a large absolute contribution to the sum of the errors of the whole problem. Omitting the field boundary condition at the end is allowed, since the local character of the singularity of the field is guaranteed by the choice of the physical expansion fields. However, this problem arises only in the case of a free ending wire. If the wire is connected to a thick conductor or to other wires, MP's can be located also very close to the end of the wire. See fig. 2 and 3 as well as [6] for further results.

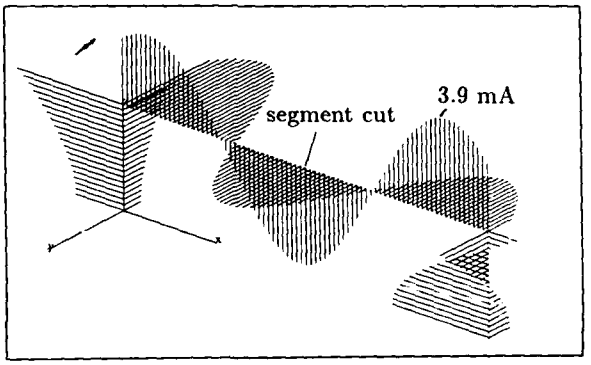

Figure 2 Real and imaginary part of the current in a rectangular loop (height: $\lambda/3$; width: $5\lambda/3$) over a good conducting ground plane, excited by the electrically small dipole shown in the left of the picture. Each vertical branch is modelled with a 10-segment-smooth-current-wire, the horizontal branch is modelled with two 20-segment-smooth-current-wires ($\rightarrow$ 68 free unknowns, 180 MP's). The continuity of the current is correct, also at the corners and at the junction in the middle of the horizontal branch, where no continuity conditions for the current are imposed.

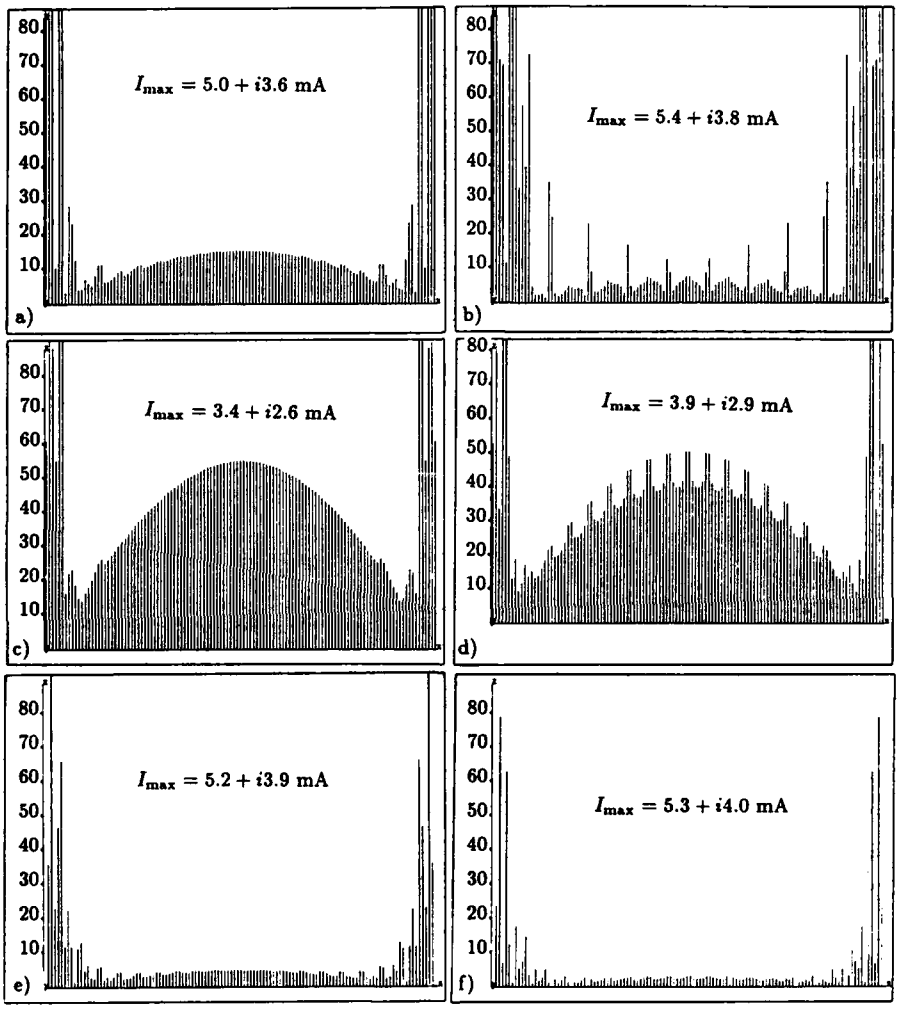

Figure 1 A $\lambda/2$-dipole antenna (diameter: $\frac{2\lambda}{1000}$) is excited with a plane wave. All pictures show the error (longitudinal electric field) on the surface of the wire in percent of the excitation. In the left column, the antenna was modelled by a single 20-segment-smooth-current-wire (22 free unknowns). In the right column, no current continuity conditions at all have been imposed. Hence, there were 60 free unknowns to fulfill the field boundary conditions. The segment length is $l = \lambda/40$. a) and b): 70 equally distant MP's ($\rightarrow$first MP is $\frac{l}{7}$ away from end). c) and d): 120 equally distant MP's ($\rightarrow$first MP is $\frac{l}{13}$ away from end). e) and f): the very first and the very last MP was omitted. ($\rightarrow$116 MP; first MP is $\frac{l}{4}$ away from end). The current is (optically) exactly sine-shaped and comes out continuous with an accuracy of at least 5 digits, but its maximum value I_{max} varies as indicated.

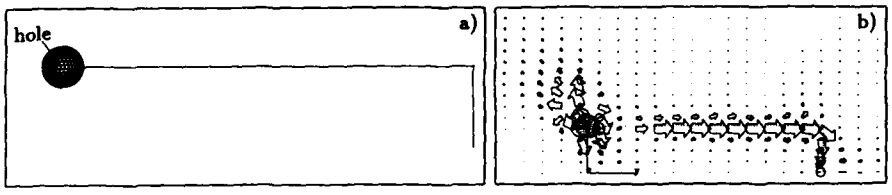

Figure 3 Conducting sphere with a radiating hole at the left hand side and a connected wire at the right hand side over conducting ground. (Loop dimensions like in fig. 2!) a) geometric model; b) time mean value of the Poynting vector in a plane, parallel to, but 10 cm in front of the loop plane.

3.2 *Model Validation*

The validation of the results is still a problem. Using the original MMP-code, examining the field at the boundaries can do the job. If the mis-matching is less than a few percent of the excitation, the result is hopefully correct. In the case of a thin wire, the field looks always correct. This is due to the fact, that the radial component of the field on the wire surface is usually orders of magnitudes larger than both the excitation and the local longitudinal field. Therefore, the electric field is usually almost perpendicular on the wire surface. But only the longitudinal electric field is used to determine the unknowns. Hence, one is obliged to compare the longitudinal component alone with the excitation. Examining only the currents does not always help! In fig. 1, the current *distribution* seems always reasonable. However, experience is needed to be sure about the correctness of the results.

Appendix: Solution of the Current Continuity Conditions by Hand

The $N-1$ continuity conditions of the current of an N-segment wire and the additional $N-1$ conditions of the derivative of the current may be solved by hand, when the local coordinate system of section 2.1 is chosen for each segment, and the segment length l_i is assumed to be smaller than a quarter of a wave length: $l_i < \pi/(2\Re k)$. Let us first consider the case with two parameters per segment. In this case, the current on the i-th segment is $I_i(z) = a_i \cos kz + b_i \sin kz$. Note: each segment starts with its own local coordinate $z = 0$. Hence, the continuity condition of the current at the beginning of the $(i+1)$-th segment is

$$a_i \cos kl_i + b_i \sin kl_i = a_{i+1}; \qquad l_i : \text{length of } i\text{-th segment.} \tag{11}$$

Now, b_i may be expressed in terms of a_i and a_{i+1} and we can write the field of the N-segment wire as

$$\vec{E} = I_b \left(\vec{E}_{c1} - \frac{\cos kl_1}{\sin kl_1} \vec{E}_{s1} \right) + I_e \frac{\vec{E}_{sN}}{\sin kl_N} + \sum_{i=2}^{N} a_i \left(\vec{E}_{ci} + \frac{\vec{E}_{s\,i-1} - \vec{E}_{si} \cos kl_i}{\sin kl_{i-1}} \right). \tag{12}$$

For $\vec{H}$, an identical formula is valid. The currents at the beginning of the wire, I_b and at the end, I_e, are free parameters, additionally to the a_i, $i = 2 \ldots N$. The whole wire is now an object with only $N+1$

free parameters. Simplifications of (12) are possible, if all the segments have the same length l. The field functions are listed in (7) and (8). Note again, that $\vec{r}$ is expressed in local coordinates for each segment.

In the second case, the current of the i-th segment is given by $I_i(z) = a_i \cos kz + b_i \sin kz + c_i$ and the continuity conditions of the current and its derivative at the end of the i-th segment are:

$$\begin{aligned} a_i \cos kl_i + b_i \sin kl_i + c_i &= a_{i+1} + c_{i+1} \\ -a_i \sin kl_i + b_i \cos kl_i &= b_{i+1} \end{aligned} \qquad l_i : \text{length of } i\text{-th segment.} \tag{13}$$

It is still possible to solve the resulting system of equations by hand, at least in the case of equal segment lengths l. In this case, one obtains for the total electric field of the N-segment wire ($C := \cos kl$, $S := \sin kl$):

$$\begin{aligned} \vec{E} = \sum_{i=1}^{N-1} a_i \Bigg(& \vec{E}_{ci} - \vec{E}_{oi} - \sum_{j=i+1}^{N} \Big(SC^{j-i-1}\vec{E}_{sj} - \big(C^{j-i-1}(1+C) - 2\big)\vec{E}_{oj} \Big) \\ & + \frac{1}{1-C}\big(C^{N-i-1}(1+C) - 2\big)(\vec{E}_{cN} - \vec{E}_{oN}) \Bigg) \\ & + b_1 \left(S\frac{1-C^N}{(1-C)^2}(\vec{E}_{cN} - \vec{E}_{oN}) + \sum_{j=1}^{N} \left(C^{j-1}\vec{E}_{sj} + \frac{S}{1-C}(1-C^{j-1})\vec{E}_{oj} \right) \right) \\ & + I_b \left(\sum_{j=1}^{N} \vec{E}_{oj} + \frac{1}{1-C}(\vec{E}_{cN} - \vec{E}_{oN}) \right) - I_e \frac{1}{1-C}(\vec{E}_{cN} - \vec{E}_{oN}). \end{aligned} \tag{14}$$

An identical expression is valid for $\vec{H}$. The wire has now $N+2$ free parameters, $a_1 \ldots a_{N-1}$, b_1, I_b and I_e.

For completeness, we give also the derivatives I' of the current at the wire ends as a function of the $N+2$ unknowns:

$$I'_b = kb_1; \tag{15-1}$$

$$I'_e = \frac{k}{1-C}\left(S(I_e - I_b) + b_1(2C^N - C - 1) + 2S\sum_{j=1}^{N-1} a_j\big(1 - C^{N-j}\big) \right). \tag{15-2}$$

References

[1] Ch. Hafner, *The GMT-technique for computational electromagnetics* (prospective title), to be published by Artech House Inc., 1990.

[2] P. Leuchtmann, "A completely automated procedure for the choice of functions in the MMP-method," in *Proc. of the International Conference on Computational Methods in Flow Analysis*, (Okayama), pp. 71-78, June 1988.

[3] G.J. Burke and A.J. Poggio, "Numerical electromagnetics code (NEC) — Method of Moments", NOSC Technical Document 116, Vol. 1, Lawrence Livermore Laboratory, Livermore, CA, January 1981.

[4] N. Kuster and R. Tell, "A dosimetric assesment of the significance of high intensity rf field exposure resulting from reradiating structures," in *Proc. of the 11th Annual Meeting of the Bioelectromagnetic Society.*, (Tucson), June 1989.

[5] Ch. Hafner, *Numerische Berechnung elektromagnetischer Felder*. Springer Verlag, 1987.

[6] L. Bomholt, P. Regli, Ch. Hafner, P. Leuchtmann, "MMP-3D: A package for computation of 3D electromagnetic fields on PCs and Workstations." In this conference.

ULTRA HIGH GAIN ANTENNA ARRAYS

Ross A. Speciale
General Dynamics, Ontario, California
and
Paul F. Wacker
Retired NBS Senior Scientist

1 SUMMARY

A new, rigorous vectorial theory of Ultra High Gain Antenna Arrays has been developed, to identify and analyze physically possible finite-aperture field-distributions, consistent with the "Curl-Curl" or "Vector Helmoltz" equation, that would generate practically feasible approximations to non-diffracting electromagnetic beams.

The new theory expresses the radiated array field as a two- dimensional vector linear combination of exact solutions of Maxwell's equations, in circular cylindrical coordinates (cylindrical modes), and imposes three fundamental conditions: a) That the radial component of the time-averaged energy flow be everywhere zero, b) That the axial component k_z of the wave number **k** be real, and c) That the time-averaged real energy flow within a broadside beam-cylinder, with cross-section equal to the array aperture, be as large as possible, as compared to the total radiated energy.

The energy flow within the broadside beam-cylinder and the approximate total radiated energy are first computed by integrating the real part of the z-component of the complex Poynting's vector, azimuthally and radially, from the beam axis to the array edge, and again to a much larger finite radius. An expression of the ratio of the average energy density within the beam-cylinder to the approximate total energy density is then computed, and analyzed for possible maxima as function of: a) The maximum electrical radius at the array edge, and b) The spectrum of cylindrical modes used to define the finite-aperture field-distribution across the array radiating surface.

The new theory shows that the maximization of the energy flow within the beam-cylinder can be pursued independently for each set of cylindrical modes with equal azimuthal symmetry index m in the spectrum, and that the individually maximized results can be subsequently added to attain an almost uniform energy-density distribution across the given array aperture.

With the only exception of one rapidly converging series expansion, closed-form expressions of the integral of the z- component of the Poynting's vector along the radius have been obtained, in terms of Bessel functions of the first kind, of various integer and half-integer orders. A substantial volume of numerical computations has already been performed, to characterize the new beam fields. These fields are steady-state, time-harmonic solutions of Maxwell's equations that approximate, in a physically realizable way, non-diffracting, vectorial electromagnetic beams, characterized by both finite axial and azimuthal energy flow and zero radial energy flow. Should sufficiently accurate and practically feasible approximations be found, ultra high gain antenna arrays could be designed that would generate beams of essentially constant cross-section characterized by little or negligible axial attenuation over very large propagation distances. Such beams are of obviously exceptional interest in many practical electromagnetic systems at microwave and millimeter wave frequencies. An intensive program of numerical computation is in progress.

2 PATTERN SYNTHESIS IN THE SPECTRAL DOMAIN

In an effort to design broadside arrays with especially high directivity, we use, as a first approximation, linear combinations of exact solutions of Maxwell's equations, solutions for which the radial com-

ponent of time-averaged energy flow is everywhere zero. We choose combinations for which the axial (z direction) component of total energy flow from within the diameter of the array is large.

We express the fields in terms of circular cylindrical coordinates, using the complex exponential forms of Hansen's **m** and **n** functions

$$\mathbf{m}_{m\lambda} = e^{im\phi} \left[m\, i\, \xi\, \hat{\mathbf{e}}_R - \delta\, \hat{\mathbf{e}}_\phi \right] \tag{1}$$

and

$$\mathbf{n}_{m\lambda} = \frac{e^{im\phi}}{k} \left[i\, h\, \delta\, \hat{\mathbf{e}}_R - h\, m\, \xi\, \hat{\mathbf{e}}_\phi + \lambda^2\, R\, \xi\, \hat{\mathbf{e}}_z \right] \tag{2}$$

where:

$h = k_z$, $\lambda = k_R = \sqrt{k^2 - h^2}$, $\xi = Z_m(\lambda R)/R$, and $\delta = \frac{\partial}{\partial R} Z_m(\lambda R)$, where m is the azimuthal index (a signed integer), and Z_m is a cylindrical Bessel function of any kind. Then the contributions to the field for given values of m and λ are:

$$\mathbf{E}_{m\lambda} = -\left(a_{m\lambda}\, \mathbf{m}_{m\lambda} + b_{m\lambda}\, \mathbf{n}_{m\lambda} \right) e^{(ihz - i\omega t)} \tag{3}$$

and

$$\mathbf{H}_{m\lambda} = -\, k\, \left(b_{m\lambda}\, \mathbf{m}_{m\lambda} + a_{m\lambda}\, \mathbf{n}_{m\lambda} \right) \frac{e^{(ihz - i\omega t)}}{i\omega\mu} \tag{4}$$

Confining attention to fields in which all the modes have the same constant value of ω, the time-average intensity of energy flow is the real part of the complex Poynting's vector, i.e., of

$$\mathbf{S}^* = \frac{1}{2}\, \mathbf{E} \times \tilde{\mathbf{H}} = \frac{1}{2} \begin{vmatrix} \hat{\mathbf{e}}_R & \hat{\mathbf{e}}_\phi & \hat{\mathbf{e}}_z \\ \mathbf{E}_R & \mathbf{E}_\phi & \mathbf{E}_z \\ \tilde{\mathbf{H}}_R & \tilde{\mathbf{H}}_\phi & \tilde{\mathbf{H}}_z \end{vmatrix} , \tag{5}$$

where $\tilde{}$ indicates that the complex conjugate is to be taken [4]. (Although this analysis is only for a single constant value of ω, there may be any number of co-located independent systems, provided that each system a) transmits only a single frequency, and b) receives only one of the transmitted frequencies.) To obtain the total energy flow from within a given radius or annulus on the infinite $z = 0$ plane, integration is first carried over ϕ, which eliminates both the $e^{im\phi}$ factors and every product which involves two different m values. Therefore, the integrations over R can be carried out for each m value separately and the results then added if desired.

Hence, we confine attention to individual m values and to fields with zero radial propagation, i.e., fields for which the real part of the $\hat{\mathbf{e}}_R$ component of (5) is everywhere zero. Further, to simplify both analytical integrations and numerical computations, we confine attention, at least initially, to fields for which a) the Bessel functions are of the first kind ($J_m(\lambda R)$'s), b) ω, λ, and h are real, and c) for each m

value there is only one value each of h and λ. Note that this eliminates, from (5), modes with radial energy propagation and the $e^{(ihz-i\omega t)}$ factors (the time dependence and attenuation in the z direction). Suppressing the subscripts on the a's, b's, m's, and n's, the integral over ϕ for a given m is:

$$\int_0^{2\pi} \mathbf{S}^* d\phi = -\frac{\pi\tilde{k}}{\bar{i}\omega\tilde{\mu}} \begin{vmatrix} \hat{e}_R & \hat{e}_\phi & \hat{e}_z \\ ami\xi + bih\delta/k & -a\delta - bhm\xi/k & b\lambda^2 R\xi/k \\ -\bar{b}mi\bar{\xi} - \bar{a}ih\bar{\delta}/\tilde{k} & -\bar{b}\bar{\delta} - \bar{a}hm\bar{\xi}/\tilde{k} & \bar{a}\bar{\lambda}^2 R\bar{\xi}/\tilde{k} \end{vmatrix} \tag{6}$$

Then assuming that k, μ and the a and b coefficients are real, there is no radial energy flow in the fields. Also, the flow is unchanged if the phases of a and b are increased (or decreased) by the same amount.

With the dimensionless abbreviation $\zeta = h/k$, the z component of the energy flow within a given radius or annulus is given by:

$$Re\ \{ \frac{\pi k}{[-i]\omega\mu} \int_{R_1}^{R_2} [(ami\xi + bi\zeta\delta)(-b\delta - am\zeta\xi) - (-a\delta - bm\zeta\xi)(-bmi\xi - ai\zeta\delta)]\ RdR \ \} \tag{7}$$

$$= \frac{\pi k}{\omega\mu} \int_{R_1}^{R_2} [(am\xi + b\zeta\delta)(b\delta + am\zeta\xi) + (a\delta + bm\zeta\xi)(bm\xi + a\zeta\delta)]\ RdR \tag{8}$$

$$= \frac{\pi k}{\omega\mu} \int_{R_1}^{R_2} [(a^2 + b^2)\zeta(m^2\xi^2 + \delta^2) + 2abm\xi\delta(1 + \zeta^2)]\ RdR \tag{9}$$

(The azimuthal flow is not pertinent, in itself, to directivity.) Replacing λR by ϱ , the individual integrals (for integer m) are:

$$\int_0^{R_M} \xi\delta R\ dR = \int_0^{\varrho_M} J_m(\varrho)\ (\partial/\partial\varrho) J_m(\varrho)\ d\varrho = \frac{1}{2}\{\ [J_m(\varrho_M)]^2 - [J_m(0)]^2\ \} \tag{10}$$

$$\int_0^{\infty} \xi\delta R\ dR = -\delta_{m0}/2 \qquad (\delta_{m0}\ is\ Kronecker\ \delta) \tag{11}$$

$$\int_0^{R_M} \xi^2 R\ dR = \int_0^{\varrho_M} J_m(\varrho)\ J_m(\varrho)/\varrho\ d\varrho \tag{12}$$

$$m \neq 0: \quad = \frac{1}{2m} \int_0^{\varrho_M} J_m(\varrho)[J_{m-1}(\varrho) + J_{m+1}(\varrho)]\ d\varrho \tag{13}^5$$

$$m = 1: \quad = \frac{1}{2m}\ \{\ 1 - [J_0(\varrho_M)]^2 - [J_1(\varrho_M)]^2\ \} \tag{14}^6$$

$$m > 1: \quad = \frac{1}{2m} \left\{ 1 - [J_0(\varrho_M)]^2 - [J_m(\varrho_M)]^2 - 2 \sum_{n=1}^{m-1} [J_n(\varrho_M)]^2 \right\} \tag{15}^6$$

$$\int_0^\infty \xi^2 \, R \, dR = \frac{1}{2m} \qquad (m \neq 0) \tag{16}$$

$$\int_0^{R_M} \delta^2 R \, dR = \int_0^{\varrho_M} [(\delta/\delta\varrho) J_m(\varrho)]^2 \, \varrho \, d\varrho = \int_0^{\varrho_M} \left[-J_{m+1}(\varrho) + \frac{m}{\varrho} J_m(\varrho) \right]^2 \varrho \, d\varrho \tag{17}$$

$$= \frac{1}{4} \int_0^{\varrho_M} \left\{ [J_{m+1}(\varrho)]^2 - \frac{2m}{\varrho} J_m(\varrho) \, J_{m+1}(\varrho) + (m/\varrho)^2 [J_m(\varrho)]^2 \right\} \varrho \, d\varrho \tag{18}^5$$

$$m = 0: \quad = \int_0^{\varrho_M} [J_1(\varrho)]^2 \, \varrho \, d\varrho = \frac{\varrho_M^2}{2} \left\{ [J_1(\varrho_M)]^2 - J_0(\varrho_M) \, J_2(\varrho_M) \right\} \tag{19}^5$$

$$m \geq 1: \quad = \frac{\varrho_M^2}{2} \{ [J_{m+1}(\varrho_M)]^2 - J_m(\varrho_M) \, J_{m+2}(\varrho_M) \}$$

$$- \frac{m}{2} \{ 1 - [J_0(\varrho_M)]^2 - 3 [J_m(\varrho_M)]^2 - 2 \sum_{n=1}^{m-1} [J_n(\varrho_M)]^2 \} \tag{20}^{6,9}$$

An equivalent analytic expression of the integral (17) should be:

$$m \geq 1: \quad = \frac{\varrho_M^2}{8} \left\{ [J_{m-1}(\varrho_M)]^2 + [J_{m+1}(\varrho_M)]^2 - J_{m-2}(\varrho_M) \, J_m(\varrho_M) - J_m(\varrho_M) \, J_{m+2}(\varrho_M) \right\}$$

$$- \frac{\sqrt{\varrho_M} \; \Gamma(m+1)}{2^{2(m+1)} \, \Gamma(m) \, [\Gamma(m+2)]^2} \sum_{n=0}^{\infty} \frac{(2m + 2n + \frac{3}{2}) \, \Gamma(2m + n + \frac{3}{2}) \, J_{2m+2n+\frac{3}{2}}(2\varrho_M)}{n!}$$

$$\times \; {}_5F_4 \left| \begin{matrix} m + \frac{1}{2} , & m+1 , & m+1 , & 2m + n + \frac{3}{2} , & -n \\ m+2 , & m , & 2m+1 , & m+2 & \end{matrix} \right| \tag{20a}$$

where the ${}_5\mathbf{F}_4$ factor is a generalized hypergeometric function of unit argument [5], [7], [8]. (The cross-term of (18) is evaluated as Bailey's (4.1) [7], where $\nu = m-1$, $\lambda = m+1$, $\varrho = z \sin\theta$, $d\varrho = z \cos\theta \, d\theta$, $\mu = 0$, $\kappa = 0$, $\alpha = 3/2$, $z = \varrho_{max}$, and the ${}_5\mathbf{F}_4$ function of page 145 replaces the ${}_4\mathbf{F}_3$ function in the equation on page 144. With the arguments given in equation (20), the ${}_5\mathbf{F}_4$ function is Saalschutzian, but not well-poised, and cannot, apparently, be summed. The negative fifth numerator parameter will, however cause truncation of its series expansion.)

The summation in the second term of equation (20) includes a finite number $m-1$ of positive terms, and can therefore be easily evaluated numerically in a very short time. On the contrary, the infinite series in

the second term of equation (20a) includes terms of alternating sign, and has so far failed to converge to the expected right value of its sum.

As a first approximation to a design for a given array radius, we choose a combination of m, λ, a, and b based upon the z component of flow [Eq. (9)] from the z = 0 plane. Specifically, we choose the combination which maximizes the ratio of the flow from within the given radius to that from within a radius many times as large. The ratio is given by

$$\frac{(1+\beta^2)u+\beta v}{(1+\beta^2)U+\beta V} \tag{21}$$

where β = b/a, u and U are the values of $\int_0^{R_M} \zeta\ (m^2\ \xi^2+\delta^2)R\ dR$ for the given and large radii respectively, and v and V are the respective values of $2m\int_0^{R_M} \xi\ \delta\ (1+\zeta^2)R\ dR$. Setting the derivative of (21) equal to zero yields the conditions

$$[(1+\beta^2)U+\beta V](2\beta u+v) = [(1+\beta^2)u+\beta v](2\beta U+V)$$

$$Uv+\beta(2uU+vV)+\beta^2(Uv+2uV)+2\beta^3uU = uV+\beta(vV+2uU)+\beta^2(2Uv+uV)+2\beta^3uU$$

$$Uv+\beta^2(Uv+2uV) = uV+\beta^2(uV+2Uv)$$

$$\beta = \sqrt{\frac{uV-Uv}{Uv+2uV-uV-2Uv}} = \pm 1. \tag{22}$$

For one of the two signs (plus or minus), (22) gives the "optimal" ratio of b to a, given m and λ. (Dividing both numerator and denominator by a^2 rather than b^2 introduces no loss of generality since (9) is invariant with respect to an interchange of a and b.)

To simplify the choice of m and λ, we make use of the fact that, for a fixed m, (10), (12), and (17) are functions of a single variable, the upper limit $\varrho_M = \lambda R_M$, and plot their contributions to (9) as functions of the limit. More precisely, we renormalize their contributions to (9) for computational convenience and divide by both ϱ_M^2 and k^2 to simplify estimation of the z component of flow per unit area of the array. Specifically, we define F and G as $2m(10)/\varrho_M^2$ and $[m^2(12)+(17)]/\varrho_M^2$, respectively, yielding

$$\frac{\lambda^2}{k^2}\ [(1+\beta^2)\zeta G+\beta(1+\zeta^2)F] \tag{23}$$

(23) as the renormalized z component of energy flow per unit area. Since all the quantities in are positive, except possibly β, β must be positive for a maximum, giving

$$(1-\zeta^2)[2\zeta G+(1+\zeta^2)F] \tag{24}$$

since $\lambda^2/k^2 = 1-\zeta^2$. For G = 0, (24) is a maximum for $\zeta = 0$ (λ = k), while for F = 0, it is maximum for $\zeta = (1/3)^{1/2}$ ($\lambda = (2/3)^{1/2}$k). More generally, a maximum of (24) must satisfy the condition

$$\zeta^3+3g\zeta^2-g = 0, \tag{25}$$

where g = G/2F. Hence, the desired root may be plotted as a function of g; moreover, the ratio of the maximum to G may also be plotted as a function of g. Note that the procedure for determining the

"optimal" values of m, λ, ζ, and a/b is independent of the values of ω, k, and μ. F and G are plotted, for a given m, as functions of the dimensionless variable ϱ_M, while both the "optimal" value of $\zeta = k_z/k$ and the dimensionless ratio of the maximum (of (24)) to G are plotted as functions of the dimensionless variable g. Note that these functions of g are independent of m as well as of ω, k, μ, and ϱ_M. However, the radius of the array in terms of wavelength, kR_M, determines the range of ϱ_M values of interest for F and G and, in turn, the "optimal" values of m, ζ, and λ. To minimize truncation effects, the integrands (e.g., the slope of $\varrho^2(23)/(1-\zeta^2)$) should presumably be small at the chosen array radius.

Because Bessel functions of higher order build very slowly for small arguments, m should not be very large, particularly for small arrays. However, because larger m values permit closer azimuthal changes of phase (without change of λ or h), m should not be too small, particularly for large arrays. For a large array, it may be that a combination of a large m (for close azimuthal spacing at the outer rings) and a small m (to fill in the inner rings) would be desirable. Note that there is no z component of energy flow on axis, even for $m = 0$ [(9),(19)]. Large values of λ permit close radial spacing, but $\lambda = k$ causes ζ to be zero in (9) and (23), and larger values cause exponential damping in the z direction. Note also that both (12) and (17) are real and non-negative and that (12) cannot be greater than $1/2m$.

Having found "optimal" values of the m's, λ's, a's, and b's, the pattern may be "fine tuned" with the aid of the variational method in combination with computation of the far-field directivity from the near-field pattern.

3 PATTERN SYNTHESIS STRATEGY.

In an effort to determine broadside-array patterns of especially high directivity, the fields are expressed as linear combinations of exact global three-dimensional six-vector solutions of Maxwell's equations in circular cylindrical coordinates. (These may be considered to be the modes of an infinitely-long circular cylindrical waveguide of infinite radius.) To obtain the high directivity, the constituent solutions are confined to those for which the radial component of the time-averaged energy flow is everywhere precisely zero. Assuming that the propagation constant k and the magnetic susceptibility μ are real and that there is a single real frequency ω, the complex Poynting vector shows that the total fields have zero time-averaged radial components if all the Bessel functions are of the first kind and the propagation-constant components k_z and k_R are real. (Any number of frequencies may be used, with each frequency being considered as a separate problem, if each transmitter transmits only a single frequency and no receiver receives more than one of the frequencies.)

The effect of truncation of the array radius to any given practical value R_{max} is minimized by a) maximizing the total z-component of energy flow from within the given array radius on the $z = 0$ plane and b) minimizing its rate of change at that radius. (The azimuthal component does not (in itself) affect the directivity nor does the m value affect the relation between k, k_z, and k_R.) Henceforth, 'flow' will indicate the z-component of the energy flow. To obtain the total flow from within a radius or annulus, integration is first carried out over the azimuthal angle ϕ and then with respect to the radius. The azimuthal integration eliminates every term with two <u>different</u> m values, permitting investigations to be carried out <u>for each m</u> value separately, followed by simple addition if desired. By confining k_R (and therefore k_z) to a single value for each m and confining the modal coefficients to real values, it was possible to carry out all the integrations analytically. Under these conditions, it was shown that maximum total flow from within a given radius R_{max} occurs when the coefficients of the TE and TM solutions for the given m are equal in both magnitude and sign. Further, it was then shown that the total flow per unit area <u>for each m</u> is proportional to a weighted sum of two explicit functions F_m and G_m of the dimensionless variable $k_R R_{max}$, where the weights are simple functions of k_z/k. Differentiating with respect to k_z/k, it was shown that the maximum flow is obtained when k_z/k is a root of an explicit cubic equation with the single constant $g_m = G_m/2F_m$; further, the ratio of the maximum total flow per unit area to G_m (or to F_m) is a function of g, independent of the m value. For a given ω and R_{max}, maxima in the plots of the F_m's and G_m's, together with the latter ratio function, thus permit choice of

k_R for each m value of interest. (The rate of change of the energy flow at R_{max} is proportional to $(k_R R_{max})^2/[1-(k_z^2/k^2)]$ times the preceding total energy flow per unit area and is usually small near its maxima.)

Because of the slow growth of Bessel functions for large m, m should not be too large, particularly for small $k_R R_{max}$. However, for large $k_R R_{max}$, large m permits closer azimuthal spacing at the outer radii. Particularly for large radii, two or more m values may be desirable, e.g., large m for outer radii and small m for the inner radii. The k_R values for the different m's may be chosen so that one curve roughly fills in the minima of the other, permitting increased total output from a given area when the output per element is limited. (Changing the value of k_R for one or more m values permits shifting of maxima or minima.) The fields obtained with the preceding choices of the m's, k_R's, and the ratios of the TE to TM coefficients may be "fine tuned" with the variational method in combination with computations of the far-field directivity from the near finite-aperture fields.

4 NUMERICAL RESULTS

Very preliminary numerical results, and graphic displays have already been generated (Figures 1 - 6). Three MATLAB functions, that evaluate the three partial Bessel function integrals expressed by equations (10), (12) - (15), and (17) - (20), were first written. Four more MATLAB functions use the three integrals to evaluate the functions F, G, g, and to find the roots of the cubic (25). One of the three roots of the cubic, identified as root 3, is always real for $g > 0$, and it has been assumed to represent the optimum value of the normalized radial wave number $\zeta = k_r / k$, and used to determine the normalized radial wave number, $\lambda_M = k_r / k$. The optimum values of ζ, λ_M, and the values of the functions F and G have then been used to evaluate the optimized, time-averaged axial component of the radiated energy density, expressed by Real $(S_z^*)/\pi \times R_M$, where Real (S_z^*) is given by equation (9).

The obtained values of the time-averaged axial component of the energy density are displayed in Figures 1 - 3, as functions of the array maximum radius R_M, measured in free-space wavelengths, for the integer values 0 to 10 of the azimuthal symmetry index m of the different sets of cylindrical modes. The time-averaged axial component of the energy density is maximum on axis only for $m = 1$, while the maximum moves to a larger radius for $m = 0$, and to increasingly larger radii for increasing $m > 1$ values.

The fundamental implication of these results is that the determined radial dependence of the radiated energy density, displayed in Figures 1 - 3, is independent of time and of the downrange distance z from the array aperture surface, assumed to be at $z = 0$.

The Figures 4 to 8 illustrate various aspects of the aperture distribution, for a cylindrical mode with azimuthal symmetry index $m = 1$, and with a normalized radial wave number $\lambda_N = (2/3)^{1/2}$. The length L of the square aperture side is ten free-space wavelengths, and the patterns have been truncated at an arbitrary maximum radius. Figure 4 shows the amplitude distribution fo the radial electric field component E_R, and Figure 5 shows the phase pattern of the azimuthal electric field component E_P, while Figures 6 and 7 show the amplitude distributions of the X-axis and Y-axis electric field components E_X and E_Y. Finally, Figure 8 shows the amplitude distribution of the axial component S_z^* of the complex Poynting's vector.

Further numerical evaluations are in progress to determine the structure of the optimized aperture field distributions, corresponding to different m values and in terms of the E, H, and S* vectors, and to determine the truncation effects induced by the choice of a finite optimum maximum radius R_M for the array aperture.

5 REFERENCES.

[1] P.F. Wacker, "Unified theory of near-field analysis and measurement: Scattering and inverse scattering," IEEE Trans. Antennas and Propagation., vol. AP-29, pp. 342-351, 1981.

[2] J.A. Stratton, Electromagnetic Theory. New York: McGraw-Hill, p. 397, 1941.

[3] J.A. Stratton, Electromagnetic Theory. New York: McGraw-Hill, pp. 394, 396, 1941.

[4] J.A. Stratton, Electromagnetic Theory. New York: McGraw-Hill, (29), (30), p. 137, 1941.

[5] P.M. Morse and H. Feshbach, Methods of Theoretical Physics. New York: McGraw-Hill, p. 1322, 1953.

[6] A. Erdelyi, Tables of Integral Transforms, vol. 2, (35), (36), p. 338, New York: McGraw-Hill, 1956.

[7] W.N. Bailey, "Some integrals involving Bessel functions," Quart. J. Math. Oxford Ser., vol. 9, pp. 141-147, 1938.

[8] A. Erdelyi, Higher Transcedental Functions, vol. 1, Chaps. II and IV, New York, McGraw-Hill, 1956.

[9] G. N. Watson, A Treatise on the Theory of Bessel Functions, 5.11, Equation (11), p. 135, and 5.12, Equation (6), p. 137, 2nd Edition, Cambridge at the University Press, 1962.

ACKNOWLEDGEMENTS

The authors wish to express their deepest appreciation and gratitude for the unrelenting and persistent efforts delivered by Mr. Ramon Suehrstedt and Miss Laurie Kristinat in carefully composing and editing the manuscript of this paper.

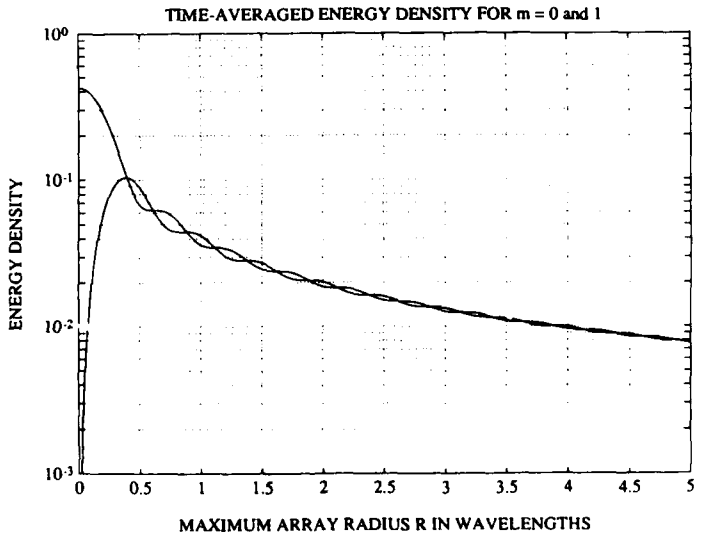

Figure 1 – Optimized Axial Component of the Radiated Energy Density, as Function of the Array Maximum Radius R_M, in Free-Space Wavelengths, for Modes with Azimuthal Symmetry Index m = 0, and m = 1, and for R_M from 0 to 5.

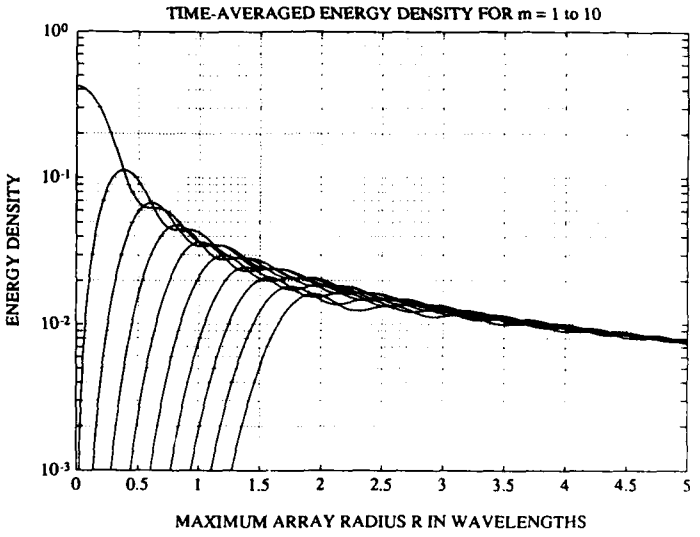

Figure 2 – Optimized Axial Component of the Radiated Energy Density, as Function of the Array Maximum Radius R_M, in Free-Space Wavelengths for Modes with Azimuthal Symmetry Index m = 1 to 10, and for R_M from 0 to 5.

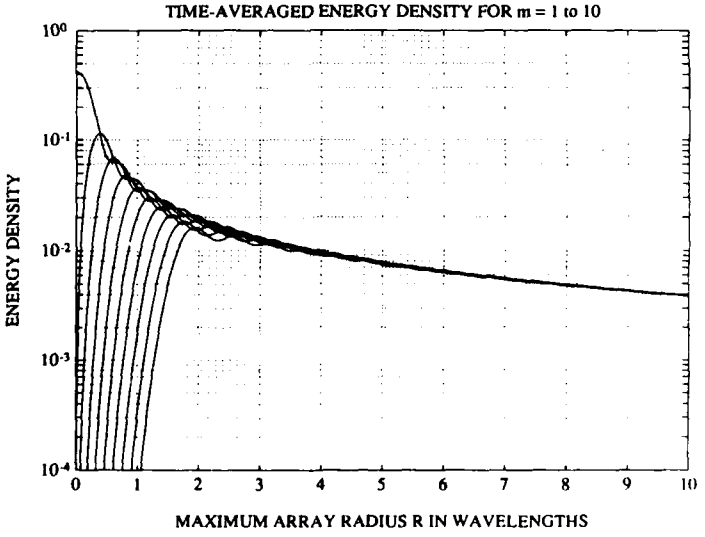

Figure 3 – Optimized Axial Component of the Radiated Energy Density, as Function of the Array Maximum Radius R_M, in Free-Space Wavelengths, for Modes with Azimuthal Symmetry Index m = 1 to 10, and for R_M from 0 to 10.

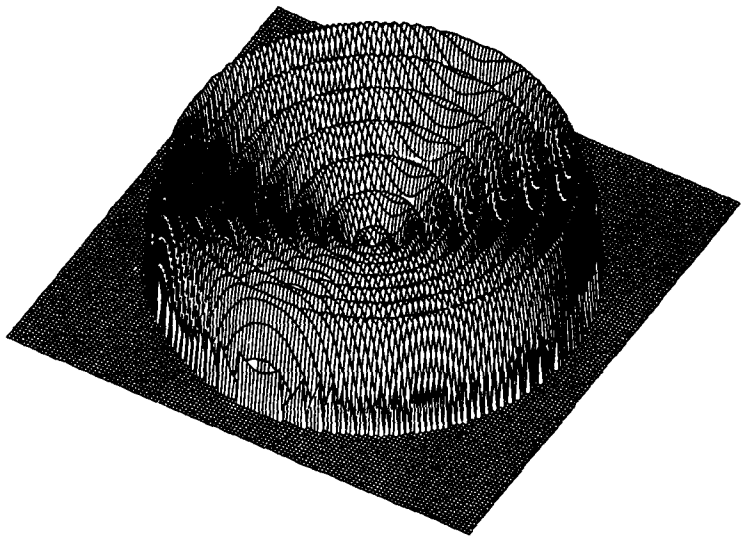

Figure 4 – Amplitude Distribution of the Radial Electric Field Component E_R, of a Cylindrical Mode, with Azimuthal Symmetry Index m = 1, and Normalized Radial Wave Number $\lambda_N = (2/3)^{1/2}$. The Size of the Square Aperture is 10 by 10 Free–Space Wavelengths.

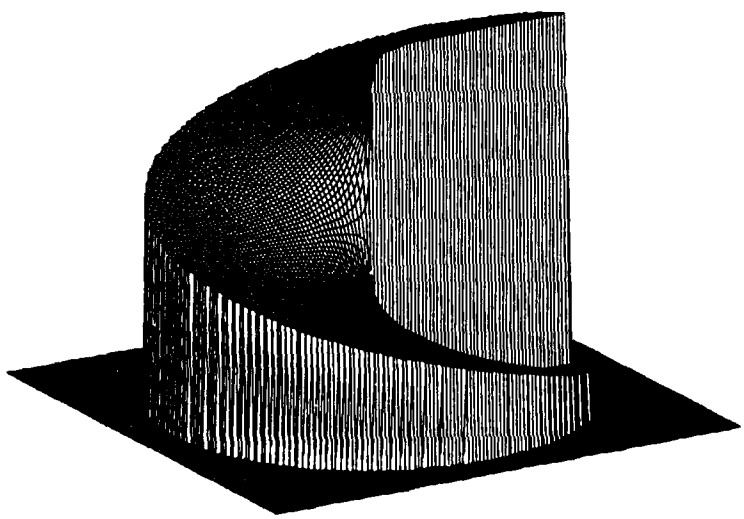

Figure 5 – Phase Distribution of the Azimuthal Electric Field Component E_P, of a Cylindrical Mode, with Azimuthal Symmetry Index m = 1, and Normalized Radial Wave Number $\lambda_N = (2/3)^{1/2}$. The Size of the Square Aperture is 10 by 10 Free–Space Wavelengths.

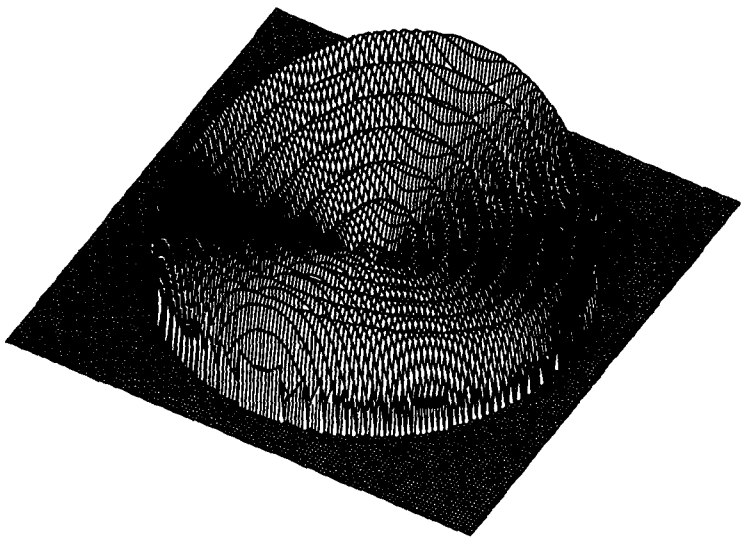

Figure 6 – Amplitude Distribution of the X-Axis Electric Field Component E_X, of a Cylindrical Mode, with Azimuthal Symmetry Index m = 1, and Normalized Radial Wave Number $\lambda_N = (2/3)^{1/2}$. The Size of the Square Aperture is 10 by 10 Free-Space Wavelengths.

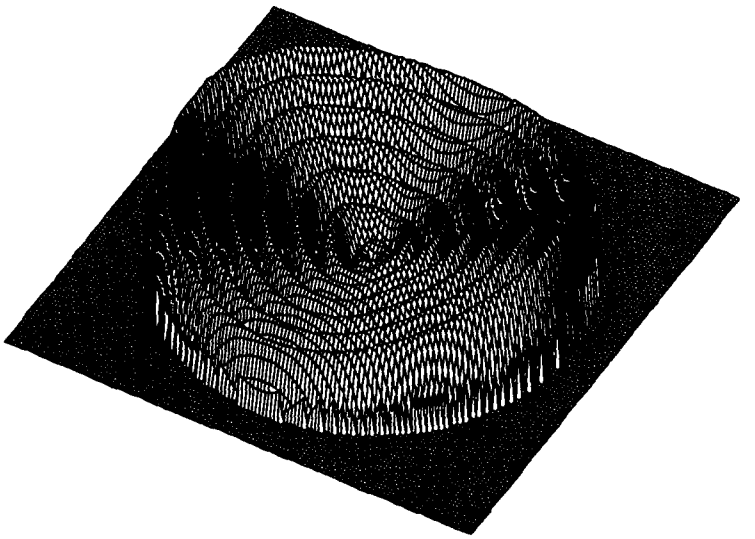

Figure 7 – Amplitude Distribution of the Y-Axis Electric Field Component E_Y, of a Cylindrical Mode, with Azimuthal Symmetry Index m = 1, and Normalized Radial Wave Number $\lambda_N = (2/3)^{1/2}$. The Size of the Square Aperture is 10 by 10 Free-Space Wavelengths.

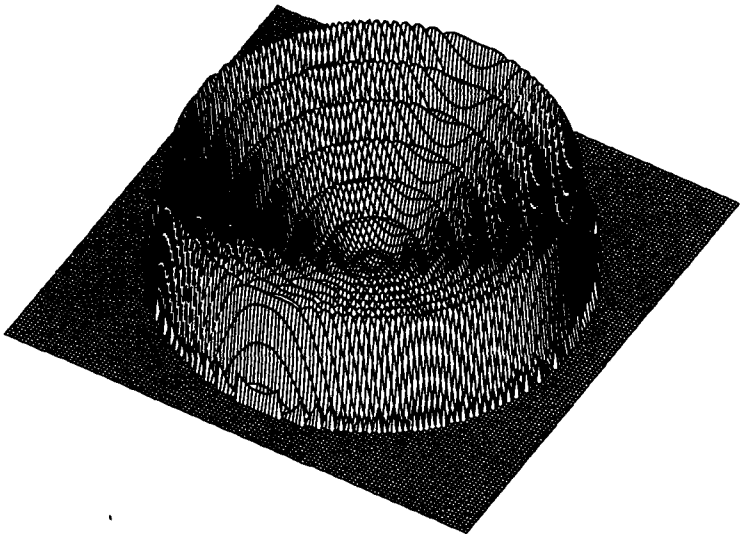

Figure 8 – Amplitude Distribution of the Axial Component S_z^*, of the Poynting's Vector for a Cylindrical Mode, with Azimuthal Symmetry Index m = 1, and Normalized Radial Wave Number $\lambda_w = (2/3)^{1/2}$. The Size of the Square Aperture is 10 by 10 Free-Space Wavelengths.

Parallel Modelling of Electromagnetic Field Scattering For Coupled Antenna-Dielectric Systems

G.W. Chege R.W. Taylor J.M. Tealby
Department of Electronics, University of York

1 Introduction.

Work has been carried out to investigate how novel parallel computing environments may be used in modelling electromagnetic (EM) field scattering for coupled wire antenna-dielectric systems. This is important for such diverse applications as printed circuit board design, hyperthermia therapy, control of radar cross sections and design of microwave devices. The techniques developed have made use of a number of different processor topologies, exploiting the natural properties of distributed arrays to provide efficient implementations.

In the frequency domain, open boundary EM scattering is normally treated in three ways: (1) Integral equation formulation of which *moment method* is best known, (2) partial differential equation formulation with finite elements and finite diferences being more widely used, and (3) hybrid techniques which combine integral and partial differential formulations. The integral techniques are advantageous in terms of simple discretization of regions and simple numerical implementation. However, they suffer from costly full matrices and are difficult to implement for complex media. Partial differential formulations have simple numerical implementation but require far field radiation conditions resulting in a large number of unknowns. The hybrid techniques combine the advantages of both integral and differential forms and eliminate their weaknesses, though they require more effort to implement.

Two numerical techniques (viz: the *finite element method* and the *moment method* have been attempted. The finite element method (FEM) is a compute intensive technique especially for 3-D problems requiring thousands of element discretizations and has therefore become a candidate for parallel processing. It has led to a search for efficient numerical algorithms especially of the sparse matrix type. An MIMD research machine bearing its name (the Finite Element Machine) has been built at NASA Langley Research Centre, underlining the importance of the coupling between the finite element method and distributed computing [Jordan78]. FEM has been implemented in this work [Chege88] and has been found adequate for uncoupled antennas but despite its attractive properties for modelling arbitrarily shaped objects, it is deemed unsuitable for generalized 3-D unbounded scattering (some methods for handling unbounded problems exist; e.g. [Silv77, Brauer82, Emson88]). Hence, the technique has not been used for 3-D problems. This is mainly due to the open boundary far field condition mentioned above. Moment methods (MM) plays a central role in the integral formulation of scattering problems [Harri68]. A computer code (Numerical Electromagnetics Code - NEC) for analysis of wire antennas and surfaces has been developed at Lawrence Livermore Labs, California, and is available to researchers in von Neumann computing environments [Burke81]. The general MM technique has been adopted in this work and a complex conjugate gradient technique used to solve the resulting complex matrices.

This work is based on the Edinburgh Concurrent Supercomputer (ECS), currently under development at the University of Edinburgh [Stro88]. Started in 1986 the ECS MIMD system has 500 T800 transputers each with 4MB of RAM and is targeted to have 1024 T800s on completion. Each of these modules provide performance equivalent to that of a DEC VAX 8600 when executing a standard Fortran 77 application. The transputer (*trans*istor com*puter*) is a computer on silicon having four major subsystems: CPU, RAM, communication links module, memory interface module and a floating point engine in the case of the T800 series. Processes executing on a single transputer commununicate via 'soft' internal channels while interprocessor communication which is unbuffered is via one of four serial links. Occam, the native parallel processing language of the transputer, is used here as a large scale numeric vehicle. It is based

on Hoare's Communicating Sequential Processes (CSP) paradigm of concurrency [Hoare78], [Hoare85] and has some similarities with ADA.

The overall effort from problem formulation through discretization and solution of the resulting complex matrices for problems of the type under consideration here, is mainly compute bound and expensive. As far as we are aware, this kind of work has not been done in parallel environments. Most researchers upto date have used von Neumann computing techniques [Casey88], [Kari80], [Live74]. In this work, a transputer based MIMD parallel computing environment is used in an effort to bring parallel computing to EM engineering problems and it is here that we hope to raise awareness in the potential benefits to computational electromagnetics. Work has been carried out on 5 and 17 processor platforms and some preliminary work on 128 processors is discussed here. A new model for investigating EM scattering in dielectric cages excited by a wire antenna is also discussed.

Occam is used throughout as a large scale numeric compiler. Some of the parallel computing pitfalls to be overcome include load balancing, problem mapping to minimize interprocessor communications, and the more common ones like deadlocks and livelocks.

2 Theory: Mathematical Formulation

2.1 Simple coupling problems

Here, a short integral formulation for coupled antenna-body systems is described. Consider a wire antenna in the presence of a dielectric body as shown in Fig.1. For simplicity, we consider a hollow straight wire of length L and a dielectric of uniform cross section (these generalisations do not restrict the formulation, although adjustments are necessary for thick cylindrical antennas), with conductivity $\sigma(\mathbf{r})$, permitivity $\varepsilon(\mathbf{r})$ and with free space permeability μ_0.

By the equivalence theorem, the antenna-dielectric system can be replaced by free space and equivalent current densities $\mathbf{J_a(r)}$ for the antenna and $\mathbf{J_{eq}(r)}$ for the dielectric body. By definition the scattered fields are the difference between total fields $\mathbf{E_T(r)}$ and the incident field $\mathbf{E^i(r)}$. In the equivalent problem, the scattered fields are the free space fields of $\mathbf{J_a(r)}$ and $\mathbf{J_{eq}(r)}$ which we label $\mathbf{E^a(r)}$ and $\mathbf{E^b(r)}$ respectively. The total fields are therefore given by

$$\mathbf{E_T(r)} = \mathbf{E^a(r)} + \mathbf{E^b(r)} + \mathbf{E^i(r)} \tag{1}$$

and

$$\mathbf{H_T(r)} = \mathbf{H^a(r)} + \mathbf{H^b(r)} + \mathbf{H^i(r)} \tag{2}$$

where the superscripts 'a' and 'b' refer to scattered fields by antenna and body and 'i' refers to incident fields. Using Green's free-space dyadic, we can obtain electric field integral equations (EFIEs) for the equivalent currents.

By assuming a thin wire kernel, we can take an axial current I(s) on the antenna surface giving

$$\mathbf{E^a(r)} = \int_{\mathbf{L}} \mathbf{I(s')\hat{s}'.\vec{G}(r,s')ds'} \tag{3}$$

and for the dielectric body,

$$\mathbf{E^b(r)} = \mathbf{PV} \int_{\mathbf{L}} \mathbf{J_{eq}(r).\vec{G}(r,r')dV'} - \frac{\mathbf{J_{eq}(r)}}{\mathbf{3j\omega\varepsilon_0}} \tag{4}$$

where $\vec{\mathbf{G}}(\mathbf{r},\mathbf{r}')$ is the free space Greens dyadic funtion given by,

$\vec{\mathbf{G}}(\mathbf{r},\mathbf{r}') = -j\omega\mu_0(\vec{\mathbf{I}} + \frac{\nabla\nabla}{k^2})\mathbf{g}(\mathbf{r},\mathbf{r}')$; $\mathbf{g}(\mathbf{r},\mathbf{r}') = \frac{e^{-jkR}}{4\pi R}$; $R = |\mathbf{r}-\mathbf{r}'|$; $k = w\sqrt{(}\mu_0\varepsilon_0)$;

r is a field observation point, r' is a source point inside V. s' is a source point along antenna; $\hat{s}'$ is a unit vector along antenna at s'; the symbol PV denotes principle value of the integral carried out by ommiting an infinitesimal volume around r [Bladel61].

From equation 1 the free space electric field $\mathbf{E}(\mathbf{r})$

$$\mathbf{E}(\mathbf{r}) = \mathbf{E}^{\mathbf{a}}(\mathbf{r}) + \mathbf{E}^{\mathbf{b}}(\mathbf{r}) \tag{5}$$

The dielectric's conductivity is complex, made up polarization and conduction currents with,

$$\mathbf{J_{eq}}(\mathbf{r}) = \tau(\mathbf{r})\mathbf{E}(\mathbf{r}) \tag{6}$$

where the complex conductivity is given by,

$$\tau(\mathbf{r}) = \sigma(\mathbf{r}) + j\omega(\mathbf{r})(\varepsilon(\mathbf{r}) - \varepsilon_0). \tag{7}$$

Substituting equation 3 and equation 4 into equation 5 and using equation 6 leads to :

$$\int_{\mathbf{L}} \mathbf{I}(\mathbf{s}')\hat{\mathbf{s}}'.\vec{\mathbf{G}}(\mathbf{r},\mathbf{s}')\mathbf{ds}' + [1 + \frac{\tau(\mathbf{r})}{3j\omega\varepsilon_0}] - PV \int_L \mathbf{J_{eq}}(\mathbf{r}).\vec{\mathbf{G}}(\mathbf{r},\mathbf{r}')dV'. = 0 \tag{8}$$

The second EFIE is obtained by applying boundary conditions to the perfectly conducting antenna surface. The total field must vanish $\Rightarrow \mathbf{E}_T(s) = 0$ (tangential components on antenna).

Hence,

$$\hat{s}.[\mathbf{E}^a(s) + \mathbf{E}^b(s)] = -\mathbf{E}^i(s). \tag{9}$$

Substituting equation 3 and equation 4 into equation 9 and using equation 6, we get :

$$\hat{s}. \int_L \mathbf{I}(\mathbf{s}')\hat{\mathbf{s}}'.\vec{\mathbf{G}}(\mathbf{s},\mathbf{s}')\mathbf{ds}' + \int_L \mathbf{J_{eq}}(\mathbf{r}).\vec{\mathbf{G}}(\mathbf{s},\mathbf{r}')dV'. = -\mathbf{E}^i(s) \tag{10}$$

These equations were developed in [Casey88, Kari80] but are given here for completeness. The second tensor integral in equation 10 is not a principle value integral because the field point is outside V. Equation 8 and Equation 10 must now be solved for the surface current $I(s)$ and volume current density $\mathbf{J_{eq}}(\mathbf{r})$ or equivalently $\mathbf{E}(\mathbf{r})$). By divinding the antenna into Na segments and the dielectric into Nb cells, we can approximate $I(s)$ and $\mathbf{E}(\mathbf{r})$ by expanding them using a set of basis functions. Suppose the following expansions are chosen :

$$I(s) = \sum_{n=1}^{Na} \alpha_n f_n(s) \tag{11}$$

$$\mathbf{E}(\mathbf{r}) = \sum_{n=1}^{Nb} c_n(\mathbf{r})\mathbf{E}^{\mathbf{n}} \tag{12}$$

where ,
α_n = expansion coefficient of the nth basis function
$\{f_n(s)\}$ = set of N linearly independent current basis functions
$\mathbf{E}^n$ = induced electric field in the nth cell

$$c_n(\mathbf{r}) = \begin{cases} 1 & \text{if r in } (\Delta V)_n \\ 0 & \text{otherwise} \end{cases}$$

The current basis functions $f_n(s)$ have been taken as

$$f_n(s) = (a_n + b_n \cos k(s - s_n) + c_n \sin k(s - s_n)); \tag{13}$$

where s_n is the position of segment n and $\mid s - s_n \mid < \Delta_n/2$, $\Delta_n/2$ being the segment length.

Using equation 11 and equation 12 in equation 8 and equation 10 and point matching at current segment centers and cell centers leads to a system of equations of order $(N_a + 3N_b)$ of the form,

$$\begin{bmatrix} \mathbf{M_1} & \mathbf{M_{2X}} & \mathbf{M_{2Y}} & \mathbf{M_{2Z}} \\ \mathbf{M_{3X}} & \mathbf{M_{4XX}} & \mathbf{M_{4XY}} & \mathbf{M_{4XZ}} \\ \mathbf{M_{3Y}} & \mathbf{M_{4YX}} & \mathbf{M_{4YY}} & \mathbf{M_{4YZ}} \\ \mathbf{M_{3Z}} & \mathbf{M_{4ZX}} & \mathbf{M_{4ZY}} & \mathbf{M_{4ZZ}} \end{bmatrix} \begin{bmatrix} \alpha_1 \\ \alpha_2 \\ \vdots \\ \alpha_{\mathbf{N_a}} \\ \mathbf{E_X} \\ \mathbf{E_Y} \\ \mathbf{E_Z} \end{bmatrix} = \begin{bmatrix} -\mathbf{E_1^i} \\ -\mathbf{E_2^i} \\ \vdots \\ -\mathbf{E_{N_a}^i} \\ \vdots \\ 0 \\ \vdots \end{bmatrix}$$

2.2 Formulation of the Many Body Problem

A Mathematical model for an antenna radiating in a many body problem is developed here. Essentially, the antenna is in an optionally completely closed shell of a dielectric material and is in the presense of other dielectrics placed anywhere within the shell. Fig.2 shows the geometrical model. Extending the work in [Kari80] and [Casey88] for the single antenna single dielectric class of problems above, one gets the results shown below.

$$\hat{s}.\int_L \mathbf{I(s')}\hat{\mathbf{s}}'.\vec{\mathbf{G}}(\mathbf{s},\mathbf{s}')\mathbf{ds}' + \sum_{i=1}^{N}\int_{V_{b_i}} \mathbf{J_{eq}(r)}.\vec{\mathbf{G}}(\mathbf{s},\mathbf{r}')dV' = -\mathbf{E}^i(s). \tag{14}$$

and

$$\int_{\mathbf{L}} \mathbf{I(s')}\hat{\mathbf{s}}'.\vec{\mathbf{G}}(\mathbf{r},\mathbf{s}')\mathbf{ds}' - \sum_{i=1}^{N} PV\int_{V_{b_i}} \mathbf{J_{eq}(r)}.\vec{\mathbf{G}}(\mathbf{r},\mathbf{r}')dV' + [1+\frac{N\tau(\mathbf{r})}{3j\omega\varepsilon_0}]\mathbf{E(r)} = 0. \tag{15}$$

where N is the total number of bodies including the shell, V_{bi} is the volume of the i^{th} body and $\mathbf{r}' \in V_{bi}$ and the rest of the symbols retain the same meaning as before.

Equation 14 and equation 15 form a coupled system of EFIEs which must be solved for the antenna surface currents and induced fields inside the N bodies. Using expansion functions and basis functions, equation 14 and equation 15 may be reduced to a system of linear equations of the following form;

$$\begin{bmatrix} \mathbf{M_1} & \mathbf{M_2^1} & \mathbf{M_2^2} & \cdots & \mathbf{M_2^N} \\ \mathbf{M_3^1} & \mathbf{M_4^{11}} & \mathbf{M_4^{12}} & \cdots & \mathbf{M_4^{1N}} \\ \mathbf{M_3^2} & \mathbf{M_4^{21}} & \mathbf{M_4^{22}} & \cdots & \mathbf{M_4^{2N}} \\ \vdots & \vdots & \vdots & \vdots & \vdots \\ \mathbf{M_3^N} & \mathbf{M_4^{N1}} & \mathbf{M_4^{N2}} & \cdots & \mathbf{M_4^{NN}} \end{bmatrix} \begin{bmatrix} \alpha_1 \\ \alpha_2 \\ \vdots \\ \alpha_{\mathbf{N_a}} \\ \mathbf{E^1} \\ \mathbf{E^2} \\ \vdots \\ \mathbf{E^N} \end{bmatrix} = \begin{bmatrix} -\mathbf{E_1^i} \\ -\mathbf{E_2^i} \\ \vdots \\ -\mathbf{E_{N_a}^i} \\ \vdots \\ 0 \\ \vdots \end{bmatrix};$$

where the submatrices have the following physical meaning,

- $[\mathbf{M_1}]$ represents the interactions on a segment of the antenna by other parts of the antenna.
- $[\mathbf{M_2^i}]$ represents the interactions on body b_i by the antenna.
- $[\mathbf{M_3^i}]$ represents the interactions by the antenna on body b_i.
- $[\mathbf{M_4^{ij}}]$ represents the interactions on body b_i by body b_j.

$i = 1, 2, ..., N; j = 1, 2, ..., N; N_\alpha$ = number of antenna segments.

Each $[\mathbf{M}_2^{\mathbf{i}}]$ and $[\mathbf{M}_3^{\mathbf{i}}]$ contains three block matrices while each $[\mathbf{M}_4^{\mathbf{ij}}]$ contains 9 submatrices. Hence, the total number of submatrices is $(9N^2 + 6N + 1)$.

We may reorganize the above coefficient matrix to the form:

$$\begin{bmatrix} \mathbf{M_1} & \mathbf{M_{2X}^{1...N}} & \mathbf{M_{2Y}^{1...N}} & \mathbf{M_{2Z}^{1...N}} \\ \mathbf{M_{3X}^{1...N}} & \mathbf{M_{4XX}^{1...N}} & \mathbf{M_{4XY}^{1...N}} & \mathbf{M_{4XZ}^{1...N}} \\ \mathbf{M_{3Y}^{1...N}} & \mathbf{M_{4YX}^{1...N}} & \mathbf{M_{4YY}^{1...N}} & \mathbf{M_{4YZ}^{1...N}} \\ \mathbf{M_{3Z}^{1...N}} & \mathbf{M_{4ZX}^{1...N}} & \mathbf{M_{4ZY}^{1...N}} & \mathbf{M_{4ZZ}^{1...N}} \end{bmatrix};$$

where,

$$\mathbf{M_{2X_p}^{1...N}} = \begin{bmatrix} \mathbf{M_{2X_p}^1} & \mathbf{M_{2X_p}^2} & \cdots & \mathbf{M_{2X_p}^N} \end{bmatrix};$$

$$\mathbf{M_{3X_p}^{1...N}} = \begin{bmatrix} \mathbf{M_{3X_p}^1} \\ \mathbf{M_{3X_p}^2} \\ \vdots \\ \mathbf{M_{3X_p}^N} \end{bmatrix};$$

and,

$$\mathbf{M_{4X_pX_q}^{1...N}} = \begin{bmatrix} \mathbf{M_{4X_pX_q}^{11}} & \mathbf{M_{4X_pX_q}^{12}} & \cdots & \mathbf{M_{4X_pX_q}^{1N}} \\ \mathbf{M_{4X_pX_q}^{21}} & \mathbf{M_{4X_pX_q}^{22}} & \cdots & \mathbf{M_{4X_pX_q}^{2N}} \\ \vdots & \vdots & \vdots & \vdots \\ \mathbf{M_{4X_pX_q}^{N1}} & \mathbf{M_{4X_pX_q}^{N2}} & \cdots & \mathbf{M_{4X_pX_q}^{NN}} \end{bmatrix};$$

where $p = 1, 2, 3; q = 1, 2, 3;$ and $X_1 = X, X_2 = Y, X_3 = Z$. The reorganization is dictated by the mapping technique described below.

3 Mapping Problems onto Processors

3.1 The Edinburgh Concurrent Supercomputer

Fig.3 shows the Edinburgh Concurrent Computer (ECS) which is made up of a number of domains, each domain having local transputers which are software configurable [Stro88]. A user gets exclusive access to a domain at a time. Software configurability of each of the four transputer links means that one can design any interconnection topology within a domain - for example one can make a k connected cube by making supernodes of k processors to increase communication space; in short the four links per node need not be a barrier to interconnection topologies optimal to a given problem.

Each domain is file served by a host transputer **H** connected to the UNIX file servers through a communications guardian transputer, and a communications spine. Users currently have a choice of Occam, C, or Fortran.

3.2 Five Processor Mapping

A 5-processor topology for the single antenna single dielectric is shown in Fig.4. A heuristic attempt at balancing the load during matrix build up is shown below. This is based on an iterative process of different submatrix mappings.

- P1 computes : [M2Y] and [M4ZZ]; communicates: [M2Y] to PP3 and [M4ZZ] to P5; also acts as master.
- P2 computes : [M1], [M2Z], [M4XY]; communicates: [M2Z] to P3 and [M4XY] to P5.
- P3 computes : [M2X] and [M4XZ]; communicates: [M4XZ] to P5.
- P4 computes : [M3X], [M3Y], [M3Z] and [M4YZ]; communicates: [M4YZ] to P5.
- P5 computes : [M4XX] and [M4YY].

This topology completely balances P1, P2, and P3 with P5 having a slightly heavier load for $N_b > N_a$. Here block symmetries, corresponding to cells of the same size in body V_b have been extracted and utilized. If $N_b \gg N_a$, P4 will considerably slow down the network.

With [M1] residing in P2, [M2] in P3, [M3] in P4 and [M4] in P5, the Complex Conjugate Gradient (CCG) method is used to solve the equations. The CCG has the advantage of rapid convergence in n iterations with $n \leq N$ where N is the order of the system. With the absence of round-off error, the CCG would yield an exact solution and is comparable to direct methods in that sense. The CCG algorithm used is shown below.

3.2.1 *The Complex Conjugate Algorithm*

Suppose we have the system $Ax = b$, with both the matrix A and vector b complex. Then the following algorithm defines a version of the conjugate gradient method [Hest80]. Normally, the coefficient matrix A is restricted to a symmetric matrix. However, the algorithm shown applies to any general complex matrix. First initialize $\mathbf{x_0}(= [0], \text{say})$. Then initialize the residual vector $\mathbf{r}$ and direction vector $\mathbf{p}$ as :

$$\mathbf{r_0} = \mathbf{A}\mathbf{x_0} - \mathbf{b}, \tag{16}$$

$$\mathbf{p_1} = -\mathbf{A}^*\mathbf{r_0}, \tag{17}$$

where $\mathbf{A}^*$ is the complex conjugate transpose of $\mathbf{A}$. Then at step j,

$$\alpha_j = \frac{\| \mathbf{A}^*\mathbf{r_{j-1}} \|^2}{\| \mathbf{A}\mathbf{p_j} \|^2} = \frac{(\mathbf{A}^*\mathbf{r_{j-1}})(\mathbf{A}^*\mathbf{r_{j-1}})^*}{(\mathbf{A}\mathbf{p_j})(\mathbf{A}\mathbf{p_j})^*}, \tag{18}$$

$$\mathbf{x_j} = \mathbf{x_{j-1}} + \alpha_j \mathbf{p_j}, \tag{19}$$

$$\mathbf{r_j} = \mathbf{r_{j-1}} + \alpha_j \mathbf{A}\mathbf{p_j}, \tag{20}$$

$$\beta_j = \frac{\| \mathbf{A}^*\mathbf{r_j} \|^2}{\| \mathbf{A}\mathbf{r_{j-1}} \|^2} = \frac{(\mathbf{A}^*\mathbf{r_j})(\mathbf{A}^*\mathbf{r_j})^*}{(\mathbf{A}\mathbf{r_{j-1}})(\mathbf{A}\mathbf{r_{j-1}})^*}, \tag{21}$$

$$\mathbf{p_{j+1}} = \beta_j \mathbf{p_j} - \mathbf{A}^*\mathbf{r_j}, \tag{22}$$

This phase represents matrix build up which takes the bulk of the computation. After building up the matrices, data is redistributed to take advantage of the CCG algorithm. Fig.6 shows the CCG solution stage mapping that takes advantage of the data space. This is a semi-geometric, semi-algorithmic problem decomposition arising from data dependencies of the problems under discussion. It is a generalized model for problems of this kind formulated in Moment Methods.

The technique developed computes local product vectors **V** which are then partially built up to correspond to pertinent matrix sub-blocks and transmitted to the master for evalution of the solution vector **x**. Obviously, it is possible to have a scheme where every processor computes its own **x** but the communication costs involved are prohibitive.

3.4 128 Processor Mapping

It is important to study the behaviour of computational EM scattering using a massively parallel approach. Towards this goal a 128-processor environment is described here both for loaded wire antenna problems and the many body problems discussed in Section 2.2.

3.4.1 Mapping For Loaded Wire Antennas

It is possible to extract a simple mapping from the problem domain and the number of processors available. For p processors having a factor f we can decompose the problem such that a portion n of the problem is assigned to n processors, i.e. $n = p/f$. From the matrices in Section 2.2, we can extract a value of 16 for factor f and with $p = 128$. $n = 8$, the following decomposition results.

From the $N_a \times N_a$, $N_a \times N_b$, $N_b \times N_a$, and the $N_b \times N_b$ blocks, we can write:

$$N_a = nV_1 + R_1,$$

$$N_b = nV_2 + R_2.$$

with $V_1 = N_a DIV n, V_2 = N_b DIV n, R_1 = N_a MOD n, R_2 = N_b MOD n$

For the $N_a \times N_a$ block, each processor p_j has the following mapping :

$$i_{st} = \begin{cases} ((p_j - 1)(V_1 + 1) + 1), & R_1 \neq 0, \quad p_j \geq R_1 \\ ((p_j - 1)V_1 + 1), & R_1 = 0, \quad \text{other } p_j \end{cases}$$

$$i_{end} = \begin{cases} (i_{st} + V_1), & R_1 \neq 0, \quad p_j \geq R_1 \\ (i_{st} + V_1 - 1), & R_1 = 0, \quad \text{other } p_j \end{cases}$$

where $j = 1$ and i_{st} refers to the first row in the $(V_1/(V_1 + 1) \times N_a)_j$ subblock and i_{end} is the last row. If $V_1 = 0$, then the first R_1 processors in $j = 1$ are assigned all the blocks (refer to Fig.7).

For the $N_a \times N_b$ blocks, each processor p_j has the following mapping :

$$j_{st} = \begin{cases} ((p_j - 1)(V_2 + 1) + 1), & R_2 \neq 0, \quad p_j \geq R_2 \\ ((p_j - 1)V_2 + 1), & R_2 = 0, \quad other\ p_j \end{cases}$$

$$j_{end} = \begin{cases} (j_{st} + V_2), & R_2 \neq 0, \quad p_j \geq R_2 \\ (j_{st} + V_2 - 1), & R_2 = 0, \quad other\ p_j \end{cases}$$

where $j = 2, 3, 4$ and j_{st} refers to the first column in the $(V_2/(V_2 + 1) \times N_b)_j$ subblock and j_{end} is the last column. If $V_2 = 0$, then the first R_2 processors for $j = 2, 3, 4$ are assigned all the blocks.

For the $N_b \times N_a$ and $N_b \times N_b$ blocks, each processor p_j has the following mapping :

$$i_{st} = \begin{cases} ((p_j - 1)(V_2 + 1) + 1), & R_2 \neq 0, \quad p_j \geq R_2 \\ ((p_j - 1)V_2 + 1), & R_2 = 0, \quad other\ p_j \end{cases}$$

where $\mathbf{x_j}, \mathbf{r_j}, \mathbf{p_j}$ are vectors and α_j, β_j are scalars.

A good and reliable measure of accuracy is beleived to be the root mean square error per sample defined as

$$\delta_j = \frac{(\| r_j \|)^{1/2}}{N} \tag{23}$$

which is a monotonically decreasing quantity. A more meaningful measure of accuracy is

$$\gamma_j = \frac{\delta_j}{\| x_j \| / N} \tag{24}$$

or $\gamma_j = \frac{\|r_j\|}{\|x_j\|} = (\frac{(r_j, r_j^*)}{(x_j, x_j^*)})^{1/2}$; a value of $\gamma_j = 10^{-4}$ means that the solution is at best 4 significant digits.

3.2.2 Form of computation

During the matrix build up stage a combination of Gaussian quadrature and a variant of Romberg integration are used. Analysis of our functions shows that they do not oscillate rapidly over integration intervals and the techniques are valid. Once the matrices are built up and positioned in their respective processors (i.e. $[\mathbf{M1}]$ residing in P2, $[\mathbf{M2X_p}]$ in P3, $[\mathbf{M3X_p}]$ in P4 and $[\mathbf{M4X_pX_q}]$ in P5), the CCG is executed as follows.

Let

$$[\mathbf{B}]\{\mathbf{s}\} = \left\{ \begin{array}{c} \{Q_t\} \\ \{Q_b\} \end{array} \right\}$$

where $\mathbf{B} = \mathbf{A}, \mathbf{A}^*$ and $\mathbf{s} = \mathbf{r_k}, \mathbf{r_{k-1}}, \mathbf{p_k}$. Suppose the submatrices $\mathbf{Q_{t1}}, \mathbf{Q_{t2}}, \mathbf{Q_{b1}}, \mathbf{Q_{b2}}$ are computed by the processors P2, P3, P4, P5 and communicated to processor P1 (master) as depicted below.

$$\begin{array}{lll} P2 & \xrightarrow{Q_{t1}} & P_1 \\ P3 & \xrightarrow{Q_{b1}} & P_1 \\ P4 & \xrightarrow{Q_{t2}} & P_1 \\ P5 & \xrightarrow{Q_{b2}} & P_1 \end{array}$$

Then, P1 computes vector Q where,

$$Q = \left\{ \begin{array}{c} Q_t \\ Q_b \end{array} \right\},$$

with

$$\begin{aligned} (Q_t)_i &= (Q_{t1})_i + (Q_{t2})_i \\ (Q_b)_j &= (Q_{b1})_j + (Q_{b2})_j \end{aligned} \tag{25}$$

where i, j denote vector elements with $i = 1, 2, \cdots, N_a$ and $j = 1, 2, \cdots, N_b$. P1 uses the resulting vector Q to: execute step 19, step 19 and step 20 ; communicate $\mathbf{r_k}$ to network; check for convergence while waiting for the current $Q_y, y = t_1, t_2, b_1, b_2$; and execute step 22 and step 22. The iteration step is repeated if convergence hasn't occurred else the network is terminated.

3.3 17 Processor Mapping

Fig.5 shows the seventeen processor mapping for the coupled antenna-dielectric system described in Section 2.1. The load distribution scheme is developed from results of the five processor model. The topology and interconncetion mechanism which forms a 'disturbed torus' is chosen so as to maximize usage of available links and to minimize communication hops between the master $P1$ and slaves $P2, \ldots, P17$.

$$i_{end} = \begin{cases} (i_{st} + V_2), & R_2 \neq 0, \quad p_j \geq R_2 \\ (i_{st} + V_2 - 1), & R_2 = 0, \quad other\ p_j \end{cases}$$

where $j = 5, 6, 7$ for the $(V_2/(V_2+1) \times N_a)_j$ blocks and $j = 8, 9, ...16$ for the $(V_2/(V_2+1) \times N_b)_j$ blocks. j_{st} refers to the first row in the relevant block and j_{end} is the last row. If $V_2 = 0$, then the first R_2 processors for $j = 8, 9, ..., 16$ are assigned all the blocks.

This model is not well balanced especially during matrix build up but yields a regular structure for communications during the CCG stage. Each processor p_j is identified by a cordinate point $(i, j), i = 1, \cdots, n; j = 1, \cdots, f$ which is used during the the CCG solution stage. Unlike the 5 and 17 processor models described above, no data positioning across the network takes place after matrices are built up.

3.4.2 Mapping For the Many Body Problem

A mapping that utilizes the technique in Section 3.4.1 has been tried for the many body problem described in Section 2.2. However, due to the complexity of the data space, communication imbalances result giving a poor load balance. A better balanced scheme is shown in Fig.8 which groups processors together to form supernodes.

In this scheme, $SN1$ (supernode-1) is a 3×3 processor computing surface; it is assigned to the enclosing cage b_N in Fig.2, and also generates all network communication addresses. $SN2$ is a 5×5 supernode and is assigned to $M^{1,\cdots,N}_{2\hat{X}_p}, p = 1, 2, 3$. $SN3$ is a 3×4 supernode and is assigned to $M^{1,\cdots,N}_{3\hat{X}_p}, p = 1, 2, 3$. $SNx, x = 4, \ldots, 12$ is a 3×3 supernode and each is assigned to $M^{1,\cdots,N}_{4\hat{X}_p\hat{X}_q}, p = 1, 2, 3; q = 1, 2, 3$ as described in Section 2.2; each x corresponds to a (p, q) set. This mapping preserves somewhat the natural layout of the problem and does not introduce alot of communication overhead.

3.5 Results

Results for the antenna-body problem on 5 and 17 processor models are shown Fig.10 (a,b,c) and Fig.11 (a,b,c). Fig.9 shows both the free space current distribution and coupled distribution. The coupling reduces the free space values. The induced **E**-fields are shown with their (x, y, z) orientations as in Fig.1. Fig.12(a) shows the processor utilization for the 17-processor model during matrix build-up stage and the busy time as percentages of total computation time. The busy time tracks arithmetic time in most processors. The communication time complexity for the same model is shown in Fig. 12(b)-this is far less than system computation time with the highest value being 0.05%. The penalties in this model are therefore not in interprocessor communications, but in the unequal processor loads during matrix build-up. In migrating from 5 to 17 processors an efficiency of 93.8% was achieved, this being a reflection of the relatively high degree of balancing in the 17 processor environment.

4 Conclusions

An attempt has been made to model EM scattering problems on a highly parallel MIMD environment. A generalized many body model has been developed and a solution methodology indicated. The complex conjugate approach has been shown to be ammenable to parallel computation for problems that use MM methods. Although more work needs to be done to model complex problems, the present model has shown some promise and has led to the development of techniques for parallel decomposition of EM problems of this type. The diverse applications of the general model covering: modelling of EM effects on biological bodies, radiation interference in printed circuit boards and the stringent radiation requirements by regulatory bodies all point to the enormous potential benefits that may come from parallel computing.

References

[Chege88] Chege, G.W., Taylor, R.W., Tealby, J.M. : "A survey and analysis of parallel processing and numerical techniques applied to electromagnetic field problems", Research Report (Y88/3), Dept. of Electronics, Univ. of York (July 1988).

[Bladel61] Bladel, J.V.: "Some remarks about Green's dyadic for infinite space", *IRE Trans. Antennas Prop.* , vol. AP-9, (1961), pp. 563-566.

[Brauer82] Brauer, J.R.: "Open boundary finite elements for axi-symmetric magnetic and skin effect problems", *J. Appl. Phys.*, 53(11), (1982), pp. 8366-8368.

[Burke81] Burke, G.J., Poggio, A.J.: "Numerical Electromagnetics Code (NEC) - Method of moments, Part III : Program description - Users Guide", Lawrence Livermore Laboratory, Jan. 1981.

[Casey88] Casey, J.P., Bansal, R.: "Dielectrically loaded wire antennas", *IEE Proceedings*, vol. 135, Pt. H, no.2,(1988), pp. 103-110.

[Emson88] Emson, C.R.I.: "Methods for solution of open boundary electromagnetic field problems", *IEE Proceedings*, vol. 135, Pt. A, no.3, (1988), pp. 151-157.

[Harri68] Harrington, R.F.: "Field computation by moment methods", MacMillan Company, NY (1968).

[Hest80] Hestenes, M.R.: " Conjugate Direction Methods in Optimization", Springer-Verlag, New York, (1980), Chapt. IV.

[Hoare78] Hoare, C.A.R.:"Communicating Sequential Processes", *Communications of the ACM*, vol. 21, no.8, pp. 666-677, (1978).

[Hoare85] Hoare, C.A.R.:"Communicating Sequential Processes", Prentice-Hall International, UK (1985).

[Jordan78] Jordan, H.F.: "A special purpose architecture for finite element analysis", Proc. 1978 Conference on Parallel Processing, (Aug. 1978), pp. 263-266.

[Kari80] Karimullah, K., Chen, K.M. and Nyquist, D.P.: "Electromagnetic coupling between a thin wire antenna and a neighbouring biological body: theory and experiment", *IEEE Trans., Microwave Theory and Tech.*, MTT-28, (1980), pp. 1218-1225.

[Live74] Livesay, D.E., Chen, K.M.: "Electromagnetic fields induced inside arbitrarily shaped biological bodies", *IEEE Trans., Microwave Theory and Tech.*", vol. MTT-22, no.12, (1974), pp. 1273-1280.

[Silv77] Silvester, P.P., Lowther, D.A., Carpenter, C.J.: "Exterior finite elements for 2-dimensional field problems with open boundaries", *IEE Proceedings*, vol. 124, no.12, (1977), pp. 1267-1270.

[Stro88] Stround, N.: "The Edinburgh Concurrent Supercomputer Project - report of first users meeting, 10th Feb. 1988" , *British Computer Society PPSG Newsletter*, no. 5, (1988), pp. 41-47.

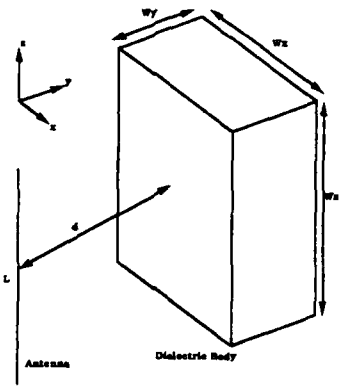

Fig. 1: Antenna Body System

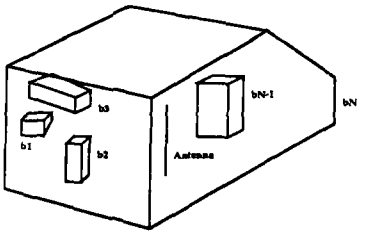

Fig. 2 : Planar faced arbitrarily shaped cage with many dielectrics exited by an antenna.

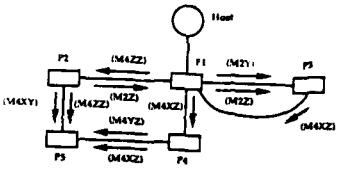

Fig.4: Balancing and communications for the five processor Mapping

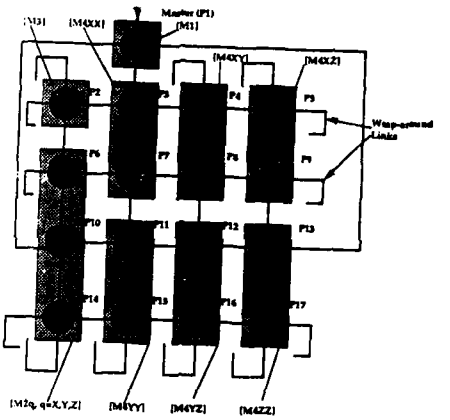

Fig.5: 17_Processor Matrices Computation/Load Balancing Phase Topology: (P2....P17 are Slave Processors)

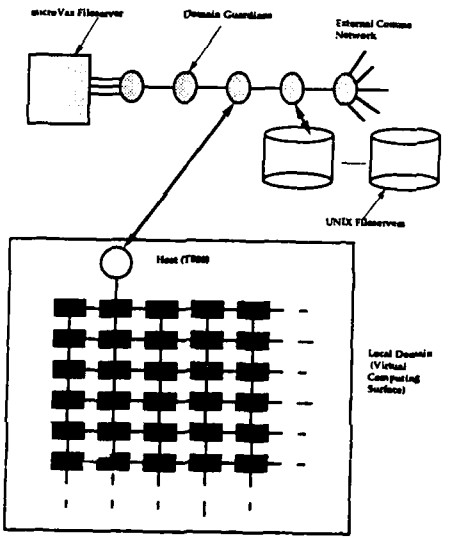

Fig.3: The Domains Structure of the SCS (from [Stu88])

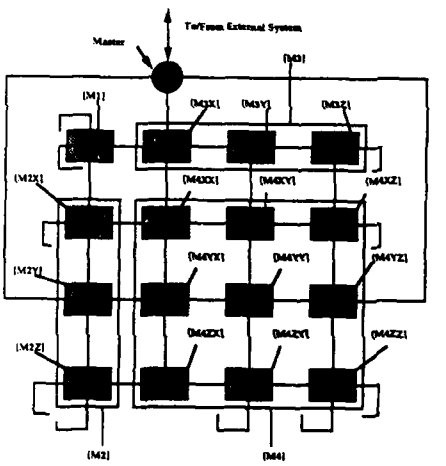

Fig.6: 17_Processor Solution Phase Balancing Topology

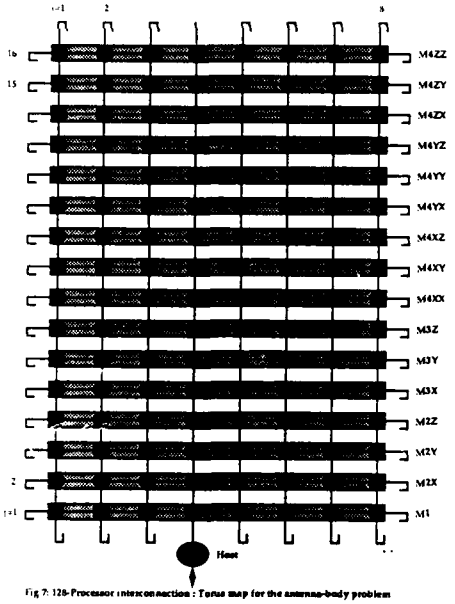

Fig 7: 128-Processor interconnection : Torus map for the antenna-body problem

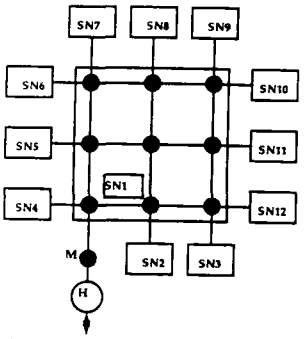

Fig. 8: 128 Processor Supernode Model For The Many Body Problem.

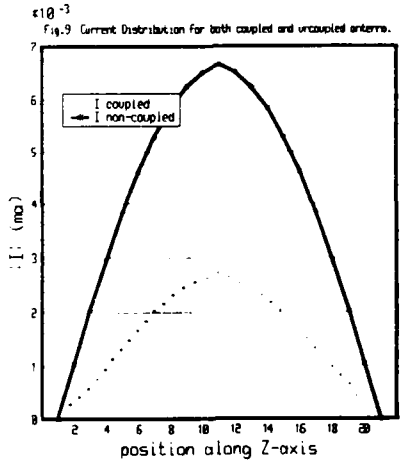

Fig.9 Current Distribution for both coupled and uncoupled antenna.

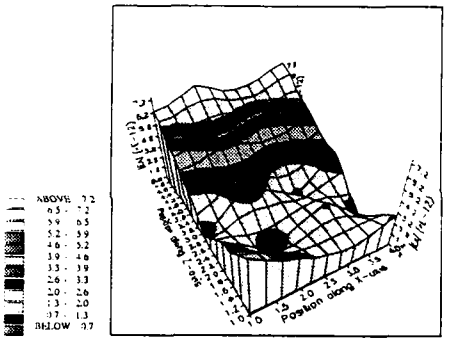

Fig 10(a): |Ex| Field Distribution (5 Processor Model)

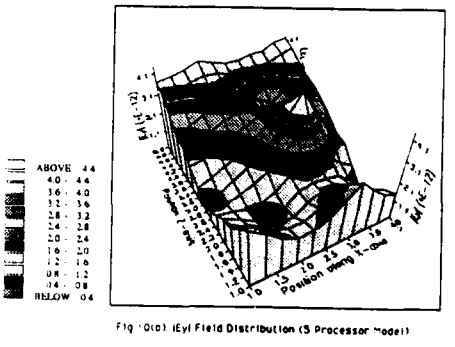

Fig 10(b): |Ey| Field Distribution (5 Processor Model)

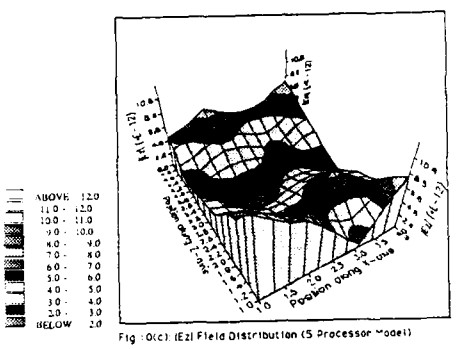

Fig. 10(c): |Ez| Field Distribution (5 Processor Model)

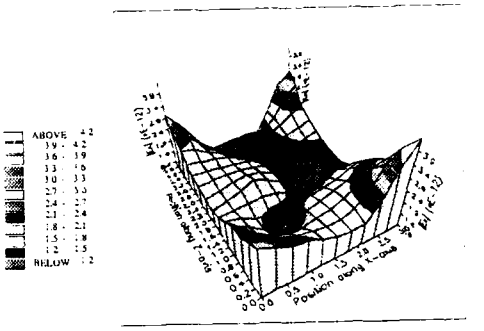

Fig. 11(a): |Ex| Field Distribution (17 Processor Model)

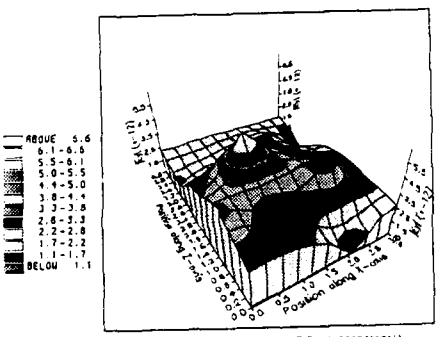

Fig. 11(b): |Ey| Field Distribution (17 Processor Model)

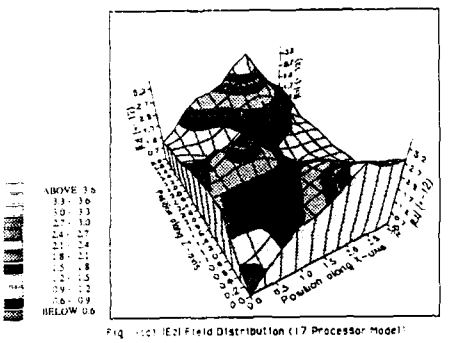

Fig. 11(c): |Ez| Field Distribution (17 Processor Model)

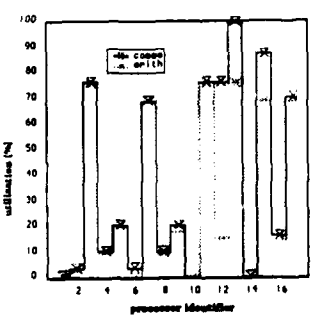

Fig. 12(a): 17-Processor Utilization

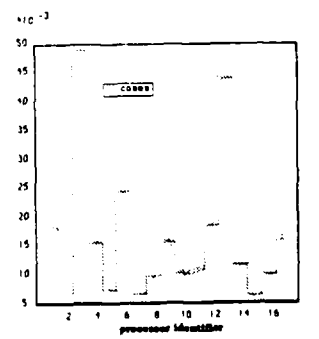

Fig. 12(b): 17-Processor Communications

SESSION 7 - "NEC APPLICATIONS"

The Effect Of The Ground Plane on the Log-Periodic Dipole Antenna

William G. Marzullo
Wright Research and Development Center
Wright Patterson AFB, Ohio
(513) 255-3050

Abstract

A computer analysis of a six element log-periodic dipole array was undertaken using the Numerical Electromagnetics Code (NEC). Following verification of log-periodicity in current, gain, and impedance for the free space environment, the antenna is placed over both perfect and real grounds. Although the type of ground was shown to have an effect on the gain and take-off angle of the main beam of radiation, it was seen to be of secondary importance as compared to the perfect ground environment. The height of the antenna was shown to be the most important parameter. Specifically, it is shown that a log-periodic antenna should be placed no higher than .5 λ above the ground

Introduction

Although the performance characteristics of the log-periodic dipole antenna have been examined in detail, most of the available material limits its discussion to the free space case. This paper will briefly examine the performance of the log-periodic dipole array in both the perfect and non-perfect ground cases.

Foe very high frequency applications in the microwave and radar bands, the performance of an antenna closely resembles that of an antenna in free space. This occurs because the electrical distance between the antenna and the ground is large enough that free space effects predominate. At lower frequencies, however, including HF and VHF, boom and mast length restraints dictate that the antenna either be fractions of a wavelength of a few wavelengths above the ground. At these heights the effect of the ground alters the performance of the antenna.

Method of Investigation

A number of software tools were examined for use in this project, i.e. MathCAD, MININEC, before the Numerical Electromagnetics Code (NEC) was decided upon. NEC is a method of moments code which has three options for calculating grounds: the Sommerfield Integral, solving for currents over a perfect ground using image theory, and modified image theory using Fresnel plane wave reflection coefficients. Although the latter is not accurate in describing near field interactions, it has been found useful for structures at least .1λ above the ground [1].

Antenna Design

The original design used was based upon the presentation in Antenna Theory and Design by Dr's Stutzman and Thiele [2]. Although this procedure is based upon the work of Carrel [3], the above reference does not include feeder design considerations. This omission led to an unacceptable condition.In order to simplify analysis and computation, a 2:1 structure bandwidth was chosen. Choosing the nominal gain at 8.5 db, the appropriate values of τ and σ are:

$\tau = .822$ and $\sigma = .149$
BW = 30 - 60 mhz
$\lambda_L = 10$ meters
$\lambda_U = 5$ meters
Length to diameter ratio = 200

Although only 5 elements were required the 2:1 bandwidth, I decided to add an extra element to improve band-edge performance. Table 1 shows the appropriate element number and its length and diameter. Length is in lambda and diameter is in meters.

TABLE 1 : SEGMENT AND ELEMENT SUMMARY

ELEMENT #	6	5	4	3	2	1
LENGTH @ 30 MHZ	0.6	0.5	0.4	0.3	0.27	0.22
NUMBER OF SEGMENTS	9	9	7	7	5	5
DIAMETER	0.0304	0.025	0.020	0.016	0.013	0.011

For proper feeding of the LPDA, the centers of each antenna were connected by transmission line alternating the connection between adjacent dipoles. The impedance of the feeder line was chosen to be 50 ohms.

Discussion Of Free Space Results

Currents were calculated and showed expected results. At 30 mhz element no. 5 is at $\lambda/2$. At this frequency, most of the current falls on elements 4 and 5 with element 5 having a 62.17 + j31.19 impedance, close to the half-wave dipole value. The structure continued this behavior throughout its bandwidth.

E-field gains were also calculated. As predicted, the area of maximum radiation occurs off the small end of the antenna. The HPBW is approximately 60° and the gain was 7.5 db.

Next, the VSWR values were calculated using the antenna input impedances at each of the frequencies tested. The normalized values are shown below.

TABLE 2 : NORMALIZED INPUT IMPEDANCE - NO FEEDER DESIGN

FREQUENCY	RESISTANCE /50	REACTANCE /50	VSWR
30 MHZ	1.45	0.45	1.7
40 MHZ	0.16	-0.63	10.0
50 MHZ	0.49	-0.12	2.1
60 MHZ	0.73	0.58	2.1

This table demonstrates that this design procedure is clearly not acceptable. The VSWR of 10 at 40 mhz indicates that a large amount of power is residing on the feeder line at that frequency. Before continuing with a discussion of the perfect ground case, another design procedure must be followed.

Augmenting the original design with feeder considerations, we proceed as follows. The antenna feeder impedance Z_o, depends on the mean radiation resistance level R_o, the average characteristic impedance of the elements, σ, and the length to diameter ratio [4]. From Weeks [5]

$$Z_a = 120 \, (\ln h/a - 2.25)$$

With $h/a = 200$, $Z_a \cong 365$ where Z_a is the average characteristic impedance of the antenna elements. Finding the mean relative spacing factor σ' [6]

$$\sigma' = \frac{\sigma}{\sqrt{\tau}}$$

$$\sigma' = \frac{.149}{\sqrt{.822}} = .164$$

Choosing a mean radiation resistance level, R_o, of 75 Ω we can find Z_o from [7]

$$Z_o = \frac{R_o^2}{8\sigma' Zav} + R_o \sqrt{\left(\frac{R_o}{8\sigma' Zav}\right)^2 + 1}$$

$$Z_o = 87.66 \, \Omega$$

This design procedure takes into account the loading of the antenna elements. In effect, we are saying that we should design the parallel-rod feeder line as if it had a characteristic impedance of 87.66 ohms. Notice that the mean value of the input impedance, R_o, is less than the characteristic impedance of the feeder, Z_o. This is due to the shunt capacitance that is added by the presence of the short dipoles in the transmission region. As a result of this design change, the VSWR values were changed to 1.5,1.2,1.7, and 2.2 at 30 to 60 mhz respectively.

The Perfect Ground Case

From image theory, we can prove that an antenna above a perfect ground may be replaced by the antenna and its image placed below the ground with the ground removed. The field of the image antenna is added to the actual antenna to produce a total field, above the plane, which is the vector sum of the two. By using this method, we can reduce the problem of a horizontal dipole above a perfectly conducting ground to that of an endfire array [8].

For this case, the LPDA was placed over a perfectly conducting ground, i.e. $\sigma = \infty$. In this model, the ground plane is considered infinite in extent on the xy plane. This may be contrasted with another procedure for handling grounds in which the ground is composed of finite patches. Using the infinite ground approach, the array was placed at both $\lambda/4$ and $\lambda/2$, referenced to 30 mhz, above it. These two electrical distances were chosen to keep within the program limits of placing the structure at least .2 λ above the ground. If we assume that equal power is delivered to both the antenna and its image, we should see a corresponding increase in gain of approximately 3 db over the free space case. Moreover, because the antenna and its image have currents of equal magnitude but opposite phase, there should be zero gain at the horizontal plane or at theta equal 90°. This is exactly found to be the case as the gain has increased from 7.62 db to 10.81 db. This has been achieved at the expense of beamwidth which is halved. Also, no gain was achieved at theta equal 90°.

Considering now two specific cases above a perfect ground. Figure 1 and 2 below show the difference between 30 and 60 mhz. Thirty mhz at 5 meters above the ground is almost identical to 60 mhz at 2.5 meters (not shown). At 60 mhz and 5 meters we find that the beam has split into two lobes with a deep null at 60°. Serious reception problems will occur if the take-off angle was chosen in this area. The complete data shows, in fact, that serious lobing problems began to occur at only 40 mhz and 5 meters above the ground!

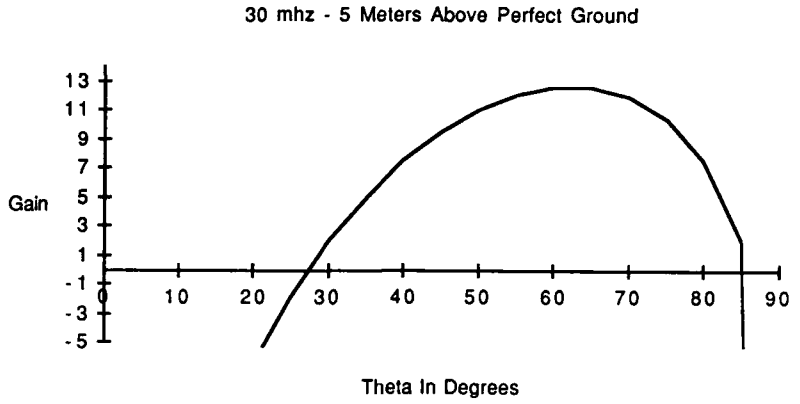

FIGURE 1 : 30 MHZ AT 5 METERS ABOVE A PERFECT GROUND

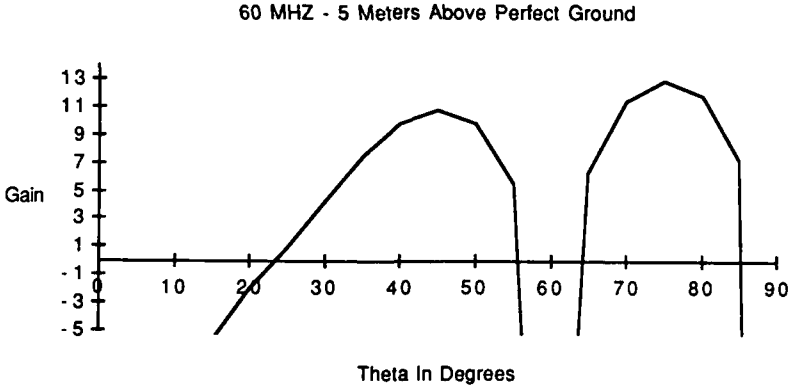

FIGURE 2 : 60 MHZ AT 5 METERS ABOVE A PERFECT GROUND

The Real Earth Ground

Under the case of a perfect ground, it was found that an antenna should be placed no higher than $\lambda/2$ of the highest frequency of operation above a

perfect ground. In order to find a good representation of grounds in the United States, three grounds were chosen and are shown in the table below [9].

TABLE 2 : MATERIAL CONSTANTS (PERMITTIVITY, CONDUCTIVITY)

MATERIAL	RELATIVE PERMITTIVITY	CONDUCTIVITY mhos/m
Sandy Soil	10	0.002
Clay Soil	14	0.005
Urban Ground	4	0.0002

The pattern of an antenna over a real earth ground is different from the pattern when the antenna is operated over a perfect ground. The sane principles as the perfect ground case apply except that the strength of the image will be reduced over that in the perfect case. As in the previous sections, the antenna was placed at both 2.5 and 5 meters above the ground. In each of the soil types it was found that the antenna's performance mimicked the performance above a perfect ground. Below, figure 2 shows a representative example comparing perfect and sandy soil cases. The open squares show the perfect ground while the filled in ones depict the sandy soil case.

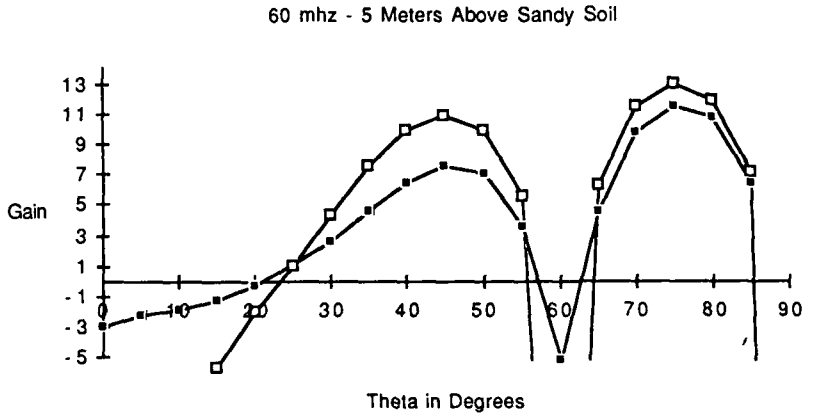

FIGURE 3 : GAIN AT 60 MHZ - SANDY SOIL AND PERFECT GROUND

Conclusion

The study undertaken demonstrated that the presence of a ground has a significant effect on the take-off angle of the beam of maximum gain. In addition, changing the ground conditions from a perfect ground to a real ground only served to lower the achieved gain, with the takeoff angle experiencing only minimal fluctuation in going from the perfect to real case. Furthermore, it was shown (in the complete study) that as the height of the antenna is raised above

2 lambda above the ground, referenced to the highest frequency of operation, wide fluctuations in gain resulted.

References

[1] G.J. Burke and A.J. Poggio, Numerical Electromagnetics Code (NEC) - Method of Moments, Part III (Lawrence Livermore National Laboratory, 1981), p. 11.

[2] W.L. Stutzman and G.A Thiele, Antenna Theory and Design (Wiley, 1981), pp. 295-299.

[3] Robert L. Carel, "Analysis and Design of the Log-Periodic Antenna" (PhD Dissertation, Univ of Illinois, Urbana, 1961), p. 20.

[4] Gerald L. Hall, The AARL Antenna Book (AmericanRadio Relay League, 1984), pp. 6-25.

[5] W.L. Weeks, Antenna Engineering (McGraw-Hill, 1968), p. 286.

[6] Hall, The AARL Antenna Book, pp.6-25.

[7] Ibid.

[8] John D. Krauss, Antennas, 2d ed., (McGraw-Hill, 1968), p. 462.

[9] Ibid., p. 851

MF-TRANSMITTING ANTENNA COMBINED WITH HIGH GROUNDED SUPPORTING MASTS

G.Potschkat and W.Tippe
Institut für Rundfunktechnik
Floriansmühlstr. 60, D8000 München 45

ABSTRACT

The article describes a medium-frequency transmitting antenna comprising specially arranged angle-radiators suspended from a high support mast. This type of MF-antenna offers much broader bandwidth than conventional cylindrical cage antennas and can be used for omnidirectional and directional radiation. Two full-scale antennas have been constructed around masts with different numbers of guy-ropes, and optimized by computations using the method of moments and by model measurements. For directional radiation various constructions are specified. A front-to-back ratio better than -10 dB can be achieved in configurations using a single support mast. Worthwhile savings are therefore possible in terms of materials and construction costs.

1. INTRODUCTION

For the terrestrial radiation of radio and TV frequencies in the bands I to IV/V highly focused beam transmitting antennas are used which - for better coverage - are fit to high grounded supporting masts (up to 300 meters in Germany). Repeatedly, efforts have been made to utilize these high and passive supporting masts by fixing additional cage constructions for the radiation of Medium Wave (MF-) frequencies.

According to the specific literature its utilization is restricted to some special tasks only / 1 /, and there has been no significant spreading so far. This state of development is due to hard conditions being the close electro-magnetical cross coupling of such a combined radiation system and the interference of all characteristics of the MF-antenna.

Usually, supporting installations (supporting mast and its guy ropes) do not have a major ground network. They are grounded on the base and have grounded guy ropes without being subdivided by insulators. Above all, by the overall height of the supporting mast and the length of its guy ropes a particularly strong influence on the characteristics of such a combined MF- transmitting antenna is achieved, if its electric dimensions are more or less equivalent to resonances ($1/2\lambda$; $3/4\lambda$) of the MF-frequency to be radiated.

This paper presents a new combined MF-transmitting antenna supporting-installation, whose most important design features are the angular and outwardly-sloping single-wire radiators forming the MF-antenna. This type of MF-antenna - called "angle-radiator-antenna" - is designed in such a way that the supporting installation is essentially supplemented by a complete ground network. The special arrangement and form of these angle radiators allow a rather loose coupling between the MF-antenna and the mast with its guy ropes respectively. Due to the considerable number of variable design parameters this system would meet very precise requirements for the MF-propagation. In respect of characteristics and efficiency, this angle-radiator-antenna is at least as powerfull as all other standard MF-vertical transmitting antennas.

The generation of directed radiation patterns via only one supporting installation is another essential advantage of this combined arrangement. This can easily be obtained; by adding one or two passive radiators serving as a reflector or a director it is possible to achieve differently directed radiation patterns. Even in the case of different phases in the feed-currents of single angle-radiators, directed patterns are obtained. By this means supply requirements of most different kinds can be complied with at low costs for material and construction.

II. DESIGN and CONSTRUCTION

Fig. 1 represents a model of this angle-radiator antenna type combined with a supporting mast. All single angle-radiators (e.g. three or six in number) are positioned around the mast, between the guy-ropes, with equal angular spacing. The base of each angle-radiator is attached to a conducting ring suspended around the mast base, just above the ground. This feed supply has been insulated from the supporting mast and the ground. For the purpose of terminating angle-radiators, span-ropes or short masts can be fixed to their angular points. These, points of attachment must be insulated.

Various types of parameters can be used for impedance and pattern optimization. In this regard, the positioning of the angle-radiators in respect of their azimuth distance to guy wire planes and supporting mast are of utmost importance. They are determinated by the position of the angular point by (s. Fig. 2):

A = radial distance from the supporting mast and
H = distance from the ground.

Further influential factors are the overall electric length (L= L1+L2) as well as the element angle ß of the angle-radiator which is determined by fixed points at the feed supply just at a variable height of the supporting mast.

III. INFLUENCE of GUY ROPES

One characteristic of self-radiating MF-vertical antennas is the fact that guy ropes - indispensable for the termination of the mast - are actively connected with the mast-radiator. Their influence on the features of the aerial is very critical if non-insulated dimensions show exactly or nearly a quarter wave resonance length of the MF- operating wave length. In order to keep these effects as low as possible, guy ropes of self-radiating masts are usually divided into short segments $\lambda/10$ by means of insulators / 2 /.

By contrast, the supporting mast and its guy ropes of the angle-radiator supporting installation are only passive elements. The azimuthal position of the guy ropes in respect of the angle-radiators has proven the advantage that the induced currents on the non-insulated guy ropes can be used very well for pattern optimization. In single cases only, where the height of the supporting mast has a $\lambda/2$ or $3/4\lambda$ resonance wave length, a partial insulation of the guy ropes is necessary. Here, the supporting mast is loaded with an additional top capacitance producing a de-tuning out of the resonance.

IV. METHODS of RESEARCH

IV.1 Calculations

The technological development of this type of MF-angle radiator antennas combined with a supporting installation has been performed principally by comprehensive theoretical analyses. For this purpose the well-known computer code "NEC" (Numerical Electromagnetics Code) - originally developed at the Lawrence Livermore Laboratory of the University of California - has been used in a modified way / 3 /.

With the aid of the so-called Method of Moments according to Harrington / 4 / this code is a computer program for analyzing the electromagnetic response of an arbitrary antenna system consisting of wires or other metal structures. The analysis is accomplished by the numeric solution of integral equations for currents induced on the structures by local sources or incident fields. The structures can be positioned either in a free space or above a perfectly or finitely conducting earth. In addition, this program covers non-radiating networks, transmission line modeling, lumped or distributed loading and free ends of finite wires with various radius thicknesses by means of highly functional physical models. The output may include current and charge density, near or far zone electric or magnetic fields, and antenna input impedances or admittances. Pre-requisite for this task was the creation of a complete simulation of the supporting mast and its guy ropes, also, the ropes of the angle-radiators including their feed system and terminations were taken into consideration. Fig. 3 represents one example of a calculation model.

IV.2. Model Measurements

The theoretical analyses are backed up by model measurements on a realistic reproduction of this antenna system. It has only been completed by a ground network.

A scale of 1 : 100 for an unsymmetrical model and 1 : 200 for a symmetrical model is the basis for dimensions of the supporting installation and the different antenna combination. The unsymmetric model of the combined supporting system - set up above the ground network - serves to measure input impedance. Its ground network consists of a circular metal plate having a sufficiently wide radius. The base of the supporting mast - just as the bases of the guy ropes - have been provided with a conductive connection with the metal plate. The upper final points of the guy ropes have a conductive connection with the supporting mast.

Regarding the symmetric model, the conductive ground has been simulated by supplementing a reliable mirror reflection. The symmetric aerial is set up on a positioner which can be turned under full control within a conventional indoor range.

The MF-frequency of 1 MHz serves as indication for the frequency of this model. Multiplied by the respective scale factor, it results in scale model frequencies of 100 MHz and 200 MHz respectively. The construction concept of both models permits an optional conversion with different forms of MF-antennas and lengths of supporting installations.

V. RESULTS

The results given here are related to presently installed supporting masts with different heights and terminations. Fig. 4a and Fig. 4b represent real dimensions of two systems of such a kind. For both types the dimensions for an optimized MF-angle radiator antenna having an omni-directional characteristic have been indicated additionally. Concerning other heights of supporting masts with combined MF-transmitting angle-radiator antennas, please refere to the report / 5 /.

5.1 Input Impedances

The input impedances of this antenna combination have been measured according to the method described in chapter 3.1. Transfer curves for a frequency bandwidth of ± 1 MHz (i.e. in real terms: ± 10 kHz at 1 MHz) have been plotted at a model frequency of 100 MHz. Fig. 5 shows a Smith chart representation of the transfer curves, for the case where Z_Φ = 60 Ohm and for various support mast heights (in an un-matched condition). As results prove, the frequency bandwidth of ± 1 MHz remains under a standing wave ratio of s = 1.2. Due to the fact that AM-radio requires a frequency bandwidth of ± 5 kHz for this standing wave ratio in Germany, there is obviously a redundancy in the frequency behavior of the MF- angle radiator antenna. This reserve will have a positive effect on the system under meteorological conditions (e.g. wind and ice formations). The input impedance with a real component of about 30. Ohm can be adapted to the characteristic impedance of the feeder cabel by minimum tuning means.

5.2 Radiation Patterns for omni-directional Radiation

Fig. 6a and 6b show calculated horizontal and vertical radiation patterns for a 3/4λ supporting mast height installed on a perfect ground according to Fig. 4a. The three upper guy ropes of each set have not been subdivided by insulators and they have been grounded. The upper guy ropes of each set have

been also non-insulated first and a second time along a rope length at a distanca of 0.16λ have been subdivided by a insulator. It is clear that induced currents running through the upper guy ropes exercise a strong influence on the radiation pattern of this MF-antenna combination. To a large extent, the analysis shows that the horizontal pattern is omnidirectional, and that the vertical pattern is similar to that of a base-fed mast radiator.

As can be seen in Fig. 7a and 7b, a comparison has been made between a λ/4 vertical radiator and the MF- angle radiator combination concerning the radiation characteristics. The MF-angle-radiator antenna is combined with a supporting mast according to Fig. 4a with the upper guy ropes of each set partly insulated.

The second example (see Fig. 4b) is represented by a graphic description of calculated patterns for horizontal and vertical radiation. Fig. 8a and 8b show the radiation characteristics of non-insulated guy ropes. In order to obtain an optimal omnidirectional pattern for this type, the lowest and central guy ropes of each set have to be insulated close to the mast. Fig. 8a and 8b show also the optimal form of the farfield patterns (dashed line). The structural dimensions for this optimal antenna combination is given in Fig. 4b. The patterns have been calculated for a MF-frequency of F = 567 kHz. Consequently, the electric length of the supporting mast and of the angle-radiators result in: L supp.mast = 0.44λ ; L angle-rad. = 0.33λ .

5.3 Radiation Patterns for directional Operation.

In conclusion, results are shown proving that the MF-angle radiator antenna combined with a high supporting mast can also be used for directional radiation. For this purpose additional measures can be made use of:

5.3.1 Grounding of one or various angle-radiators

Fig. 9 shows horizontal radiation patterns, two angle radiators of a 60-degree sector having been grounded, i.e. not being directively connected with the feeder. The difference between the two pattern shown in Fig. 9 is the diversified overall length of the grounded angle radiators. With this feeding supply it is obviously no problem to achieve a front-to-back ratio lower than -10 dB. Here, however, a bandwidth deterioration must be expected.

5.3.2 Additional passive Radiators

A similar tune-out effect as described in 5.3.1 can be achieved if - in addition to six excited angle-radiators - further passive linear radiators are terminated. The azimuthal position of this linear radiators is optimal if it is placed between two angle-radiators. The rope length of the passive ropes should be about λ/4 wave length. Fig. 10 represents the radiation pattern calculation and measured as a reflector. The depth of the tune-out effect (nul) can be

varied by changing the azimuth position of the linear radiator, or its length, or its angle relative to the mast. Regarding the input impedance, this tune-out effect has proven that no major changes are to be expected; as the broadband characteristic of the relatively high effect of the impedance values are retained.

5.3.3 Different Current Phases in opposite angle-radiators

Another way of producing directional patterns by means of one supporting installation is to feed angle-radiators pointing in opposite direction with different current phases. Fig. 11, e.g., represents a calculated radiation pattern, whereby of the six fed angle-radiators, two - having an opposite azimuthal position - are fed with a phase difference of the input currents of 170 degree. The form of the directional pattern can be influenced by changing the current phase. In this case, also, the broadband characteristics remain unchanged.

V. CONCLUSION

All results described above demonstrate that angle-radiators are an efficient form of MF-transmitting antenna and that they can conveniently be integrated into a high support mast structure. The angle-radiator antenna is not one of the "standard" types. The choise of overall dimensions is nonethless made in the same way as for standard vertical radiators, i.e. in terms of electrical length ($\lambda/4$, $\lambda/2$, 0.625λ, etc). Nevertheless, the variable dimensions of the angle-radiators must be optimized for each individual support mast configuration, because the non insolated or partially insolated guy-ropes contribute to the overall radiation characteristics.

The antenna combination offers economic advantageous compared to conventional mast radiators or twin-mast directional antennas, or situations where VHF/UHF and MF services use completely separate support structures. Problems resulting from the acquisition of real estate and often lengthy negotiations thereto can be ruled out by the possibility of integrating an angle-radiator antenna into a supporting installation. There is no necessity for an installation of a separate MF-mast together with guy ropes and its expensive insulation.

There are a number of other technical advantages, and notably the fact that the integrated antenna has excellent protection against lightning. Electrostatic charges built up during thunder-storms are leaked directly to earth via the grounded mast and guy-ropes. Also, since the mast remains earthed, staff can climb to the VHF/UHF antennas in safety without having to interrupt the MF service.

VI. REFERENCES

/ 1 / Peter Bruger, Gert Otten and Bernd Waniewsky, "Mittelwellen-Richtantennen aus TÜrmen mit mitten- gespeisten Seilreusen" (Directional antennas using self-supporting towers with driven wire cages). ITG-Fachberichte 99, 1987,pp. 221 - 226.

/ 2 / S.M. Wright, P.W. Klock and J.D. Jubera, "The impedance of the guyed quater wave monopole", IEEE Transactions on Broadcasting, Vol. BC-29, No. 1, pp. 22-30, 1983

/ 3 / W. Tippe, "NEC, ein universelles Rechenprogramm zur Analyse komplexer Antennensysteme" (NEC, an universal computer programme for the analysis of complex antenna systems). IRT Technical Report B 46/83, 1983

/ 4 / R.F. Harrington, "Field computation by Moment Methods", New York: Mc Millan Company, 1968

/ 5 / G. Potschkat, "Modelltechnische Untersuchungen an Kombinationen von Mittelwellensendeantennen mit Träger-mastanlagen" (Modelling techniques for investigations of combinations of MF antennas with support masts). IRT Technical Report B 99/89, 1989.

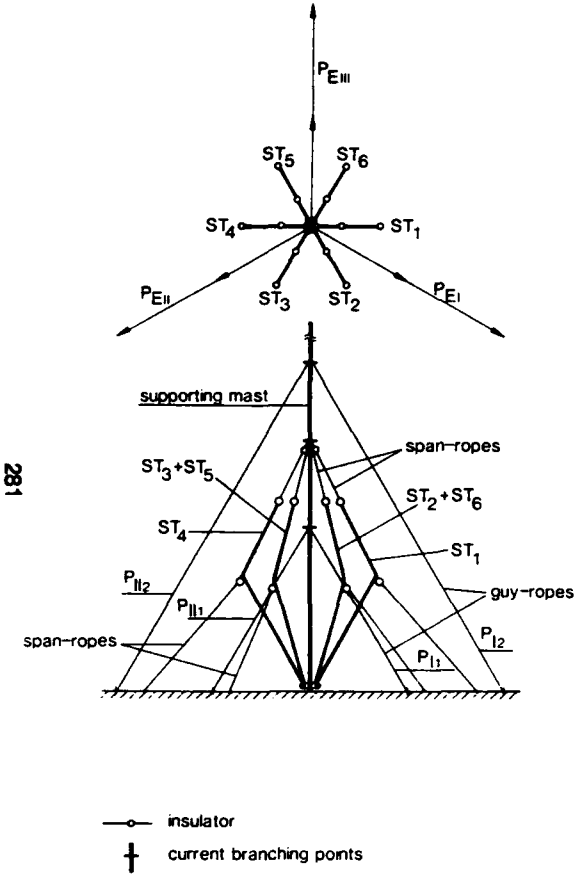

Fig. 1: Top and front view of a MF-angle-radiator antenna combination with a high supporting mast

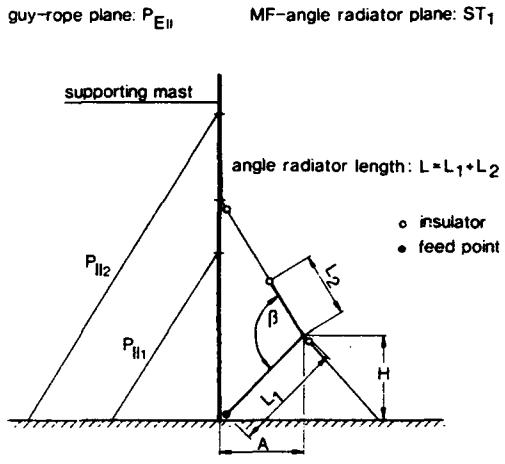

Fig. 2: Dimensions of the MF-angle-radiators

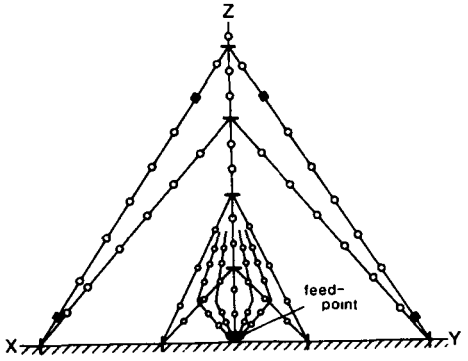

points,where the current is calculated
points with series impedance
points with current branching
feed-point

Fig. 3: Computer model of the antenna combination

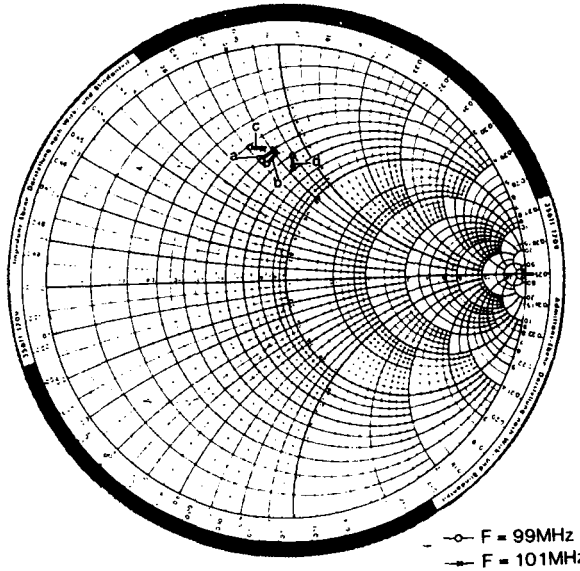

mast length

a : 0,5λ_o b : 0,667λ_o c : 0,75λ_o d : 0,833λ_o

Fig. 5: Measured impedances of optimized MF-angle-radiator antennas combined with supporting masts with various mast length

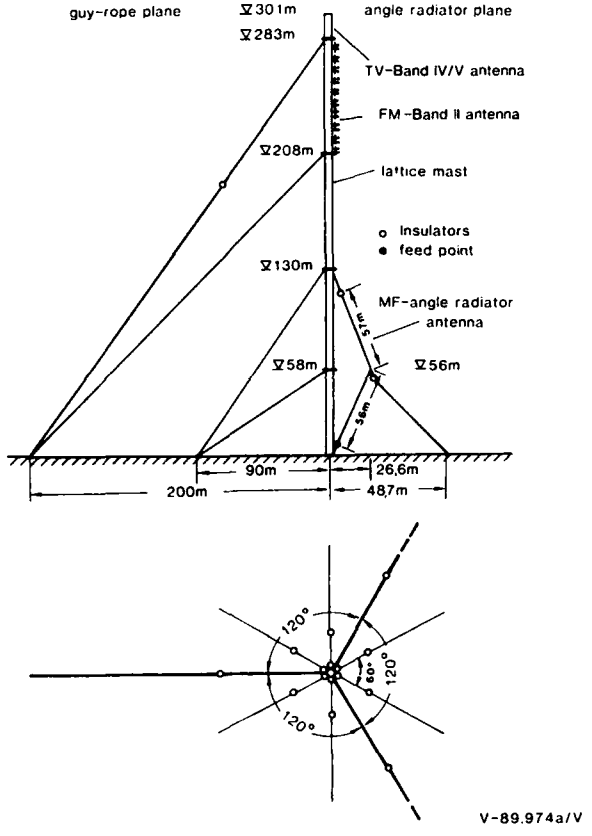

Fig. 4a: Top and front view of 300m supporting mast with 4 sets of guy ropes and combined with an optimal dimensioned MF-angle-radiator antenna.

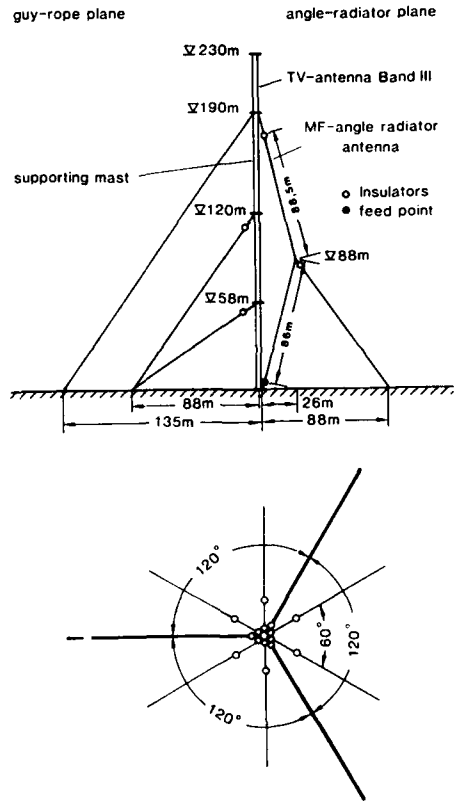

Fig. 4b: Top and front view of 230m supporting mast with 3 sets of guy ropes and combined with an optimal dimensioned MF-angle-radiator antenna.

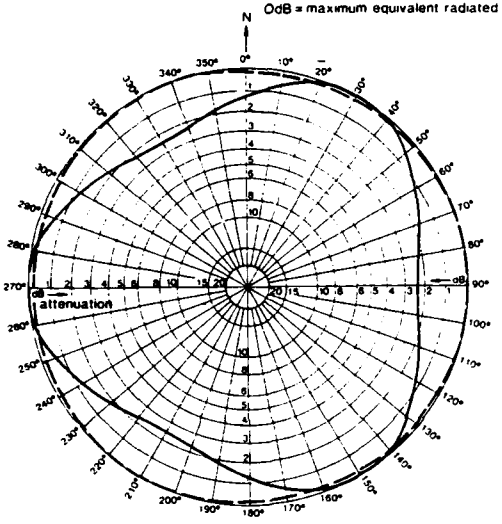

horizontal pattern

V-88.873a/V

Fig. 6: Relative gain pattern of a MF-angle-radiator antenna combined with a real erected supporting mast after Fig. 4a over perfect ground

Parameter: ——— upper guyes not insulated
– – – upper guyes partial insulated

a. horizontal pattern
$\vartheta = 90°$

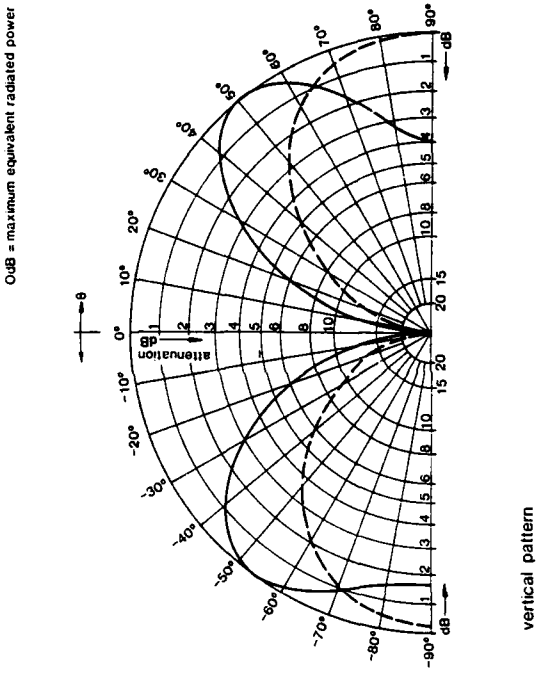

vertical pattern

Fig. 6: Relative gain pattern of a MF-angle-radiator antenna combined with a real erected supporting mast according to Fig. 4a over perfect ground

Parameter: ——— upper guyes not insulated
– – – upper guyes partial insulated

b. vertical pattern
$\varphi = 90°$

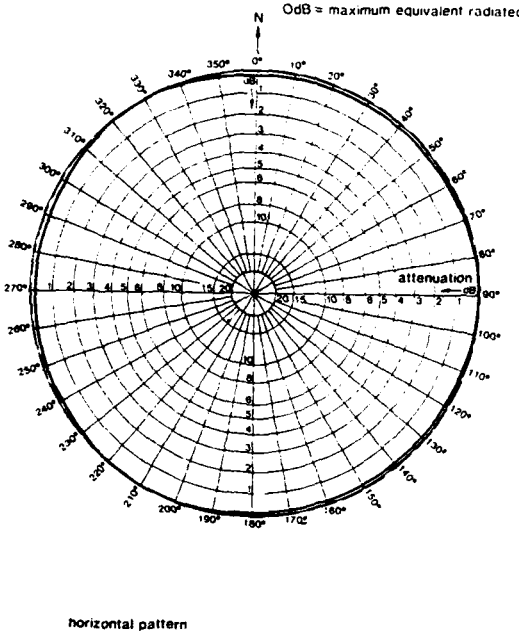

horizontal pattern

Fig. 7: Comparison concerning the relative gain patterns of a $\lambda/4$ vertical radiator and the optimal dimensiond angle-radiator combination after Fig 4a.

Parameter: --- $\lambda/4$ vertical radiator
——— Angle-radiator combination

a. horizontal pattern
$\varphi = 90°$

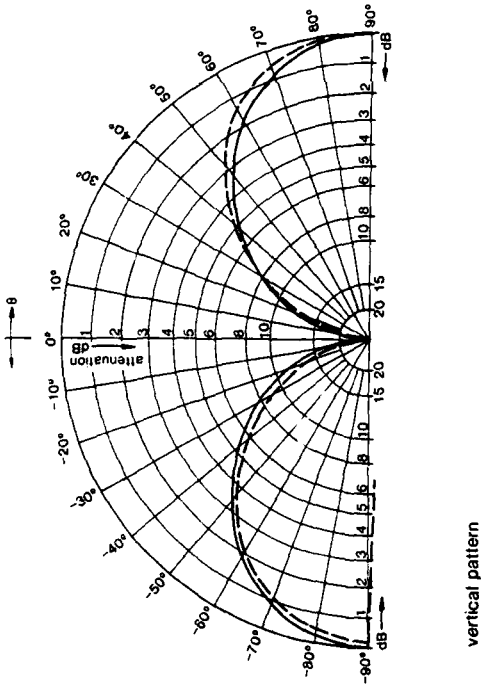

vertical pattern

Fig. 7: Comparison concerning the relative gain patterns of a $\lambda/4$ vertical radiator and the optimal dimensiond angle-radiator combination according to Fig. 4a over perfect ground

Parameter: — — — $\lambda/4$ vertical radiator
——— Angle-radiator combination

b. vertical pattern
$\varphi = 90°$

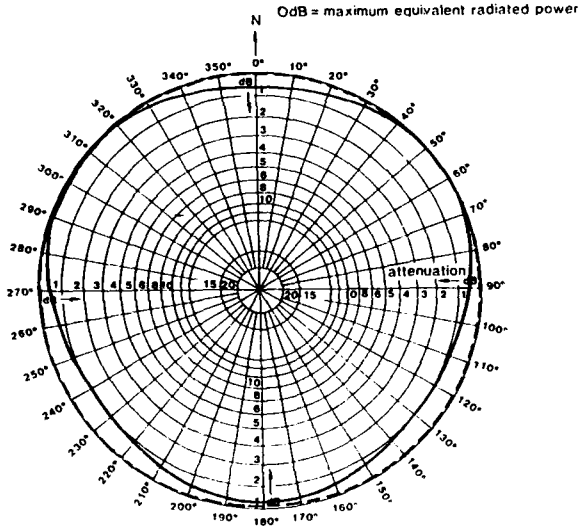

horizontal pattern

Fig. 8: Relative gain pattern of a MF-angle-radiator antenna combined with a real erected supporting mast after Fig. 4b over perfect ground

Parameter: —— all guy ropes not insulated
– – – lower guy ropes insulated near mast

a. horizontal pattern
$\theta = 90^\circ$

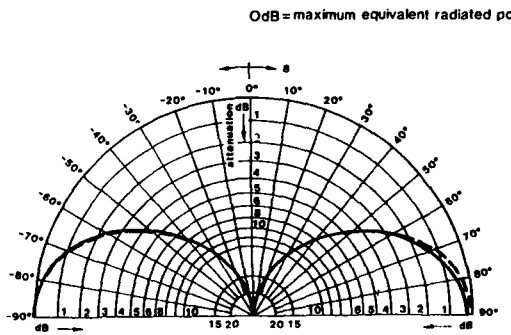

vertical pattern

Fig. 8: Relative gain pattern of a MF-angle-radiator antenna combined with a real erected supporting mast according to Fig. 4b over perfect ground

Parameter: —— all guy ropes not insulated
– – – lower guy ropes insulated near mast

b. vertical pattern
$\varphi = 90^\circ$

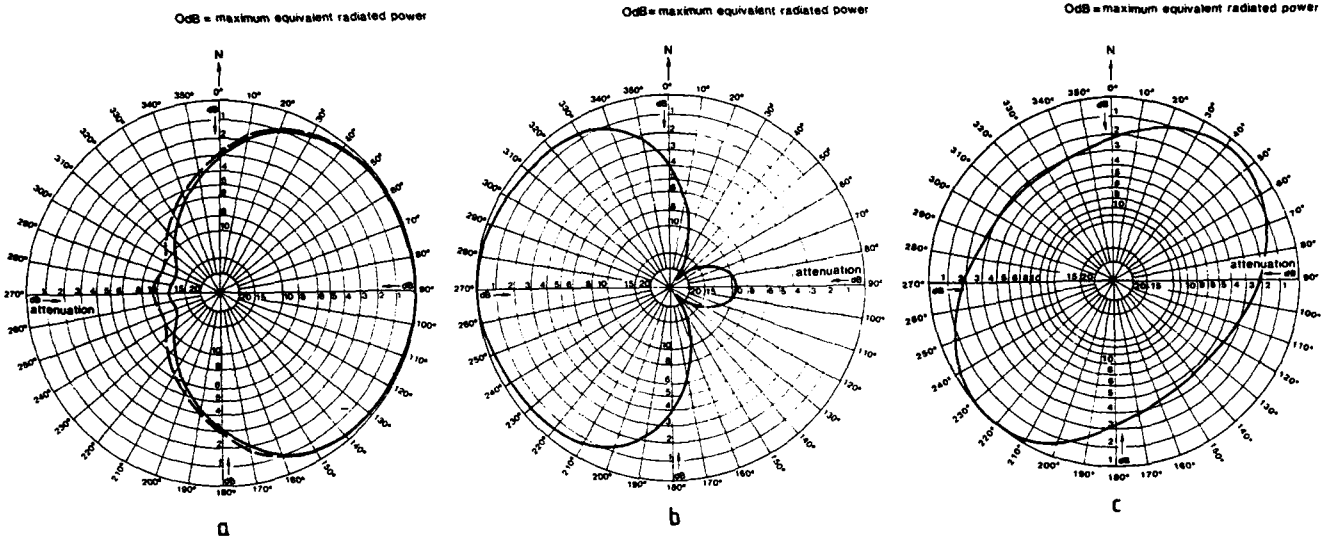

Parameter:
two angle-radiators with an electr.
—— length of 0.23 λ, grounded
two angle-radiators with an electr.
---- length of 0.245 λ, grounded

Parameter:
six angle-radiators feeded and one covered by two additional passive linear radiators

Parameter:
four angle-radiators feeded with equal current phase and two pointed in opposite with a current-phase difference of 170 degrees.

Fig. 9: Relative gain patter of a directive MF-angle-radiator antenna combined with a real erected supporting mast according to Fig.4a.

IMPROVED NIGHT INTERFERENCE PROTECTION FOR AM STATIONS

James B. Hatfield
Hatfield & Dawson Consulting Engineers Inc.
4226 6th Ave. N.W.
Seattle, Wa 98107

ABSTRACT

Radiation from standard broadcast AM stations travels greater distances at night than during the day due to skywave propagation. This can cause interference to other stations operating on the same frequency at relatively great distances. To maintain interference levels below specified limits the FCC regulations provide a method for determining radiation limits at calculated angles above the horizon. The radiation at these vertical angles is given by the "vertical plane radiation" formula (Equation (2)), and the FCC AM directional antenna formula (Equation (1)) when a station uses a directional antenna.

The formulas that are used to calculate the radiation at angles above the horizon are derived by assuming a sinusoidal current distribution. The phase shift of the antenna current over the length of the tower is ignored. A more realistic current distribution and hence vertical angle radiation can be computed using numerical methods. Several different AM antenna systems have been analyzed using MININEC to determine vertical angle radiation and the results compared to the vertical angle radiation predicted by formulas presently used by the FCC.

The improved computation of the AM nighttime interfering fields indicates that existing FCC methods underpredict the levels of potential interference in many instances where tall towers are used. AM antenna design using modern numerical techniques such as the method of moments produce more accurate radiation calculations resulting in reduced interference potential at night from new facilities.

COMPUTING FCC DIRECTIONAL ANTENNA PATTERNS

The directional antenna patterns for AM medium wave broadcast facilities in this country are determined through the use of equations (1) and (2). The angular variables are given in terms of the clockwise azimuth from true north, the vertical angle in degrees above the horizon and spacings and phases in electrical degrees. These expressions yield the far field, no loss, inverse distance field strength at one kilometer. The far field is assumed to exist at distances from the array great enough for rays from the antenna elements to the observation point to be effectively parallel. Equation (1) is the summation of a series of polar numbers, one for each tower, with the magnitude given by the product of the pattern size factor, the relative far field contribution from the given tower, and a weighting factor that is proportional to the radiation from the tower at a given vertical angle. The angle of the polar number is determined from the distances between elements, the phase angle of the far field contribution of the given element, and the path length differences resulting from the horizontal angular displacement of the element from the reference point and

the angle of the observation point above the horizontal.

The angles of the polar numbers are determined by parallel ray geometry while the magnitudes of the polar numbers are determined by functions that are derived from an assumed sinusoidal tower current distribution. The effects of the phase shifts of the tower currents as a function of the tower heights are not included in these equations. In situations where tower current phase shift is significant the fields at vertical angles that are computed using these expressions may be unrealistic.

The limits established by the FCC on the radiated fields from AM directional antennas are derived from the "theoretical pattern" equations just described and are called the "Standard Pattern".

DETERMINING LIMITS ON VERTICAL RADIATION

The signals radiated at various vertical angles at night from AM antennas can be transmitted greater distances via skywave propagation than daytime ground wave signals. Variability in the reflections from the ionosphere make skywave propagation a statistical phenomenon. Various measurements and calculation techniques have been combined over the years in an attempt to arrive at a reasonable prediction methodology. Figure (1) is typical of the curves used by the FCC for determining skywave signal strength as a function of distance from an AM antenna, and the vertical plane field strength of that antenna, at the "pertinent vertical angle". Figure(2) depicts the geometry by which the "pertinent vertical angles" are determined.

Equations (1) and (2) are used to design AM directional antennas to limit the radiation in the vertical plane so as not to exceed the interference limits determined by the skywave methodology outlined above, in combination with other administrative rules and procedures.

A MORE REALISTIC VERTICAL PLANE FIELD COMPUTATION

Method of moments programs yield tower current distributions that are likely to be more realistic than the sinusoidal current distributions used to calculate the fields from AM towers and directional arrays. The differences between the fields calculated using the two methods are likely to be greater for taller towers where the tower current phase shift, which is ignored by the sinusoidal approach, is greater. The following examples illustrate the effects that occur in a variety of situations.

I. A Single Tall Tower

An example of how a tall tower can be used to limit skywaves at relatively high vertical angles is shown in Figure (3). This curve depicts the relative field in the vertical plane, calculated for an assumed sinusoidal distribution, from a tower .6 wavelengths tall. The minimum can be used to reduce the interference to co-channel stations within a few hundred miles of the tower.

Figure (4) shows the fields from this tower in the vertical plane as computed by MININEC and by Equation (2). The minimum given by MININEC is not as deep as that calculated by Equation (2) and it occurs at a different vertical angle. The actual interference levels will obviously be much higher than those predicted by Equation (2).

II. Four Tower Array

The horizontal plane pattern of a four tower in line array is shown in Figure (5). These towers are 0.3 wavelengths tall. The vertical plane fields for this array in the region of the horizontal plane minima are shown in figure (6). Fields computed by MININEC and Equation (1) are depicted in comparison the maximum fields allowed at these angles by the FCC Standard Pattern.

It can be seen that the numerically computed fields agree reasonably well with the fields computed by Equation (1) and are all within the standard pattern limits. This is caused by the fact that the phase shifts of the tower currents are small enough that the two computation methods yield similar results.

III. Unequal Height Two Tower Array

The horizontal plane pattern of an unequal height two tower array is shown in Figure (7). One of the towers is 0.45 wavelengths tall while the other tower is half as tall. Figure (8) shows the FCC standard pattern limits in the vertical plane at an azimuth near the horizontal plane pattern minimum and the vertical plane fields for two sets of antenna adjustment parameters as calculated by MININEC.

The vertical plane pattern for this array was computed by MININEC using the design field parameters. The inverse fields exceeded the standard pattern limits in the horizontal plane by almost 50%. At the higher vertical angles the fields fell within the standard pattern limits. When the actual array was adjusted in the field to obtain the design field parameters, the measured fields agreed with those calculated by MININEC and the array was readjusted so that the horizontal plane field fell to 82.3 mV/m (see Figure (8)). The fields at the lower vertical angles are within the standard pattern limits for this adjustment, while the fields at the higher vertical angles exceed the standard pattern limits.

DISCUSSION

These three examples demonstrate that the accuracy of FCC Equations (1) and (2) in predicting vertical plane radiation from AM antennas is a function of the phase shifts of the currents flowing along the antennas. The total phase shift of the current in the single tall tower (0.6 wavelength) from its base to its top is +170 degrees. The total phase shift of the antenna currents in the four tower example (equal heights of 0.3 wavelengths) ranges from -25 to -40 degrees. Accurate computation of the phase shift of the currents in taller towers must be considered if excessive vertical angle radiation from these towers is to be avoided. Numerical computation techniques provide a means of reducing nighttime AM interference by giving a more complete picture of the current distributions in AM broadcast antennas.

When a program such as NEC or MININEC is used to compute the horizontal plane pattern of an AM broadcast station's directional antenna the agreement achieved with the pattern given by FCC Equation (1) is very good when the base drive voltages that result in the correct far field parameters (field ratios and phases used in FCC Equation (1)) are used. The exception to this rule is the unequal height two tower array discussed in example III above. The horizontal plane pattern given by FCC Equation (1) has minima that are 50% lower than the MININEC far field pattern minima for the same field parameters. The measured field strengths for the actual antenna system agree with the MININEC computations.

Using FCC far field parameters for the design of AM directional antennas does not always result in as much field suppression at specified angles as is indicated by the use of FCC Equation (1). To provide nighttime interference protection by reducing the fields at the higher vertical angles for the unequal height two tower array discussed above the horizontal plane standard pattern field limits must be exceeded in the pattern minima. When field parameters are used that do not cause the horizontal plane standard pattern limits to be exceeded the radiation at vertical angles above thirty degrees exceeds the limits of the vertical plane standard pattern and nighttime interference is increased.

The FCC requires that an AM directional antenna "proof of performance" be conducted for all new AM directional antenna installations. The FCC rules state that the Proof of Performance must show that the measured horizontal plane ground wave pattern of an AM directional antenna installation is within the confines of the FCC horizontal plane standard pattern. This results in increased nighttime interference from this particular array.

FCC EQUATIONS

1. *General equations*

The theoretical directional antenna radiation pattern is calculated by means of the following equation, which sums the field strength from each element (tower) in the array.

where:

$$E_T(\varphi,\theta) = \left| K_L \sum_{i=1}^{n} F_i f_i(\theta) \angle \underline{\Psi_i + S_i \cos\theta \cos(\varphi_i - \varphi)} \right| \qquad (1)$$

$$f_i(\theta) = \frac{\cos(G_i \sin\theta) - \cos G_i}{(1-\cos G_i)\cos\theta} \qquad (2)$$

where:

$E_T(\varphi, \theta)$: theoretical inverse distance field strength at one kilometre in mV/m for the given azimuth and elevation;

K_L : multiplying constant in mV/m which determines the pattern size (see paragraph 2.5 below for derivation of K_L);

n : number of elements in the directional array;

i : denotes the ith element in the array;

F_i : ratio of the theoretical field strength due to the ith element in the array relative to the theoretical field strength due to the reference element;

θ : vertical elevation angle, in degrees, measured from the horizontal plane;

$f_i(\theta)$: ratio of vertical to horizontal plane field strength radiated by the ith element at elevation angle θ;

G_i : electrical height of the ith element, in degrees;

S_i : electrical spacing of the ith element from the reference point in degrees;

φ_i : orientation of the ith element from the reference element (with respect to True North), in degrees;

φ : azimuth with respect to True North, in degrees;

Ψ_i : electrical phase angle of field strength due to the ith element (with respect to the reference element), in degrees.

Equations (1) and (2) assume that:

- the current distribution in the elements is sinusoidal,
- there are no losses in the elements or in the ground,
- the antenna elements are base-fed, and
- the distance to the computation point is large in relation to the size of the array.

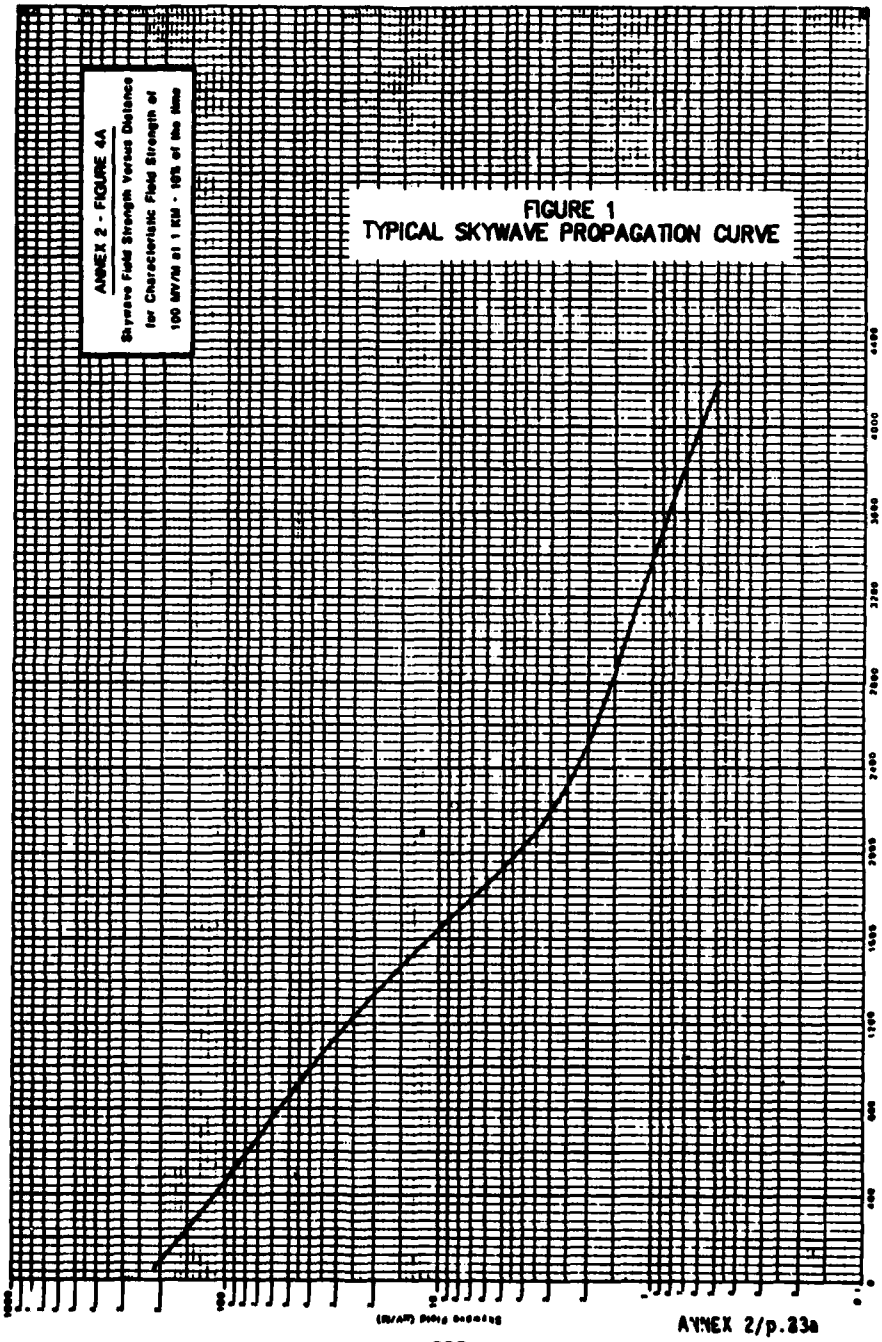
ANNEX 2 - FIGURE 4A
Skywave Field Strength Versus Distance
for Characteristic Field Strength of
100 dBuV/m at 1 KM - 10% of the time
FIGURE 1
TYPICAL SKYWAVE PROPAGATION CURVE

ANGLES OF DEPARTURE
VERSUS
TRANSMISSION RANGE

1 for use in computing 50% signals

2 and 3 for use in computing 10% signals

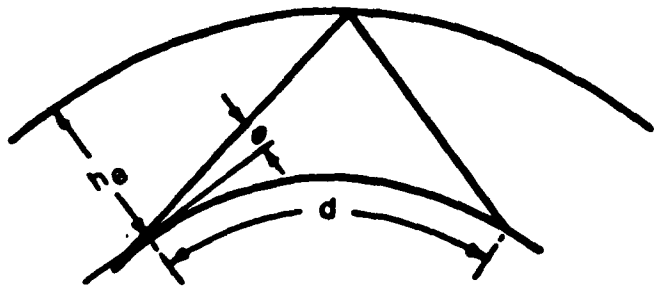

FIGURE 2
GEOMETRY FOR DETERMINING
PERTINENT VERTICAL ANGLES

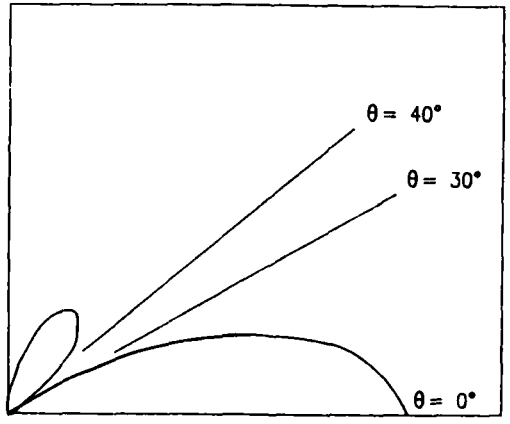

FIGURE 3
RELATIVE 0.6 WAVELENGTH TOWER
FIELDS IN THE VERTICAL PLANE

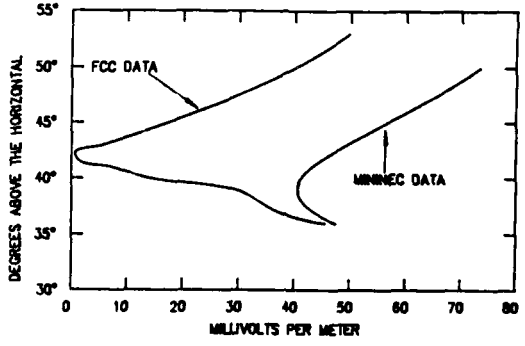

FIGURE 4
0.6 WAVELENGTH TOWER

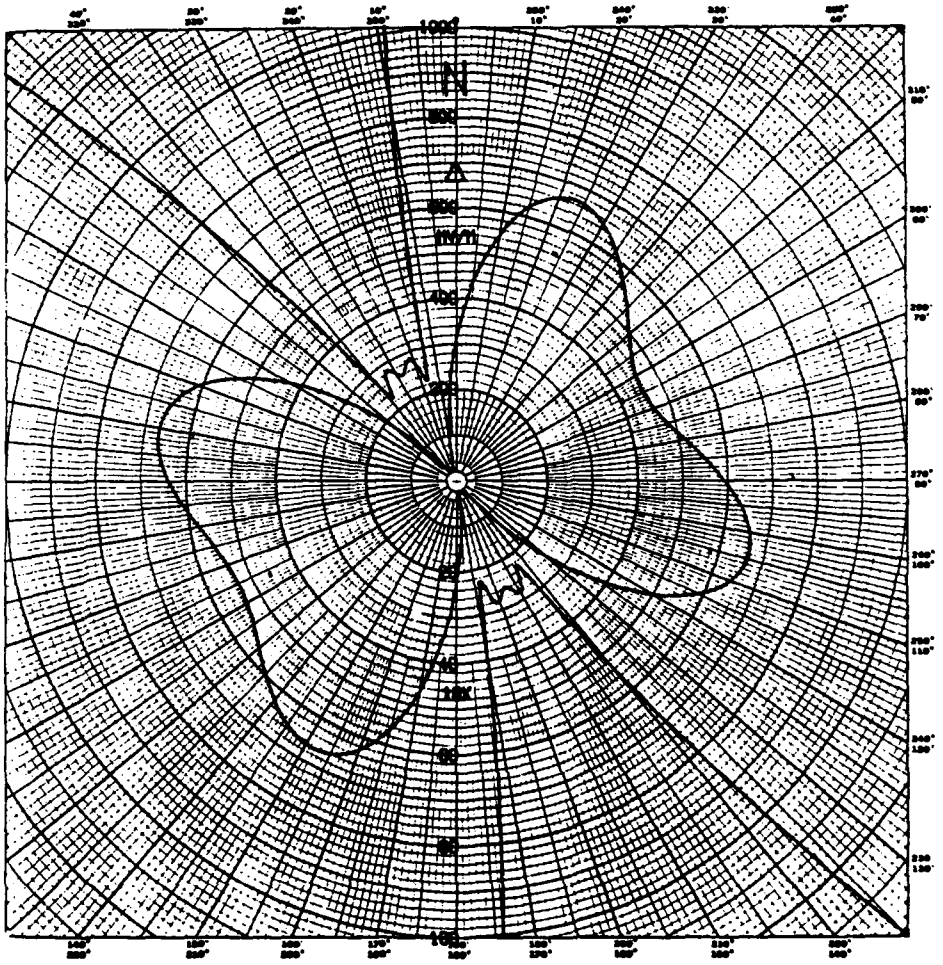

FIGURE 5
HORIZONTAL PLANE STANDARD PATTERN FOR FOUR TOWER
0.3 WAVELENGTH EQUAL HEIGHT IN LINE ARRAY

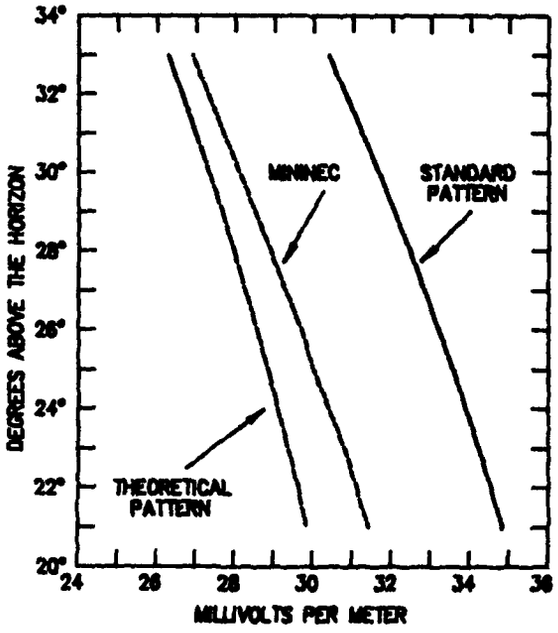

FIGURE 6
FOUR TOWER ARRAY

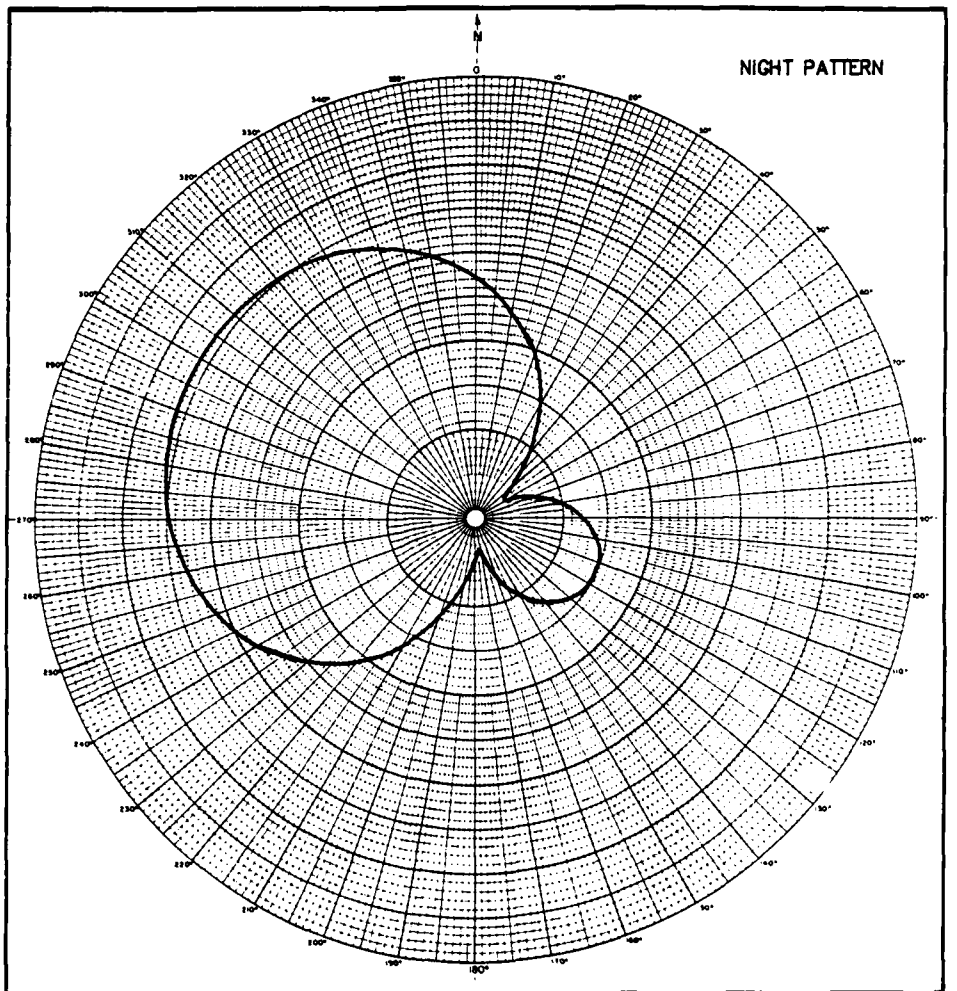

TOWER No.	AZIMUTH IN DEG.	SPACING IN DEG.	FIELD RATIO	PHASE ANGLE	TOWER HEIGHT IN DEGREES
1	0.0	0.0	1.00	0.0	160.2
2	297.5	90.0	0.84	-134.0	80.1

SHORTEST TOWER IN ARRAY IS #2 TOWER. NO TOP LOADED TOWERS.

FIGURE 7
HORIZONTAL PLANE STANDARD PATTERN FOR
UNEQUAL HEIGHT TWO TOWER ARRAY

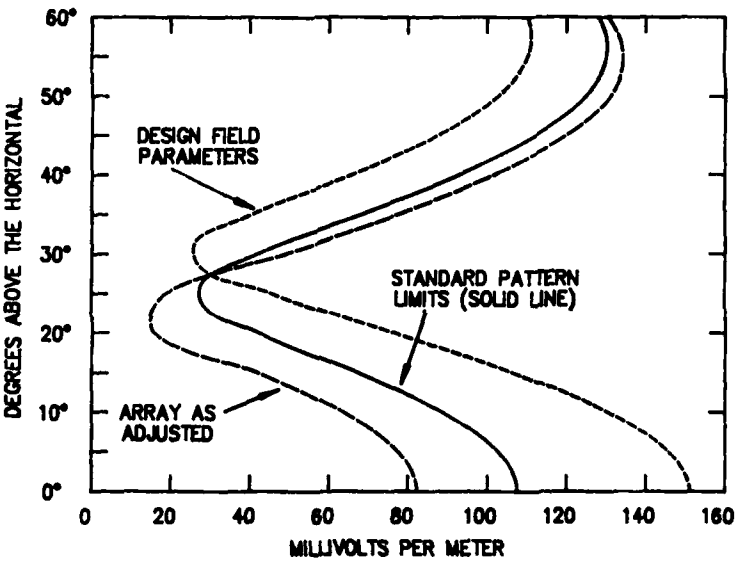

FIGURE 8
UNEQUAL HEIGHT TWO TOWER ARRAY

CHARACTERIZATION OF A HIGH–FREQUENCY VERTICAL HALF RHOMBIC

M.D. Fanning and W.P. Wheless, Jr.
University of Alabama Electrical Engineering Department
Tuscaloosa, Alabama 35487

D.L. Faust and M.B. King
Eyring, Inc. Communications Systems Division
Provo, Utah 84601

Abstract – Selected radiation pattern characteristics of the commercially available Barker & Williamson model AC–1.8–30 antenna, above finite ground, are investigated experimentally and numerically at several frequencies in the hf (3–30 MHz) frequency range. Emphasis is placed on examination of the capability of personal computer software, the Numerical Electromagnetics Code (NEC–81, ver. 2.2), to reliably predict the radiation patterns of this antenna. Numerous graphical comparisons of measured versus computed radiation patterns are presented.

INTRODUCTION

Design of hf wire antennas using NEC2 (specifically, NEC–81 version 2.2) [1,2] on a personal computer (pc) is attractive from the viewpoint of convenience. Many hf antennas are in near proximity to finite ground and may involve ancillary devices, like ground rods, which question the practical utility of NEC2. In this paper, graphical comparisons of several measured and computed radiation patterns are presented. The results offer a sampling of the accuracy and reliability of NEC2 pattern predictions for hf antennas close to real ground.

The antenna used for NEC2 analysis and measurements was the Barker & Williamson model AC–1.8–30. While commonly referred to as a vertical half rhombic (VHR), the antenna illustrated in Figure 1 could be described as a "balanced–feed, loaded pyramid" configuration. Antenna wire is stranded #14 AWG. The center support for this study was a 10.7–meter fiberglas pole. The axis of the antenna was along a precise East–West line, with the balun feed at the East end and the 804Ω termination resistor at the West end.

Measurements were carried out using Eyring's Broadband Antenna Test System (BATS) at its Cedar Valley, Utah, test range. BATS is a computer–controlled, integrated test system which incorporates the capability for airborne pattern measurements of antenna power gain. The test system is referenced to standard dipoles [5] for obtaining hf pattern profiles with an overall accuracy on the order of 1 dB. The BATS configuration and methodology is described in references [3] and [4], with details on the antenna measurement beacon in [5]. Test site ground parameters ϵ_r (dielectric constant) and σ (conductivity) are measured for each pattern profile as described in reference [7].

COMPARISON OF NEC2 AND MEASURED PATTERNS

Measurements were conducted at the Eyring facility to acquire pattern profiles at frequencies including 3.195, 10.12, 19.0475, and 22.9 MHz. Corresponding NEC2 radiation patterns were subsequently computed. BATS software, running on an IBM PC, was used to overlay the NEC2 data on the measured data plots.

A sample of results was selected for presentation. Three gain versus elevation and

seven gain versus azimuth pattern profiles (involving five different elevation angles) were chosen. NEC2 patterns are shown with computed gain values, compensated for efficiency, except for Figures 2,7,8, and 10. For ease of qualitative pattern comparison, the NEC2 gains for these four figures were respectively reduced by 4.9, 5.9, 5.9 and 3 dBi.

The measured data in Figures 2–4 was derived from airborne flyovers along a North–South course (perpendicular to the axis of the antenna). The respective frequencies were 3.1925, 10.12, and 19.0475 MHz, with Horizontal polarization attitude. The correspondence between the NEC2 computed pattern shape and the measured results in Figure 2 is excellent. Measurements at 10.12 and 19.0475 MHz (Figures 3 and 4), conducted four days earlier, illustrate manifestations of high winds aloft in measured flyover patterns. The NEC2 predicted patterns for Figures 3 and 4 are believed to be as reliable as the Figure 2 results.

Figures 5 through 9 present gain versus azimuth results for Vertical polarization at various frequencies and elevation angles (from 5° to 40° above the horizontal) indicated by the figure captions. Figures 10 and 11 give two similar Horizontal polarization case studies. The NEC2 predicted patterns are satisfactory for many hf applications except for the minor lobe predictions associated with Figures 7 and 8. A distinct minor lobe exists about 270° azimuth in Figure 7. Figure 8 shows that the minor lobe is substantially larger at the higher elevation angle of 40°. In contrast, NEC2 predicts that the incipient null in Figure 7 about 270° azimuth continues to deepen as the elevation angle is raised to 40°. Other cases also exhibited the same tendency in NEC2 results.

CONCLUSIONS

The primary objective of this work has been to sample the validity of NEC2 pattern shape predictions for hf wire antennas in close proximity to finite ground. Generally good correspondence between NEC2 and measured patterns was observed in this study. From the results obtained, it appears that NEC2 can compute the radiation patterns of such antennas to a degree of accuracy that is useful for many intended applications. Pattern shapes may be interpolated with reasonable confidence when the NEC2 computational program is supplemented by a modest pattern measurement series at a few discrete frequencies.

REFERENCES

1. Burke, G.J. and A.J. Poggio, "Numerical Electromagnetics Code (NEC) – Method of Moments," vol. 2, Naval Ocean Systems Center Technical Document 116, January 1981.
2. Burke, G.J. and A.J. Poggio, "Numerical Electromagnetics Code (NEC) – Method of Moments, Part III: User's Guide", NEEDS 2.0 Version, Lawrence Livermore National Laboratory, Livermore, California, Report UCID–18834, January 1981.
3. Faust, D.L. and M.B. King, "Broadband HF antenna testing," *Proc. of RF Technology Expo '86*, pp. 625–631, Anaheim, CA, January 1986 (Eyring Document No. 800–0758).
4. Faust, D.L., "The low profile antenna/rollout hf antenna: a new tactical communications option," *HF Radio Clinic*, St. Louis, MO, September 1986 (Eyring Document No. 900–0013).
5. _____, "Antenna measurement beacon," January 1989, Eyring Document No. 900–0034.
6. Faust, D.L., "Selected pattern measurements of four full–scale tactical HF antennas," *Proc. 2nd Annual Rev. of Progress in Applied Computational Electromagnetics*, Monterey, CA, March 1986 (updated September 1986 as Eyring Document No. 900–0009).
7. _____, " Ground measurement probe," March 1990, Eyring Document No. 900–0036B.

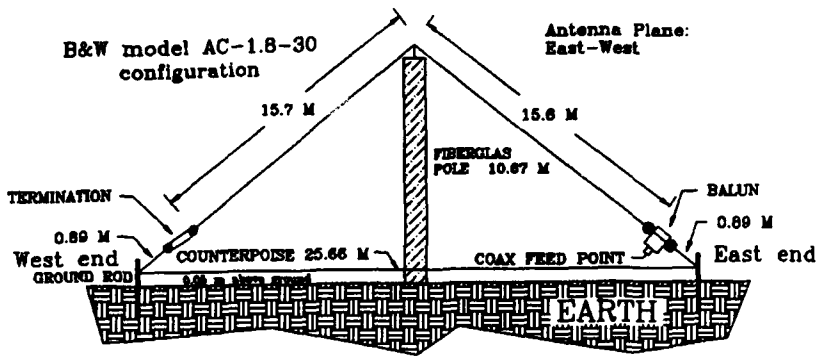

Figure 1. Antenna geometry.

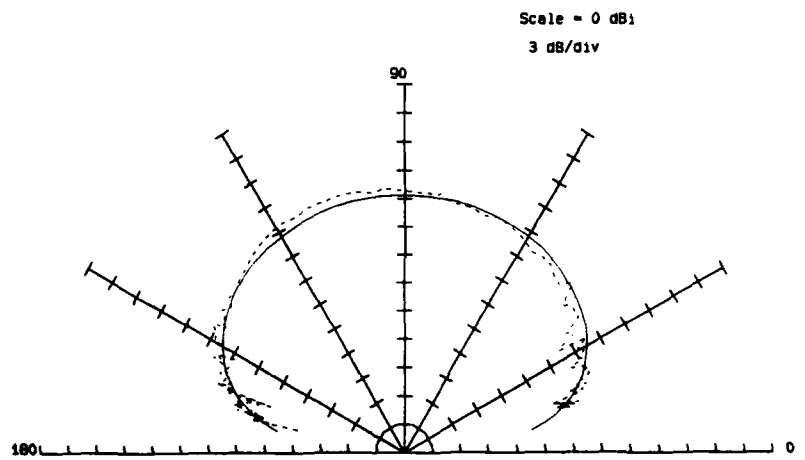

——— COMPUTED (adjusted by -4.9 dB) ----- MEASURED

Figure 2. Gain versus elevation for horizontal polarization at 3.1925 MHz, compass azimuth = 0° (ϵ_r = 18.5, σ = 4.3 mS/m).

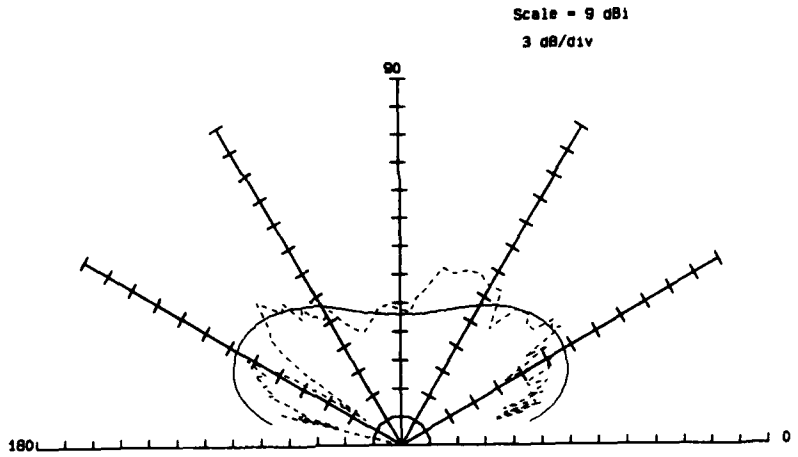

——— COMPUTED ----- MEASURED

Figure 3. Gain versus elevation for horizontal polarization at 10.12 MHz, compass azimuth = 0° (ϵ_r = 8.7, σ = 6.7 mS/m).

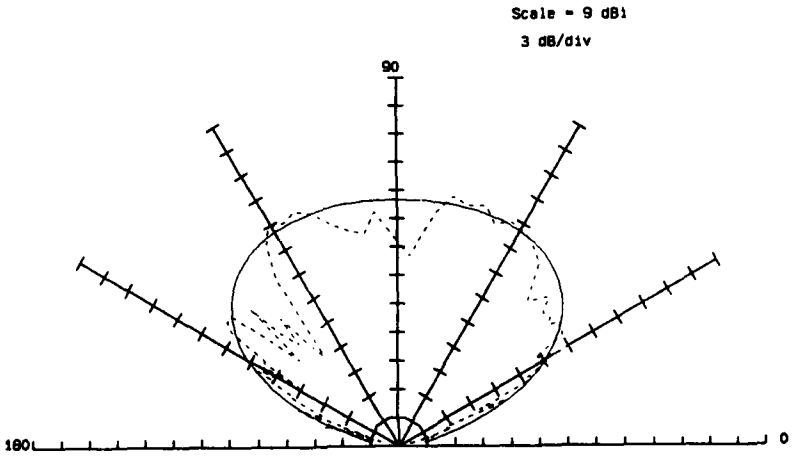

——— COMPUTED ----- MEASURED

Figure 4. Gain versus elevation for horizontal polarization at 19.048 MHz, compass azimuth = 0° (ϵ_r = 7.8, σ = 8.9 mS/m).

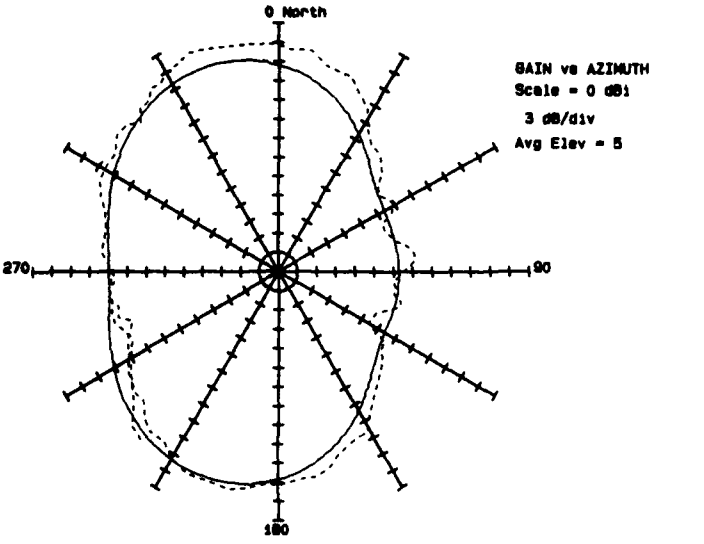

Figure 5. Gain versus azimuth for vertical polarization at 10.12 MHz, 5° elevation (ϵ_r = 10., σ = 8.0 mS/m).

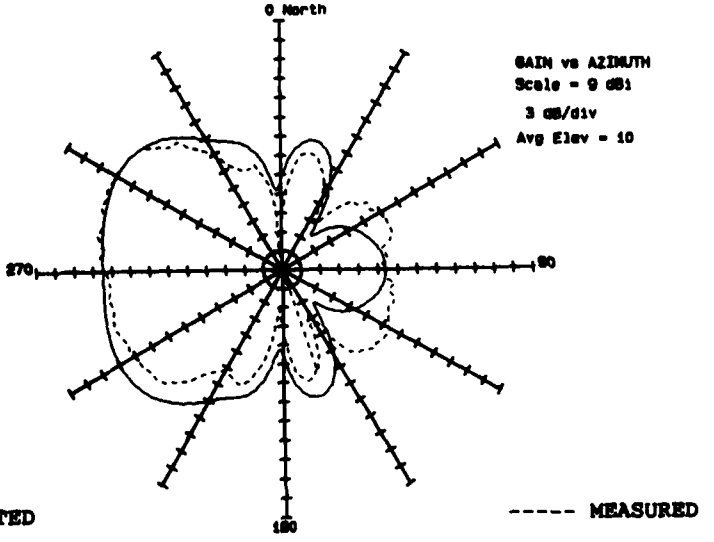

Figure 6. Gain versus azimuth for vertical polarization at 22.9015 MHz, 10° elevation (ϵ_r = 6.3, σ = 8.5 mS/m).

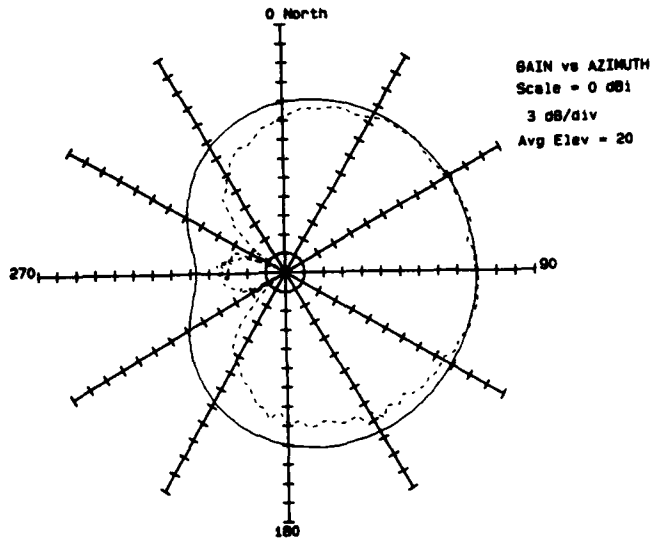

——— COMPUTED (adjusted by -5.9 dB) ----- MEASURED

Figure 7. Gain versus azimuth for vertical polarization at 3.1925 MHz, 20° elevation (ϵ_r = 18.5, σ = 4.3 mS/m).

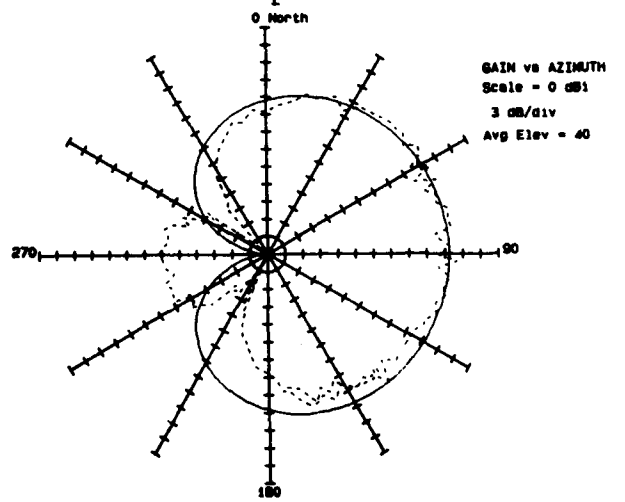

——— COMPUTED (adjusted by -5.9 dB) ----- MEASURED

Figure 8. Gain versus azimuth for vertical polarization at 3.1925 MHz, 40° elevation (ϵ_r = 18.5, σ = 4.3 mS/m).

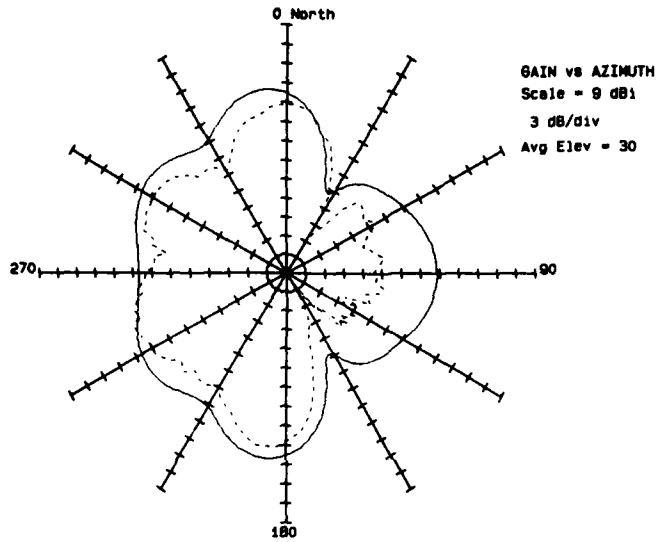

——— COMPUTED ----- MEASURED

Figure 9. Gain versus azimuth for vertical polarization at 19.0475 MHz, 30° elevation (ϵ_r = 8.9, σ = 10.9 mS/m).

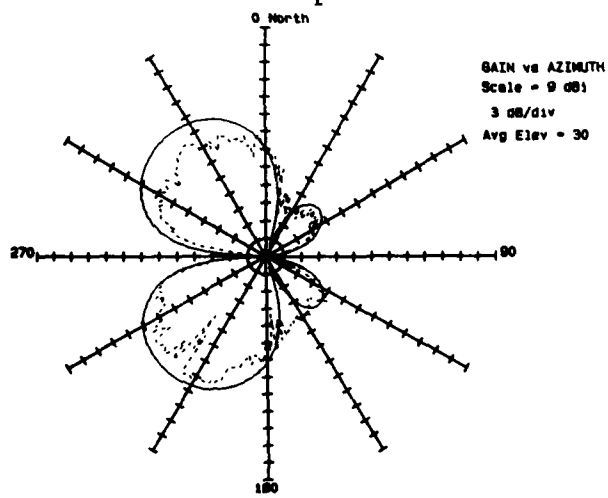

——— COMPUTED (adjusted by -3 dB) ----- MEASURED

Figure 10. Gain versus azimuth for horizontal polarization at 10.12 MHz, 30° elevation (ϵ_r = 8.7, σ = 6.7 mS/m).

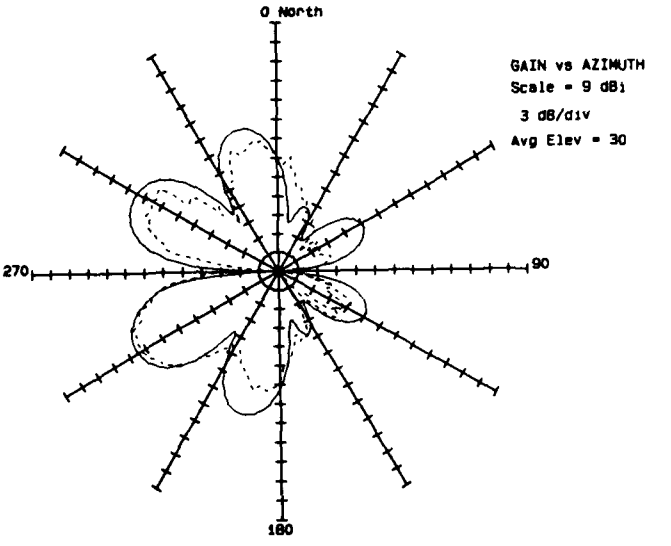

——— COMPUTED ----- MEASURED

Figure 11. Gain versus azimuth for horizontal polarization at 19.0475 MHz, 30° elevation (ϵ_r = 8.9, σ = 10.8 mS/m).

COMPARISON OF NECGS TO MEASURED DESIGN CURVES FOR VLF MONOPOLES

Submitted by

James P. Cahill
Kershner, Wright & Hagaman P.C.
Alexandria, VA

ABSTRACT

The applicability of the NEC-GS program to the design of VLF top-loaded monopoles is evaluated by comparing its results against measured data. Effective height, resonant frequency, and static capacitance values computed from the NEC-GS output are compared with measured design curves published by the U.S. Navy Electronics Laboratory. NEC-GS results obtained using both the current-slope-discontinuity source and the applied E-field source are presented to establish which source model is best suited for the VLF top-loaded monopole problem.

1.0 INTRODUCTION

A top-loaded, base insulated monopole is often used as a VLF transmitting antenna. To determine the accuracy of the NEC-GS solution for this type of antenna and to discover the modeling techniques which provide the most accurate and consistent results, several important antenna characteristics derived from NEC-GS output were compared with measured data. One specific goal of this study was to determine which of the two voltage source models available in the NEC-GS code, the applied E-field source or the current-slope discontinuity CSD source, provides the more accurate results. [1] [2]

The measured data against which the NEC-GS results were compared were obtained from a U.S. Navy Electronics Laboratory (NEL) report.[3] Contained in the NEL report are a series of effective height, resonant frequency, and static capacitance curves which were derived from numerous scale model measurements. Effective height, resonant frequency and static capacitance were measured, because if these quantities are known, most other significant VLF monopole properties can be calculated.

2.0 NEL CURVES

The NEL measurements were performed on a scale model with the geometry defined in Figure 1. A number of equally-spaced top radials were attached to a cylindrical tower which was insulated from ground at its base. For all measurements, the height (h) of the structure was 76.5 inches, the height-to-tower diameter ratio (h/d) was very nearly 200, and the height-to-radial diameter ratio (h/d_1) was 7630. To provide a reference for later measurements, the characteristics of the model monopole without any top radials were determined, and from this information, curves showing the effective height, resonant frequency, and static capacitance versus monopole height (Figures 2, 4 and 6) were calculated. The effective height curve was derived by assuming that the effective height of the monopole was one-half of its physical height. After the resonant frequency of the model monopole was measured, the resonant frequency curve was plotted by recognizing that for a constant h/d ratio, the height-resonant frequency product remains constant. Similarly, the static capacitance curve was calculated from the reference measurement using the fact that the static capacitance is proportional to the antenna height for constant h/d.

When the top radials were added, the static capacitance was again measured directly, but the resonant frequency and effective height were measured relative to the properties of the reference monopole alone. The relative effective height values were found by measuring the far-field strength levels with a constant current input at 5 MHz.

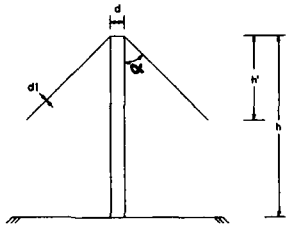

Figure 1 - Simplified model geometry.

Although the NEL report presents curves for several top-radial configurations, this paper considers only the case where the angle between the tower and radials (α) was 45° and the number of radials is 12. This case is representative of many antennas now operating and should sufficiently indicate the suitability of the NEC-GS program for VLF top loaded monopole design.

3.0 NEC-GS MODEL

A NEC-GS model was created which was practically identical to that described in the previous section except that a full size antenna was modeled at 50 kHz. The h/d and h/d_1 ratios were 200 and 7600, respectively. When top radials were present, twelve were used and α was 45°. The cylindrical tower was divided into five segments. Depending on the h'/h ratio, between one and five segments were specified on each radial.

3.1 *Effective Height*

Figure 2 displays the effective height data for a monopole without top radials as derived from NEC-GS as well as the corresponding NEL curve. NEC-GS effective height values are shown for both the E-field and CSD sources. These values were calculated from the computed input resistance. Clearly, the CSD source provides a closer fit to the NEL data. It is not surprising that the CSD source gives the more accurate input resistance, because it attempts to compute the impedance from the current at the base of the tower rather than at the center of the lowest segment as the E-field source does.

Effective height data for a top-loaded tower are presented in Figure 3. In this figure, the effective height data relative to a monopole without radials are plotted against the h'/h ratio. (h'/h is the ratio of the projected length of the radials onto the tower divided by the tower height.) The NEC-GS relative values were found by dividing the results for a 633 ft top-loaded monopole by those for a 633 ft monopole alone. Once again, the CSD source data agree more closely with the measured curve.

Total effective height values for a 633 ft monopole are given in Table I. This table again shows the CSD source to be in better agreement with the NEL data. However, VLF top-loaded monopoles are usually designed with h'/h ratios between 0.5 and 0.7, and the E-field source gives satisfactory results in this range.

Effective height values can also be determined from the NEC-GS results for the far E-field (E) and base current (I). For the E-field source, the effective height figures calculated in this manner were within

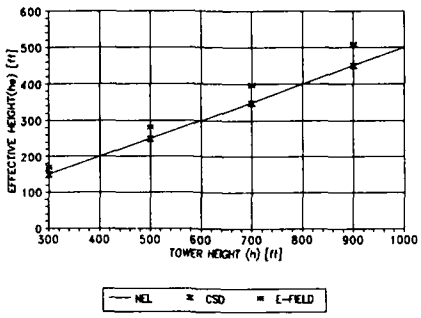

FIGURE 2 - EFFECTIVE HEIGHT OF AN UNLOADED MONOPOLE
NEC-GS VALUES WERE CALCULATED FROM THE INPUT RESISTANCE

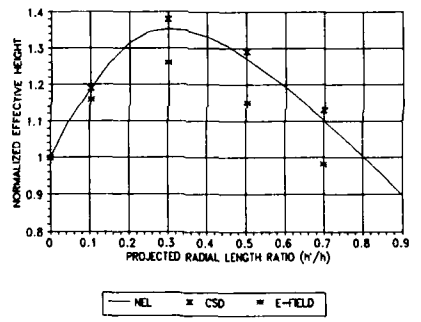

FIGURE 3 - EFFECTIVE HEIGHT OF A TOP-LOADED MONOPOLE RELATIVE TO THAT OF THE REFERENCE MONOPOLE

one percent of those determined from the resistance. For the CSD source, however, the values calculated using E and I were approximately 4.0 percent lower than those found from R. This difference probably occurred because NEC-GS does not account for the higher base current of the CSD source when computing the field strength.

From the information presented above, it can be seen that the NEC-GS program is able to provide an accurate estimate for the effective height of a VLF monopole. It appears that the CSD source generally

TABLE I

Effective Height (m) of a
633 Foot Top-Loaded Monopole

b'/h	NEL	CSD*	E-FIELD*
0	96.5	95.9	109
0.1	115	114	125
0.3	130	132	137
0.5	123	124	125
0.7	106	108	107

*From base resistance

provides more accurate results than does the E-field source. Furthermore, the best and simplest way to find the effective height is by calculating it from the computed radiation resistance.

3.2 Resonant Frequency

An efficient way to estimate the resonant frequency using NEC-GS is to compute the reactance at two frequencies and then calculate the resonant frequency assuming that the antenna can be modeled as a series RLC circuit. Figure 4 shows the resonant frequencies calculated from the 50 and 100 kHz base reactance for several tower heights. Both sources give higher resonant frequencies than the NEL measurements did, and the CSD source is greater by a considerable amount. These discrepancies are understandable considering that the simple RLC circuit approximation was used. A more accurate, although more time consuming, way to locate resonance is by trial and error. Table II reveals that the trial and error method produces results remarkably close to the NEL data.

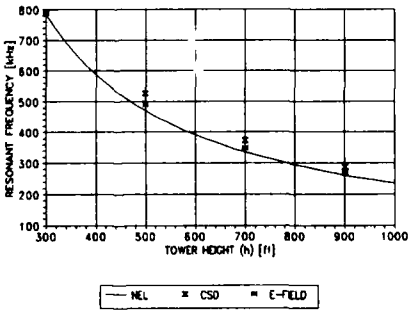

FIGURE 4 - RESONANT FREQUENCY OF AN UNLOADED MONOPOLE
NEC-GS RESULTS WERE FOUND BY THE TWO-FREQUENCY METHOD

TABLE II

Resonant Frequency (kHz) for
Unloaded Monopoles

h(ft)	NEL	CSD*	E-FIELD*
300	784	784	783
700	336	336	335

*Trial and error method

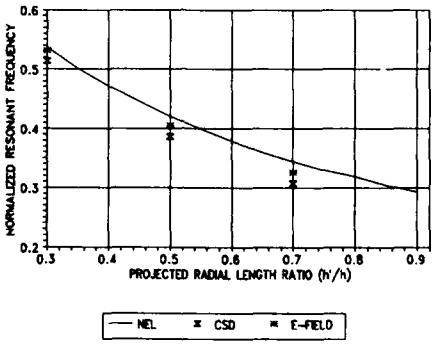

FIGURE 5 - RESONANT FREQUENCY OF A TOP-LOADED MONOPOLE RELATIVE TO THAT OF THE REFERENCE ANTENNA

The relative resonant frequency versus radial length curves are provided in Figure 5, and Table III contains the resonant frequency values of a 633 ft tower for several h'/h ratios. All calculated values were determined by the two-frequency method from the 50 and 80 kHz reactances. Notice that better agreement was obtained between the NEC-GS and NEL values for the longer radial lengths. The agreement improves because the RLC approximation is more appropriate when the capacitance between the top radials and ground is large.

The resonant frequency of VLF monopoles with h'/h ratios of 0.5 or greater can be found quite accurately from the NEC-GS output using the two-frequency method. For monopoles with shorter radials, the resonant frequency can be estimated by the two-frequency method and then established more closely by trial and error.

TABLE III

Resonant Frequency (kHz) of a
633 Foot Top-Loaded Monopole

h'/h	NEL	CSD*	E-FIELD*
0	372	414	387
0.3	200	213	206
0.5	157	160	157
0.7	128	127	126

*From two-frequency method

3.3 Static Capacitance

Static capacitance values were found by two methods. The first method involved computing NEC-GS reactances at two frequencies below resonance and then calculating the static capacitance by assuming that the antenna could be modeled as a series RLC circuit. Fifty and 100 kHz were the two computation frequencies for the tower alone, while 50 and 80 kHz were used when top radials were included. In the second method, the static capacitance was calculated directly from the NEC-GS reactance at the extremely low frequency of 30 Hz. Interestingly, both methods produced identical results to three significant figures for all cases considered.

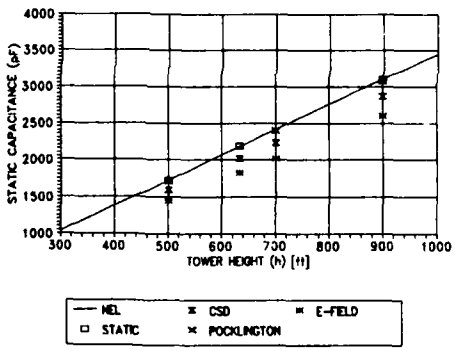

FIGURE 6 - STATIC CAPACITANCE OF AN UNLOADED MONOPOLE
NEC-GS AND POCKLINGTON RESULTS WERE FOUND BY THE TWO-FREQUENCY METHOD

As Figure 6 shows, the capacitance of the tower alone derived from NEC-GS is significantly lower than the NEL curve. Also provided in the figure are results obtained from a Kershner, Wright & Hagaman (KWH) static moment method program and from a KWH moment method program which solves Pocklington's equation using a sinusoidal basis and testing functions along with a delta function generator.

The KWH results agree very well with the NEL data and, therefore, call into question the accuracy of the NEC-GS values.

Initially, it was thought that because the segment lengths were extremely short compared to a wavelength at 30 Hz, numerical errors might have occurred. The modeling notes in the NEC User's Guide[4] suggest that the segment lengths should not be less than 0.001 wavelengths. However, it would be difficult to explain why the two methods gave identical answers if numerical errors were the problem. As a further check, the static capacitance of a 700 foot tower was calculated directly from the 30 kHz NEC-GS reactance. Thirty kHz was chosen because the segments are longer than 0.004 wavelengths and the effect of the tower inductance is small since the frequency is less than one tenth of the resonant frequency. It was found that the 30 kHz capacitance was less than one percent higher than the 30 Hz capacitance. A slightly higher 30 kHz capacitance would be expected, since the tower inductance was neglected. Therefore, it is unlikely that numerical errors caused the NEC-GS values to be low.

Turning to the relative capacitance of the top-loaded towers displayed in Figure 7, it is seen that the CSD source results closely follow the NEL measured data.

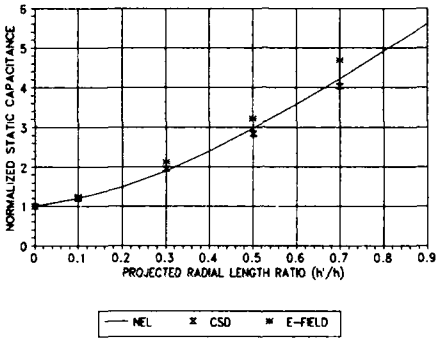

FIGURE 7 - STATIC CAPACITANCE OF A TOP-LOADED MONOPOLE RELATIVE TO THAT OF THE REFERENCE ANTENNA

Table IV provides the total NEL, KWH static, and NEC-GS capacitances for a 633 foot top-loaded monopole. The KW&H values agree more closely with the NEL data than do the NEC-GS results regardless of the source model employed. The CSD source capacitances are approximately 11 percent below the NEL data for h'/h ratios between 0.5 and 0.7, while the E-field source results are around 8 percent lower over the same h'/h range.

4.0 CONCLUSIONS

NEC-GS results have been compared against measured data to evaluate the accuracy of the program and to establish guidelines for modeling VLF top-loaded monopoles. It was found that the agreement between the NEC-GS results and the measured effective height and resonant frequency data was very good, but the agreement for the static capacitance was somewhat poorer.

TABLE IV

Static Capacitance (nF) of a
633 Foot Top-Loaded Monopole

h'/h	NEL	CSD	E-FIELD	STATIC
0	2.18	2.02	1.83	2.19
0.3	4.14	3.91	3.89	4.25
0.5	6.43	5.73	5.89	6.26
0.7	9.22	8.17	8.56	8.86
0.9	12.2			12.3

In estimating the effective height, the CSD source model was superior to the F-field source. Also, calculating the effective height from the radiation resistance provided better agreement with the measured results than if the effective height were found from the far-field and the base current. In fact, the effective heights determined from the resistance using the CSD source were always within two percent of the measured values for all tower heights and radial lengths considered.

The trial and error method with the CSD source proved to be the best technique to establish the resonant frequency, especially when the top radials were short. For a tower with short top radials, the two-frequency method over-estimated the resonant frequency by seven to ten percent, but the trial and error method agreed with the measured data to three significant figures. For h'/h ratios between 0.5 and 0.7, however, the two-frequency method exhibited improved accuracy. Under these conditions, both sources produced resonant frequencies within two percent of the measured results for a 633 foot tower.

Results for the static capacitance were not quite so good. The main problem seemed to be that the NEC-GS capacitance for a tower without radials was too low. The total capacitance of a 633 foot tower with a h'/h ratio between 0.5 and 0.7 was found to be about eight percent low for the E field source and 11 percent low for the CSD source. Exactly the same answers were obtained whether the capacitance was calculated by the two-frequency method or directly form the 30 Hz reactance.

Static capacitance estimates are mainly used to predict the bandwidth-efficiency product and the voltages on a VLF antenna. Because the bandwidth-efficiency is directly proportional to the static capacitance, a top-loaded monopole designed using NEC-GS results would have slightly more bandwidth than anticipated. Also, the antenna voltage is proportional to the reactance for constant power, so the antenna would operate at a lower voltage than NEC-GS predicted. In other words, the antenna would be slightly over-designed.

REFERENCES

1. Burke, G.J. and Poggio, A.J., Numerical Electro-Magnetics Code (NEC) - Method of Moments, Technical Document 116, Part I, Naval Ocean Systems Center, San Diego, CA, 1980.

2. Adams, R.W., Poggio, A.J., and Miller, E.K., Study of a New Antenna Source Model, UCRL-51693, Lawrence Livermore Laboratory, 1974.

3. Devany, T.E., Hall, R.F., Gustafson, W.E., Low-Frequency Top-Loaded Antennas, U.S. Navy Electronics Laboratory, San Diego, CA, 1966.

4. Burke, G.J. and Poggio, A.J., Part III.

SESSION 8 - "PARTIAL DIFFERENTIAL EQUATION BASED METHODS"

STOCHASTICAL FINITE ELEMENT FOR ELECTROMAGNETICS

Tarek Galal

ABSTRACT: - A new finite element technique is introduced. This technique would provide us with the means to numerically solve a variety of electromagnetic problem with stochastical nature.

A brief interpretation for a possible application and a future formulation concepts, regarding local and global models are discussed.

INTRODUCTION

The finite element method is an approximation procedure of numerical methodology required for solving differential, and/or integral equations of boundary and/or inital-value, in engineering types problem [1]. When the problem involving random variation of a relevant coefficient or parameter, approaches are been made to adapt the used technique to yield for stochastical numerical applications [2-9] .

This paper discuss the possible application and formulation of a stochastical finite element analysis for solving a variety of electromagnetic engineering problems,with stochastical nature. Examples are: Wave propagation with random refractive index; with fluctuating frequency; with random located scatterers; and with random rough geometry scatterer.

APPLICATION

Consider the scattering of electromagnetic waves from rough surface. Ref. [10] gives the scattered field in one dimension by:

$$E_{2j} = F_1 \int_{(j-1)h}^{jh} (a\,\xi_x - b)\, e^{i(\gamma_x x + \gamma_z \xi)} \, dx \qquad (1)$$

The author address is: P.O. Box 334, St. Brossard
Brossard, P.Q. J4Z 3N3
Canada

$j = 1,2,.....,n$

with 'n' is the number of elements and 'n+1' is the number of nodes

$\xi(x)$: the surface height ; varies randomly in the z direction .

$F_1 = \frac{ike^{ikR_0}}{4\pi R_0}$:

$K = 2\pi/\lambda$

R_0 : distance of the receiver from the origion

θ_1 : angle of incidence

θ_2 : scattering angle

R : Fresnel reflection cooficient for a smooth surface

$v_x = k(\sin\theta_1 - \sin\theta_2)$

$v_z = -k\,(\cos\theta_1 + \cos\theta_2)$

$a = (1-R)\sin\theta_1 + (1+R)\sin\theta_2$

$b = (1+R)\cos\theta_2 - (1-R)\cos\theta_1$

Through the following formulation [2], we obtain the three most important characteristics of a random proccess: the mean value, the variance, and the co-variance [11].

The average value of a local scattered field from an element j(having a length L in x direction), is given by:

$$< E_{2j} >^{(e)} = < e^{iv_z \xi(x)} >^{(e)} \left[F_1 \int_{(j-1)l}^{jl} (a\,\xi'(x) - b)\; e^{iv_x x}\; dx \right]^{(e)} \qquad (2)$$

The expression of the local element equations can be written as:

$$\bar{E}_{2j}^{(e)} = A_j^{(e)}\, \Gamma_j^{(e)} \qquad (3)$$

$$with\ \ A_j^{(e)} = \langle e^{ivr_s\xi(x)} \rangle^{(e)}\ ,\ \text{and}\ \ \Gamma_j^{(e)} = [F_1 \int_{(j-1)l}^{jl} (a\,\xi'(x) - b)\ e^{ivr_s x}\ \ dx]^{(e)} \quad (4)$$

The average value of the global scattered field from the surface is given by:

$$\Sigma_{e=1}^{n} \langle E_{2j} \rangle^{(e)} = \Sigma_{e=1}^{n} [\langle e^{ivr_s\xi(x)} \rangle^{(e)} [F_1 \int_{(j-1)l}^{jl} (a\xi'(x) - b) e^{ivr_s x}\ \ dx]^{(e)}] \quad (5)$$

The expression of the global finite element equation can be written as:

$$\bar{E}_2^{(g)} = A_j^{T_{(e)}} \Gamma_j^{(e)} \quad (6)$$

with

$$A_j^{T_{(e)}} = [A_1^{(e)}, A_2^{(e)}, \ldots\ldots A_n^{(e)}] \quad (7)$$

and

$$\Gamma_j^{T_{(e)}} = [\Gamma_1^{(e)}, \Gamma_2^{(e)}, \ldots\ldots \Gamma_n^{(e)}] \quad (8)$$

On the following we give expressions for local and global variences [10].

The local varience for an element j is given by:

$$Var(E_{2j})^{(e)} = \langle E_{2j}\ E_{2j}^{*} \rangle^{(e)} - \bar{E}_{2j}^{(e)}\ \bar{E}_{2j}^{*(e)} \quad (9)$$

The global varience associated with the total surface, is given by:

$$Var(E_2)^{(g)} = \langle E_2\ E_2^{*} \rangle^{(g)} - \bar{E}_2^{(g)}\ \bar{E}_2^{*(g)} \quad (10)$$

with

$$\langle E_2\ E_2^{*} \rangle^{(g)} \quad is\ given\ by \quad (11)$$

$$\Sigma_{e=1}^{n} \langle E_{2j}\ E_{2j}^{*} \rangle^{(e)} = \Sigma_{e=1}^{n} [\langle e^{ivr_s(\xi_1 - \xi_2)} \rangle^{(e)} [\ F_2^2 \int_{(j-1)l}^{jl} e^{ivr_s(x_1 - x_2)}\ \ dx]^{(e)}\ ] \quad (12)$$

and $F_2 = \dfrac{-ibke^{ikR_0}}{4\pi R_0}$:

The covarience between any two locally scattered fields E_{2j} and E_{2k} can be obtained from:

$$Cov(E_{2j}, E_{2k})^{(e)} = \langle E_{2j}\, E_{2k} \rangle^{(e)} - \bar{E}_{2j}^{(e)} \bar{E}_{2k}^{(e)} \qquad (13)$$

FORMULATION

We are currently embarking on pursuing the research to include the following aspects:

1. Green's function

Any electromagnetic problem described by a partial differential equation, with stochastical nature, and subject to dictated boundary conditions, can be performed in integral equation form. Such a formulation requires searching the suitable green's function [12].

2. Local maxima and high-level excursions

Ref [13] gives material covers the following subjects:
- The mean number of local maxima above high levels.
- Excursion characteristics above high levels.
- The local structure of high maxima.
- The local structure of excursions above high levels.
- The global maximum.

Using this preceding material, we would formulate necessary concepts regarding local and global stochastical finite element.

CONCLUSION

The method of stochastical finite element has been introduced. Through given demonstration, the technique would show potential for solving electromagnetic problems with stochastical nature.

REFERENCES

1. Baker, A.J., Finite Element Computational Fluid Mechanics, McGraw-Hill book co, Inc., New York, 1983.
2. Vanmarcke, E., Asce, M., and grigoriu, M., "Stochastic Finite Element Analysis of Simple Beams", ASCE, J. Eng. Mech. Div., 109 (5), 1983, pp.1203-1214.
3. Vanmarcke, E., Random Fields: analysis and synthesis, The MIT press, Cambridge, Mass., 1983.

4. Vanmarcke, E., Shinozuka, M., Nakagiri, J., Schueller, G.I., and Grigoriu, M., "Random Fields and Stochastic Finite Elements", Structural Safety, 3, 1986, pp.143-166.
5. Handa, K., and Andersson, K., "Application of Finite Element Methods in the Statistical Analysis of Structures", Proc. 3rd Int. Conf. on Structural Safety and Reliability, 1981, pp.409.
6. Hisada, T., and Nakagiri, S., "Stochastical Finite Element Method developed for Structural Safety and Reliability", Proc. 3rd Int. Conf. on Structural and Reliability, 1981, pp.395.
7. T. Galal, "Interactions Ondes Electromagnetiques et Surfaces Rugueuses Applications a la Surface Cutanee" doctorat thesis, Franche-Comte Besancon, France, 1989.
8. T. Galal, J. Mignot, P. Agache, "Technique d' Element Finis Stochastiques Appliquee a une Grandeur Physique a la Surface Cutanee", presented atITBM/Quatrieme Forum des Jeunes Chercheurs d'Innovation et Technologie en Biologie et Medecine, Paris, May 26-27, 1988, pp.40-41.
9. T. Galal, D. Rondot, J. Mignot, "Stochastic Finite Element Applied to Simulated Problem on Skin", presented at IEEE/Ninth Annual conference of the Engineering in Medicine and Biology Society, Boston, Ma., Nov. 13-16 1987, pp.40-41.
10. Beckmann, P., and Spizzichino, A., "The Scattering of Electromagnetic Waves from Rough Surfaces", New York, Macmillan, 1963.
11. Beckmann, P., "Probability in Communication Engineering", Harcourt, Brace of World Inc., New York, 1967.
12. Silvester, P.P., and Ferrari, R.L., "Finite Elements for Electrical Engineers", Cambridge University Press, 1983.
13. Adler, R.J., "The Geometry of Random Fields", John Wiley & Sons, Chichester, 1981.

A FINITE ELEMENT/BOUNDARY INTEGRAL EQUATION APPROACH TO THE ACCURATE PREDICTION OF RADAR CROSS SECTION

E. Thomas Moyer Jr.
Associate Professor of Engineering and Applied Science
School of Engineering and Applied Science
The George Washington University
Washington, DC 20052

Erwin Schroeder
Research Mathematician
Applied Mathematics Division
David Taylor Research Center
Bethesda, Maryland 20084

ABSTRACT

Maxwell's equations of electromagnetics are solved for problems of radiation and scattering using the finite element approach. In two-dimensions, second order scalar dampers and in three-dimensions, infinite elements are used to truncate the problem domain. The scattering cross section is calculated by integrating the electric field integral equations on a near-field surface surrounding the target. The technique is employed to solve the problems of a two-dimensional circular cylinder, a two-dimensional strip and a three-dimensional flat plate. Results agree well with reference solutions.

INTRODUCTION

Maxwell's equations are the governing equations for electromagnetic field and wave problems. For a time-harmonic formulation the equations involve only spatial derivatives and the solution for the scattered field can be obtained by solving the problem of a radiating scatterer where the surface conditions are determined from the boundary conditions and the far-field condition. Numerical solutions of these equations have been obtained by: the finite element method, the boundary element method (also called the Method of Moments in electromagnetics literature), and the finite difference method (and its recent offspring, the finite volume method).

The boundary element method models only the surface of the scatterer and solves the integral equation for either the electric field or the magnetic field on the surface [1,2]. This method produces a full, complex and nonsymmetric linear system of equations which is singular at internal resonances of the scatterer geometry.

The finite element and finite difference methods model the full field by solving the partial differential equations in the region. Both produce systems of linear algebraic equations which are banded, symmetric and complex. Significantly more degrees of freedom are required for these methods than for the boundary element method. Since the physical domain is infinite, an outer boundary must be established sufficiently far from the scatterer so an approximate boundary condition can be applied.

If the outer boundary can be applied close enough to the scatterer, either finite element or finite difference would be the method of choice for solving scattering problems due to the *banded and symmetric system matrices*. This paper presents a finite element approach which

shows significant potential for scattering applications. Infinite elements are employed to allow truncation of the domain only a few elements from the scatterer.

FINITE ELEMENT APPROACH

For a linear, isotropic, homogeneous and source free medium and harmonic time dependence, each component of the electric and magnetic field vectors satisfies the Helmholtz equation. Maxwell's equations, therefore, can be recast as [3]

$$\nabla^2\mathbf{E} + \frac{1}{c^2}\mu_r\epsilon_r\omega^2\mathbf{E} = 0 \tag{1}$$

$$\nabla^2\mathbf{H} + \frac{1}{c^2}\mu_r\epsilon_r\omega^2\mathbf{H} = 0 \tag{2}$$

where **E** is the electric field intensity, **H** is the magnetic field intensity, ω is the circular driving frequency, c is the speed of light, ϵ_r is the permittivity of the medium and μ_r is the permeability of the medium. A standard Galerkin finite element approach reduces the solution to a system of linear algebraic equations:

$$\mathbf{K} \cdot \mathbf{U} = \mathbf{F} \tag{3}$$

where **U** are the discrete values of the field and the vector **F** arises from derivative boundary conditions. Element stiffness matrix entries for each component are given by

$$K_{ij} = \int \left[\frac{\partial N_i}{\partial X_k} \frac{\partial N_j}{\partial X_k} - \kappa^2 N_i N_j \right] d\Omega \tag{4}$$

where κ is the wave number. Standard Dirichlet and Neuman boundary conditions can be directly applied in this formulation. Linear combinations of the field quantities can be tied on the boundary using standard techniques [4]. This formulation is not the easiest to use for general problems. For certain applications, however, it directly admits scalar analogies which significantly reduce computation time.

Two-dimensional problems can be reduced to two scalar problems with TM and TE polarizations and, therefore, become scalar Helmholtz equations with appropriate boundary conditions. Scalar Helmholtz equations can be solved by most structural finite element programs using scalar analogies [5,6]. The two-dimensional examples in this paper were solved using the NASTRAN computer program [7].

For three-dimensional problems, the situation is much different. As a first step, a three-dimensional scalar finite element program has been developed for the solution of Helmholtz equation. A unique feature of this program is the inclusion of infinite elements which allow truncation of infinite domains extremely close to the scattering surface. The flat plate was chosen as the test problem. Near normal incidence with TE polarization, the radar cross section is dominated by the transverse component of the electric field and the resulting magnetic field. A scalar approach, therefore, provides a first approximation to the solution and demonstration of the approach.

Quadratic isoparametric finite elements, which provide excellent convergence properties, were used for near-field modelling [4]. Approximately four elements are required for each wavelength of domain. In two-dimensions the elements are curvilinear quadrilaterals and in three-dimensions they are curvilinear hexahedra.

OUTER BOUNDARY CONDITIONS AND INFINITE ELEMENTS

With finite elements or finite differences, the standard approach for truncating the infinite outer domain is to use an approximation of the Sommerfeld radiation condition. A second order approximation is obtained by using a linear spring and dashpot with appropriate constitutive parameters [6]. These elements are available in most structural finite element codes and appear to be an adequate truncation assumption if the outer boundary is between two and four wavelengths from the scatterer. Many authors have discussed higher order approximations [8,9].

Zienkiewicz and others suggested constructing an element which maps a standard finite element into an infinite region in the physical domain. The finite face of the element is then applied to the near-field modeling as shown schematically in Figure 1 (for two-dimensional problems). The extrapolation functions

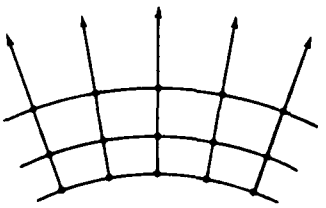

Fig. 1. Finite and Infinite Element

for the element are assumed to have the correct wave component. The geometry and extrapolation mappings are:

$$r = \frac{\Lambda}{(1-t)} \tag{5}$$

$$N_i(p,s,t) = M_i(p,s,t)\cdot\exp\left[i\kappa\frac{\Lambda}{(1-t)}\right]\left[-i\kappa\frac{\Lambda}{2}\right] \tag{6}$$

where $M_i(p,s,t)$ are the standard quadratic shape functions, Λ is a constant related to the location of the centroid of the element face and p,s are the standard mapped coordinates which relate to the two finite spatial dimensions [10]. The extrapolation functions decay radially with leading order $1/r$ in three-dimensions and with $1/\sqrt{r}$ for two-dimensions (where r is measured from the centroid of the physical domain).

The infinite elements allow for a general quadratic variation over the finite face of the element and for decay in a three term series expansion. The leading term in the shape

function is the three- dimensional free-field Green's function for the Helmholtz equation. With this approach, the infinite elements can be placed quite close to the scattering object. For a sound hard sphere, results suggest that one element in the field is sufficient for accurate surface solution, and reasonable results can be obtained with only infinite elements applied to the surface [11]. For surfaces close to the scatterer, the number of degrees of freedom is of the same order as the boundary element approach, but with banded and symmetric matrices. In the worst case, the order of bandwidth is $\sqrt{N}$ (where N is the number of surface nodes).

SURFACE INTEGRAL COMPUTATION OF THE ELECTRIC FAR-FIELD VECTOR

To compute the scattering cross section, values of the electric field must be obtained at points far from the scattering object. These far-field values of the electric field are computed using near-field values that have been obtained from a finite element solution in a bounded region containing the object. The far-field is computed by a surface integral whose integrand is a function of the near-field electric and magnetic field vectors. The surface over which the integral is evaluated is contained in the region that is represented by the finite element solution.

To compute the finite element solution of the field scattered by the object, a region containing the object is modeled with finite elements, and this region will be bounded. The surface integral requires that values of the electric and magnetic fields are given on a surface containing the scattering object. The surface S, is defined so that it contains the scattering object and is contained in the region modeled with finite elements. To obtain values of the magnetic field intensity, $\mathbf{H}$ on the surface, derivatives of the electric field are approximated using values of $\mathbf{E}$ at nearby grid points, and the $\mathbf{H}$ field is computed using the Maxwell equation

$$\mathbf{H} = \frac{i}{\omega\mu}\nabla \times \mathbf{E} \tag{7}$$

For this problem, the hexahedral finite elements are cubes, so the surface consists of element faces, but in general, field values on the surface would be interpolated from values computed at nearby points. With the values of the fields $\mathbf{E}$ and $\mathbf{H}$ given on the surface, the surface integrals for values at far-field points are:

$$\mathbf{E} = \frac{1}{4\pi}\int_S [-i\omega\mu(\hat{\mathbf{n}}' \times \mathbf{H})\phi + (\hat{\mathbf{n}}' \times \mathbf{E}) \times \nabla'\phi + (\hat{\mathbf{n}}' \cdot \mathbf{E})\nabla'\phi]ds' \tag{8}$$

$$\mathbf{H} = \frac{1}{4\pi}\int_S [i\omega\varepsilon(\hat{\mathbf{n}}' \times \mathbf{E})\phi + (\hat{\mathbf{n}}' \times \mathbf{H}) \times \nabla'\phi + (\hat{\mathbf{n}}' \cdot \mathbf{H})\nabla'\phi]ds' \tag{9}$$

In these integrals, $\mathbf{r}'$ is the integration variable on S, $\mathbf{r}$ is the vector to the far-field point, $\phi = \frac{e^{-ikr}}{r}$ is the fundamental solution for the distance r given by $r = |\mathbf{r}' - \mathbf{r}|$, and $\hat{\mathbf{n}}'$ is the unit vector normal to S at $\mathbf{r}'$ [1]. The integrals are evaluated by Gaussian quadrature.

EXAMPLE PROBLEMS

The first example is a two-dimensional perfectly conducting strip 0.3 wavelength wide, and an incident field with TE polarization. The uniform finite element mesh had 144 elements and second order spring-dashpots on the outer boundary. Table I shows the

predicted total scattering cross section from the finite element/boundary integral calculation vs. the reference solution (the reference solution is graphical and the reported numbers where digitized from the graph) [12]. The results agree quite closesly for all incidence including grazing (90 degreee angle of attack). The worst case was a difference of 5%. It is expected that the digitizing errors may account for much of the reported difference.

TABLE 1: TOTAL SCATTERING CROSS SECTION FOR A PERFECTLY CONDUCTING 0.3 WAVELENGTH STRIP

ANGLE OF ATTACK (DEGREES)	NUMERICAL PREDICTIONS	REFERENCE SOLUTION	DIFFERENCE (PERCENT)
0	1.971	1.994	1.15
10	1.943	1.891	2.75
20	1.856	1.796	3.34
30	1.709	1.662	2.83
40	1.518	1.468	3.41
50	1.316	1.274	3.29
60	1.137	1.099	3.46
70	1.002	0.967	3.62
80	0.921	NA	NA
90	0.894	0.850	5.14

Figure 2 shows the backscatter cross section (RCS) vs. angle of attack. Plotted for comparison is the physical optics solution. The physical optics solution obviously does not predict the RCS accurately for angles of attack more than 30 degrees from normal. Figure 3 shows the RCS for a 5.5 wavelength wide perfectly conducting strip. The results are plotted with the Karp-Keller solution with single diffraction [12]. Agreement is quite good qualitatively except the depths of the troughs are overpredicted by Karp-Keller and the solution degrades near grazing incidence. The numerical solution is consistent with expected results.

The second example is a perfectly conducting circular cylinder with radius of ten wavelengths. The incident radiation was polarized with the TE polarization. The predicted bistatic cross section is shown in Figure 4 compared with the analytic solution. Figure 4 compares the predicted bistatic cross section with the analytic solution and shows excellent agreement at all bistatic angles. The cylinder has been studied previously for both the TE and TM polarizations with excellent comparison between the numerical and analytical solutions [11].

The third example is fully three-dimensional. The RCS was computed for a perfectly conducting five wavelength square plate. If the incident field is polarized in the plane of the plate, it is anticipated that the cross section may be dominated by this component of the **E** field and the resulting **H** field (especially if the bounding surface is near the plate). The domain was modeled by standard hexahedral finite elements. Infinite elements were applied to the outer boundary of the mesh at about one wavelength away from the plate. The nearest infinite element was 0.6 wavelength from the plate. The predicted RCS is plotted as a

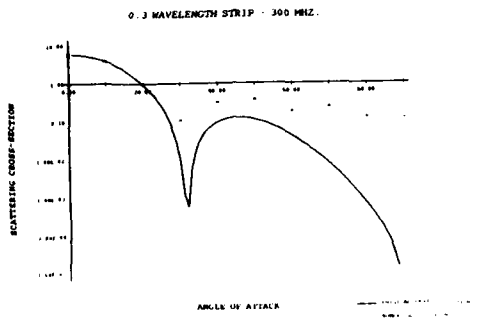

Fig. 2. RCS FOR 0.3 WAVELENGTH STRIP

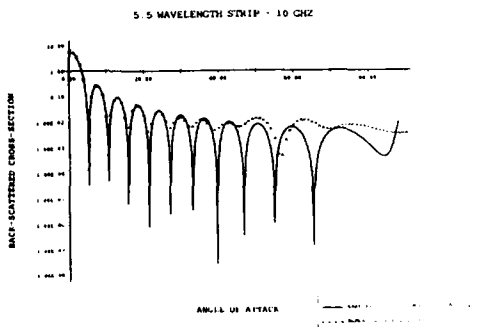

Fig. 3. RCS FOR 5.5 WAVELENGTH STRIP

function of incident angle in Figure 5. The experimental results shown are from Ross [13]. Out to an incident angle of about 40 degrees from normal incidence, the solution is quite good. Beyond that point, the scalar near-field assumption is not a good approximation and the solution degrades. Where the approximation is valid, however, the finite element solution truncating the domain with infinite elements and integrating the far-field using boundary integrals is an accurate approach.

CONCLUDING REMARKS

The finite element method with infinite elements approximating the far-field absorbtion is shown to be an accurate way to solve scalar Helmholtz problems. The far-field solution and cross section can be predicted using the electric field integral equation. The infinite

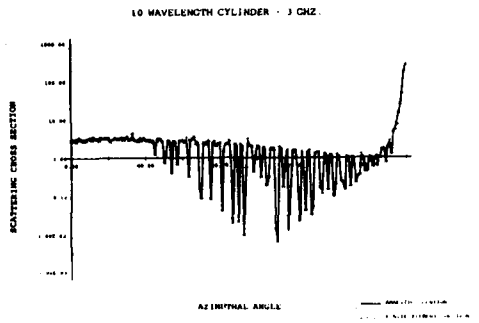

Fig. 4. PERFECTLY CONDUCTING 10 WAVELENGTH CYLINDER

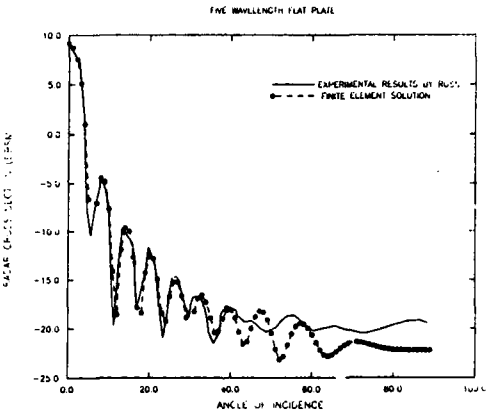

Fig. 5. PERFECTLY CONDUCTING 5 WAVELENGTH FLAT PLATE

elements allow for minimal field modeling and, therefore, smaller system matrices. The formulation produces banded and symmetric matrices that reduce computational requirements, and produces accurate results.

The methodology is being extended for the full vector Maxwell equations. The shape function assumptions used in the infinite element are correct independent of formulation (i.e. independent of whether a Helmholtz or curl-curl formulation is employed). The finite element matrices are not only banded, but are also extremely sparse; a typical finite element matrix in three-dimensions has approximately 82 nonzero entries in each row independent of problem size. If robust iterative solvers were available, this sparsity would render the solution time of order N.

ACKNOWLEDGEMENT

This work was supported in FY-90 by the David Taylor Research Center's (DTRC) Independent Research (IR) program, sponsored by the Office of the Chief of Naval Research (OCNR), Office of Naval Research (ONR), and administered by the Research Director, DTRC 0112, under Program Element 61152N, Task Area ZR 014 02 01, and DTRC Work Unit 1844-147, DN 500052.

REFERENCES

1. A.J. Poggio and E.K. Miller, "Solutions of Three-dimensional Scattering Problems" *Computer Techniques for Electromagnetics*, R. Mittra, editor, Pergamon Press, Oxford, 1973, page 166, Equation (4.13a)
2. R.F. Harrington, *Field Computation By Moment Methods*, New, York, Macmillan, 1968.
3. P. Lorain and D. Corson, *Electromagnetic Fields and Waves*, San Francisco, Freeman and Comp., 1970.
4. O.C. Zienkiewicz, *The Finite Element Method*, London, McGraw Hill, 1977.
5. G.C. Everstine, "Structural Analogies for Scalar Field Problems," **Int. J. Num. Meth. in Engrg.**, Vol 17, pp. 471-476 (1981).
6. E.T. Moyer Jr. and E. Schroeder, "Finite Element Modeling of Electromagnetic Fields and Waves Using NASTRAN", **Seventeenth NASTRAN Users' Colloquium**, NASA CP-3029, National Aeronautics and Space Administration, Washington, DC, pp. 214-246, 1989.
7. *COSMIC NASTRAN User's Manual*, Computer Software Management and Information Center, University of Georgia, Athens, Ga. 1986.
8. B. Enquist and A. Majda, "Absorbing Boundary Conditions for the Numerical Simulation of Waves", **Mathematics of Computation**, Vol. 31., pp. 629-651, 1977.
9. A. Bayliss and E. Turkel, "Radiation Boundary Conditions for Wave-Like Equations", **Commun. on Pure and Applied Math.**, Vol. 33, pp. 707-725, 1980.
10. O.C. Zienkiewicz, K. Bando, P. Bettess, C. Emson and T.C. Chiam, "Mapped Infinite Elements for Exterior Wave Problems", **Int. J. Num. Meth. in Engrg.**, Vol. 21, pp. 1229-1251, 1985.
11. E.T. Moyer Jr. and E.A. Schroeder, "Combined Finite Element/Boundary Integral Approach to the Prediction of Acoustic Signatures and Radar Cross Sections", Proc. of IMSE-90, Hemisphere Publishing Comp., IMSE-90 May, 1990, Arlington, Texas.
12. J.J. Bowman, T.B.A. Senior and P.L.E. Uslenghi, *Electromagnetic and Acoustic Scattering by Simple Shapes*, New York, Hemisphere Publishing Col., 1987.
13. R.A. Ross, "Radar Cross Section of Rectangular Flat Plates as a Function of Aspect Angle", **IEEE Trans. on Antennas and Propagation**, Vol. 14, pp. 329-335, 1966.

Application of Generalized Vertex Splines to Boundary Element Method For Electromagnetic Scattering[1]

A. K. Chan, C. K. Chui and T. X. He
Department of Electrical Engineering and
Department of Mathematics
Texas A&M University, College Station, Texas 77843

Abstract

A Boundary Element formulation using the *generalized vertex splines* is presented in this paper. These splines are generated using lower degree piecewise polynomials in order to keep the same degree of smoothness offered by the vertex splines. The Barycentric coordinates and the Bézier representation of the generalized vertex splines are presented. The characteristics of the generalized vertex splines and their applications are discussed. An example of scattering of an infinite conducting cylinder is shown.

I. Introduction

Boundary element method (BEM) has been the major numerical technique in marine hydrodynamics for many years. Recently, it has been used to solve electromagnetic boundary value problems such as waveguide discontinuities, multilayer dielectrics and electromagnetic scattering [1-3]. Essentially, this method is similar to the finite element method with the exception that the BEM discretizes only the boundaries. This reduces the memory requirements for computations. On the other hand, the BEM method is based on Green's theorem, and boundary integral equations must be set up for a given boundary value problem. Singularities associated with the Green's function must be taken care of in the numerical evaluation of the boundary integrals. Sometimes, the integrals cannot be evaluated due to the strong singularities in the Green's function. Hence, the choice of the shape functions (or interpolation

[1]Research partially supported by NSF CDR-8721512 Offshore Technology Research Center; Texas Higher Education Coordinating Board Advanced Research Program Nos. 32123-70030, 32130-70440, and 32130-70420; and by SDIO/IST managed by the U.S. Army Research Office under contract No. DAAL 03-87-K-0025.

functions) is crucial to the success of this method. Currently, choices of the shape function include piecewise polynomials up to degree two. These shape functions are defined over individual elements and are joined together at the element boundary to form the approximate solution. Generally, these approximation solutions are continuous but are discontinuous in the first derivative. Such approximate solutions may pose problems in computation if the boundary integral is strongly singular.

In this paper, we present a different approach to solve the boundary element equation by using the generalized vertex splines as the basis functions. The unknown is represented by a spline series which is continuously differentiable in the entire boundary. In this manner, boundary integrals with strong singularities can be converted to weakly singular integrals. The solution of the boundary value problem is given in terms of its values at the discretization nodes.

II Bézier representation of piecewise polynomials

Traditional representation of a polynomial P(x) using the global basis is inconvenient for describing the shape function in the finite (or boundary) element method. The Barycentric coordinate system (u,v) gives a much more compact local description of the polynomial P(x) within a given interval (x_0,x_1). The coordinates u and v, are defined by

$$u = (x_2 - x)/(x_2 - x_1)$$
$$v = (x - x_1)/(x_2 - x_1) \qquad (1)$$

so that u+v=1. They are known as the Bernstein's polynomials of the first degree if the interval of interest is (0,1). The variable x in (1) is expressed in terms of u and v as $x = x_1u + x_2v$. Any n^{th} degree polynomial can be expressed as a linear combination of the Bézier polynomial basis given by

$$\phi_{ij}^{(n)}(u,v) = \frac{n!}{i!\,j!}u^i v^j, \quad i,j = 0,1,\ldots,n \text{ and } i+j = n. \qquad (2)$$

For example, a second degree polynomial $P_2(x)$ can be expressed

$$P_2(x) = \sum_{i+j=2} a_{ij}\, \phi_{ij}^{(2)}(u,v) \qquad (3)$$

where a_{ij} are called the Bézier coefficients. These coefficients uniquely determine the polynomial $P_2(x)$ within the interval (x_1,x_2) and are invariant relative to the location of the interval.

The arrangement of the coefficients for an univariate piecewise polynomial within its support is called the Bézier net. The Bézier nets for a second degree and a third degree polynomial are shown below

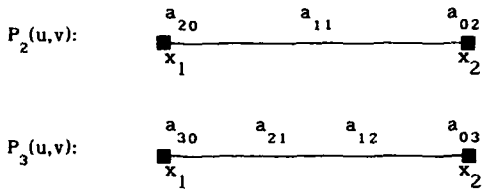

For example, if the interval (x_1,x_2) is $(0,1)$ and $P_2(x)=x^2$, the Bézier net is $(0,0,1)$. Likewise, if $P_3(x)=x^3-1$, its Bézier net is given by $(-1,-1,-1,0)$.

III. C^1 quadratic generalized vertex splines

A polynomial spline is defined to be a function consisting of piecewise polynomials joining together smoothly at the knots (grid points). A function is said to be of C^n smoothness if it has continuous derivatives up to the n^{th} order. Popular spline functions include the linear, quadratic and the cubic splines. However, the most useful form of the spline functions are the B-splines (basis splines) because any continuous smooth function can be expanded as a series of B-splines. The linear and cubic B-splines are shown in figure 1.

It is not difficult to see that the support of the B-spline is enlarged as the order of smoothness is increased. The B-splines with large support are not very useful for the tradiational finite element formulation. Hence, there exist a need to find spline functions with small support, reasonable degree of smoothness, and good approximation order. The vertex spline is developed to

satisfy this need.

A vertex spline is defined as a locally supported piecewise polynomial function in C^n on an interval Δ whose support contain **AT MOST** one grid point in the interior. The familiar triangular function is a linear vertex spline with C^0 smoothness. Univariate vertex splines with C^1 and C^2 smoothness are the Hermite cubics and the Hermite quintics as shown in figure 2. Vertex splines of higher degree of smoothness are desirable as shape functions in finite element method and boundary element method. An example of their usage is given in [4]. However, elements with higher degrees of smoothness must be constructed using piecewise polynomials of higher degrees, which, in some applications, may not be desirable. For this reason, generalized vertex splines are developed by using lower degree polynomials and expanding the support without the sacrifice of smoothness. One way to accomplish this is to refine the grid partition. In finite element literature, the element obtained in this way is called the **Macro element**. The details of spline constructions are shown in [5]. The Bézier net for the C^1 quadratic generalized vertex spline is given as follows:

$\Phi(x)$ 0 0 .5 1 1 1 .5 0 0

The graph of $\Phi(x)$ is shown in figure 3.

IV Formulation and computation using generalized vertex splines

Following Kagami and Fukai [1], the equation for a two-dimensional scattering problem formulated using the boundary integral approach is given by

$$u_i + \int_B u(\partial G/\partial n)dc - \int_B (\partial u/\partial n)Gdc \approx 0 \qquad (4)$$

where the u_i is the known incident field and G is the appropriate Green's function for the boundary value problem. As a trial case, we consider the

two-dimensional scattering problem of TM wave incident on an *infinitely long* circular conducting body of radius a. Since the electromagnetic fields must obey the radiation condition at infinity, the contribution from the boundary at infinity to the integral in (4) is zero. Putting the observation point on the boundary of the conducting body, the integral equation for the unknown magnetic field H^s is

$$[1-\alpha/2\pi]E_z^s(x_i,y_i)=\int G(x,y|x_i,y_i)H^s(x,y)dc-\int E_z^s(x,y)[\partial G(x,y|x_i,y_i)/\partial n]dc \qquad (5)$$

where E_z^s is the scattered field at the boundary and α is the angle around the singular point at which $r=[(x-x_i)^2+(y-y_i)^2]^{1/2}$ is zero. Here, $\int$ denotes the Cauchy's principle value of the integration and α is π for smooth boundary. The known field E_z^s and the unknown field H^s are expanded as series of generalized vertex spline basis as follow:

$$E_z^s(\theta) = \sum_j E_j \, \Phi(\theta-\theta_j)$$

$$H^s(\theta) = \sum_j H_j \, \Phi(\theta-\theta_j)$$

where $\Phi(\theta-\theta_j)$ is the generalized vertex spline shown in figure 3. The boundary integral in (5) can be expressed in matrix form as

$$[P][e] = [S][h]$$

where the elements of the column vector [e] are known values of the scattered E field at the nodal points on the boundary. The elements p_{ij} and s_{ij} are integrations over the support of the spline functions at the j^{th} node. Mathematically, they are expressed as

$$p_{ij} = \int[\partial G(\theta|\theta_i)/\partial n]\Phi(\theta-\theta_j)dc(\theta) + \delta_{ij}/2$$

$$s_{ij} = \int G(\theta|\theta_i)\Phi(\theta-\theta_j)dc(\theta)$$

where δ_{ij} is the Kronecker delta. The column vector [h] contains the values of the unknown H^s field at the nodal points.

V Conclusions

The results of using the generalized vertex splines in the BEM for the problem of plane wave scattering by an infinite conducting cylinder are compared to those using linear elements for the case where $a = \lambda$. The number of segments is 60 so that the segment length is approximately $.1\lambda$. The graphs in figure 4 indicate that the solutions using generalized vertex splines are smooth and the average amplitude error is smaller than that using linear element.

Several advantages can be pointed out in using the generalized vertex spline as basis for the boundary element method. (1) It is not necessary to map an arbitrary segment of the boundary into a standard segment where the shape function is defined over a given coordinate system. (2) The smoothness of the solution is guaranteed because the basis function is smooth everywhere. (3) Strong singularities can be reduced to weak singularities so that numerical integration can be performed if needed. (4) The order of approximation is known so that the segment length can be predetermined for a given accuracy requirement.

References

[1] Kagami, S., and I. Fukai, "Application of Boundary-Element Method to Electromagnetic Field Problems" IEEE-MTT 32, No. 4, April, 1984, pp.455-461.

[2] Yashiro, K. and S. Ohkawa, "Boundary Element Method for Electromagnetic Scattering from Cylinders" IEEE-AP 33, No. 4, April, 1985, pp.383-389.

[3] Koshiba, M., and M. Suzuki, "Application of the boundary-element method to waveguide discontinuities," IEEE-MTT 34, No. 4, April, 1986, pp.301-307.

[4] Chan, A. K., and C. K. Chui,"A Novel Finite Element Formulation using Quintic Vertex Splines for Field Analysis in Closed Structures" Proceedings of ACES 5th Annual Review, March, 1989, pp. 524-531

[5] Chui, C. K., *Multivariate Splines*, CBMS-NSF Series in Applied Mathematics No. 54, SIAM Publications, Philadelphia, Pa., 1988.

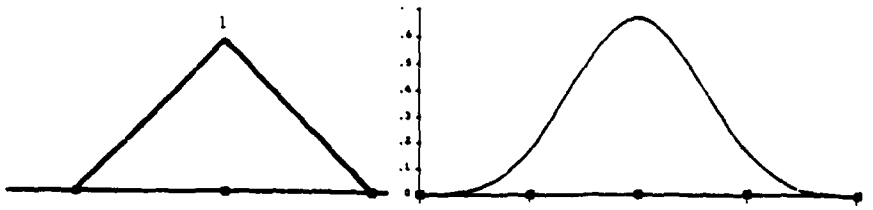

(a) Linear B-spline

(b) Cubic B-spline

Figure 1

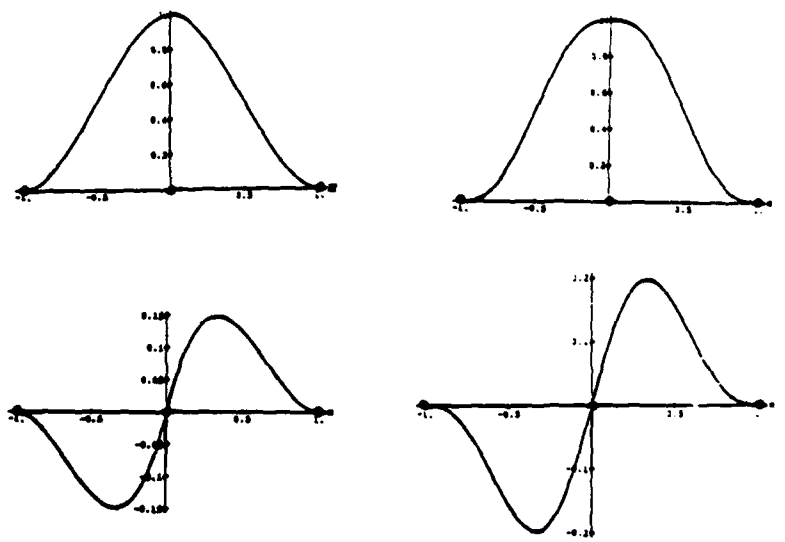

(a) Hermite cubics

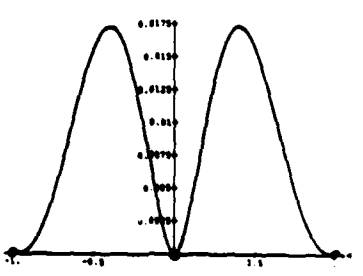

(b) Hermite quintics

Figure 2

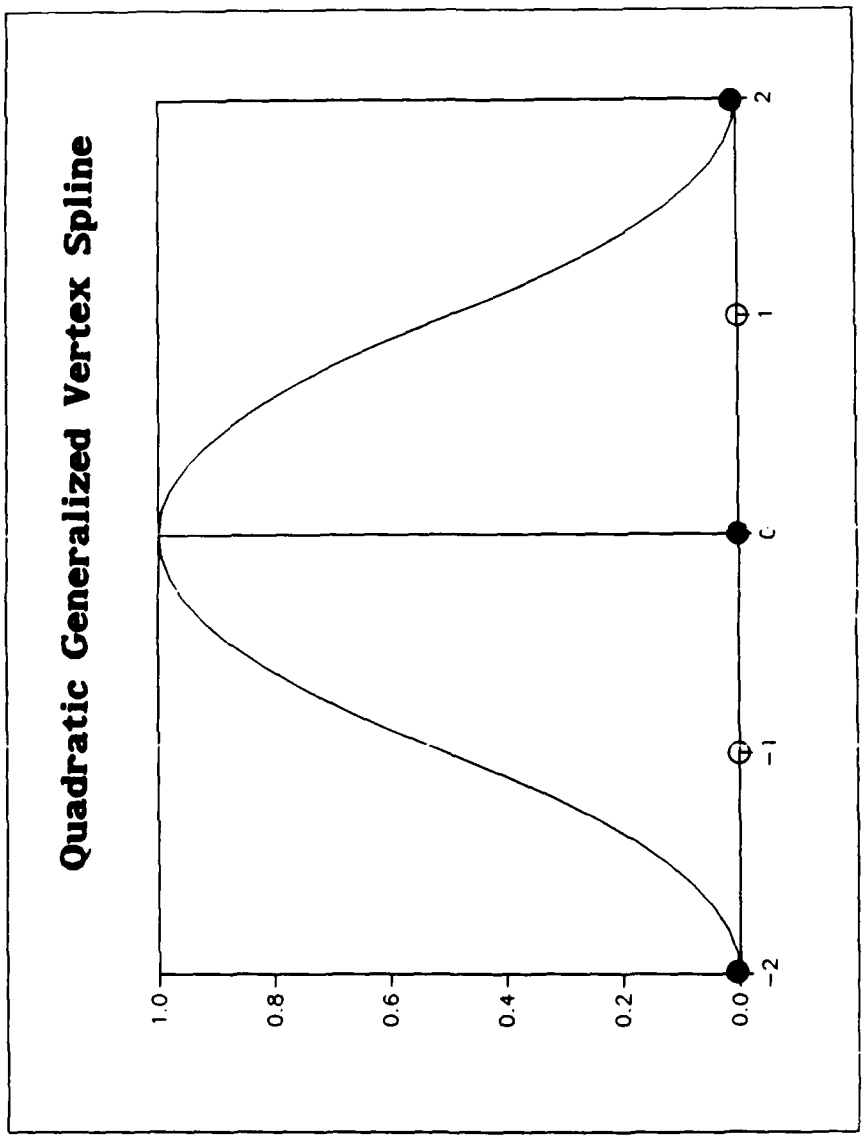

Figure 3

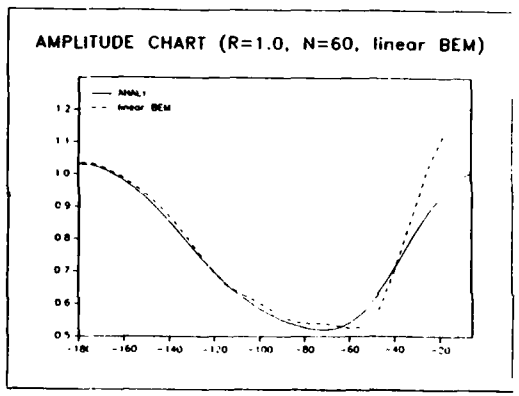

(a)

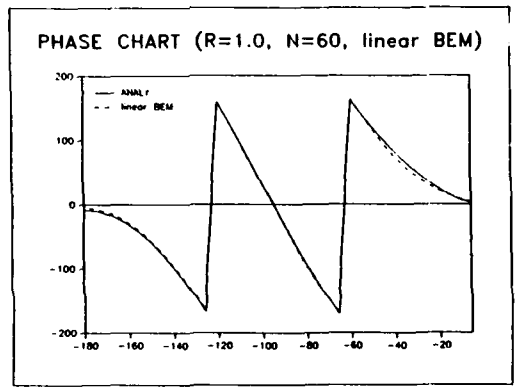

(b)

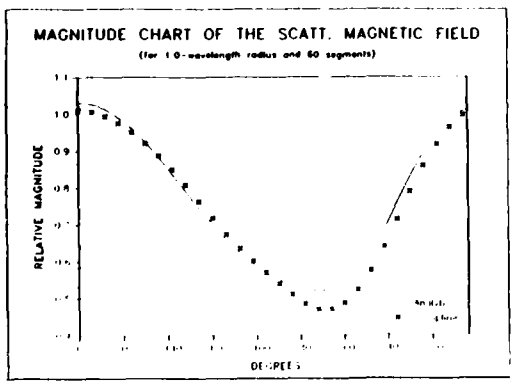

(c)

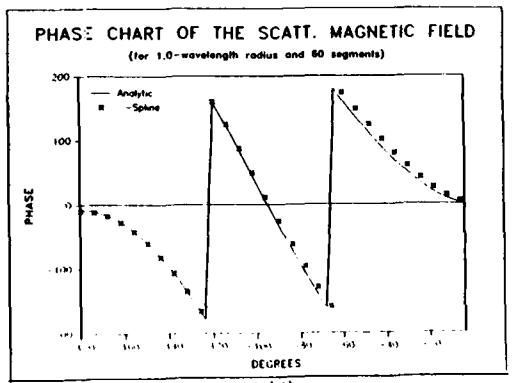

(d)

Figure 4

SESSION 9 - "HIGH FREQUENCY METHODS AND CODES"

A HYBRID ASYMPTOTIC-MODAL ANALYSIS OF THE EM SCATTERING BY OPEN-ENDED S-SHAPED RECTANGULAR WAVEGUIDE CAVITIES

P.H. Law, R.J. Burkholder and P.H. Pathak
The Ohio State University ElectroScience Laboratory
1320 Kinnear Road
Columbus, Ohio 43212

Abstract

The electromagnetic (EM) backscatter from 3-dimensional perfectly conducting S-shaped open-ended waveguide cavities with a planar termination is analyzed when they are illuminated by an external plane wave. The cavities which are modeled in this analysis are built up by smoothly joining straight and annular shaped uniform waveguide sections with constant rectangular cross-sections. The analysis is based on a self-consistent multiple scattering method which accounts for the multiple wave interactions between the open end, the junctions between waveguide sections, and the interior termination. The scattering matrices which describe the reflection and transmission coefficients of the waveguide modes reflected and transmitted at each junction between the different waveguide sections, as well as the scattering from the edges at the open end are found via asymptotic high frequency methods such as the geometrical and physical theories of diffraction used in conjunction with the equivalent current method. It is noted that the modes within the annular section include the whispering gallery type. This hybrid method is expected to yield very accurate results and is much more efficient than conventional mode matching procedures for analyzing these types of waveguide cavities with electrically large cross-sections which accomodate a large number of propagating modes.

The numerical results for the backscatter from an S-shaped waveguide cavity are compared with the backscatter from a straight waveguide cavity of the same length; the backscattered patterns are different in the sense that the curvature of an S-shaped cavity redistributes the energy reflected from the interior termination in a way that is different from that of a straight cavity.

1 Introduction

The EM scattering by large open-ended waveguide cavities with an interior termination are of interest in radar cross section (RCS) applications. From a high frequency asymptotic point of view, the electric field scattered from an open-ended cavity due to an incident plane wave is composed of the three scattering mechanisms shown in Figure 1. The total scattered field is written as

$$\vec{E}^s = \vec{E}^{ext} + \vec{E}^{rim} + \vec{E}^{cav} \quad (1)$$

where $\vec{E}^{ext}$ is the scattering from the exterior of the cavity, not including the rim at the open end, $\vec{E}^{rim}$ is the scattering from the rim at the open end of the cavity, and $\vec{E}^{cav}$ is the scattering from the interior of the cavity. $\vec{E}^{ext}$ is not of interest here because it depends on the cavity's supporting structure and could be found using other high frequency methods such as physical optics [1], the geometrical theory of diffraction (GTD) [2] or its uniform extension [3], etc. Only $\vec{E}^{rim}$ and $\vec{E}^{cav}$ will be considered here.

The open-ended cavity geometries analyzed here are made up of alternate sections of uniform rectangular straight and annular waveguides for which the waveguide modes are known in closed form, as shown in Figure 1. The annular waveguides are simply straight rectangular waveguides bent with a constant radius. The multiple scattering matrix (MSM) method [4], also referred to as the generalized scattering matrix method, is used to find the cavity scattered fields in such a way that all multiple wave interactions between the open end, junctions and termination are included self-consistently. The MSM is made up of modal scattering matrices which describe the isolated reflection and transmission of waveguide modes at junctions between waveguide sections and between the first waveguide section and the external region. It also contains the termination modal reflection matrix. These component matrices are computed efficiently element-by-element using high frequency asymptotic methods, rather than by the more conventional and numerically intensive mode matching procedure which requires solution of a system of equations of the order of the number of propagating modes. The hybrid modal method used here has been used in a broad class of open-ended cavity scattering problems [5-10].

For the waveguide cavity configuration of interest shown in Figure 1, it has been found that the modal reflections from the junctions between sections are negligable because the junctions are smoothly continuous. It has also been found that higher order wave interactions between the open end and the termination are negligable compared with the first order scattering from the interior of the cavity. Therefore, the MSM, which intrinsically includes all higher order interactions, reduces to a simple matrix which includes just the first order scattering from the rim at the open end and the scattering due to energy which couples into the cavity via the open end, propagates in the form of waveguide modes to the termination, reflects, propagates back to the open end and re-radiates into the external region. This simplification is important computationally because the complete MSM requires several matrix inversions of the order of the number of propagating modes, which can be quite large. The details of this analysis can be found in [8] and will only be summarized here. An $e^{j\omega t}$ time convention is assumed and suppressed throughout.

2 Formulation

The incident plane wave electric and magnetic fields can be written in terms of their $\hat{\theta}$ and $\hat{\phi}$ components as

$$\vec{E}^i = \left(\hat{\theta}A^i_\theta + \hat{\phi}A^i_\phi\right)e^{-j\vec{k}\cdot\vec{r}} \quad (2)$$

$$\vec{H}^i = Z_o^{-1}\hat{k}^i \times \vec{E}^i, \quad (3)$$

where $\vec{k}^i = \hat{k}^i k$ is the free space propagation vector of the incident plane wave ($k = 2\pi/\lambda$), Z_o is free space impedance ($Z_o \approx 377\Omega$), and $\vec{r}$ is a vector from the origin located in the vicinity of the open end of the cavity. The scattered electric field of (1) can be written in terms of its $\hat{x}, \hat{y}, \hat{z}$ components as

$$\vec{E}^s = \hat{x}E^s_x + \hat{y}E^s_y + \hat{z}E^s_z, \quad (4)$$

which can be in the near or far field region of the cavity. $[S]$, the MSM which relates the components of the scattered and incident fields is then defined by

$$\begin{bmatrix} E^s_x \\ E^s_y \\ E^s_z \end{bmatrix} = [S]\begin{bmatrix} A^i_\theta \\ A^i_\phi \end{bmatrix}. \quad (5)$$

The electric and magnetic fields $\vec{E}_w, \vec{H}_w$ in any component waveguide section of the cavity can be expanded as a sum of forward ($+\hat{\eta}$) and backward ($-\hat{\eta}$) propagating ortnogonal waveguide modes as

$$\left(\vec{E}_w, \vec{H}_w\right) = \sum_{mn} A^+_{mn}\left(\vec{e}^{\,+}_{mn}, \vec{h}^{\,+}_{mn}\right)e^{-j\beta_{mn}\eta} + A^-_{mn}\left(\vec{e}^{\,-}_{mn}, \vec{h}^{\,-}_{mn}\right)e^{j\beta_{mn}\eta}, \quad (6)$$

where $A^\pm_{mn}$ are the modal expansion coefficients, $\vec{e}^{\,\pm}_{mn}, \vec{h}^{\,\pm}_{mn}$ are the fields of the mn^{th} mode in a transverse cross section of the waveguide, β_{mn} is the propagation constant of the mn^{th} mode, and η is the axial coordinate of the waveguide. For a straight rectangular waveguide η is a cartesian coordinate such as z, in which case β_{mn} has dimensions of length^{-1}, and for an annular waveguide η is the cylindrical coordinate ϕ, in which case β_{mn} is dimensionless. The rectangular waveguide modes are in the form of sines and cosines, and the annular waveguide modes are in the form of sines, cosines and Bessel functions. The exact form of these modes can be found in [8]. It is noted that the sum in (6) is over the propagating modes in a given waveguide section. Evanescent modes are not included because the waveguides are assumed to be electrically large; such that enough propagating modes are supported to adequately describe the fields in the waveguides. For smaller waveguides, a finite number of evanescent modes could also be included in (6) to improve the accuracy.

The simplified MSM for the 5-section waveguide cavity of interest here which includes only the first order scattering from the open end and the cavity interior with no multiple interactions is given by

$$\begin{aligned}[S] = {} & [S_{00}] + [S_{10}][P_1][S_{21}][P_2][S_{32}][P_3][S_{43}][P_4][S_{54}][P_5][S_\Gamma] \\ & \cdot[P_5][S_{45}][P_4][S_{34}][P_3][S_{23}][P_2][S_{12}][P_1][S_{01}], \end{aligned} \quad (7)$$

with the component scattering matrices illustrated in Figure 2. $[S_{00}]$ relates the components of the scattered field due to the scattering by the rim at the open end to the components of the incident plane wave. $[S_{01}]$ relates the components of the incident plane wave to the modal expansion coefficients of the modal fields coupled through the open end into the first waveguide section, and $[S_{10}]$ relates the components of the cavity scattered field to the modal expansion coefficients of the modal fields incident on the open end from within the first waveguide section. The transmission matrices associated with junctions between waveguide sections relate the transmitted modal expansion coefficients to those incident on the junction from the adjacent waveguide section. $[S_\Gamma]$ is the modal reflection matrix of the termination of the cavity and relates the modal expansion coefficients of the modal fields incident and reflected from the termination within waveguide section 5. The propagation matrices $[P_i]$, $i = 1,2,3,4,5$, are diagonal matrices composed of the terms $e^{-j\beta_{mn}l_i}$, where l_i is the length of the i^{th} section (l_i is linear for a straight rectangular guide and angular for an annular guide). These matrices describe the propagation of the waveguide modes from junction to junction.

The scattering matrices which make up the MSM of (7) are found using high-frequency asymptotic methods. $[S_{00}]$ is found by replacing the rim at the open end with equivalent line currents which are found using GTD, based on the incident plane wave field and the location of the observer. The junction transmission matrices are found by replacing each incident modal field with equivalent surface currents based on the Kirchhoff approximation in the plane of the junction and then finding the excitation of the transmitted modes due to these currents radiating inside an unbounded waveguide (i.e., with no junctions or terminations present). $[S_{01}]$ is found in a similar manner by replacing the incident plane wave with equivalent Kirchhoff surface currents in the open end and allowing them to excite modes in the first waveguide section. The modal excitation coefficients due to the equivalent electric and magnetic surface currents, $\vec{J}_s$ and $\vec{M}_s$, respectively, radiating in an unbounded waveguide can be found from the following equation [4]:

$$A_{mn}^{\pm} = -\frac{1}{2}\int_{S_{ij}} \left(\vec{e}_{mn}^{\pm} \cdot \vec{J}_s - \vec{h}_{mn}^{\pm} \cdot \vec{M}_s\right) dS \tag{8}$$

where S_{ij} is the surface of the junction between waveguide sections i and j. It is noted that (8) applies only to waveguide modes which are normalized to carry unit power. It is also noted that for the cavity configurations of interest here, there is always a simple reciprocity relationship which relates all matrices of the form $[S_{ij}]$ to the corresponding matrix $[S_{ji}]$. Finally, the termination reflection matrix for the case of a perfectly conducting (PEC) planar termination is given by

$$[S_\Gamma] = -[I], \tag{9}$$

where $[I]$ is an identity matrix of the order of the number of propagating modes in the last waveguide section. The termination is not limited to this simple planar PEC case and may be completely arbitrary as long as it is characterized by a known $[S_\Gamma]$.

3 Numerical Results

The monostatic radar cross section (RCS) is plotted as a function of aspect angle in Figure 3 for a straight rectangular and an S-shaped cavity. In this figure the scattering from the rim and the scattering from the cavity interior are plotted separately, in addition to the sum total of these two RCS components. The units of the RCS are decibels relative to a square wavelength (dBSW) and the aspect angle given in degrees. Of interest in these plots is that the patterns peak near axial incidence for the straight rectangular cavity but do not for the S-shaped cavity. This is because the S-bend has the effect of offsetting the termination so that it is not directly visible looking through the open end, and it redistributes the scattered fields asymmetrically in the RCS patterns. It is also noted that the scattering from the rim at the open end is generally much less significant than the interior cavity scattering.

4 Conclusions

The hybrid asymptotic-modal technique for analyzing the EM scattering by large open-ended waveguide cavities is accurate because it uses the natural waveguide modal fields of the cavities and it is efficient because all the scattering matrices are calculated one element at a time using high frequency asymptotic techniques rather than by solving a large system of equations numerically. In the case of the cavities of interest in this paper, it was seen that the scattering by the rim is generally much less significant than the scattering from the cavity interior and that the S-shape causes the cavity scattered fields to be redistributed in the RCS pattern so that they do not peak near axial incidence.

Ongoing work in this area is concerned with finding ways to track the fields inside non-uniform lossy cavities for which waveguide modes cannot be defined in the conventional sense. Also, it is of interest to be able to characterize more realistic, complex terminations with a modal reflection matrix $[S_\Gamma]$.

References

[1] P.H. Pathak, "Techniques for High Frequency Problems," Chapter 4 in ANTENNA HANDBOOK - Theory, Applications, and Design, eds. Y.T. Lo and S.W. Lee, Van Nostrand Reinhold, 1988.

[2] J.B. Keller, "Geometrical Theory of Diffraction," J. Opt. Soc. Am., Vol. 52, pp. 116-130, 1962.

[3] R.G. Kouyoumjian and P.H. Pathak, "A Uniform Geometrical Theory of Diffraction for an Edge in a Perfectly Conducting Surface," Proc. IEEE, Vol. 62, pp. 1448-1461, November 1974.

[4] R. Mittra and S.W. Lee, Analytical Techniques in the Theory of Guided Waves, The Macmillan Company, New York, 1971.

[5] P.H. Pathak, C.W. Chuang and M.C. Liang, "Inlet Modeling Studies," The Ohio State University ElectroScience Laboratory Technical Report 717674-1, prepared under Contract No. N60530-85-C-0249, for Naval Weapons Center, China Lake, California, October 1986.

[6] A. Altintas, P.H. Pathak, W.D. Burnside, "Electromagnetic Scattering from a Class of Open-Ended Waveguide Discontinuities," The Ohio State University ElectroScience Laboratory Technical Report 716148-9, prepared under Grant No. NSG-1613, for NASA/Langley Research Center, Hampton, Virginia, March 1986.

[7] C.W. Chuang, P.H. Pathak, R.J. Burkholder, "A Hybrid Asymptotic Modal-Moment Method Analysis of the EM Scattering by 2-D Open-Ended Linearly Tapered Waveguide Cavities," The Ohio State University ElectroScience Laboratory Technical Report No. 312436-1, prepared for McDonnell Douglas Corporation, St. Louis, MO, December 1988.

[8] P.H. Law, R.J. Burkholder, and P.H. Pathak, "A Hybrid Asymptotic-Modal Analysis of the EM Scattering by an Open-Ended S-Shaped Rectangular Waveguide Cavity," The Ohio State University ElectroScience Laboratory Technical Report No. 719630-2, prepared under Grant NAG 3-476, for NASA/Lewis Research Center, Cleveland, Ohio, December 1988.

[9] P.H. Pathak, R.J. Burkholder, "Modal, Ray and Beam Techniques for Analyzing the EM Scattering by Open-Ended Waveguide Cavities," IEEE Trans. Antennas Prop., vol. AP-37, No. 5, pp. 635-647, May 1989.

[10] R.J. Burkholder, "High-Frequency Asymptotic Methods for Analyzing the EM Scattering by Open-Ended Waveguide Cavities," R.J. Burkholder, Ph.D. dissertation, The Ohio State University, June 1989. Also see The Ohio State University ElectroScience Laboratory Technical Report No. 719630-3.

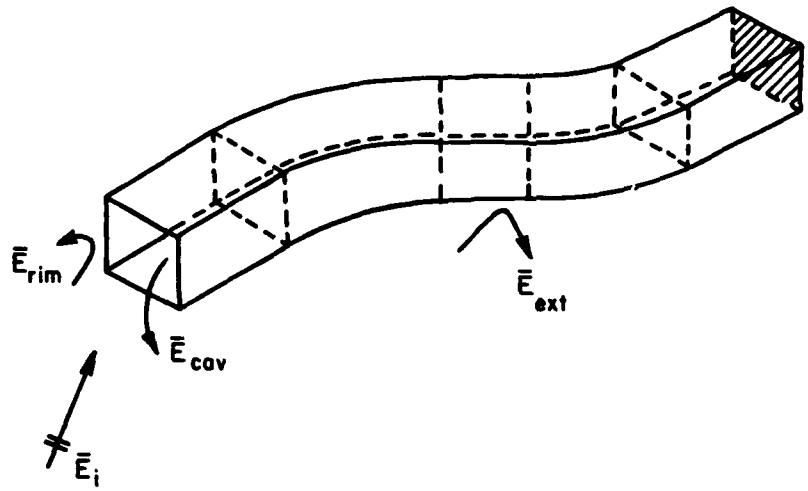

Figure 1: Scattering mechanisms of an open-ended S-shaped waveguide cavity.

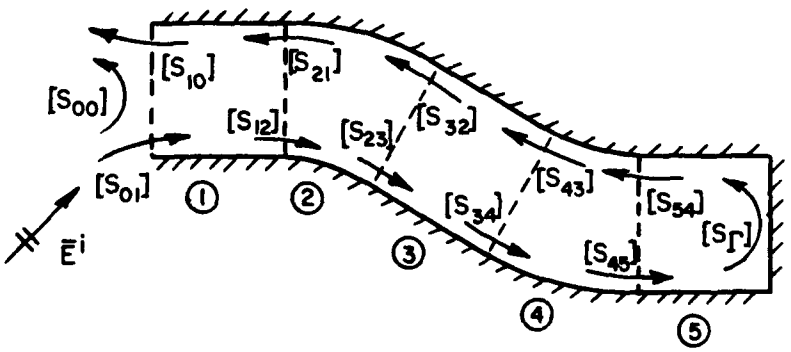

Figure 2: Modal propagation and scattering matrices of the waveguide cavity.

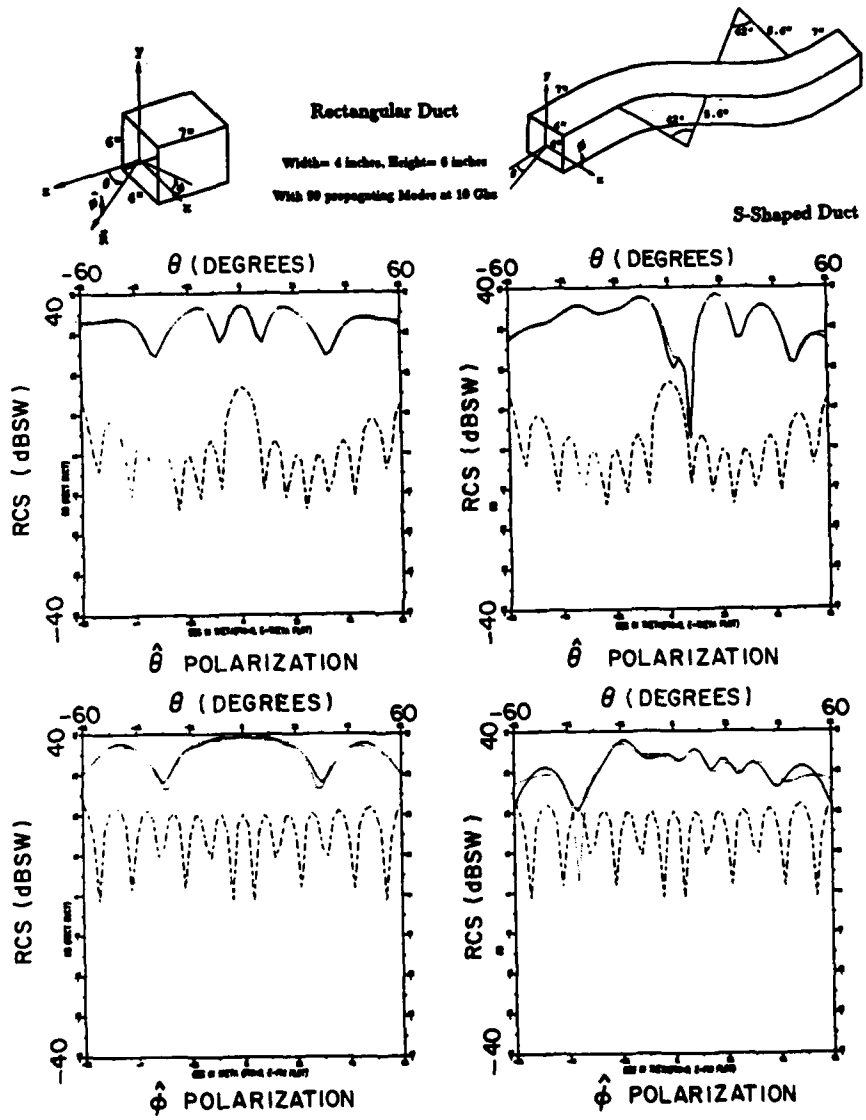

Figure 3: RCS vs. θ in the x-z plane ($\phi = 0°$) for a straight and S-shaped rectangular cavity at 10 GHz.

APPLICATION OF THE GENERALIZED RAY EXPANSION FOR ANALYZING THE EM SCATTERING BY OPEN-ENDED NON-UNIFORM WAVEGUIDE CAVITIES WITH A VARYING SUPER-ELLIPTIC CROSS SECTION

C.W. Chuang, R.J. Burkholder, R.-C. Chou and P.H. Pathak
The Ohio State University ElectroScience Laboratory
1320 Kinnear Road, Columbus, Ohio 43212

1. Introduction

The generalized ray expansion (GRE) method [1,2] was developed recently to analyze the complex problem of electromagnetic (EM) scattering by large open-ended waveguide cavities of relatively arbitrary shape. Basically, the scattering from just the open end alone can be found via the geometrical theory of diffraction used in conjunction with the equivalent current method, whereas, the field scattered into the exterior due to the presence of the interior waveguide termination is found by discretizing the aperture at the open end into a relatively small number of sub-apertures and by launching the rays from each sub-aperture into the cavity with the initial ray amplitudes weighted by the far field radiation pattern of the sub-aperture. This approach has the advantage in that, unlike the conventional geometrical optics ray shooting approach, the GRE method launches and tracks a grid of rays within the cavity just once, independent of the external plane wave incidence angle, and the fields diffracted into the cavity by the edges at the open end are implicitly included in the analysis.

A GRE based computer code has been developed to analyze the EM scattering by perfectly conducting waveguide cavities that can be modeled mathematically using a super-elliptic cross section which changes its shape gradually from rectangular at the open end of the cavity to an arbitrary super ellipse at the planar termination. Furthermore, the axis of the cavity may have a lofting function described by a fifth order polynomial to model cavities with bends. At present, the code can only handle cavities with rectangular apertures (open ends) normal to the waveguide cavity axis, but in the near future it will be modified to analyze cavities with arbitrary

super-elliptic apertures which may be slanted with respect to the waveguide axis. It is noted that the present code allows the planar termination to be slanted with respect to the waveguide axis. A brief theoretical background of the GRE approach and numerical results for the backscatter by several 3-D open-ended super-ellipse cavity geometries which have rectangular cross sections at the open end are given in the following.

2. Theoretical Background

The electromagnetic scattering from open-ended cavities consists of three distinctive scattering mechanisms, namely, the scattering by the front end rim, the scattering by the external structure of the cavities, and the interior irradiation. In the high frequency range, the coupling between the three different scattering mechanisms is negligible so that they can be treated separately. Here we are concerned with the interior irradiation, which is the scattering due to EM energy coupled into the interior of the cavity and reflected back to reradiate into the exterior region.

In the GRE approach for evaluating the interior irradiation, we assume that the open end aperture fields for launching rays into the interior of the cavity are those of the incident plane wave. The aperture area is divided into a relatively small number of sub-apertures and rays are launched from each sub-aperture into the cavity with the initial ray amplitudes weighted by the far field radiation pattern of the sub-aperture as shown in Figures 1 and 2. The ray path and ray field are determined by the geometrical optics. Specifically, at each point along the ray path the ray field is given by

$$[E_{p\ell}] \sim \left\{ \frac{e^{-jkr_{po}}}{r_{po}} \left(\prod_{q=1}^{N(p)} [R_{pq}] [\mathcal{T}_{pq}] \right) \left| \sqrt{\frac{\Delta S_o}{\Delta S_N}} \right| e^{j\frac{n\pi}{2}} e^{-jk\sum_{q=1}^{N(p)} r_{pq}} \right\} \cdot [C_{p\ell}] \tag{1}$$

$$\bar{C}_{p\ell} = \frac{jkZ_o}{4\pi} \int\int_{S_\ell} [\hat{r}_{po} \times \hat{r}_{po} \times d\bar{p}_e(\bar{r}'_\ell) + Y_o \hat{r}_{po} \times d\bar{p}_m(\bar{r}'_\ell)] \, e^{jk\hat{r}_{po}\cdot\bar{r}'_\ell} \tag{2}$$

where $N(p)$ is the number of reflections, R_{pq} is the reflection coefficient, $\mathcal{T}_{pq}$ decomposes the ray fields just before each reflection into TE and TM

components, $\left|\sqrt{\frac{\Delta s_n}{\Delta s_N}}\right|$ is the ray divergent factor, m is the number of caustics traversed by the ray, $\bar{C}_{pt}$ is the radiation pattern of each sub-aperture, and $d\bar{p}_e$ and $d\bar{p}_m$ are the equivalent electric and magnetic current dipoles at the open end associated with the incident plane wave fields.

After going through several internal reflections, the rays will exit the open end aperture. Huygen's principle is then applied to integrate each ray field at the aperture to obtain the scattered field due to the internal irradiation.

3. Numerical Results

Several numerical results of the GRE approach for the EM scattering by open-ended cavities with a super-elliptic cross section are shown in Figures 3, 4, 5, and 6. The cavities in these figures are of different shapes, but they all can be modeled by a super ellipse. A super ellipse is described by

$$\left[\frac{x - a^{(3)}(z)}{a^{(1)}(z)}\right]^q + \left[\frac{y - a^{(4)}(z)}{a^{(2)}(z)}\right]^q = 1 \qquad (3)$$

By letting $a^{(1)}$, $a^{(2)}$, $a^{(3)}$, $a^{(4)}$, and q varying with z, the super ellipse can be used to model an S-bend cavity while transitioning from a rectangular cross section at the open end to a circular one at the termination of the cavity.

The scattered fields shown in Figures 3, 4, 5 and 6 include only the internal irradiation from the cavity. In Figure 3, the GRE solution is compared with a hybrid modal reference solution[1] and a solution obtained using the shooting and bouncing ray (SBR) technique[3]. The good agreement between the three solutions indicates the accuracy of the GRE approach. The cavities in Figures 4, 5, and 6 are non-uniform and the GRE solutions are compared with those obtained by the SBR technique in these figures. In all the cases shown, the termination of the cavity is a planar conductor. Use of more complicated terminations and other improvements will be performed in future work.

References

[1] R.J. Burkholder, "High-Frequency Asymptotic Methods for Analyzing the EM Scattering by Open-Ended Waveguide Cavities," Ph.D. dissertation, The Ohio State University, June 1989. Also see The Ohio State University ElectroScience Laboratory Technical Report No. 719630-3.

[2] P.H. Pathak, R.J. Burkholder, R.C. Chou and G. Crabtree, "A Generalized Ray Expansion Method for Analyzing the EM Scattering by Open-Ended Waveguide Cavities," presented at the IEEE AP-S International Symposium and URSI Radio Science Meeting, June 26-30, 1989, San Jose, California.

[3] H. Ling, R. Chou and S.W. Lee, "Shooting and Bouncing Rays: Calculating RCS of an Arbitrary Cavity," *IEEE Trans. on Antennas and Propagation*, Vol. AP-37, No. 2, pp. 194-205, February 1989.

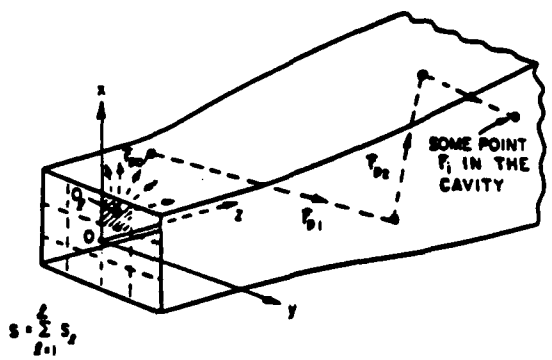

Figure 1: Generalized Ray Expansion Method

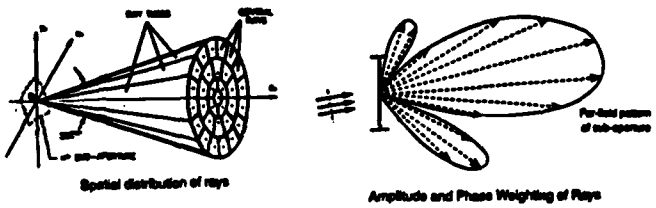

Figure 2: Rays of Each Sub-Aperture

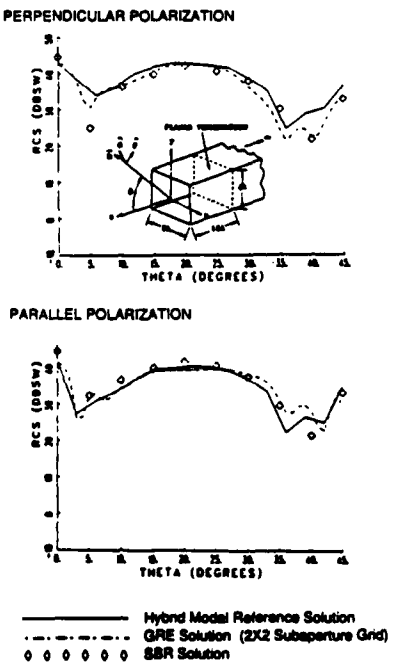

Figure 3: Straight rectangular duct

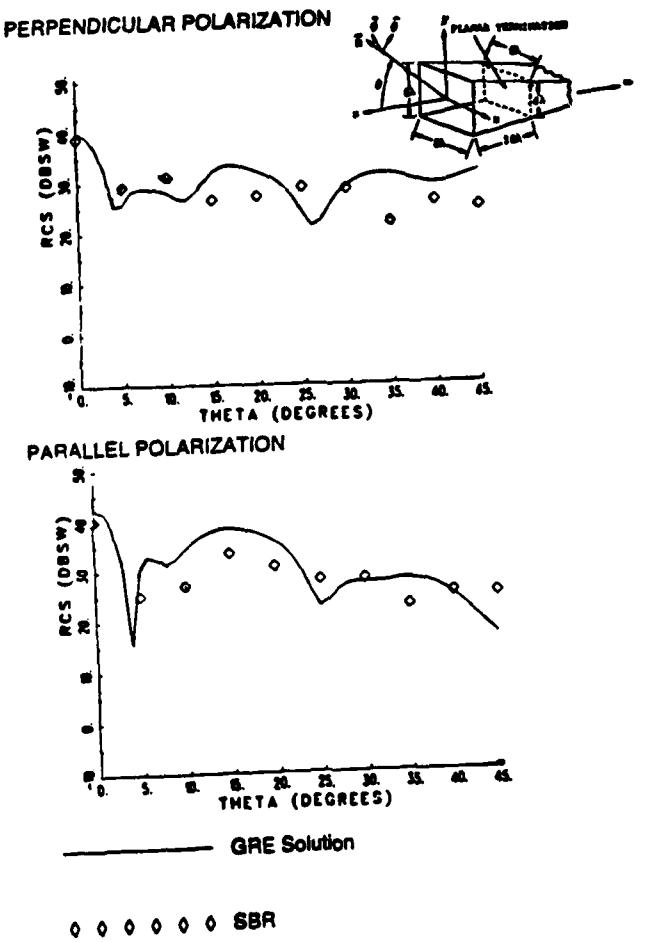

Figure 4: Tapered Rectangular Duct

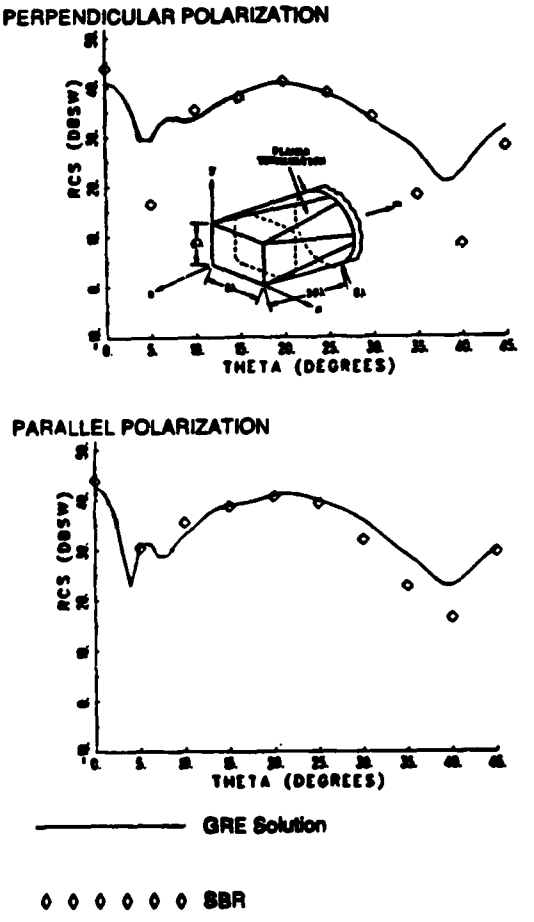

Figure 5: Straight Rectangular to Circular Transition Duct

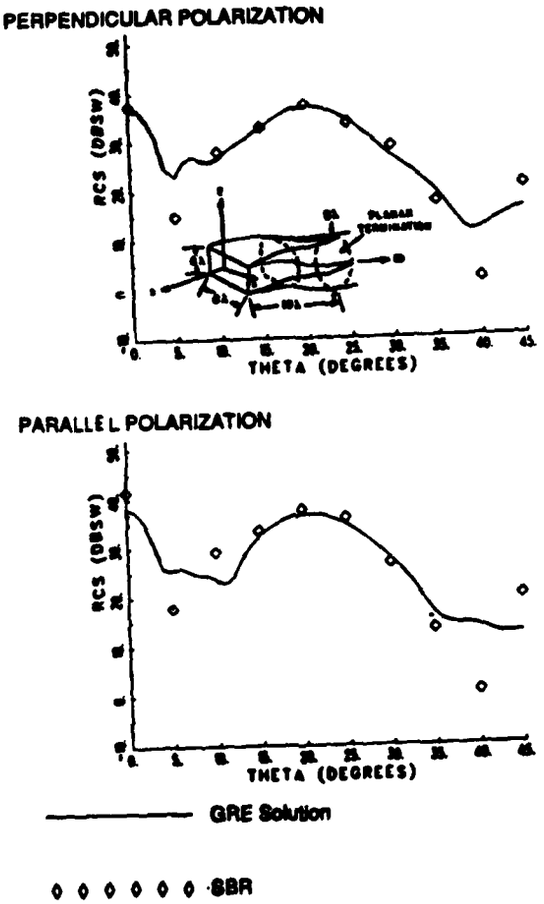

Figure 6: S-Bend Rectangular to Circular Transition Duct

A SATCOM ANTENNA SITING STUDY ON AN AIRCRAFT USING THE NEC-BSC V3.1

R. J. Marhefka and D. Bensman
The Ohio State University
ElectroScience Laboratory
1320 Kinnear Road
Columbus, Ohio 43212-1156

D. DeCarlo
Naval Air Test Center
Mail Code SY80AE
Patuxent River, MD 20670

Abstract

The performance of a UHF SATCOM antenna on a P-3C aircraft is studied using the NEC-Basic Scattering Code V3.1 (NEC-BSC31). It is desired for the system to provide performance to maintain the satellite link in areas of high signal fading to multipath effects. Potential locations of the antenna system to achieve a desired pattern and polarization coverage is the ultimate goal. This paper concentrates on the modeling and validation effort that should first take place in such studies.

The antenna modeled in this study represents a Dorne & Margolin DM 1501341 "Batwing" airborne UHF satellite communications antenna. This antenna produces a circular polarized antenna pattern. The antenna model used in the code is validated by comparing with measurements on a flat finite ground planes taken at Naval Air Test Center. Procedures for referencing the results to a circular polarized isotropic radiator are discussed.

Various types of computer models are used for different locations of the antenna. Some of the relevant background of the modeling effort pertaining to UTD and the NEC-BSC31 are discussed. The P-3C computer models are validated by comparing with scale model measurements taken independently by two different companies.

I Introduction

This paper discusses the use of the NEC - Basic Scattering Code Version 3.1 (NEC-BSC31) to predict the patterns of a UHF SATCOM antenna on an aircraft. The ultimate objective is to find a location or locations of the antenna to maintain the satellite link in areas of high signal fading to multipath effects. In this case, the

antenna is a commercially available circularly polarized crossed dipole type system. The aircraft is a P-3C.

The use of a code, such as the NEC-BSC31, in studies like this can ease costs by reducing though not eliminating measurements. Many locations can be tried in a reasonably fast time. Measurements are still needed, however, to validate the code. This paper concentrates on the model set up and the validation steps. First, setting up the code to present the circular polarization normalized to circular isotropic is discussed. Next, how the antenna is modeled is presented. The methodology of defining the aircraft model is next discussed. Finally, the validation of the model is presented.

II Background

The analysis is performed using the NEC - Basic Scattering Code Version 3.1 [1]. The complete capabilities of this code are detailed in the manual and have been summarized in previous papers [2]. The theory, based on UTD, has also been discussed in many references [3,4]. The main discussion here is centered around using the code to define a particular type of model and validation of the model.

In defining a model, it is necessary to compare the needs of the applications with the limitations of the available capabilities of the code. Some of the missing elements can be added. Others will have to be circumvented by careful definitions of similar cases that can supply at least partial information. Any problems beyond that need to be bounded.

In this case, the first step is defining an antenna model in the code that gives a good description of the real antenna. Since this is a circular polarized antenna, a means of plotting the results is developed. This is done externally to the existing code using the plotting program.

It is also desired to represent the results in absolute directive gain. This question arises frequently by users of the code. Since the NEC-BSC is not an antenna code per se. It is necessary to provide the normalizing information to the code. The surest way to obtain this information is to calculate a volumetric pattern. Integrating the volumetric pattern provides a figure for the power radiated. This number is then used to normalize the pattern. The volumetric pattern can be calculated using an ideal situation of the antenna in free space or over an infinite ground plane, which ever is more appropriate. In this case, it is an antenna over a ground plane. If one assumes that power is conserved when the model is changed, and that the current distribution does not change significantly, then this is a reasonable number to use for all the various model configurations calculated subsequently. All the results below are shown as absolute directive gain relative to circular isotropic or linear

isotropic depending on the situation.

III Antenna Study

The antenna used is a Dorne & Margolin DM 1501341 (Batwing) airborne UHF satellite communication antenna. It is a circular polarized type antenna built into an aerodynamic casing. It radiates like a simple set of crossed dipoles around 16.5" in length. They are oriented parallel to the fuselage and 7.6" off of it.

One way to model an antenna in the code is to first calculate the current distribution from a method of moments code. This is done using the ESP4 code [5]. An infinite ground plane is simulated by using image elements. The results proved to be almost exactly that of using the standard dipole model in the NEC-BSC31 over an infinite ground plane. The simpler built in model is, therefore, used.

Naval Air Test Center measured the Batwing antenna on a 6 foot ground plane. The patterns are for the vertical and horizontal polarization taken at 300 MHz for various elevation cuts. Just a couple of which are shown here. The calculated and measured results for the horizontal and vertical polarized fields in the principal elevation cut of the antenna (between the two elements) is shown in Figure 1. The calculated and measured results for the horizontal and vertical polarized field in the elevation cut along one of the element arms is shown in Figure 2.

The results compare very well. If the standard model in the code had not worked out so well, then the measured result could have been used in the table look up feature of the code. The ground plane would first have to be processed out.

IV Model Study

Defining the model to use is the next step. The best model to use depends on the location of the antenna. Simple plan view drawings of the aircraft are usually sufficient to help define the needed parameters. The measurements can be taken off the drawings then translated into the appropriate commands. The input set can then be run through the GKS geometry code, NECBSCGM, being supplied with version 3. Properly scaled this drawing can be overlaid on the plan view to see the accuracy of the input numbers.

In the case of the P-3C being studied here, any one of the three curved surface shapes can be used for the location of the antenna location used in the measurements. Figure 3 illustrates the use of a cylinder to represent the fuselage. An advantage of the cylinder at the present time is that the creeping waves can be calculated. For other locations closer to the nose it would be better to use on ellipsoid

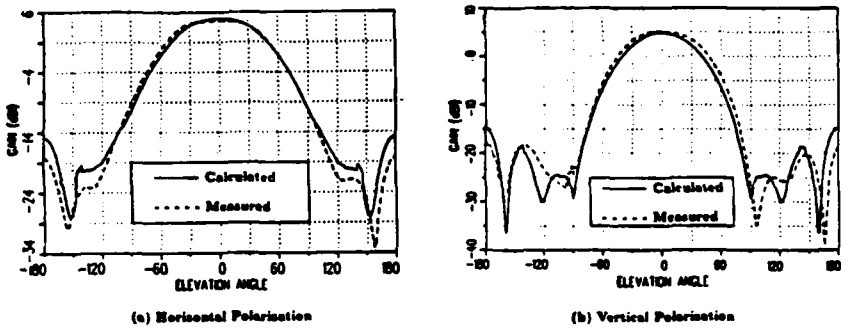

(a) Horizontal Polarization (b) Vertical Polarization

Figure 1: Comparison of calculated result using the NEC-BSC with measured result from NATC for horizontal and vertical polarizations of the antenna on a 6' ground plane in an elevation cut between the elements.

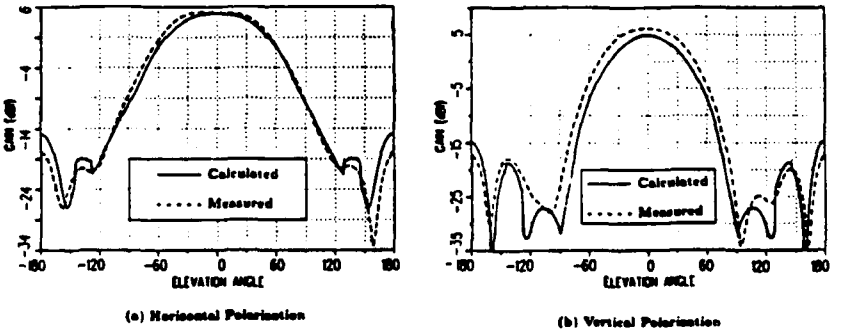

(a) Horizontal Polarization (b) Vertical Polarization

Figure 2: Comparison of calculated result using the NEC-BSC with measured result from NATC for horizontal and vertical polarizations of the antenna on a 6' ground plane in an elevation cut along one of the elements.

model. Cone frustum models are possible for other locations. In any case, it is best to start simple. Only five plates are used at first representing the wings, horizontal and vertical stabilizers.

A sensitivity study of the model is next in order. This entails running some pattern cuts with and without various parts of the structure included. If a plate representing a wing or a cylinder representing an engine does not produce significant scattering then it can be left out. It is determined by this type of analysis that the geometry in Figure 3 is sufficient for the indicated antenna location.

Another concern, for this particular problem, is that the antenna is only a quarter - wavelength off the surface. This pushes the largeness assumption for the UTD. This is tested by using an exact solution [6] to check the pattern in the roll plane. The dipoles are mounted on the top and oriented axially and circumferentially to an infinite cylinder in this case. The results are compared in Figure 4 for right and left hand polarization. This confirms that the code gives a reasonable approximation in the roll plane. Other cone angles gave similar comparisons, however, results could not be taken for very small cone angles.

The next step is to compare the patterns in the principal plane with scale model measurements. The measurements are made on a 1/17 scale model by Boeing [7]. The antenna elements are parallel to the fuselage but rotated 45° with respect to the fuselage axis. The results are compared for the roll, elevation, and azimuth planes for the right circular component in Figures 5a,b,c, respectively. A single pattern cut took about 1.5 minutes of CPU time on a VAX 8550. Notice that the roll plane results compare excellently. The elevation and azimuth planes show deviation near the nose and tail. This is due to the interactions with the wings and stabilizers. The code does not presently have the cylinder - plate terms. These have been approximated by superimposing an interaction of a plate image of the antenna with the wings. On the whole, however, the comparisons are quite good over most of the patterns.

V Conclusions

The NEC-BSC V3.1 has been used to predict the directive gain of a circular polarized antenna on an aircraft. The antenna model is validated against measurements on a circular ground plane. The aircraft model for a P-3C used is based on a circular cylinder fuselage with five flat plate wings and stabilizers. The model is validated by comparison with scale model measurements. The comparisons indicate that the code gives good results in most regions of the illuminate pattern. The exception is where the fuselage wing interactions have been approximated.

Numerous conic cuts have been calculated and compared with measurements

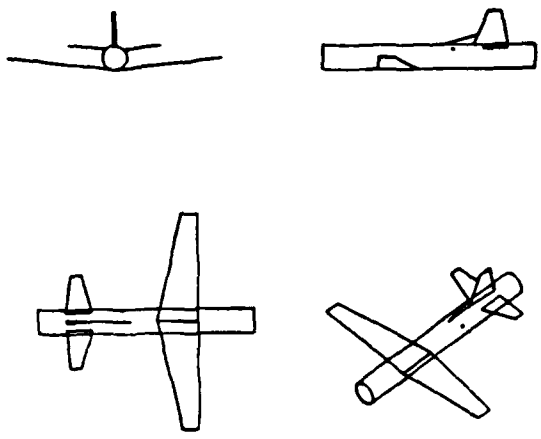

Figure 3: Illustration of a model of P-3C used in the NEC-BSC.

with similar conclusions. Various other locations for the antenna also have been investigated. The model for the various locations are essentially the same as the one given here. When the antenna is mounted near the nose, however, a composite ellipsoidal fuselage is used. More details of this study are provided in Reference [8].

References

[1] R. J. Marhefka and J. W. Silvestro, "Near zone - basic scattering code, user's manual with space station applications," Technical Report 718422-13, The Ohio State University ElectroScience Laboratory, Department of Electrical Engineering, March 1988. Prepared under Grant No. NSG 1613 for National Aeronautics and Space Administration.

[2] R. J. Marhefka, "Development and validation of a new version of the NEC-BSC," in *4th Annual Review of Progress in Applied Computational Electromagnetics*, March 22-24 1988.

[3] P. H. Pathak, "Techniques for high-frequency problems," in *Antenna Handbook: Theory, Applications, and Design*, (Y. T. Lo and S. W. Lee, eds.), ch. 4, New York: Van Nostrand Reinhold Co. Inc., 1988.

[4] W. D. Burnside and R. J. Marhefka, "Antennas on aircraft, ships, or any large, complex environment," in *Antenna Handbook: Theory, Applications, and Design*, (Y. T. Lo and S. W. Lee, eds.), ch. 20, New York: Van Nostrand Reinhold Co. Inc., 1988.

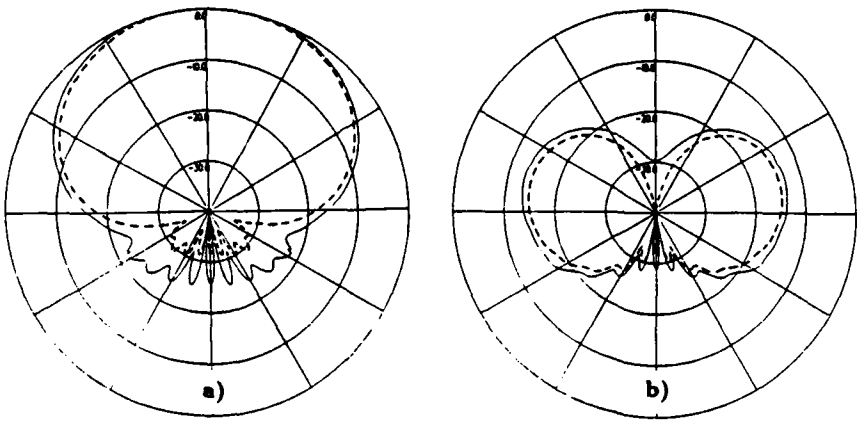

Figure 4: Comparison of NEC-BSC results (solid) versus an eigenfunction (dashed) solution in the roll plane of a cylinder for (a) right and (b) left circular polarization.

[5] E. H. Newman and R. L. Dilsavor, "A user's manual for the electromagnetic surface patch code: ESP version III," Technical Report 716148-19, The Ohio State University ElectroScience Laboratory, Department of Electrical Engineering, May 1987. Prepared under Grant No. NSG 1613 for National Aeronautics and Space Administration.

[6] R. F. Harrington, *Time-Harmonic Electromagnetic Fields*, pp. 232–238. McGraw-Hill Book Co., 1961.

[7] S. Hunter, "P-3 update IV antenna test report," Document No. D385-66744-1, Boeing, Airborne Antenna System Group, May 1988. Prepared under Contract No. N00019-87-C-0269 for Naval Air Test Center.

[8] D. Bensman and R. J. Marhefka, "SATCOM antenna siting study on a P-3C using the NEC-BSC V3.1," Technical Report 721711-2, The Ohio State University ElectroScience Laboratory, Department of Electrical Engineering, To be published 1990. Prepared under Grant No. NAG2-542 for Naval Air Test Center and National Aeronautics and Space Administration.

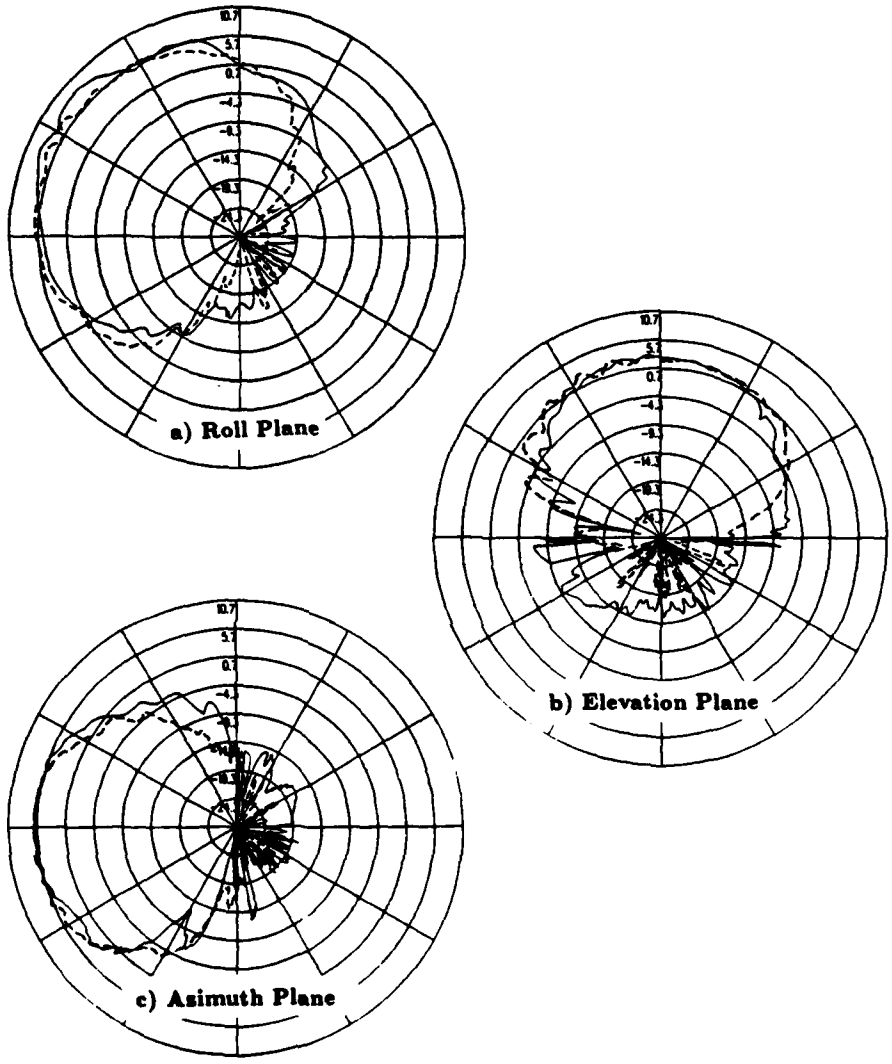

Figure 5: Comparison of NEC-BSC results (solid) with scale model measurements (Boeing) (dashed) for the right circular polarization in the (a) roll, (b) elevation, and (c) azimuth planes.

ANALYSIS OF LOW DIRECTIVITY ANTENNAS ON STRUCTURES

P R Foster, Microwave and Antenna Systems, UK

ABSTRACT

A computer program, ALDAS, has been developed which computes the radiation pattern of a low gain antenna installed on a structure using the methods of the Geometrical and Unified Theories of Diffraction (GTD/UTD). 7 antenna types are included with provision for the input of measured feed data. Linear and circular polarisation can be accommodated. The structure may consist of cylinders and flat plates, and incorporates a choice of 3-D curvatures for a single item, that is, the fuselage of an aircraft. The program is user-friendly with full screen editing for input, a comprehensive filing system as well as tabular and graphical output for the radiation patterns and structure geometry. It is intended for 80387 machines running under DOS and DEC machines running under VMS.

INTRODUCTION

This program has been developed primarily for low gain antennas on air and space vehicles. It has also been used for ground vehicles and ships.

The development of a complex program for electromagnetic problems is a compromise between accuracy of the input and output, runtime and ease of use. The major problems encountered in writing a program to deal with low gain antennas on large structures are deciding on the mathematical/geometrical approach and ensuring a standard entry of data which is acceptable to the user and will provide consistent results.

The heart of a GTD/UTD program is not primarily an electromagnetic problem but a decision as to the approach to the solution of the geometry. A general description of the structure in terms of the surface in three dimensional coordinates, while possible, assumes the availability of good manufacturing drawings. These might not be available but, even if they were, the modelling of surfaces which are not good conductors such as windscreen, radome and other dielectric sectors of an aircraft would be questionable. The decision in this case was to break up the structure into a range of permitted canonical shapes and calculate only reflection, blockage and first diffraction effects. This avoids the need for ray-tracing which is very time-consuming.

DATA ENTRY

The entry of data is dealt with by taking the user through a menu which leads to a set of 'pages' to be edited and creating standard files which can be reused or edited to take care of new parameters.

The data entry is divided into four sections, feed type, feed position, structure geometry and required radiation pattern output. Each section has its own menu and a capability to file the current data, to read an existing file or to write the current data to file. Thus if it is required to move an antenna position on an aircraft, only an alteration to the ANTENNA POSITION file is required. Each file is an exact replica of the screen data which makes the files easy to read and understand.

1) FEED

Seven types of feed are available as follows

dipole (plus optional parasitics)
monopole (plus optional parasitics)
rectangular horn (plus optional dielectric)
circular horn (plus optional dielectric)
spiral
polyrod
annular slot

There is also a facility for the input of measured free space radiation patterns. Figure 1 shows a typical entry page for a feed. The top section shows the input data while the lower section shows the resultant parameters pertaining to the feed.

2) ANTENNA POSITION

This must be defined in the same global coordinates as the structure although the units may be different. Internal to the program, all coordinates and dimensions are in metres. The angular direction of the antenna boresight is also required (Figure 2).

3) STRUCTURE GEOMETRY

There are several screens or 'pages' for a structure. It is basically described on the first page as a 'fuselage' which may be

- absent
- ellipsoidal
- cylindrical with an elliptical cross-section
- 'cylindrical' with a rectangular cross-section.

There is provision for adding a truncated nose-cone to the last two entries. The first page also contains entries for the number of cylinders, flat plates and obstacles which make up the structure.

Cylinders (up to 10) have to be circular in cross-section but may be orientated in any direction. Typical items to be modelled this way would be engines or stores on an aircraft.

Flat plates (up to 10) can have between 4 and 10 corners and the data entry is checked to ensure that the entered points are in deed coplanar. There is a facility for allowing either the user or the program to correct any such errors. Figure 3 shows a typical page of data. The attachment parameters allow a decision to made by the program as to whether diffraction should be calculated for a particular edge and, if so, whether wedge diffraction or cylindrical diffraction is to be used.

Obstacles (up to 10) are for modelling such things as UHF blades and each is assumed to be a flat plate with four corners. These are again checked for consistency. Edge diffraction parameters are also entered.

An additional facility is available which provides an onscreen or hardcopy plot of the structure. This does not have hidden line removal as its primary function is to check that all geometry is correctly entered and all sections are correctly attached. Figures 4 and 5 show examples.

4) RADIATION PATTERNS

A typical page for requesting a radiation pattern allows the entry of three types of cut, constant phi, constant theta or a bank angle (Figure 5). The three data entry files must be specified.

5) DATA VALIDATION

Each data entry is validated for type and range and is provided with a default value to ensure the program is robust [1]. Additional checking of interactive parameters is carried out as in the entry of geometry for the fuselage and plates.

COMPUTATIONS

Items included in the diffraction analysis [2 - 4] include

- direct ray
- creeping waves for a feed on a conducting surface
- reflected waves (curved and flat surfaces)
- creeping waves on curved surfaces

The majority of computation time is taken up with computing ray geometry and checking that input and output rays are not intersected by other parts of the structure. The diffraction computation of two rather than one linear polarisation adds little to the total time. Thus calculations of circularly polarised radiation patterns take very little longer than those for one linear polarisation. Provision is made for the input of radiation patterns in two orthogonal polarisations so that a final slant or circular polarisation can be computed.

VALIDATION

Over the last five years, a considerable body of comparison data has been collected. At the simplest level, it is possible to show predicted and measured radiation patterns on single structures (Figure 7). At a higher level, comparison has been made between predicted and scale model results (Figure 8 and 9). A detailed examination was carried out of antennas on a helicopter where the radiation patterns were measured in free space and installed while the computations used the measured free space results. The difference between the measured and predicted patterns for the installation had an RMS value of 0.35 dB for gain above -8 dBi.

In general, it can be said that the error in a predicted radiation pattern is a function of the gain level with peak errors being less than 1.0 dB for gain levels greater than -5 dBi, rising to 3 dB at -15 dBi and 5 dBi at -25 dBi. One problem is that aircraft dimensions are not exact and a 1% change is quite common in civil aircraft. The predicted results may not represent the aircraft which is measured. This means that gross features are reproduced quite well but a sharp null may occur at a slightly different angle to that predicted. Systematic measurements on several aircraft of the same type do not appear to have been made with a view to inter-comparison of the results.

RUNTIMES

Runtimes are a function of the machine used and the complexity of the structure. The runtime for a single radiation pattern of a monopole on a ground plane will be less than one minute on a 25 MHz PC with a 80387 chip. On the other hand, a radiation pattern on a structure which contains a fuselage, four engines, some stores and several planes will take up to 30 minutes.

REFERENCES

1 Browning D J and Foster P R
Data Entry and Validation Techniques for Electromagnetic Problems
IEE Colloquium No 1989/121 on 'Large Scale Programs for Use in Antenna Performance Prediction', October 1989

2 Kouyoumjian R G and Pathak P H
A Uniform Geometrical Theory of Diffraction for an Edge in a Perfectly Conducting Surface
Proc IEEE, 62, No 11, 1974, p1448 - 1461

3 Kouyoumjian R G
The Geometrical Theory of Diffraction and its Application
'Topics in Applied Physics, 1975, ed R Mittra

4 Bach H
Introduction to GTD Applications
'Theoretical Methods for Determining the Interaction of Electromagnetic waves with Structures', 1981, ed J K Skwirzynski

5 Albertsen N C and Jensen Fl
Pattern Prediction for L-band antennas on aircraft
TICRA Rept S-77-03, Nov 1977

6 Burnside W
Analysis of On-aircraft Antenna Patterns
PhD Thesis,1972, Ohio State University

12-03-90 ANALYSIS OF LOW DIRECTIVITY ANTENNAS ON STRUCTURES 11:32:42

FEED DEFINITION EDITOR

Feed type (? for poll)	Dipole
Polarisation (Horiz, Vertical or Slant)	Vertical
Centre frequency (GHz)	10.000
Length of driven element (mm)	15.000
Number of parasitics	0
H-plane half-power beamwidth (Deg)	360.000
E-plane half-power beamwidth (Deg)	60.000
Peak gain (dBi)	2.150
Fractional Bandwidth	0.200

^Z Exit ^E Up ^X Down

FIGURE 1 Edit Page for Feed Entry

19-01-90 ANALYSIS OF LOW DIRECTIVITY ANTENNAS ON STRUCTURES 16:15:02

Antenna Position Editor

Number of antennas	1
Units (metres or millimetres)	Millimetres
Antenna 1	
X-coordinate	0.000
Y-coordinate	0.000
Z-coordinate	7.300
Azimuth boresight	0.000
Elevation boresight	90.000

^Z Exit ^E Up ^Z Down

FIGURE 2 Edit Page for Antenna Position Entry

19-01-90 ANALYSIS OF LOW DIRECTIVITY ANTENNAS ON STRUCTURES 16:15:02

Geometry Definition Editor Page 3

Current Units	Metres
Current plane number	5
Number of corners	4

Corner Number	Coordinates -- X --	-- Y --	-- Z --	Edge Attached	Edge Type	Edge Radius	Edge Angle
1	-8.486	0.000	0.813	No	Wedge		20.000
2	-8.480	-2.340	0.813	No	Wedge		20.000
3	-9.930	-2.340	0.813	No	Wedge		20.000
4	-9.930	0.000	0.813	Yes	Wedge		20.000

^Z Exit ^E Up ^Z Down ^S left ^D Right ^A Previous page ^F Next page

FIGURE 3 Edit Page for Flat Plate Entry

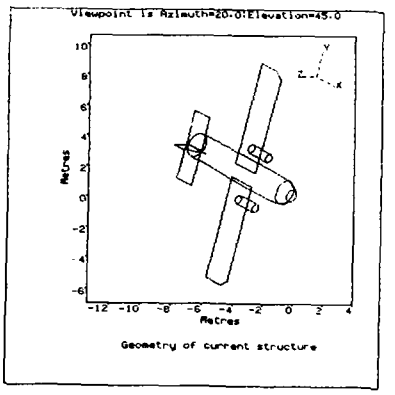

FIGURE 4 Geometry output for an ISLANDER

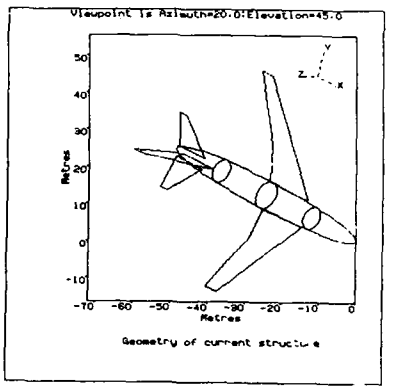

FIGURE 5 Geometry output for a BOEING 747

19-01-90 ANALYSIS OF LOW DIRECTIVITY ANTENNAS ON STRUCTURES 16:15:02

Radiation Pattern Data

Frequency (GHz)	2.000
Angular Cut (Theta or Phi constant)	Phi
Elevation Start Angle (deg)	-270.000
Elevation Stop Angle (deg)	90.000
Elevation Step Angle (deg)	5.000
Azimuth Start Angle (deg)	0.000
Azimuth Stop Angle (deg)	90.000
Azimuth Step Angle (deg)	0.000
Name of Feed file	DIPV.FD
Name of Feed Position file	DIPV.POS
Name of Geometry file	PLATE.GEO
Title	FEED PATTERN - HOR DIPOLE OVER FLAT PLATE
Type of radiation pattern plot	Polar

^Z Exit ^E Up ^Z Down

FIGURE 6 Data Entry for Radiation Pattern Output

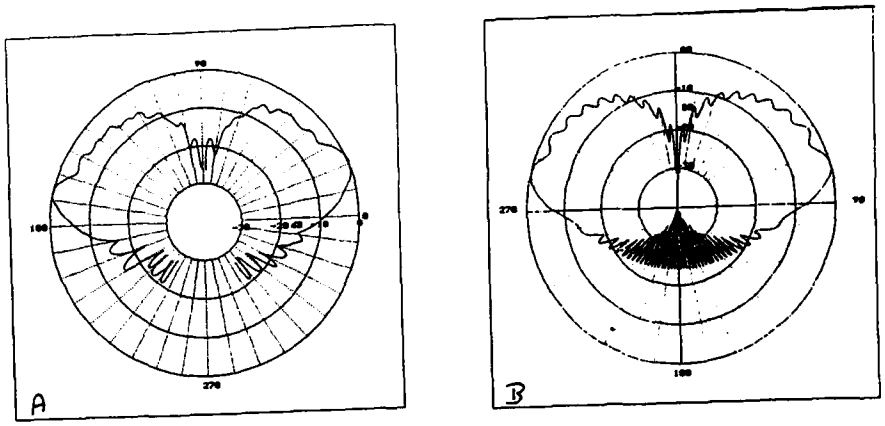

FIGURE 7 Radiation pattern of a monopole
on a 20 wavelength square ground plane
A) Measured B) Computed

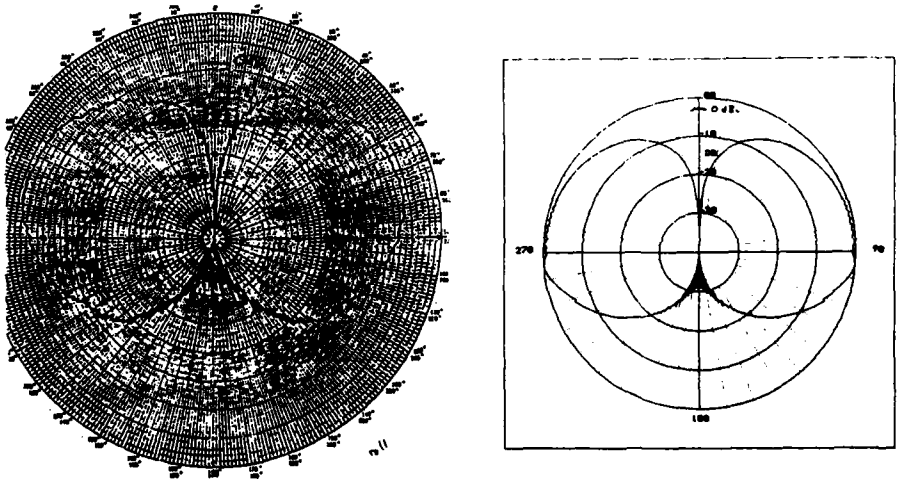

FIGURE 8 Roll plane radiation pattern of a
monopole on a BOEING 747
A) Measured [5] B) Predicted

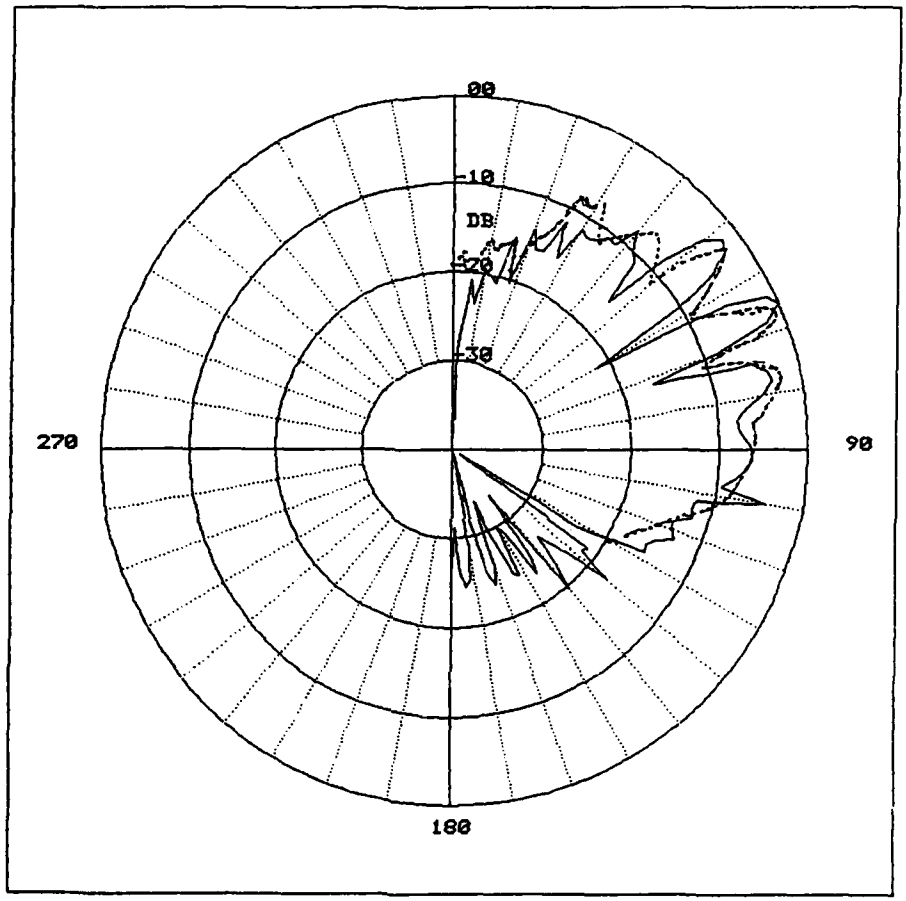

FIGURE 9 Roll plane radiation pattern of
a monopole on a schematic aircraft
Solid line Computed
Dashed line Measured [6]

High Frequency Scattering from an Edge Bounded by Nonperfectly Conducting Surfaces

Robert T. Brown
Lockheed Aeronautical Systems Company
Dept. 77-22, Bldg. 311, Plant B-6
P.O. Box 551
Burbank, California 91520

The Maliuzhinets approach [1] to the problem of scattering by an edge bounded by nonperfectly conducting surfaces has the advantage that it provides an exact solution to the problem of diffraction by an edge with different material properties on either side, but has the disadvantage that it has not yet been fully developed for oblique incidence, although some progress has recently been reported in this area [2], [3], and is applicable only to the less generally valid impedance boundary condition (IBC), not arbitrary reflectance. It has the further disadvantage of being computationally intensive. Burnside *et al.* have shown that within the limitations of a penetrable, possibly lossy, knife edge, or planar discontinuity, good results can be obtained by using reflection and transmission coefficients to modify the GTD diffracted field [4], [5]. Luebbers has extended this method to a study of propagation path loss, and has obtained good agreement with both measured data and results from the exact Maliuzhinets diffraction coefficient [6], [7].

This paper describes a study of the feasibility of using reflection coefficients to modify PTD edge diffraction coefficients [8], [9] in a way consistent with the way they are used to modify physical optics [10]. A simple weighted average reflection coefficient is used in the case of illumination on both faces of the edge. Although the method is applicable to arbitrary reflectance, so far it has been tested only against moment method results for edges bounded by impedance surfaces. Excellent agreement is obtained for cases in which there is not too great a jump in reflectance properties across the edge. Agreement is not as good when the jump corresponds to a change in normal incidence reflected power of 10dB or more.

SCATTERING FROM EDGES BOUNDED BY NONPERFECTLY CONDUCTING SURFACES–REQUIREMENTS

- Suitable for general purpose computer code
- Large number of finite length edge segments
- Arbitrary orientation (incidence angle and polarization)
- Backscatter only

TECHNIQUES FOR PREDICTING HIGH FREQUENCY SCATTERING BY NONPERFECTLY CONDUCTING EDGES

- Maliuzhinets Theory
  - + Exact solution
  - + Successfully combined with GTD as well as PTD
  - – Impedance surfaces only
  - – Numerically intensive
  - – Not fully developed for oblique incidence
- Reflectance modification of diffraction coefficients
  - + Arbitrary complex reflectance
  - + Successfully applied to GTD
  - + Numerically simple
  - – No firm theoretical basis

COORDINATE SYSTEMS USED TO DESCRIBE DIFFRACTION BY AN ARBITRARILY ORIENTED EDGE

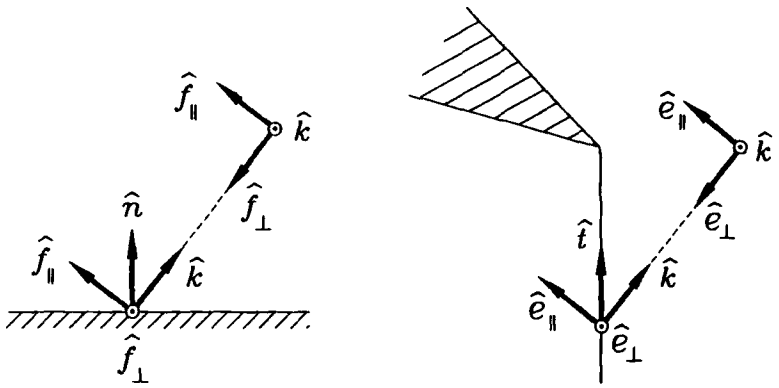

PO/PTD SCATTERING MATRIX ELEMENT FOR EDGE WITH ONE FACE ILLUMINATED

Incident field $\mathbf{E}_e$ in the edge-oriented coordinate system

$$\mathbf{E}_e = (\hat{\mathbf{p}}_i \cdot \hat{\mathbf{e}}_\parallel)\hat{\mathbf{e}}_\parallel + (\hat{\mathbf{p}}_i \cdot \hat{\mathbf{e}}_\perp)\hat{\mathbf{e}}_\perp$$

Modified by the diffraction coefficients:

$$\mathbf{E}_d = (\hat{\mathbf{p}}_i \cdot \hat{\mathbf{e}}_\parallel)\hat{\mathbf{e}}_\parallel f + (\hat{\mathbf{p}}_i \cdot \hat{\mathbf{e}}_\perp)\hat{\mathbf{e}}_\perp g$$

Then projected on the face-oriented basis:

$$\mathbf{E}_{d+r} = (\mathbf{E}_d \cdot \hat{\mathbf{f}}_\parallel)\hat{\mathbf{f}}_\parallel R_\parallel - (\mathbf{E}_d \cdot \hat{\mathbf{f}}_\perp)\hat{\mathbf{f}}_\perp R_\perp$$

Finally, for an arbitrary receiver polarization $\hat{\mathbf{p}}_s$:

$$\begin{aligned} A_{is} &= \mathbf{E}_{d+r} \cdot \hat{\mathbf{p}}_s \\ &= \hat{\mathbf{p}}_i \cdot [\hat{\mathbf{e}}_\parallel \hat{\mathbf{e}}_\parallel f + \hat{\mathbf{e}}_\perp \hat{\mathbf{e}}_\perp g] \cdot [\hat{\mathbf{f}}_\parallel \hat{\mathbf{f}}_\parallel R_\parallel - \hat{\mathbf{f}}_\perp \hat{\mathbf{f}}_\perp R_\perp] \cdot \hat{\mathbf{p}}_s \end{aligned}$$

PTD DIFFRACTION COEFFICIENTS

One face illuminated:

$$f = F_d + F_p$$
$$g = G_d + G_p$$

Two faces illuminated:

$$f = F_d + F_p(1) + F_p(2)$$
$$g = G_d + G_p(1) + G_p(2)$$

Sum of "GTD" and "PTD" terms; "GTD" independent of face from which illumination is measured.

TERMS IN PTD DIFFRACTION COEFFICIENTS

"GTD" Terms ($s = \alpha/\pi$):

$$F_d = \frac{\sin \pi/s}{s}\left[\frac{1}{\cos \pi/s - 1} - \frac{1}{\cos \pi/s - \cos 2\phi/s}\right]$$

$$G_d = \frac{\sin \pi/s}{s}\left[\frac{1}{\cos \pi/s - 1} + \frac{1}{\cos \pi/s - \cos 2\phi/s}\right]$$

"PO" Terms:

$$F_p(1) = -\frac{1}{2}\tan \phi$$
$$G_p(1) = \frac{1}{2}\tan \phi$$
$$F_p(2) = -\frac{1}{2}\tan(\alpha - \phi)$$
$$G_p(2) = \frac{1}{2}\tan(\alpha - \phi)$$

PO/PTD SCATTERING MATRIX ELEMENT FOR EDGE WITH TWO FACES ILLUMINATED

For external wedge angle greater than $3\pi/2$

$$\begin{aligned} A_{is} &= \hat{\mathbf{p}}_i \cdot \left\{ [\hat{\mathbf{e}}_\parallel \hat{\mathbf{e}}_\parallel F_d + \hat{\mathbf{e}}_\perp \hat{\mathbf{e}}_\perp G_d] \cdot [w_1 \mathcal{R}(1) + w_2 \mathcal{R}(2)] \right. \\ &+ [\hat{\mathbf{e}}_\parallel \hat{\mathbf{e}}_\parallel F_p(1) + \hat{\mathbf{e}}_\perp \hat{\mathbf{e}}_\perp G_p(1)] \cdot \mathcal{R}(1) \\ &+ \left. [\hat{\mathbf{e}}_\parallel \hat{\mathbf{e}}_\parallel F_p(2) + \hat{\mathbf{e}}_\perp \hat{\mathbf{e}}_\perp G_p(2)] \cdot \mathcal{R}(2) \right\} \cdot \hat{\mathbf{p}}_s \end{aligned}$$

The reflectance dyadic $\mathcal{R}(\ell)$ is

$$\mathcal{R}(\ell) = \hat{\mathbf{f}}_\parallel(\ell)\hat{\mathbf{f}}_\parallel(\ell)R_\parallel(\ell) - \hat{\mathbf{f}}_\perp(\ell)\hat{\mathbf{f}}_\perp(\ell)R_\perp(\ell)$$

where the index ℓ refers to face 1 or 2, and the weights are the fractional projected angles

$$w_1 = \frac{\phi - \phi_L}{\alpha - 2\phi_L}$$

and

$$w_2 = \frac{\alpha - \phi_L - \phi}{\alpha - 2\phi_L}$$

REFLECTION COEFFICIENT MODIFICATION OF PO/PTD DIFFRACTION COEFFICIENTS

EXTERNAL WEDGE ANGLE GREATER THAN $3\pi/2$

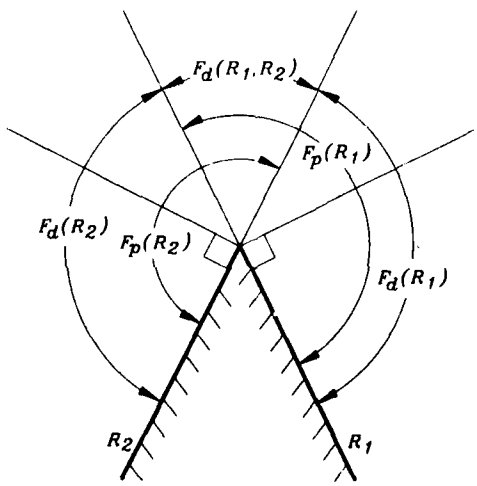

GEOMETRY OF MONOSTATIC WEDGE DIFFRACTION

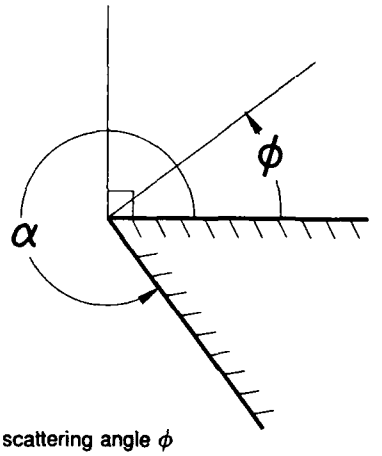

- External wedge angle α
- Projected incidence and scattering angle ϕ
- GTD singularity at $\phi = \pi/2$

EFFECT OF SINGULARITIES ON USE OF WEIGHTED REFLECTION COEFFICIENTS

- Singularities in f and g when $\phi \to \pi/2$, or $\alpha - \phi \to \pi/2$
- Second terms in F_d and G_d approach division by zero
- "PO" terms approach ∞ as $\tan \pi/2$
- Indeterminate form $\infty - \infty$ has finite limit

$$f \to \frac{\sin \pi/s}{s(\cos \pi/s - 1)} + \frac{1}{2s \tan \pi/s}$$

$$g \to \frac{\sin \pi/s}{s(\cos \pi/s - 1)} - \frac{1}{2s \tan \pi/s}$$

- Therefore "GTD" and "PO" terms must be modified in same way in region of singularity

PO/PTD SCATTERING MATRIX ELEMENTS IN THE INTERMEDIATE REGION

- Two Faces Illuminated, external wedge angle less than $3\pi/2$
- Singularities limit use of weighted reflection coefficients
- For the case $\phi \leq \pi/2$ as measured from face 1

$$\begin{aligned} A_{is} &= \hat{\mathbf{p}}_i \cdot \left\{ \left[\hat{\mathbf{e}}_\parallel \hat{\mathbf{e}}_\parallel [F_d + F_p(1)] + \hat{\mathbf{e}}_\perp \hat{\mathbf{e}}_\perp [G_d + G_p(1)] \right] \cdot \mathcal{R}(1) \right. \\ &+ \left. [\hat{\mathbf{e}}_\parallel \hat{\mathbf{e}}_\parallel F_p(2) + \hat{\mathbf{e}}_\perp \hat{\mathbf{e}}_\perp G_p(2)] \mathcal{R}(2) \right\} \cdot \hat{\mathbf{p}}_s \end{aligned}$$

- For the case $\phi \leq \pi/2$ as measured from face 2

$$\begin{aligned} A_{is} &= \hat{\mathbf{p}}_i \cdot \left\{ \left[\hat{\mathbf{e}}_\parallel \hat{\mathbf{e}}_\parallel [F_d + F_p(2)] + \hat{\mathbf{e}}_\perp \hat{\mathbf{e}}_\perp [G_d + G_p(2)] \right] \cdot \mathcal{R}(2) \right. \\ &+ \left. [\hat{\mathbf{e}}_\parallel \hat{\mathbf{e}}_\parallel F_p(1) + \hat{\mathbf{e}}_\perp \hat{\mathbf{e}}_\perp G_p(1)] \mathcal{R}(1) \right\} \cdot \hat{\mathbf{p}}_s \end{aligned}$$

- Reflectance dyadic $\mathcal{R}$ as defined previously

REFLECTION COEFFICIENT MODIFICATION OF PO/PTD DIFFRACTION COEFFICIENTS

EXTERNAL WEDGE ANGLE LESS THAN $3\pi/2$

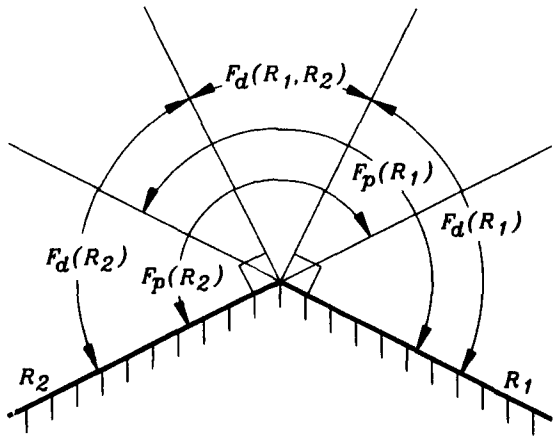

COMPARISON OF RESULTS FOR SQUARE CYLINDER, TWO WAVELENGTHS PER SIDE

ALL SIDES PERFECTLY CONDUCTING

TE POLARIZATION

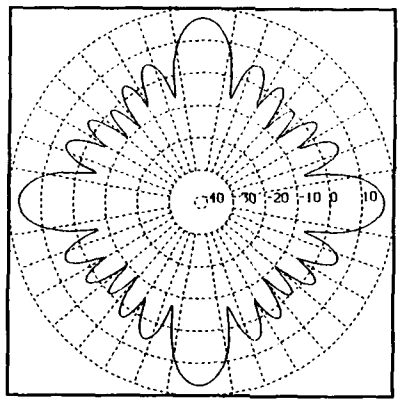

MoM

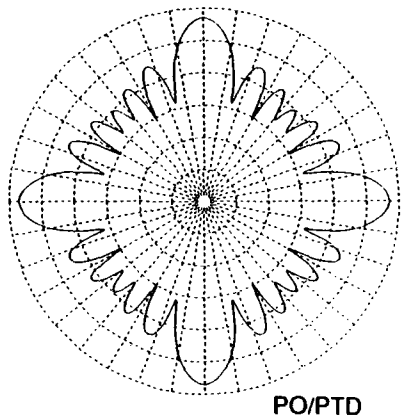

PO/PTD

COMPARISON OF RESULTS FOR SQUARE CYLINDER, TWO WAVELENGTHS PER SIDE

TWO SIDES PERFECTLY CONDUCTING, TWO SIDES Z=(.3,.3)

TE POLARIZATION

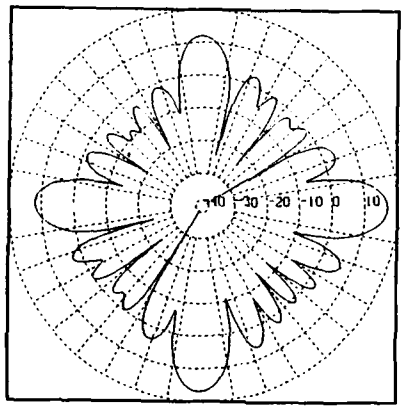

MoM

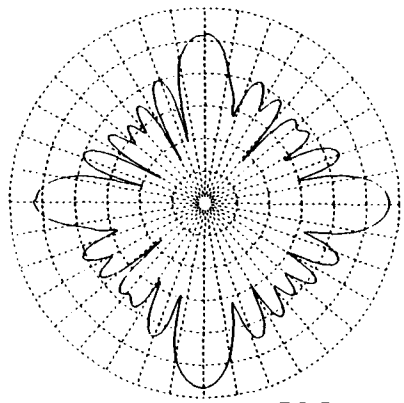

PO/PTD

COMPARISON OF RESULTS FOR SQUARE CYLINDER, TWO WAVELENGTHS PER SIDE

ALL SIDES PERFECTLY CONDUCTING

TM POLARIZATION

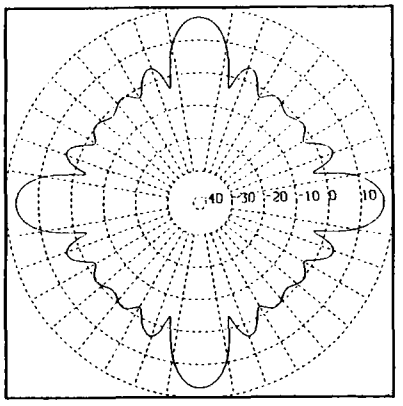

MoM

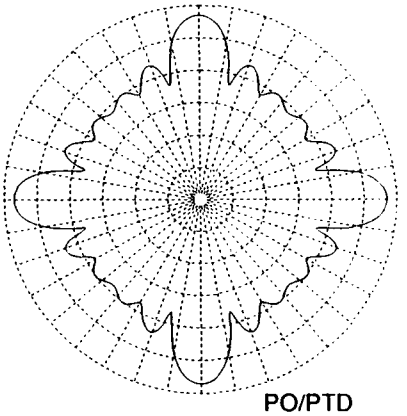

PO/PTD

COMPARISON OF RESULTS FOR SQUARE CYLINDER, TWO WAVELENGTHS PER SIDE

TWO SIDES PERFECTLY CONDUCTING, TWO SIDES Z=(.3,.3)

TM POLARIZATION

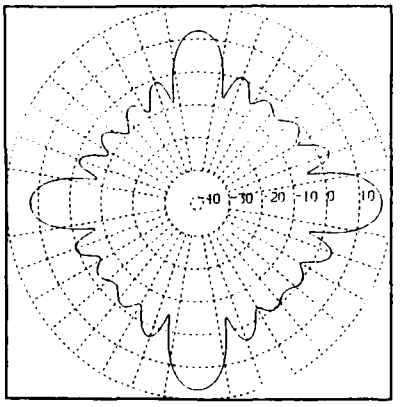

MoM

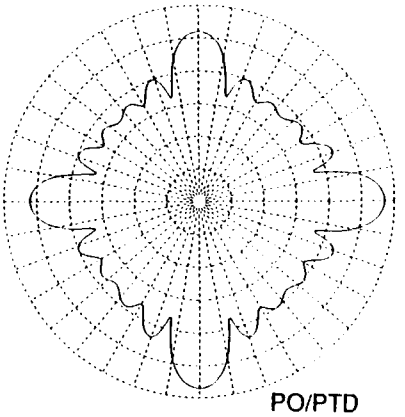

PO/PTD

References

[1] G. D. Maliuzhinets, "Exitation, Reflection, and Emission of Surface Waves from a Wedge with Given Face Impedances," *Sov. Phys. Doklady,* vol. 3, pp. 752-755, 1958.

[2] E. Bleszynski, H. B. Tran and M. Bleszynski, "Physical Theory of Diffraction for Scattering of Electromagnetic Waves of an Arbitrary Incidence Angle from Impedance Edges." 1989 IEEE-APS International Symposium, San Jose, California, June 1989.

[3] E. Bleszynski and M. Bleszynski, "A Perturbative Approach to Scattering of Electromagnetic Waves of an Arbitrary Incidence Angle from A Wedge with Different Face Impedances," 1989 IEEE-APS International Symposium, San Jose, California, June 1989.

[4] R. G. Rojas-Teran and W. D. Burnside, "GTD Analysis of Airborne Antennas in the Presence of Lossy Dielectric Layers," Ohio State University, ElectroSci. Lab. Rept. 710964-8, Aug. 1981.

[5] W. D. Burnside and K. W. Burgener, "High Frequency Scattering by a Thin Lossless Dielectric Slab," *IEEE Trans. Antennas Propogat.* vol. AP-31, pp. 104,110, Jan. 1983.

[6] R. J. Luebbers, "Finite Conductivity Uniform GTD Versus Knife Edge Diffraction in Prediction of Propagation Path Loss," *IEEE Trans. Antennas Propagat.* vol. AP-32, pp. 70-76, Jan. 1984.

[7] R. J. Luebbers, "Comparison of Lossy Wedge Diffraction Coefficients with Application to Mixed Path Propagation Loss Prediction," *IEEE Trans. Antennas Propagat.* vol. AP-36, pp. 1031-1034, Jul. 1988.

[8] P. Ya. Ufimtsev, "The Method of Edge Waves in the Physical Theory of Diffraction," Translation by USAF Foreign Technology Division, Wright-Patterson AFB, Ohio, FTD-HC-23-259-71, 1971, AD 733 203.

[9] K. M. Mitzner, "Incremental Length Edge Diffraction Coefficients," AFAL-TR-73-296, Air Force Avionics Laboratory, Wright-Patterson AFB, Ohio, 1973, AD 918 861.

[10] G. T. Ruck,D. E. Barrick, W. D. Stuart and C. K. Krichbaum, *Radar Cross Section Handbook*, New York:Plenum Press, 1970, pp. 55-58.

SESSION 10 A - "VALIDATION"

IS GALERKIN'S METHOD REALLY BETTER?

Andrew F. Peterson
School of Electrical Engineering
Georgia Institute of Technology
Atlanta, GA 30332-0250

Roy E. Jorgenson
Sandia National Laboratories
PO Box 5800
Albuquerque, NM 87185

ABSTRACT: The selection of basis and testing functions within a method-of-moments discretization is an important issue in computational electromagnetics. There appears to be widespread belief that Galerkin's method (selecting the same functions for basis and testing) will generally produce better results than some other choice. To investigate this issue, a variety of discretizations have been studied for several canonical electromagnetics problems. Results suggest that the accuracy of the discretization depends primarily on the order or "smoothness" of the basis and testing functions, and that there is nothing particularly noteworthy about the accuracy obtained with Galerkin's method.

1. THEORETICAL DEVELOPMENT

The method of moments [1] has proven effective for solving a variety of electromagnetic radiation and scattering problems described by a continuous operator equation Lf=g. The linear operator L maps functions in its domain (such as the unknown f) to functions in its range (such as the excitation g). As a general rule, the domain and range are different linear spaces. For instance, in the case where L is a differential operator, the domain of L will generally include boundary conditions not imposed on functions in the range.

It is convenient to introduce the notion of an inner product, which is a scalar quantity denoted <a,b> satisfying the following properties:

$$\langle a,b\rangle = \langle b,a\rangle^* \tag{1}$$

$$\langle \alpha a, \beta b + c\rangle = \alpha^*\beta \langle a,b\rangle + \alpha^* \langle a,c\rangle \tag{2}$$

$$\langle a,a\rangle \begin{cases} >0 & \text{if } a\neq 0 \\ =0 & \text{if } a=0 \end{cases} \tag{3}$$

where a, b, and c are functions and α and β are scalars. Complex conjugation is denoted using an asterisk (*). Any inner product satisfying these properties can be used to define a natural norm

$$\|a\| = \sqrt{\langle a,a\rangle} \tag{4}$$

and the associated metric

$$d(a,b) = \| a - b \| \tag{5}$$

The metric provides us with the notion of "distance" between two functions.

Two functions a and b in an inner product space are said to be *orthogonal* if <a,b>=0. In a similar fashion, functions $\{B_n\}$ in an inner product space form an orthogonal set if

$$<B_m,B_n> = 0 \qquad m \neq n \tag{6}$$

The set $\{B_n\}$ is said to be *complete* if the zero function is the only function in the inner product space orthogonal to each member of the set. A set $\{B_n\}$ that is both complete and orthogonal is said to be a basis, and can be used to represent any function in the inner product space in the sense that

$$\| f - \sum_n \alpha_n B_n \| = 0 \tag{7}$$

where the $\{\alpha_n\}$ are scalar coefficients uniquely determined by

$$\alpha_n = \frac{<B_n,f>}{<B_n,B_n>} \tag{8}$$

In practice, we are forced to project the functions of interest onto a finite-dimensional subspace of the original inner product space. In the subspace, the basis is truncated to the form $\{B_1, B_2, ..., B_N\}$ and the representation is given by

$$f \cong f^N = \sum_{n=1}^{N} \alpha_n B_n \tag{9}$$

The scalar coefficients $\{\alpha_1, \alpha_2, ... \alpha_N\}$ are selected to minimize the distance between the function f and the representation f^N. The error $d(f,f^N)$ is minimized when the coefficients are chosen to make the error orthogonal to the N-dimensional basis, i.e.,

$$<B_n, f - f^N> = 0 \qquad n = 1, 2, ..., N \tag{10}$$

This is known as an orthogonal projection. Because of the orthogonality of the basis functions, the coefficients α_n are the same in the subspace as in the original inner product space. Unfortunately, when attempting a solution of Lf=g, the coefficients $\{\alpha_n\}$ can not be determined directly from Equation 8 since f is an unknown function.

On the other hand, quantities defined on the range of the linear operator L are known and might be more convenient to work with. If the set $\{T_n\}$ forms a basis for the range space of the operator L, any function on the range may be represented in the N-dimensional subspace spanned by $\{T_1, T_2, ..., T_N\}$ according to

$$g \cong g^N = \sum_{m=1}^{N} \beta_m T_m \tag{11}$$

The projection that minimizes the error $d(g,g^N)$ employs coefficients

$$\beta_m = \frac{\langle T_m, g \rangle}{\langle T_m, T_m \rangle} \tag{12}$$

Using Equation 9, the representation of Lf^N is

$$Lf^N = \sum_{n=1}^{N} \alpha_n LB_n \tag{13}$$

Projecting this function on the N-dimensional subspace spanned by the set $\{T_1, T_2, ..., T_N\}$ yields

$$Lf^N \cong \sum_{m=1}^{N} \sum_{n=1}^{N} l_{mn} \alpha_n T_m \tag{14}$$

where the coefficients $\{l_{mn}\}$ that provide the "best" approximation in the range space as measured by the metric are

$$l_{mn} = \frac{\langle T_m, LB_n \rangle}{\langle T_m, T_m \rangle} \tag{15}$$

Equating this representation for Lf^N with the representation g^N from Equation 11 produces the discrete system of equations

$$\sum_{n=1}^{N} l_{mn} \alpha_n = \beta_m \qquad m = 1, 2, ..., N \tag{16}$$

This system is an NxN matrix equation that can be solved for the coefficients $\{\alpha_n\}$.

Although the above procedure provides a way of obtaining the coefficients of f^N, the coefficients $\{\alpha_1, \alpha_2, ..., \alpha_N\}$ obtained from the solution of Equation 16 are generally *not* the same as those specified in Equation 8. In other words, despite the fact that the projections in the range space are orthogonal, Equation 16 does not ensure an orthogonal projection in the domain space, and will usually not produce the "best" approximation as measured by the metric $d(f,f^N)$.

From an operational standpoint, Equation 16 can be obtained by substituting Equation 9 into Lf=g and forcing the residual

$$L\left(\sum_{n=1}^{N}\alpha_n B_n\right) - g = \sum_{n=1}^{N}\alpha_n LB_n - g \qquad (17)$$

to be orthogonal to a set of testing functions $\{T_1, T_2, ..., T_N\}$. This produces the conventional "method of moments" matrix equation $L\alpha=\beta$ where l_{mn} and β_m are, within a normalization, defined in Equations 12 and 15.

Although the matrix equation $L\alpha=\beta$ is formally identical to Equation 16, the method of moments procedure can be applied to produce an approximate solution regardless of whether the functions $\{B_n\}$ and $\{T_m\}$ form complete, orthogonal sets. Basis and testing functions used in electromagnetics, such as the subsectional "triangle" and "rooftop" functions, often do not comprise orthogonal sets. (We continue to denote these as "basis functions" despite the fact that they do not satisfy the definition of a basis in the strict sense.) Subsectional functions typically differ from the classical basis in a second way: increasing the order of the approximation usually alters every element of the set $\{B_1, B_2, ..., B_N\}$, rather than just adding an additional function. Even if the basis functions are orthogonal, the method of moments projection of the domain space onto the basis functions is not guaranteed to be orthogonal. This makes it difficult to make firm statements about the convergence of the numerical approximation to the exact solution as $N \to \infty$.

Because of the widespread use of the method of moments approach for electromagnetics, much research has been devoted to the proper choice of basis and testing functions [1-2]. However, there also appears to be a certain amount of "folklore" surrounding the selection of basis and testing functions. A notable example concerns the use of Galerkin's method, which involves the same set of functions for both basis and testing. The authors have often encountered the statement that "the best answers will be obtained by the use of Galerkin's method."

The supposed superiority of Galerkin's method appears to originate with classical variational methods. It is widely appreciated that Galerkin's method for discretizing a linear operator equation produces the identical system of equations as the Rayleigh-Ritz procedure applied to the associated quadratic functional [3]. In the classical literature, one frequently encounters the statement that the Ritz procedure produces the "best" answer possible for a given set of trial or basis functions [4-5]. But this notion is usually taken out of context when discussed in conjunction with the method of moments. In the classical literature, the idea of a "best" answer invariably refers to the value of the functional itself, not the approximate solution obtained from the expansion. Assumptions about the mathematical character of the original continuous operator are also involved, and the concept of "best" does not apply unless the functional of interest is positive definite [6].

From a theoretical perspective, Galerkin's method may have one advantage over a more general choice of basis and testing functions. If the operator L is self-adjoint with respect to the inner product, so that $\langle La,b\rangle = \langle a,Lb\rangle$, and if L is positive definite, i.e.,

$$\langle a,La\rangle > 0 \quad \text{for all nonzero } a \qquad (18)$$

then a second inner product space can be defined in terms of the new inner product

$$\langle a,b\rangle_2 = \langle a,Lb\rangle \qquad (19)$$

If $T_m=B_m$, the orthogonal projection onto the original testing functions is equivalent to

$$\langle B_m,L(f^N-f)\rangle = \langle B_m,f^N-f\rangle_2 = 0 \qquad (20)$$

In the special case where L is a positive definite self-adjoint operator and the basis functions form a complete, orthogonal set in the *new* inner product space, Equation 20 shows that the method-of-moments projection of the solution onto the basis is guaranteed to be orthogonal in the new space. It follows that the numerical approximations will converge to the exact solution as N -> ∞. Unfortunately, the equations of electromagnetics do not involve self-adjoint, positive definite operators except in the static limit. Since the integral equations used for frequency-domain radiation and scattering problems (the electric, magnetic, and combined field equations) do not possess the positive definite character, there is no obvious theoretical merit to the use of Galerkin's method with these equations.

2. A NUMERICAL EXAMPLE

The electric-field integral equation for TM scattering from perfectly conducting cylinders is defined

$$E_z^{inc}(t) = jk\eta \int J_z(t') \frac{1}{4j} H_0^{(2)}(kR)\, dt' \tag{21}$$

where

$$R = \sqrt{[x(t) - x(t')]^2 - [y(t) - y(t')]^2} \tag{22}$$

and t is a parametric variable around the contour of the cylinder. We wish to test the accuracy of the method of moments discretization of this equation using various order spline basis and testing functions. The family of splines we employ includes the Dirac delta function as a "zero-order" spline, the pulse or piecewise constant function

$$B_1(t) = p\left(t; -\frac{\Delta}{2}, \frac{\Delta}{2}\right) = \begin{cases} 1, & -\frac{\Delta}{2} < t < \frac{\Delta}{2} \\ 0, & \text{otherwise} \end{cases} \tag{23}$$

as the first-order spline, and higher-order splines defined by the convolution

$$B_n(t) = B_{n-1}(t) * \frac{1}{\Delta} p\left(t; -\frac{\Delta}{2}, \frac{\Delta}{2}\right)$$

$$= \int_{\frac{-\Delta}{2}}^{\frac{\Delta}{2}} B_{n-1}(t-t')\, dt' \tag{24}$$

(The second-order spline is the piecewise-linear "triangle" function; the third-order spline is the conventional quadratic spline, etc.)

For circular cylinders excited by a uniform plane wave, exact and numerical solutions can be systematically compared as a function of the order of the basis and testing functions. Tables 1 and 2 summarize the results for cylinders of size ka=2 and ka=6, respectively. For the example of Table 1, 10 basis and testing functions are employed to produce a density of 5 basis functions per wavelength on the cylinder contour. For the ka=6 example, 20 basis and testing functions are used to provide a density of 3.3 functions per wavelength. These tables present the normalized error

$$\frac{\| J_z^{exact} - J_z^{numerical} \|}{\| J_z^{exact} \|} \tag{25}$$

as a function of the order of the splines employed as basis and testing functions, using the norm

$$\| J_z^{exact} - J_z^{numerical} \| = \sqrt{\int | J_z^{exact}(t) - J_z^{numerical}(t) |^2 \, dt} \tag{26}$$

The integration required in Equation 26 is performed over the actual basis function set used in each case to represent the current density; no additional smoothing or interpolation is carried out after the coefficients are determined. The examples demonstrate that the accuracy is primarily a function of the order or "smoothness" of the basis function set. There is little variation with testing function choice. In addition, there is no clear indication of any special advantage associated with Galerkin's method.

TABLE 1

Error in the moment method solution as measured by Equation 25 for a circular cylinder of radius a, as a function of the order of the splines employed as basis and testing functions. Cylinder has ka=2.0; ten basis and ten testing functions of the indicated order were employed to construct the matrix equation.

order of basis	order of testing	error
1	0	0.303
1	1	0.304
1	2	0.313
1	3	0.315
1	4	0.317
1	5	0.318
2	0	0.0965
2	1	0.0955
2	2	0.0960
2	3	0.0965
2	4	0.0973
3	0	0.0550
3	1	0.0540
3	2	0.0540
3	3	0.0542

TABLE 2

Error in the moment method solution as measured by Equation 25 for a circular cylinder of radius a, as a function of the order of the splines employed as basis and testing functions. Cylinder has ka=6.0; twenty basis and twenty testing functions of the indicated order were employed to construct the matrix equation.

order of basis	order of testing	error
1	0	0.349
1	1	0.350
1	2	0.356
1	3	0.358
1	4	0.360
1	5	0.362
2	0	0.117
2	1	0.117
2	2	0.118
2	3	0.119
2	4	0.119
3	0	0.0656
3	1	0.0651
3	2	0.0653
3	3	0.0655

REFERENCES

[1] R. F. Harrington, *Field Computation by Moment Methods*. Malabar, FL: Krieger, 1982.

[2] D. R. Wilton and C. M. Butler, "Effective methods for solving integral and integro-differential equations," *Electromagnetics*, vol. 1, pp. 289-308, 1981.

[3] D. S. Jones, "A critique of the variational method in scattering problems," *IRE Trans. Antennas Propagat.*, vol. AP-4, pp. 297-301, 1956.

[4] P. M. Morse and H. Feshbach, *Methods of Theoretical Physics*. New York: McGraw-Hill, 1953.

[5] R. F. Harrington, *Time-harmonic Electromagnetic Fields*. New York: McGraw-Hill, 1961.

[6] E. F. Kuester and D. C. Chang, "A unified approach to the derivation of bivariational principles in acoustics and electromagnetics," Electromagnetics Laboratory Scientific Report No. 80, contract DAAG 29-82-K-0096, University of Colorado, Boulder, CO, July 1985.

Comparison of Methods for Determining Currents on a Plate

T. J. Brinkley and R. J. Marhefka
The Ohio State University
ElectroScience Laboratory
1320 Kinnear Road
Columbus, Ohio 43212-1156

Abstract

Development of classic asymptotic diffraction coefficients have been based on exact canonical problems. The tractable problems, however, are primarily two dimensional in nature. To extend the diffraction coefficients into three dimensional geometries, such as corners or vertices, solutions are being based on approximate asymptotic currents. In order to validate the assumed currents and help direct improvement of them, various numerical techniques are being explored.

The currents on fairly large perfectly conducting flat plates are studied for oblique incidence. The currents calculated using the Conjugate Gradient FFT (CG-FFT) method and moment methods (MM) are compared with the current predicted by analytical expressions based on Physical Theory of Diffraction and Uniform Geometrical Theory of Diffraction concepts. The analytical expressions supplement the physical optics current with a correction current based on the exact solution for the current on a half plane.

I Introduction

In order to isolate the current near the vertex of a flat perfectly conducting plate while keeping the numerical solution of the problem fairly simple, the current on a three wavelength square plate is investigated. The plate needs to be small enough to allow the CG-FFT and MM solutions to be easily found, but also large enough so that the effects of the back edges and other vertices are small near the front vertex. A square plate was chosen for reasons indicated in Section II. The surface currents on a three wavelength perfectly conducting square plate found using each of these three methods are illustrated in Section V. The far zone fields radiated by these currents are also given for two different pattern cuts.

II Conjugate Gradient FFT Method

The conjugate gradient method is an iterative technique which may be used to solve integral equations. When the conjugate gradient method is combined with the Fast Fourier Transform (CG-FFT method) so that most of the calculations are done in the spectral domain, one obtains a fairly efficient numerical technique for finding the currents on a flat plate. Descriptions of the CG-FFT method may be found in References [1], [2], and other recent papers. The CG-FFT results presented here are found using a computer code written at Ohio State University [3] which implements the CG-FFT method for scattering from perfectly conducting flat plates.

In order to get a fairly smooth representation of the currents on a flat plate structure, it has been found that several conditions must be met. First, the bases funtions used in the CG-FFT method must fit the edges of the flat plate. In this case pulse bases functions are used so the plate must be rectangular. Second, the segment size must be very small. In this case about 0.025λ (for pulse bases functions) or smaller. Finally, the intial guess must be smooth or the result may not be smooth even with error levels of around 0.01, where the term error is the same as the tolerance level described in [2]. It should be emphasized that the far zone scattered fields may have converged to essentially the final result even if the above conditions are not met.

The relevant CG-FFT parameters used for the calculations shown in Section V are the number of sample points taken in each direction on the plate ($N_x = N_y = 120$), the number of points taken in the FFT in each direction ($N_{fx} = N_{fy} = 512$), and the segment lengths in each direction ($\Delta x = \Delta y = 0.025\lambda$). The level of zero padding used in the calculations may not be large enough to prevent aliasing in the FFT from significantly affecting the answer. This may be one of the reasons that the CG-FFT and MM field calculations in Section V do not match in some regions of the patterns. For these calculations, increasing the amount of zero padding is not practical. Decreasing the number of sample points on the plate (N_x and N_y) will mean the current is no longer reasonably smooth. Increasing the number of points in the FFT is not computationally practical, since the problem already requires approximately 15 minutes of Cray Y-MP time for 500 iterations (required to reduce the error to 0.01).

III Moment Method

The moment method results shown in Section V are found using the Elemagnetic Surface Patch code (ESP) [4]. It solves the electric field integral equation (EFIE) using piecewise sinusoidal rectangular surface patch bases and test modes. The

segment size for the examples given here is fairly large, a quarter of a wavelength, so that the problem could be run quickly on a VAX 8550 computer. The current on the plate at any given point may be easily calculated from the modes using

$$\begin{aligned} \vec{J}(x,y) &= \hat{x}\left[\frac{A_{x1}\sin k(x-x_1)+A_{x2}\sin k(x_2-x)}{2w_y\sin k(x_2-x_1)}\right] \\ &+ \hat{y}\left[\frac{A_{y1}\sin k(y-y_1)+A_{y2}\sin k(y_2-y)}{2w_x\sin k(y_2-y_1)}\right] \end{aligned} \tag{1}$$

where

$$w_y = \frac{1}{2}(y_2-y_1), \quad w_x = \frac{1}{2}(x_2-x_1) \tag{2}$$

and A_{x1} and A_{x2} are the complex values of the $\hat{x}$ directed modes centered at $[x_1, \frac{1}{2}(y_1+y_2)]$ and $[x_2, \frac{1}{2}(y_1+y_2)]$, respectively. Similarly A_{y1} and A_{y2} are the complex values of the $\hat{y}$ directed modes centered at $[\frac{1}{2}(x_1+x_2), y_1]$ and $[\frac{1}{2}(x_1+x_2), y_2]$, respectively. Even though the segment size was fairly large the field results have converged to within a dB of the results for 0.2λ segments. Reducing the segment size to 0.025λ or smaller so the current appears fairly smooth on a 3-D plot would not be practical at this time, even with the resources of a Supercomputer. Utilizing 32 MW on a Cray Y-MP the largest problem which may be run using ESP is approximately 45 segments in each direction [5] corresponding to a segment size of about 0.07λ on a three wavelength plate and requiring approximately 15 minutes of CPU time.

IV Analytic Expressions

In many cases one desires to approximate the currents on the surface of a scattering structure. Physical optics is a well known approximation to the currents on the body of an electrically large scatterer. However, a better representation of the currents on a planar structure may be obtained if the nonuniform components of the current from each edge of the plate are included. The nonuniform currents on a half plane arising from a plane wave of arbitrary polarization and incidence angle may be easily derived from the closed form expressions for the total current given in [6]. The expressions are found by simply subtracting the PO current component from the total current and may be found in [7].

The nonuniform currents given above may be used on plates other than a half plane by terminating the currents in the proper manner. To extend these currents to other scatterers, the nonuniform current from each edge must be included in the total. The nonuniform current from each edge is included if the diffraction point associated with the particular current element and the particular edge lies on the physical edge of the plate. If the diffraction point associated with the particular

current element and the particular edge does not lie on the physical edge, but lies instead on the infinite extension of the edge, the nonuniform current contribution from that edge is zero. This obviously creates discontinuities in the total current where the nonuniform current from a given edge is suddenly terminated.

The discontinuities in the total current where the nonuniform current is terminated may be compensated by corresponding discontinuities in the current emanating from an associated vertex. The form of this current is the subject of further research at this time.

V Results

Several results for the current on a three wavelengths square perfectly conducting plate lying in the x-y plane are given here. In all cases, it is assumed that a plane wave is incident from the direction $\theta^i = 55°$ and $\phi^i = 225°$, with the E field polarized in the $\hat{\phi}^i$ direction. The incident field level is $1V/\lambda$ and the surface current is plotted in units of A/λ. The peak level in each plot gives an indication of how the relative levels of the different plots compare. The current is separated into $\hat{\rho}$ and $\hat{\phi}$ components since the problem is symmetric along the diagonal of the square corresponding to the line $y = x$. Note also that all $\hat{\phi}$ components of the current are viewed from the direction of the incident field, while all $\hat{\rho}$ components of the current are viewed from the direction $\theta^r = 55°$ and $\phi^r = 45$ which is the direction of the reflected field off the plate.

The $\hat{\phi}$ and $\hat{\rho}$ components of the current for an incident field polarized in the $\hat{\phi}^i$ direction are shown in Figures 1, 2, and 3 for the CG-FFT, MM, and PO+NU methods, respectively. Note how the CG-FFT and MM solution have the same basic overall behavior, but the MM solution is much less detailed since the segment size is significantly larger. Also the PO+NU solution appears to duplicate the general behavior of the CG-FFT solution except in regions near the back edges and near the discontinuities in the $\vec{J}^{NU}$ components. Since the PO+NU solution is only a first order solution, this indicates that vertex and higher order currents are needed in these regions to accurately predict the currents.

The far zone bistatic fields radiated by the three different currents illustrated previously in this section are calculated for two different pattern cuts. Figure 4 illustrates the co-polarized RCS for a $\phi = 225°$ pattern cut and the co and cross polarized RCS for a $\phi = 135°$ pattern cut (both with a fixed source: $\theta^i = 55°$ and $\phi^i = 225$). The cross polarized RCS for the $\phi = 225°$ cut is essentially zero for all three currents, although the segment size of the MM solution had to be reduced significantly to obtain convergence.

VI Conclusions

Currents on a perfectly conducting plate calculated using three separate methods have been illustrated for oblique plane wave incidence. Bistatic far zone patterns indicate that the differences in the currents on the plate only create differences in the fields in some far zone directions. The results indicate the CG-FFT may be the best candidate to help derive empirical approximations for a vertex current using rectangular structures. A method for non-right angled structures needs further investiation. It is hoped that this will then lead to improved diffraction coefficients for scattering from a flat plate.

VII Acknowledgements

The Cray Y-MP computer time used to make the CG-FFT calculations was donated by the Ohio Super Computer Center.

References

[1] T. Sarkar and S. M. Rao, "The application of the conjugate gradient method for the solution of electromagnetic scattering from arbitrarily oriented wire antennas," *IEEE Trans. Antennas Propagat.*, vol. AP-32, pp. 398–403, Apr. 1984.

[2] T. Peters and J. L. Volakis, "Application of a conjugate gradient FFT method to scattering from thin planar material plates," *IEEE Trans. Antennas Propagat.*, vol. AP-36, pp. 518–526, Apr. 1988.

[3] J. Fichtner. Personal communication.

[4] E. H. Newman and R. L. Dilsavor, "A user's manual for the electromagnetic surface patch code: ESP Version III," Technical Report 716148-19, The Ohio State University ElectroScience Laboratory, Department of Electrical Engineering, May 1987.

[5] M. Kluskens. Personal communication.

[6] M. Born and E. Wolf, *Principles of Optics*, ch. 11, pp. 578–580. Pergamom Press, 1975.

[7] T. J. Brinkley, L. Ivrissimtzis, and R. J. Marhefka, "Uniform theory of diffraction analysis of electromagnetic scattering from corners and vertices," Technical Report 312506-1, The Ohio State University ElectroScience Laboratory, Department of Electrical Engineering, Nov. 1989. Prepared under Contract No. Z90115.

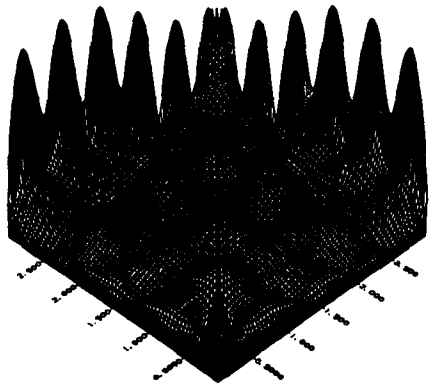

(a) $peak = 0.017A/\lambda$

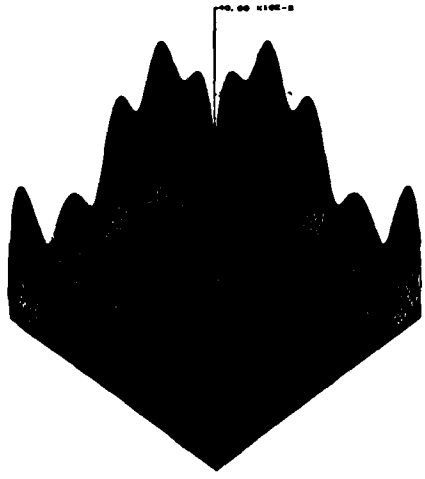

(b)$peak = 0.041A/\lambda$

Figure 1: $\hat{\phi}$ (a) and $\hat{\rho}$ (b) components of the CG-FFT current for $\vec{E}^i_{\phi^i}$ incidence from $\theta^i = 55°$, $\phi^i = 225°$ on a 3λ plate.

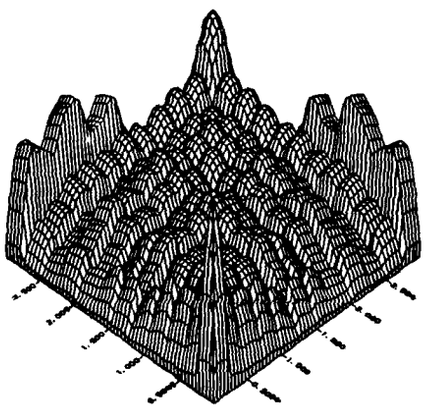

(a)$peak = 0.0089A/\lambda$

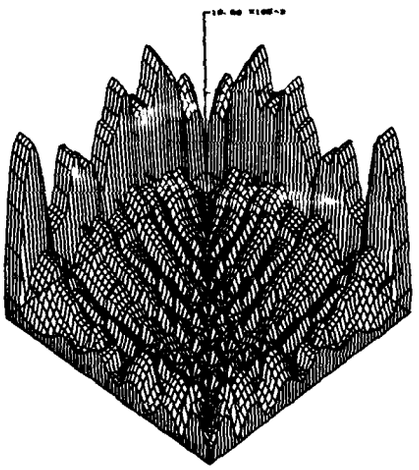

(b)$peak = 0.011A/\lambda$

Figure 2: $\hat{\phi}$ (a) and $\hat{\rho}$ (b) components of the MM current for $\vec{E}^i_{\phi^i}$ incidence from $\theta^i = 55°$, $\phi^i = 225°$ on a 3λ plate.

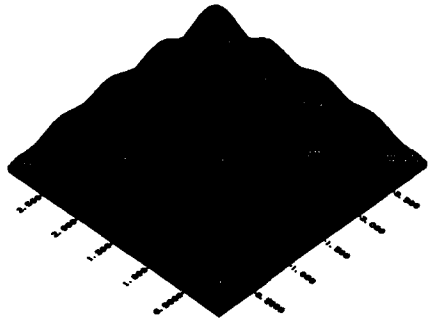

(a)$peak = 0.02A/\lambda$

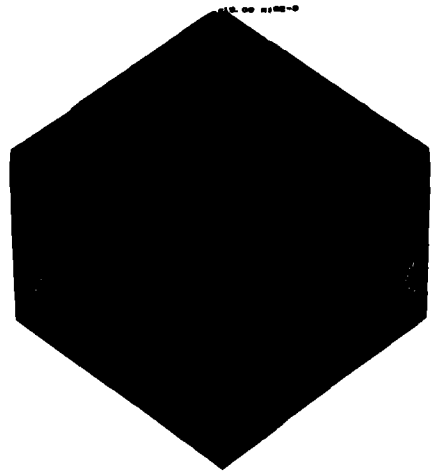

(b)$peak = 0.015A/\lambda$

Figure 3: $\hat{\phi}$ (a) and $\hat{\rho}$ (b) components of the $\vec{J}^{PO} + \vec{J}^{NU}$ for $\vec{E}^i_{\phi^i}$ incidence from $\theta^i = 55°$, $\phi^i = 225°$ on a 3λ plate.

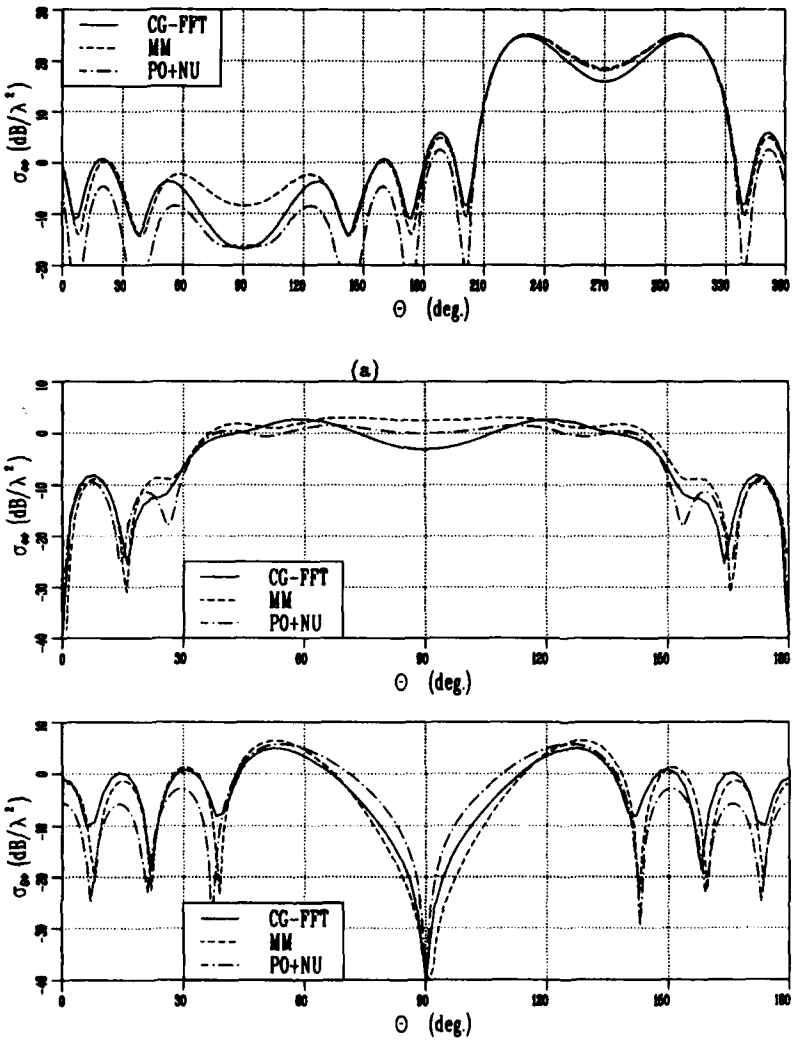

Figure 4: Bistatic RCS of a 3λ square plate for a $\hat{\phi}^i$ polarised source fixed at $\theta^i = 55°$, $\phi^i = 225°$ for (a) $\phi = 225°$ and (b) $\phi = 135°$.

SESSION 10 B - "MODELING EM INTERACTION WITH BIOLOGICAL MEDIA"

FINITE-DIFFERENCE TIME-DOMAIN CALCULATIONS IN HUMAN DOSIMETRY

P J Dimbylow
National Radiological Protection Board
Chilton
Didcot
Oxon OX11 0RQ
England

SUMMARY

This paper presents finite-difference time-domain (FDTD) calculations of the short-circuit current and the specific energy absorption rate (SAR) in the ankle. Plane wave exposures from 10 to 100 MHz for an adult, a 10-year old and a 5-year old are considered. Gandhi et al [1] have pointed out the likelihood of high local values of SAR in the ankle due to its narrow, bony structure. Currents will tend to preferentially flow through the high conductivity muscle and this will lead to high local values of SAR in the muscle at the ankle.

The calculations are performed in two parts. Firstly, the coupling between a homogeneous whole body phantom and the applied field is calculated. The region around a lower leg is then expanded, the leg being described by a realistic, fine-scale, heterogeneous model. In this expansion technique [2] an initial calculation is made for the body and the electric fields scattered from the body and tangential to a sub-boundary are stored on disk. The region inside the sub-boundary, the lower leg and surrounding air, is subdivided into smaller cells and the sub-boundary tangential fields provide the boundary conditions for the second calculation. The 1.8 m tall adult phantom that is used (see figure 1)

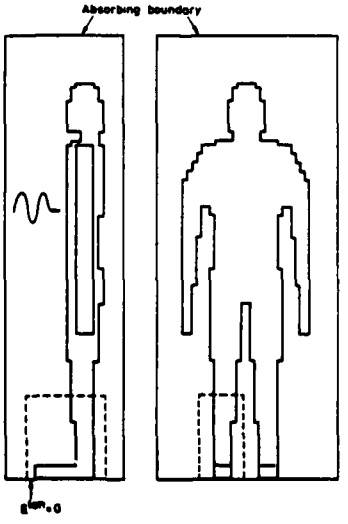

Figure 1. Whole body phantom

was described in a previous study to calculate current densities from exposure to extremely low frequency fields [3], except that the present limb model structure was attached below the knee. The phantom is located on a perfectly conducting ground plane and is surrounded by a region of air. The cells are 0.02 m cubes and the absorbing boundaries are positioned 10 cells from the nearest anatomical feature. This configuration results in a total of 168,000 cells, with 8324 describing the phantom giving a mass of 67 kg. To ease problems of computer time and storage a symmetry about the sagittal axis was invoked to halve the number of cells.

The heterogeneous model of the lower limb beneath the knee was constructed [4] from an atlas of anatomical cross-sections. There are 5 tissue types:- skin, muscle, cortical bone, trabecular bone and remainder labelled "connective tissue" which includes fat, tendons and ligaments. In all there are 14261 cells in the model arranged in 43 slices up to top of the tibia. Figure 2 shows the grid structure at the ankle and at the narrowest part of the leg. Histograms of the current densities for these slices in the adult phantom at 40 MHz are presented in figure 3. In the ankle, the maximum current density occurs in the extensor hallucis longus muscle at the front of the ankle. The histogram for the narrowest part of the leg clearly shows the bone structure, the surrounding muscle and the composite skin layer.

A more detailed description of these calculations has been submitted for publication [5].

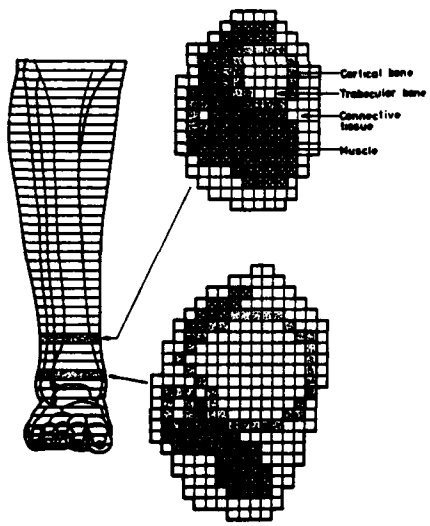

Figure 2. The mesh structure at slice 8, the ankle, and at slice 12, the narrowest part of the leg.

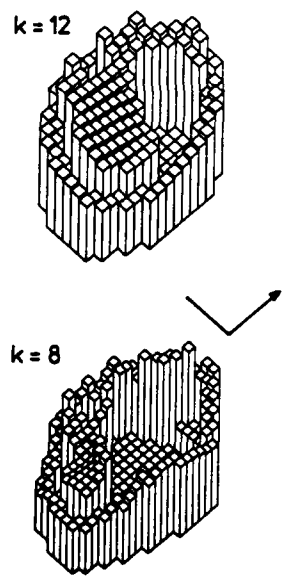

Figure 3. Histograms of the current density at 40 MHz. The arrow points to the front of the leg.

References

[1] O P Gandhi, J-Y Chen and A Riazi, "Currents induced in a human being for plane-wave exposure conditions 0-50 MHz and for RF sealers", IEEE Trans. Biomed. Eng., vol BME-33, pp 757-767, 1986.

[2] R J Spiegel, M B E Fatmi and K S Kunz, "Application of a finite-difference technique to the human radiofrequency dosimetry problem", J. Microwave Power, vol 20, pp 241-254, 1985.

[3] P J Dimbylow, "Finite-difference calculations of current densities in a homogeneous model of a man exposed to extremely low frequency electric fields, "Bioelectromagnetics, vol 8, pp 335-375, 1987.

[4] P J Dimbylow, "The calculation of induced currents and absorbed power in a realistic, heterogeneous model of the lower leg for applied electric fields from 60 Hz to 30 MHz", Phys. Med. Biol., vol 33, pp 1453-1468, 1988.

[5] P J Dimbylow, "Finite-Difference Time-Domain calculations of absorbed power in the ankle for 10-100 mHz plane wave exposure", submitted to IEEE Trans. Biomed. Engng.

SESSION 11 - "SURFACE INTEGRAL EQUATION CODES AND APPLICATIONS"

ENHANCEMENT TO FERM

ELIZABETH YIP [1], RUSSELL BOWERS [1] BRIAN TOMAS [2]

[1]Boeing Military Airplanes, [2]Boeing Helicopters

Abstract. This paper presents our enhancement to the Finite Element Radiation Model (FERM) code from the Lincoln Laboratory. FERM is a three dimensional moment method code that uses the Electric Field Integral Equation (EFIE) and the Rao, Wilton, and Glisson (RWG) basis functions. Our modifications to the code include the following: I–DEAS input, integration involving resistive patches, improvement of out-of-core solver, Sherman-Morrison-Woodbury updating and optimization. These modifications improve the "user-friendliness" of the code, run time and create a useful tool for iterative design processes.

I. INTRODUCTION

This paper presents our enhancement to the Finite Element Radiation Model (FERM) code from the Lincoln Laboratory. FERM is a three dimensional moment method code that uses the Electric Field Integral Equation (EFIE) and the Rao, Wilton, and Glisson (RWG) basis functions. Our modifications to the code include geometric input, integration on resistive patches, reduced I/O in the out-of-core solver and the Sherman-Morrison-Woodbury updating and optimization.

II. GEOMETRIC INPUT

For perfectly conducting bodies, the original FERM[4] provides an adequate geometric input in module EFIE1. However for the input of patch resistivity in EFIE1R, the user is expected to provide the corresponding internal patch indices. This is impractical for electrically large bodies.

For computation sites with I–DEAS, a geometric package from SDRC, we have an interface between I–DEAS and the internal data of FERM, and bypass EFIE1, and EFIE1R, which is the input modules of FERM. Fig. 1 presents the system flow of our interface.

For computation sites without I–DEAS, we use EFIE1, and replace EFIE1R with a module called FERMRES. In FERMRES, for each resistivity, the user provides a set of lines. Then as illustrated in Fig. 2, FERMRES tags the patches whose edges intersect with these lines.

III. INTEGRATION ON RESISTIVE PATCHES

In this section, we present the computation of an analytical form of the integral related to the resistive patches. The tangential electric field of such patches is represented in equation (1).

$$E^i_{tan} = ZJ + j\omega\mu_0 \int JGds + \frac{j}{\omega\epsilon_0}\nabla \int \nabla \cdot JGds, \tag{1}$$

with

$$Z = \sum_\ell Z_\ell \chi_\ell,$$

where $\chi_\ell = 1$ on the $\ell-$th patch and $\chi_\ell = 0$ otherwise, and

$$J = \sum_n I_n f_n$$

where f_n is the RWG basis function, and I_n is the expansion coefficient. Then the matrix element corresponding to the first term of equation (1) can be represented as

$$A_{mn} = \sum_\ell Z_\ell \int_{S_\ell} f^1_n \cdot f^2_n ds. \tag{2}$$

The original FERM does a "one point approximation" to the integral in equation (2). The example illustrated in Fig. 3 shows that this approximation is too coarse when the corresponding triangular patch is not equilateral. In this example the patch to be on the $x-y$ plane. The three vertices are $(1.,0.),(0.,\sqrt{3}.)$, and $(-\sqrt{3}.,0.)$, and the $n-$th edge is defined by the first two vertices $(1.,0.)$ and $(0.,\sqrt{3}.)$. The exact solution is .2886758; the FERM approximation is $-.8591167$.

Fig. 4 illustrates an arbitrary triangular patch, with δS_1 representing the corresponding $n-$th edge in equation (2). The integrand in equation (2) can be written as

$$\langle x - v_1, x - v_2\rangle = \langle x - v_1, x - v_1\rangle + \langle v_1 - v_2, x - v_1\rangle. \tag{3}$$

Motivated by Gorden[3], we choose two functions F_1 and F_2 such that

$$(\nabla \times F_1)\cdot \hat{n} = \langle x - v_1, x - v_2\rangle$$

and

$$(\nabla \times F_2)\cdot \hat{n} = \langle v_1 - v_2, x - v_1\rangle.$$

Then Stokes' theorem can be applied:

$$\int_{\delta S} F_1 \cdot \hat{t} dp = \int_S (\nabla \times F_1) \cdot \hat{n} dS = \int_S \langle x - v_1, x - v_2 \rangle, \tag{4.1}$$

and

$$\int_{\delta S} F_2 \cdot \hat{t} dp = \int_S (\nabla \times F_1) \cdot \hat{n} dS = \int_S \langle v_1 - v_2, x - v_1 \rangle, \tag{4.2}$$

If v_1 is the origin, the following choice of F_1 and F_2 serves our purpose:

$$F_1 = \frac{1}{3}(-(x^2)^3, (x^1)^3, 0), \tag{5.1}$$

and

$$F_2 = \frac{1}{2}(-v_2(x^2)^2, v_2^1(x^1)^2, 0). \tag{5.2}$$

($x^k, k = 1, 2, 3$ denotes the $k-$th element of the vector x; $v_j^k, j, k = 1, 2, 3$ denotes the $k-$th element of the vector v_j.) To conserve space, we do not present the details of the computations of the integrals in equation (4).

III. IMPROVEMENT OF THE OUT-OF-CORE SOLVER

The out-of-core linear equation solver, EFIE3, in FERM stores each row as a logical record and brings in one row at a time in the Gaussian elimination process. We modify EFIE3 by bringing r rows into core at a time, and reduce the I/O count from order $O(n^3/6)$ to $O(\frac{1}{r}n^3/6)$.

To improve the computation time, we replace the innermost loop of the Gaussian elimination from straight FORTRAN code to calls to BLAS (Basic Linear Algebra Subroutines). Assembler versions of the BLAS are available for most "supercomputers".

Table 1 illustrates our computation improvement for a problem with 2665 unknowns on a SCS40 version of FERM.

For an indication of the condition of the MOM matrix, we monitor the size of the diagonal elements in the Gaussian elimination process. A diagonal element whose magnitude is small relative to the average magnitude of the other matrix elements indicates that the MOM matrix is ill-conditioned. This is usually due to improper user input.

We also modify EFIE5B to solve more than one incident vectors at a time, thus reducing the I/O count during the forward and backward substitutions.

IV. SMW UPDATING AND OPTIMIZATON

We are building an optimal loading code based on FERM. Mathematically, we have a non-linear optimization problem with linear constraints. NPSOLN[2] in level II of BC-SLIB is used as optimization procedure. NPSOLN is the Boeing version of NPSOL which was developed at the Systems Optimization Laboratory (SOL) of Stanford University Department of Operations Research. NPSOL uses the latest advances in active set strategies and projected Lagrangian methods, and is considered the state-of-the-art.

As in most optimization software, NPSOLN requires an external function to compute the objective function and its gradient. The SMW (Sherman-Morrison-Woodbury) formula is used to compute our objective function.

The form of the SMW described in Yip and Tomas[1] yields an operation count of $O((n^2p + nm))$ for each evaluation of the objective function, where n is the size of the original problem, p is the number of variables updated and m is the number of incident angles. In the case of multiple frequencies (say h frequencies), the operation count would be $O((n^2p+nm)h)$ which becomes prohibitive as h increases and the number of iterations increases. Also in each evaluation of the objective function, we have to bring h matrices of order $n \times n$ from disk into core; having h too large would "beat the disk to death".

In the rest of this section, a scheme of eliminating the factor n from the operation count of the evaluation of the objective function and its gradient is discussed.

Recall that our assumption is that the problem to be optimized has a MOM matrix A of the form:

$$A = B - UV^T \tag{6}$$

so that we can apply the SMW formula for $s^TA^{-1}b$:

$$s^TA^{-1}b = s^TB^{-1}b + s^TB^{-1}U(I - V^TB^{-1}U)^{-1}V^TB^{-1}b. \tag{7}$$

with s and b related to the scattering and incident vectors.

But if A can be written as

$$A = B - UDV^T \tag{8}$$

where D contains all the resistivity information, and U and V^T are independent of the resistivities, then equation (7) becomes:

$$s^TA^{-1}b = s^TB^{-1}b + s^TB^{-1}UD(I - V^TB^{-1}UD)^{-1}V^TB^{-1}b \tag{9}$$

The motivation for using equation (8) is immediate in equation (9); since all the terms dependent on D are of order p and not of order n. Suppose all the terms independent of D are computed and stored before the start of the optimization procedure, (this part of the code is called the "set-up" procedure) then each computation of the objective function in the optimization procedure only involves decomposing a $p \times p$ matrix and other operations with operation count of the order $O(p^3 + p^2 m)$.

As indicated in Yip and Tomas[1], the gradient of the objective function is a sum of terms of the form:

$$-\Re(s^T A^{-1} \frac{\partial A}{\partial Z_j} x) \tag{10}$$

Using the matrices computed in the "set-up" procedure, one can compute the gradient of the objective function with the same efficiency as the computation of the objective function.

III SUMMARY

In this paper we present a series of modifications done to FERM to improve execution time, user-friendliness, and to reduce the amount of I/O. We are also building an optimal loading code based on FERM using a variant of the SMW for the computation of the obective function and its gradient.

REFERENCES

1. E.Yip, B. Tomas, *Obtaining Scattering Solutions for Perturbed Geometries and Materials from Moment Method Solutions*, Applied Computational Electromagnetics Society Journal and Newsletter 3 No.2 (1988), 95–118.

2. M. Healy, "Guide to the Numerical Optimization Software Libraries Provided by the Mathematical/Statistical Library Project of Boeing Computer Services, ETA-LR-32," Engineering & Scientific Services Division, Boeing Computer Services, Seattle.

3. W. Gorden, *Far-Field Approximations to the Kirchoff-Helmholtz Representations of Scattered Fields*, IEEE Trans. Antennas Propoga., AP-23, (1975), 590–592.

4. S. Lee, D.A. Shnidman, F.A. Lichanco, "Numerical Modeling of RCS and Antenna Problems, Technical Report 785," Lincoln Laboratory, MIT, 1987.

FIG. 1 IDEAS & FERM Interface

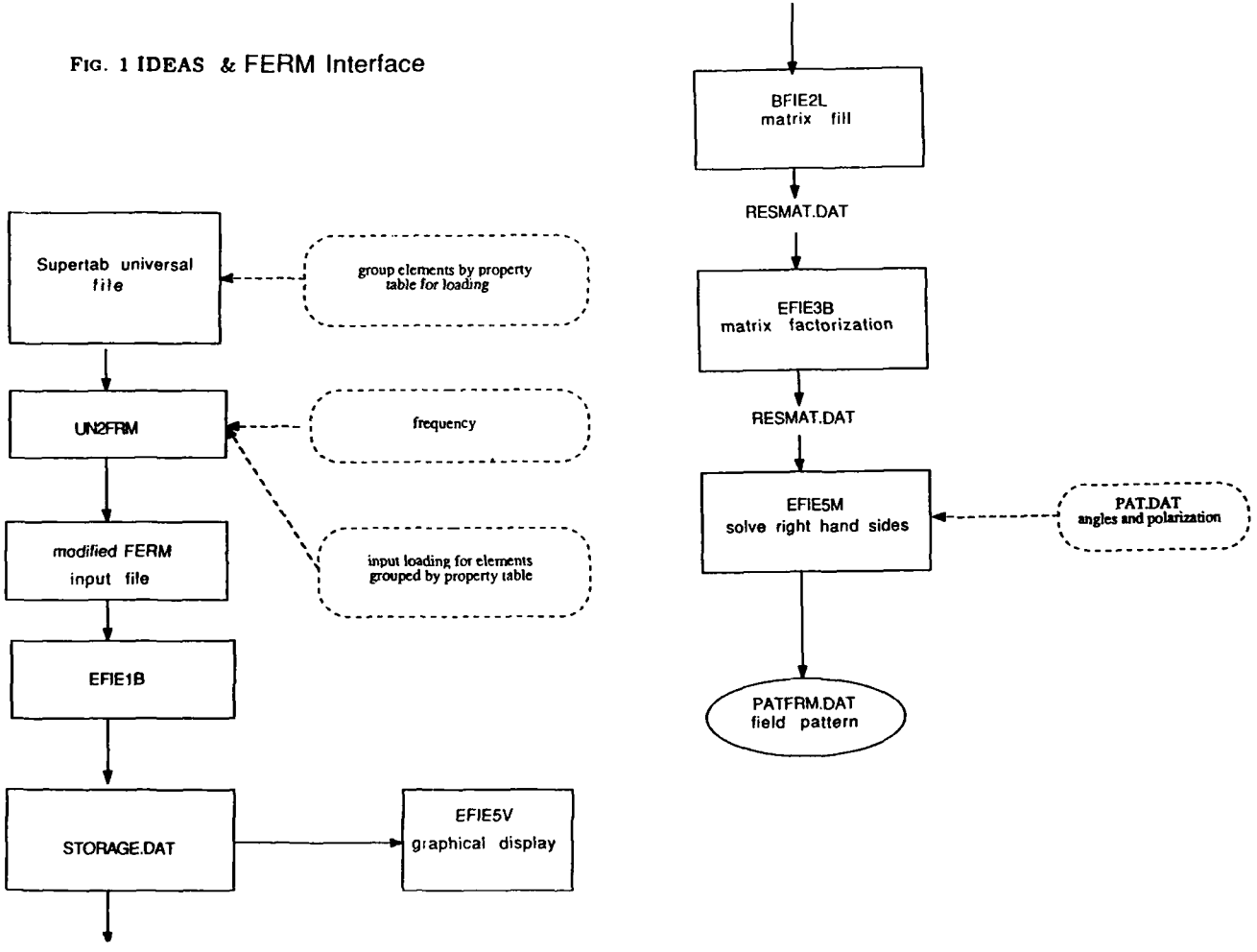

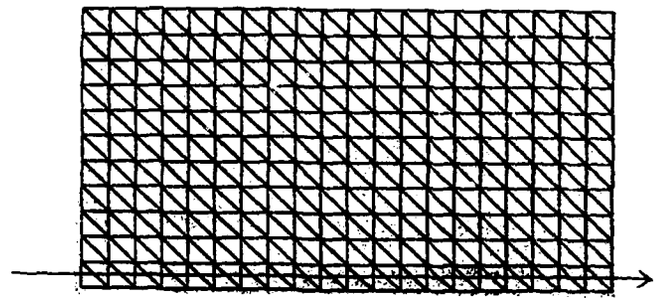

FIG. 2 INTERSECTION OF USER-INPUT LINE & PATCH EDGES

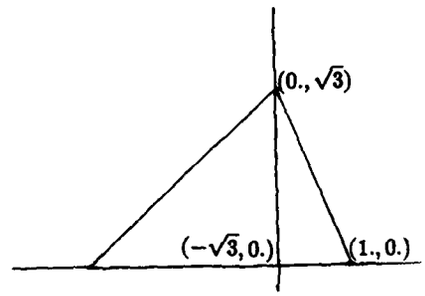

FIG. 3 EXAMPLE OF INTEGRATION OF RESISTIVE PATCH

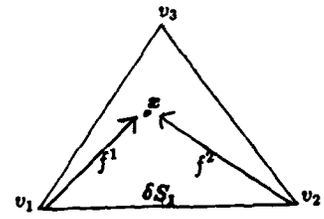

FIG. 4 ARBITRARY TRIANGULAR PATCH

	Old	New	Ratio
CPU Fill	24,045	24,038	1
CPU Factor	56,811	9,696	5.9
Total I/O	86,910	13,956	6.2
total time	167,766	47,690	3.5

TABLE 1 COMPUTER RESOURCES (SECONDS) : (2665 UNKNOWNS)

EQUIVALENT SURFACE CURRENT FORMULATION FOR CALCULATING THE ELECTROMAGNETIC SCATTERING BY A CONDUCTOR PARTIALLY COVERED WITH DIELECTRIC

Robert J. Burkholder and Nan Wang
The Ohio State University ElectroScience Laboratory
1320 Kinnear Road
Columbus, Ohio 43212

1 Introduction

A computer code has been developed to calculate the scattered field for a two-dimensional conducting cylinder partially covered with dielectric material. The formulation is based on the general equivalence principle in which surface currents along the boundaries of the geometry are used to find the fields inside the dielectric as well as the external scattered field [1]. Pulse basis functions and point matching are employed in the method of moments to solve for the surface currents by enforcing the boundary conditions. This technique is very efficient compared with method of moments techniques which incorporate equivalent volume polarization currents to represent the dielectric material because, generally, far fewer unknowns are required in a surface current formulation [2]. Also, in this surface current formulation, four matrices of the order of the number of basis functions along each separate boundary require inversion. This is generally more efficient than inverting one large matrix of the order of the total number of basis functions, as is often required in these types of numerical approaches.

The code is accurate and user friendly and can handle both transverse electric (TE) and transverse magnetic (TM) polarizations. Furthermore, monostatic or bistatic scattering data can be generated. Numerical results will be presented for both the TE and TM polarizations and compared with an independent solution. An $e^{j\omega t}$ time convention is assumed and suppressed in the following formulation.

2 Formulation

Figure 1(a) shows the basic geometry of a 2-D perfectly conducting cylinder partially covered with a dielectric/ferrite material and illuminated by an incident plane wave. To apply the general equivalence principle, the original problem is split into an interior and an exterior problem where equivalent $\hat{z}$ directed surface currents placed along the boundaries replace the dielectric-conductor geometry, as shown in Figures 1(b) and (c). Figure 1(b) shows the outer boundary with the current I_1 placed along the dielectric-air boundary and the current I_4 placed along the conductor-air

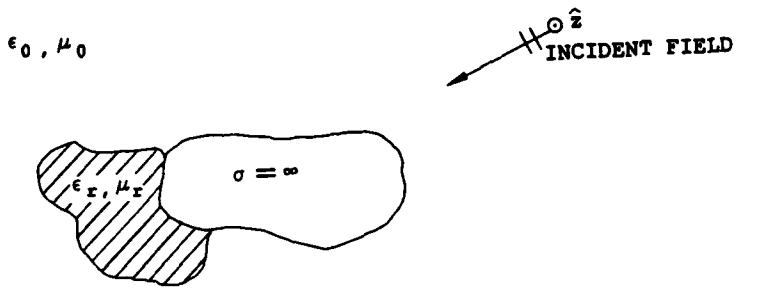

(a) Original problem

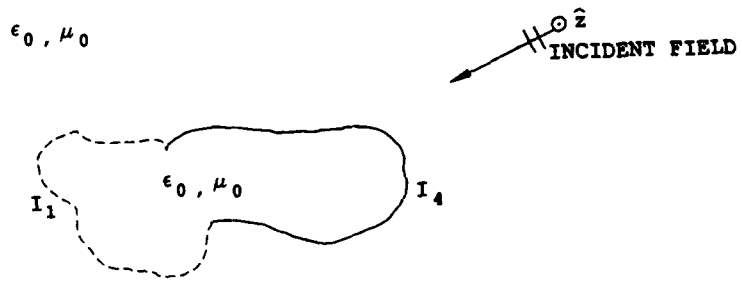

(b) Exterior problem

(c) Interior problem

Figure 1: 2-D dielectric-conductor illuminated by a plane wave and the associated exterior and interior problems.

boundary, and Figure 1(c) shows the dielectric boundary with the current I_2 placed along the dielectric-air boundary and the current I_3 placed along the dielectric-conductor boundary. It is important to note that I_1 and I_4 radiate the scattered field in free space with the incident field present and I_2 and I_3 radiate in unbounded dielectric without the incident field, as illustrated in the figures. It is also noted that the currents are all $\hat{z}$ directed and that they are electric or magnetic currents for a TM_z or TE_z polarized incident field, respectively. Only one type of current (electric or magnetic) is necessary, with no transverse currents. This greatly simplifies the computation of the fields radiated by these currents.

The four unknown equivalent surface currents are found by forcing the the tangential electric field to be zero along the conductor-air boundary and the conductor-dielectric boundary, and the tangential electric and magnetic fields to be continuous across the dielectric-air boundary. The method of moments is used to find the unknown surface currents. Pulse basis functions are used to represent the currents and point matching is used to test the fields of these currents on the boundaries. In matrix form, the four unknown currents can be found from the following four equations which enforce the boundary conditions:

Conductor-air boundary:

$$[Z_{44}][I_4] + [Z_{41}][I_1] + [E_4^i] = 0 \tag{1}$$

Conductor-dielectric boundary:

$$[Z_{33}][I_3] + [Z_{32}][I_2] = 0 \tag{2}$$

Dielectric-air boundary:

$$[Z_{11}][I_1] + [Z_{14}][I_4] + [E_1^i] = [Z_{22}][I_2] + [Z_{23}][I_3] \tag{3}$$

$$[Y_{11}][I_1] + [Y_{14}][I_4] + [H_1^i] = [Y_{22}][I_2] + [Y_{23}][I_3]. \tag{4}$$

The $[I_j]$ matrices are column matrices whose elements are the unknown currents associated with each pulse basis function representing I_j, $j = 1,2,3,4$, and the $[Z_{ij}]$ and $[Y_{ij}]$ relate the tangential electric and magnetic fields, respectively, evaluated at the boundary of I_i to the currents of I_j. $[E_j^i]$ and $[H_j^i]$ are column matrices containing the tangential components of the incident electric and magnetic fields, respectively, evaluated along the boundary of I_j. The mn^{th} elements of these matrices are given by the following:

TM_z polarization:

$$[Z_{ij}]_{mn} = \begin{cases} -\frac{1}{4}kZ\Delta_n H_0^{(2)}(k\rho_{mn}) & : \text{ for } \rho_{mn} \neq 0 \\ -\frac{1}{4}kZ\Delta_n \left[1 + \frac{i2}{\pi} - \frac{i2}{\pi}\log\left(\frac{1}{4}\gamma k\Delta_n\right)\right] & : \text{ for } \rho_{mn} = 0 \end{cases} \tag{5}$$

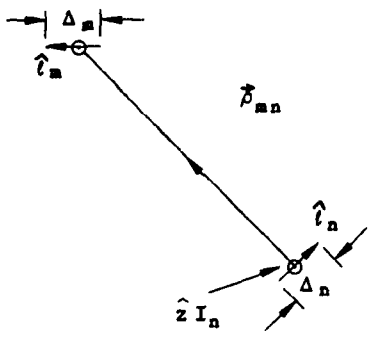

Figure 2: The n^{th} $\hat{z}$ directed current element radiating to the m^{th} element.

$$[Y_{ij}]_{mn} = \begin{cases} \hat{l}_m \cdot (\hat{z} \times \hat{\rho}_{mn}) \frac{1}{j4} k \Delta_n H_1^{(2)}(k\rho_{mn}) & : \text{ for } \rho_{mn} \neq 0 \\ \pm \frac{1}{2} & : \text{ for } \rho_{mn} = 0 \end{cases} \tag{6}$$

<u>TE_z polarization</u>:

$$[Y_{ij}]_{mn} = \begin{cases} -\frac{1}{4} kY \Delta_n H_0^{(2)}(k\rho_{mn}) & : \text{ for } \rho_{mn} \neq 0 \\ -\frac{1}{4} kY \Delta_n \left[1 + \frac{j2}{\pi} - \frac{j2}{\pi} \log \left(\frac{1}{4} \gamma k \Delta_n \right) \right] & : \text{ for } \rho_{mn} = 0 \end{cases} \tag{7}$$

$$[Z_{ij}]_{mn} = \begin{cases} -\hat{l}_m \cdot (\hat{z} \times \hat{\rho}_{mn}) \frac{1}{j4} k \Delta_n H_1^{(2)}(k\rho_{mn}) & : \text{ for } \rho_{mn} \neq 0 \\ \mp \frac{1}{2} & : \text{ for } \rho_{mn} = 0 \end{cases} \tag{8}$$

Figure 2 shows the relevant quantities associated with the n^{th} current element of width Δ_n radiating to the m^{th} current element located at a distance of ρ_{mn}. $\hat{l}_m$ and $\hat{l}_n$ are unit vectors tangent to the boundary, transverse to $\hat{z}$, at the m and n^{th} current element locations, respectively. $H_0^{(2)}$ and $H_1^{(2)}$ are Hankel functions of the second kind and $\gamma = 1.781$ is Euler's constant. k is the wave propagation number, Z is the impedance and Y is the admittance $(1/Z)$ of the media in which the above matrix elements are evaluated. It is noted that $[Z_{44}]$, $[Z_{41}]$, $[Z_{11}]$, $[Y_{11}]$,

$[Z_{14}]$, and $[Y_{14}]$ are evaluated in free space and $[Z_{33}]$, $[Z_{32}]$, $[Z_{23}]$, $[Y_{23}]$, $[Z_{22}]$, and $[Y_{22}]$, are evaluated in unbounded dielectric. For free space, $k = 2\pi/\lambda$, where λ is the free space wavelength, and $Z = \sqrt{\mu_o/\epsilon_o}$. For the dielectric, $k = 2\pi/\lambda\sqrt{\epsilon_r\mu_r}$ and $Z = \sqrt{\mu_r/\epsilon_r}\sqrt{\mu_o/\epsilon_o}$, where ϵ_r and μ_r are the relative permittivity and permeability, respectively. For the $\pm 1/2$ and $\mp 1/2$ terms in (6) and (8), use the top sign if the field is to be evaluated on the $\hat{l}_n \times \hat{z}$ side of the boundary, and use the bottom sign if the field is to be evaluated on the $-\hat{l}_n \times \hat{z}$ side of the boundary.

The $[Z_{ij}]$ and $[Y_{ij}]$ matrices are computed very efficiently using (5)-(8), involving no numerical integrations. The set of equations (1)-(4) is then solved simultaneously to yield the unknown current matrices $[I_j]$ which are then allowed to radiate in their respective media to give the fields scattered by the dielectric-conductor geometry. It is noted that this method can easily be extended to analyze more complex 2-D geometries consisting of multiple dielectric and/or conducting regions with and without common boundaries.

3 Numerical Results

Figures 3 and 4 show the bistatic echo width in decibels relative to a wavelength as a function of observation angle for a dielectric-conductor geometry with normal incidence. The results of Figure 3 are computed using the surface current formulation described in this paper and the results of Figure 4 are computed using equivalent surface currents to replace the conductor and volume currents to replace the dielectric. For a pulse width of $\Delta = .15\lambda$, the surface current formulation has a total of 65 unknown current elements while the volume current formulation has a total of 102 unknowns. It is noted that the number of unknowns increases quadratically as the size of the dielectric increases for the volume current formulation, while the number increases linearly for the surface current formulation described here.

References

[1] R.F. Harrington and A. Konrad, "Scattering by a dielectric cylinder partially covered by a conductor," presented at the 1986 IEEE Antennas and Propagation Society International Symposium, Philadelphia, PA.

[2] N. Wang, "A Simple Pulse-Galerkin Formulation for the Scattering by a Coated Cylinder," presented at the 1988 URSI Radio Science Meeting, Syracuse, NY.

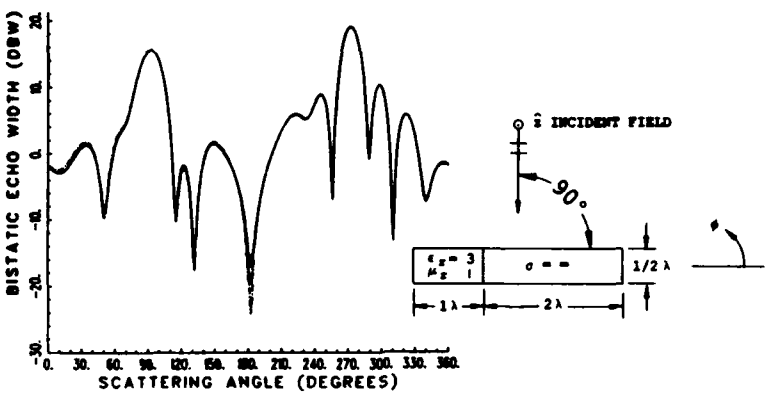

(a) TM_z polarization

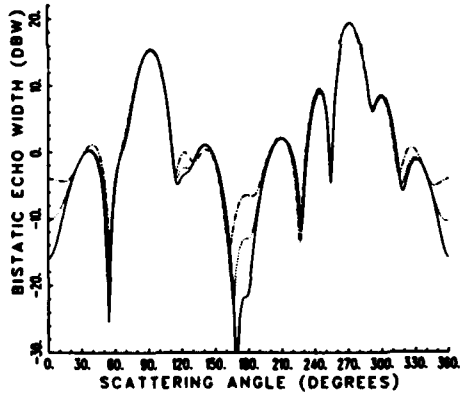

(b) TE_z polarization

—— $\Delta = .1\lambda$ - - - - - $\Delta = .15\lambda$ — · — $\Delta = .2\lambda$

Figure 3: Bistatic echo width vs. observation angle for a 2-D dielectric-conductor with normal incidence calculated using surface equivalent currents. Δ is the size of the pulse basis functions used in the calculation.

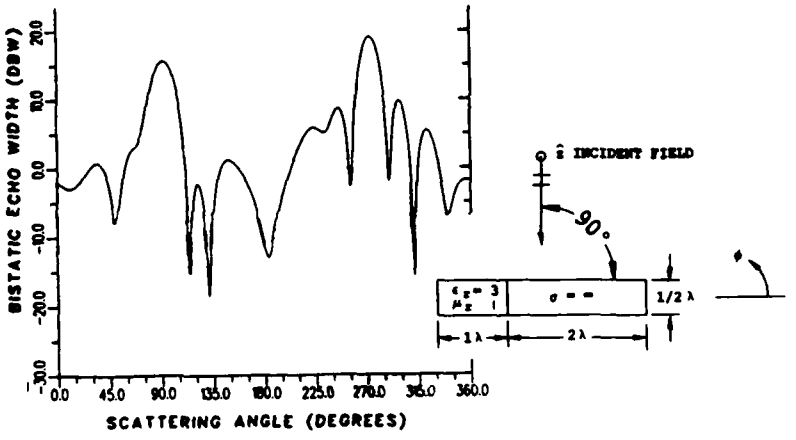

(a) TM_z polarization

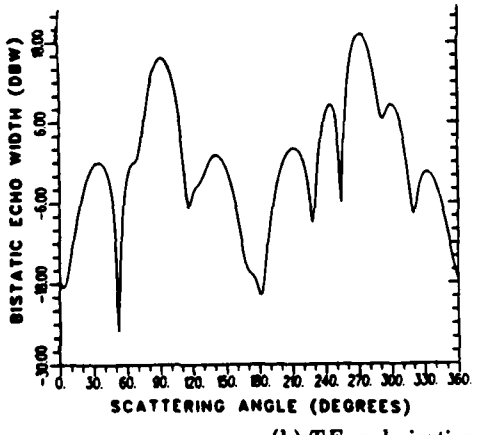

(b) TE_z polarization

Figure 4: Bistatic echo width vs. observation angle for a 2-D dielectric-conductor with normal incidence calculated using equivalent surface currents for the conductor and volume currents for the dielectric. $\Delta = .15\lambda$ is the size of the pulse basis functions used in the calculation.

A COMPUTER SIMULATION OF MONOSTATIC RADAR CROSS SECTION MEASUREMENTS

Kenneth R. Johnson, Naval Weapons Support Center, Crane
Microwave Components Division, Code 80312, Crane, IN 47522

Jovan Lebaric, Rose-Hulman Institute of Technology
5500 Wabash Avenue, Terre Haute, IN 47803

Abstract

A method for computer calculation of radar cross section of arbitrarily shaped metallic objects is presented, based on a generally available MOM computer code. Computer simulation of RCS measurements, as performed by a monostatic CW radar, is employed, and the conditions for obtaining accurate results are discussed. Polar plots of RCS for PEC plate and a PEC corner reflector are presented, as well as data for the mainframe/supercomputer resources used in the RCS calculation.

I. Introduction

Radar Cross Section (RCS) can be measured using an actual radar system and a full-scale object, or a conveniently scaled model and a correspondingly scaled operating frequency [1]. Measurements require that the instrumentation radar and the target are shielded from external electromagnetic fields and that all non-target reflections are either prevented or eliminated. An alternative may be a computer calculation of RCS for various objects to the extent allowed by the availability of three major components: computer memory, software, and time. The computer also allows calculation of RCS in early design stages, before a model or the actual object may be available.

This paper addresses the use of NEEDS (Numerical Engineering Electromagnetic Design System) [2][3] to calculate and plot monostatic RCS of arbitrarily shaped PEC objects. A method, using NEEDS software for simulating RCS measurements by a CW monostatic radar, is outlined, and results for the monostatic RCS of a PEC plate and 90° dihedral PEC corner reflector are presented. The accuracy of computer RCS calculations, memory requirements, and a comparison of RCS calculations using a 386-class PC, a VAX mainframe, and a CRAY supercomputer are also given.

II. Brief Description of NEEDS

NEEDS software package consists of a MOM [4] computer program and a pre-processing graphics utility for interactive geometry definition of an electromagnetic radiation or scattering problem.

Numerical Electromagnetic Code (NEC) is the MOM computer program included in NEEDS, developed at the Lawrence Livermore National Laboratory [5]. The NEC source code has been somewhat modified for this project as it was ported to a CRAY XMP-48 supercomputer and vectorized, allowing RCS evaluation for electrically larger structures.

A major program supporting NEC is the NEEDS graphic utility called IGUANA. IGUANA is a CAD type "model maker" program that takes user-defined top and side views of a structure to be analyzed and creates a three dimensional model. The three dimensional structure can be displayed, rotated, enlarged or reduced, edited, plotted, and translated into a NEC input file. The use of IGUANA for complex structures simplifies NEC input file creation and editing. Furthermore, the process

is less error-prone than text editing of a NEC input file, since the changes in the input geometry can be visualized on the computer screen.

III. RCS Calculation

RCS is defined as [1]:

$$RCS = \lim_{R \to \infty} 4 \cdot \pi \cdot R^2 \cdot |E_r|^2 / |E_i|^2 \qquad (1)$$

R is the distance between radar and target
E_r is the reflected field strength at the radar
E_i is the strength of incident field at the target.

For practical applications the distance R in (1) cannot be infinite. The RCS in (1) can be evaluated at some finite distance R as:

$$RCS = 4 \cdot \pi \cdot R^2 \cdot |E_r|^2 / |E_i|^2 \qquad (2)$$

provided that R is in the far-field zone (Fraunhofer region) [7]:

$$R \geq R_f = 2 \cdot D^2 / W \qquad (3)$$

R_f is the far-field distance
D is the target's largest linear dimension (aperture)
W is the wavelength.

It is advantageous to factor out the distance R from the RCS calculation. This can be accomplished by using a "test" target with a known RCS (RCS_T), and comparing the reflected fields from the actual target and the test target at the same distance. In such a case the reflected RCS of a target can be expressed as the ratio of two reflected fields:

$$RCS = RCS_T \cdot |E_r|^2 / |E_{rT}|^2 \qquad (4)$$

RCS_T is the known RCS of the test target
E_r is the reflected field for the actual target
E_{rT} is the reflected field for the test target.

RCS can then be expressed in decibels relative to the wavelength squared:

$$RCS_{dB} = 10 \cdot \log_{10}(RCS/W^2). \qquad (5)$$

IV. Computer Simulation of RCS Measurements

The objective is to simulate RCS measurements as performed by a monostatic CW radar on an actual target in free space. NEC allows almost unrestricted selection of the transmitter power and eliminates reflections other than from the target by defining the single target as residing in free space. Consequently, the radar antennas can be remarkably simple; a center-fed half-wavelength dipole as the transmitting antenna and a short (tenth of a wavelength) dipole as the receiving antenna have been selected. A short dipole rather than a resonant one has been selected as the receiving antenna to reduce secondary reflections and the amount of coupling to the transmitting antenna. To further reduce the coupling the receiving dipole is positioned directly above the radiating dipole, two

wavelengths apart. Although the transmitting and the receiving antennas are not exactly collocated, the effect of their separation is negligible for distances much larger than several wavelengths. The antenna setup used for the computer calculation of RCS is shown in Figure 1 below.

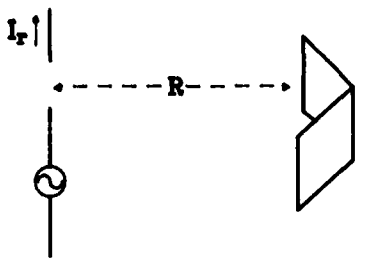

Figure 1 (Antenna Setup)

A current will be induced on the receiving dipole even in the absence of a target, due to mutual coupling of the two antennas. The current measured on the receiving dipole when a target is present is the addition of this antenna coupling current and the current induced by the target-reflected wave.

$$I_m = I_r + I_o \quad (6)$$

or

$$I_r = I_m - I_o \quad (7)$$

I_m is the measured current phaser
I_r is the current phaser induced by a target-reflected wave
I_o is the current phaser due to mutual coupling.

The following procedure for computer RCS calculation may now be devised:
- calculation of current $|I_o|$ induced on the receiving dipole with the target absent
- calculation of current $|I_{rT}|$ induced on the receiving dipole by the wave reflected off the test target
- calculation of current $|I_r|$ induced on the receiving dipole by the wave reflected off the actual target
- computation of the RCS of the actual target using :

$$RCS = RCS_T \cdot |I_r|^2 / |I_{rT}|^2 \quad (8)$$

The test target has been chosen to be a PEC plate perpendicular to the direction of propagation of the incident wave as the RCS is known to be :

$$RCS_{PLATE} = 4 \cdot \pi \cdot A^2 / W^2 \quad (9)$$

A is the surface area of the plate.

For different targets, or for the same target but with different orientations relative to the direction of the incident wave, it is only the numerator of (8) that has to be recalculated, since the denominator is in essence calibrated to a known RCS. Typical application of (8) may involve rotation of the target and calculation, for each of the target positions, a value for $|I_r|$ and consequently the target RCS. The results can then be presented as polar plots of RCS versus the angle of azimuth or elevation, and with a horizontal or vertical polarization.

V. Modelling Considerations

Surface of a PEC object should be approximated, for NEC analysis, by a collection of flat PEC patches which may be of arbitrary shape but "small" compared to the wavelength of operation. Each patch introduces two unknown elements: two patch currents perpendicular to each other that need to be solved for. In order to ensure the accuracy of the computer solution, it is recommended [4] that no less than five patches per wavelength are employed for modelling a PEC object. Figure 2 below is an example of sporadic results when too few patches are used.

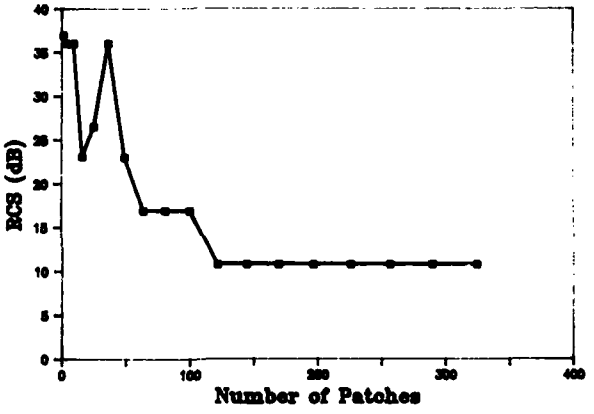

Figure 2 (RCS_{dB} of 5x5 wavelength PEC plate)

Adopting the "five patches per wavelength" recommendation results in :

$$N = 25 \cdot A/W^2 \qquad (10)$$

N is the number of patches.

With two elements per patch the number of elements is equal to 2N and the system of linear equations is equal to the square of the number of elements, $(2N)^2$. Thus a $1m^2$ plate at 1 GHz results in a 309,136 element matrix of coefficients. As the wavelength decreases or the PEC structure modelled gets larger, the matrix size and the computer memory required to store the matrix increases as a power of two. This large memory requirement is the major limitation in employing MOM codes in RCS

computations of electrically large metallic objects.

VI. Results

The drawback of not meeting the far-field condition in (3) is shown in Figure 3 below.

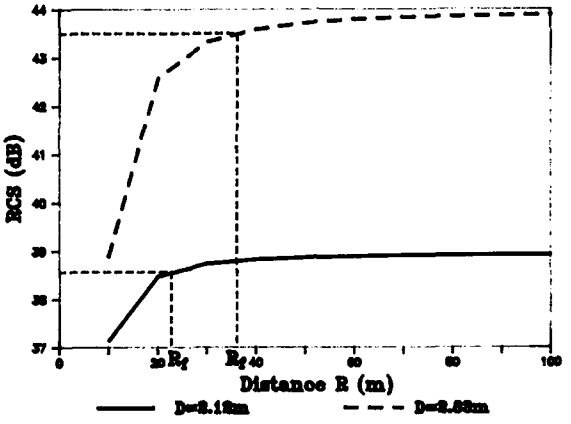

Figure 3 (Computer calculated R_f)

Figure 3 presents the computer calculated RCS_{dB} plots (at 1 GHz) for two square plates with apertures D of 2.12m and 2.83m. From Figure 3 the R_f was found to be 22m and 38m, while (3) gives 30m and 53.4m respectively. This demonstrates that (3) gives a good estimate for the distance R_f, somewhat greater than the computer calculated R_f.

Two targets have been selected for RCS calculations: a five-by-five wavelength PEC plate and a 90° dihedral PEC corner reflector. The total area of the dihedral reflector is equal to the five-by-five wavelength

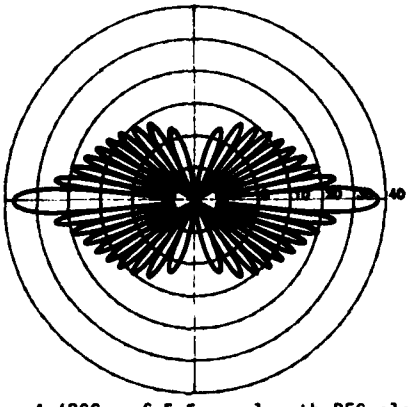

Figure 4 (RCS_{dB} of 5x5 wavelength PEC plate)

plate. The targets were rotated to determine RCS as a function of angles of azimuth and elevation. Figures 4 through 6 are the polar plots of the data obtained through the computer simulation.

Figure 4 on the previous page represents the RCS_{dB} of the five-by-five wavelength square PEC plate as a function of either azimuth or elevation angles. Polarization invariance is shown, due to the symmetry of the square plate. A rapid fluctuation in monostatic RCS_{dB} is clearly visible as the direction of the incident wave moves away from being perpendicular to the plate (horizontal axis on the graph). The half-RCS angle, defined as the angle between the points where the monostatic RCS drops 6dB of its maximum value is about 7°.

The next two graphs (Figures 5 & 6 below) are polar plots of the RCS_{dB} for the 90° dihedral PEC corner reflector.

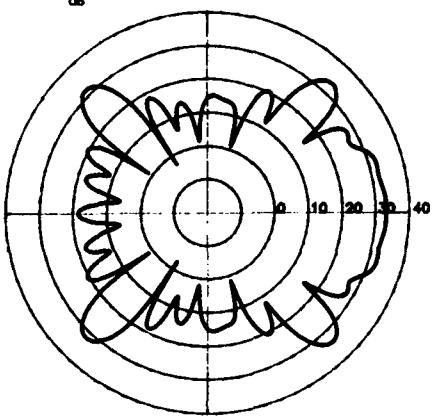

Figure 5 (Vertical Polarization)

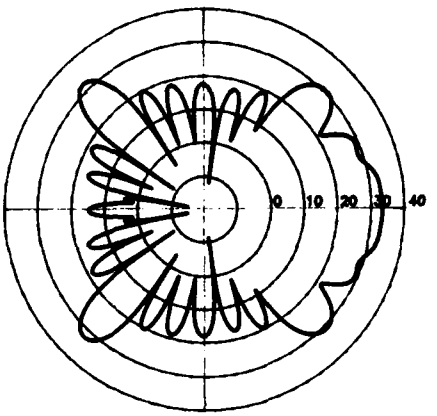

Figure 6 (Horizontal Polarization)

Figure 5 shows RCS_{dB} for the dihedral PEC corner reflector as a function of the angle of azimuth with the horizontal axis in the figure corresponding to the perpendicular incidence of a vertically polarized wave. A very significant increase in the half-RCS angle to about 48° in the horizontal plane is evident from the figure. Furthermore, the maximum RCS_{dB} is only reduced by about 5 dB compared with the maximum RCS_{dB} for the square plate of the same surface area. A simple calculation shows that, for normal incidence, the corner reflector area projected onto the plane perpendicular to the direction of incidence is:

$$RCS = 4 \cdot \pi \cdot (2.5 \cdot W \cdot 5 \cdot W)^2 / W^2 = 50.0 \cdot \pi \cdot W^2 \quad (11)$$

$$RCS_{dB} = 10 \cdot \log_{10}(RCS/W^2) = 32.9dB. \quad (12)$$

This area is smaller than the surface area of the plate by 6 dB which confirms the computer-calculated RCS for the corner reflector at normal incidence. Four RCS_{dB} "lobes", each 6 dB below the maximum RCS_{dB} of the square plate, are visible at +45°, -45°, +135°, and -135°. They correspond to perpendicular incidences onto the left or the right half of the corner reflector, respectively.

Figure 6 shows RCS_{dB} for the dihedral PEC corner reflector as a

function of the angle of azimuth with the horizontal axis corresponding to the perpendicular incidence of a horizontally polarized wave. The difference between Figure 5 and Figure 6 is in the polarization of the incident wave : the incident electric field is either parallel to the centerline of the corner reflector (referred to as the vertical or the parallel polarization in Figure 5), or perpendicular to the centerline (referred to as the horizontal or cross polarization if Figure 6). A significant increase in half-RCS angle, from 48° for parallel polarization to 54° for the cross-polarization, is evident by comparing Figure 5 and Figure 6. A simple corner reflector thus provides a relatively wide 54° angle in the plane of azimuth, with the RCS_{dB} within 3 dB of its maximum value for the perpendicular incidence of a cross-polarized wave. Table I below summarizes the half-RCS angles in the plane of azimuth for the five-by-five wavelength PEC plate and the 90° dihedral PEC corner reflector of the save area, at 1 GHz.

	Vertical Polarization	Horizontal Polarization
Square PEC Plate	7°	7°
Dihedral PEC Corner Reflector	48°	54°

Table I (Half-RCS Angle)

VII. Computer Run Times

NEEDS package can be used for RCS calculations as a stand-alone PC package, provided that the particular machine used has sufficient memory and that the user can tolerate long execution times if the problem geometry requires a large number of elements. An alternative is to use the PC-based NEEDS package in conjunction with a mainframe computer running the NEC code. The latter is a preferred concept, since it assigns appropriate tasks to the best suited computer environments: highly interactive pre- and post- processing (geometry definition and plotting) is performed by a PC, whereas extensive "number crunching" is performed by a mainframe or a supercomputer, with small size files transferred between the two. The decrease in CPU time required for RCS calculation is of two orders of magnitude between a 386-class PC (16MHz, 387 co-processor, and Microsoft Fortran) and a VAX 8530 mainframe; and another two orders of magnitude between a VAX 8530 mainframe and CRAY XMP-48 supercomputer.

Table II below shows the amount of CPU time needed to calculate a 600 element problem on a VAX 8530 and a CRAY XMP-48.

	Total CPU Time	Time Factoring	% of Time Factoring
VAX 8350	556.60s	527.93s	94.84%
CRAY XMP-48	5.34s	3.59s	66.48%

Table II (Computer Run Times)

An increase in speed of about 104 times resulted from porting the NEC code to the supercomputer. Furthermore, time of the RCS computer calculations has revealed that 95% of the CPU time in the NEC code was spent in factoring the matrix of coefficients. Consequently, most of the attention in porting the NEC code to the CRAY XMP-48 has been concentrated on improving the performance of the matrix factoring subroutine. "Unrolling" of the innermost DO loop in the subroutine and compiling NEC using CFT77 [6] vectorizing FORTRAN compiler reduced the portion of total CPU time spent in this subroutine to about 66.5%, which also contributed to the increase in computation speed over the VAX 8530 mainframe.

VIII. Conclusion

A computer simulation of RCS measurements of metallic objects has been devised using the NEEDS software package. The requirements for the number of patches per wavelength needed to model an object surface, and the minimum distance between the transmitting/receiving antennas and the target have been investigated. The method has been applied to calculate RCS, as a function of the angle of incidence in the two principal planes, for a PEC plate and a dihedral PEC corner reflector. Polar plots of RCS and the half-RCS angles for the parallel (vertical) and cross (horizontal) polarizations were generated from the results obtained using a supercomputer and a vectorized version of the NEC computer code. The computer-calculated RCS agreed very well with the results that had been theoretically predicted, such as for the RCS of a large (relative to the operating wavelength) PEC plate at perpendicular incidence. Finally, the NEEDS/NEC concept for computer simulation of RCS measurements applies to PEC targets of arbitrary shape, limited in modelling of electrically large objects by the available computer memory.

Acknowledgements

Authors would like to acknowledge the Academic Affiliates Program of the National Center for Supercomputing Applications (NCSA) at Urbana-Champaign, IL, for its support for supercomputer applications in advanced electromagnetic courses at Rose-Hulman Institute of Technology.

References

[1] M.I. Skolnik, ed., Chapter 27 in Radar Handbook, McGraw-Hill, New York, 1970.

[2] NEEDS: The Numerical Electromagnetic Engineering Design System, VErsion 1.0, The Applied Computational Electromagnetic Society (ACES), February 1988.

[3] ACES SOFTWARE LIBRARY, Applied Computational Electromagnetic Society Journal and Newsletter, Vol. 3, No. 2, Fall 1988.

[4] M.M. Ney, "Method of Moments as Applied to Electromagnetic Problems", IEEE Transactions on Microwave Theory and Techniques, Vol. MTT-33, No. 10, pp. 972-980, October 1985.

[5] G.J. Burke and A.J. Poggio, Numerical Electromagnetics Code (NEC), Lawrence Livermore National Laboratory, January 1981.

[6] UNICOS User's Guide, Version 1.0, University of Illinois at Urbana-Champaign, January 1989.

[7] M.I. Skolnik, Chapter 7 in Introduction to Radar Systems, McGraw-Hill, New York, 1962.

THE AUGMENTED MAGNETIC FIELD INTEGRAL EQUATION WITH TRIANGULAR PATCHES FOR THE ANALYSIS OF SCATTERING BY CONDUCTING BODIES

Luis M. Correia and Afonso M. Barbosa
Centro de Análise e Processamento de Sinais and
Departamento de Engenharia Electrotécnica e de Computadores,
Instituto Superior Técnico, Universidade Técnica de Lisboa
Av. Rovisco Pais, 1096 LISBOA CODEX, PORTUGAL

ABSTRACT

The solution by the Moment Method of the Augmented Magnetic Field Integral Equation, when triangular patch basis functions are used, is obtained. The choice of the test function for the normal component is discussed. Numerical results are presented for the sphere and the cube (condition numbers of the matrices, back and forward scattering cross sections). The CPU time is also discussed.

I. INTRODUCTION

The analysis of scattering by conducting bodies, when its dimensions are in the order of the wavelength, is usually done by using either the Electric or the Magnetic Field Integral Equations (EFIE or MFIE) [1]. However, it is known that when the frequency of the incident wave is in the vinicity of a resonant frequency of the body, these equations cannot be used. Among the integral equations that have been proposed to overcome this problem are the Augmented Electric and Magnetic Field Integral Equations (AEFIE or AMFIE) proposed by Yaghjian [2]; in [2] only the AMFIE was implemented, using square patches with pulse basis and delta test functions.

When one wants to analyze the scattering by arbitrary shape bodies, the square patch does not seem much appropriate, because it may be difficult to model the surface of the scatterer. The triangular patch basis function proposed by Rao [3] seems a good choice for that purpose. In a previous work [4] a test function for the normal component of the AEFIE was developed, implementing this equation with Rao's basis function.

In this communication, a study for the choice of the normal component's test function of the AMFIE, using Rao's triangular patch basis function, is presented. The singularity, existing for the "self-contributions" of the triangles is analyzed for constant test functions. Two test functions are implemented. In order to evaluate the procedure, the sphere and the cube are used as scatterers. The condition number of the matrix resulting from the matrix product in the normal equation is presented. Also the back and forward scattering cross sections are calculated.

II. PROBLEM FORMULATION AND SOLUTION

II.1 Electromagnetic Formulation

Given a perfectly conducting scatterer, defined by its closed surface S with exterior normal $\mathbf{n}$, and an incident wave $(\mathbf{E}^i, \mathbf{H}^i)$, the Augmented Magnetic Field Integral Equation is [2]

$$-\frac{1}{2}\,\mathbf{n}\times\mathbf{J}_S(\mathbf{r}) - \frac{1}{4\pi}\int_S \mathbf{J}_S(\mathbf{r}')\times\nabla'\Psi(\mathbf{r},\mathbf{r}')\,dS' = \mathbf{H}^i(\mathbf{r})\ ,\quad P(\mathbf{r})\in S \tag{1}$$

where $\mathbf{J}_S$ is the induced surface electric current density, and $\Psi(\mathbf{r},\mathbf{r}')$ is the free-space Green's function

$$\Psi(\mathbf{r},\mathbf{r}') = \frac{e^{-jkR}}{R} \tag{2}$$

so that

$$\nabla'\Psi(\mathbf{r},\mathbf{r}') = (1+jkR)\,\frac{e^{-jkR}}{R^3}\mathbf{R} \tag{3}$$

where

$$\mathbf{R} = \mathbf{r}-\mathbf{r}' \tag{4}$$

$$R = |\mathbf{r}-\mathbf{r}'| \tag{5}$$

Introducing

$$\mathbf{H}^s(\mathbf{r}) = \frac{1}{4\pi}\int_S \mathbf{J}_S(\mathbf{r}')\times\nabla'\Psi(\mathbf{r},\mathbf{r}')\,dS'\ ,\quad P(\mathbf{r})\in S \tag{6}$$

the tangential component of the AMFIE (the Magnetic Field Integral Equation) can be written as

$$\frac{1}{2}\mathbf{J}_S(\mathbf{r}) - \mathbf{n}\times\mathbf{H}^s(\mathbf{r}) = \mathbf{n}\times\mathbf{H}^i(\mathbf{r})\ ,\quad P(\mathbf{r})\in S \tag{7}$$

and the normal component is

$$-\mathbf{n}\cdot\mathbf{H}^s(\mathbf{r}) = \mathbf{n}\cdot\mathbf{H}^i(\mathbf{r})\ ,\quad P(\mathbf{r})\in S \tag{8}$$

II.2 Numerical Solution

To solve the AMFIE by the Method of Moments [5], $\mathbf{J}_S$ is expanded in terms of Rao's basis function $\mathbf{b}_n$ [3]

$$\mathbf{b}_n(\mathbf{r}) = \begin{cases} \frac{l_n}{2S_n^+}\,\boldsymbol{\rho}_n^+(\mathbf{r}) & ,\ P(\mathbf{r})\in T_n^+ \\ \frac{l_n}{2S_n^-}\,\boldsymbol{\rho}_n^-(\mathbf{r}) & ,\ P(\mathbf{r})\in T_n^- \\ \mathbf{0} & ,\ \text{elsewhere} \end{cases} \tag{9}$$

As far as the test functions are concerned, Galerkin's Method [5] is used for the tangential component of the AMFIE, $\mathbf{t}_m^t = \mathbf{b}_m$; to test the normal component, the function $\mathbf{t}_m^n$

$$\mathbf{t}_m^n(\mathbf{r}) = \begin{cases} f_m^+(\mathbf{r})\,\mathbf{n}_m^+ & , \quad P(\mathbf{r}) \in T_m^+ \\ f_m^-(\mathbf{r})\,\mathbf{n}_m^- & , \quad P(\mathbf{r}) \in T_m^- \\ \mathbf{0} & , \quad \text{elsewhere} \end{cases} \tag{10}$$

is introduced, where the functions $f_m^{\pm}(\mathbf{r})$ have to be defined. The inner product is simply

$$< \mathbf{f}, \mathbf{g} > \; = \; \int_S \mathbf{f} \cdot \mathbf{g}\, dS \tag{11}$$

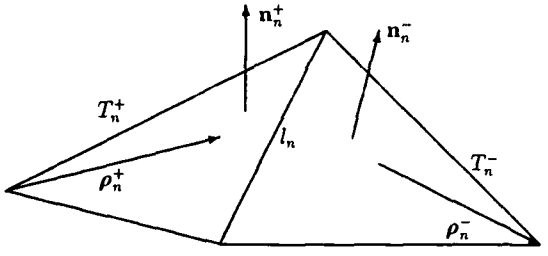

Figure 1: *Parameters defining basis and test functions.*

By applying this procedure, an overdetermined matrix equation is obtained

$$\mathbf{M}\,\mathbf{J}_S^N = \mathbf{I} \tag{12}$$

$\mathbf{M}$ being a $2N \times N$ matrix (N is the number of basis functions in the expansion), composed by two square submatrices related to the components of the integral equation, $\mathbf{M}^t$ and $\mathbf{M}^n$; $\mathbf{I}$ is a $2N$ vector, also composed by two subvectors, $\mathbf{I}^t$ and $\mathbf{I}^n$; $\mathbf{J}_S^N$ is the vector of the unknowns (of dimension N). The submatrix and subvector related to the tangential component are the same as for the MFIE, and the details can be found in [3]. For the normal component, the submatrix and subvector coefficients are given by

$$M_{mn}^n = < -\mathbf{H}^s, \mathbf{t}_m^n > = \int_S -\mathbf{H}^s(\mathbf{r}) \cdot \mathbf{t}_m^n(\mathbf{r})\, dS \tag{13}$$

$$I_m^n = < \mathbf{H}^i, \mathbf{t}_m^n > = \int_S \mathbf{H}^i(\mathbf{r}) \cdot \mathbf{t}_m^n(\mathbf{r})\, dS \tag{14}$$

The test functions are null outside the pair of triangles where they are defined, so these integrals over S reduce to integrals over the triangles $T_m^{\pm}$. By analogy with the MFIE, the coefficients are calculated by summing the contributions $C_{\mathbf{M}^n}^{pq}$, $C_{\mathbf{I}^n}^{p}$ for each pair of triangles T^p,T^q (with edges l_i^q and l_j^p); the integrals expressing these contributions, as well as those related to the MFIE, are approximated by the midpoint formula (except for $C_{\mathbf{M}^n}^{pp}$, which will be discussed later),

$$C_{\mathbf{M}^n}^{pq} = -\int_{T^p} f_j^p(\mathbf{r})\,\mathbf{n}^p \cdot \mathbf{H}_i^{pq}(\mathbf{r})\,dS \simeq -S^p\, f_j^p(\mathbf{r}^{cp})\,\mathbf{n}^p \cdot \mathbf{H}_i^{pq}(\mathbf{r}^{cp}) \tag{15}$$

$$C_{\mathbf{I}^n}^{p} = \int_{T^p} f_j^p(\mathbf{r})\,\mathbf{n}^p \cdot \mathbf{H}^i(\mathbf{r})\,dS \simeq S^p\, f_j^p(\mathbf{r}^{cp})\,\mathbf{n}^p \cdot \mathbf{H}^i(\mathbf{r}^{cp}) \tag{16}$$

where

$$\mathbf{H}_i^{pq}(\mathbf{r}^{cp}) = \frac{1}{4\pi}\int_{T^q} \frac{s_i^q l_i^q}{2S^q}\,\boldsymbol{\rho}_i^q(\mathbf{r}') \times \nabla'\Psi(\mathbf{r}^{cp},\mathbf{r}')\,dS' \tag{17}$$

(it is assumed that the vectors $\boldsymbol{\rho}_i^q$ are directed inwards the triangle, the sign being given by $s_i^q = \pm 1$). The integrals in (17) are calculated numerically.

II.3 Choice of the Normal Component's Test Function

The test function for the normal component of the integral equation must be in the range of this operator [6]. In this way, the sign of $\mathbf{t}_m^n$ in the pair of triangles must be chosen according to the magnetic field radiated by that pair, when the current distribution matches the basis function.

As can be seen in Fig. 1, both vectors $\boldsymbol{\rho}_n^{\pm}$ are directed in the same way, so there will be no change of sign in the magnetic field radiated by the two triangles. Therefore, the test function must keep the same sign in both triangles; the simplest will be a constant function in each triangle, with a unitary amplitude, $f_m^{\pm}(\mathbf{r}) = 1$. Nevertheless, a test function with alternated signs in the triangles, $f_m^{\pm}(\mathbf{r}) = \pm 1$, has also been implemented, in order to show its influence on the results.

II.4 "Self-Contributions" of the Triangles

The contribution of a triangle to itself must be evaluated analytically, because there is a singularity in the integrand function. Substituing the basis function, and since the test function is constant, one can write (the index p of the triangle is omitted)

$$C_{\mathbf{M}^n}^{pp} = -\frac{s_i l_i f_j}{8\pi S}\,\mathbf{n} \cdot \mathbf{T} \tag{18}$$

where

$$\mathbf{T} = \int_T \left[\int_T \boldsymbol{\rho}_i(\mathbf{r}') \times \nabla'\Psi(\mathbf{r},\mathbf{r}')\,dS'\right]\,dS \tag{19}$$

The vector $\boldsymbol{\rho}_i(\mathbf{r}')$ can be expressed in terms of $\boldsymbol{\rho}_i(\mathbf{r})$, Fig. 2,

$$\boldsymbol{\rho}_i(\mathbf{r}') = \boldsymbol{\rho}_i(\mathbf{r}) - \mathbf{R} \tag{20}$$

therefore

$$\boldsymbol{\rho}_i(\mathbf{r}') \times \nabla'\Psi(\mathbf{r},\mathbf{r}') = \boldsymbol{\rho}_i(\mathbf{r}) \times \nabla'\Psi(\mathbf{r},\mathbf{r}') \tag{21}$$

On the other hand,

$$\nabla'\Psi(\mathbf{r},\mathbf{r}') = -\nabla\Psi(\mathbf{r}',\mathbf{r}) \tag{22}$$

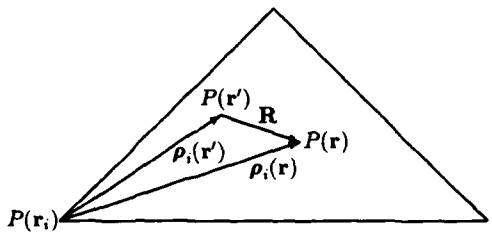

Figure 2: *Vectors* $\rho_i(\mathbf{r}')$ *and* $\rho_i(\mathbf{r})$.

thus, $\mathbf{T}$ can be written as

$$\mathbf{T} = -\int_T \left[\int_T \boldsymbol{\rho}_i(\mathbf{r}) \times \nabla\Psi(\mathbf{r}', \mathbf{r})\, dS'\right] dS \tag{23}$$

Changing the order of integration (this is possible [7] since the inner integral converges in the domain of the outer integral and the integrand function is sectionally continuous in the domain of the inner integral [8]), $\mathbf{T}$ can be written as

$$\mathbf{T} = -\int_T \left[\int_T \boldsymbol{\rho}_i(\mathbf{r}) \times \nabla\Psi(\mathbf{r}', \mathbf{r})\, dS\right] dS' \tag{24}$$

but, except for the minus sign, this is just another way of writing (19), interchanging $\mathbf{r}'$ with $\mathbf{r}$. Hence

$$\mathbf{T} = \mathbf{0} \tag{25}$$

i.e., the "self-contributions" are null, whatever are the test functions, as long as they are constant in each triangle.

If the test function is not constant, the singularity may be removed by adding and subtracting the singular term of the integrand function ($[1+(k^2/2)]\mathbf{R}/R^3$), and integrating the non-singular term numerically and the singular term analytically.

II.5 Computer Implementation

The solution of the overdetermined matrix equation is obtained by computing the solution of the normal equation (the superscript ^{H} stands for hermitian) [9]

$$\mathbf{M}^H \mathbf{M}\, \mathbf{J}_S^N = \mathbf{M}^H \mathbf{I} \tag{26}$$

The calculation of the AMFIE matrix coefficients differs only slightly from the MFIE (the inner product of the normal is evaluated along with the cross product of the MFIE, for both $\mathbf{H}_i^{pq}(\mathbf{r}^{cp})$ and $\mathbf{H}^i(\mathbf{r}^{cp})$). A special purpose routine has been written to do the matrix product in the normal equation, accounting for the characteristics of the matrix. The ZHPCO and ZHPSL routines in the LINPACK [9] package were used to solve the equations system.

III. NUMERICAL RESULTS

In order to evaluate this procedure, the sphere (radius a) and the cube (side L), both modelled with 96 patches (144 unknowns), have been used as test scatterers. A plane wave is used as incident wave. The condition number for both objects, Fig. 3, clearly shows that the AMFIE is stable in the resonance frequencies. It can also be seen that the alternate sign test function leads to lower values of the condition number; however, in both cases, those values are acceptable.

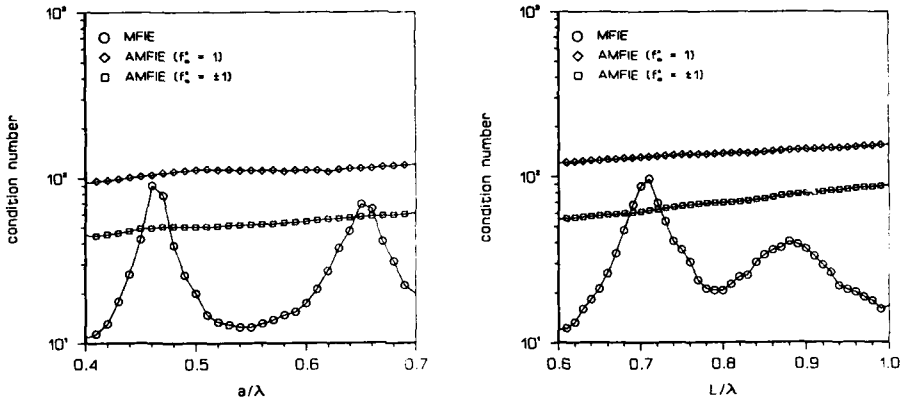

(a) *sphere* (b) *cube*

Figure 3: *Condition numbers for* $\mathbf{M}^H\mathbf{M}$.

As far as the back (σ_b) and forward (σ_f) scattering cross sections are concerned, Fig. 4-5, the constant sign test function gives better results, as could be expected from the criteria used to choose the test function; good results are obtained, although in the case of the sphere there are some differences in the amplitude of the oscillations of σ_b. The discrepancies in the results are probably due to the approximations used in (15) and (16) (this has already been pointed in [3], where the same approximation has been used with the MFIE), and from the fact that the MFIE is sensible to the geometry of the scatterer [1].

Concerning the CPU time, typically the calculation of the AMFIE matrix takes 19% more time than the MFIE matrix, depending both on N^2. The factorization of $\mathbf{M}^H\mathbf{M}$ is faster than the one of the MFIE matrix, because the first one is hermitian (while the second has no special characteristics); the first factorization takes about 40% of the time of the second, but both vary essentially with N^3. The AMFIE has the matrix product, which the MFIE has not; the CPU time for this product depends mainly on N^3, and is responsible for the greatest difference in the total computational time between the AMFIE and the MFIE (roughly 2.3 times when N is 144, but growing with N).

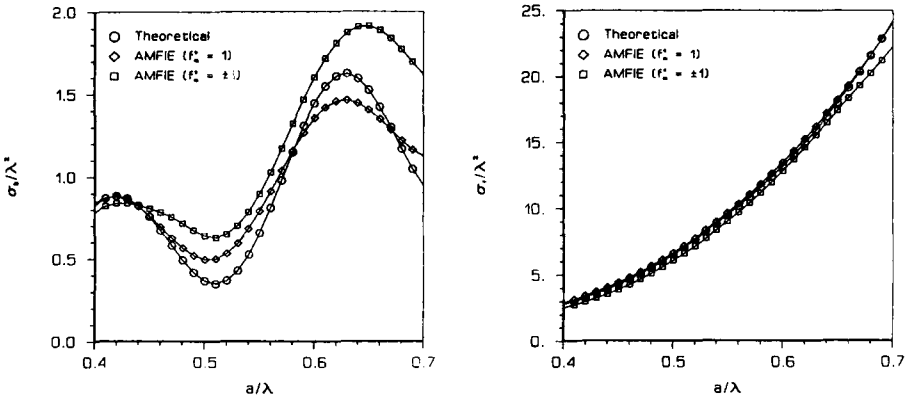

(a) σ_b/λ^2 (b) σ_f/λ^2

Figure 4: *Back and forward scattering cross sections for the sphere.*

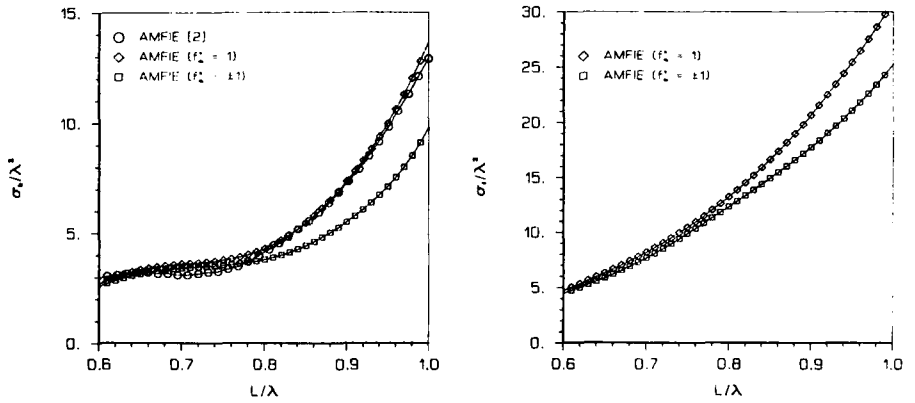

(a) σ_b/λ^2 (b) σ_f/λ^2

Figure 5: *Back and forward scattering cross sections for the cube (broadside incidence).*

IV. CONCLUSIONS

The Augmented Magnetic Field Integral Equation has been implemented with triangular patch basis functions. An overdetermined matrix equation $(2N \times N)$ is obtained, with two submatrices $(N \times N)$ for the tangential and the normal components of the integral equation. The Method of Galerkin is used for the tangential component of the integral equation. An analysis of the normal component of the equation is done, and the test function for this component is chosen according to the characteristics of the radiated magnetic field. The "self-contributions" of the triangles for the coefficients of the normal component submatrix are null, when the test function is constant. The solution of the matrix equation is obtained by solving the normal equation. The sphere and the cube are used as test objects. The condition number of the matrix of the normal equation shows that the AMFIE is stable. The scattering cross sections (back and forward) are calculated, and show a reasonable agreement with theoretical or previous numerical results. As far as the CPU time is concerned, the AMFIE takes about twice the time of the MFIE, when the number of unknowns is circa 100, but this ratio increases with N.

REFERENCES

[1] Poggio,A.J. and Miller,E.K., *"Integral Equation Solutions of Three-Dimensional Scattering Problems"*, in Mittra,R. (ed.), *"Computer Techniques for Electromagnetics"*, Pergamon Press, New York, N.Y., 1973.

[2] Yaghjian,A.D., *"Augmented Electric- and Magnetic-Field Integral Equations"*, Radio Science, Vol. 16, No. 6, Nov.-Dec. 1981, pp. 987-1001.

[3] Rao,S.M., *"Electromagnetic Scattering and Radiation of Arbitrarily-Shaped Surfaces by Triangular Patch Modeling"*, Ph. D. Dissertation, Univ. of Mississippi, Aug. 1980.

[4] Correia,L.M. and Barbosa,A.M., *"A Procedure for the Analysis of Scattering by Arbitrary Shape Conducting Bodies in the Resonance Region"*, IEEE AP-S International Symposium, Syracuse, N.Y., June 1988.

[5] Harrington,R.F., *"Field Computation by Moment Methods"*, Macmillan, New York, N.Y., 1968.

[6] Sarkar,T.K., *"A Note on the Choice of Weighting Functions in the Method of Moments"*, IEEE Trans. Antennas Propagat., Vol. AP-33, No. 4, Apr. 1985, pp. 436-441.

[7] Courant,R. and John,F., *"Introduction to Calculus and Analysis"*, Vol. 2, John Wiley & Sons, New York, N.Y., 1974.

[8] Müller,C., *"Foundations of the Mathematical Theory of Electromagnetic Waves"*, Springer-Verlag, Berlin, 1960.

[9] Golub,G.H. and Van Loan,C.F., *"Matrix Computations"*, The Johns Hopkins Univ. Press, Baltimore, Maryland, 1983.

[10] Dongarra,J., Bunch,J.R., Moler,C.B. and Stewart,G.B., *"LINPACK Users' Guide"*, SIAM Publications, Philadelphia, 1978.

BENCHMARK TESTING WITH AN OPEN-ENDED CYLINDER PROBLEM

A.C. Hamilton and S.M. Gittins
Hunting Engineering Limited
Ampthill,
Bedford MK45 2HD
England
Telephone: 525-403431

R.W.M. Lau and R.J. Sheppard
Curlsol Microwave Limited
Braemar Hamlet
Chetnole, Sherborne
Dorset DT9 6NY
England
Telephone: 935-872925

ABSTRACT

The problem chosen for the benchmark testing was that of plane wave irradiation of a cylinder open at one end. The cylinder dimensions in wavelengths were 0.68 length by 0.19 diameter. The direction of propagation was parallel to the cylinder axis.

The codes tested were as follows:

1. STRIPES - a commercial transmission line method (TLM) code;
2. TDFDS - a commercial time domain finite difference code;
3. NEC - the numerical electromagnetics code;
4. CHAOS - a wire grid moment method code;
5. BOR2,BOR3 - two moment method codes.

These codes were compared with data from waveguide mode analysis and experimental data.

Within the known limitations of the various numerical methods the agreement between all five methods, the waveguide analysis and experimental data was good. However, some important differences emerged between the codes and these are discussed fully below.

INTRODUCTION AND OBJECTIVE

The interior fields in a structure obtained due to an incident field penetrating the structure, e.g. via an aperture, are difficult to estimate because often they are small compared to the incident field and so any errors due to the method of estimation are likely to be comparable to these interior fields. The objective in benchmarking codes for the open ended cylinder is to compare their ability to estimate accurately the very small fields known to be obtained deep inside this cylinder.

THE PROBLEM CHOSEN

As stated above, the problem chosen was that of a plane wave irradiation of an open ended cylinder of dimensions in wavelengths 0.68 length by 0.19 diameter - see **Figure 1.** The excitation was a linearly polarised unit plane wave axially incident on the open end. The output was the amplitude of the component of the E -field in the direction of polarisation at different points along the central axis.

Apart from the expected low internal fields mentioned above, this problem was chosen because it has previously been investigated in the open literature, see **References 1 - 4,** and because it lies within the applicable frequency range of the codes tested.

CODES TESTED

FREQUENCY CONSTRAINTS

All the codes tested, namely STRIPES, TDFDS, NEC, CHAOS and BOR2,BOR3 have to be considered "low frequency" codes. For example the cell length in STRIPES and the element length in a NEC wire grid model have to be small compared with the wavelength and are recommended to be less than one tenth the wavelength at the frequency of interest in both cases. Computer storage constraints limit the number of cells/elements that can be used to describe a problem: this means that the object size cannot exceed a few wavelengths.

The codes also have a lower frequency limit. For example in NEC it is recommended that the wire grid element lengths are greater than $\lambda/1000$. With the time domain codes STRIPES and TDFDS, it is necessary to run the model for several cycles of the propagating wave to ensure convergence to a steady state solution: this implies a lower frequency limit if the number of timesteps simulated is not be prohibitive.

STRIPES

STRIPES is a commercially available TLM code, developed by the University of Nottingham and KCC Limited. TLM (Transmission Line Matrix) is a time domain numerical technique which models the propagation of EM waves by filling space with a network of transmission lines (References 5 - 7).

TDFDS

TDFDS is a commercially available total field time domain finite difference code based on the Yee algorithm (Reference 8). It has been developed by Kings College London and Curlsol Microwave Limited and is described in Reference 9.

THE STRIPES/TDFDS MODEL

In order to carry out as far as possible a like-with-like comparison between STRIPES and TDFDS, the same model of the cylinder problem was used in both cases - see Figure 2. The cell size, 0.025 wavelengths, and problem space, 20 x 36 x 20 cells, chosen was a compromise between the need to have a sufficiently small cell size to describe the cylinder accurately in Cartesian coordinates, and to have a large enough workspace round the cylinder so that reflections from the problem space walls did not significantly affect the results.

The problem space boundaries were modelled in STRIPES using zero reflection coefficient walls and in TDFDS using a first order extrapolation of field within the problem space. In the latter case the boundary was chosen mainly to reduce the possibility of 'late time ringing' and in the former to reduce bias due to problem space boundary reflections. The excitation plane was chosen to be five cells away from the mouth of the cylinder: preliminary studies showed that the results to be relatively insensitive to choice of excitation plane stand off.

In order to ensure convergence to the steady state solution the TDFDS model was run to the equivalent of four complete cycles of the propagating wave. Similarly, STRIPES was run for 800 timesteps simulating 3.75 cycles. In addition, in order to test the sensitivity of the results to the number of timesteps, STRIPES was re-run with 1000 timesteps, i.e. 12.5 cycles.

The CW excitation was simulated directly by TDFDS. With STRIPES the main solver assumes a Dirac pulse at time zero. Thus to obtain the CW response it was necessary to convolve the Dirac pulse results with the CW excitation.

STRIPES assumes zero loss in the air cells. In the case of TDFDS a slight loss in the air cells of the model was introduced to obtain the field convergence within the cylinder as recommended in Reference 3.

MOMENT METHOD CODES

The Lawrence Livermore code NEC is described in References 4 and 10. The cylinder was modelled by the wire grid shown in Figure 3, which contained 354 segments, the average segment length being 0.051λ. In order to examine the effect of wire thickness, two radii were considered namely 0.0038 and 0.0076λ (surface area of all the wires = 1 and 2 times the surface area of the cylinder respectively). Because NEC is a scattered field code, to obtain accurate internal fields it was necessary to run NEC twice, once with the cylinder ends closed, and once with the end cap removed as in Figure 3. The internal field was then estimated by subtracting the scattered fields with and without the end cap.

The code CHAOS is described in detail in Reference 4. CHAOS, like NEC uses a wire grid model (Figure 4) to describe the cylinder. The main difference between the codes is in the way they represent the currents on the wire segments, NEC using sinusoidal and CHAOS overlapping triangle functions.

BOR2 and BOR3 are body of revolution codes. They are described in detail in Reference 1. The differences between them are that while BOR2 is a conventional near-field scattering code, BOR3 uses an equivalent aperture excitation method for predicting the internal fields more accurately.

RESULTS AND DATA

The internal fields obtained from the six codes are compared with those obtained from a waveguide mode analysis and experimental data in Figures 5 - 7. In the waveguide mode analysis (WMA) the model components were determined by requiring zero tangential E -field on the cylinder surface except in the aperture where the E -field predicted by BOR3 was prescribed. In the anechoic chamber experiment an electrically short diode - loaded probe and a high resistance transmission line were used to minimise measurement apparatus interference. The WMA and the experiment are discussed in more detail in Reference 1.

In the figures the amplitude of the E -field component parallel to the incident field is plotted against penetration in wavelengths. The data plotted is as follows:

Figure 5 WMA, experiment, BOR2, BOR3, CHAOS

Figure 6 WMA, experiment, NEC (0.0038 and 0.0076λ wire radius)

Figure 7 WMA, experiment, TDFDS, STRIPES (300 and 1000 timesteps)

All codes predict the same negative exponential trend of field amplitude with penetration shown by the WMA and the experiment. However, there are some significant differences between the codes and these mainly concern the range of operation of the codes and the field amplitudes. The effective ranges of operation of the codes are as follows: BOR2 0 - 0.25λ, CHAOS 0 - 0.15λ, NEC 0.1 - 0.25λ, STRIPES (300 timesteps) and TDFDS 0 - 0.35λ, BOR3 and STRIPES with 1000 timesteps operating for the full range of penetrations considered. The field amplitudes tend to be consistent with the WMA in the case of the moment method codes: in the particular case of BOR3 the agreement with WMA is exact. With the time domain codes the field amplitudes tend to be above those predicted by experiment.

DISCUSSION

The upper bound on the depth of penetration of the BOR2, CHAOS and NEC codes arises because these are scattered field codes: the total internal field is obtained from the difference of the incident and scattered field and any error in estimating the scattered field may be comparable to the computed small internal field.

The reason that NEC is inaccurate for penetrations below 0.1 wavelengths is that with the end cap in place, errors arise due to the sample points being near the end cap wire grid. Nevertheless, within its range of operation, NEC is surprisingly accurate considering that the single precision version NEC2S was used. The results are also shown to be relatively insensitive to wire radius.

With about four periods of the waveform simulated, TDFDS and STRIPES are accurate to 0.35 wavelengths penetration. A longer period needs to be simulated if accurate results at deeper penetrations are required. The small differences between the TDFDS and STRIPES arise due to small differences in the estimated slope of the exponential decay and in the field amplitude at the open end of the cylinder. The higher field amplitudes obtained with STRIPES and TDFDS codes compared with the moment method codes are likely to be due to the effect of reflections from the problem space walls (a difficulty also common to the experiment where reflections are likely from the anechoic chamber walls) and the discretisation of the cylinder cross section.

CONCLUSION

Within the known limitations of the various numerical methods, the agreement between the six codes, the waveguide mode analysis and experimental data was good. The main constraints to be taken into account in the estimation of the low internal fields expected in the cylinder are the relative lack of accuracy of scattered as opposed to total field codes, and in the case of codes such as TDFDS and STRIPES the need to define the object with sufficient accuracy while yet enclosing the object in a problem space that is sufficiently large to prevent reflections from the walls significantly affecting the result.

ACKNOWLEDGEMENT

This work has been carried out with the support of the Procurement Executive, UK Ministry of Defence.

REFERENCES

1. Schuman, H.K., Warren, D.E., Coupling Through Rotationally Symmetric Apertures in Cavities of Revolution, RADC-TR-77-214, Rome Air Development Center, June 1977.

2. Glisson, A.W., Wilton, D.R., A Simple Approach to the Problem of Coupling Through Azimuthally Symmetric Apertures in Bodies of Revolution, Internal Memo, University of Mississippi, June 1978.

3. Taflove, A., Application of the Finite-Difference Time-Domain Method to Sinusoidal Steady-State Electromagnetic-Penetration Problems, IEEE Trans., Vol. EMC-22, No.3, pp 191-202, August 1980.

4. Moore, J., Pizer, R., Moment Methods in Electromagnetics, Research Studies Press, John Wiley, 1984.

5. Hoefer, W., The Transmission Line Matrix Method - Theory and Applications, IEEE Trans., Vol. MTT-33, No. 10, 1985.

6. Johns, P., New Symmetrical Condensed Node for Three-Dimensional Solution of Electromagnetic Wave Problems by TLM, Electronics Letters, Vol. 22, No.3, pp 162-164, 1986.

7. KCC Ltd., STRIPES User Manual Version 1.0, 1986.

8. Yee, K.S., Numerical Solution of Initial Boundary Value Problems Involving Maxwell's Equations in Isotropic Media, IEEE Trans., Vol. AP-14, pp 302-307, May 1966.

9. Curlsol Microwave Ltd., TDFDS - Time Domain Finite Difference Simulator User Manual Version 1.0, 1988.

10. Burke, G.J., Poggio, A.J., Numerical Electromagnetics Code - Method of Moments - Parts I, II and III, Lawrence Livermore National Laboratory, UCID 18834, 1981.

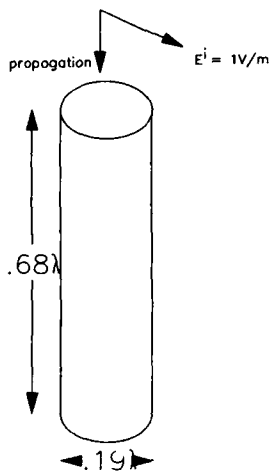

Fig. 1 Cylinder with Open End Showing Excitation

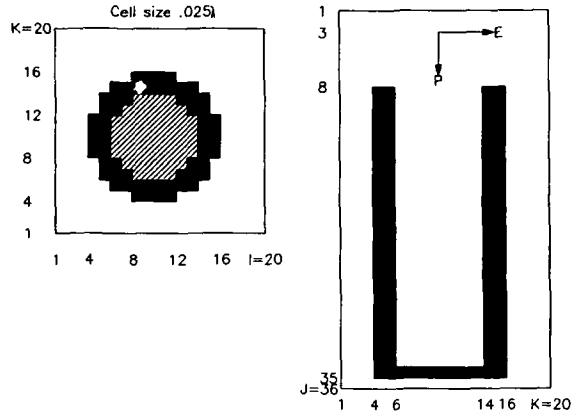

(a) Transvere Cross Section

(b) As viewed at plane I=10

Fig. 2 Model of Cylinder and Excitation used for TDFDS and STRIPES Codes with 20x36x20 Cell Workspace

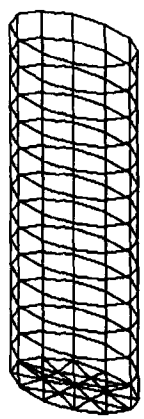

Fig. 3 NEC Wire Grid Model

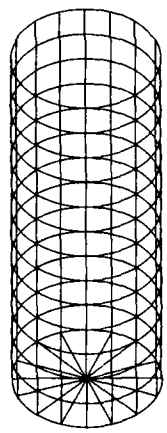

Fig. 4 CHAOS Wire Grid Model

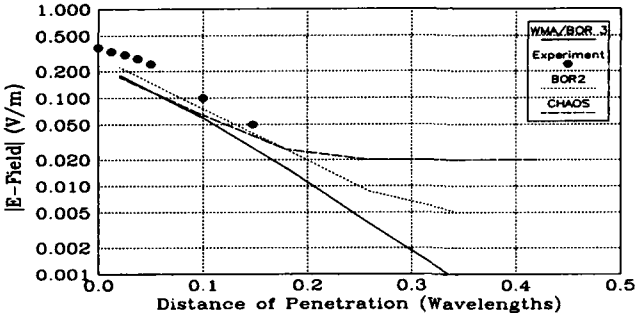

Fig. 5 Comparison of Moment Method Codes BOR2, BOR3 and CHAOS with Waveguide Mode Analysis and Experimental Data

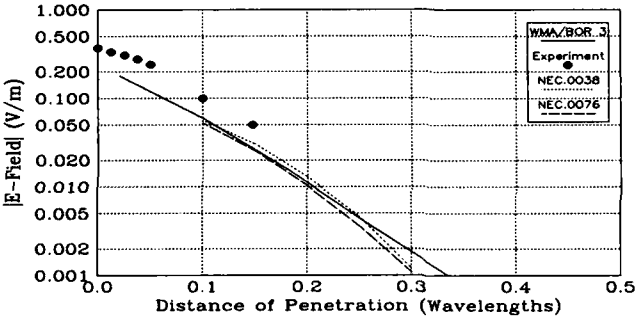

Fig. 6 Comparison of NEC (0.0038 and 0.0076λ Radius Wire Grid Models) with BOR3/Waveguide Mode Analysis and Experimental Data

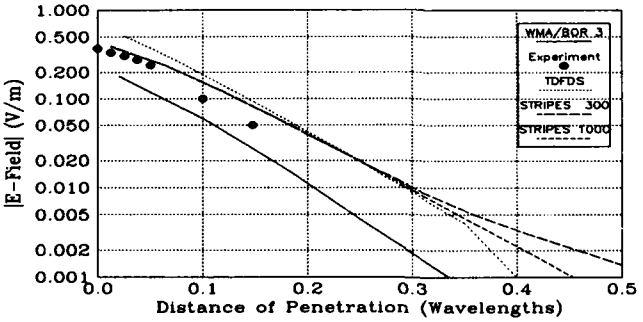

Fig. 7 Comparison of STRIPES (300 and 1000 Timesteps Simulated) and TDFDS with BOR3/Waveguide Mode Analysis and Experimental Data

AUTHOR INDEX